Measurement of Nitrogen Dioxide, Sulphur Dioxide, Formaldehyde and Glyoxal by Using Car MAX-DOAS Observations in and around the Megacity of Lahore, Pakistan

Dissertation

zur Erlangung des Grades

"Doktor der Naturwissenschaften"

im Promotionsfach Chemie

am Fachbereich Chemie, Pharmazie,

Geographie und Geowissenschaften

der Johannes Gutenberg-Universität Mainz

Maria Razi

geboren in Lahore

Mainz, 2021

1. Berichterstatter:

2. Berichterstatter:

Tag der mündlichen Prüfung: 17.02.2022

D77

The work presented in this thesis was performed at the Max Planck Institute for Chemistry (MPIC), Mainz, Germany.

DECLARATION

I hereby declare that I wrote the dissertation submitted without any unauthorized external assistance and used only sources acknowledged in the work. All textual passages which are appropriated verbatim or paraphrased from published and unpublished texts as well as all information obtained from oral sources are duly indicated and listed in accordance with bibliographical rules. In carrying out this research, I complied with the rules of standard scientific practice as formulated in the statutes of Johannes Gutenberg-University Mainz to ensure standard scientific practice.

Mainz, November 2021

Maria Razi

ABSTRACT

Since the industrial revolution in the 19th century, urbanization is continuously increasing. Nowadays, more than half of the world's population lives in cities leading to the expansion of urban areas and giving rise to the formation of megacities. As a result of the enhanced industrial and power generation activities as well as traffic loads, megacities face severe problems of air pollution. Lahore, the second largest city of Pakistan with a population of more than 11 million is no exception to this. During the last few years, Lahore has been ranked among the topmost polluted cities in the world.

In the current thesis, results of simultaneous measurements of four important tropospheric trace gases: NO_2, SO_2, HCHO and CHOCHO by using the car Multi Axis Differential Optical Absorption Spectroscopy (car MAX-DOAS) in and around Lahore are presented. Measurements were performed on many days during five campaigns in different years and seasons. The spatial distribution of tropospheric vertical column densities (VCDs) is retrieved from the observations. By combining the measurements with wind information, the total emissions/fluxes of NO_2, SO_2 and HCHO from the city of Lahore are estimated.

In this study, the data analysis is based on previous studies, but also important improvements were developed and implemented. In particular, a modified approach was introduced to calculate the VCDs derived from the spectra obtained during campaigns when the instrument motor did not work properly. The new approach was tested based on data when the motor worked accurately, and good consistency was found between the modified and the standard methods. Also a correction method was developed to deal with the problem of spectral interference between O_3 and SO_2 at high solar zenith angles (SZA). The new method improved the data quality and allowed to analyze the data also at high SZA. Both improvements are important for future studies.

In the following, the most important measurement results are summarized. In general, enhanced tropospheric trace gas VCDs were observed in the city center and along the areas of enhanced industrial activities. The derived emissions of NO_x and the underlying NO_2 VCDs were found comparable with those in other large cities like Shanghai, China and Delhi, India. For the other trace gases, only the tropospheric VCDs could be compared to similar measurements at other locations. Here much higher SO_2 VCDs were found compared to other large Asian cities like Hefei, Nanjing or Shanghai (China). For HCHO similar values were observed as in other polluted regions, like, e.g. Yangtze River Delta, China, (YRD). The CHOCHO VCDs around Lahore were comparable to the glyoxal VCDs at other polluted regions like, e.g. Beijing, China.

No prominent seasonality was observed for the NO_x emissions and HCHO fluxes. In contrast, a clear seasonal variability was observed for SO_2 with emissions in spring approximately two times higher than in summer. The glyoxal VCDs were found higher in summer than in spring by about a factor of two.

The car MAX-DOAS results were also compared with TROPOMI satellite observations and the bottom-up emission inventory EDGAR. A good qualitative agreement (R^2 = 0.56 and 0.62) was observed with the tropospheric NO_2 VCDs from TROPOMI. However, like in previous studies, the satellite data was found around 40 to 50% lower than the car MAX-DOAS results. For SO_2 and HCHO, the comparison of the car MAX-DOAS results to TROPOMI could not be performed on an individual satellite pixel basis because the satellite results are close to or below the detection limit. Nevertheless, for both trace gases, a similar range of tropospheric VCDs was found in the averaged satellite and car MAX-DOAS data.

The NO_x emissions estimated from the car MAX-DOAS observations were compared with those estimated from the TROPOMI satellite observations. Here, consistent with the VCD comparison, an underestimation of 30-65% was found. In contrast, the comparison with the EDGAR emission inventory showed very good agreement within 5-15%. For the SO_2 emissions larger differences (36-47%) were found, indicating that the SO_2 emissions from Lahore in the EDGAR database probably need to be updated accordingly.

This research has established an unprecedented insight into the spatio-temporal variability of the studied four trace gases in and around Lahore. The results of this thesis added new and significant information on the air quality and related trace gas emissions. These new findings can help to improve the air quality of the city by devising better policies, and the improved analysis techniques will also be helpful for the execution of similar studies in other megacities.

ZUSAMMENFASSUNG

Seit dem Beginn der industriellen Revolution nimmt die Urbanisierung stetig zu. Derzeit lebt bereits mehr als die Hälfte der Weltbevölkerung in Städten, was zu einer Ausbreitung der Stadtgebiete und der Entstehung sogenannter „Megacities“ führt. Industrie, Stromerzeugung und eine hohe Verkehrsdichte (Verbrennungsmotoren) erhöhen die Luftverschmutzung in diesen Städten erheblich. Lahore, die zweitgrößte Stadt in Pakistan mit einer Bevölkerung von über 11 Millionen Menschen, ist hier keine Ausnahme. In den letzten Jahren wurde Lahore unter den am stärksten verschmutzten Städten der Welt aufgelistet.

In dieser Arbeit werden die Ergebnisse simultaner Messungen von vier wichtigen troposphärischen Spurengasen vorgestellt (NO_2, SO_2, HCHO und CHOCHO). Hierzu wurden Spektren ausgewertet, die zuvor mit einem sogenannten „Car Multi Axis Differential Optical Absorption Spectroscopy“ (Car MAX-DOAS) Instrument in und um Lahore aufgenommen wurden. Die Messungen wurden an mehreren Tagen während 5 Meßkampagnen durchgeführt. Der Gesamtzeitraum erstreckt sich über mehrere Jahre zu verschiedenen Jahreszeiten. Zum einen wurde die räumliche Verteilung der troposphärischen vertikalen Säulendichte (VCD) aus den Beobachtungen bestimmt. Zum anderen wurden aus den Messdaten zusammen mit Informationen zu Windrichtung und -geschwindigkeit die Emissionen von NO_2, SO_2 und HCHO in Lahore abgeschätzt.

Für diese Studie wurde die Datenanalyse, die auf vorhergehenden Studien basiert, weiterentwickelt. Hierzu wurde ein neuer Ansatz implementiert, der es ermöglicht auch jene Messungen zu verwenden, bei denen der Motor zur Steuerung des Elevationswinkels ausgefallen war. Die Ergebnisse der modifizierten Methode wurde anhand von Messungen, bei denen der Motor funktionierte, mit den Ergebnissen der Standard-Methode verglichen, wobei sehr gute Konsistenz gefunden wurde. Zusätzlich wurde eine Korrektur für die spektrale Interferenz zwischen O_3 und SO_2 bei hohen Sonnenzenithwinkeln (SZA) eingeführt, was die Auswertung selbst bei hohem SZA und eine präzisere Nutzung der vorhandenen Daten ermöglicht. Diese Änderungen sind wichtig für zukünftige Studien.

Im Folgenden werden die wichtigsten Ergebnisse der Arbeit zusammengefasst: Generell wurden erhöhte troposphärische Säulendichten der verschiedenen Spurengase im Stadtzentrum und in den Industriegebieten gefunden. Die berechneten Emissionen von NO_x und die zugrundliegende NO_2 VCDs sind vergleichbar zu anderen Großstädten, wie zum Beispiel Shanghai (China) oder Delhi (Indien). Für die anderen Spurengase konnten nur die troposphärischen Säulendichten mit ähnlichen Messungen an anderen Orten verglichen werden: Hier wurden zum Beispiel deutlich höhere SO_2 Säulendichten als in anderen asiatischen Großstädten wie Hefei, Nanjing oder Shanghai (China) gemessen. Die

Säulendichten von HCHO und CHOCHO waren mit anderen verschmutzen Regionen vergleichbar (z.B. Peking oder dem Yangtze River Delta, China).

Weder für NO_x, noch für die HCHO-Emissionen/Flüsse konnten signifikante jahreszeitliche Verläufe festgestellt werden. Im Gegensatz dazu wurde für die SO_2 Emissionen eine starke saisonale Variation festgestellt mit etwa doppelt so hohen Emissionen im Frühling wie im Sommer. Die Säulendichten von Glyoxal sind im Sommer etwa zweimal so hoch wie im Frühling.

Die Ergebnisse aus den Car MAX-DOAS Messungen wurden zusätzlich mit Satellitenmessungen (TROPOMI) und dem Emissionsdatensatz von EDGAR verglichen. Mit den Satellitenmessungen der NO_2 Säulendichten konnte eine gute qualitative Übereinstimmung gefunden werden ($R^2 = 0.56$ und 0.62). Die Satellitendaten waren jedoch systematisch um etwa 40-50% niedriger als die Car MAX-DOAS Daten, was vorhergehende Studien bestätigt. Für SO_2 und HCHO konnte kein Vergleich mit den individuellen Satellitendaten durchgeführt werden, da die Satellitenmessungen beider Spurenstoffe über Lahore nah am/unter dem Detektionslimit des Satelliten waren. Für gemittelte Daten waren die troposphärischen Säulendichten beider Messungen jedoch vergleichbar. Zusätzlich zum Vergleich der Säulendichten wurden für NO_x auch die Emissionen zwischen den Messungen mit dem Car MAX-DOAS und den Satellitenmessungen verglichen. Ähnlich wie schon beim Vergleich der Säulendichten, konnte hier eine systematische Unterschätzung durch die Satellitendaten von etwa 30-65% festgestellt werden. Im Gegensatz dazu konnte eine sehr gute Übereinstimmung mit den Emissionen aus dem EDGAR Datensatz gefunden werden (Unterschiede von 5-15%). Die berechneten Emissionen von SO_2 zeigen hingegen größere Unterschiede (36-47%) zum EDGAR Datensatz, woraus sich die Notwendigkeit einer Aktualisierung dieses Datensatzes ableiten lässt.

Diese Arbeit liefert einen beispiellosen Datensatz, welcher die räumliche und zeitliche Variation der vier vorgestellten Spurengase in der Region um die Megacity von Lahore beschreibt. Die Ergebnisse liefern neue Erkenntnisse, die dabei helfen können, die Luftqualität in dieser Stadt durch neue Maßnahmen und Gesetze zu verbessern. Die in dieser Arbeit entwickelte verbesserte Analyse wird auch helfen, die Ausführung und Analyse zukünftiger Studien in anderen „Megacitys“ zu verbessern.

Table of Contents

List of Tables

List of Figures

1. INTRODUCTION

The Anthropocene, the present era having a strong influence of human activities on the planet's atmosphere, biosphere, hydrosphere, and geosphere, started with the accelerated industrial revolution around 1950 (Haq, 2012; United Nations, 2018). This enhanced industrial revolution encouraged large fractions of people to live in cities, and this shift from rural to urban resulted in the emergence of the megacities. A large city with a population of 10 million or more is termed as megacity. By the 1950s, New York and Tokyo were the two known megacities. In 1990, there were ten such megacities, while in 2018, the number of megacities increased to 33, representing 13% of the planet's total population (United Nations, 2018). Megacities capture special attention as they are home to a large number of inhabitants and have a large concentration of economic activity. In parallel, an escalating population has increased the energy demands, industrialization, and on-road motor vehicles in the past several decades. This has all led to rapid and unplanned urbanization. Urban activities are mainly related to the high usage of fossil fuels. Various urban area associated activities like power generation, transportation and industrial operations consume fossil fuel and thereby emit numerous pollutants in the urban atmosphere. Many of these pollutants and trace species are long-lived and can travel over 100 kilometers or more, creating urban areas as major sources of global and regional pollution. The ambient pollutants produced in the urban areas or megacities not only deteriorate the local air quality but also negatively impact the air quality of the nearby rural areas and smaller cities. The pollutants with longer atmospheric residence times can travel farther distances, while reactive pollutants with shorter lifetimes can act as precursors for the production of secondary pollutants (Taylor & Ann, 2014).

The quality of air is of utmost importance as human beings continuously need clean air to sustain life. According to WHO (2018), 91 percent of the world's population is breathing air of poor quality. According to the 'state of global air' report, air pollution has been responsible for about 6.7 million deaths globally in 2019 (Health Effects Institute, 2020). Around 4.2 million deaths occur each year as a result of ambient air pollution worldwide (WHO, 2018).

Pollution affects the developed, developing, and underdeveloped countries and regions disproportionately. More than 90% of the pollution-related mortalities occur in low and middle-income countries, and the poor are more vulnerable to the effects of pollution than the rich. During 2015, the largest number of pollution-related deaths occurred in southeast Asia (3.2 million) and the western pacific regions (2.2 million) (Landrigan et al., 2018).

Atmospheric pollution not only negatively impacts human health but also disturbs natural ecosystems, deteriorates building materials, impairs visibility and damages forests and agriculture (Marquez & Smith, 1999). Air pollution is also responsible for production losses and reduced gross domestic products (GDP) of countries. So, air pollution is not only an environmental but also a social and economic issue of the highest priority (Landrigan et al., 2018).

Trace gases like oxides of nitrogen and sulfur, especially NO_x (NO + NO_2), SO_2, and volatile organic compounds, e.g., formaldehyde, are anthropogenically released as a result of fossil fuel combustion and other industrial activities. Particulate matter and ozone (O_3) are also considered as ambient pollutants with significant adverse impacts on human health. NO_2, SO_2, $PM_{2.5}$ (particulate matter with diameter < 2.5 micrometers), and tropospheric O_3 are included in the list of six criteria air pollutants and can cause potential damage to human health, environment and infrastructure (US EPA, 2021c). The short- and long-term exposures to these pollutants aggravate or develop respiratory diseases like asthma and chronic obstructive pulmonary disease (COPD) (Gurjar et al., 2010; William & Kenneth, 2000). NO_x negatively impacts the environment by forming acid rain and smog (US EPA, 2018). Similarly, SO_2 also attacks the human respiratory system and forms acid rain. Furthermore, SO_2 damages vegetation, decreases visibility by forming haze, and forms sulfuric acid aerosols (US EPA, 2019). Formaldehyde (HCHO) is included in the list of hazardous air pollutants (HAPs) by US EPA and is classified as a carcinogen (Zhu et al., 2017). Primarily, HCHO is emitted as a result of biomass and fossil fuel burning. Secondarily, HCHO is formed by photochemical oxidation of non-methane and methane hydrocarbons (De Smedt et al., 2008). Glyoxal is the most abundant dicarbonyl in the troposphere and is emitted due to various anthropogenic and biogenic activities. Both formaldehyde and glyoxal are used as proxies of the photochemical degradation of volatile organic compounds (VOCs) in the troposphere (Myriokefalitakis et al., 2008; Volkamer et al., 2005a and references therein). All the above-mentioned trace gases have multiple adverse impacts on human health and the environment. Therefore, a thorough understanding of their sources, sinks and distribution patterns in urban environments is of utmost importance.

Therefore, continuous pollution monitoring is crucial in interpreting the state of the air quality of a region. The in-depth understanding of the behavior of emissions and their sources does not only give an insight into the damage caused by them but is also helpful in future planning, policy-making and introduction of abatement technologies and measures. Air quality monitoring can for example, be done by emission estimations of the pollutants from their sources or by quantifying the pollutant concentrations in the atmosphere through monitoring stations (Jung et al., 2019).

Various monitoring techniques, instruments and platforms are being used to monitor the air quality globally. Each technique has its advantages and limitations. Developed countries have well-established networks of pollution monitoring compared to underdeveloped or low- and middle-income countries. Developing countries are often less concerned about environmental degradation, and many factors contribute to this. They usually lack the

resources and technology to monitor and control the pollution sources. In parallel, these countries are already striving to provide basic amenities to their citizens. According to UNEP (2019), in low and middle-income countries, laws are often not only weak but their enforcement is also challenging. Moreover, emission standards are lenient, and clean fuels are not common.

Since the onset of rapid industrialization and consequent air pollution, several studies have been performed globally to understand the chemistry of the atmosphere. The existing air quality database of megacities is available at various levels, ranging from global measurements to single megacities or even street canyons of a city (Marlier et al., 2016). Various techniques, e.g. ground-based in situ and remote sensing instruments, satellite remote sensing instruments (in combination with chemical transport models, CTM) and emission inventories, provide insight into the ambient air state. However, a detailed understanding of urban chemistry requires dense networks of long-term continuous measurements. Harrison (2018) mentioned that extensive research projects like REPARTEE (London), MEGAPOLI (Paris), ClearfLo (London) and CalNex4 are needed (with high spatial and temporal coverage and resolution) to comprehend the chemical processes happening in the urban atmosphere. These kinds of projects are rarely found in developing countries as they require high operational costs.

The densely populated Asian continent is especially facing the problem of air pollution. People in China and South Asian countries like India, Pakistan and Bangladesh are inhaling polluted air with pollutant concentrations exceeding the WHO prescribed limits. In 2019, the world's 30 out of 40 topmost polluted cities belonged to this region (IQAir, 2019). Pakistan being a South Asian country and a home of more than 200 million people, is experiencing poor air quality for the last three decades. Since 1990, Pakistan's air quality has been continuously deteriorating (Colbeck et al., 2010; Ilyas, 2007). As mentioned earlier, irrespective of the detrimental effects of air pollution on the economy, environment and human health, pollution monitoring and abatement are still much-neglected issues in many developing countries, and especially also Pakistan is no exception to this. In Pakistan, around 150–300 deaths per 1 million inhabitants per year can be attributed to air pollution. (Landrigan et al., 2018). In 2016, Pakistan ranked number five with respect to the worst air quality (Greenstone & (Claire) Fan, 2019). Moreover, the unavailability of proper monitoring networks and the lack of priority to the air pollution studies have worsened the matter. Also, the extensive urbanization and surge in the vehicle count have contributed a considerable share in increasing the pollutant levels (Anjum et al., 2021 and references therein).

Lahore, the megacity of Pakistan, is no exception to this. The air quality of the city is deteriorating at alarming rates. Lahore, like other megacities is also failing to combat the effects of the escalated surge in vehicle numbers and industrial activities. Since the last five years Lahore is being ranked among the topmost polluted cities of the world. According to an IQAIR report, Lahore stands at ninth position in the ranking of the world's most polluted cities in 2018 with respect to $PM_{2.5}$ (IQAIR, 2018). Furthermore, since October 2016, the city has been experiencing extreme episodic smog events every winter (Kashif et al., 2019).

In the last two decades, several but limited studies were performed in Lahore to investigate the emission patterns of trace gases like nitrogen oxides (NO_x), sulfur dioxide (SO_2) and particulate matter (PM) in the city. Whereas, as far as VOCs like formaldehyde (HCHO) and glyoxal (CHOCHO) are concerned, no prominent study was conducted at the Lahore city level. To get an overview, some of the important studies executed during this period to assess the ambient air quality of Lahore are briefly described below.

Hameed et al. (2000) investigated the reasons for heavy fog in Lahore during the winter months. They collected aerosol samples from the city during and after fog periods. The samples were analyzed for NO_3^- and SO_4^- ions and some trace elements. They found high concentrations of SO_4^- during the fog period as compared to the post-fog period. Based on wind information and measured SO_4^-/Se ratios, coal combustion activities were assumed as the primary source of the sulfate ions. However, the study also mentioned significant uncertainties due to the lack of knowledge of aqueous phase oxidation in fog.

Another study was conducted by the Pakistan Space and Upper Atmosphere Research Commission (SUPARCO) during 2003-2004 in major cities of Pakistan, including Lahore. In the study, concentrations of SO_2, NO_x, CO & CO_2 and O_3 were measured using ultraviolet (UV) fluorescence, chemiluminescence, gas filter correlation (GFC) and UV photometry techniques, respectively. All these analyzers were installed in a mobile lab, and measurements were performed at seven busy locations of the city for several days during the study period (2003-2004). O_3, NO_x and SO_2 concentrations were found highest in Lahore amongst the other cities. The authors also mentioned that the current study plan could not explain the complete picture of the emissions. The measurements were performed only for a few fixed locations, so the data cannot be regarded as representative of the emission patterns of the whole city (Ghauri et al., 2007).

Jafary & Faridi (2006) also estimated the motor vehicle exhaust emissions and roadside dust levels. Levels of CO, SO_2 and NO_2 were measured from the exhaust of the automobiles by using direct reading colorimetric dräger tubes from 23 busy road sites of Lahore. The study reported that these trace gases were found high compared to similar studies for other regions and countries. The study also indicates that vehicular emissions are primarily responsible for the high levels of SO_2 and NO_2 in Lahore.

In another study, air pollution patterns of Lahore city were identified by using the geographic information system (GIS) for the period from 1999-2007 by Younes et al. (2009), including patterns of NO_2, SO_2, ozone and CO. For CO concentrations of 9 years were presented, whereas, for the other gases, one-year data were reported. They found high pollution patterns over all the sampled locations as a result of the high vehicular density.

Ali & Athar (2010) studied the impact of industrial and vehicular emissions on the ambient air quality of Lahore. The sampling was performed for three days on 10 different sites of the city and concentrations of six criteria pollutants, NO_2, SO_2, O_3, CO, Pb and particulate matter were monitored. The ambient levels of SO_2, particulate matter and Pb were found far higher than the prescribed standards whereas, CO and NO_2 concentrations were found within limits.

An effort was also made by Ashraf et al. (2013) to evaluate the status of ambient air quality in Lahore city. They measured concentrations of particulate matter ($PM_{2.5}$), NO, NO_2, CO and SO_2 from 19 different industrial, commercial and residential locations for three months (June- August). The methods or instruments used were non-dispersive infrared detection, gas-phase chemiluminescence and a carbon monoxide analyzer (KANECO91 /UK). NO, NO_2 and ($PM_{2.5}$) were found higher than the USEPA limits, while SO_2 levels were found well below the standards.

Mirza et al. (2013) performed spatio-temporal monitoring of atmospheric SO_2 in Lahore city. This study was executed in 49 locations for the pre-monsoon, monsoon and post monsoon seasons. A fluorescence method SO_2 analyzer (U.S. EPA Reference Method EQSA-0506-159) was used in the study. They identified SO_2 hot-spot zones within the city. The variability in mean SO_2 values was found with respect to different land-use patterns and seasons. The highest levels were found at the busy road crossings, near the brick kilns and in the vicinity of the industrial zones during the pre-monsoon season. Whereas moderate levels were observed in the post monsoon season, and the lowest levels were found during winter. Another study was performed by Yasar et al. (2013) to compare emissions from different vehicles using different fuels in Lahore. NO, SO_2, CO and hydrocarbons were measured from the exhaust of automobiles. They found higher smoke opacity, hydrocarbon and NO levels in the exhaust from diesel vehicles compared to gasoline and compressed natural gas (CNG) vehicles.

ul-Haq et al. (2014) presented results for tropospheric distributions of NO_2 over Pakistan for the year 2005 using OMI satellite data. Lahore was identified as one of the NO_2 hotspots along with three other cities. They also compared the NO_2 columns over Lahore, retrieved from OMI and SCIAMACHY (Scanning Imaging Absorption Spectrometer for Atmospheric Chartography) and tried to find out the main emission sources and prominent anthropogenic sources included motor vehicles, fossil fuel combustion in industries and crop residue burning

Ahmad et al. (2014) collected suspended particulate matter (SPM) at 13 different outdoor locations in Lahore and analyzed the samples for trace elements. Trace elements like Cd, Pb, Zn, Cu and Ni were found in all the samples.

Ali et al. (2015) also measured particulate matter at two roads with high traffic loads in Lahore. They found a positive correlation between traffic density and PM levels.

Another study was performed by Hamid et al. (2019) for eight months during July 2015 and February 2016. They monitored NO, SO_2, CO, and total suspended particles (TSP) at four different busy locations in Lahore for three consecutive days each month. The gases and TSP were monitored using MX6 iBrid air analyser and Micro Dust Pro Casella Cell/CEL-712, respectively. They found elevated levels of CO, TSP and NO at the measurement sites.

Tabinda et al. (2020) performed a comparative analysis of ambient air quality of five major cities of Punjab Province, including Lahore. They measured CO, SO_2, NO_x and PM_{10} at

fixed sites in five cities for three months during 2018. The highest levels of CO and NO_x were found in Lahore during the study period.

Khokhar et al. (2015) studied seasonal trends of tropospheric NO_2 over Pakistan using satellite observations for the period of 2002-2012. They also presented NO_2 levels for major cities of Pakistan including Lahore. Jalees & Asim, (2016) performed statistical modelling of heavy metals from four locations in Lahore. ul-Haq et al, (2016) studied the spatio-temporal SO_2 variability over Lahore using OMI (observations and MACCity emission data for 2004-2015. Haider et al. (2017) studied monthly and diurnal trends of trace species like NO_x, SO_2, CO, CH_4, O_3 and particulate matter in Lahore for 2007-11 and 2014 by using mobile and fixed monitoring stations. Riaz & Hamid. (2018) highlighted the problem of smog in Lahore to bring into notice the severity of the pollution problem to the relevant authorities. Ashraf et al. (2019) analyzed ambient concentrations of trace species (NO_X, SO_2, CO, O_3, VOC and PM) at three busy locations in Lahore for 2-5 November 2016. They also studied the relationship between smog events and eye diseases. Kashif et al. (2019) analyzed the impact of vehicular emissions on the air quality of Lahore during the smog phase in 2017. Zeb et al. (2019) used satellite observations and statistical models to study the decadal spatio-temporal trends of NO_2, HCHO, O_3 and CO over Pakistan including Lahore.

Results of all the above-mentioned studies give an overall impression of an increasing trend of ambient air pollutant levels (trace gases and particulate matter) in the city of Lahore during the last two decades. The results indicate that for most pollutants very high ambient concentrations were measured. This has led to the continuous degradation of air quality of the city. However, the measurements were performed on limited temporal and spatial scales. Instruments and techniques used for most of the ground-based observations were in-situ and were capable of providing a picture of the measured site only whereas satellite observations provided only limited spatial resolution. Table 1.1 presents a quick overview of some of the important studies performed to evaluate the status of ambient air in the megacity of Lahore.

To have a better picture of the trace gas concentrations, their emissions and emission sources for the whole city of Lahore, a detailed study with an extended spatial coverage was required. To fill this gap, an effort has been made in the current study by using the ground based remote sensing technique of car MAX-DOAS observations. Based on these observations also a top-down emission approach was applied for the entire area. In this thesis, an effort has also been made to investigate the tropospheric emission patterns of the above-mentioned trace species from the megacity of Lahore. Based on the spatial pollution patterns, individual emission sources (Dios et al., 2012) could be identified. Also the seasonal variation was investigated.

Table 1.1: Important ambient air monitoring studies performed in Lahore during the last two decades (for more details, see text).

Reference	**Species monitored**	**Study period**	**Study location**	**Important findings**
Hameed et al., (2000)	NO_3^- and SO_4^- ions, Cr, Sc, Fe, Zn metals	Jan 1999	SUPARCO, Lahore	High concentrations of SO_4^- during the fog period
Ghauri et al., (2007)	SO_2, NO_x, CO & CO_2, O_3	2003-2004	Busy locations in major cities of Pakistan including Lahore	O_3, NO_x and SO_2 concentrations were found highest in Lahore
Jafary & Faridi, (2006)	Total Suspended Particulates (TSP), CO, SO_2, NO_2	1 day in 2002	Busy road-crossings	High CO, SO_2 and NO_2 levels
Younes et al. (2009).	SO_2, NO_2, CO, O_3	1999-2007	Lahore	High levels of trace gases monitored
Raja et al. (2010)	$PM_{2.5}$, Trace metals	Nov 2005 - Jan 2006	Lahore	Secondary particles and diesel emissions were found as major $PM_{2.5}$ contributors
Ali & Athar, (2010)	CO, NO_2, SO_2, O_3, TSP, PM_{10}, Pb	3 days	Industrial and high traffic density roads	The levels of SO_2, particulate matter and Pb were found higher than the standards
Ashraf et al. (2013)	$PM_{2.5}$, NO, NO_2, CO, SO_2	Jun-Aug 2012	Marketplaces and residential locations	NO, NO_2 and $PM_{2.5}$ levels exceeded the standards
Mirza et al. (2013)	SO2	Apr - Oct	residential areas, main road crossings, educational institutions, hospitals, parks, and suburban areas	High SO_2 levels near brick kilns, industries, and busy roads
Yasar et al. (2013)	NO, SO_2, CO and hydrocarbons from vehicular exhaust.	No information	Lahore	Smoke opacity, hydrocarbon and NO levels were found higher in the diesel vehicles emissions

Reference	Species monitored	Study period	Study location	Important findings
ul-Haq et al. (2014)	NO_2	2005	Pakistan	Lahore was identified as NO_2 hotspot
Ahmad et al. (2014)	SPM, Trace metals	Dec 2001 and Jan 2002.	Lahore	PM levels exceeding standards and trace metals were identified in SPM samples
Khokhar et al. (2015)	NO_2	2002-2012	Pakistan	7% per year increase in NO_2 columns was observed for Lahore
Ali et al. (2015)	PM	1 day	Two busy road sites in Lahore	PM levels exceeding standards
Haider et al. (2017)	NO_x, SO_2, CO, CH_4, O_3, PM	2007-2011 and 2014	Lahore	Vehicles are major NO_x emitters and industries are major emitters of SO_2
Ashraf et al. (2019)	NO_X, SO_2, CO, O_3, VOC, PM	2-5 Nov 2015 and 2016	Busy locations in Lahore	Higher ambient levels of trace gases were found on a smog day
Hamid et al. (2019)	NO, SO_2, CO, TSP	July 2015 - Feb 2016	Lahore	CO, TSP and NO levels exceeding the standards
Kashif et al. (2019)	Vehicular emissions	2017	Lahore	Two stroke and public transport vehicles were major pollutant emitters
Tabinda et al. (2020)	CO, SO_2, NO_x and PM_{10}	3 months in 2018	Lahore, Multan Rawalpindi, Gujranwala, and Faisalabad	Highest levels of CO and NO_x were found in Lahore

1.1. OBJECTIVES

This study aims to broaden the present knowledge of the spatio-temporal variation and the emission sources of the four tropospheric trace gases (NO_2, SO_2, formaldehyde and glyoxal) in Lahore.

The main objectives of the thesis are:

i. To estimate NO_x, SO_2 and HCHO emissions (or net fluxes) from Lahore.

ii. To study the spatial distributions of NO_2, SO_2 and HCHO and CHOCHO in Lahore.

iii. To identify the seasonal variations of these gases in Lahore.

iv. To identify the major emission sources of NO_x, SO_2, HCHO and CHOCHO along the driving routes.

Additional objectives of the study include:

a. The comparison of the measurements with satellite data and emission inventories for the city of Lahore.

b. To study the trace gas spatial distributions in the vicinity of power plants within the city of Lahore.

c. To study the trace gas spatial distributions for other large cities of Punjab.

1.2. OUTLINE

The above mentioned objectives are achieved by applying Differential Optical Absorption Spectroscopy (DOAS) (Platt & Stutz, 2008). MAX-DOAS instruments were operated on mobile platforms (cars) for different routes inside and encircling the city of Lahore.

The remainder of this chapter provides basic information about the study area, basic properties of the atmosphere, and characteristics and atmospheric reactions of the measured trace species.

Chapter 2 gives a general description of the measurement technique and the data analysis.

Chapter 3 describes various details of the different measurement campaigns performed during the study period.

Chapter 4 presents the derived emission estimates of NO_x and SO_2. Similarly, also the net formaldehyde fluxes from the city of Lahore (including secondary formation) are presented. For glyoxal no net fluxes could be derived, because of the smaller signal too noise ratio but the spatial distribution patterns are presented.

Chapter 5 presents the results of additional measurements performed in the vicinity of power plants and for other major cities in the region of Punjab.

In chapter 6, the results from the car MAX-DOAS measurements are compared to other data sets. The derived spatial distributions are compared to TROPOMI satellite

observations. The emission estimates for the city of Lahore are compared with existing emission inventories.

Finally, chapter 7 concludes the study, by highlighting the key findings from the previous chapters and gives recommendations for future studies.

1.3. DESCRIPTION OF THE STUDY AREA

Lahore, the main study area, is the second largest city of Pakistan and the capital of the Punjab province. Lahore is located in the northeast of the Punjab province having a border with eastern India. The city is the most populous city of Punjab with a population of more than 11 million inhabitants (Pakistan Bureau of Statistics, 2017). According to the 1998 census, Lahore's population was reported as 6.39 million. These figures show that the population in the city has almost doubled in the last two decades, which represents a rapid and unplanned urbanizing trend. The city is also the educational centre of the province with several universities attracting students from all over Punjab. The area of the city is around 300 km^2, has a flat terrain, and is located at an average elevation of 217 m above sea level. The weather of the city is represented by five seasons i.e. summer, monsoon, winter, spring and autumn (Table 1.2). The temperature in the hottest summer months rises up to 48℃ and during the coldest winter months it rarely goes down near the freezing point (Colbeck et al., 2019). As far as the transportation system of the city is concerned, it has a well-developed road network of 1265 km with around 4 million registered vehicles in 2015 (Punjab Bureau of Statistics, 2015). In 2012, this number was 2.7 million (Rasheed, 2014) and the count has risen up to 6.2 million in 2020 (Zahid, 2020). Abubakar, 2016 also mentioned that in Lahore, rapid and uncontrolled urbanization is changing the city's infrastructure and increasing the vehicular count resulting in increased emissions from the vehicles.

In 2014, there were about 2233 industries in Lahore, and of these 727 were large industries with more than 100 employees (Punjab Bureau of Statistics, 2017). The study area of Lahore with major emission sources, power plants and industrial areas is shown in Figure 1.1. The major zones with high industrial activities are Quaid e Azam industrial Estate (QIE) at Kot Lakhpat (northeast), Sundar Industrial Estate (SIE), along the G.T. road (north to northeast), Multan Road (southwest) and Manga-Raiwind Road (south). In the north of the city, major industries are related to iron works, steel re-rolling and metal parts casting. Figure 1.2 exhibits emissions from one such industry in the north. Ali & Athar, (2010); Stone et al, (2010) (see also references therein), mentioned that the presence of the large number of vehicles and industries in the city has intensified the issues of the city's poor air quality, which is further aggravated due to the lack of efficient pollution control systems and a good mass transport system. Furthermore, intense smog episodes in the winter months impair visibility, disturb transportation, and aggravate respiratory tract infections.

Table 1.2: Seasons in the study area

Season	Duration
Winter	mid-Nov to mid-Feb
Spring	mid-Feb to mid-Apr
Summer	mid-Apr to mid Jul
Monsoon	mid-Jul to mid-Sep
Autumn	mid-Sep to mid-Nov

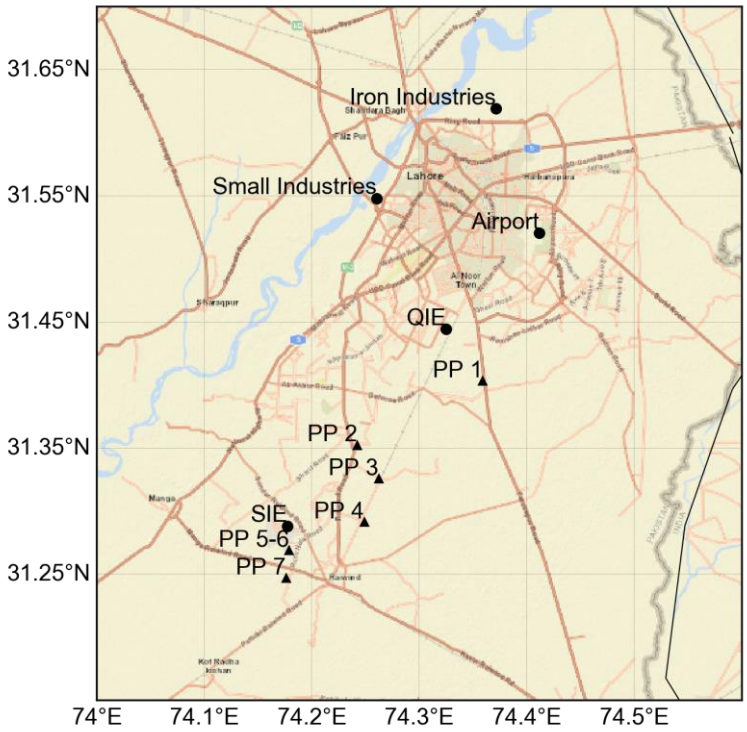

Figure 1.1: The study area of Lahore with major emission sources. Power plants (solid triangles) and industrial areas (solid circles) are marked.

Figure 1.2: Black smoke emerging from one of the iron industries located in the north of Lahore.

1.4. COMPOSITION AND STRUCTURE OF THE ATMOSPHERE

In the following section, a short overview on the earth's atmospheric composition and structure based on Platt & Stutz (2008) is presented.

The Earth's atmosphere is divided vertically into various layers based on differences in temperature, pressure, chemical reactions and mixing processes. The lowermost layer is the troposphere, and extends from ground until 8 to 18 km at the poles and the equator, respectively. This layer can be divided into two sub layers: the atmospheric boundary layer and the free troposphere. The atmospheric boundary layer is typically located in the lowest 500 to 4 km, depending on location, season and time of the day. The free troposphere extends from the boundary layer to the tropopause. The troposphere is the most dynamic layer of the atmosphere and most of the chemical processes occur in this region.

The layer up to approximately 50 km above the troposphere is called the Stratosphere. This layer is not well mixed and contains the ozone layer. The atmosphere above the stratosphere, comprises the mesosphere, thermosphere and exosphere.

The Earth's atmosphere is composed mainly of Nitrogen (78%), Oxygen (~21%) and Argon (0.93%). These species are responsible for more than 99% of the Earth's atmosphere. The gases and species which consist less than about 1% of the atmospheric composition are termed trace gases. These trace gases are important in shaping the chemistry of the atmosphere due to their reactivity and for the atmosphere's radiative budget. Trace species are also important as they are responsible for disturbing the stratospheric ozone layer, causing environmental pollution, smog and climate change.

A variety of sources both anthropogenic and natural are responsible for the emissions of these species into the atmosphere. Anthropogenic activities include mainly fossil fuel combustion in industries, power plants and vehicles. Natural sources include biogenic (from biological organisms), biomass burning and non-biogenic sources (volcanoes).

It is, therefore, very important to study the chemistry of the trace species in the atmosphere. Different analytical methods are used to observe the atmospheric gases. Of these techniques, differential optical absorption spectroscopy (DOAS) is a well-recognized method to observe various gases. In the next sub-sections, the chemistry of the tropospheric trace gases observed in the study by using the DOAS method is discussed.

1.4.1. Tropospheric Chemistry

In this section, the chemical behavior of ozone, nitrogen oxides, sulfur dioxide, formaldehyde and glyoxal in the troposphere is discussed. The description presented here is mainly based on Pitts & Pitts, (2000); Jacob, (1999); Koppmann, (2007); Seinfeld & Pandis, (2006) and Wallace & Hobbs, (2006)

1.4.1.1. Ozone

Ozone (O_3) is one of the most important gases in both stratosphere and troposphere. The ozone in the stratosphere provides protection from exposure to harmful ultraviolet solar radiation while in the troposphere it contibutes to smog formation. In the stratosphere ozone production is triggered by the photolysis of molecular oxygen present at higher altitudes by ultraviolet radiation (Seinfeld & Pandis, 2006).

$$O_2 + h\nu \rightarrow 2O\ (^3P)\ (\lambda < 242\ nm) \qquad (1.1)$$

As a result of the photolysis of O_2, two highly reactive oxygen atoms are produced which further react with O_2 molecules in the presence of a collision partner M (N_2 or O_2) to form ozone.

$$O(^3P) + O_2 + M \rightarrow O_3 + M \qquad (1.2)$$

The O_3 molecule is then photolyzed back via photons at lower energy to form an O_2 molecule at slower rate.

$$O_3 + h\nu \rightarrow O_2 + O\ (\lambda < 320\ nm) \qquad (1.3)$$

Ozone cannot be formed in troposphere due to the photolysis of the oxygen molecule, as the troposphere lacks the shorter wavelength ultraviolet radiation required for the process. However, a small percentage of stratospheric ozone may be transferred to the troposphere. Fishman & Crutzen (1978) found out that there must be some important sources of O_3 present in the troposphere. In urban areas nitrogen oxides are significant anthropogenic precursor species of tropospheric ozone. The production of O_3 in the troposphere via reactions with NO_x is discussed in section 1.4.1.2. CH_4, CO and hydrocarbons contribute to produce tropospheric O_3 in the presence of nitrogen oxides. It should be noted that ozone is also a precursor of the hydroxyl radical (OH) and acts as an oxidizing agent. OH is produced when water vapor reacts with O (^1D), (reactions 1.4-1.6).

$$O_3 + h\nu \rightarrow O_2 + O(^1D)\ (\lambda < 320\ nm) \qquad (1.4)$$

$$O(^1D) + M \rightarrow O + M \qquad (1.5)$$

$$O(^1D) + H_2O \rightarrow 2OH \quad (1.6)$$

Tropospheric ozone, on the one hand plays a positive role, steering the oxidizing capabilities of the troposphere and on the other hand it acts as a pollutant gas in the lower troposphere (Jacob, 1999). High levels of tropospheric ozone are detrimental to human health and plants. O_3 is a strong oxidant and so can destroy cellular material of plants and negatively affect lungs in humans (European Environment Agency, 2015; US EPA, 2021d).

1.4.1.2. Nitrogen Oxides (NO_x)

Oxides of Nitrogen NO_x (NO+ NO_2) are one of the most important trace species of the earth's atmosphere and are key players in the tropospheric chemistry. NO and NO_2 are readily interconverted in the daytime and so are classified together as NO_x. In this section their tropospheric chemistry, sources, sinks and effects are outlined.

NO_x are produced both by natural and anthropogenic sources like from soils, biomass burning, lightening, oxidation of ammonia, fossil fuel combustion in industries and vehicles (Wallace &. Hobbs, 2006). They are formed when atmospheric nitrogen as well as nitrogen present in fuels reacts with atmospheric oxygen at high temperatures.

At our study area, industrial, vehicular and power plant emissions are the major sources of NO_x.

The primary source of NO_x is NO, but during daytime a quasi-instant equilibrium is established between NO and NO_2 through the following chain of reactions. NO in the presence of O_3 forms NO_2 over a period of few minutes:

$$NO + O_3 \rightarrow NO_2 + O_2 \quad (1.7)$$

In the presence of radiation of wavelengths lower than 424 nm, NO_2 is photolyzed to $O(^1D)$ and NO.

$$NO_2 + h\nu \xrightarrow{\lambda<424\,nm} NO + O(^1D) \quad (1.8)$$

The resulting oxygen atom reacts with O_2 and forms ozone which is the primary source of O_3 in the troposphere.

$$O + O_2 \rightarrow O_3 + M \quad (1.9)$$

Reactions (1.7) and (1.8) describe the rapid equilibrium mechanism between NO and NO_2. M is the collision molecule (N_2 or O_2) which is needed to conserve the momentum. At night-time, in the absence of solar radiation the photolysis of NO_2 (Eq 1.8) is not possible and most of the NO_x exists in the form of NO_2. (Seinfeld & Pandis, 2006)

During daytime, the most important sink of NO_x is the reaction with OH and finally the oxidation to Nitric acid (HNO_3).

$$NO_2 + OH + M \rightarrow HNO_3 + M \quad (1.10)$$

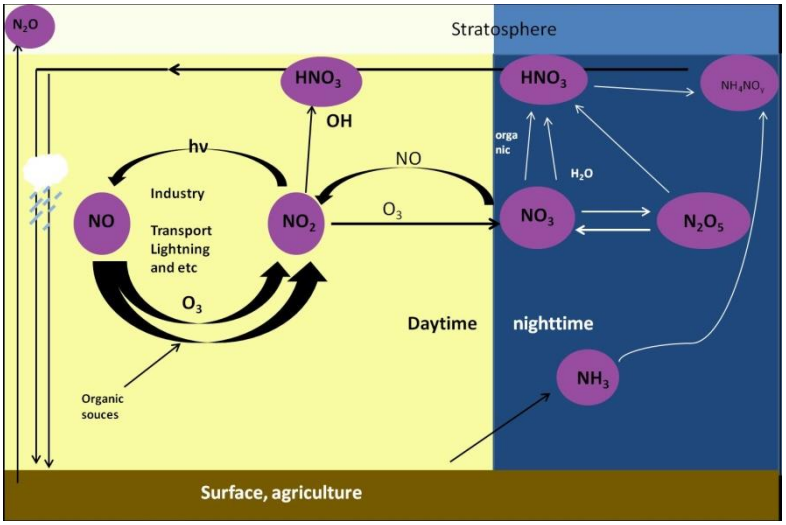

Figure 1.3: An overview of day and night-time tropospheric chemistry of oxides of nitrogen. Figure taken from Shaiganfar, (2012).

HNO_3 is removed from the troposphere in approximately 1 week by wet and dry deposition (Seinfeld & Pandis, 2006; Wallace & Hobbs, 2006).

During night-time, ozone oxidizes NO_2 to nitrate (NO_3). The nitrate radical then further reacts with NO_2 and forms nitrogen pentoxide (N_2O_5);

The day and night time reactions of the nitrogen oxides in troposphere are also depicted in Figure 1.3.

$$NO_2 + O_3 \rightarrow NO_3 + O_2 \quad (1.11)$$

$$NO_2 + NO_3 + M \rightarrow N_2O_5 + M \quad (1.12)$$

Nitrogen pentoxide then further reacts with H_2O on particles and produces HNO_3.

$$N_2O_5 + H_2O + M \xrightarrow{aerosols} 2HNO_3 \quad (1.13)$$

PAN (Peroxyacetyl nitrate) is produced in the troposphere when carbonyl compounds are photo-oxidized in the presence of NO_x. PAN is a major reservoir of NO_x. PAN reproduces nitrogen oxides as a result of their thermal decomposition. The peroxyacetyl radical, $CH_3C(O)O_2$ reacts with nitric oxide (NO) and NO_2 to form PAN;

$$CH_3C(O)O_2 + NO \rightarrow NO_2 + CH_3C(O)O \quad (1.14)$$

$$CH_3C(O)O + O_2 \rightarrow CH_3O_2 + CO_2 \quad (1.15)$$

In sum:

$$CH_3C(O)O_2 + NO \xrightarrow[O_2]{} NO_2 + CH_3O_2 + CO_2 \quad (1.16)$$

PAN is also formed when the peroxyacetyl radical reacts with NO_2, and in the presence of heat, it decomposes back to NO_2 and the peroxyacetyl radical.

$$CH_3C(O)O_2 + NO_2 + M \rightarrow CH_3C(O)O_2NO_2 + M \quad (1.17)$$

PAN is not very water soluble, so it is removed from the atmosphere by photolysis and thermal decomposition and not by wet deposition.

Tropospheric NO_x is primarily produced as a result of both anthropogenic and natural activities. Anthropogenic sources are the high temperature combustion processes in vehicles, industry and power production. Natural or biogenic sources include lightning, soil bacterial activity and biomass burning. The anthropogenic formation of NO_x usually takes place at high temperatures (>1800 ℃). Molecular nitrogen in air is combined with oxygen at high temperatures and gives NO. This mechanism was introduced by (Zel'dovich, 1946). At temperatures above 1800 ℃ the molecular oxygen is broken into atomic oxygen, [O]:

$$O_2 + M \leftrightharpoons O + O + M \quad (1.18)$$

Ambient nitrogen then reacts with atomic oxygen and yields NO and atomic nitrogen, N.

$$O + N_2 \leftrightharpoons NO + N \quad (1.19)$$

This atomic N further reacts with molecular oxygen present in air and produces NO and atomic oxygen:

$$O_2 + N \leftrightharpoons NO + O \quad (1.20)$$

At higher temperatures, the equilibrium for the last two reactions is more towards the right-hand side (Moesl, 2012).

NO_x badly impacts the respiratory system by not only developing but also further deteriorating the health conditions of persons, already suffering from asthma and other respiratory diseases (EPA, 1999).

As discussed previously, NO and NO_2 are responsible for the formation of tropospheric ozone and PAN. They also play a major part in the formation of nitrate aerosols. Tropospheric ozone, PAN and aerosols are all pollutants and have adverse impacts on the environment (Varshney & Singh, 2003).

1.4.1.3. Formaldehyde (HCHO)

Formaldehyde (HCHO) belongs to a larger group, named oxygenated volatile organic compounds (OVOCs). They play a significant role in air quality and photochemistry of the troposphere. HCHO is an intermediate product of the oxidation of methane and a majority of non-methane volatile organic compounds (NMVOC). OVOCs have various primary and secondary sources which are both natural and anthropogenic. Formaldehyde drives the formation of new radicals that are responsible for ozone formation (Luecken et al., 2012 and references therein). Fossil fuel combustion, biomass burning, use as solvent or industrial and biogenic emissions are the primary direct sources (Parrish et al., 2012). Direct anthropogenic emitters of HCHO also include exhausts of diesel cars and various industrial processes like paint industry, petrochemistry or refineries, incinerators and power plants (Koppmann, 2007). Formaldehyde is formed as a secondary product when methane

and non-methane hydrocarbons are oxidized photochemically and peroxy radicals are formed (Atkinson et al., 2008). Isoprene (C_5H_8) is emitted by vegetation and its oxidation by ambient OH is the most important biogenic source of HCHO (Anderson et al., 1996; Kesselmeier, 2001).

Thus, measurements of formaldehyde help in understanding the oxidation processes in the troposphere including isoprene oxidation and formation of CO from methane and non-methane VOCs. The understanding of these phenomena further helps in quantifying OH levels. Furthermore, the measurement of the ratio of the HCHO to NO_2 concentration (or tropospheric columns) can give insights to the tropospheric ozone formation regimes (De Smedt et al., 2021 and references therein).

Peroxy radicals (RO_2), responsible for the secondary formation of formaldehyde show a positive correlation with HCHO and can be seen as a proxy of the total VOCs reactivity. At global scales, the secondary formation is the dominant source of HCHO but in regions with enhanced anthropogenic activities like urban areas, the primary formation cannot be neglected (Su et al., 2019 and references therein).

The most abundant source of HCHO in the atmosphere is the oxidation of organic compounds (e.g., methane) via reaction with the OH radical (Koppmann, 2007). The following series of reactions explains the secondary production of HCHO from the oxidation of methane. These reactions are also valid for non-methane hydrocarbons (Koppmann, 2007; Seinfeld & Pandis, 2006).

Methane is oxidized by OH radicals and yields methyl radicals:

$$CH_4 + OH \rightarrow CH_3 + H_2O \quad (1.21)$$

The methyl radical then instantly reacts with atmospheric oxygen and yields methyl peroxy radicals (CH_3O_2):

$$CH_3 + O_2 + M \rightarrow CH_3O_2 + M \quad (1.22)$$

The methyl peroxy radical then further reacts with NO and yields methoxy radical (CH_3O) and NO_2. The methoxy radical reacts with oxygen and yields formaldehyde.

$$CH_3O_2 + NO \rightarrow CH_3O + NO_2 \quad (1.23)$$

$$CH_3O + O_2 \rightarrow HCHO + HO_2 \quad (1.24)$$

CH_3O_2 can also react with HO_2 and yields methyl hydroperoxide (CH_3OOH). It is then photolyzed or reacts with the OH radical and yields HCHO.

NO can react with HO_2 produced in reaction (1.24) and yields NO_2 and OH which then affect the tropospheric O_3 production.

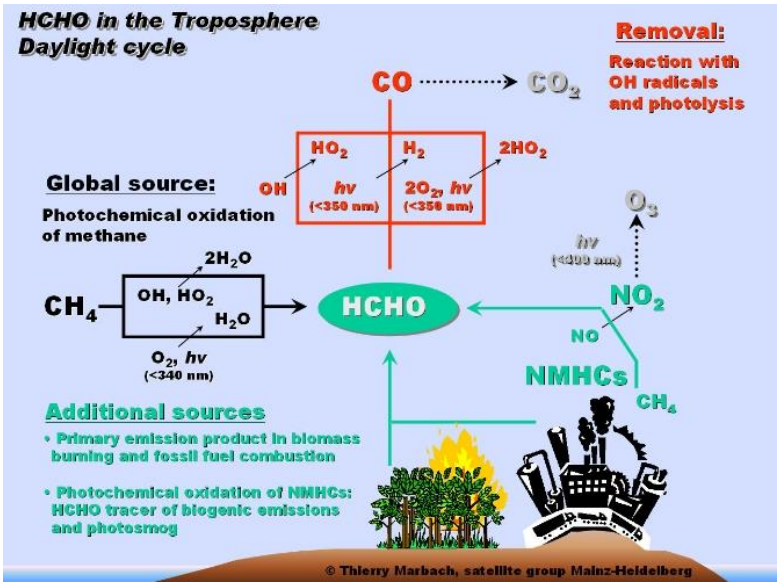

Figure 1.4: Various sources and sinks of HCHO in the troposphere. Figure is taken from Marbach, (2021).

HCHO is primarily lost by either photolysis or by reaction with OH. The photolysis of formaldehyde yields carbon monoxide (CO).

$$HCHO + h\nu \rightarrow CO + H_2 \quad (1.25)$$

HCO can also be formed by photolysis of HCHO at wavelengths shorter than 325 nm.

$$HCHO + h\nu \rightarrow HCO + H \quad (1.26)$$

The reaction with the hydroxyl radical (OH) leads to its removal from the atmosphere:

$$HCHO + OH \rightarrow HCO + H_2O \quad (1.27)$$

At night, NO_3 is responsible for the HCHO removal from the atmosphere:

$$HCHO + NO_3 \rightarrow HNO_3 + HCO \quad (1.28)$$

H and HCO produced in the above reactions react with O_2 and yield CO and HO_2. Wet and dry deposition are also responsible for the removal of this group of VOCs. An overview of the HCHO chemistry in the troposphere during daytime is depicted in Figure 1.4. Formaldehyde has a short lifetime of few hours (Arlander et al., 1995) and is thus mainly found proximal to its emission sources. Due to its short lifetime, HCHO is responsible for the release of several other short lived volatile organic species (De Smedt et al., 2021).

Like other air pollutants, HCHO is also detrimental to human health in outdoor as well as indoor Formaldehyde exposures may cause acute health effects like eye problems, coughing, nausea and may also cause leukemia (National Cancer Institute, 2011).

1.4.1.4. Glyoxal (CHOCHO)

Glyoxal is the smallest dicarbonyl formed as a result of the oxidation of VOCs (Calvert et al., 2000). Differentiation between primary and secondary sources of glyoxal is not fully understood due to the lack of sufficient observations. However, Volkamer et al. (2005) argued that secondary emissions are more prominent than the primary ones. Glyoxal is produced when hydrocarbons containing at least two carbon atoms are oxidized. About 65-70% of the total CHOCHO abundance originates from the oxidation of biogenic isoprene. Among anthropogenic sources, biomass burning and the oxidation of acetylene are the major source of glyoxal. Glyoxal can also be emitted from tail pipe emissions in minute amounts (Grosjean, Grosjean, & Gertler, 2001).

Glyoxal is removed from the atmosphere through a number of reactions like photolysis, oxidation by OH radicals and also by dry and wet deposition. On the basis of these sinks and sources, the chemical lifetime of glyoxal is about three hours. Enhanced glyoxal concentrations are predominantly present in the boundary layer, close to surface. Glyoxal, in addition to HCHO, may also be considered as a good indicator of the oxidation of VOCs present in environments polluted by vehicular emissions (Vrekoussis et al., 2009 and references therein).

1.4.1.5. Sulfur Dioxide (SO_2)

Sulfur dioxide is the most abundant member of the group of sulfur oxide gases in the atmosphere. It is emitted in the atmosphere by different natural and anthropogenic processes. The prominent natural sources of SO_2 in the troposphere are volcanic eruptions, oxidation of CS_2 and dimethyl sulphide (DMS) (Seinfeld & Pandis, 2006). Biomass burning also contributes to the natural emissions of SO_2. With the advancement in industrialization and urbanization, anthropogenic sources of SO_2 became predominant over natural emissions (Smith et al., 2001). Combustion of sulfur containing fuels like coal for power production and other industrial processes are the major anthropogenic contributors of SO_2 emissions in the atmosphere. Emissions from vehicles using fuel with high sulfur content and extraction of metals from ore are also human induced sources of SO_2.

SO_2 is oxidized by the OH radical and removed from the atmosphere by forming sulfuric acid (H_2SO_4) and acid rain (Jacob, 1999) :

$$SO_2 + OH + M \rightarrow HSO_3 + M \quad (1.29)$$

M may be N_2 or O_2 molecules.

$$HSO_3 + O_2 \rightarrow SO_3 + HO_2 \quad (1.30)$$

$$SO_3 + H_2O + M \rightarrow H_2SO_4 + M \quad (1.31)$$

SO_2 negatively impacts both the environment and human heath. Short term exposure to SO_2 may lead to respiratory illness including difficuilty in breathing. Asthamatic patients, childern and elderly are even more susceptible to such exposure. Long term exposure may aggravate existing lung and heart diseases. SO_2 emissions in higher concentrations may

also form other oxides of sulfur that lead to the formation of particulate matter on reaction with other compounds. These fine particles impair visibility and form haze (US EPA, 2021b). Sulfur oxides also damage plants by destroying leaves and impairing their growth. Moreover, SO_2 contributes to the acid rain that damages the aquatic and other ecosystems by aluminium leaching (US EPA, 2021a).

2. METHODOLOGY[1]

This study describes the measurement of tropospheric NO_x, SO_2, HCHO and CHOCHO in and around the city of Lahore. These trace species inherent characteristic narrowband absorption structures which allows to detect them in the atmosphere by using the Differential Optical Absorption Spectroscopy (DOAS) technique introduced by Platt & Stutz, (2008). In this chapter, the DOAS principle and other details related to the methodology are presented.

2.1. ABSORPTION SPECTROSCOPY

2.1.1. Beer - Lambert Law

Absorption spectroscopy is an important method to study the chemical composition of gases in the atmosphere. In this spectroscopic technique, electromagnetic radiation absorbed by matter is used and can be described by Lambert–Beer's law (or Bouguer–Lambert law).

The Beer-Lambert law is the basis of many quantitative trace gas measurement methods in the atmosphere and the laboratory. The law was discovered by Pierre Bouguer before 1729. It is often misattributed to Johann Heinrich Lambert, who cited Bouguer's Essai d'Optique sur la Gradation de la Lumiere (Claude Jombert, Paris, 1729), and even quoted from it, in his Photometri in 1760. Much later, August Beer extended the exponential absorption law in 1852 to include the concentration of solutions in the absorption coefficient.

The photons are absorbed by the atmospheric molecules and as a result electronic, vibrational and rotational transitions occur in the molecules. Each molecule has its specific characteristic absorption spectrum which is dependent upon the above-mentioned transitions states. So, the identification of the absorber along with its concentration can be done on the basis of the strength and type of the absorption.

The Lambert Beer's law thus explains the relationship between the concentration and the absorption of the absorber. Radiation is absorbed by molecules in the atmosphere (trace gases and aerosols). The light intensity I at a specific wavelength λ will be reduced by the amount dI, after passing the absorbing layer of the thickness ds:

$$dI(\lambda) = -I(\lambda)\sigma(\lambda)Nds \qquad (2.1)$$

[1] The part of this chapter written in italic font is copied from Shaiganfar, (2012).

Where, $\sigma(\lambda)$ is the absorption cross section of the absorber at wavelength λ and N is the number density.

Integration of the formula 2.1 yields:

$$\ln\left(\frac{I_0}{I}\right) = \sigma(\lambda) \int_0^L N ds \qquad (2.2)$$

where I_0 represents the initial intensity and L the thickness of the layer.

With $S = \int_0^L N ds$, and dD=σ(λS) ds we derive:

$$I(\lambda, L) = I_0(\lambda) e^{-\sigma(\lambda) S} = I_0(\lambda) e^{-D} \qquad (2.3)$$

which is known as Beer-Lambert Law. D is referred to as optical density. Figure 2.1 explains the application of the Lambert-Beer Law.

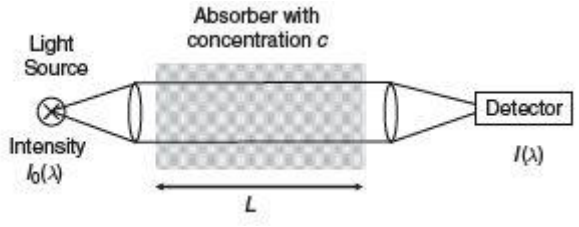

Figure 2.1 Application of the Lambert-Beer Law for absorption spectroscopy. Radiation travels through a path of length L with an absorber of concentration c. I(λ) is the attenuated light which is measured by the detector. Figure adopted from Platt and Stutz, (2008).

2.1.2. Ground-based Observations

The absorption of photons by atmospheric molecules changes the state of the molecules by causing electronic, vibrational and rotational transitions. The absorption cross-section is characteristic for the absorbing molecules.

The absorption of radiation by matter is described by the Beer-Lambert Law (see previous section). Light with an intensity $I_0(\lambda)$ passes through a volume (open atmosphere) with absorbers and scatterers (trace gases and aerosols). From the reduced intensity $I(\lambda)$, we can derive information about these absorption and scattering processes.

Here, the optical density is denoted by D that can also be expressed as;

$$D = \ln\left(\frac{I_0(\lambda)}{I\ (\lambda, \mathrm{L})}\right) = \int_0^L \sum_j \sigma_j(\lambda) c_j dl \qquad (2.4)$$

where σ_j is the absorption cross sections of the j^{th} trace species and c_j is its concentration:

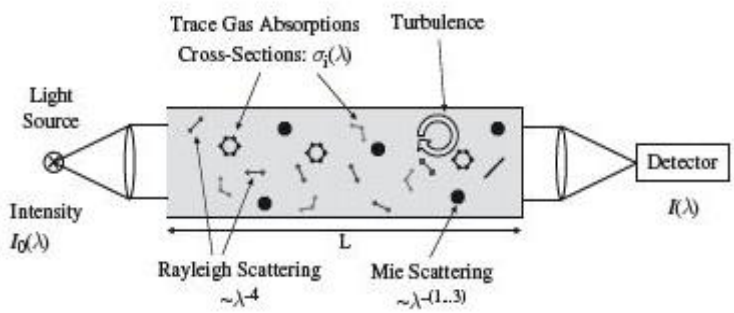

Figure 2.2: Schematic representation of the experimental setup for the measurement of trace gases in the open atmosphere. Various scattering and absorption processes are also mentioned. Figure adopted from Platt and Stutz, (2008).

If only one absorber is present, for the calculation of the average concentration c of the given absorber, the following relation can be used;

$$c = \frac{\ln\left(\frac{I_{0(\lambda)}}{I(\lambda)}\right)}{\sigma(\lambda)L} = \frac{D}{\sigma(\lambda)\cdot L} \qquad (2.5)$$

The corresponding slant column density (S) is the concentration integrated over the light path in the atmosphere. It is calculated as:

$$S = \frac{D}{\sigma(\lambda)} \qquad (2.6)$$

In the laboratory, the concentration of a given absorber can be determined by measuring I and I_0. Whereas, in the real atmosphere, $I_0(\lambda)$ cannot be determined, because the instrument cannot put outside the atmosphere. Moreover, in addition to the absorption processes of several trace gases also scattering of the light occurs (e.g., by aerosols, water droplets and gas molecules). In Figure 2.2, simultaneous processes of absorption, scattering and turbulence that lead to the light attenuation in the open air are depicted. So, the Eq. (2.3) cannot be applied straightforwardly to determine the trace gas concentrations in the atmosphere. This limitation was addressed by the differential optical absorption spectroscopy (DOAS) method explained in the following subsection.

2.1.3. Differential Optical Absorption Spectroscopy (DOAS)

In order to measure the trace gas concentrations in the open atmosphere, the Lambert - Beer's law in the simple form could not suffice the purpose, as the determination of the true $I_0(\lambda)$ is not possible, and as several absorbers and scattering agents are present in the atmosphere. So, Eq. (2.3) needs to be modified for the atmospheric application as Eq (2.7):

$$I(\lambda, \mathrm{L}) = \mathrm{I_0}(\lambda)\cdot \exp\left[-\int_0^{\mathrm{L}} \cdot \sum\left(\sigma_{\mathrm{j}}(\lambda)\cdot \mathrm{c_j}(\mathrm{s})\right) + \varepsilon_R(\lambda, s) + \varepsilon_M(\lambda, s)\cdot ds\right]\cdot A(\lambda) \qquad (2.7)$$

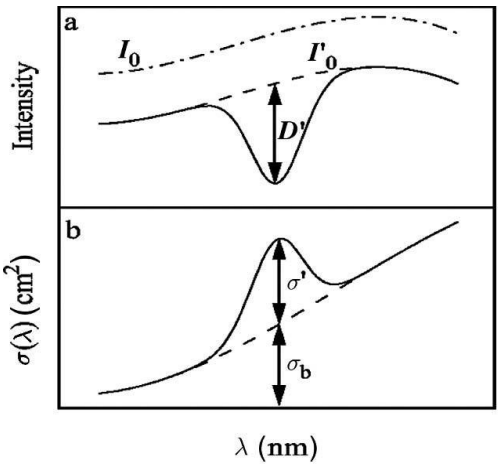

Figure 2.3: The basic DOAS principle: Separation of I_0 and σ by the filtering process into a narrow (D' andσ') and broad band part (I'_0 and σ_b). Figure and caption taken from Platt & Stutz, (2008).

Here, $\varepsilon_{M\,(\lambda)}$ and $\varepsilon_{R\,(\lambda)}$ are the extinction coefficients for Mie and Rayleigh scattering, respectively, and $A(\lambda)$ represents instrumental effects and also accounts for the efficiency of the scattering procedures that are responsible for the scattering of sunlight into the instrumental line of sight.

For the calculation of the trace gas concentrations in the open atmosphere, it is necessary to accurately quantify all the factors that contribute to the attenuation of the initial light intensity (I_0), which is impossible. This limitation is however, solved by the Differential Optical Absorption Spectroscopy (DOAS) technique (Platt & Stutz, 2008). Many trace species, turbulence and aerosol extinction exhibit broadband and smooth absorption features while some trace gases show narrowband absorptions structures. DOAS makes use of this and separates narrow and broadband structures of the absorption spectrum (Figure 2.3)[2].

These narrow and broadband features, collectively constitute the total absorption cross section as:

$$\sigma_j(\lambda) = \sigma_{j0}(\lambda) + \sigma'_{j0}(\lambda) \qquad (2.8)$$

Here, σ_{j0} and σ'_{j0} represent the broad and narrow band contributions, respectively. The broad band contributions are mainly due to the Mie and Rayleigh scattering processes.

By taking into account both narrow and broadband absorptions, the Eq. (2.4) can also be written as Eq (2.9):

[2] Figure 2.3 illustrates the basic principle, but in practice the described procedure is not being done exactly in this way currently. The approximation of the broadband component of the measured spectrum is done by the polynomial function.

$$I(\lambda, L) = I_0(\lambda) \cdot \exp\left[-\int_0^L \cdot \left(\sum_j \left(\sigma_j'(\lambda) \cdot c_j(s)\right) \cdot ds\right)\right] \cdot \exp\left[-\int_0^L \cdot \left(\sum_j \left(\sigma_{j0}(\lambda) \cdot c_j(s)\right) + \varepsilon_R(\lambda, s) + \varepsilon_M(\lambda, s)\right) \cdot ds\right] \cdot A(\lambda) \quad (2.9)$$

In the above equation (Eq. 2.9), narrow band absorptions by the trace gases are represented by the first exponential function, whereas the second exponential term accounts for the broad-band variations due to the absorption and scattering (Mie and Rayleigh) by the gases and the aerosols. So, after the separation of the broadband and differential parts, the initial intensity is modified in to I_0' and can be defined as;

$$I_0'(\lambda) = I_0(\lambda) \cdot \exp\left[-\int_0^L \cdot \left(\sum_j \left(\sigma_{j0}(\lambda) \cdot c_j(s)\right) + \varepsilon_R(\lambda, s) + \varepsilon_M(\lambda, s)\right) \cdot ds\right] \cdot A(\lambda) \quad (2.10)$$

The differential absorption cross-section, $\sigma_j'(\lambda)$ of the trace gas is calculated from the original absorption cross-section which was measured under controlled laboratory conditions. The differential optical density (D') can be determined as:

$$D' = \ln \frac{I_0'(\lambda)'}{I(\lambda)} = \int_0^L \cdot \left(\sum_j \left(\sigma_j'(\lambda) \cdot c_j(s)\right)\right) \cdot ds \quad (2.11)$$

Differential optical density D', and absorption cross-sections $\sigma_j'(\lambda)$ substitute the D and $\sigma(\lambda)$, respectively. As each trace gas has its characteristic absorption structure, the concentrations of each species can be calculated separately. In this section the basic principle of the DOAS is explained; for extensive details and mathematical descriptions, refer to Platt and Stutz, (2008).

The DOAS principle can be used for multiple light path set-ups and can make use of artificial light sources e.g., Xe arc lamps and lasers (active DOAS) or use natural light from sun or moon (passive DOAS).

In this thesis, Multi AXis DOAS (MAX-DOAS) set up was used, which measures scattered sun light; details of this system are described later in section 2.3.

2.2. RADIATIVE TRANSFER IN THE ATMOSPHERE

In the atmosphere, the transfer of solar radiation is determined by scattering and absorption processes.

Through absorption processes, radiation is removed from the radiation field and converted into some other form of energy. Elastic scattering changes the direction of propagation of an individual photon, but not its energy. Such scattering on air molecules is called Rayleigh scattering and on aerosols particles it is often referred to as Mie scattering. Inelastic scattering (the energy is changed) is caused by Raman scattering. For atmospheric observations in the UV / vis spectral range, the rotational Raman scattering on molecules is important.

2.2.1. Rayleigh Scattering

Elastic scattering is caused by air molecules, if the direction of photons changes but without any energy transfer.

The Rayleigh scattering cross-section is given by (Rayleigh, 1899):

$$\sigma(\lambda) \approx \frac{\sigma_0}{\lambda^4} \tag{2.12}$$

Here λ denotes the wavelength of the photon. The change of the direction is described by the so-called phase function. The phase function for Rayleigh scattering is given by:

$$\varphi(\cos(\theta)) = \frac{3}{4}\,(1 + cos^2(\theta)) \tag{2.13}$$

Here θ is the scattering angle, which is defined as angle between the direction of the incoming and the scattered photon.

2.2.2. Mie Scattering

Scattering and absorption of light on aerosol particles is often described by Mie theory (Mie, 1908), which can be applied if the dimensions of the particles are comparable to the wavelength of the incident radiation. For this kind of elastic interactions, there is a weaker wavelength dependency compared to Rayleigh scattering.

2.2.3. Raman Scattering

Inelastic scattering processes change the energy of the photon. Energy can be transferred from photons to the molecules (Stokes line), and vice versa (Anti-Stokes). The term rotational Raman scattering is used if only the rotational excitation is affected (Platt & Stutz, 2008).

2.3. MULTI AXIS DIFFERENTIAL OPTICAL ABSORPTION SPECTROSCOPY (MAX-DOAS)

The Multi-Axis Differential Optical Absorption Spectroscopy (MAX-DOAS) is a passive DOAS measurement technique that observes scattered sunlight under different elevation angles between zenith and horizon (Hönninger et al., 2003; Leser et al., 2003; Van Roozendael et al., 2004; Wagner et al., 2004). Passive DOAS means that natural light sources (sun or moon) are used as the light source. The relatively simple experimental setup is an advantage of passive DOAS. Using different elevation angles gives us the possibility to derive the vertical distribution of trace gases. This technique allows to quantify the column densities of trace gases for low as well as higher elevation angles. The instrument's sensitivity to the trace gases varies with the elevation angle. At lower elevation angles, the light path traversing the trace gas layer is enhanced and so, the sensitivity for the tropospheric trace gases is. Whereas, for the stratospheric absorbers, the sensitivity is almost independent of the elevation angle (Wagner et al., 2010). In Figure 2.4, the measurement geometry of the MAX-DOAS set-up is depicted. It can be seen that for lower elevation angles, light paths are longer and thus allows increased sensitivity to the lowermost trace gas layers.

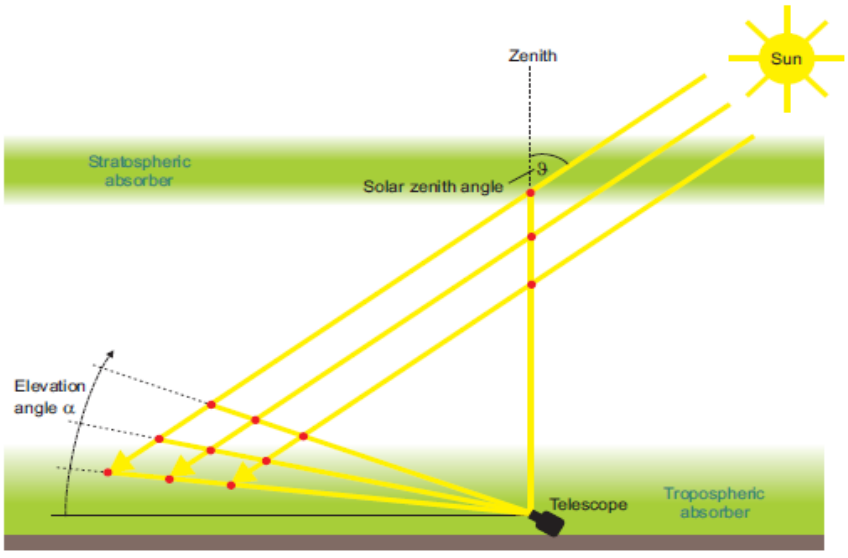

Figure 2.4: MAX-DOAS setup showing observations at different elevation angles from zenith to lower ones. Light intensity from the sun is entering the atmosphere at specific solar zenith angles (SZA). The red points denote the scattering processes, in the line of sight of the instrument. Trace gas layers are represented by the green shaded zones. Figure is taken from Sinreich, (2008).

2.4. DATA ANALYSIS

After the acquisition of the spectra, they are analyzed to retrieve the profiles of trace gas concentration (or aerosol extinction) or the corresponding integrated quantities, the so-called vertical column density (VCD) or aerosol optical depth (AOD). In this section details of the data analysis are described

2.4.1. Correction of the Spectra

The MAX-DOAS spectra need to be corrected before the analysis. They have to be corrected by offset and dark current spectra, which are recorded by the same instrument.

2.4.1.1. Offset

The analogue-digital converter transforms the signals to digital form. Before this step an offset is added to the measured spectra to avoid negative signals. Therefore, this offset has to be subtracted from the spectra. The corrected spectrum can be obtained by:

$$I_{corr}(\lambda) = I_{meas}(\lambda) - \frac{N_{meas}}{N_{offset}} I_{offset} \quad (2.14)$$

Here;

$I_{meas}(\lambda)$ *is the raw spectrum*

$I_{corr}(\lambda)$ *is the corrected spectrum.*

I_{offset} *is the Offset spectrum.*

N_{meas} *is the number of scans of the measured spectrum,* N_{offset} *is the number of scans of the offset spectrum and* $I_{meas}(\lambda)$ *is the intensity of the measured spectrum. An offset spectrum is a measured spectrum (without being illuminated) with a high number of scans and a short integration time (to reduce the dark current).* An example of offset spectrum is shown in Figure 2.5.

2.4.1.2. Dark Current

This is the signal measured by the detector without illumination. This effect is caused by thermal excitation. The probability of this excitation is proportional to the Boltzmann function. To reduce the dark current signals, detectors are usually cooled to a constant temperature. The corrected spectrum can be obtained by:

$$I_{corr}(\lambda) = I_{meas}(\lambda) - \frac{t_{meas}}{t_{DC}} I_{DC}(\lambda) \quad (2.15)$$

Here,$I_{meas}(\lambda)$ is the intensity of the raw spectrum. $I_{corr}(\lambda)$ is the corrected spectrum and t_{meas} and t_{DC} are the integration times of measured and dark current spectrum.

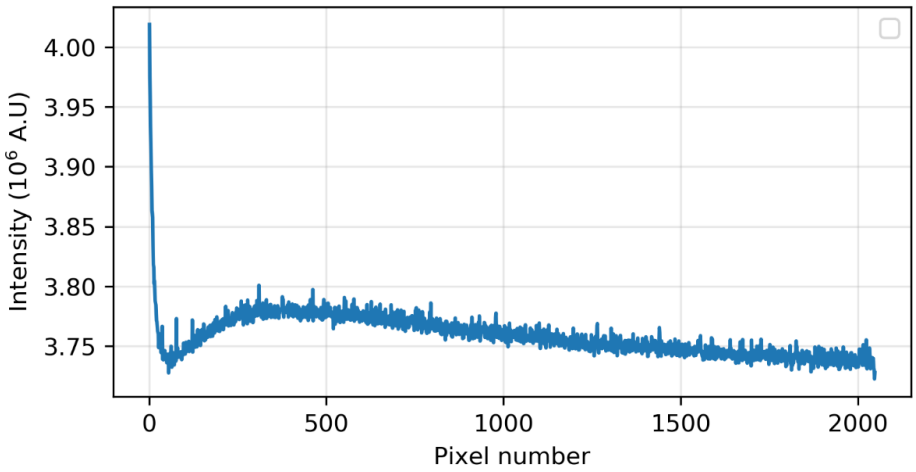

Figure 2.5: A typical offset spectrum, measured on 1 June 2017 having 10,000 scans with an integration time of 3 ms.

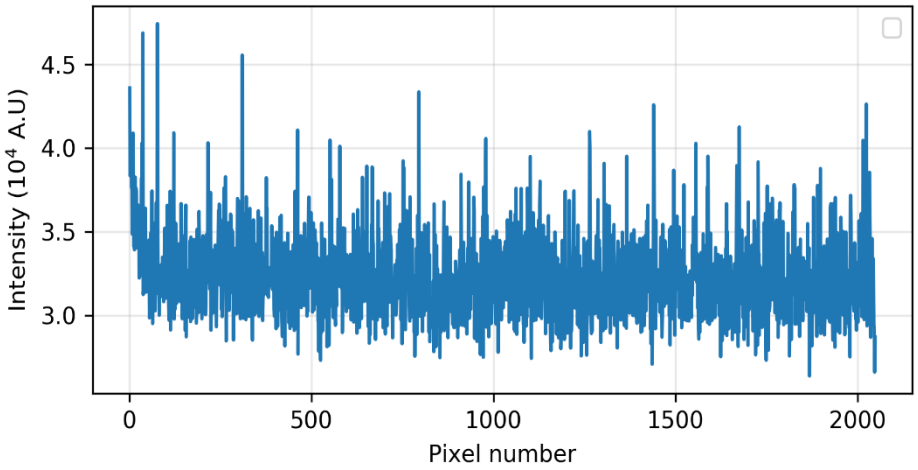

Figure 2.6: A typical dark current spectrum, measured on 1 June 2017, having one scan, with an integration time of 20,000 milliseconds.

$I_{DC}(\lambda)$ represents the dark current spectrum, which is a measured spectrum with one scan and a long integration time. An example of a dark current spectrum is shown in Figure 2.6.

2.4.2. DOAS Retrieval

The measured spectra are analyzed using the DOAS method (Platt & Stutz, 2008). Several trace gas absorption cross sections as well as a Fraunhofer reference spectrum, a so-called Ring spectrum and a polynomial (order 5) are included in the spectral fitting process by means of a least square fitting routine. The QDAOS software (Danckaert, Fayt, & Van Roozendael, 2017) was used to analyze the spectra.

The Levenberg-Marquardt Algorithm (LMA) (Levenberg, 1944) is used in the DOAS fit (Platt & Stutz, 2008). *The LMA is a combination of linear and non-linear fitting processes.*

During the fitting process the difference between the measured spectrum $I(\lambda)$ and simulated spectrum $F(\lambda)$ is minimised:

$$\sum_i \left(\ln\left(I_i(\lambda)\right) - F_i(\lambda)\right)^2 \rightarrow min \tag{2.16}$$

where i is the detector pixel number.

The simulated spectrum can be shown in this form; $F(\lambda) = \sum \sigma(\lambda)\, SCD + P$ where $\sigma(\lambda)$ represent the absorption cross-sections (and Ring spectrum, see next section) and P the polynomial. The difference between the first term (optical depth of the measured spectrum) and the second term (the simulated spectrum) in equation 2.16 is the residual, which should be minimized. The output of the spectral analysis is the so-called slant column density (SCD), the integrated trace gas concentration along the light path through the atmosphere.

2.4.2.1. Ring Effect

Rotational Raman scattering in the atmosphere causes a reduction of the optical density of the solar Fraunhofer lines. Because of this reduction, a correction has to be applied during the spectral analysis. Light intensity scattered into a passive DOAS instrument can be written as: (Platt & Stutz, 2008; Solomon & Sanders, 1987)

$$I_{meas} = I_{Rayleigh} + I_{Mie} + I_{Raman} = I_{elastic} + I_{Raman} \tag{2.17}$$

If we rewrite this equation we get:

$$\ln(I_{meas}) = \ln(I_{elastic}) + \ln\left(1 + \frac{I_{Raman}}{I_{elastic}}\right)$$

$$\approx \ln(I_{elastic}) + \ln\left(\frac{I_{Raman}}{I_{elastic}}\right) \tag{2.18}$$

where the last ratio of the Raman and the elastic part of the intensity is defined as Ring spectrum:

$$I_{Ring} = \frac{I_{Raman}}{I_{elastic}} \tag{2.19}$$

The Ring spectrum is included as pseudo-absorber in the DOAS retrieval. The Ring spectrum was calculated from the Fraunhofer reference spectrum (FRS) by using the DOASIS software (Kraus, 2006). An additional Ring spectrum with different broad band spectral dependence was also used in the fitting process (Wagner et al., 2009).

2.4.2.2. Stratospheric Correction

MAX-DOAS observations are in principle sensitive to both the tropospheric and stratospheric trace gas absorptions. Our focus in this study is the tropospheric part.The SCD is the sum of the SCDs of the troposphere and the stratosphere:

$$SCD_{meas} = SCD_{trop} + SCD_{strat} \quad (2.20)$$

The result of the DOAS retrieval is the difference between the SCDs of the measured spectrum and the Fraunhofer reference spectrum SCD_{ref}, since the Fraunhofer reference spectrum also contains atmospheric trace gas absorptions. This DSCD (differential slant column density) can be written as:

$$DSCD_{meas} = SCD_{meas} - SCD_{ref} \quad (2.21)$$

For the Fraunhofer reference spectrum usually a spectrum with small trace gas absorption, e.g., in zenith direction, is chosen.

For trace gases, for which the stratospheric part can be comparable to or smaller than the tropospheric part, an assumption is feasible that the stratospheric absorption is the same in all spectra taken during one elevation sequence (Wagner et al., 2010).

$$DSCD_{meas}(\alpha) = SCD_{trop}(\alpha) + SCD_{strat} - SCD_{trop}(ref) - SCD_{strat}$$

$$= SCD_{trop}(\alpha) - SCD_{trop}(ref) = DSCD_{trop}(\alpha) \quad (2.22)$$

Here $DSCD_{trop}(\alpha)$ is the tropospheric differential slant column density for the low elevation angle, which contains only tropospheric absorption signals.

2.4.2.3. Determination of the tropospheric vertical column density

The vertical column density is defined as the concentration of a trace gas vertically integrated over the entire extent of the atmosphere. The airmass factor (AMF) (Solomon et al., 1987) is defined as:

$$AMF = \frac{SCD}{VCD} \quad (2.23)$$

Here AMF is the proportionality factor between the observed slant column density and the vertical column density.

For a slant viewing geometry, the absorption paths through the lower atmosphere (and thus also the AMF) can become rather large. MAX-DOAS observations are especially sensitive to tropospheric trace gases.

The accuracy of the airmass factor calculations directly affects the accuracy of the vertical column densities. For many applications, the AMF is retrieved from radiative transfer simulations (Solomon et al., 1987). The tropospheric AMF is defined as:

$$AMF_{trop}(\alpha) = \frac{SCD_{trop}(\alpha)}{VCD_{trop}} \quad (2.24)$$

This equation can be rewritten as:

$$\frac{SCD_{trop}(\alpha)}{AMF_{trop}(\alpha)} = \frac{DSCD_{trop}(\alpha) + SCD_{trop}(ref)}{AMF_{trop}(\alpha)} \tag{2.25}$$

$$DSCD_{trop}(\alpha) = AMF_{trop}(\alpha) \cdot VCD_{trop} - AMF_{trop}(ref) \cdot VCD_{trop} \tag{2.26}$$

$$VCD_{trop} = \frac{DSCD_{trop}(\alpha)}{AMF_{trop}(\alpha) - AMF_{trop}(ref)}$$

$$VCD_{trop} = \frac{DSCD_{trop}(\alpha)}{DAMF_{trop}(\alpha)} \tag{2.27}$$

with,

$$DAMF_{trop}(\alpha) = AMF_{trop}(\alpha) - AMF_{trop}(ref).$$

2.4.2.3.1. Geometrical approximation for ground-based observations

In many cases, we can use an approximation for the airmass factor, the so called geometric approximation (Brinksma et al., 2008). The tropospheric *airmass factor can be described by:*

$$AMF_{trop} \approx \frac{1}{\sin(\alpha)} \tag{2.28}$$

Thus, the tropospheric vertical column density can be determined as:

$$VCD_{trop} = \frac{DSCD_{trop}(\alpha)}{\frac{1}{\sin(\alpha)} - \frac{1}{\sin(ref)}} \tag{2.29}$$

If a Fraunhofer reference spectrum measured at zenith is used this equation can be rewritten as:

$$VCD_{trop} = \frac{DSCD_{trop}(\alpha)}{\frac{1}{\sin(\alpha)} - 1} \tag{2.30}$$

The geometric approximation can usually be applied only for high elevation angles (larger than about 10°).

2.4.2.3.2. Mobile MAX-DOAS observations

The determination of the tropospheric vertical column density is more difficult for mobile MAX-DOAS observations. Because of the movement of the platform, the trace gas concentrations can considerably change during one measurement sequence. Furthermore,in contrast to stationary MAX-DOAS measurements usually only one pair of elevation angles are used. Besides observations in zenith direction, measurements are also performed at an elevation angle between about 15 and 30°. Thus, a slightly modified analysis approach has to be used, which is described below.

The basic formula to retrieve the tropospheric VCD is:

$$VCD_{trop} = \frac{SCD_{meas}(\alpha) - SCD_{strat}(\alpha)}{AMF_{trop}(\alpha)} \quad (2.31)$$

Here α represents the non-zenith angle.

$$= \frac{DSCD_{meas}(\alpha) + SCD_{ref} - SCD_{strat}(SZA)}{AMF_{trop}(\alpha)} \quad (2.32)$$

$$= \frac{DSCD_{meas}(\alpha) + DSCD_{offset}}{AMF_{trop}(\alpha)} \quad (2.33)$$

The SCD_{ref} and $SCD_{strat}(SZA)$ are usually unknown. While SCD_{ref} is constant, $SCD_{strat}(SZA)$ depends on the solar zenith angle. For high SZA, this dependency is large, but for low SZA it is usually negligible. The difference of these two terms is referred as $DSCDo_{ffset}$ (SZA) as follow;

$$DSCD_{offset}(SZA) = SCD_{ref} - SCD_{strat}(SZA). \quad (2.34)$$

Wagner et al., (2010) determined the $DSCD_{offset}$ (SZA) from the MAX-DOAS observations. Then, by using Eq. (2.32) absolute values for the VCD_{trop} can be determined.

By equating Eqs. (2.27) and (2.32) we get;

$$DSCD_{offset}(SZA) = \frac{AMF_{trop}(ref) \cdot DSCD_{meas}(\alpha) - AMF_{trop}(\alpha) \cdot DSCD_{meas}(ref)}{AMF_{trop}(\alpha) - AMF_{trop}(ref)} \quad (2.35)$$

This term can in principle be derived from a single pair of measurements from one elevation sequence. However,to minimise the effect of the moving platform, we apply this method to all the measurements. The $DSCDo_{ffset}$ (SZA) is dependent on the solar zenith angle, and simple averaging of all the $DSCDo_{ffset}$ (SZA) values does not work well. Thus the time series of the $DSCDo_{ffset}$ (SZA) are expressed as follow:

$$DSCD_{offset}(t) = \frac{AMF_{trop}(ref) \cdot DSCD_{meas}(\alpha, t) - AMF_{trop}(\alpha) \cdot DSCD_{meas}(ref, t)}{AMF_{trop}(\alpha, t) - AMF_{trop}(ref, t)} \quad (2.36)$$

Here, t is the time of an individual measurement. The time dependent $DSCD_{offset}$ can be approximated by a polynomial, which is fitted to all data points calculated by Eq. (2.35).

2.5. TRACE GAS ANALYSIS

In this section various steps of the DOAS retrievals as presented in section 2.4 are described individually for each trace gas.

2.5.1. Nitrogen Dioxide Analysis

The recorded spectra are analyzed according to the DOAS technique (Platt and Stutz, 2008) by using the QDOAS software V2.112.1. (Danckaert et al., 2017). The wavelength calibration was performed by using a high resolution solar spectrum (Chance & Kurucz, 2010). Daily, fixed Fraunhofer reference spectra (FRS), taken around noon at an elevation angle of 90 degrees were used. The wavelength range for the fitting window used was 400-460 nm except for the 2015-I campaign where the wavelength range used was 400-442 nm as the spectral range of the spectrometer was 287 to 445 nm for the instrument used in the first campaign. A Ring spectrum calculated from the daily FRS using the DOASIS software and a second Ring spectrum with a different broadband spectral dependence calculated from the first ring were included in the spectral fitting process. A polynomial of fifth order was used in the spectral analysis. For the Tube MAX-DOAS measurements, gaps were also introduced to minimize the influence of hot pixels and residual structures. A typical fit result is shown in Figure 2.7. The fitted absorption cross-sections are mentioned in Table 2.1.

Table 2.1: Fitted cross sections for the NO_2 analysis

Fitted Cross Sections	Details
NO_2	at 294 K (Vandaele et al., 1998), I_0-correction with $1x10^{17}$ molec/cm^2 (Aliwell et al., 2002; Pinardi et al., 2013). NO_{2a} at 220 K (Vandaele et al., 1998) NO_2 squared at 294K (Vandaele et al., 1998)
O_3	at 233 K (Serdyuchenko et al., 2014)
O_4	at 293 K (Thalman & Volkamer, 2013)
H_2O	at 296 K (Rothman et al., 2010)
CHOCHO	at 296 K (Volkamer et al., 2005)

2.5.1.1. Data Quality

Some measurements have significant errors, which might occur as a result of low intensity or other issues like fluctuations in the temperature of the spectrometer. The dark current signal is temperature dependent and needs to be corrected for each spectrum. If the temperature of the instrument is not stable, it yields variable dark current signals and hence impacts the correction of the spectra. Moreover, temperature fluctuation of the spectrometer may also result in changes in optical properties e.g., the so-called slit function of the instrument, which also affects the spectral analysis. Unfortunately, on some days, due to some error in the instrument, temperature stabilization did not work.

2.5.1.1.1. Root mean square (RMS) filtering

The root mean square (RMS) of the residual is one of the criteria to determine the fit quality. Data were filtered out before further processing using a temporally varying NO_2 RMS threshold. For that purpose, a polynomial of 4th order (Eq. 2.34) as a function of the solar zenith angle (SZA) is used to filter out unreliable data. The threshold depends on SZA, as for the low sun, less light is received, which results in high RMS even for measurements of good quality. The polynomial was determined by visual inspection of the derived RMS values of NO_2 analysis. An example is shown in Figure 2.8

$$\frac{(1\times10^{-9}\times SZA^4)-(1\times10^{-8}\times SZA^3)+(3\times10^{-7}\times SZA^2)-(4\times10^{-6}\times SZA)+(5\times10^{-4})}{scaling\ factor} \quad (2.37)$$

SZA is the solar zenith angle of the individual measurement.

The threshold polynomial was scaled according to the RMS level of the individual days. While the overall SZA dependence stayed the same, the absolute values changed from campaign to campaign because of changing instrumental properties. Moreover, even between the individual days of a campaign slight variations of RMS were found. Therefore, the SZA dependence was manually adjusted by applying a scaling factor on daily basis to remove the obvious outliers. On most of the days a scaling factor of 7×10^{-4} was used. The same filter was also applied for the other three trace gases (SO_2, HCHO and CHOCHO) DSCDs to filter out the bad quality data. This procedure was chosen for simplicity, because it was found that the RMS of the different trace gas analyses are highly correlated (see Figure 2.9). In Figure 2.9, the NO_2 RMS is plotted against the filtered (lower panel) and unfiltered RMS values (upper panel) of the SO_2 and formaldehyde analyses for 18 June 2018. From this figure, it can be seen that the effect of the low quality spectra are consistently found for all trace species. For the measurements performed in spring 2018, the instrument received low intensity of light which resulted in large residuals. The reason for the reduced intensity is not completely known, but probably the coupling of the glass fiber to the spectrometer was not performed accurately. Due to the corresponding low signal to noise ratio, higher scaling factors were used, so that good quality data with high RMS values can also be used.

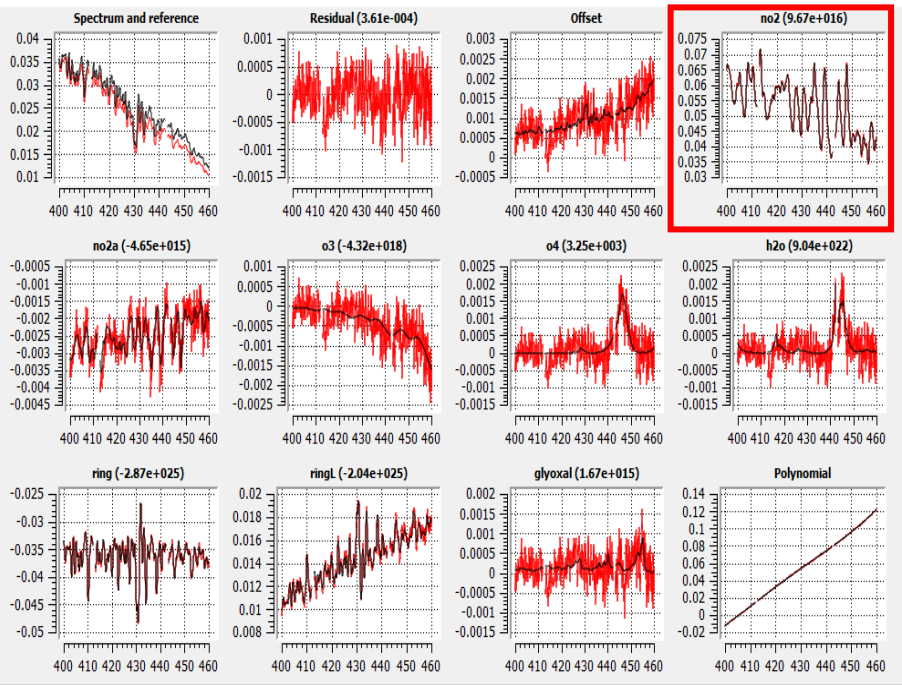

Figure 2.7: Example of a typical DOAS fit result for NO_2. The red lines show the measured optical densities for various absorbers used for the fitting process and the black lines indicate the fitted spectra. The spectrum shown was taken on 1st June 2017 at 07:24 UTC at the elevation angle of 22°.The fit in the red box represents NO_2

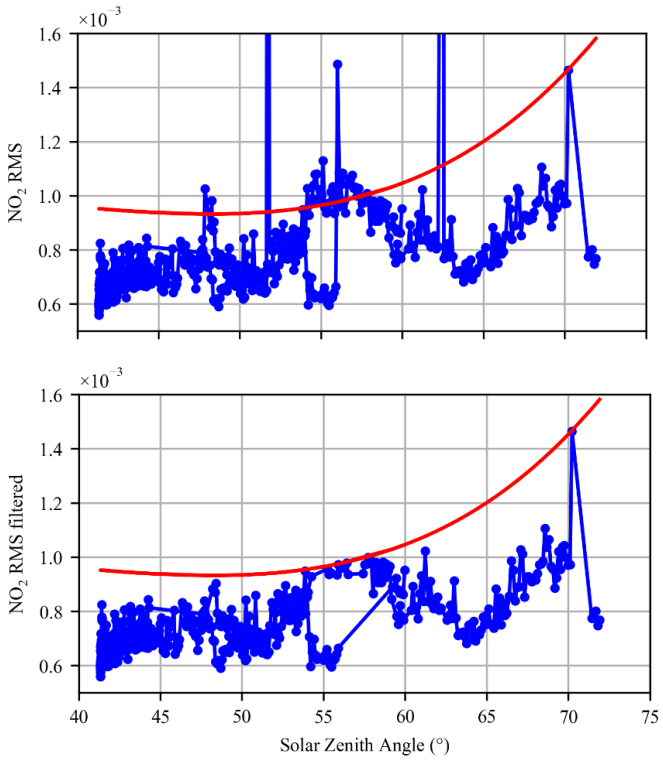

Figure 2.8: Effect of the quality filter. RMS values of the raw (upper panel) and filtered (lower panel) measurements plotted against SZA for 23.02.2018. The red line is the polynomial used as threshold..

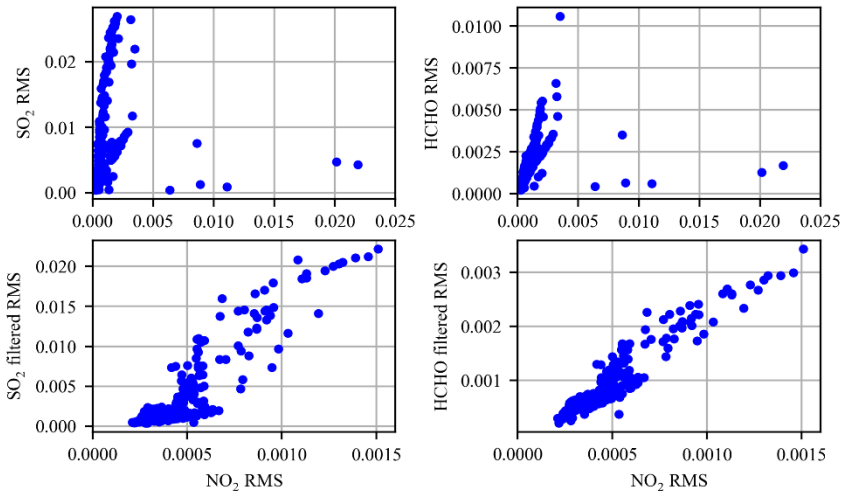

Figure 2.9: Scatter plot between the RMS values of the SO_2 and HCHO analyses versus those of the NO_2 analysis for the observations performed on 18.06.2018.

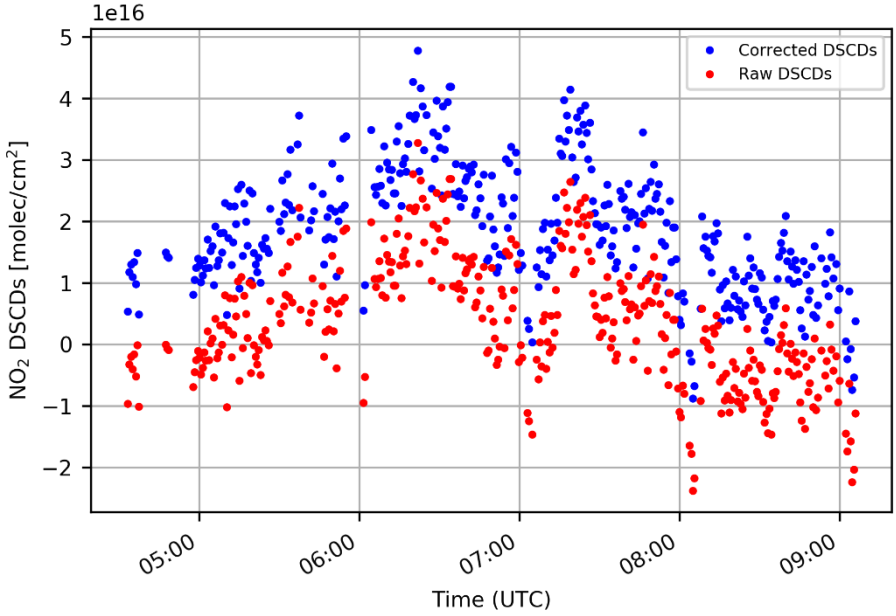

Figure 2.10: Timeline plot of NO_2 DSCDs on 18.02.2018 retrieved with a fixed reference spectrum (red). The blue data represents the DSCDs after application of the bias correction.

2.5.1.2. Determination of the tropospheric vertical column density for the non-working motor period

Due to some technical problem in the instrument, the motor did not work automatically for the 2018-II measurements (the details of which are explained in the next chapter). During that period, the calculation of $DSCD_{offset}$ (SZA) according to Eq.(2.36) was not possible as 90-degree measurements were not available for each elevation angle sequence. To retrieve VCDs for these conditions, the following routine was adopted. The correction was done in two steps as described below.

2.5.1.2.1. Lowest values correction

In an ideal case, a reference spectrum in clean air (trace gas SCD ~ 0) can be used. However, usually, such a clean reference spectrum is not available. Using a reference spectrum with enhanced trace gas absorptions would result in a negative bias of the retrieved results and sometimes even negative DSCDs. In the standard analysis this issue is resolved by fitting an offset, which is determined by a combination of DSCDs from the low elevation angle and 90° (see Eq. 2.35). However, for the measurements where the motor did not work, and sequential 90° DSCDs were not measured, this method is not applicable. Therefore, the DSCDs were treated in the following manner before the calculation of VCDs: The whole time series of a day is analysed with a fixed 90° reference spectrum. If there were negative DSCDs, a bias was added to the whole time series to make the lowest DSCDs equal to zero. Here it should be noted that obvious outliers with very strong negative values were filtered out before. Secondly, if all DSCDs were positive, a bias was subtracted from the whole time series to make the lowest positive values equal to zero. The underlying assumption is that the NO_2 DSCDs of the cleanest measurements should have values close to zero. An example of the correction of negative DSCDs is shown in Figure 2.10. On this day (18.02.2018) a bias of 1.5×10^{16} was added. After adding the bias, still some negative values may exist as can be observed around 8 and 9 am (Figure 2.10), which were considered as outliers and were filtered out before the bias was determined. The SZA threshold used for NO_2 was 85 degrees.

2.5.1.2.2. Stratospheric correction

As mentioned in section 2.2.4.2, Eq. (2.20) the slant column density (SCD) is the sum of the SCDs in the stratosphere and troposphere;

$$SCD_{meas} = SCD_{trop} + SCD_{strat}$$

As the current study focuses only on the tropospheric part, a correction was done to remove the stratospheric part. Usually this is achieved by calculating the time dependent $DSCD_{offset}$ according to Eq. (2.35). However, for the periods without working motors, a different approach has to be applied. A solar zenith angle (SZA) dependent offset is calculated and expressed as follow:

$$Offset_{str} = \left(\frac{1}{\cos\theta} - AMF_{ref}\right) \times \ scaling\ factor \qquad (2.38)$$

This correction takes into account that for low and medium SZA (θ), the stratospheric absorption can be approximated using a geomeric AMF. The scaling factor represents the stratospheric trace gas VCD. For NO_2 a VCD of 2.0×10^{15} was used as for this value the retrieved tropospheric VCDs were found in close agreement with the standard method (Eq. 2.36). The stratospheric DSCD is subtracted from the NO_2 DSCD obtained in the previous step. The resulting values represent the tropospheric NO_2 DSCDs. Typical values of the stratospheric NO_2 VCD as derived e.g. from GOME-1 observations over Lahore are about $\sim2\times10^{15}$ in February/March and 2.8×10^{15} in summer (Wenig et al., 2004). That means that the stratospheric influence in summer is more significant than in spring. Since the scatter of the measurements is higher in spring 2018 than for the other periods, and because the stratospheric DSCD is typically by far lower than the tropospheric DSCD, no stratospheric correction is done for the spring 2018 measurements This can also be observed in Figure 2.11 a.

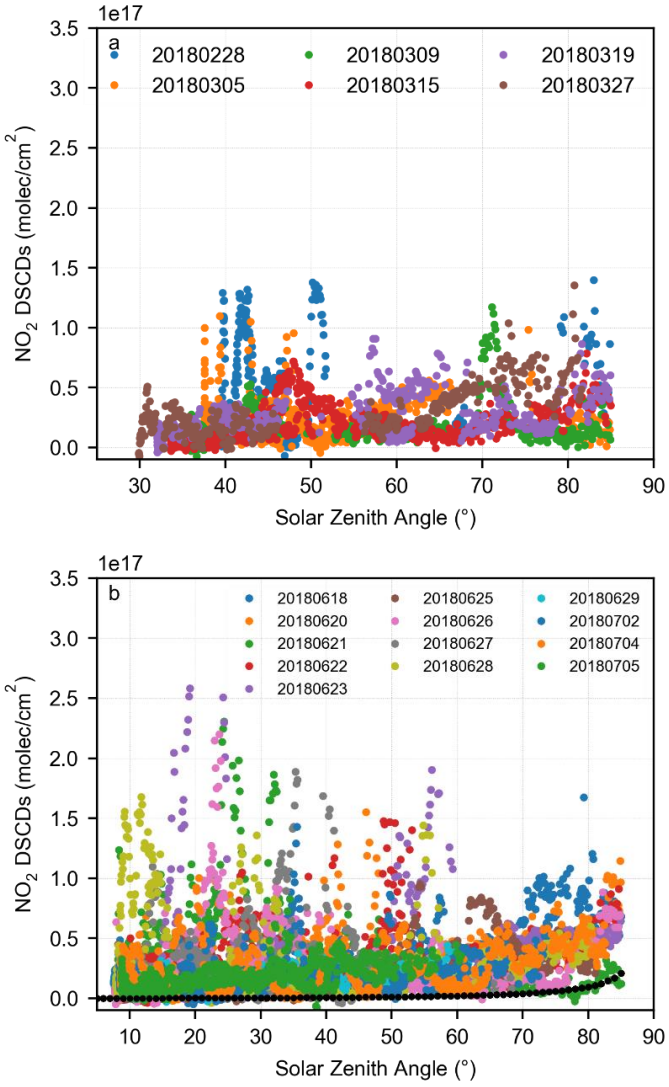

Figure 2.11: a) NO_2 DSCDs (after bias correction) for spring 2018 measurement. b) NO_2 DSCDs for summer 2018 measurements. Black dots represent the stratospheric DSCDs (Eq.2.37).

2.5.1.2.3. Comparison of VCDs determined by two methods

In this section the VCDs calculated by the modified approach were compared with those from the standard method. For that purpose, measurements for which the motor worked well were used. For such measurements both methods can be applied, and the corresponding results can be compared. Although the comparison showed overall quite good agreement, the VCDs calculated with the modified method are systematically smaller than those from the standard method. This indicates that the trace gas absorption in the reference spectrum are not negligible. Figure 2.12 shows a comparison for 29 May 2017 (top), where the retrieved raw DSCDs had negative values and for 18 May 2017 (bottom) where the raw DSCDs had positive values. Although systematic differences are obvious, for the high tropospheric VCDs the errors caused by the alternative approach are of the order of only a few percent. It should also be noted that for the flux calculations such systematic biases almost entirely cancel out.

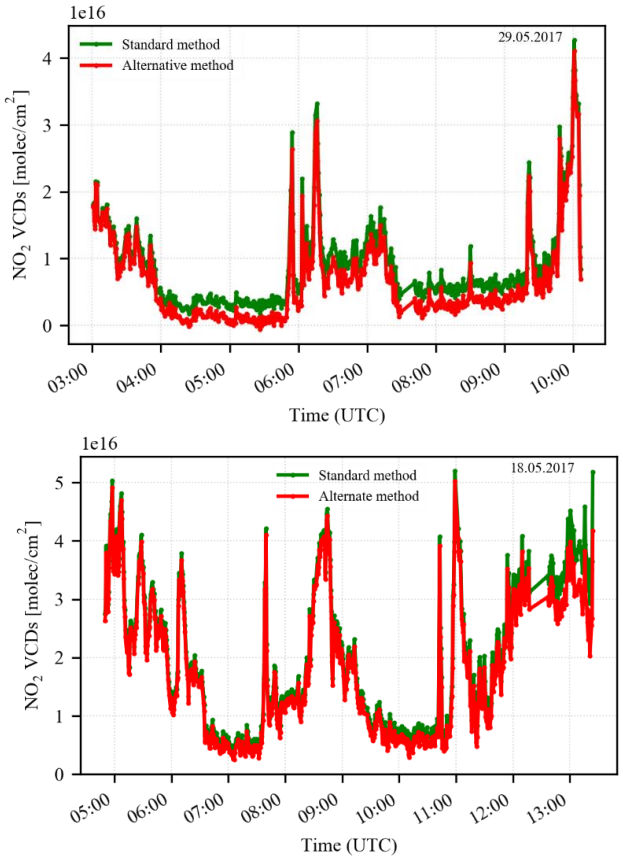

Figure 2.12: NO_2 VCDs calculated by the different SCD correction methods for 18.05.2017 and 29.05.2017. The green lines indicate the results of the standard method and the red lines are for the alternative method.

2.5.2. Sulfur Dioxide Analysis

In this section, details of the SO_2 analysis are described. The recorded spectra were analyzed according to the DOAS technique (Platt & Stutz, 2008) by using the QDOAS software (Fayt et al., 2011). As Fraunhofer reference spectrum, a fixed spectrum, taken around noon at the elevation angle of 90° was used for each day. The wavelength range for the fitting window used was 310-325 nm. A Ring spectrum calculated from the daily Fraunhofer reference spectrum and a second Ring spectrum with a different broad band spectral dependence (calculated from the first Ring spectrum) and a polynomial of 5th order were also included in the spectral fitting process. The fitted cross sections are summarized in Table 2.2. A fit result is shown in Figure 2.13. Bad quality data was filtered based on the RMS of the fit residual as mentioned in section 2.5.1.1.1.

Table 2.2: Fitted cross sections for the SO_2 analysis.

Fitted Cross Sections	References
SO_2	at 298K (Vandaele, Hermans, & Fally, 2009)
O_3	at 233 K (I_0 corrected) (Serdyuchenko et al., 2014)
NO_2	at 294K (Vandaele et al., 1998)
HCHO	at 297K (Meller, 1992)

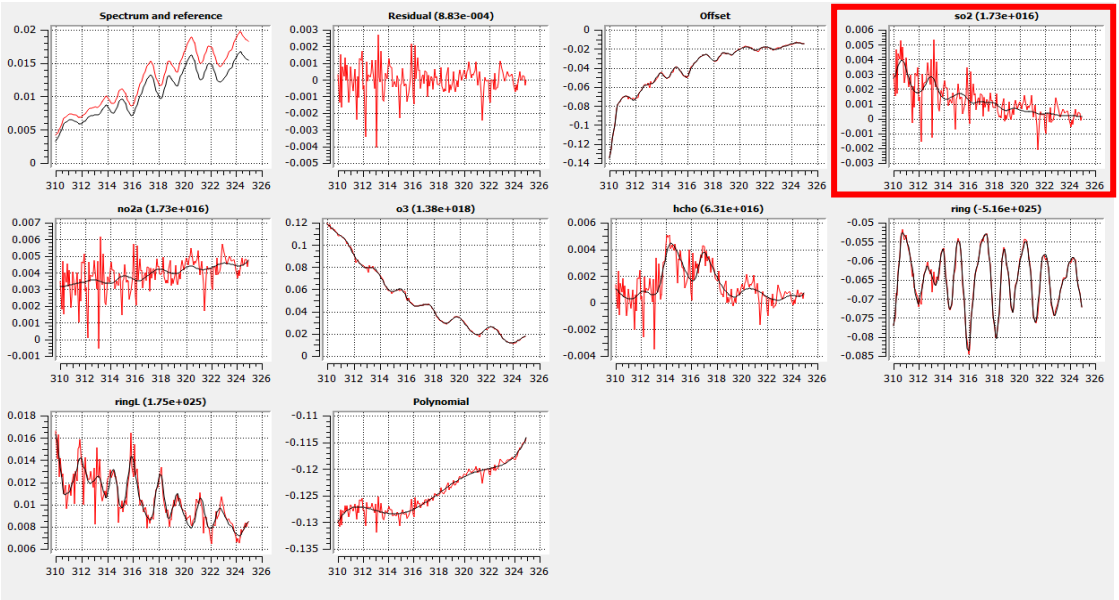

Figure 2.13: Example of a typical DOAS fit result for SO_2. The red lines show the measured optical densities for various absorbers used for the fitting process, whereas the black lines indicate the fitted spectra. The spectrum shown was taken on 1st June 2017 at 07:02 UTC at an elevation angle of 22° using the Tube MAX-DOAS instrument.

2.5.2.1. Determination of the tropospheric vertical column density

VCDs for the period where motor was in working condition were determined by the method mentioned in section 2.4.
However, before this conversion could be applied, a correction for an ozone interference has to be applied. Such an interference was especially observed for the measurements performed in summer 2018. In the wavelength window used for the SO_2 analysis (310 to 325 nm), strong O_3 absorptions are present (Platt & Stutz, 2008) (see Figure 2.14) Especially at high SZA, this interference can affect the retrieved SO_2 SCDs. In most of the days, during summer 2018, such a strong interference of O_3 with SO_2 was observed causing enhanced SO_2 DSCDs for measurements with high O_3 absorptions (at high SZA) (Figure 2.15). Interestingly, no obvious SZA dependence was observed for the other two measurement periods (i.e., summer 2017 and spring 2018). One probable reason might be the change in the spectral resolution of the spectrometer for these campaigns. Full width half-maximum (FWHM) values for three measurement periods are shown in Table 2.3.

Table 2.3: Full width at half maximum (FWHM) values for the SO_2 analysis window for the different measurement campaigns

Campaign	Min FWHM at 310 nm	Max FWHM at 310 nm	Min FWHM at 325 nm	Max FWHM at 325 nm
2017	0.645	0.695	0.625	0.650
2018-I	0.640	0.700	0.570	0.640
2018-II	0.595	0.645	0.585	0.621

So, to minimize the effect of the O_3 interference, SO_2 VCDs were calculated after subtracting a time dependent $DSCD_{offset}$ similar to NO_2. The $DSCD_{offset}$ (t) Eq. (2.36) is calculated from the combination of 22° and 90° DSCDs and applied to correct for the O_3 interference. In contrast, for the campaigns where no such interference has been observed, a constant DSCD offset is determined and added to the DSCDs before the conversion to SO_2 VCDs (dividing by AMF_α).

For the measurements without functioning motor, where only very few 90° measurements were available, the DSCDs were corrected in the similar way as for NO_2 as described in section 2.5.1.2. The corrected DSCDs were then divided by the geometric AMF to derive the VCDs. Again, the VCDs calculated without the 90° measurements were found to be close to the ones determined by the standard method. Figure 2.16 shows a comparison of the VCDs calculated from both methods.

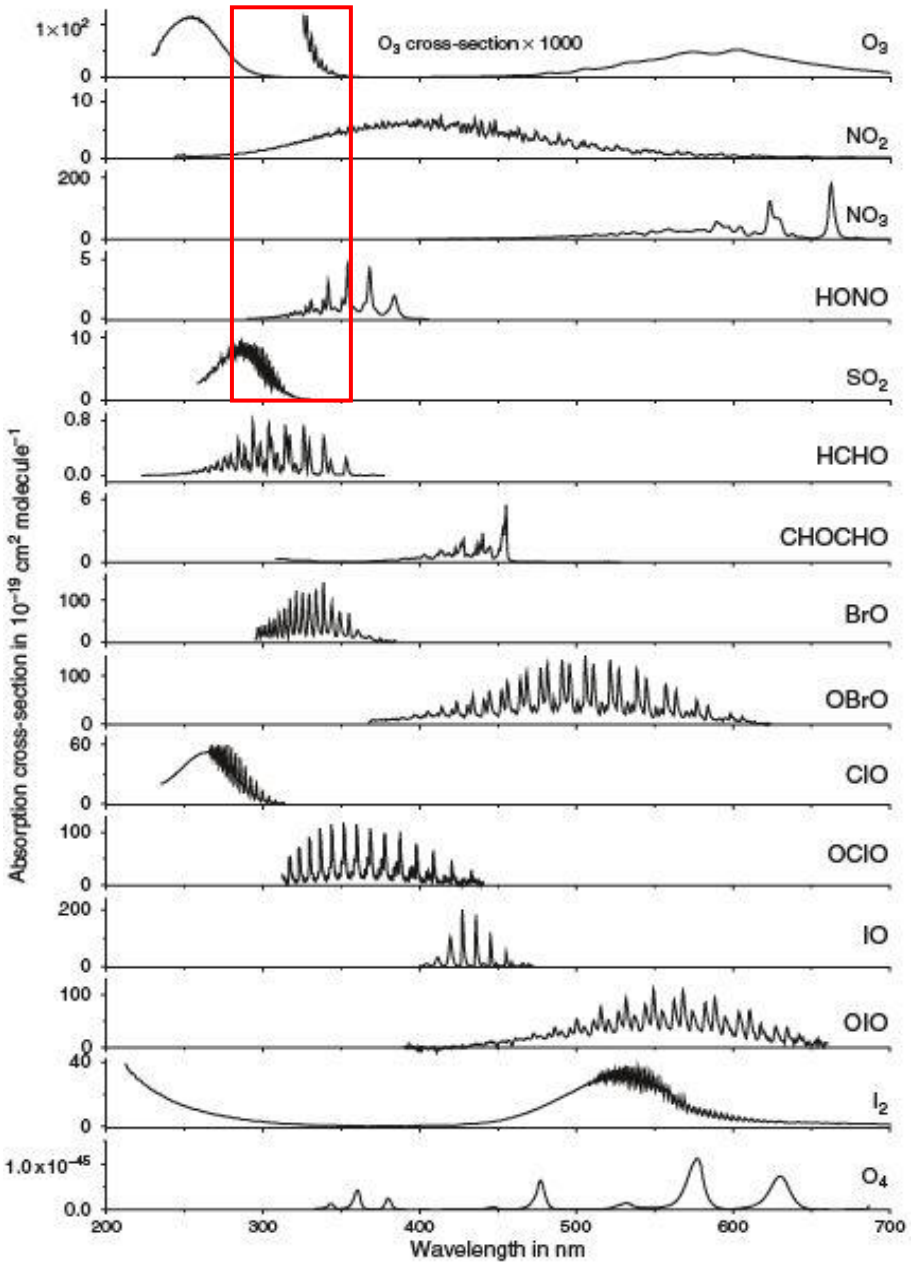

Figure 2.14: Absorption cross-sections of various atmospheric trace species. The red lines indicate the wavelength window used for the SO_2 analysis. The corresponding cross sections of O_3 and SO_2 are shown in the 1st and 5th panel, respectively. The figure is taken from (Platt & Stutz, 2008).

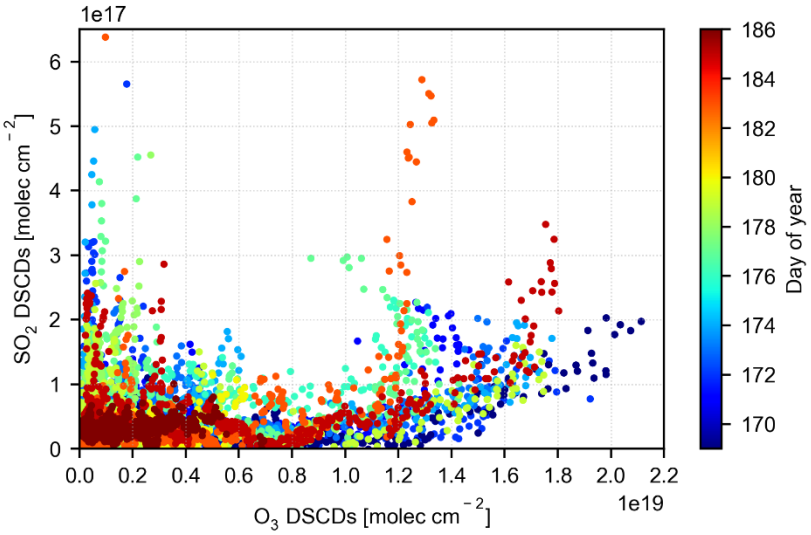

Figure 2.15: Scatter plot between the SO_2 and O_3 DSCDs during the summer 2018-II measurements.

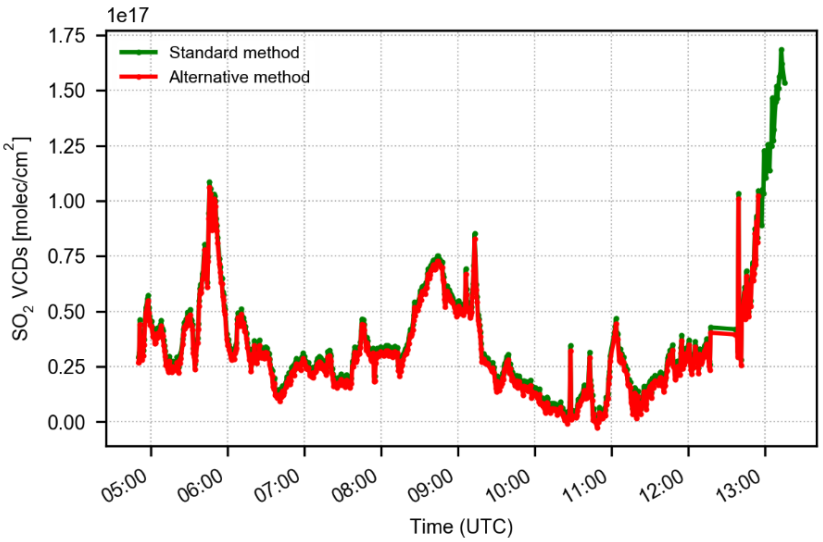

Figure 2.16: SO_2 VCDs calculated with the standard method (green) and with the alternative method for periods in which the motor did not wotk (red) for the observations performed on 18.05.2017.

2.5.3. Formaldehyde Analysis

In this section, details of the formaldehyde analysis are described. The recorded spectra are analyzed according to the DOAS technique (Platt and Stutz, 2008) by using the QDOAS software (Fayt et al., 2011). One daily fixed Fraunhofer reference spectrum at the elevation angle of 90 degrees was used. The wavelength range for the fitting window used is 324-359 nm. The SZA threshold used for the formaldehyde analysis is 85 degrees. The data is filtered on the basis of the NO_2 RMS as described in section 2.5.1. All cross sections are calibrated in air wavelengths. The fitted cross sections are presented in Table 2.4, and an example of DOAS fit analysis is presented in Figure 2.17.

Table 2.4: Fitted cross sections for HCHO analysis

Fitted Cross-Sections	Details
HCHO	at 297K (Meller, 1992)
BrO	at 223K (Fleischmann et al., 2004)
O_3	O_3 at 233K (Serdyuchenko et al., 2014)
	O_3a at 223 K (Serdyuchenko et al., 2014)
O_4	at 293 K (Thalman & Volkamer, 2013)
NO_2	at 294 K (Vandaele et al., 1998)

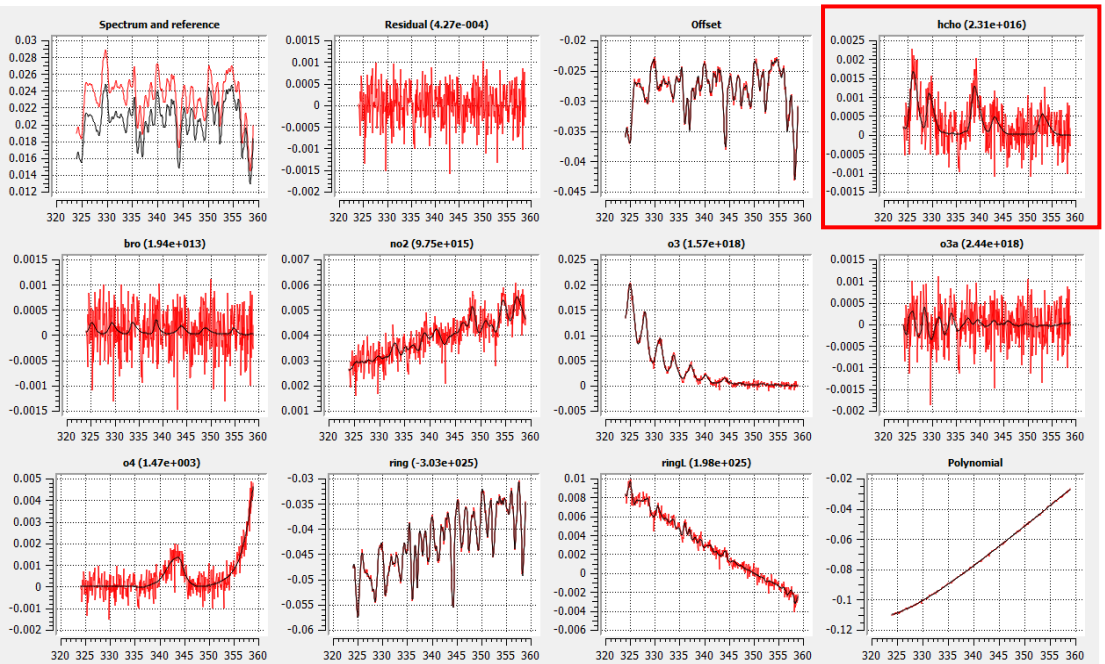

Figure 2.17: Example of a typical DOAS fit result for formaldehyde. The red lines show the measured optical densities for various absorbers used for the fitting process, whereas the black lines indicate the fitted spectra. The spectrum shown was taken on 01 June 2017 at 07:02 UTC at an elevation angle of 22°.

2.5.3.1. Determination of the tropospheric vertical column density

As for the other two trace gases, the VCDs for formaldehyde were also determined by two methods for periods with working or non-working motor. For the measurements where the motor worked, the $DSCD_{offset}$ (2.35) is determined by the combination of measurements at a low elevation angle (α) and 90 degrees (standard method). A mean of the DSCD offset is added to the DSCDs at 22 degrees. The corrected DSCDs are then divided by the (geometric) AMF for an elevation angle of 22° (~ 2.67).

For the period with only few measurements at 90°, the corrected DSCDs (as described in section 2.5.1.2) are simply divided by the geometric AMF. But for HCHO, in contrast to NO_2 and SO_2, a large difference is found if the lowest HCHO DSCD is set to zero. This can be explained by the fact that, an enhanced background value exists for all measurements for HCHO, while the DSCDs for NO_2 and SO_2 can reach rather low values outside of the pollution plumes. Figure 2.18 represents a comparison of the VCDs calculated by the different methods (with and without using zenith measurements).

To correct this bias, a constant SCD_{ref} was added to the whole time series which is calculated as follows.

The first outcome of the analysis, the DSCD, is the difference between the SCD_{meas} and SCD_{ref} (section 2.4.2.2).

The $DSCD_{meas}$ can be written as

$$DSCD_{meas} = SCD_{meas} - SCD_{ref} \tag{2.39}$$

or;

$$DSCD_{90} = SCD_{90} - SCD_{ref} \tag{2.40}$$

and

$$DSCD_{22} = SCD_{22} - SCD_{ref} \tag{2.41}$$

And also;

$$AMF = \frac{SCD}{VCD}$$

or

$$SCD = AMF \times VCD$$

Eqs. (2.40) and (2.41) can also be written as;

$$DSCD_{meas} = (VCD \times AMF_{meas}) - SCD_{ref} \tag{2.42}$$

or

$$VCD = \frac{DSCD_{90} + SCD_{90}}{AMF_{90}} \quad (2.43)$$

and

$$VCD = \frac{DSCD_{22} + SCD_{ref}}{AMF_{22}} \quad (2.44)$$

Equating Eqs. (2.43) and (2.44); value of SCD_{ref} can be obtained as follow;

$$SCD_{ref} = -\frac{2.67 \times DSCD_{90} - DSCD_{22}}{1.67} \quad (2.45)$$

where, AMF_{90} = 1, and AMF_{22} = 2.67

For the non-working motor period, the VCDs calculated after the addition of the constant (Eq. 2.45) were considered as they agreed very well with the VCDs calculated from the standard method (see Figure 2.19).

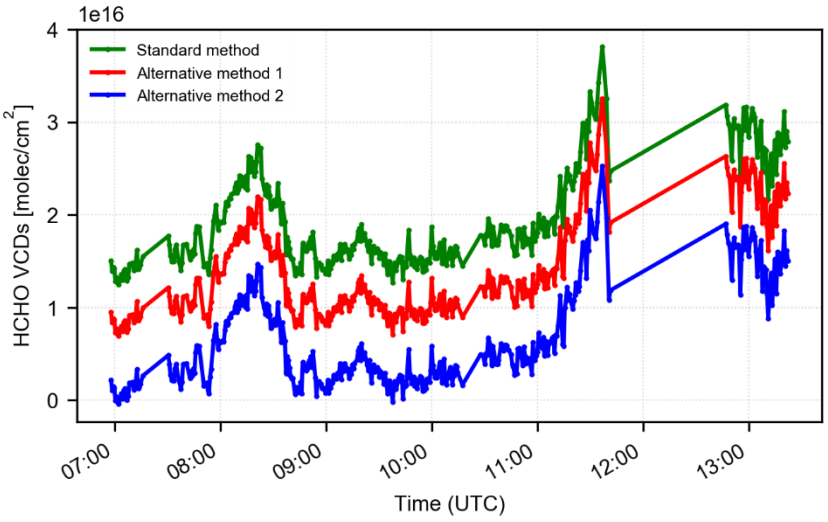

Figure 2.18: Formaldehyde VCDs calculated by differently treated DSCDs for the measurements performed on 20.05.2017. The standard and alternative method represent the VCDs, calculated with and without sequential 90° SCDs, respectively. The alternative method 1 indicates the VCDs where no correction was performed on low elevation angle DSCDs and the alternative method 2 represents the VCDs calculated where the lowest DSCDs were set to zero.

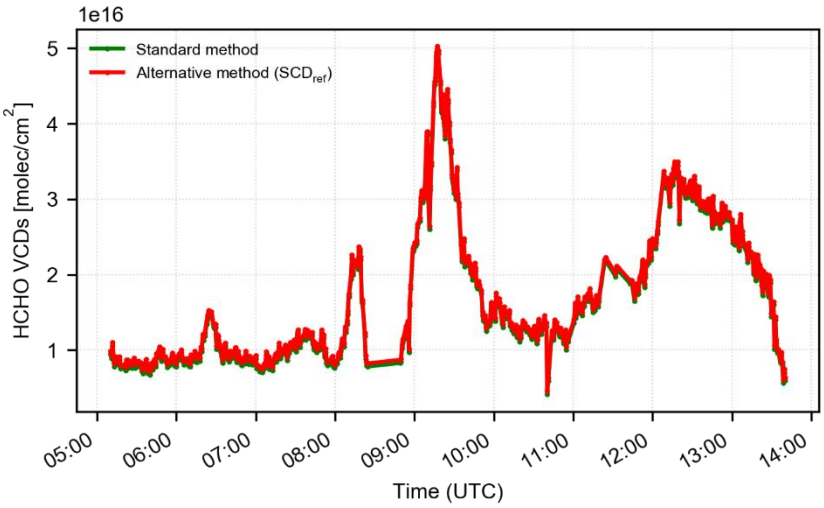

Figure 2.19: Formaldehyde VCDs calculated for the 23.06.2018 measurements. VCDs calculated by assuming a constant SCD_{ref} (alternative method) were found closely agreeing to the VCDs calculated by using the standard method.

2.5.4. Glyoxal Analysis

In this section, the settings for spectral analysis of glyoxal are described in detail. The recorded spectra were analyzed according to the DOAS technique (Platt and Stutz, 2008) by using the QDOAS software (Fayt et al., 2011). The wavelength range for the fit window used is 400-460 nm. The SZA threshold used for the glyoxal analysis is 85 degrees. For the Fraunhofer reference spectrum, a fixed spectrum, taken around noon at an elevation angle of 90° was used for each day. A Ring spectrum calculated from the daily Fraunhofer reference spectrum) and a second Ring spectrum with different broad band spectral dependence (calculated from the first Ring spectrum) and a polynomial of 5th order were also included in the spectral fitting process. Low quality data was filtered out on the basis of NO_2 RMS as described in the section 2.5.1.1.1. Gaps were also introduced to minimize the influence of hot pixels. The fitted cross sections are presented in Table 2.5, and an example of the DOAS analysis for CHOCHO is presented in Figure 2.20.

The tropospheric VCDs of glyoxal were determined in the same way as for formaldehyde as described in the previous section (2.5.3.1).

Table 2.5: Fitted cross-sections for the glyoxal analysis

Fitted Cross Sections	Details
CHOCHO	at 296 K (Volkamer et al., 2005)
NO_2	at 294 K (Vandaele et al., 1998) (I_0-correction with 1×10^{17} molec/cm^2 (Aliwell et al., 2002; Pinardi et al., 2013))
O_3	at 233 K (Serdyuchenko et al., 2014)
O_4	at 293 K (Thalman & Volkamer, 2013)
H_2O	at 296 K (Rothman et al., 2010)

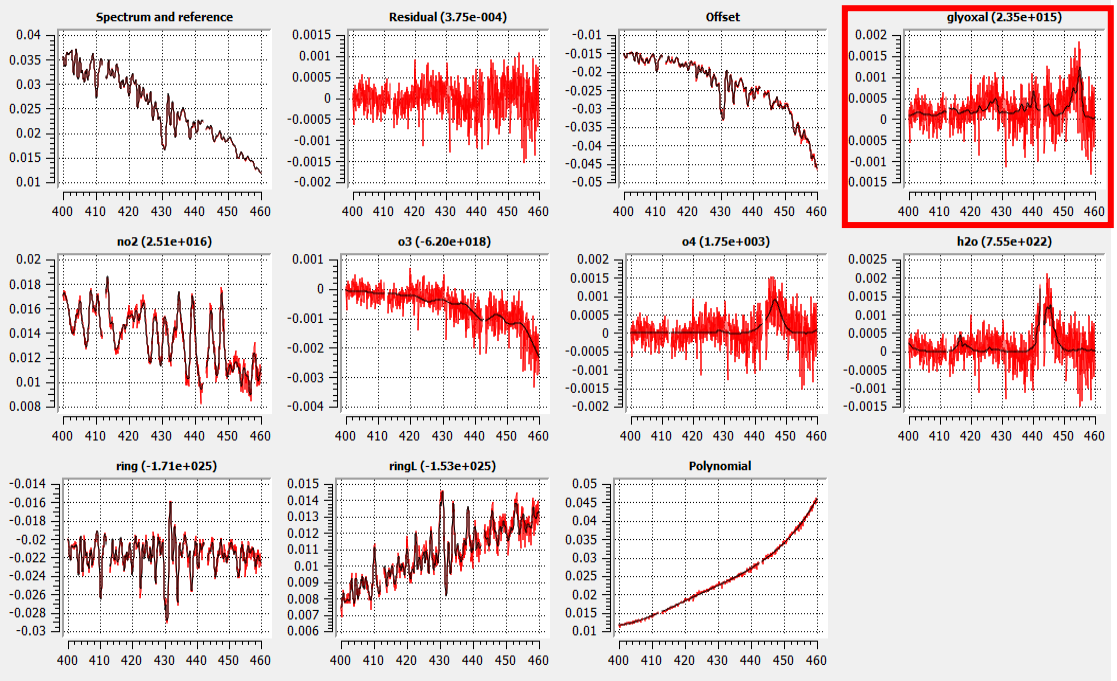

Figure 2.20: Example of a typical DOAS fit result for glyoxal. The red lines show the measured optical densities for various absorbers used in the fitting process, whereas the black lines indicate the fitted spectra. The spectrum shown was taken on 1st June 2017 at 08:07 UTC.

2.6. EMISSION ESTIMATION OF POLLUTION SOURCES

The mobile MAX-DOAS technique, in combination with the wind information allows the estimation of total emissions by encircling the source (see e.g., Johansson et al., 2008; Rivera et al., 2009; Wagner et al., 2010). The encircled area or the source can be as small as an industrial area (Claudia Rivera et al., 2010), an airport (Frins et al., 2016) or a power plant (Wu et al., 2017) or as large as a megacity (Ibrahim et al., 2010; Shaiganfar et al., 2011; Shaiganfar, 2012; Shaiganfar et al., 2017). In this study, the emissions from the mega city Lahore and power plants have been estimated, using car MAX-DOAS observations. Determining emissions from mobile MAX-DOAS measurements is a top-down emission estimation procedure that quantifies real-time emissions. This procedure can also be used to testify bottom-up emission inventories (Shaiganfar, 2012).

For car MAX-DOAS measurements, an additional horizontal integration is achieved along with the inherent vertical integration because of the moving platform. By using this two-dimensional integration in combination with wind data, the total flux of trace gas molecules from the encircled area can be calculated by using the closed integral method (CIM) as described in Shaiganfar (2012):

$$F = \oint_S VCD(s)\vec{\omega} \cdot \vec{n} \cdot ds \tag{2.46}$$

The integral is replaced by the sum of the fluxes, calculated for the individual measurements along the whole driving route and Eq. (2.46) can be rewritten as:

$$F \approx \sum_i VCD_i \cdot \omega_i \cdot sin(\beta_i) \cdot ds \tag{2.47}$$

The different symbols represent the following quantities:

VCD_i = trace gas VCD at each measurement point (here the average between the start and stop time of a measurement is chosen)

$\vec{n}$ = the vector perpendicular to the driving direction and parallel to the ground.

$\vec{\omega}_i$ = the averaged wind speed over the measurement area

The angle β_i is the angle between the driving direction and the averaged wind vector.

The distance (ds) between two consecutive measurements and the angle β between the driving route and the wind direction was calculated from the positions of the two measurements for each section of the route.

The flux at each individual measurement point is determined through Eq. (2.47). The total Flux (F) is the difference between the out-flux and in-flux of the trace gas. The in-flux and the out-flux are determined according to the wind direction.

A schematic diagram of the flux calculation is shown in Figure 2.21. Each dot in the circle represents the VCDs at the corresponding measurement location, while the black arrows represent the respective wind vectors at each point.

The fluxes of HCHO, NO_2 and SO_2 are calculated according to Eq. (2.47) whereas for the calculation of the total NO_x emissions, corrections for the NO_x lifetime and the partitioning between NO and NO_2 needs to be applied. The lifetime correction factor ($C\tau$) can be determined by the following relation (Shaiganfar, 2012)

$$C_\tau = e^{\frac{t}{\tau}} = e^{\frac{\frac{r}{\omega}}{\tau}} \tag{2.48}$$

where r is the radius of the circle, ω is the averaged wind speed over the encircled area, and τ is the lifetime of NO_x. So, t is the ratio between r and ω. The NO_x lifetime is assumed to be 4 hours ± 0.5 hours (Beirle et al., 2011).

NO_2 is primarily emitted as NO. The rate of the NO_2 photolysis and the ozone concentration determine the partitioning between NO and NO_2 (Shaiganfar, 2012). These processes are faster than transport times of the species from the emission source to the measurement location. So, to compensate for the NO_x partitioning, a chemical transformation factor is applied:

$$c_L = \frac{[NO_x]}{[NO_2]} \tag{2.49}$$

According to Seinfeld & Pandis, (2006) a chemical partitioning factor c_L of 1.32 was used.

After applying both corrections, the NO_x emissions can be estimated as;

$$F_{NO_x} = C_L \cdot C_\tau \cdot F_{NO_2} \tag{2.50}$$

Due to technical problems or bad quality data (section 2.5.1.1), sometimes large gaps occurred between individual measurements. To estimate the corresponding uncertainties the flux in the current study was calculated in both forward and backward driving directions (for more details please refer to section 4.1.3).

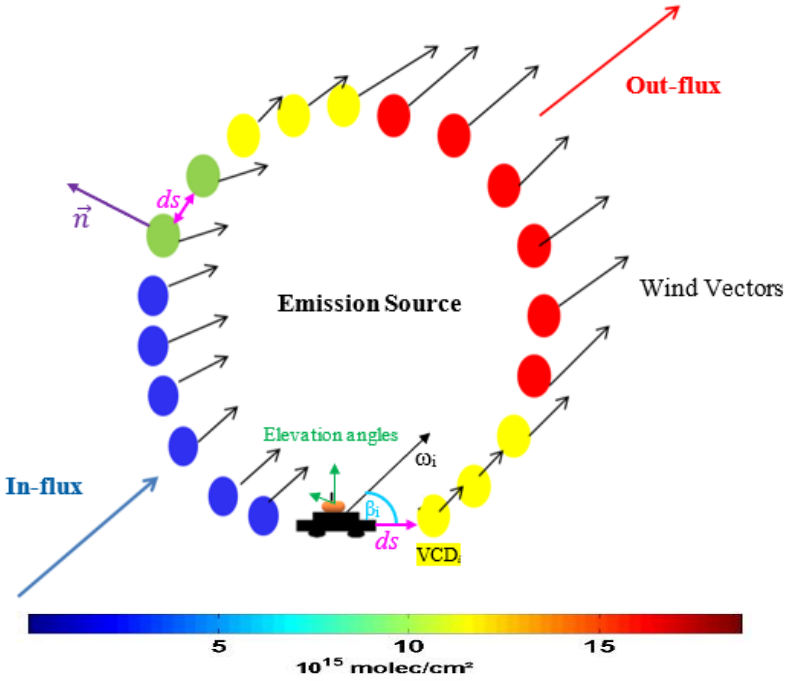

Figure 2.21: A schematic representation of car MAX- DOAS measurements encircling a source (e.g., a city or a power plant). The colored solid circles represent trace gas VCDs. (Figure adapted from Shaiganfar, 2012)

2.6.1. Wind Data

Wind plays a crucial part in the flux determination. Suitable wind conditions are of utmost importance to calculate the emissions from the encircled area. In this thesis, wind information is taken from the operational analysis data of the European Centre for Medium-Range Weather (ECMWF). ECMWF was chosen as data is available over the whole measurement area. The horizontal resolution of the data is 0.1 degree, whereas vertically data is available up to about 80 km above sea level, distributed in 137 levels. The temporal resolution of the data is six hours with four outputs at 00, 06, 12 and 18 UTC for each day. The six hourly outputs of wind speeds and directions were averaged up to the altitude of approximately 500 m above ground level, for which the lowest 14 levels were considered. Wind speeds and directions were interpolated spatially and temporally. For the temporal interpolation the mean time of the measurement period was calculated, and the wind averages were interpolated according to this time. For example, if the measurement start time of the circle was 08:09 and measurement end time of the circle was 13:17 UTC then the mean time is 10:43 UTC, and so, the temporal interpolation of the wind data was done between the 6 and 12 UTC outputs. Spatially, the wind information is interpolated according to the individual MAX-DOAS measurement.

ECMWF wind data was also compared with the wind observations from EHS (Enhanced Surveillance) and ADS-B (Automatic Dependence Surveillance-Broadcast) data of aircraft radars. Measurements from aircrafts were obtained through a DVB-T (Digital Video Broadcasting-Terrestrial) antenna at the frequency of 1090 MHz. The antenna was

connected to a laptop. To receive and calculate the data, the software dump1090 and the python module pyModeS from GitHub were used (Sun et al., 2019). For the decoding a self-written decoding software[3] was used. Observations from aircrafts at ± one hour of the ECMWF output times (0, 6, 12 and 18 UTC) were averaged over the area of 1×1 degree at altitude intervals of 200 meters. For the comparison, winds with speeds below 2 m s^{-1} and variable directions were not considered. In Figure 2.22, wind rose plots for winds averaged between 400-600 m above sea level or approximately 200-400 meters above ground level are presented. For this altitude range only 14 data points are valid and so these windrose plots are based on the only 14 values. To gather better statistical data an additional altitude ranges up to 1000 m above sea level was used. The averaged wind directions for this additional altitude range showed a bias of around 45 degrees between both datasets (Figure 2.23). Here it should be noted that winds calculated from the aircraft observations are also prone to uncertainties and errors. According to the "Aircraft Meteorological Data Relay" reference manual, for aircraft winds, the uncertainty sources can be errors of the airspeed, of the Mach number, of the navigation system etc. (For details of these errors please refer to the manual WMO, (2003)). The World Meteorological Organization, (2017), also reported a bias of around 10-15 degrees in wind directions. Moreover, as a result of the poor observational network in Pakistan, ECMWF modelled winds are also prone to large uncertainties, as ECMWF data is based on assimilation of model and observations. Since both data sets have their uncertainties, it is difficult to judge from this comparison, which data set is closer to the truth. Since the aircraft wind data are not available for all measurement campaigns, we decided to use the ECMWF wind data for the flux calculation. However, to estimate the flux uncertainties related to the uncertainties of the wind direction, we performed several flux calculations using the original ECMWF wind data and modified ECMWF wind data, for which the wind direction was changed in steps of 0.1° between the original averaged ECMWF winds and the original averaged ECMWF winds plus 45°. The averaged flux values within this range yielded the estimated emission values for each circle. The standard deviation of the flux values for the chosen interval represents the flux uncertainty caused by the uncertainty of the wind direction. This procedure is further illustrated in Figure 2.24 and Figure 2.25, where the fluxes for varying wind directions are calculated for two selected days. On 17.02.2018 (Figure 2.24) the maximum flux is found for assumed wind directions close to the original ECMWF wind direction and the shifted ECMWF wind direction indicating that the ECMWF wind data are well suited for the flux calculation on that day. Also, the difference between the maximum and minimum flux values in the considered wind direction interval is rather small. It should be noted that the flux calculations are presented for two integration directions i.e., clockwise, and counterclockwise. The difference between both results represents the error related to gaps in the measurement time series (see also sections 2.6 and 4.1.3).

[3] The code is written and provided by Kornelia Mies, Satellite Remote Sensing Group, MPIC, Mainz.

In contrast, for the measurements on 31.05.2017 (Figure 2.25) not very consistent results of the flux calculations are found. The derived fluxes are even negative indicating that the wind conditions on that day were not well suited for the calculation of emission fluxes. Moreover, the wind fields on this day also showed large variability between the 0, 6 and 12 UTC ECMWF outputs. Here it should be noted that on that day similar results were also found for the other trace gases.

The flux calculation results for all the trace gases for the other days can be found in appendix A.

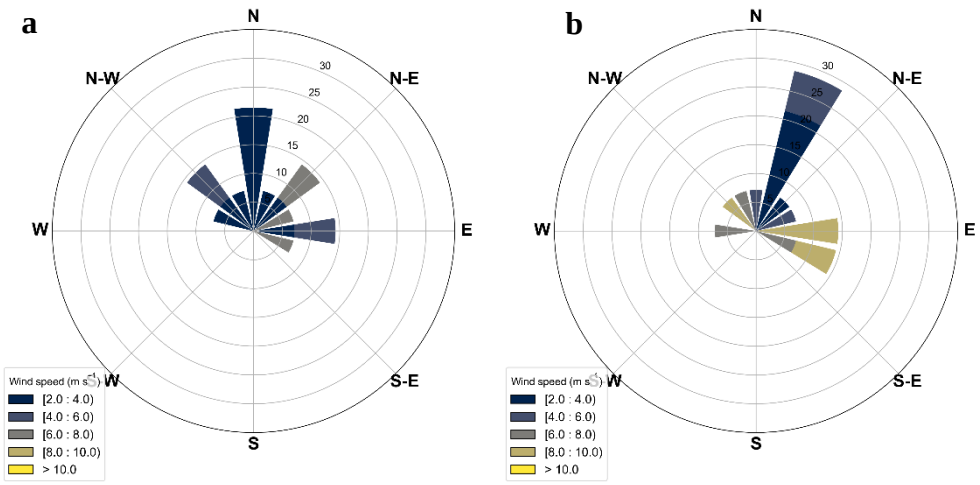

Figure 2.22: Windrose plots for ECMWF (a) and aircaft (b) wind data, averaged over 400 to 600 m altitude.

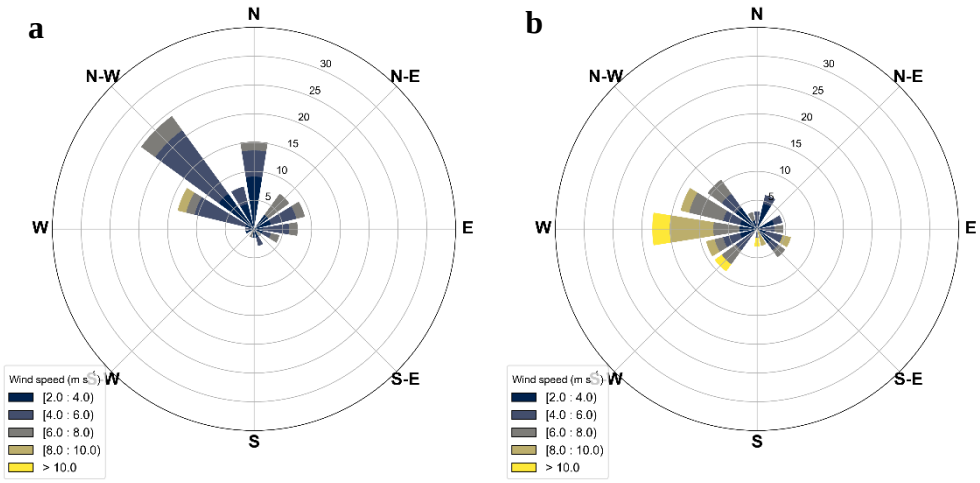

Figure 2.23: Windrose plots for ECMWF (a) and aircaft (b) wind data, averaged over 400 to 1000m asl.

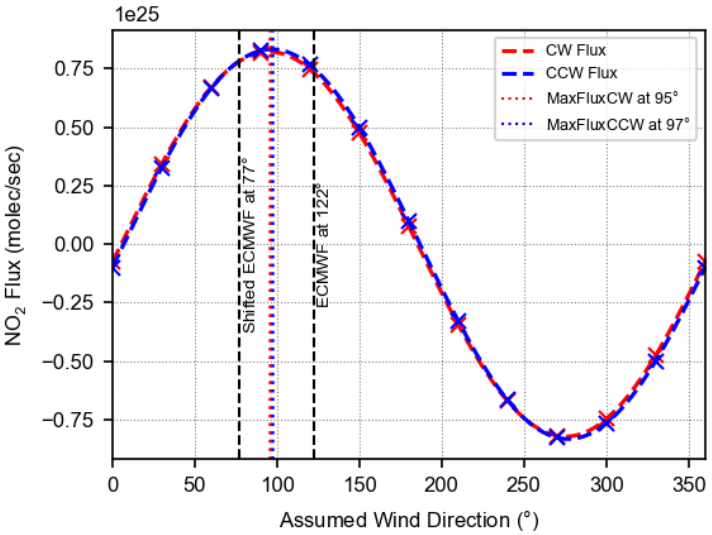

Figure 2.24: NO_2 fluxes calculated for different assumed wind directions on 17.02.2018. The dashed vertical black lines indicate the averaged original ECMWF and shifted ECMWF wind directions (122 and 77 degrees), respectively. The maximum flux is found for a wind direction of approximately 100 degrees. The red and blue symbols represent the results for clockwise (CW) and counterclockwise (CCW) directions.

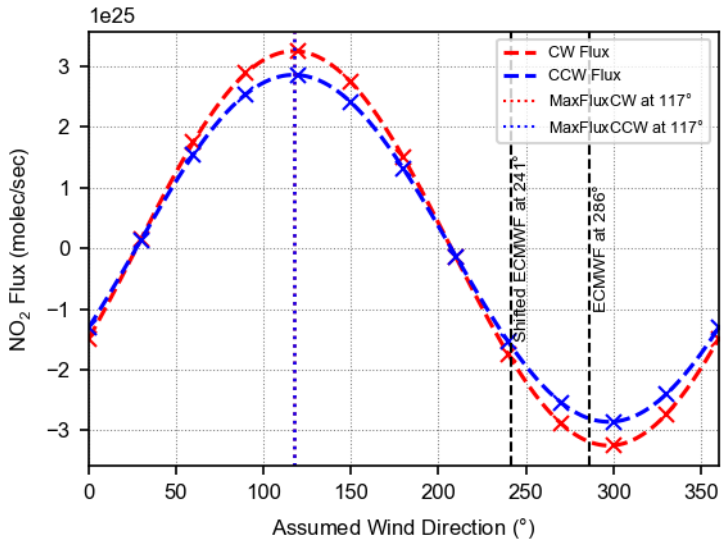

Figure 2.25: NO_2 fluxes calculated for different assumed wind directions on 31.05.2017. The dashed vertical black lines indicate the averaged original ECMWF and shifted ECMWF wind directions, respectively. The maximum flux is found for a wind direction of approximately 120 degrees. The red and blue symbols represent the results for clockwise (CW) and counterclockwise (CCW) directions.

2.6.2. Suitability Criteria for Flux Calculations

The selection of wind data needs special attention. Otherwise, it may lead to high uncertainties for the flux results.

Wind conditions suitable for emission estimations should meet the following conditions:

1. Wind speeds should not be calm or too low.
2. Wind directions should be consistent, i.e. not much variable between two interpolated outputs and also not variable over the measurement location (Ibrahim, 2009).

The equation 2.47 works well if the winds and emissions are constant for the measurement period. Therefore, for consistency, we devised certain criteria to select measurements to be suitable for flux calculations. The following three considerations were taken into account while scrutinizing the measurements for flux estimations.

1. Measurement circles with large gaps at the point of influx or out-flux were not used for the flux estimation.
2. The flux is estimated for measurement periods only with uniform wind directions.
3. The minimum threshold for wind speed for larger circles with radii around 12 km is set to 3.3 m s^{-1} (12 km h^{-1}) while for the smaller circles with radii around 8 km it is set 2.4 m s^{-1} (~8.5 km h^{-1}).

Based on the above-mentioned criteria, we divided the measurement days (or circles) into the three following categories.

The **category I** includes measurement days where the wind conditions are ideal, as mentioned above. For this category, measurement days with wind speeds $\geq$ 3.3 m s^{-1} and $\geq$ 2.4 m s^{-1} for large and small circles, respectively, were considered. In addition to the wind speeds, stable wind directions between the two interpolated ECMWF outputs were also considered (Figure 2.26). Here it should be noted that two days (17 May 2017 and 06 March 2018), for which the wind directions were different in the second ECMWF output, were still put to category I. This was done as the change in wind direction very probably occurred after the respective measurement circles were finished.

In **category II**, wind speeds are relatively low (not lower than 2.3 m s^{-1}) or directions are not uniform between the two ECMWF outputs. These days are not ideal but still provide useful information. In Figure 2.27 an example of category II wind conditions is shown.

In **category III**, fall the measurement days where speeds are rather low ($<$2 m s^{-1}) and/or directions are highly variable ($\sim \geq 30°$) within the measurement area for one ECMWF output or between the two ECMWF outputs. Figure 2.28 shows one such example. On 18 May, wind speeds were not only lower than 2 m s^{-1} but also the directions at all three outputs were different. Moreover, the days where there were significant gaps ($\sim \geq$ 10 km) at the sides of influx or out-flux also fall in this category**.** In Figure 2.29, one such day with a measurement gap of about 16 km can be seen at the west and southwest side of the route.

On this day wind speeds were also low. These measurement days have not been used for flux/emission estimation due to very high uncertainties.

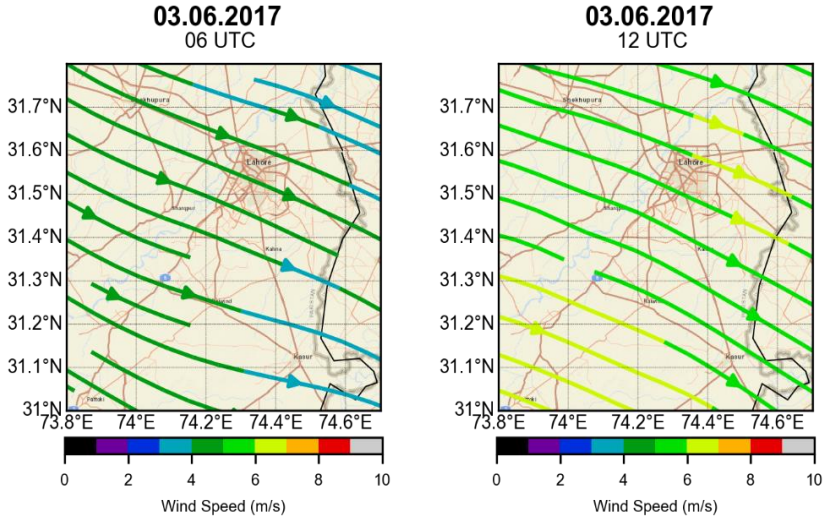

Figure 2.26: An example of category I wind conditions is shown. ECMWF averaged wind data over the measurement area on June 03, 2017 at 6 UTC (left) and 12 UTC (right). Mean measurement time on this day was 06:58. Wind direction between both interpolated ECMWF output were found to be stable. Wind speeds were also found higher than 4 m s^{-1} over the measurement zone.

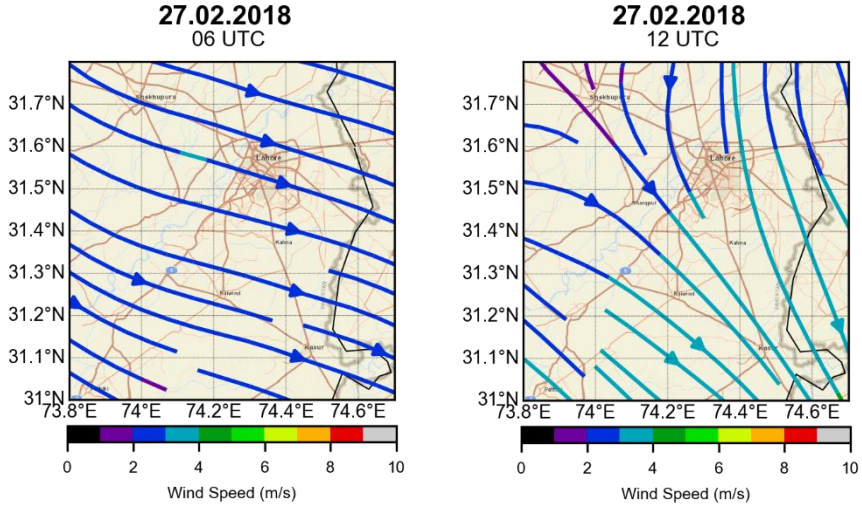

Figure 2.27: Category II wind conditions are shown. ECMWF averaged wind data over the measurement area on Feb 27, 2018 at 6 UTC (left) and 12 UTC (right). The mean measurement time on this day was 06:09. The wind direction for both ECMWF outputs were found to be systematically different. Wind speeds were rather low (<3 m s^{-1}) over the measurement area.

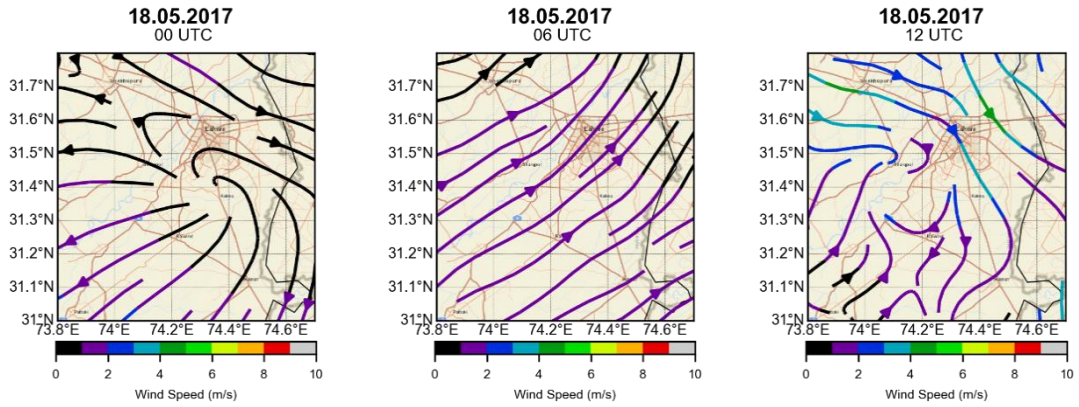

Figure 2.28: An example of category III wind conditions is shown. ECMWF averaged wind data over the measurement area on May 18, 2017 at 0, 6 and 12 UTC are plotted. Two circles were performed on that day, between 4:49 and 11:34 UTC. Highly variable wind directions with speeds lower than 2 m s^{-1} can be observed.

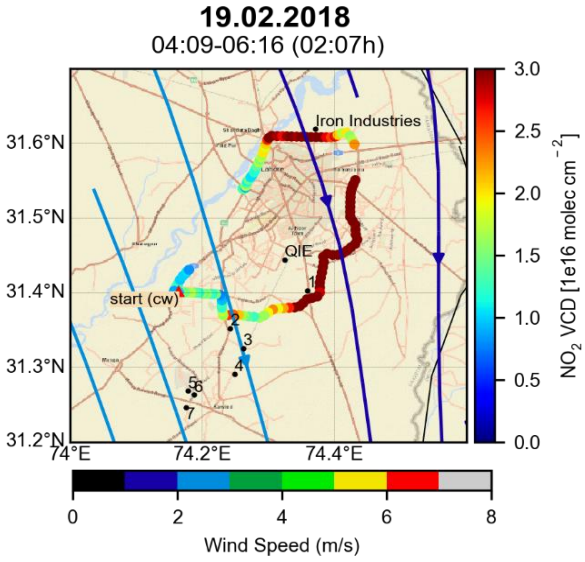

Figure 2.29: Measurements performed on 19.02.2018. A large gap at the influx side of the route occurred at the west and southwest part of the route. Therefore, also these measurements were classified under category III.

2.7. ADDITIONAL DATASETS FOR COMPARATIVE ANALYSES

In the current study, additional datasets are also used to perform the comparison with the MAX-DOAS observation. The comparisons are performed to evaluate the consistency of the measured data with other datasets. The data from the TROPOspheric Monitoring Instrument (TROPOMI) and the Emission Database for Global Atmospheric Research (EDGAR) emission inventory were used for comparison with the VCDs and emission estimates derived from the MAX-DOAS measurements, respectively. The outcomes of these comparisons are presented in chapter 6.

2.7.1. TROPOMI Satellite Data

The TROPOspheric Monitoring Instrument (TROPOMI) (Veefkind et al., 2012) was launched on the European Space Agency's (ESA's) satellite, Sentinel-5 Precursor (S-5P), on 13 October 2017. S-5P is a sun-synchronous orbiting satellite with a swath width of about 2600 km. TROPOMI has an unprecedented spatial resolution of 3.5×7 km^2 (3.5×5.5 km^2 since 6 August 2019) and measures trace gases like SO_2, NO_2, ozone, formaldehyde, methane, CO, as well as aerosol and cloud properties. The four detectors of TROPOMI operate in the ultraviolet (UV), UV–visible (UV-VIS), near-infrared (NIR) and short-wavelength infrared (SWIR) spectral bands. The satellite overpasses around 13:30 local time (LT), with daily global coverage having a measurement period of about 60 milliseconds (Veefkind et al., 2012). As a result of the high horizontal resolution, TROPOMI observations are well suited to investigate the NO_2 pollution from individual sources like powerplants, industries and highways (Liu et al., 2020).

2.7.2. EDGAR Emission Inventory Data

The Emissions Database for Global Atmospheric Research (EDGAR) is a bottom-up emission compilation and provides sector-specific global emissions of air pollutant gases and particulates for all countries. The inventory is compiled by considering all anthropogenic sources and region-wise abatement technologies in practice. For consistency with the model input[4], version 4.3.2 (Crippa et al., 2018) of the inventory was used instead of the more recent version 5 (Crippa et al., 2019). The version 4.3.2 provides data from 1970 to 2010 whereas, version 5 provides data till 2015. The comparison between the data for NO_x emissions from both versions over the study area, revealed rather small differences of around 11%. Figures 2.30 and 2.31 present emission and correlation plots between both versions, respectively.

From the database, monthly flux values are available for each cell of $0.1° \times 0.1°$ spatial resolution. The flux values of each cell were multiplied by the area of the respective cell and then summed up to get the emissions for a chosen city. Pixels with $<25\%$ coverage of the area encircled by the route were not considered. The uncertainty of emissions from

[4] For details of the model, refer to appendix E.

EDGAR was found around ±20% and was determined by also considering the cells with <25% coverage of the area encircled by the route.

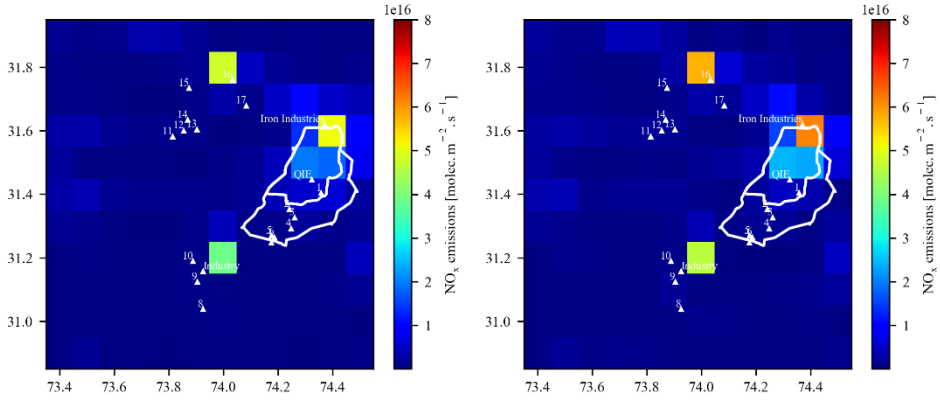

Figure 2.30: EDGAR annual averaged NOx emissions for the base years 2010 (left) and 2015 (right) for Lahore and the adjacent area. The white line represents the route adopted for the two circles around Lahore. Simlar emission patterns can be observed from both the figures.

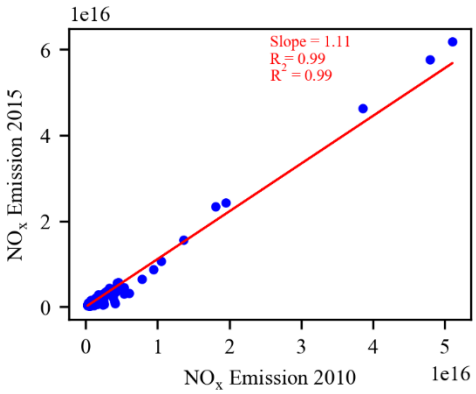

Figure 2.31: Correlation plot between the NO_x V4.3.2 (2010) and V5 (2015) EDGAR emissions for the area displayed in Figure 2.30.

3. INSTRUMENTATION AND CAMPAIGNS

In this chapter the description of the instruments used, and various details of the measurement campaigns are presented.

3.1. INSTRUMENTATION

Two types of MAX-DOAS instruments were used in the five campaigns. The instruments are developed to measure spectra of scattered sunlight for the application of the MAX-DOAS technique (Hönninger & Platt, 2002). One instrument was a so-called Mini MAX-DOAS, which is commercially available by Hoffmann Messtechnik GmbH. The other instrument was a so-called Tube MAX-DOAS, which is a prototype and built in collaboration of the satellite remote sensing group with the electronics workshop of the Max Planck Institute for Chemistry (MPIC), Mainz. The instruments are described in the following sub-sections.

3.1.1. Mini-MAX-DOAS

The Mini-MAX-DOAS instrument is an automated, small spectrometer with dimensions of 13 cm ×19 cm ×14 cm. It consists of an aluminum box which is sealed and contains a Czerny Turner spectrometer (ocean optics USB 2000+), quartz lens and optical fiber for the transmission of the scattered sunlight. A stepper motor is mounted outside the box to adjust the elevation angles of the telescope. The instrument is connected to the laptop through a USB cable. The instrument was operated by the software DOASIS (DOAS Intelligent System) (Kraus, 2006). DOASIS runs a Jscript program, which performs an automated control of various parameters like the movement of the stepper motor at various elevation angles, measurements of spectra, read-out electronics, and cooling. A car battery of 12 V was used as power supply. The temperature of the detector was maintained through a Peltier cooler. To minimize the power of the Peltier cooler, the detector temperature was maintained at least 15 °C lower than the ambient temperature. Two different Mini-MAX- DOAS instruments were used in the two campaigns. The full width at half maximum (FWHM) of the spectrometer was approximately 0.7 nm while the spectral range of the spectrometer was 287 to 445 nm for the instrument used in the first measurement campaign. The spectral range of the spectrometer used during the second campaign was from around 318 – 464 nm. An integration time of 60 seconds was used during both measurement campaigns for which the Mini MAX-DOAS instruments

were used. A typical set-up of the car MAX DOAS arrangement during the Dec. 2015 campaign is illustrated in Figure 3.1a

3.1.2. Tube MAX-DOAS

The setup of the Tube MAX-DOAS is comprised of two main parts. One includes the telescope and is fixed on the car roof (Figures 3.1b and 3.2 a). The second part is the controlling box placed in the car which contains the spectrometer, the peltier cooler along with a fan for cooling and a USB module (Figures 3.2 b). The telescope part consists of the telescope that collects the scattered sunlight and transfers it to the spectrometer through a quartz fiber bundle. This unit also contains a stepper motor inside the orange tube to adjust the elevation angles of the telescope. The telescope unit is connected to the control unit placed in the car. The control unit is also attached to the laptop via a USB cable. Power is supplied to the unit via a 12-volt DC external battery which is also connected to the controlling box. The central part of the setup is the spectrometer. An AvaSpec-ULS2048x64-RS-USB2 spectrometer from the AVANTES company is used in our instrument. The spectrometer has a symmetrical Czerny-Turner configuration. The incident light enters the spectrometer through a 100 x 900 µm slit and is passed through a BG3 filter to exclude radiation of wavelengths higher than 450 nm to minimize the spectrograph stray light. The filtered radiation is then directed to a diffraction grating through a collimation mirror. The diffraction grating resolves the radiation into its spectral components. After diffraction, the light reaches a mirror which focuses it towards the detector that converts the energy of the incident photons into an electrical signal. The spectral range of the spectrometer is around 302 - 465 nm having a full width at half maximum between 0.65 and 0.69 nm. The detector is a built-in Charge Coupled Device (CCD-chip), which is comprised of 64 rows and 2048 columns. The 64 rows are added that leads to measured spectra containing 2048 discrete values (Donner, 2016). The Peltier element encased inside the controlling unit regulates the temperature of the spectrometer according to the predefined values based on the ambient temperature. The VBUS software developed at the MPIC workshop is used to control the Peltier element and the motor. The DOASIS software (Kraus, 2006) is used to control the measurements. Spectra are recorded according to the instructions and parameters stored in the Jscript which runs through the DOASIS software.

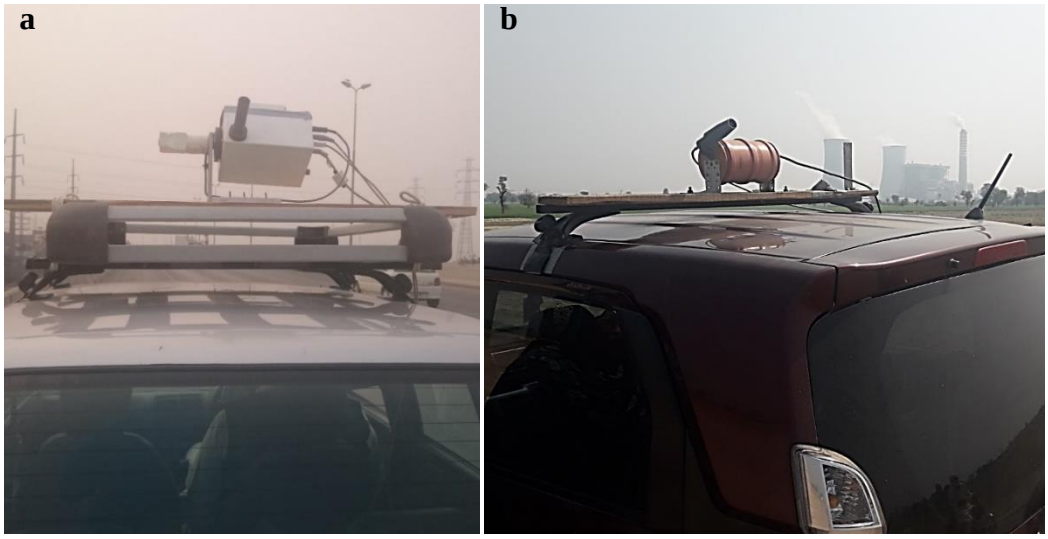

Figure 3.1: (a) Mini MAX-DOAS setup mounted on the car during the December 2015 measurement campaign. (b) The telescope unit of the Tube MAX-DOAS mounted on the car during 2018-I campaign.

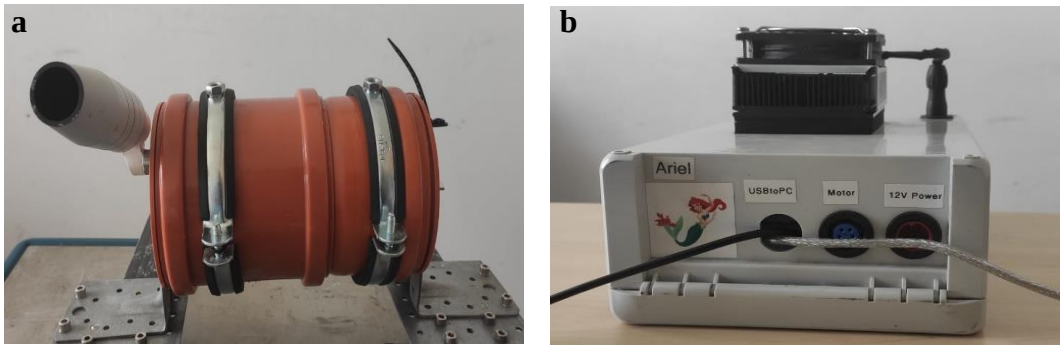

Figure 3.2: The telescope unit (a) and the control unit (b) of the Tube MAX-DOAS instrument.

3.2. MEASUREMENT CAMPAIGNS

In this section the details of the measurement campaigns performed during the PhD work are described. In total five measurement campaigns were performed during the current study. Two were performed by using the Mini MAX-DOAS instrument while the Tube MAX-DOAS instrument was used during the other three extensive campaigns. Nitrogen dioxide was measured by using the mini MAX-DOAS instrument, because for the other weaker absorbers, the signal to noise ratio of the mini MAX-DOAS instrument is not sufficient in most cases. During the other three campaigns which were executed by using the Tube MAX-DOAS instrument, four trace species, i.e., nitrogen dioxide (NO_2, sulfur dioxide (SO_2), formaldehyde (HCHO) and glyoxal (CHOCHO) were measured Table 3.1 gives an overview of these measurement campaigns. The measurement conditions and related details during these campaigns are explained in the following subsections.

Table 3.1: Overview of the measurement campaigns performed during the study

Campaign	Instrument used	Measurement period	Number of measurement days	Study area	Trace species measured
2015-I	Mini MAX-DOAS	Feb 2015	6	N5 Highway	NO_2
2015-II	Mini MAX-DOAS	Dec 2015	6	Lahore	NO_2
2017	Tube MAX-DOAS	May-Jun 2017	24	Lahore	NO_2, SO_2, HCHO, CHOCHO
2018-I	Tube MAX-DOAS	Feb-Mar 2018	33	Lahore	NO_2, SO_2, HCHO, CHOCHO
2018-II	Tube MAX-DOAS	Jun-Jul 2018	13	Power plants	NO_2, SO_2, HCHO, CHOCHO

3.2.1 Campaign 2015-I

In this section, the details of the measurements performed during 6 days of February 2015 are presented. The measurements were executed to quantify the spatial distributions of nitrogen dioxide (NO_2) along the N5 highway between major cities of the Punjab province. As mentioned earlier, during this campaign the Mini MAX-DOAS instrument was used. The results from this campaign are presented in chapter 5. The different routes adopted for the measurements are shown in Figure 3.3. A sequence of elevation angles with six measurements at 30 degrees and one measurement at 90 degrees was used. The direction of the telescope was backward, i.e., opposite to the direction of driving. The integration

time of each spectrum was 60 seconds. A handheld GPS device (HOLUX, model M247) was used to keep track of the coordinates of the route.

3.2.1.1. Details of the Study Area

During this period mobile measurements were performed along different cities including Lahore. Information about the city of Lahore is already presented in chapter 1. In this section a brief description of the other study areas is presented.

Islamabad is capital of Pakistan having a population of around 2 million and located in the north of Pakistan. **Rawalpindi** is the neighboring city of Islamabad and together both cities are termed as "twin cities". Rawalpindi has population of around 2.87 million (Pakistan Bureau of Statistics, 2017). Important stationary pollution sources for these cities are the Rawat Industrial zone; located at the junction of both cities, several industries including steel and metal works in Islamabad and an oil refinery.

The other city for which measurements were performed is **Faisalabad**. It is the third most populous city of Pakistan with an urban population of around 3.76 million. It may also be called the industrial hub of the country. Measurements at Faisalabad were performed on 19 February.

On 27 February 2015, car MAX- DOAS observations were also performed in the southern part of the province along the N5 national highway. This area comprises a mix of urban, semi urban and rural regions. There were power plants and oil refinery along the last part of the route.

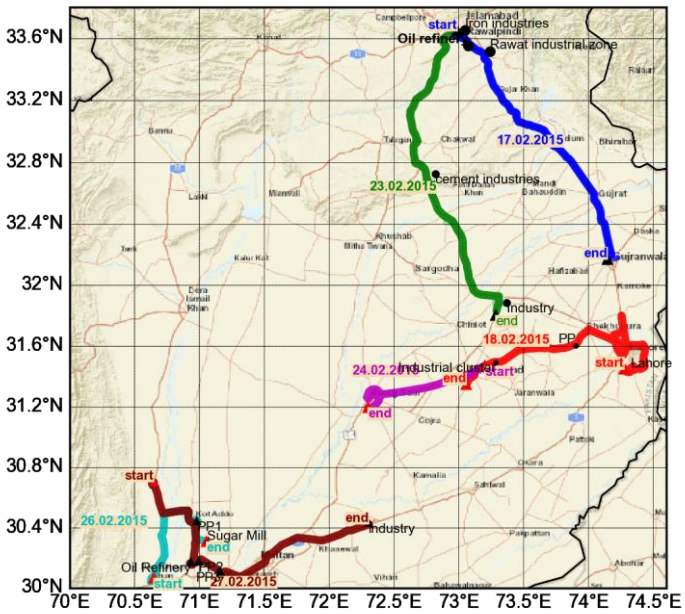

Figure 3.3: Different routes adopted during the 2015-I measurements. Different colors represent individual routes performed on different days. Important pollution sources are also indicated. PP stands for power plant.

3.2.2. Campaign 2015-II

In this section, the details of the measurements performed during six days of December 2015, around the city of Lahore are presented. The measurements were executed to estimate the NO_x emissions from the city in winter. The Mini MAX-DOAS instrument, described in section 3.1.1 was used. The route adopted for the measurements is shown in Figure 3.4 (a). Elevation angles with a sequence of six measurements at 30 degrees and one measurement at 90 degrees were used. The direction of the telescope was kept backward, i.e., opposite to the direction of driving. The integration time of each spectrum was 60 seconds. A handheld GPS device (HOLUX, model M247) was used to keep track of the coordinates of the route.

3.2.3. Campaign 2017

Measurements were performed during May and June 2017 to investigate the emissions from Lahore in summer. The tube DOAS instrument was used to measure the distributions of NO_2, SO_2, formaldehyde (HCHO) and glyoxal (CHOCHO) in the troposphere for 18 days in May and six days in June 2017. The route of the measurements is shown in Figure 3.4 (b). On all the days measurements were performed along the larger route except for 4 June 2017. On that day measurements were also performed along the smaller route in addition to the larger one. Except for two days, clockwise circles were performed around the city. Like for the previous measurement, the direction of the telescope was kept backwards. A sequence of six measurements at 22° and one measurement at 90° elevation angles was used. The integration time of each spectrum was set to 30 seconds. A handheld GPS (CANWAY) was used to keep track of the driving route.

3.2.4. Campaign 2018-I

Measurements were performed for 33 days (18 days in February and 15 days in March) to estimate the emissions from Lahore in spring. The Tube MAX-DOAS instrument was used to quantify the column densities of nitrogen dioxide, sulfur dioxide, formaldehyde and glyoxal. The ambient air temperatures during the measurement period ranged from 20 to 29° Celsius. Like for the previous campaigns, the direction of the telescope was kept backwards, i.e., opposite to the driving direction. A handheld GPS (CANWAY) was used for logging the coordinates of the driving route. During this campaign, two routes were adopted. One smaller route, to estimate the emissions from the densely populated area of the city and the other larger route to identify the additional emission sources. Figure 3.4 (c) illustrates the routes adopted during the 2018-I measurements. In addition to Lahore, measurements were also performed around the city of Faisalabad on 9 March and along the National Highway from Lahore to Islamabad on 15 March. Measurements to estimate the emissions from the Sahiwal Coal Power Plant (1,320 MW) were also performed on 5 March. The results of these days will be discussed in chapter 5.

In this campaign, some technical failure occurred, and the motor of the telescope did not work. So, the automated change of the elevation angles was not possible. To deal with this problem, the elevation angles were adjusted manually. The telescope is constructed in a way that it takes 16000 steps between zero degree and 90 degrees. Thus, the telescope was adjusted at 90 degrees manually, and the motor position was set to zero steps at the initial position by using the Vbus software.

So, by using the formula below (Eq. 3.1), the encoder position (EncPos) for the desired elevation angle was calculated. As a result, only few spectra at 90-degree were taken each day.

$$EncPos = \frac{16000 \times (Elevation\ angle - 90)}{90} \quad (3.1)$$

For the elevation angle of 22 degrees, the encoder position of -12088 was obtained. In addition to the motor problem, the instrument also received low light intensity, the reason of which is not exactly known. This might have happened due to some fault in the telescope like dust accumulation on the lens of the telescope. As a result of the low intensity, a rather high residual and low signal to noise ratio were observed. Despite these problems, the measurements during this campaign could still be analyzed as described in section 2.5.

3.2.5. Campaign 2018-II

The last measurement campaign was performed to estimate the emissions and spatial distributions of the trace gases around the power plants in the region. Three zones were identified where two or more power plants are located. Three routes were devised to encircle these power plants. Additionally, on two days one large circular route was performed to investigate the spatial distribution in the whole region. The measurements were performed for 13 days in June and July 2018. The Tube MAX- DOAS instrument was used during this period. On the last three days of the campaign (2, 4 and 5 July 2018), the motor of the instrument stopped working due to a technical failure. So, the elevation angles were adjusted in a similar manner as mentioned in section 3.2.4. For the days where motor was working, elevation angles with a sequence of six measurements at 22 degrees and one measurement at 90° were used. For the non-working motor period, only a few 90° measurements were taken by manual adjustment of the telescope.

Figure 3.5 illustrates the three powerplant zones in the region labelled as A, B and C. Figure 3.6 presents the individual routes adopted to encircle the power plants in each of these zones. These regions were identified based on the NO_2 plumes, as observed from the TROPOMI satellite measurements (Figure 3.7). The results from these measurements are discussed in chapter 5.

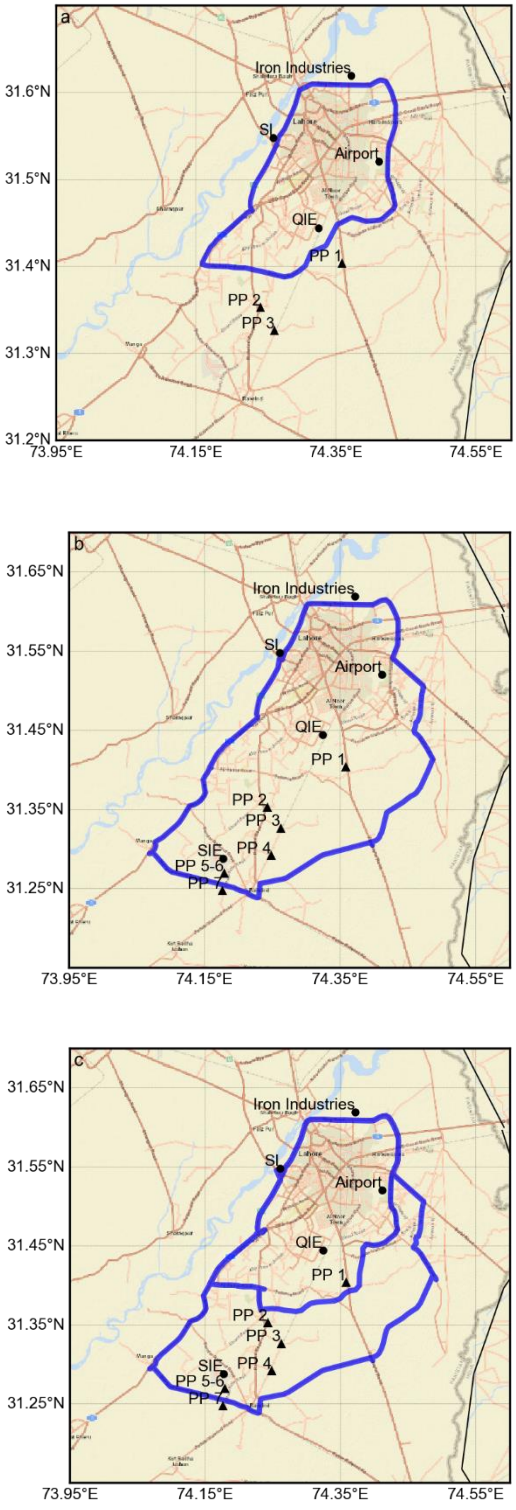

Figure 3.4: Routes around Lahore for the 2015-II (a), 2017 (b) and 2018 (c) measurements. Important pollution sources are also indicated. PP stands for power plant while SI stands for small industries, SIE stands for the Sundar industrial estate and QIE stands for the Quaid-e- Azam industrial estate.

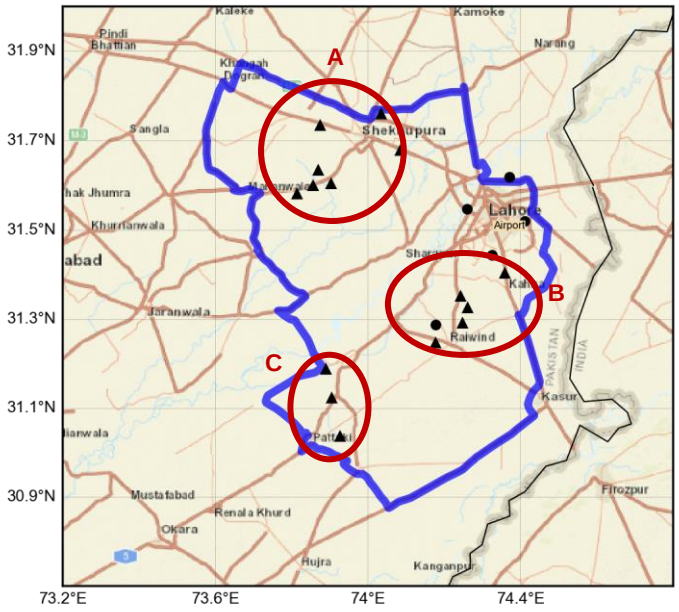

Figure 3.5: The large circle (blue line) adopted on 18th and 25th June 2018 around the power plants in the area. The black triangles represent the power plants while the black dots show the location of important industries. The red circles segregate the three zones (A, B and C) with three or more power plants.

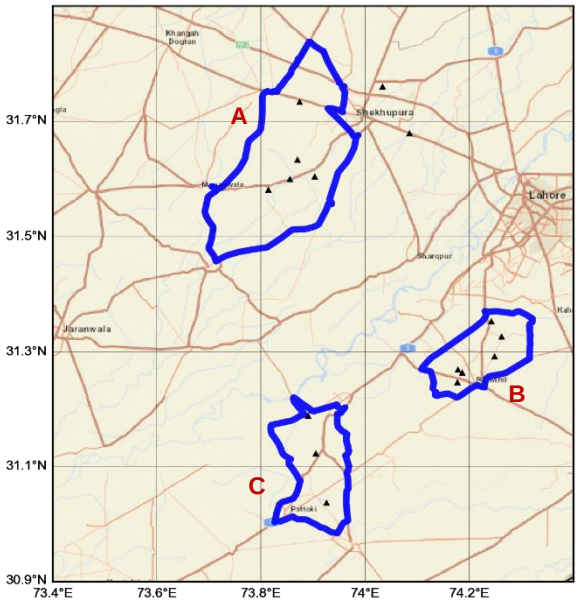

Figure 3.6: The individual routes adopted to execute the circles around zone A, B and C power plants. The black triangles indicate the power plant locations.

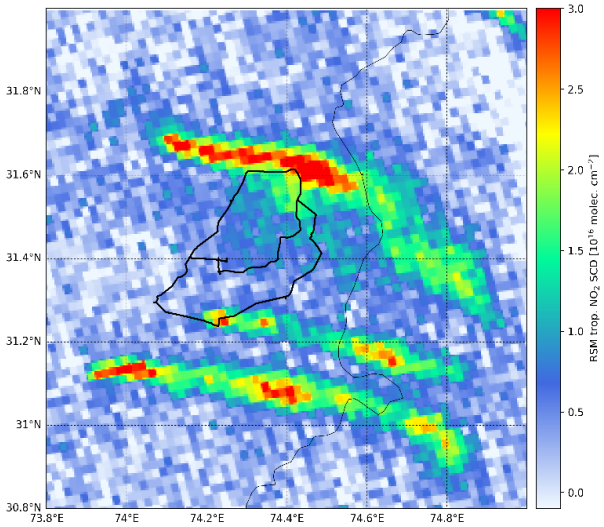

Figure 3.7: TROPOMI NO_2 SCDs over the study area observed on 07.03.2018. The measurement routes for Lahore are represented by the black lines. The three plumes represent strong NO_2 sources like power plants. (Figure courtesy: Christian Borger, Satellite remote sensing group, MPIC.

4. RESULTS

Four trace gases (nitrogen dioxide, sulfur dioxide, formaldehyde and glyoxal) were analyzed in the spectra measured around the city of Lahore. In this chapter, the results of each of these trace species are discussed in detail.

4.1. NITROGEN DIOXIDE (NO_2)

Three campaigns were performed to estimate the NO_x (NO_2 + NO) emissions and the spatial distribution of NO_2 around the city of Lahore during different seasons. Total NO_x emissions from the city are calculated by encircling the source, as described in section 2.6.

During these measurement campaigns, more than 50 circles were carried out around Lahore. Based on the suitability criteria as devised in section 2.6.2, for 9 circles the measurement conditions were found to be well-suited to derive the emissions from the encircled area (category I) while 8 circles fell into category II. The rest of the measurements (category III) were not suitable for deriving emissions (mainly because of low wind speeds or variable wind fields), but still the spatial distribution of the NO_2 VCDs could be derived.

Because of its rather short lifetime part of the emitted NO_x will be destroyed during the transport from the emission source to the measurement location. This loss can be quantified considering the wind speed, NO_x lifetime and the radius of the circle (a proxy for the distance from the source). According to Beirle et al., 2011, we assume a NO_x lifetime of 4 hours in the daytime, which results in lifetime correction factors, C_τ (Eq 2.48) in the range of 1.12 to 1.23 for the smaller circles and between 1.09 to 1.28 for the larger circles. The results for each category are discussed in the following sections.

4.1.1. NO_x Emission Estimation Results

4.1.1.1.Category I Results

Emission estimations from Lahore for circles with good conditions (category I) and low uncertainties are described in this sub-section. Measurements performed along 8 out of 9 large circles around Lahore fulfilled the criteria of category I, but only one small circle fulfilled the same.

The times of the measurement at different days are not the same which complicates the inter-comparison of the derived emissions on different days. The total NO_x emissions from Lahore are found to be between 1.20 $\times 10^{25}$ and 3.24 $\times 10^{25}$ molecules s^{-1} with total errors ranging between ±31 to ±38%. The different error sources are discussed in section 4.1.1.3.

Weighted means were also calculated for all the measurements performed under this category and weights were assigned on the basis of the estimated errors. The mean emissions for all 8 large circles are found to be $2.03\times10^{25} \pm 8.07\times10^{24}$ molecules s^{-1}. Emissions from the single small circle performed on 26 Feb 2018 were estimated as 1.51×10^{25}. The total NO_x emissions for all the circles with their respective area emissions are given in Table 4.1. The NO_2 VCDs along with the interpolated averaged ECMWF wind fields are shown in Table 4.1 for the individual days. Prominent pollution sources are also indicated in the figures with black dots. Low NO_2 VCDs can be observed at the upwind side while enhanced VCDs can be seen at the downwind side of the city. Elevated VCDs can also be observed at the northern and southern parts of the route. These high values are considered to be localized enhancements, due to various industries and power plants in the vicinity. In Table 4.1, the derived NO_x emissions for all days, selected for the category I are listed. Under this category the highest emissions were found on 26 March 2018, while the lowest emissions were observed on 3 June 2017.

In a previous study, NO_x emissions for two megacities; Delhi and Paris were also conducted by the same method. The NO_x emissions for Delhi for 3 days in April were around 1.6 $\times10^{25}$ molecules sec^{-1}. For Paris higher NO_x emissions were observed for winter as compared to summer with mean emission vales of $\sim6.0\times10^{25}$ and $\sim2.5\times10^{25}$ molec s^{-1}, respectively (Shaiganfar, 2012).

Liu et al. (2016), also estimated the NO_x emissions for 53 cities in USA and China by using OMI satellite observations. According to them, Shanghai, Wuhan and Pearl River Delta region showed high NO_x emissions ranging between $\sim1.1\times10^{25}$ and $\sim2.6\times10^{25}$ molec s^{-1}. The US cities like New York and Chicago also showed similar values (Liu et al., 2016).

4.1.1.2.Category II Results

Under this category measurements, with higher expected uncertainties were expected due to uncertainties of the wind fields, were grouped. As mentioned in section 2.6, category II measurements include days with either relatively low wind speeds (between 2 to 4 m s^{-1}) and stable wind directions or with strongly changing wind directions between the two ECMWF outputs. Eight routes around Lahore in different measurement campaigns fall in this category. Out of these eight, three were performed along the large route while the other five were executed along the small circle.

On most of the days, higher VCDs can be observed at the downwind side of the routes (Figure 4.2). On 10 December 2015, an enhancement can also be seen at the northwestern part. Along this segment of the route, a cluster of industries on both sides of the road is located. These industries caused localized enhancements in this part. On 17 and 26 February one large and one small circle were performed on each day. On most of the days, under this category, the wind directions were similar, with winds predominantly from the northwest . This resulted in higher NO_2 VCDs on the south-eastern part of the city i.e., the lee side. The highest NO_x emissions of 2.02×10^{25} molecules s^{-1} were found on 27 Feb along the smaller route while the lowest NO_x emissions (9.37×10^{24} molecules s^{-1}) were found on 25 Feb 2018.

The mean emissions for the 3 large circles were found to be $1.35\times10^{25} \pm 3.06 \times10^{24}$ molecules s^{-1} while the mean emissions for the 5 circles along the small routes, performed in the winter and spring campaigns were found to be $1.52\times10^{25} \pm 4.45 \times10^{24}$ molecules s^{-1}. The NO_2 VCDs, for the days under this category, are shown in Figure 4.2. The total NO_x emissions for all the circles with their respective area emissions are given in Table 4.2 and Table 4.3

Table 4.1: Derived NO_x emissions (category I)

Date	**NO_x emissions (molec s^{-1})**	**Mean emissions (molec s^{-1})**	**Area emissions (molec s^{-1} m^{-2})**	**Mean area emissions (molec s^{-1} m^{-2})**
17 May 2017	2.37×10^{25}		2.63×10^{16}	
28 May 2017	1.33×10^{25}		1.48×10^{16}	
28 May 2017	1.55×10^{25}		1.72×10^{16}	
29 May 2017	2.88×10^{25}	2.03×10^{25}	3.20×10^{16}	2.25×10^{16}
03 Jun 2017	1.20×10^{25}	$\pm8.07\times10^{24}$	1.33×10^{16}	$\pm8.95\times10^{16}$
14 Feb 2018	2.44×10^{25}		2.71×10^{16}	
26 Feb 2018	3.24×10^{25}		3.60×10^{16}	
06 Mar 2018	1.20×10^{25}		1.33×10^{16}	
26 Feb 2018 (small circle)	1.51×10^{25}	---------	3.50×10^{16}	---------

Table 4.2: Derived NO_x emissions for the large circles (category II)

Date	**NO_x emissions (molec s^{-1})**	**Mean emissions (molec s^{-1})**	**Area emissions (molec s^{-1} m^{-2})**	**Mean area emissions (molec s^{-1} m^{-2})**
27 May 2017	1.66×10^{25}	1.35×10^{25}	1.85×10^{16}	1.50×10^{16}
17 Feb 2018	1.33×10^{25}	$\pm3.05\times10^{24}$	1.48×10^{16}	$\pm3.38\times10^{15}$
18 Feb 2018	1.05×10^{25}		1.17×10^{16}	

Table 4.3: Derived NO_x emissions for the small circles (category II)

Date	NO_x emissions (molec s^{-1})	Mean emissions (molec s^{-1})	Area emissions (molec s^{-1} m^{-2})	Mean area emissions (molec s^{-1} m^{-2})
10 Dec 2015	1.41×10^{25}		3.27×10^{16}	
17 Feb 2018	1.33×10^{25}		3.05×10^{16}	
25 Feb 2018	9.37×10^{24}	1.52×10^{25} $\pm 4.45 \times 10^{24}$	2.17×10^{16}	3.52×10^{16} $\pm 1.03 \times 10^{16}$
27 Feb 2018	2.02×10^{25}		4.68×10^{16}	
07 Mar 2018	1.91×10^{25}		4.43×10^{16}	

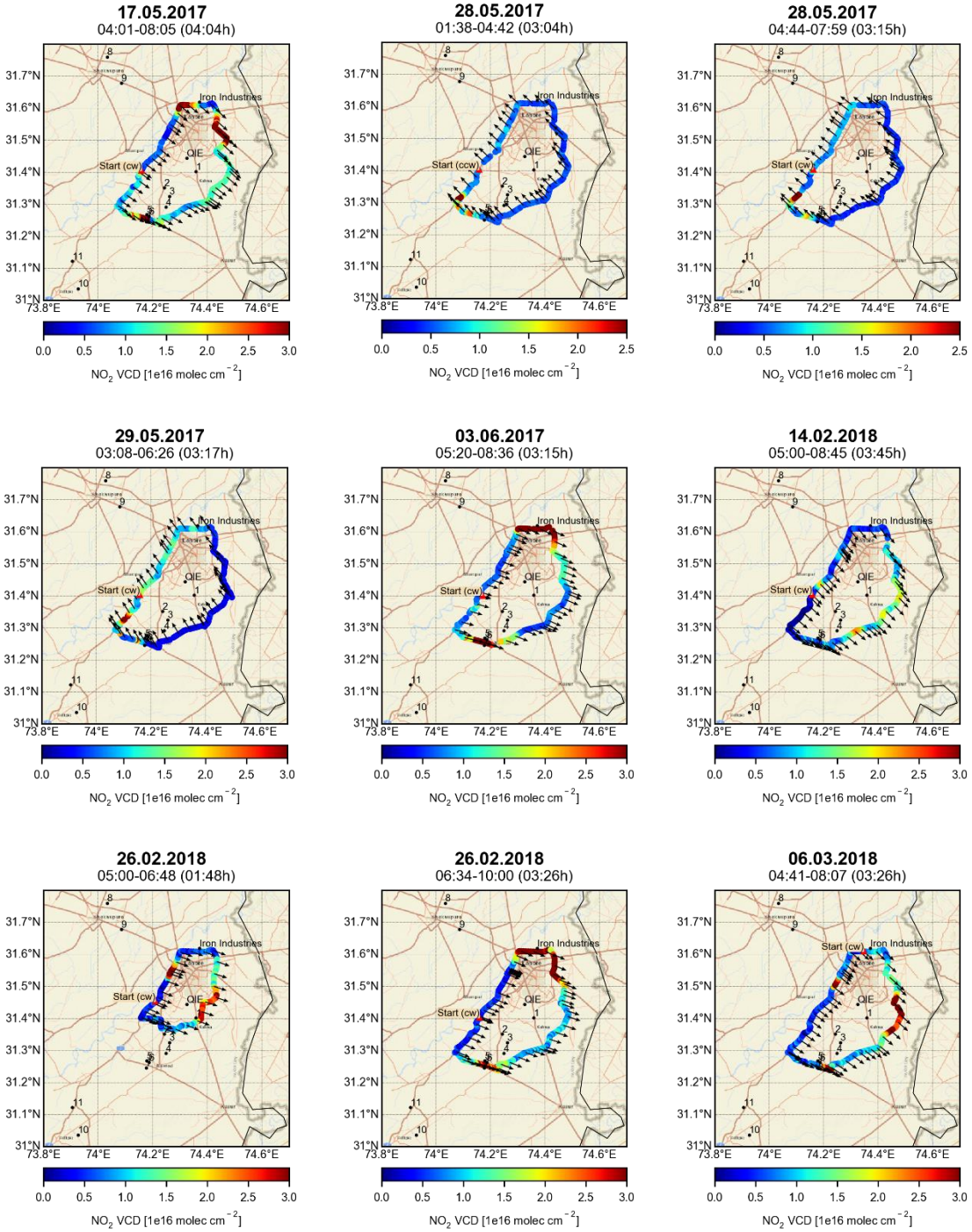

Figure 4.1: Tropospheric NO_2 VCDs for category I measurements around Lahore along with the respective wind fields, during the summer and spring measurement periods. The black arrows represent the averaged wind directions during the driving period.

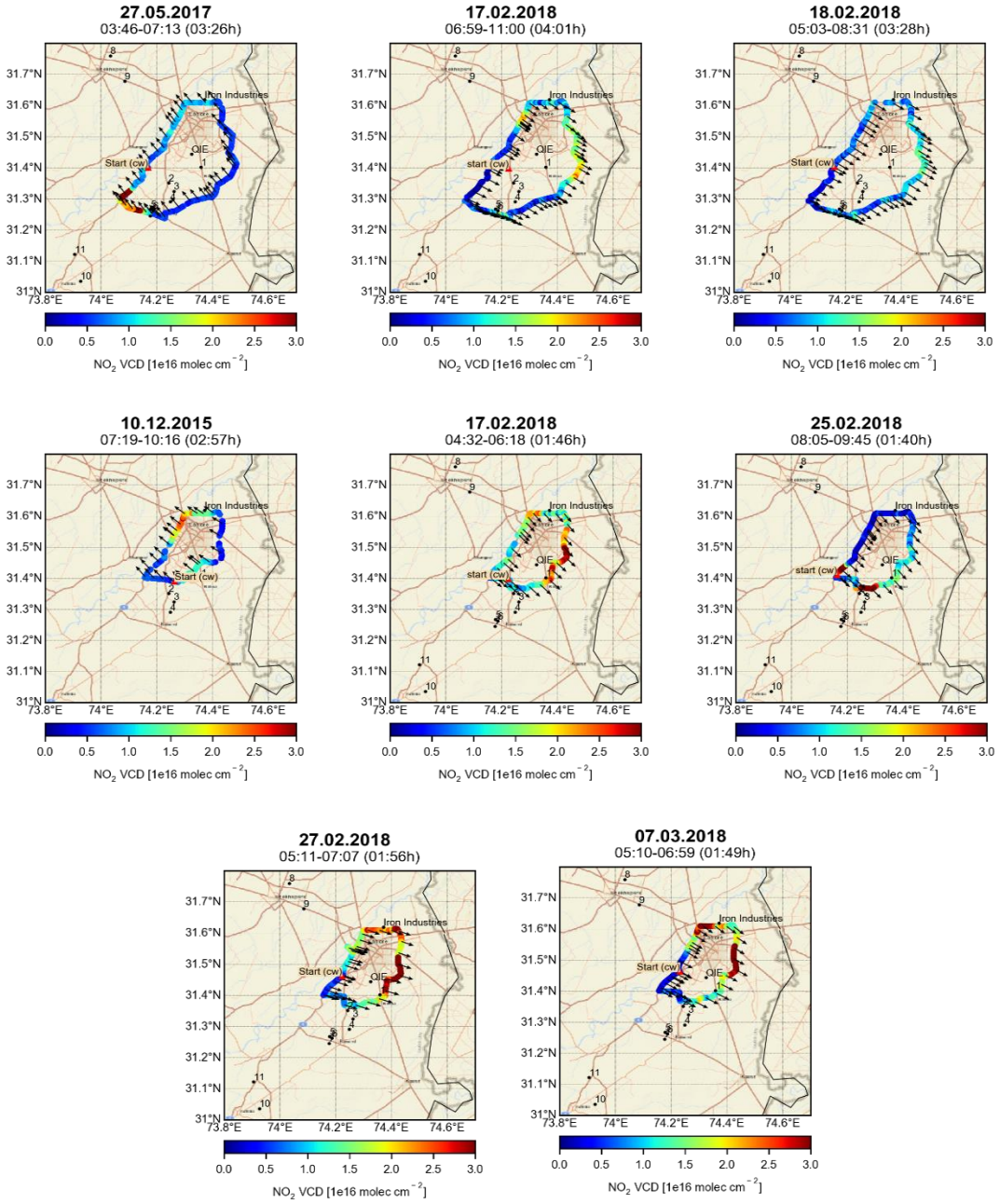

Figure 4.2: Tropospheric NO_2 VCDs around Lahore for category II measurements. Enhanced values can be clearly seen at the downwind side of the encircled area. The respective wind fields during each measurement circle are also indicated. The black arrows represent the respective wind vectors.

4.1.1.3. Error Estimation

Various sources of uncertainties like gaps in the measurements, NO_x lifetime assumptions, chemical transformations and unstable wind conditions add to the overall uncertainties (see e.g. Shaiganfar et al., 2017). Some of these error sources are described in this section.

4.1.1.3.1. Uncertainty due to gaps

As a result of the interrupted measurement routine due to the technical problems or filtering out the bad quality data, gaps in the continuous measurements happened. Such missing data are one source of uncertainties in estimating the emissions of trace gases. To cope with this, the fluxes were estimated twice; once in the clockwise (CW) direction while the second time in the counterclockwise (CCW) direction (Shaiganfar, 2012). The mean of these two calculations was then considered as the estimated emission value. To fill up the missing measurements; in both calculations the value of the last measurement, at the 'start' of the gap, was used. The corresponding deviations were then considered as the corresponding error. On most of the days the errors caused by gaps were rather small, and they ranged between ±0.16% to ±17.4%.

4.1.1.3.2. Uncertainty due to chemical transformation and lifetime

As mentioned earlier (section 2.6), a chemical transformation factor (NO_x/NO_2) of 1.32 (Seinfeld & Pandis, 2006) is used (Eq. 2.49) to convert the measured NO_2 fluxes into NO_x fluxes. Following Shaiganfar et al., (2017) the corresponding uncertainty is estimated to about ± 15%. Also, a lifetime correction factor was applied. It was determined by using Eq. (2.48) assuming a NO_x lifetime of 4 hours ± 0.5 hours (Beirle et al., 2011). This correction usually causes an uncertainty of up to about ± 15% (Shaiganfar et al., 2011).

4.1.1.3.3. Uncertainty due to wind data

Errors in the derived flux, due to the uncertainties in the wind data arise from two sources. The first source is directly related to the uncertainties of the wind fields and explained in detail in section 2.6. The second source of uncertainty associated to wind data is due to the differences in the interpolated ECMWF outputs (for details, see section 2.6.1). These errors were estimated by varying the ECMWF outputs according to the start and end times of the circles. The total estimated error of the NO_2 flux due to uncertainties of the wind field ranged between ± 4% and ± 37%.

4.1.1.3.4. Total Error

The total error, including all above-mentioned uncertainties, was calculated as the square root of the quadratic sum of all errors. The total error for the NO_x emissions, for category I, ranged between ± 31% to ± 37.4%, and for category II measurements between ± 31% to ± 48.3%. Tables 4.4 and 4.5 present the individual and total errors for measurements classified as category I and category II, respectively. The NO_x emissions with their total errors are presented in Figure 4.3.

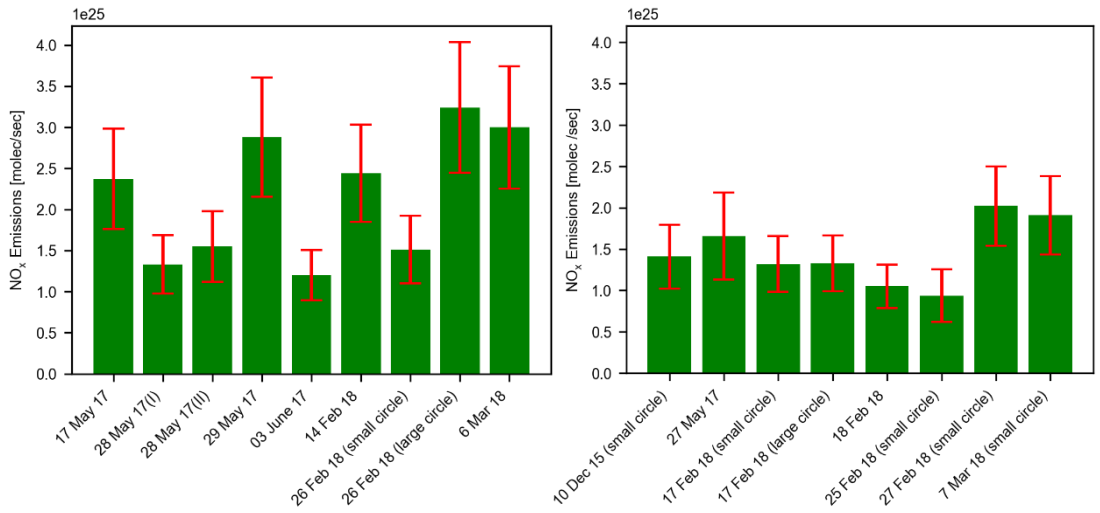

Figure 4.3: NO_x emissions for category I (left) and category II (right) measurements. The error bars represent the estimated total errors for each measurement circle.

Table 4.4: Estimated relative errors (%) of the derived NO_x emissions (category I)

Error of	Uncertainties due to		17 May 2017	28 May 2017		29 May 2017	03 Jun 2017	14 Feb 2018	26 Feb 2018	26 Feb 2018	06 Mar 2018
				I	II						
SCDs	Spectral retrieval		15	15	15	15	15	15	15	15	15
VCDs	Geometric approximation		20	20	20	20	20	20	20	20	20
NO_2 Flux	Wind	45° shift	2.7	13.6	7.7	2.8	12.6	3.5	13.5	5.3	5.2
		Tempo-ral interpo-lation	13	9	16	12	3	2.2	7	7	8
NO_2 Flux	Gaps		1	5.6	11	0.8	6	1.6	7.5	0.5	4
NO_x Flux	Partitioning factor		15	15	15	15	15	15	15	15	15
NO_x Flux	Lifetime Factor		10	10	10	10	10	10	10	10	10
Total Error (±%)			**33.6**	**35.3**	**37.4**	**33.3**	**34.0**	**31.0**	**35.0**	**32.0**	**32.5**

Table 4.5: Estimated relative errors (%) of the NO_x emissions (category II)

Error of	Uncertainties due to		10 Dec 2015	27 May 2017	17 Feb 2018		18 Feb 2018	25 Feb 2018	27 Feb 2018	07 Mar 2018
					Small	Large				
SCDs	Spectral retrieval		15	15	15	15	15	15	15	15
VCDs	Geometric approximation		20	20	20	20	20	20	20	20
NO_2 Flux	Wind	45° shift	11	8.7	8.2	2.9	2.4	32	2.6	8.4
		Tempo-ral interpo-lation	4.7	34.8	9.4	15	12	7.7	3	10.3
NO_2 Flux	Gaps		12	6.4	7.5	1.45	0.3	17.4	0.16	1.75
NO_x Flux	Partitioning factor		15	15	15	15	15	15	15	15
NO_x Flux	Lifetime Fator		10	10	10	10	10	10	10	10
Total Error (±%)			**35.1**	**47.7**	**34.0**	**34.5**	**33.0**	**48.3**	**31.0**	**33.6**

4.1.2. NO_x Seasonal Variations

In this study an attempt to identify any seasonal variation in the NO_x emissions was also made. The seasonality in NO_2/NO_x has also been previously studied, e.g., in Cairo (Khoder, 2009), in London (Bigi & Harrison, 2010), over Delhi (Sharma et al., 2010), in New Jersey (Roberts-Semple et al., 2012), in Paris (Shaiganfar, 2012) and in China (Zhang, et al., 2012). All these studies show similar findings, having the lowest values in summer and the highest values in winter. According to Roberts-Semple et al. (2012) this seasonal pattern in NO_x emissions may partly be attributed to the enhanced use of fossil fuels for domestic heating in colder months. Also the dependence of the NO_x lifetime on temperature plays a role. But in Lahore, ambient temperatures in summer are higher than 40 ºC and therefore electricity demands surge due to the domestic cooling. The Lahore Electric Supply Company (LESCO) releases performance reports on a quarterly basis. It is depicted from these reports (for 2015-2020), that electricity consumption in the Lahore region is higher in summer than in winter (LESCO, 2020). Khalil & Zaidi (2014) also mentioned that energy demands in Pakistan are higher in summer than in winter. Ghafoor et al. (2020) surveyed 300 residential buildings in Lahore and also reported higher electricity consumption during the summer months.

However, it can also be assumed that a significant portion of electricity is generated from hydropower in summer due to the high availability of water in the dams as a result of the melting of glaciers and the monsoon rains (Jamal, 2016). In contrast, in winter, electricity is mainly generated through fossil fuels combustion. The annual report published by the National Electric Power Regulatory Authority of Pakistan (NEPRA), provides details of the source wise electricity production in the country. According to the figures mentioned, in summer months (April -September), the share of electricity generated from the hydropower, is increased (NEPRA, 2018). Figure 4.4 exhibits the relative monthly share of the electricity produced by the two major electricity generation sources (hydropower and fossil fuel combustion). Moreover, higher electricity consumption in the winter months can also be observed from the figure.

The NO_x emissions were estimated for 17 routes in 3 different seasons (both category I and II measurements). Out of these 17, 6 routes were performed in summer and one in winter, while in spring, emissions for 10 circles (5 large and 5 small) were estimated. The weighted means of all estimated emissions in each season were calculated. The respective emissions and standard deviations are given in Table 4.6.

The NO_x emissions from the single small circle executed in winter is 1.41×10^{25} molec s^{-1}. The measurements performed in summer yielded averaged NO_x emissions of 1.46×10^{25} molecules s^{-1}, whereas, the averaged emissions for spring have a similar value of $\sim1.40\times10^{25}$ molecules s^{-1} and 1.41×10^{25} molecules s^{-1} for the large and small circles, respectively. In previous studies, NO_x emissions for two megacities Delhi and Paris were also conducted by the same method. Averaged NO_x emissions for Delhi for 3 days in April were around 1.6×10^{25} molecules s^{-1}. For Paris, higher NO_x emissions were observed for winter as compared to summer with mean emission vales of $\sim6.0\times10^{25}$ and $\sim2.5\times10^{25}$ molecules s^{-1}, respectively (Shaiganfar, 2012).

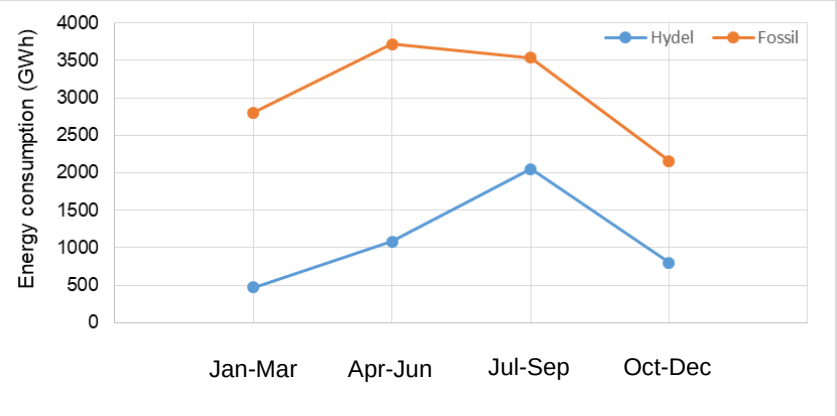

Figure 4.4: Quarterly source-wise electricity consumption in Pakistan for four years (2015-2019). (Data sources: (LESCO, 2020); (NEPRA, 2018))

Therefore, for Lahore, it can be assumed that multiple factors like high energy usage in summer and special winter meteorology in colder months may counteract for any seasonal variations. Moreover, it should also be noted that substantial NO_x sources in the city are also transport and industrial emissions which remain constant throughout the year.

Table 4.6: Averaged NO_x emissions for Lahore on seasonal basis

Details	Total Circles	Mean emissions (molec s^{-1})	Standard deviation (molec s^{-1})	Mean area emissions (molec s^{-1} m^{-2})
Winter (Small)	1	1.41×10^{25}	-----	3.27×10^{16}
Summer (Large)	6	1.46×10^{25}	1.21×10^{25}	1.63×10^{16}
Spring (large)	5	1.40×10^{25}	1.16×10^{25}	1.55×10^{16}
Spring (Small)	5	1.41×10^{25}	1.15×10^{25}	3.27×10^{16}

4.1.3. Spatial Distribution of Nitrogen Dioxide (category III)

In this section, the spatial distributions of NO_2 measured during the three measurement periods (2015-II, 2017 and 2018-I) are discussed. While for category III measurements, no meaningful emission estimates can be obtained, it is still interesting to investigate the obtained spatial distributions. Measurements were performed in three seasons, and the NO_2 sources along the driving routes are attempted to be identified.

During several days of the measurements, typical NO_2 enhancement patterns were identified at multiple locations along the route. Various localized NO_2 emission sources, e.g., power plants, industries and busy roads as mentioned in section 1.3 can be the reason of these elevated values. Emissions from local sources became more prominent on several category III days as NO_2 is tend to accumulate near the sources This prominent inhomogeneous distribution of NO_2 is most probably due to the reduced dispersion of the trace gas as a result of lower wind speeds (Chan et al., 2020).observed during the category III days. The main reasons for these elevated NO_2 values are vehicles, industries and power plants. These localized enhancements along the multiple points of the route with their potential sources are described as follow.

High values on some days can be observed along the northern part of the route (Figure 4.5). This enhancement may be attributed mainly to the cluster of industrial units related to metal and iron works. Metal industries use high temperatures (~1500-2000 ^oC) furnaces to melt iron and other metals (Figure 4.6). Due to these high temperatures, NO_x is also formed thermally, in addition to the emissions from fuel combustion as described in section 1.3.2. NO_2 VCDs are found to be even higher than 3×10^{16} molecules cm^{-2} in this part. The Allama

Iqbal International Airport located on the northeast side of the route may also contributed to the high NO_2 column densities.

On some days, enhanced NO_2 values were also observed in the western part of the route. This leg of the route was performed along the Bund Road. Along this part of the route, small industries and inter-city bus terminals are present in the vicinity and could be the contributor of localized NO_x emissions (Figure 4.7). Besides these, vehicular emissions due to high traffic density on the M2 motorway also contributed to the high values on the west and northwest sides. The M2 motorway is a busy motorway and connects Lahore to the federal capital, Islamabad and the northern part of the country.

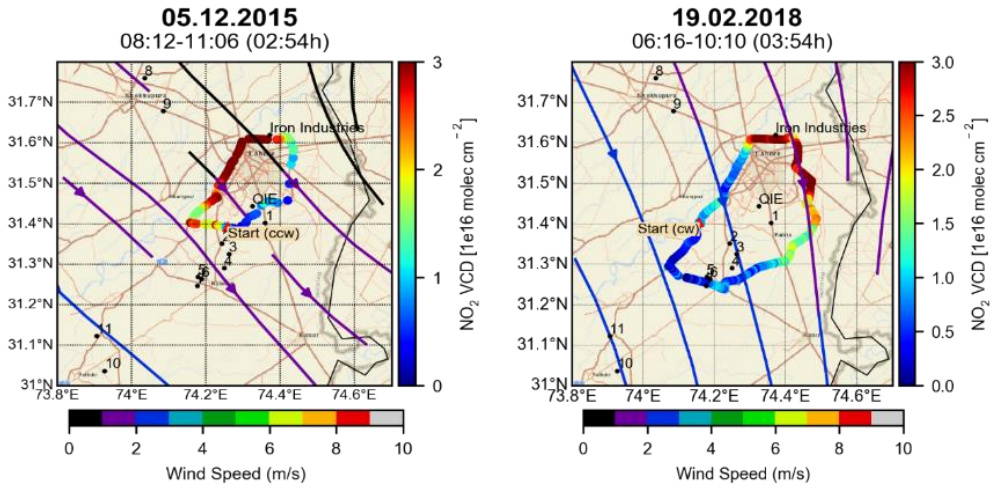

Figure 4.5: Tropospheric NO_2 VCDs measured from mobile MAX-DOAS observations around Lahore during winter and spring with wind information at 12 UTC (05.12) and 6 UTC (19.02) showing enhanced values at the north, north east and north west sides of the routes.

Figure 4.6: An example of an iron scrap melting process in a furnace located near Mahmood Booti, Lahore.

NO_2 hotspots were also observed along the south and southwestern sides. The SW part of the route was performed along the N5 highway, which connects Lahore to another big city Multan. The N5 highway is a busy road with a heavy traffic load, and also various industries are located along this road. Strong NO_2 emissions observed on the southern part of the larger route as sown in Figure 4.8, could be attributed to the cluster of industries and power plants along both sides of the road.

Elevated NO_2 VCDs can also be seen on the eastern side of the smaller circle. These enhancements may be due to the industrial area (QIE) which is around 2 km away from the road. Some of the measurements, exhibiting elevated NO_2 levels in this part, are shown in Figure 4.9. On most of the days, the wind speeds were less than 2 m s^{-1}.

The NO_2 spatial distribution results from all the other days can be found in appendix B.1

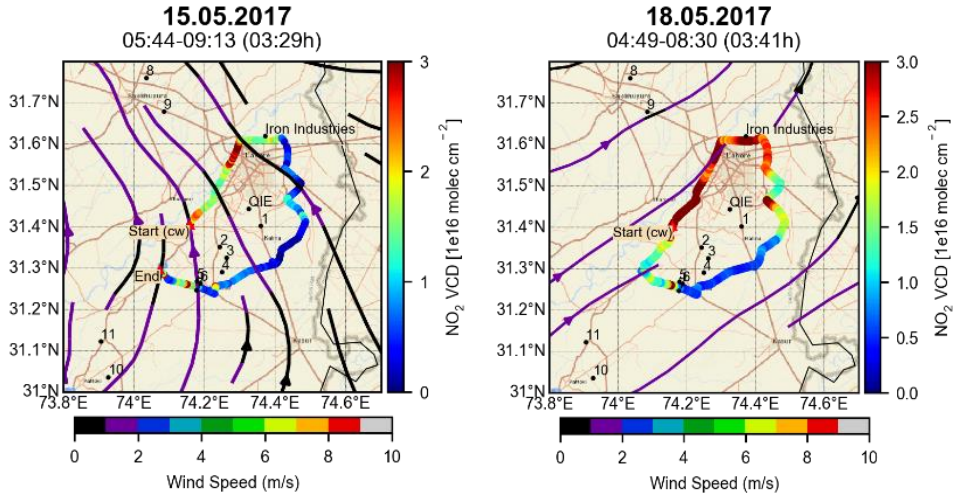

Figure 4.7: NO_2 tropospheric VCDs measured during summer together with the respective wind information at 6 UTC.

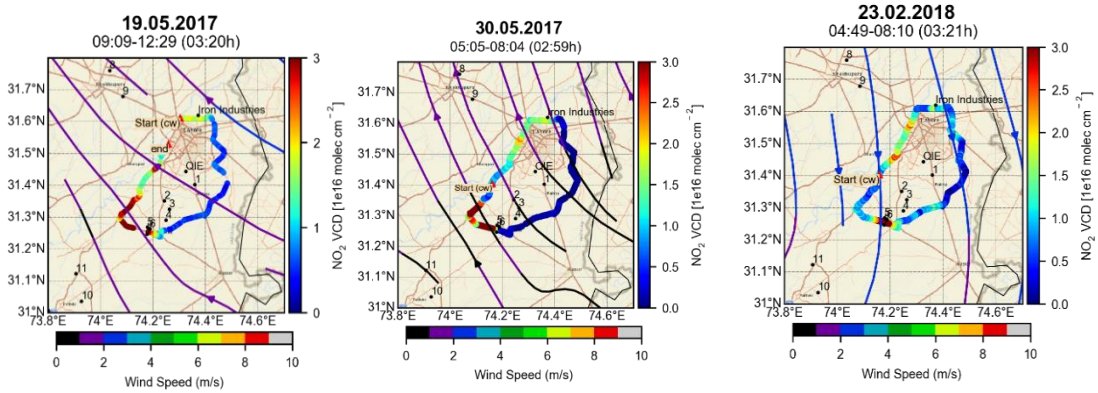

Figure 4.8: Tropospheric NO2 VCDs measured from mobile MAX-DOAS observations around Lahore on three days during the summer and spring campaigns showing enhancements at the south and southwestern parts of the route.

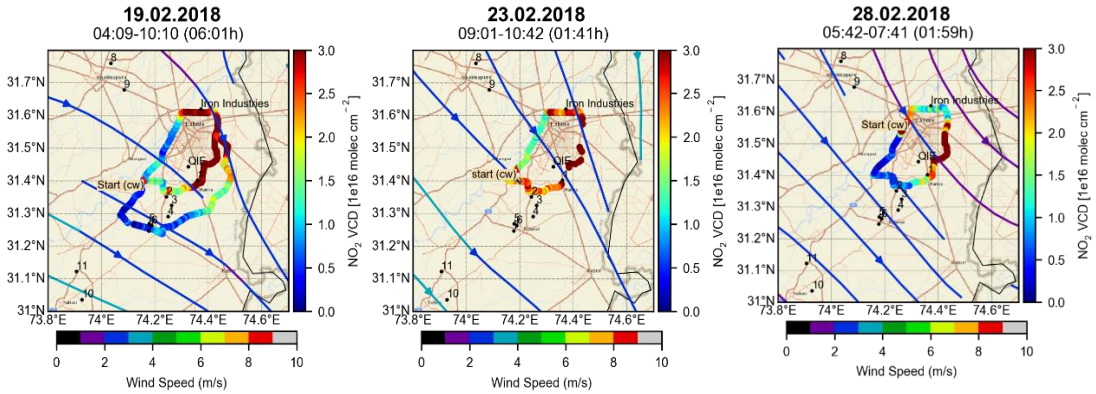

Figure 4.9: Category III tropospheric NO_2 VCDs derived from mobile MAX-DOAS observations around Lahore along with averaged wind fields on various days during the 2018-I campaign. On all these days similar wind conditions were found.

4.2. SULFUR DIOXIDE (SO_2)

Sulfur dioxide (SO_2) is an important oxide of sulfur and widely present in the urban environment as a result of anthropogenic activities like industrial processes and combustion of fossil fuels. In this study, SO_2 emissions from Lahore are estimated. The spatial distributions of SO_2 have also been studied along the driving routes. In this chapter, results from the two extensive measurement campaigns, performed in summer 2017 and spring 2018 are discussed (for details of these campaigns see sections 3.2.3 and 3.2.4.). The first two subsections present the results for SO_2 emissions from Lahore city, whereas, in the third subsection the spatial distributions of SO_2 along the driving routes are discussed with respect to the potential emission sources.

4.2.1. Emission Estimation Results

4.2.1.3. Category I Results

SO_2 emissions are estimated for nine circles under this category. Except one circle on 26 February 2018, all circles were performed along the larger route. Enhanced SO_2 VCDs were observed at the downwind side while lower values can be seen at the upwind side of the routes, as shown in Figure 4.10. The lowest emissions for the large circle (8.45×10^{24} molecules s^{-1}) were observed on 28 May 2017 (circle-II). For that circle, a smaller gradient between the outflux and the influx values was observed. The highest emissions (3.01×10^{25} molecules s^{-1}) were observed on 17 May. The mean emission for the large circles under this category is found to be 1.75×10^{25} $\pm6.87\times10^{24}$ molecules s^{-1}. The area emissions for large circles ranged between 9.37×10^{15} and 3.34×10^{16} molecules s^{-1} m^{-2}, whereas the emissions per area for the single small circle performed under this category were found 1.17×10^{16} molecules s^{-1} m^{-2}. The total errors range between ± 26.7% and ±37.5%. The total error is calculated by taking the square root of the quadratic sum of the errors due to the gaps in the measurements, uncertainties in the wind data and the retrievals of the SCDs and VCDs (see also section 4.1.1.3). The SO_2 emissions and the total error estimates for all

days under this category are presented in Tables 4.7 and 4.8, respectively. Figure 4.12 exhibits the emissions with the corresponding errors.

On three days, (17.05.17, 3.06.17 and 26.02.18) as shown in Figure 4.10 (lower most panel), substantially enhanced SO_2 VCDs were also observed at the north and south sides of the circles in addition to the downwind sides. As mentioned earlier, on the north side there is a cluster of metal industries which use refused rubber and plastic products as fuel in addition to the coal and heavy fuel oil. These fuels contain sulfur, and so after combustion, also SO_2 is emitted. On the south side, there are power plants and several industries along the road. These power plants use fuel oil for electricity generation, and several industries use coal and residual oil to operate their boilers. It can be assumed that the fuel used in power plants and the industries contains high sulfur content which may be the predominant source of SO_2 in this part of the route. Fioletov et al., (2016) prepared a global catalogue of SO_2 sources and derived the emissions from measurements of the Ozone Monitoring Instrument (OMI). According to them, in 2014 the power plants at the south of the large circle emitted 23 kilo tons ($\sim 6.86 \times 10^{24}$ molecules s^{-1}) of SO_2. On 26 February 2018 (smaller circle), at the north-western part of the route, enhanced VCDs can also be seen. These high values may be due to the small industries in the vicinity. SO_2 emissions estimated for this circle were 5.04×10^{24} molecules s^{-1}. These industries also use sulfur containing refused plastic and rubber products as fuel. Moreover, diesel generators are also used as backup energy source to generate electricity during the load-shedding in the area. Diesel combustion in heavy vehicles is also one of the sources of SO_2 emissions (Olatunji et al. (2015) and references therein). Yasin et al., (2012) tested the quality and environmental impacts of high-speed diesel fuel used in Pakistan. They reported that their analyzed diesel samples contain an average Sulfur concentration of 0.393 wt.%. This high sulfur content exceeds the permissible limits even according to the EURO 2 standards (500 ppm or 0. 05 wt.%) adopted by Pakistan during the study period

Table 4.7: Derived SO_2 emissions (category I)

Date	SO_2 emissions (molec s^{-1})	Mean SO_2 emissions (molec s^{-1})	Area emissions (molec s^{-1} m^{-2})	Mean area emissions (molec s^{-1} m^{-2})
17 May 2017	3.01×10^{25}	1.75×10^{25} $\pm7.03\times10^{24}$	3.34×10^{16}	2.15×10^{16} $\pm7.03\times10^{24}$
28 May 2017 (I)	1.10×10^{25}		1.22×10^{16}	
28 May 2017 (II)	8.45×10^{24}		9.37×10^{15}	
29 May 2017	2.27×10^{25}		2.52×10^{16}	
03 Jun 2017	1.88×10^{25}		2.09×10^{16}	
14 Feb 2018	1.83×10^{25}		2.03×10^{16}	
26 Feb 2018	2.12×10^{25}		2.35×10^{16}	
06 Mar 2018	2.44×10^{25}		2.71×10^{16}	
26 Feb 2018 (small circle)	5.04×10^{24}	----	1.17×10^{16}	----

Table 4.8: Estimated relative errors (%) of the derived SO_2 emissions (category I)

Error of	Uncertainties due to		17 May 2017	28 May 2017		29 May 2017	03 Jun 2017	14 Feb 2018	26 Feb 2018	26 Feb 2018	06 Mar 2018
				I	II						
SCDs	Spectral retrieval		15	15	15	15	15	15	15	15	15
VCDs	Geometric approximation		20	20	20	20	20	20	20	20	20
SO_2 Flux	Wind	45° shift	9.6	17.0	10.3	5.3	22.0	11.0	8.0	13.4	5.0
		Tempo-ral interpo-lation	15.0	19.5	15.0	17.0	4.4	2.7	4.6	6.8	8.0
	Gaps		2.0	1.1	19.3	0.4	3.6	15.0	2.4	4.8	1.6
Total Error (±%)			**31**	**37**	**36**	**31**	**34**	**3**	**27**	**28**	**27**

Table 4.9: Derived SO_2 emissions for the large circles (category II)

Date	SO_2 emissions (molec s^{-1})	Mean emissions (molec s^{-1})	Area emissions (molec s^{-1} m^{-2})	Mean area emissions (molec s^{-1} m^{-2})
27 May 2017	2.9×10^{24}		3.22×10^{15}	
17 Feb 2018	8.3×10^{24}	5.97×10^{24} $\pm2.26\times10^{24}$	9.17×10^{15}	6.63×10^{15} $\pm3.06\times10^{15}$
18 Feb 2018	6.7×10^{24}		7.49×10^{15}	

Table 4.10: Derived SO_2 emissions for the small circles (category II)

Date	SO_2 emissions (molec s^{-1})	Mean emissions (molec s^{-1})	Area emissions (molec s^{-1} m^{-2})	Mean area emissions (molec s^{-1} m^{-2})
17 Feb 2018	5.0×10^{24}	7.57×10^{24} $\pm2.20\times10^{24}$	1.17×10^{16}	1.76×10^{16} $\pm5.11\times10^{15}$
27 Feb 2018	9.0×10^{24}		2.08×10^{16}	
07 Mar 2018	8.7×10^{24}		2.02×10^{16}	

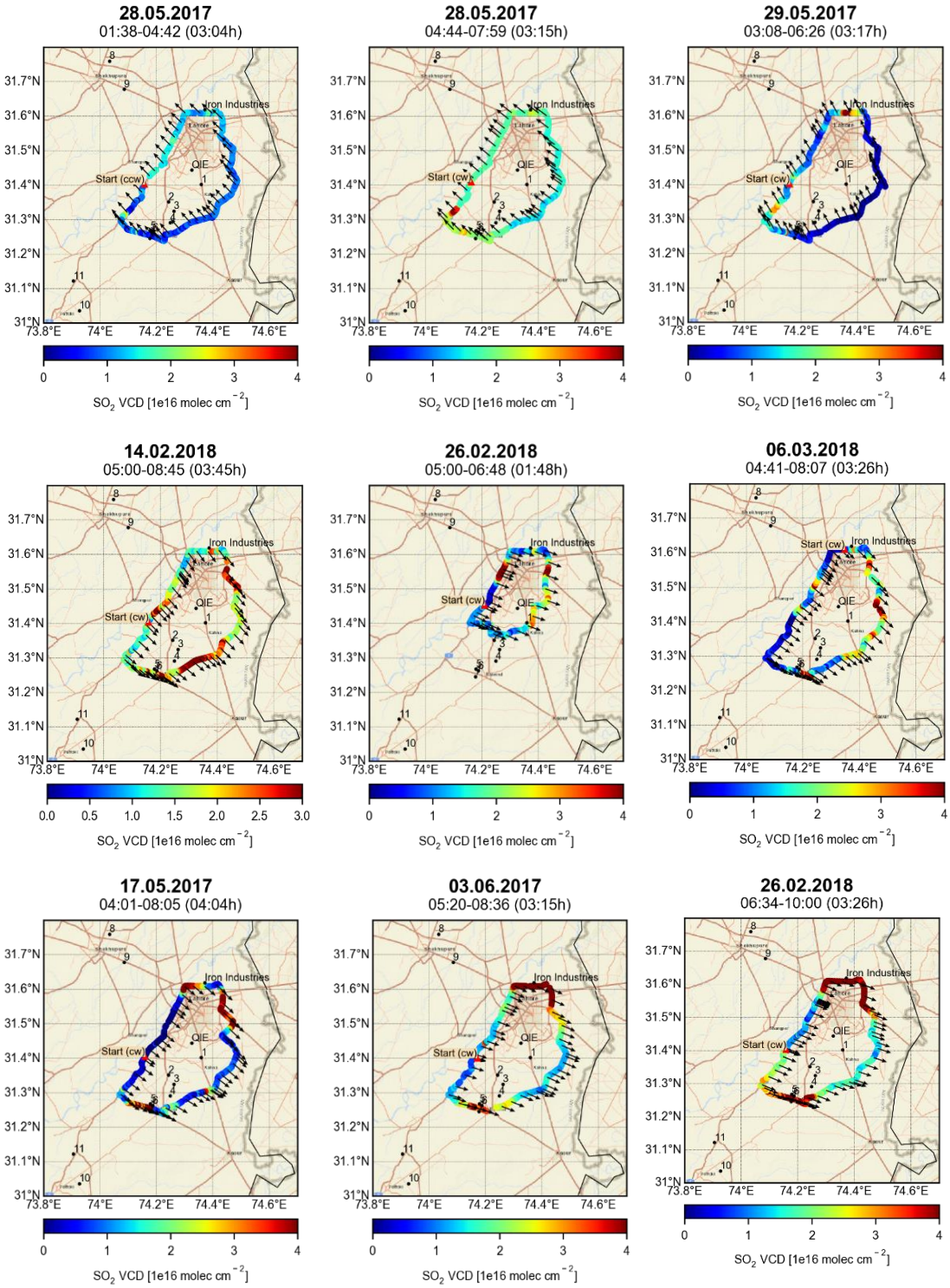

Figure 4.10: SO_2 VCDs around Lahore measured under category I conditions. High VCDs are usually observed at the downwind side of the circles. On 26.02.2018 enhancements can also be observed in the north-western part of the circle indicating influx from sources outside the circle. The black arrows represent the corresponding wind vectors. On three days in the lower most panel enhanced values can also be seen at the north and south parts of the route in addition to the downwind sides indicating emissions from nearby power plants and industrial processes (see text).

4.2.1.4. Category II Results

Measurements around six circles fall under this category with higher uncertainties than for category I. One circle was performed in the summer while the remaining five circles (3 small and 2 large) were executed during spring. On some of the measurement days, (e.g., 17, 18 and 27 Feb 2018) as shown in Figure 4.11, enhanced values can be clearly seen at the downwind sides. The SO_2 emissions under this category ranged between 2.90×10^{24} and 8.99×10^{24} molecules s^{-1} with total errors ranging between ± 26.6 % and ± 47%. SO_2 emissions for large and small circles with their corresponding estimated uncertainties are presented in Tables 4.9 - 4.11 and Figure 4.12, respectively. The lowest emission (2.9×10^{24} molecules s^{-1}) was found for the single circle performed in summer on 27 May 2017. The mean emissions for the 3 large and the 3 small circles under this category are found to be $6 \times 10^{24} \pm 2.5 \times 10^{24}$ molecules s^{-1} and $7.6 \times 10^{24} \pm 2.2 \times 1\ 0^{24}$ molecules s^{-1}, respectively.

Table 4.11: Estimated errors (%) of the SO_2 emissions (category II)

Error of	**Uncertainties due to**		**27 May 2017**	**17 Feb 2018**		**18 Feb 2018**	**27 Feb 2018**	**07 Mar 2018**
				Small	large			
SCDs	Spectral retrieval		15	15	15	15	15	15
VCDs	Geometric approximation		20.	20	20	20	20	20
SO_2 Flux	Wind	45° shift	23.7	20	13.29	25.4	4.6	25.3
		Temporal interpolation	9.7	11.3	12	11	3.9	8
SO_2 Flux	Gaps		25	32.4	11	12.5	6.8	10
Total Error (±%)			**43.6**	**47.0**	**32.7**	**9.4**	**26.6**	**42.7**

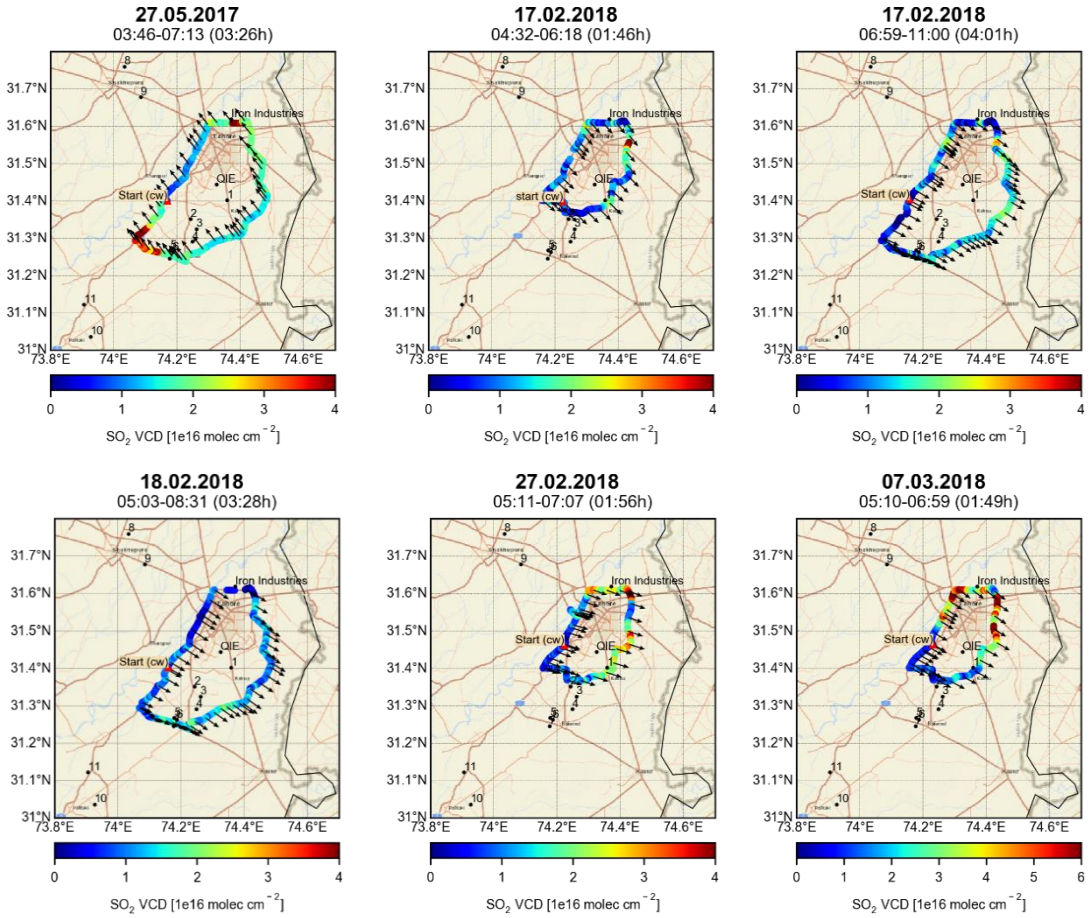

Figure 4.11: SO_2 VCDs around Lahore for measurements under category II conditions. The enhanced values can be usually observed at the downwind sides. The black arrows represent the respective wind vectors.

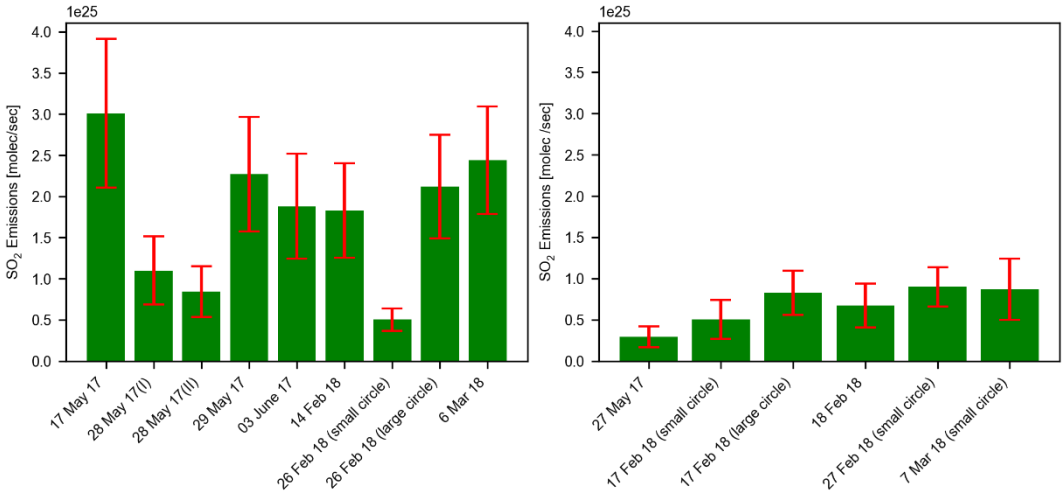

Figure 4.12: Bar graphs representing the estimated SO_2 emissions derived under category I (left) and category II (right) conditions during summer 2017 and spring 2018, respectively. The red error bars indicate the total estimated errors.

4.2.2. SO_2 Seasonal Variations

The seasonal variation of SO_2 in the study area can depend upon multiple factors. Different meteorological conditions and corresponding variable energy demands are the key factors that shape the emission patterns during different times of the year. According to the data available, high emission values were observed for the 5 circles performed in spring 2018 as compared to the averaged SO_2 emissions of the 6 circles performed in summer. The SO_2 emissions for summer ranged between 2.90×10^{24} and 3.01×10^{25} molecules s^{-1} with a mean emission value of 6.5×10^{24} molecules s^{-1} and standard deviation of 7.1×10^{24} molecules s^{-1}. In spring the mean emissions for the 6 circles are found to be 1.33×10^{25} molecules s^{-1}. Averaged SO_2 emissions with their corresponding standard deviations are presented in Table 4.12. One probable reason of the higher values for the Feb-Mar 2018 measurements might be that in colder months, natural gas is supplied to the domestic users on priority basis (Express Tribune, 2017) and industries then face shortage of natural gas supplies. So, the industrial sector has to switch to sulfur-containing fossil fuels (e.g., residual fuel oil, diesel and coal) for combustion and energy production. which results in the higher SO_2 emissions.

The mean area emissions for the 4 smaller circles (1.40×10^{15} molecules s^{-1} m^{-2}), and 5 large circles (1.48×10^{15} molecules s^{-1} m^{-2}) performed in spring 2018 showed quite comparable values that indicates that the densely populated as well as the peripheral part of the city are equally responsible in terms of the SO_2 emission shares.

Table 4.12: Mean SO_2 emissions in summer and spring

Details	Total Circles	Mean emissions (molec s^{-1})	Standard Deviation (molec s^{-1})	Mean area emissions (molec s^{-1} m^{-2})
Summer (large circles)	6	6.50×10^{24}	7.12×10^{24}	7.21×10^{15}
Spring (large circles)	5	1.33×10^{25}	8.15×10^{24}	1.48×10^{16}
Spring (small circles)	4	6.05×10^{24}	1.98×10^{24}	1.40×10^{16}

4.2.3. Spatial Distribution of Sulfur Dioxide (Category III)

The measurements, where the conditions were not suitable to estimate the emissions from the encircled area are discussed in this section. Spatial distributions of the SO_2 VCDs for the two measurement periods (summer 2017 and spring 2018) are presented. Measurements around various circles were performed during May-June 2017 and Feb-March 2018. Spatial distribution results for few selected days are presented here. Figures for rest of the measurements can be found in appendix B.2. On most of the days, similar enhancement patterns were observed. On the south and north ends of the larger circles, SO_2 VCDs were

found to be $\geq 5\times10^{16}$ molecules cm^{-2} on several days. As already discussed in the previous subsections, metal works related industries and power plants are the main reasons of enhanced VCDs in these areas. Figure 4.13 exemplifies two such days. All the power plants located south of the large circle use residual fuel oil (RFO) for combustion (NEPRA, 2018). Processing of crude oil yields RFO as residue, and its sulfur content depend upon the amount of sulfur present in the crude oil. RFO may contain sulfur up to 2.9 % (Poot et al., 2002). In addition to RFO used in the power plants, boilers in many industries, located in this area also use coal for combustion. Coal also has a rather high sulfur content. It can be assumed that power plants and industries in the south are the major emitters of SO_2 in the peripheral region.

On Fridays, the majority of the metal industries do not operate, and low values were observed at the north part of the route, e.g., on Friday, 16 March 2018 (Figure 4.14). Similarly, on few days, no high SO_2 VCDs were observed in the south. Figure 4.6 (left) shows measurements on 19 February with low SO_2 VCDs in the power plants region. This indicates that the power plants might not be operational at the time of the measurement. Enhanced SO_2 VCDs can also be observed at the east and south-eastern parts of the smaller circles. The primary sources for these enhancements can be the industries at the QIE industrial zone and along the road that use sulfur containing residual fuel oil or coal as fuel for their boilers. Figure 4.15 indicates enhanced SO_2 VCDs in this part.

The traffic in the city center is primarily light duty traffic that runs on gasoline or natural gas. Heavy-duty vehicles like trucks that run on diesel can only enter the city between 23:00 to 06:00 local time (18:00-01:00 UTC) (Ali & Athar, 2010). The Figure 4.16. (left) shows low VCD values $\leq 1\times10^{16}$ molecules cm^{-2} on the roads in the central part of the city. Whereas high VCDs in the range of $\geq 5\times10^{16}$ molecules cm^{-2} can be seen in Figure 4.16 (right) at the west and northwest parts of the route. This leg of the route was executed along parts of the N5 highway and the M2 motorway. All types of vehicles are allowed on these roads throughout the day. The trucks and buses operate on diesel fuel and the high SO_2 VCDs along this part on some days may be due to the emissions from these vehicles.

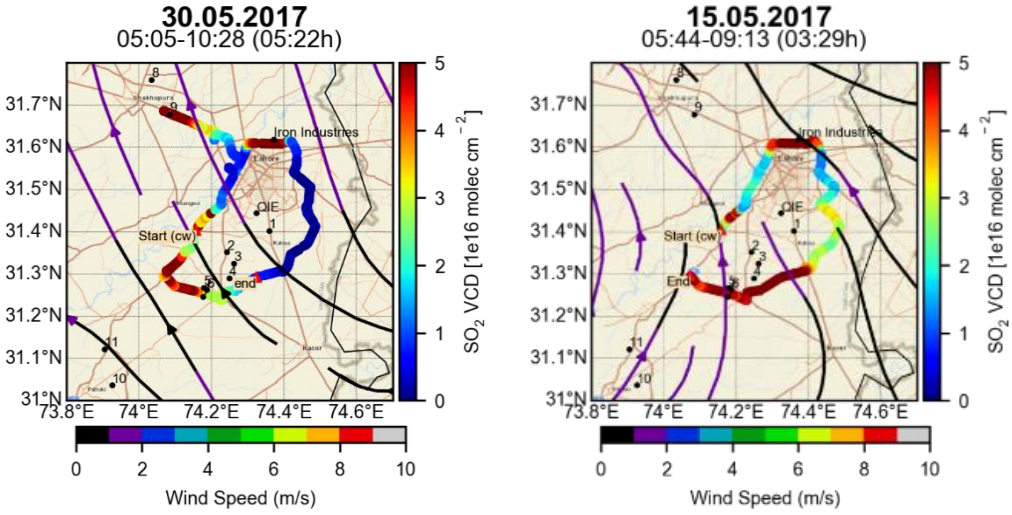

Figure 4.13: Enhanced SO_2 VCDs at the north and south parts of the circle in two selected days. On 30 May, measurements were extended in the northwest where high values were observed due to SO_2 emitted from the power plant 9 located along the road. The streamlines represent the ECMWF wind outputs at 6 UTC.

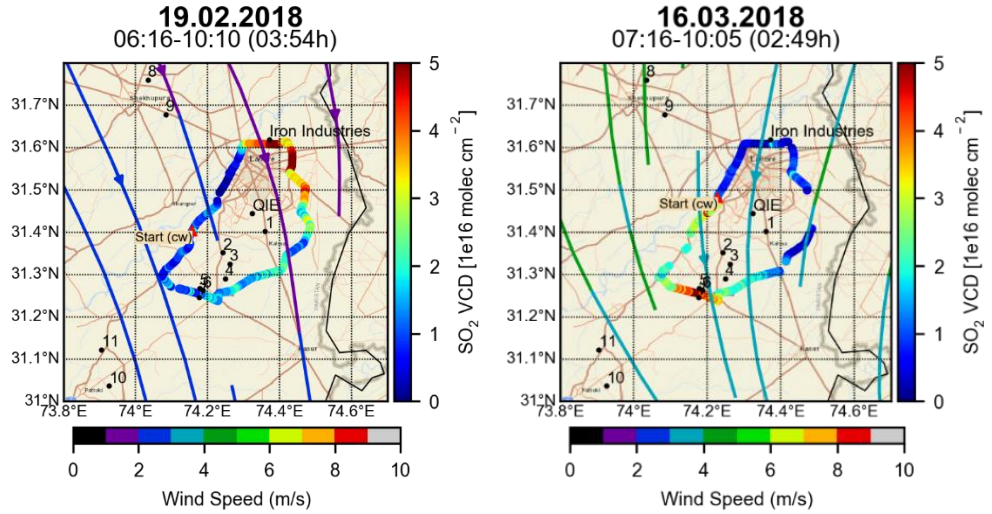

Figure 4.14: Measurements performed on 19 Feb and 16 March 2018 showing typical enhancement pattern at the south and north ends of the route. The streamlines represent the ECMWF wind output at 6 UTC.

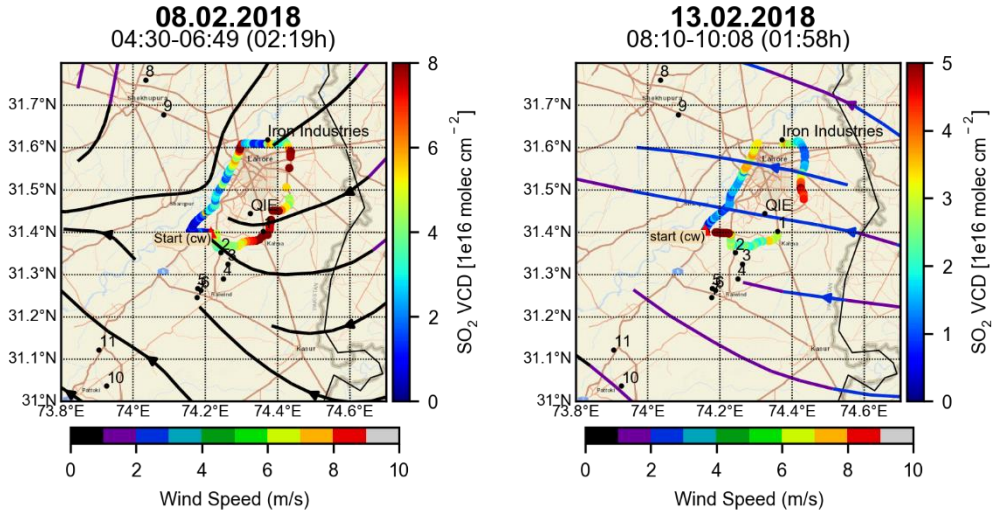

Figure 4.15: Enhanced SO_2 VCDs at the east and southeast parts of the smaller circles on two days during spring 2018. The streamlines represent the ECMWF wind output at 6 UTC.

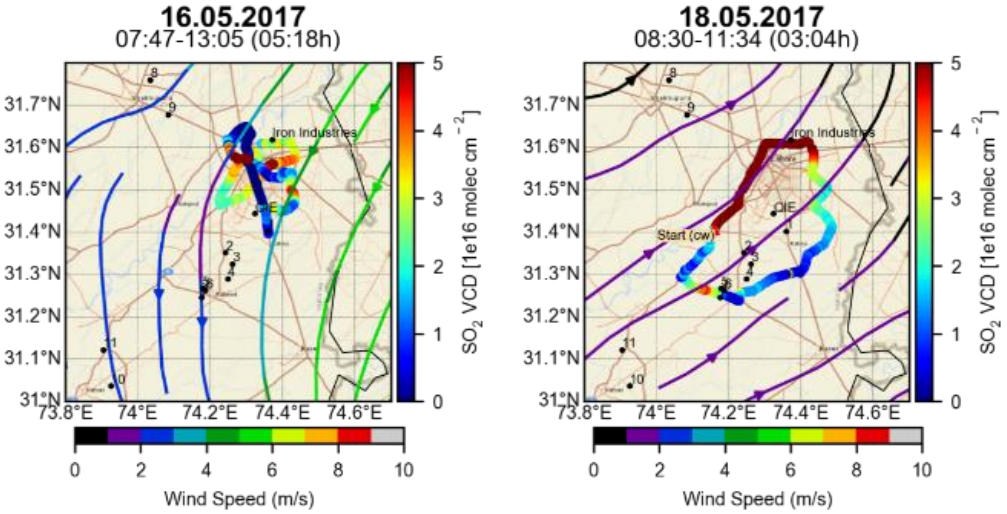

Figure 4.16: SO_2 VCDs measured on two days in summer 2017. The spatial patterns probably represent the impact of the fuel type used in different vehicles (see text).

4.3. FORMALDEHYDE (HCHO)

Formaldehyde (HCHO) is the simplest and most abundant aldehyde present in atmosphere. It is emitted directly from both biogenic and anthropogenic processes, but a substantial fraction originates from secondary formation from both natural and anthropogenic precursors (Li et al., 2014 and references therein). In addition to the estimation of NO_2 and SO_2 emissions, the total flux of formaldehyde from the city was also quantified for the summer 2017 and spring 2018 campaigns. The HCHO flux represents direct HCHO emissions and HCHO from secondary formation. Thus it can be studied as an indicator for the volatile organic compound (VOC) emissions in the area (Finlayson & Pitts., 2000). Flux The flux results for HCHO are discussed for two measurement categories, based on the conditions as described in section 2.6.2. In addition to the flux calculations, also the spatial distributions of HCHO along the driving routes are discussed with respect to the corresponding potential sources.

4.3.1. Flux Results

Collectively, 15 circles got qualified to be considered for the flux estimation. Out of these 15 circles, 8 are eligible for the category I while the remaining 7 are considered under category II according to the criteria, devised in section 2.6.2. The total formaldehyde flux of the city was calculated by using Eq. (2.47). Here, it should be noted that unlike NOx and SO2, the formaldehyde flux was calculated and not the direct emissions. The quantification of the HCHO emissions and even the total fluxes is not as straightforward. The factors like, short lifetime and complex chemistry like secondary formation in addition to the primary sources make the quantitative interpretation of the calculated flux a non-straightforward task. Thus the quantitative interpretation of the flux values should be done with care.

4.3.1.1.Category I Results

The results from the 8 circles on the days where low uncertainties are expected are presented under category I. Higher formaldehyde VCDs are observed at the downwind sides while low values can be seen at the opposite sides of the routes. The measurements performed under this category are shown in Figure 4.17. All circles except the one performed on 26 Feb 2018 were executed along the large route. The highest flux (1.28×10^{25} molecules s^{-1}) was found on 29 May 2017, while the lowest flux (2.08×10^{24} molecules s^{-1}) was observed on 26th Feb 2018 for the small circle. The mean flux for all the large circles turned out to be $7.56\times10^{24} \pm 2.08\times10^{24}$ molecules s^{-1}. The total estimated error, due to the uncertainties in the spectral analysis, VCD calculation, wind fields and measurement gaps was calculated as the square root of the quadratic sum of all individual errors. The details of the error sources are described in section 4.1.1.3. The total errors estimated for the flux measured under this category ranged between ±25.6% and ±38.5%. The calculated flux and the corresponding errors are presented in Figure 4.19 and Tables 4.13 and 4.14.

4.3.1.2. Category II Results

The 7 circles (3 large and 4 small circles), where higher errors in the derived fluxes were expected (see section 2.6.2) are presented in this section. The highest flux (9.52×10^{24} molecules s^{-1} was found on 17 Feb 2018, while the lowest flux (3.05×10^{24} molecules s^{-1}) was observed on 27 May 2017. The mean flux for the large and small circles, turned out to be $6.26\times10^{24} \pm 3.23\times10^{24}$ and $5.71\times10^{24} \pm 1.72\times10^{24}$ molecules s^{-1}, respectively. The total estimated errors ranged between ±26% and ±37%. The measurements performed under this category are shown in Figure 4.18. The estimated fluxes and the corresponding relative errors are given in Figure 4.19 and Tables 4.15-4.17

Table 4.13: Derived HCHO flux for Lahore (category I)

Date	HCHO Flux (molec s^{-1})	Mean Flux (molec s^{-1})	Area emissions (molec s^{-1} m^{-2})	Mean area emissions (molec s^{-1} m^{-2})
17 May 2017	1.11×10^{25}		1.23×10^{16}	
28 May 2017	4.90×10^{24}		5.43×10^{15}	
29 May 2017	1.28×10^{25}		1.42×10^{16}	
03 Jun 2017	7.46×10^{24}	7.56×10^{24} $\pm3.43\times 10^{24}$	8.27×10^{15}	8.69×10^{15} $\pm4.00\times10^{15}$
14 Feb 2018	8.84×10^{24}		9.80×10^{15}	
26 Feb 2018	2.08×10^{24}		2.30×10^{15}	
06 Mar 2018	7.65×10^{24}		8.48×10^{15}	
26 Feb 2018 (small circle)	6.45×10^{24}		1.50×10^{16}	

Table 4.14: Estimated relative errors (%) for the derived HCHO fluxes (category I)

Error of	Uncertainties due to		17 May 2017	28 May 2017	29 May 2017	03 Jun 2017	14 Feb 2018	26 Feb 2018	26 Feb 2018	06 Mar 2018
SCDs	Spectral retrieval		15	15	15	15	15	15	15	15
VCDs	Geometric approximation		20	20	20	20	20	20	20	20
HCHO Flux	Wind	45° shift	3.7	21.3	7.5	4.5	4.6	12.1	28.1	2.3
		Tempo-ral interpo-lation	11	14.4	14.7	5	1.7	4.7	8.1	5
HCHO Flux	Gaps		1.8	1.8	2.6	3.3	3.5	6.9	0.5	1.07
Total Error (±%)			**27.5**	**36.0**	**30.0**	**26.0**	**25.7**	**29.0**	**38.5**	**25.6**

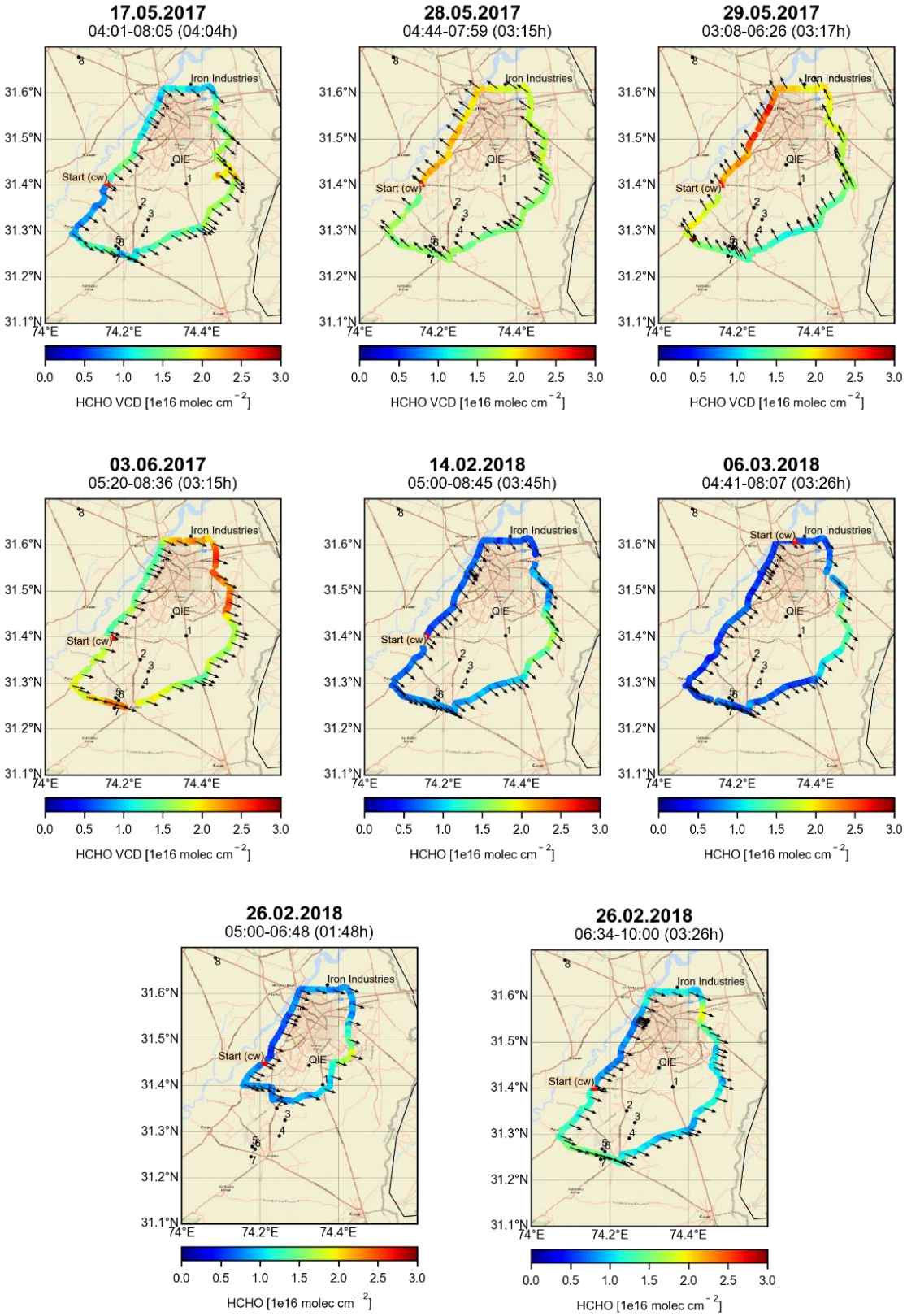

Figure 4.17: Tropospheric HCHO VCDs for category I measurements around Lahore during the summer and spring measurement periods. The black arrows represent the averaged wind directions during the driving period.

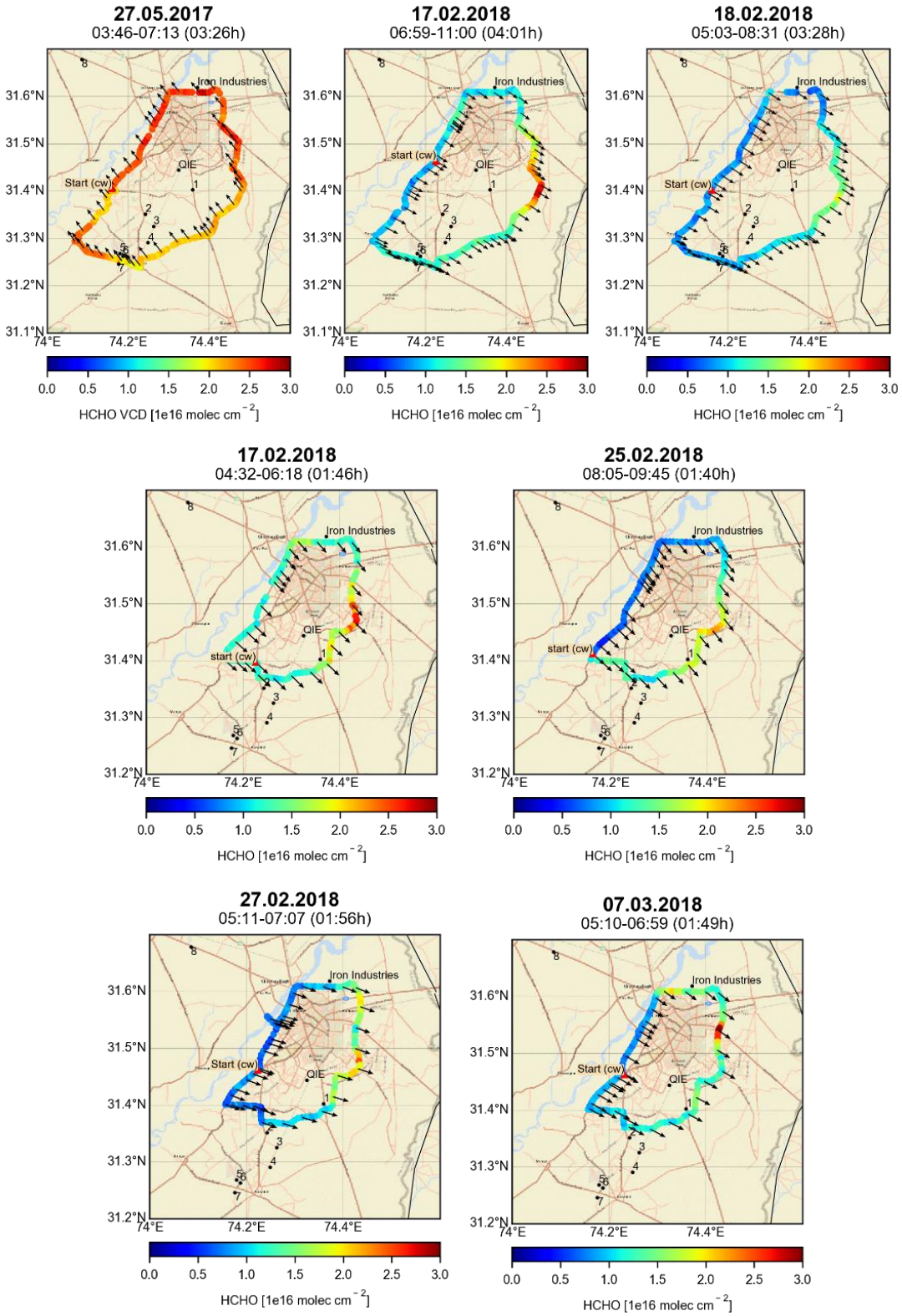

Figure 4.18: Formaldehyde VCDs around Lahore for flux measurements under category II conditions. The three figures in the top panel represent the measurements along the large circles. High values are observed on the downwind side of the circles. The black arrows represent the averged wind directions during the measuement duration.

Table 4.15: Derived HCHO fluxes for the large circles (category II)

Date	HCHO Flux (molec s^{-1})	Mean Flux (molec s^{-1})	Area Flux (molec s^{-1} m^{-2})	Mean area Flux (molec s^{-1} m^{-2})
27 May 2017	3.05×10^{24}		3.38×10^{15}	
17 Feb 2018	9.52×10^{24}	6.26×10^{24} $\pm3.23\times10^{24}$	1.05×10^{16}	6.94×10^{15} $\pm3.58\times10^{15}$
18 Feb 2018	6.20×10^{24}		6.87×10^{15}	

Table 4.16: Derived HCHO fluxes for the small circles (category II)

Date	HCHO Flux (molec s^{-1})	Mean Flux (molec s^{-1})	Area emissions (molec s^{-1} m^{-2})	Mean area Flux (molec s^{-1} m^{-2})
17 Feb 2018	4.86×10^{24}		1.13×10^{16}	
25 Feb 2018	8.10×10^{2}	5.71×10^{24} $\pm1.72\times 10^{24}$	1.32×10^{16}	1.32×10^{16} $\pm3.98\times10^{15}$
27 Feb 2018	5.70×10^{24}		1.88×10^{16}	
07 Mar 2018	4.16×10^{24}		9.65×10^{15}	

Table 4.17: Estimated relative errors (%) for the derived HCHO fluxes (category II)

Error of	Uncertainties due to		27 May 2017	17 Feb 2018 (Small)	17 Feb 2018 (large)	18 Feb 2018	25 Feb 2018	27 Feb 2018	07 Mar 2018
SCDs	Spectral retrieval		15	15	15	15		15	15
VCDs	Geometric approximation		20	20	20	20		20	20
HCHO Flux	Wind	45° shift	26.5	7.7	4.7	7.4	8.2	7	3.8
		Temporal interpolation	6.6	9.1	10.4	9.8	9.6	1.4	9.8
HCHO Flux	Gaps		1.1	9.8	0.2	1.2	1.5	0.4	1.5
Total Error (±%)			**37.0**	**29.4**	**27.5**	**28**	**28**	**26**	**27.2**

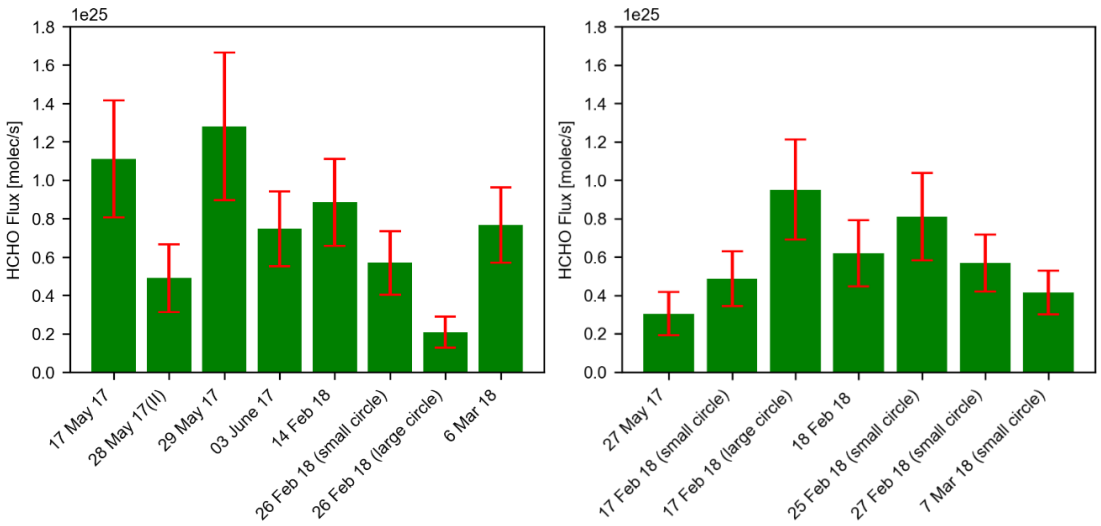

Figure 4.19: HCHO flux derived for the measurements under category I (left) and category II (right). The red error bars represent the total errors.

4.3.2. Formaldehyde Seasonal Variation

In the current study, an effort has also been made to compare formaldehyde VCDs and emissions during the spring and summer seasons. For both seasons, averaged formaldehyde flux results for 5 large circles are available. Additionally, averaged flux results for the 5 smaller circles performed during the spring are available. Table 4.18 presents weighted means of the available measurements with their respective weighted standard deviations. The results show that the mean values for the two seasons are quite similar. The values for summer and spring were found as 6.72×10^{24} $\pm2.97\times10^{24}$ and 6.82×10^{24} $\pm2.76\times10^{24}$ molecules s^{-1}, respectively. The averaged flux for the smaller route was found to be 5.23×10^{24} $\pm1.13\times10^{24}$ molecules s^{-1}. Seasonal variations of formaldehyde columns have been studied previously. E.g., Choi & Souri (2015) observed HCHO columns over Iran, Khokhar et al. (2015) studied the seasonal variation over Pakistan, and Javed et al. (2019) studied HCHO columns in China using ground based and satellite data. They reported maximum values in summer and low values during the winter. Zeb et al. (2019, and references therein) also mentioned that the high values in summer are a result of the enhanced biogenic activity and biomass burning or crop residue burning. According to Zeb et al. (2019), and references therein, biogenic emissions and agricultural fires are enhanced in periods with hot temperatures. As a result, isoprene from vegetation is emitted at enhanced rates. Khokhar, et al. (2015) reported that in Pakistan, May-June is generally attributed as the crop residue burning period and this may also lead to enhanced formaldehyde formation, whereas, in colder months, low temperatures may suppress the biogenic emissions. Chan et al. (2020) observed HCHO VCDs by using MAX-DOAS observations in Munich and reported slightly higher values during winter and attributed this enhancement to domestic heating and natural gas power plants. In the current thesis, the results showed quite similar values for the spring and summer measurements.

From this finding it can be assumed that in Lahore, the major formaldehyde sources remain unchanged throughout the year, or the variation of different sources compensate each other. Moreover, the vegetation and crop burning activities may not have a pronounced effect on the formaldehyde levels during the study period as it is probable that no event of crop residue burning activity occurred during the measurements along the 5 circles performed during summer. Moreover, the HCHO lifetime is longer in colder months (Bastien et al., 2018; Chan et al., 2020) and this factor might also contribute to the similar values in both the seasons. Furthermore, the major portion of the driving route is comprised of urban area dominated by anthropogenic activities. Agricultural fields are present along only ~30 km section of the total 130 km long route in the east to southeast directions (Sue Asal Road). Various industries are also located along this section.

Table 4.18: Seasonal mean formaldehyde fluxes for Lahore

Details	Total Circles	Mean HCHO Flux (molec s^{-1})	Standard Deviation (molec s^{-1})	Mean area emissions (molec s^{-1} m^{-2})
Summer (large)	5	6.72×10^{24}	2.97×10^{24}	7.45×10^{15}
Spring (large)	5	6.82×10^{24}	2.76×10^{24}	7.56×10^{15}
Spring (Small)	5	5.23×10^{24}	1.13×10^{24}	1.21×10^{16}

4.3.3. Spatial Distribution of Formaldehyde (category III)

The measurements where the quantification of the trace gas flux was not possible according to the suitability criteria devised in section 2.6.2 are discussed in this section. These measurements are grouped under category III and still give some interesting information about the spatial distributions of HCHO measured along the driving route during the summer 2017 and spring 2018 campaigns. Major formaldehyde sources along the driving routes are also attempted to be identified.

Around 20 circles during each measurement campaign were executed to study the formaldehyde distributions. For the summer campaign the formaldehyde VCDs ranged between ~3.5×10^{15} and ~8.3×10^{16} molec cm^{-2} and for the spring measurements, this range was between ~4.5×10^{15} and ~6.5×10^{16} molec cm^{-2}. Results from some of the measurement circles from both campaigns are discussed here. The figures for all other days depicting the HCHO spatial distributions can be found in the appendix B.3.

During the summer 2017 campaign, measurements were performed along the large circles except for three days i.e., 14.05, 16.05 and 4.06. Figure 4.20 represents the HCHO spatial distributions measured on the above-mentioned dates. On 14 and 16 May 2017, additional measurements were performed along the main roads bounded inside the large circle. On 14 May 2017, the highest VCDs (~8.3×10^{16} molecules cm^{-2}) for the whole campaign were

observed. The 6 UTC wind output shows that the wind is coming from the west with speeds between 2 and 3 m s^{-1}. The highest column densities were observed in the north and north east parts of the route. In the north, an open waste dumping site (Mehmood Booti open dumping) is located along the road. The waste is openly dumped over an area of about 0.32 km^2 (Haydar et al., 2012) and piled up to the height of ~20 m from the ground level. The municipal solid waste sites emit methane (CH_4) as a result of the anaerobic decomposition of the organic waste (Themelis & Ulloa, 2007). In the presence of OH, methane is oxidized and formaldehyde is formed (see also section 1.5.3) (Atkinson, 2000; Koppmann, 2007). Alam et al. (2017) estimated the methane emissions from the Mehmood Booti dumping site for the year 2014 by using the LandGem model and reported high methane values (5.45×10^6 Mg/year). The high HCHO column densities in the north may also be attributed to this dumping site. Enhanced HCHO VCDs ($\geq 5.5\times10^{16}$ molecules cm^{-2}) were found along the part of the route adjacent to the dumping site. A cluster of industries related to metal and iron works is also located in that part. Enhanced column densities can also be attributed to the emissions from these metal industries as formaldehyde has been detected from the emissions of industries related to metal products (Liteplo et al., 2002). On the busy roads in the city center, high formaldehyde columns around $\geq 3.5\times10^{16}$ molecules cm^{-2} were observed. It can be assumed that the traffic, iron industries and the dumping site are the main HCHO source in this part of the city.

On 16 May, measurements were performed on the busy roads of the city, and HCHO VCDs ranging between $\sim1.5\times10^{16}$ and $\sim2.5\times10^{16}$ molecules cm^{-2} were found. The 12 UTC ECMWF output indicates southerly winds.

On 4 June 2017 measurements were performed in three periods (Figure 4.20, lower panels) including measurements along one large circle and one small circle to encircle the densely populated part of the city. An additional loop along two of the main roads (Ferozepur Road and Raiwind Road) was also executed. The wind speeds at 6 UTC were quite low (around <2 m s^{-1}). It can be assumed that the enhanced values measured for the two circles on this day are localized as a result of the low wind speeds. Enhanced VCDs of around 2.5×10^{16} molec cm^{-2} were observed along the busy roads.

To further understand, the spatial distribution of formaldehyde along the large routes executed during the same campaign, some additional selected days are discussed now. The corresponding measurements are presented in Figure 4.22. Enhanced HCHO VCDs ($\geq3\times10^{16}$ molecules cm^{-2}) were found at multiple locations along the driving route on various days.

On 12 May 2017 high VCDs were seen on the southeast part of the circle. These values can most probably be attributed to agricultural activity (Wolfe et al., 2016) and burning of crop residues. Crop residue burning was observed while driving along the agricultural fields in the southeast section of the circle (Figure 4.21). As already mentioned, Khokhar et al., (2015) observed enhanced HCHO columns over Lahore using satellite data during May and they attributed these peak values to the agriculture fires.

On 15 May 2017, VCDs higher than 3×10^{16} molecules cm^{-2} can be observed along most parts of the route. The wind speeds for the 6 UTC output were calm and the enhancements

can be considered as localized. The elevated values in the south may be attributed to the combustion activities in industries, present in the vicinity. Among these industries are paper and pulp industries, which are also formaldehyde emitters (Cheremisinoff & Rosenfeld, 2010; Liteplo et al., 2002). The high HCHO VCDs in the north-west are most probably due to vehicular emissions.

On 18 May 2017 two larger circles around the city were executed and both show similar enhancement patterns i.e., enhanced VCDs on the northern part of the route. The first circle performed on that day is shown in Figure 4.22. As mentioned earlier, iron industries and a waste dumping site are located along the north part of the route, which are probably responsible for these high values.

On 30 May 2017, the route was also extended to Sheikhupura city, located 35 km NW of Lahore. Maximum values were observed along the Lahore-Sheikhupura road. Various reported formaldehyde emitters like resin, paper & pulp, paint, chemicals and metal works industries are located along this section of the route. These enhanced VCDs are attributed to the above-mentioned industrial activities in addition to mobile sources.

On 2 June 2017 also measurements along two rounds were performed. During the first circle, enhancements were found on the east and west parts of the city. The vehicular emissions and agricultural activities might be the major sources of the enhancements in these sections. In the west, enhanced values are observed on the sections of the N5 highway and the M2 motorway. In the second circle, high VCDs can be seen on the northern half of the circle and the emissions from the iron industries and the dumping site as well as the vehicular emissions are probably responsible for these enhancements.

For the spring 2018 measurements 20 circles were classified as category III. Overall, enhanced HCHO columns were observed less frequently during this campaign. However, on some days, VCDs around $\geq 3\times10^{16}$ molecules cm^{-2} were also observed. Six circles from three selected days are presented in Figure 4.23. On 13 Feb 2018 two circles were performed. The first circle was executed along the large route and low VCDs with maximum values around 1×10^{16} molecules cm^{-2} were observed. The second route was executed along the small circle and VCDs as high as 5.6×10^{16} molec cm^{-2} were observed in the SSE of the circle. A paper mill is located 200 m north-west of the road and the observed high values are most likely due to the emissions from this paper industry. It was mentioned earlier that paper and pulp industries are strong sources of formaldehyde.

Measurements along two circles (one small and one large) were also performed on 19 Feb 2018. Both circles showed enhanced values in east and southeast directions. For the large circle elevated values are most probably due to the vehicular emissions as no prominent stationary source is spotted in the vicinity.

One large and one small circle were also executed on 23 Feb 2018. Maximum values around 1.5×10^{16} molecules cm^{-2} were found along the large route whereas strong enhancements were observed extending from east to south. The highest values around $\sim4.5\times10^{16}$ molecules cm^{-2} were observed in the eastern section of the circle. These enhancements may be primarily attributed to the paper mill and traffic emissions.

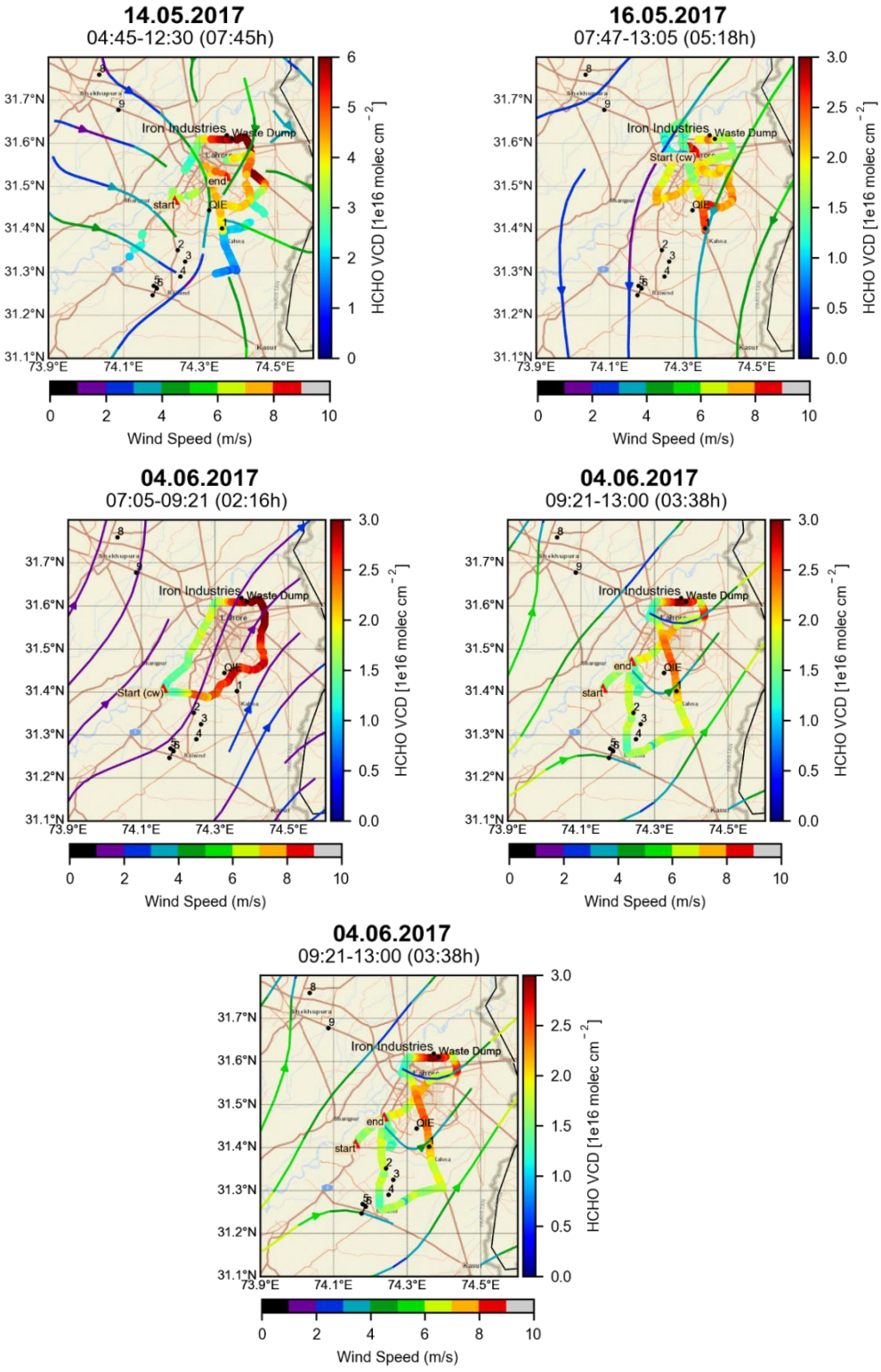

Figure 4.20: HCHO VCDs measured around Lahore on selected days along the roads inscribed in the large circle during the summer campaign. The streamlines represent the 6 hourly averaged ECMWF wind outputs with the corresponding closest times. For better depiction of the spatial distributions, the range of the VCDs' colour bar on 14th May 2017 is set higher as compared to the other days.

Figure 4.21: Crop residue burning activity observed adjacent to the road adopted for the route on 12 May 2017 at 8:11 UTC.

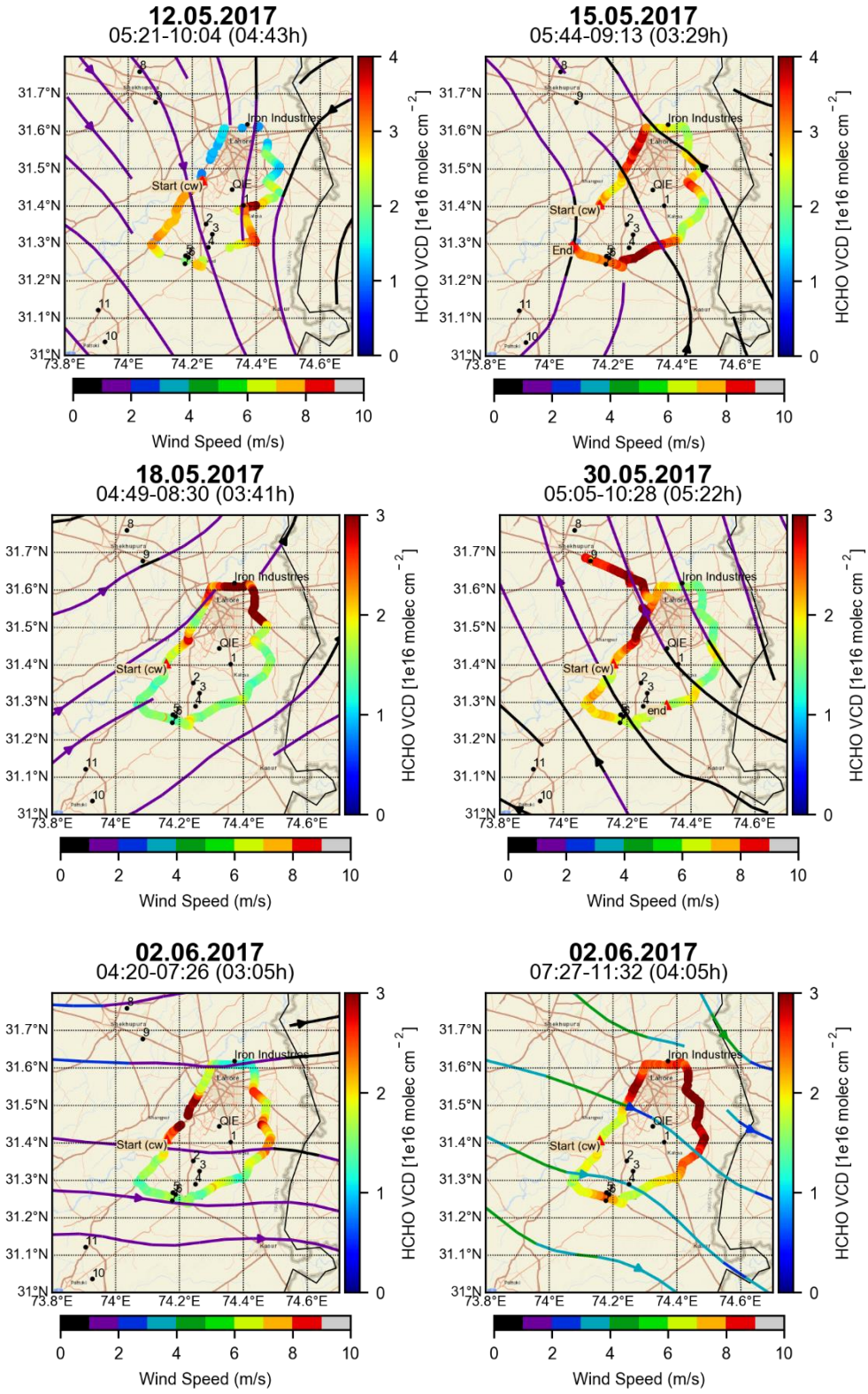

Figure 4.22: HCHO VCDs observed on selected days during the summer campaign along the large circle. The streamlines represent the corresponding averaged ECMWF wind outputs. Enhanced VCDs can be seen at multiple locations.

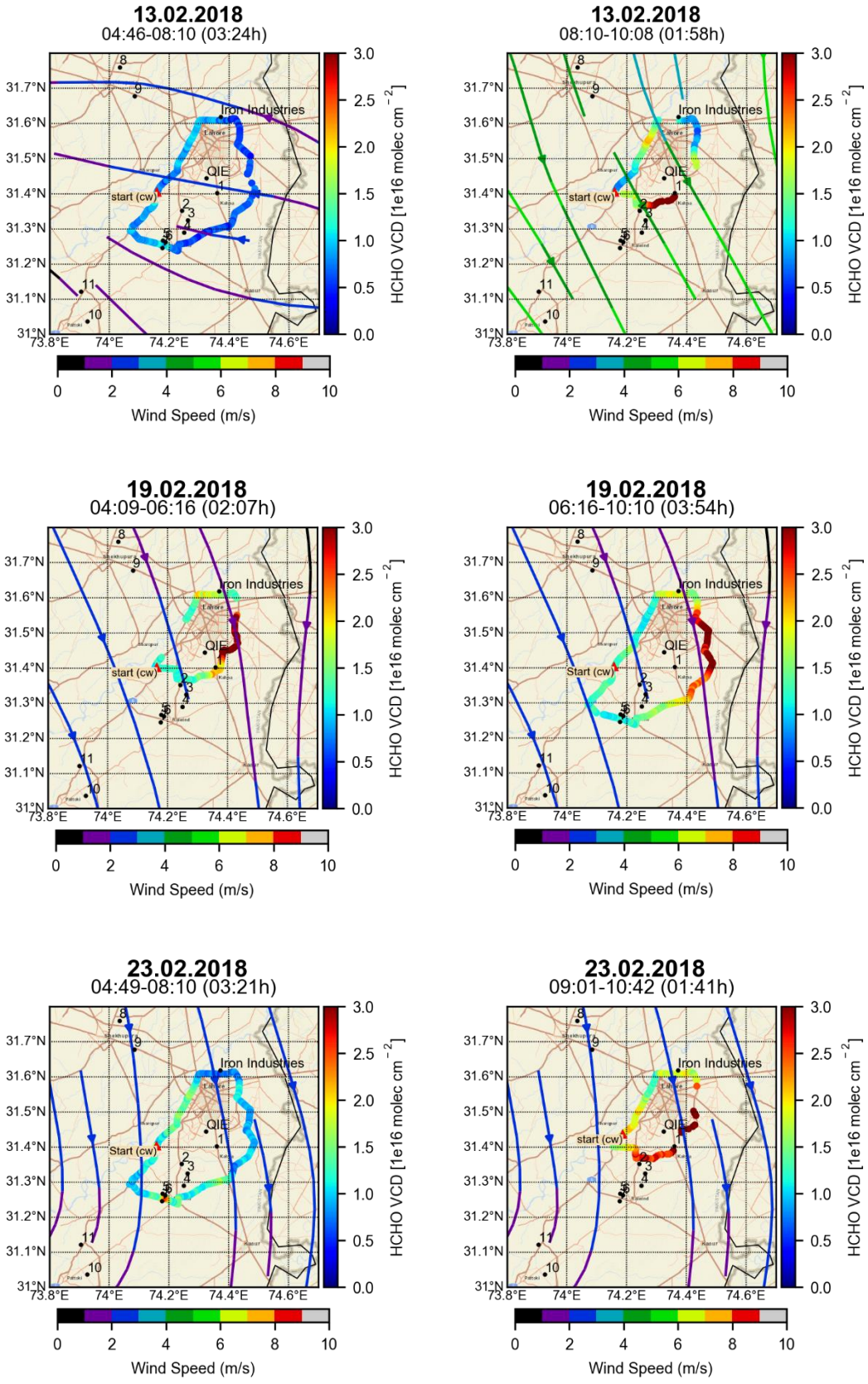

Figure 4.23: Formaldehyde VCDs on three selected days, measured during the spring 2018 campaign. The streamlines represent ECMWF wind outputs averaged for altitude of 500 m above the ground.

4.4. GLYOXAL (CHOCHO)

Glyoxal (CHOCHO) is the simplest α-dicarbonyl compound, formed from the oxidation of various VOCs emitted as a result of different anthropogenic and biogenic activities. In meagre amounts, it is also emitted from the vehicular exhaust. Like formaldehyde, glyoxal has also been used as an indicator of the VOC chemistry in the urban troposphere (Volkamer et al., 2005a and references therein).

The glyoxal distribution has also been studied previously using ground-based and satellite measurements in various regions of the world. E.g. Grosjean et al. (1990) detected glyoxal in the urban environment of Brazil. Munger et al. (1995) measured CHOCHO in cloudwater and air in a mountain area in central Virginia. Grosjean et al. (2001) studied carbonyl emissions from the exhaust of light and heavy duty vehicles, and Volkamer et al. (2001) reported secondary and primary formation of glyoxal by performing chamber simulations in Valencia, Spain. Ho & Yu. (2002) analyzed airborne carbonyls by using thermal desorption and on-sorbent derivatization in combination. Wittrock et al. (2006), Myriokefalitakis et al. (2008), Stavrakou et al. (2009) and Vrekoussis et al. (2009) presented satellite based global observations of glyoxal by using data from the Scanning Imaging Absorption Spectrometer for Atmospheric Cartography (SCIAMACHY). Glyoxal has also been retrieved from the Global Ozone Monitoring Experiment-2 (GOME-2) measurements (Lerot et al., 2010; Vrekoussis et al., 2010). Fu et al. (2008) presented global glyoxal budgets by using model simulations and reported that annually around 45 Tg of glyoxal is emitted globally.

Ground-based DOAS measurements have also been performed to measure the glyoxal distribution. For example, Volkamer et al. (2005) measured glyoxal and quantified its lifetime in the urban environment of Mexico city by using long path (LP) DOAS. The first study of glyoxal by using a MAX-DOAS instrument was done by Sinreich et al. (2007) during the ICARTT 2004 campaign. MacDonald et al. (2012) used LP DOAS and MAX-DOAS instruments to measure glyoxal over a tropical rainforest and Khokhar et al. (2016) presented glyoxal results from Pakistan observed from a mini MAX-DOAS instrument. Javed et al. (2019) also retrieved glyoxal columns in Beijing, China during haze and non-haze periods by using a mini-MAX- DOAS instrument. To best of the knowledge, no car MAX-DOAS observations have been done previously to study the spatial distribution of glyoxal and are reported for the first time in the current thesis. Additionally, an effort to identify the probable sources of glyoxal in and around Lahore along the driving routes has been made.

4.4.1. Spatial Distribution of Glyoxal

In this section, the spatial distribution of glyoxal, measured during the two extensive campaigns executed in the summer 2017 and spring 2018 are discussed.

4.4.1.1.Spatial distribution of glyoxal during summer 2017

During the summer 2017 campaign, around 30 measurements including 27 large circles one small circle and two measurements along the busy part of the city were performed to identify the spatial patterns of glyoxal. The vertical column densities during this campaign ranged between $\sim 1\times10^{12}$ and $\sim 2.8\times10^{15}$ molecules cm^{-2}. The days where enhancements higher than $\sim 1\times10^{15}$ molecules cm^{-2} were observed along the different sections of the route are presented in Figures 4.24 and 4.25. On 12 and 13 May, a slightly different route along the eastern part of the circle was adopted as compared to the other large circles performed during this campaign. On 12 May, enhanced VCDs ranging between $\sim 1\times10^{15}$ and $\sim 1.5\times10^{15}$ molecules cm^{-2} were observed along the southern half of the circle. On this day, activities of crop residue burning were observed (Figure 4.21) and the elevated CHOCHO values are most probably due to these agricultural fires as according to Fu et al. (2008), 20% of the total global glyoxal is emitted as a result of biomass burning activities. Stavrakou et al. (2016) and Zarzana et al. (2018) also reported emissions of glyoxal from agriculture waste fires and open biomass burnings, respectively. On 13 May, the enhanced VCDs along the eastern half of the circle may also be attributed to such combustion activities. For the whole campaign, the highest VCDs ($\sim 2.8\times10^{15}$ molecules cm^{-2}) were observed on 14 May. These high values were observed along the northern part of the route (Figure 4.24). A cluster of iron industries and a paint industry is located in this part of the route. Metal works industries use acetylene flames to cut the metallic sheets and for welding purposes. The high CHOCHO values in this part are most likely due to the acetylene as according to Fu et al. (2008) acetylene is the second largest precursor of glyoxal after isoprene. The paint factory in this area may also contribute to these enhancements as a variety of VOCs are used in the paint industry which may lead to the formation of CHOCHO. Ho et al. (2013) also reported the occurrence of glyoxal in paint industry. High VCDs can also be observed along the roads with high traffic density and these elevated values can probably be attributed to the vehicular emissions. On 15 May, high VCDs around 1.5×10^{15} molecules cm^{-2} along different parts of the route were observed. The high values in the northwest are most probably due to the small industries and the high-density traffic. In the east and southeast, the high values may be due to the crop residue burning activities, as this section of the route is located close to agricultural fields. On 18 May, two circles were executed, and both measurements showed similar enhancements patterns. High glyoxal VCDs, were observed in the north part of the circles which is most likely due to the use of acetylene in the iron industries.

On 19 May (Figure 4.25), in addition to the large circle around Lahore, measurements were extended on the Lahore-Sheikhupura Road and also a circle was performed around a small town (Shahdara) adjacent to Lahore in the northwest (Figure 4.25, top left image). The town is located on the other side of the river Ravi and different small industries are also

located there. High glyoxal values can be seen along the whole circle performed around this town. Elevated CHOCHO VCDs were observed in the north of the circle performed around Lahore on the same day. These enhancements are most likely due to vehicular emissions. On 20 and 26 May, enhanced VCDs can be seen in the north-west part of the circle. These elevated VCDs are most probably due to the traffic as this part of the route serves as one of the entry points to the city. The traffic in this area is characterized by heavy diesel vehicles including buses and trucks. Two circles were performed on 25 May 2017. Enhanced VCDs ($\sim 2\times10^{15}$ molecules cm^{-2}) were observed along the northwest section of the first circle while for the second one, high CHOCHO VCDs ($\sim 2.25\times10^{15}$ molec cm^{-2}) were seen along the north to the east segment. The ECMWF 6 UTC averaged wind output shows calm winds (Figure 4.25, bottom panel), from which we can assume that the sources are local. For the first circle, heavy traffic in this section could be responsible for the enhancements and for the second circle, the emissions from iron industries in the north and vehicles in the northeast probably contributed to the high glyoxal levels. The Lahore airport is also located a few kilometers away from the road in the east part of the circle. Moreover, the agricultural fields present along this section, may also contribute to the high levels.

Between 27 and 29 May 2017, 5 circles were performed. On these 3 days, wind speeds were quite high (≥ 4 m s^{-1}) and wind directions were also stable. Figure 4.26 presents the measurements performed on these days. It can be seen that high VCDs ($<1 \times 10^{15}$ molecules cm^{-2}) were observed on the downwind sides of the circles and no localized enhancements along the whole circles were noticed, indicating that due to the high speed winds, enhanced trace gas concentrations did not build-up locally.

Figure 4.27 depicts the measurements executed on 30 and 31 May 2017. On 30 May, high glyoxal values around 1×10^{15} molecules cm^{-2} were observed in the northwest section of the circle which is most probably due to vehicular emissions. On 31 May 2017, relatively low enhancements with VCDs below 1×10^{15} molecules cm^{-2} were observed along the southwest part of the circle. Low VCDs below 0.5×10^{15} molecules cm^{-2} were observed along the rest of the circle. On this day it took more than 5 hours to complete the circle as measurements had to stop due to rain.

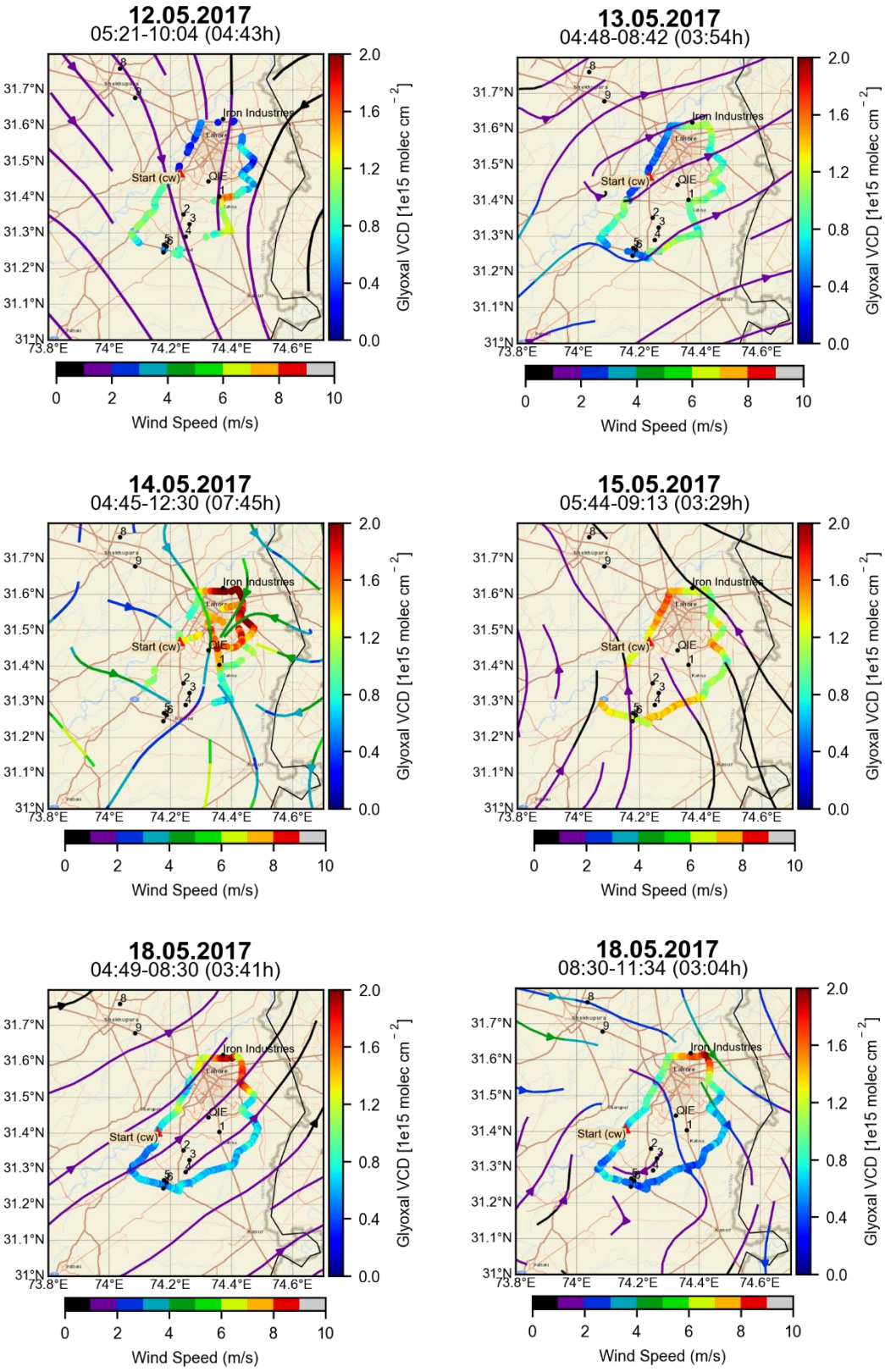

Figure 4.24: Glyoxal VCDs around Lahore, derived from mobile MAX-DOAS during the summer 2017 campaign on various days. Enhancements higher than ~1×10^{15} molecules cm^{-2} can be observed in all the circles. The streamlines represent the closest ECMWF wind outputs.

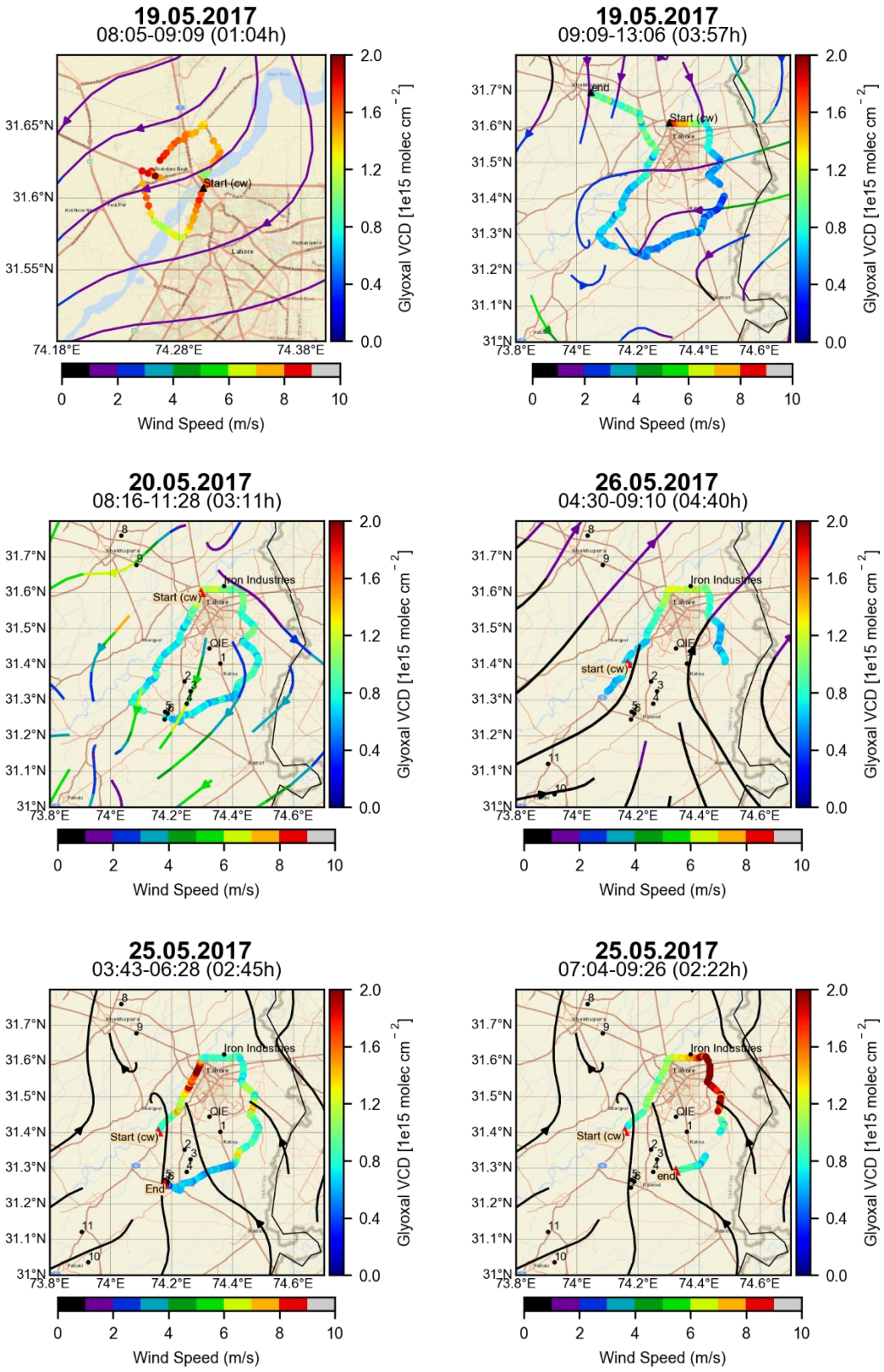

Figure 4.25: Glyoxal VCDs derived from mobile MAX-DOAS observations around Shahdra (top left) and Lahore on four days during the summer 2017 campaign. The streamlines reveal that during the measurement period the wind conditions were very different. Enhancemnets around 1×10^{15} molecules cm^{-2} or higher can be observed in all the circles.

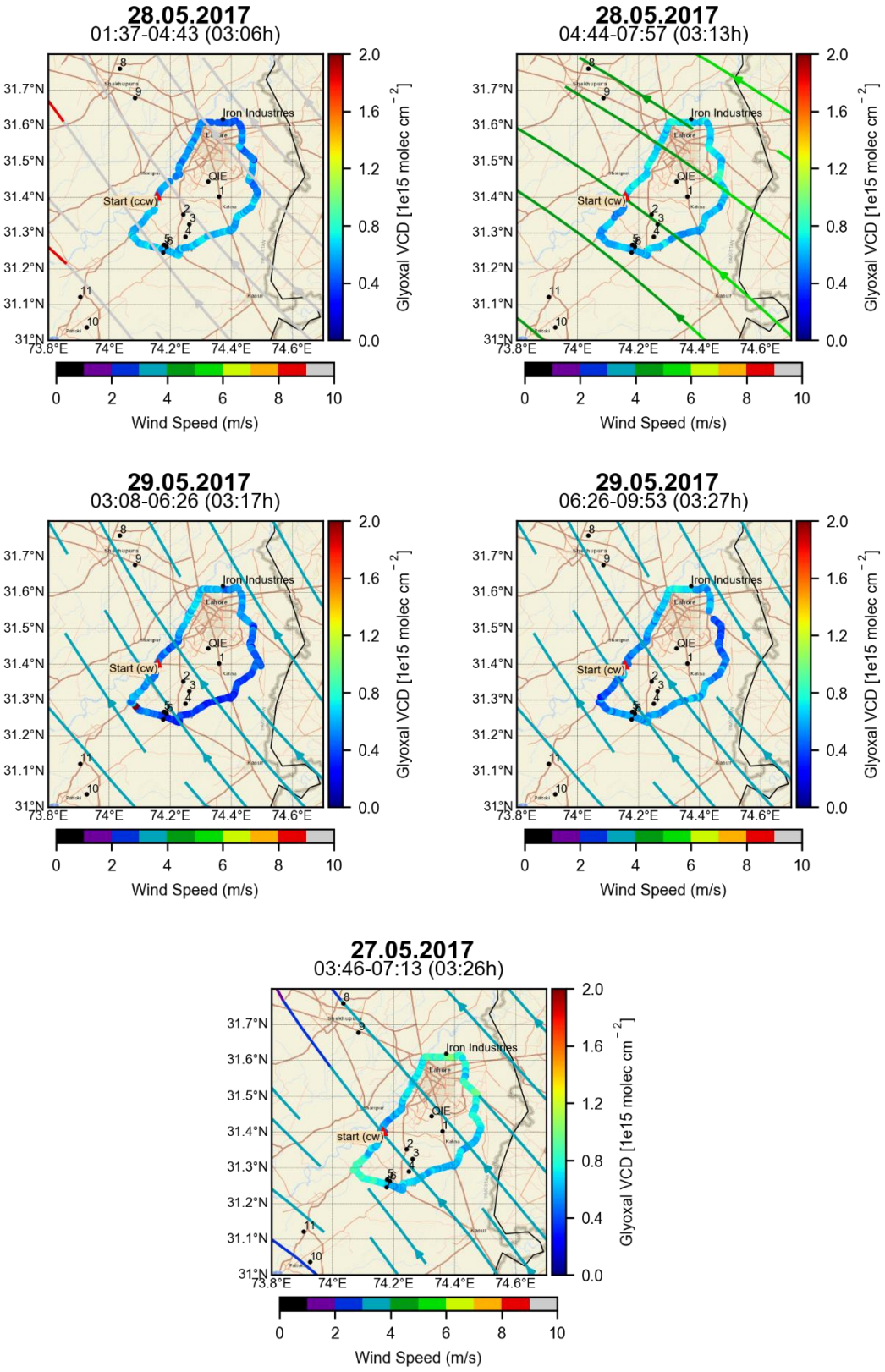

Figure 4.26: Glyoxal VCDs around Lahore on 27-29 May 2017. The ECMWF wind outputs represent winds with stable directions and speeds higher than 3 m s^{-1}. Compared to the other days, smaller CHOCHO VCDs were observed.

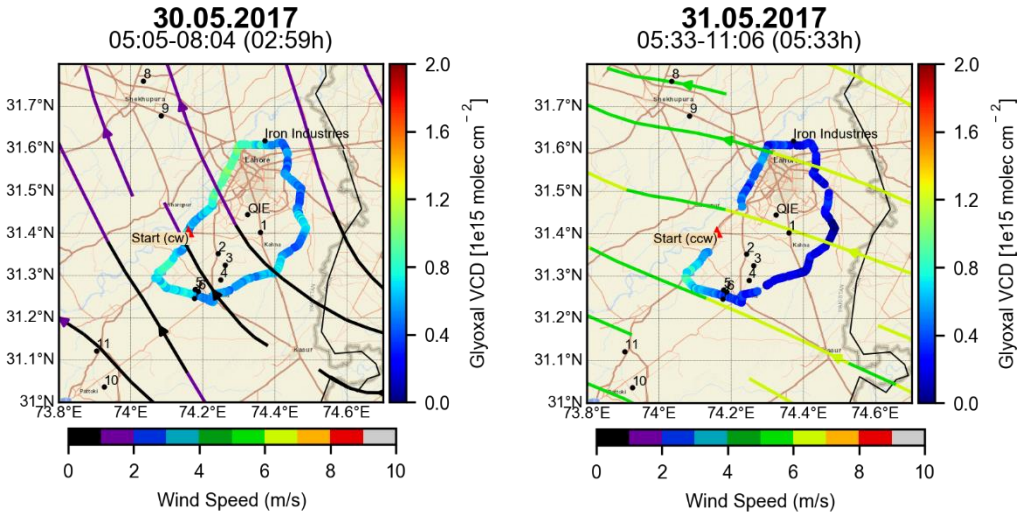

Figure 4.27: Glyoxal VCDs around Lahore, derived from the mobile MAX-DOAS observations performed on 30 and 31 May 2017.

On 1 June 2017 (Figure 4.28), two circles were carried out around Lahore. Almost similar enhancement patterns were observed for both circles. Elevated CHOCHO VCDs around 1.5×10^{15} molecules cm^{-2} were observed on the western half of the circles. In addition to the high traffic roads, different industries including an asphalt plant and paint industry are also present in the southwest part of the circle. Asphalt plants emit numbers of organic compounds including benzene, toluene and xylene (BTX) (US EPA, 2000). The BTX-OH reaction is responsible for the primary formation of glyoxal (Volkamer et al., 2001). Therefore, the enhanced glyoxal VCDs in the west and southwest part are predominantly a result of the emissions from industrial activities in the area.

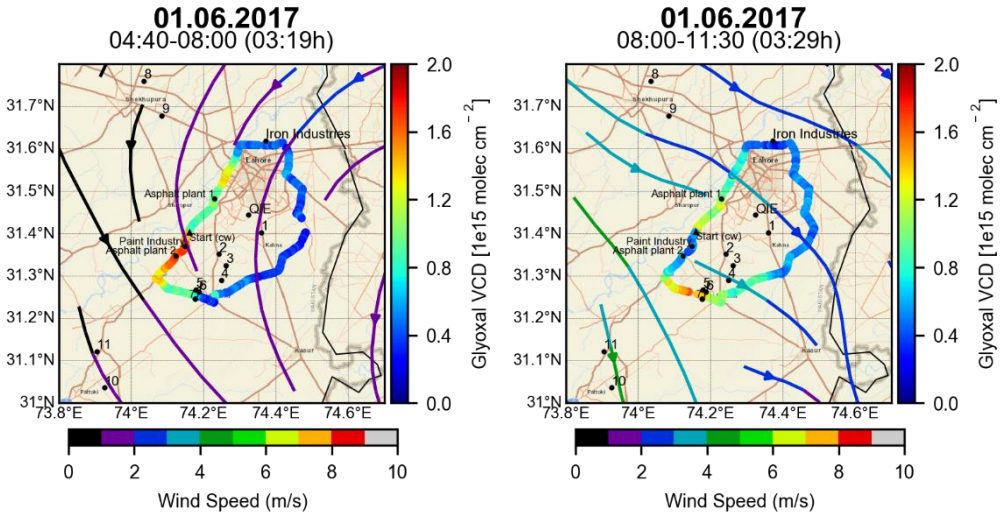

Figure 4.28: Glyoxal VCDs around Lahore, derived from the mobile MAX-DOAS observations performed on 01.06. 2017. The enhancements in the southwest can be seen in the first circle (left). In the second circle (right) enhanced VCDs can be observed in the south and the west directions.

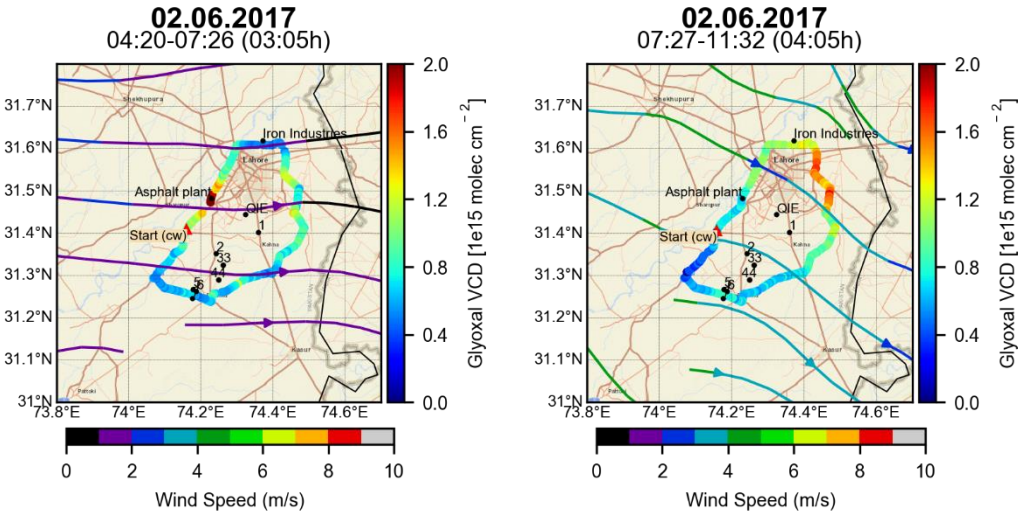

Figure 4.29: Glyoxal VCDs derived from the car MAX-DOAS measurements performed around Lahore on 2nd June 2017. The streamlines represent the closest ECMWF wind outputs.

On 2 June 2017 (Figure 4.29), also two circles were performed. Elevated CHOCHO VCDs $\geq 1\times10^{15}$ molecules cm^{-2} were found in most parts of both circles. For the first circle (Figure 4.29, left) CHOCHO VCDs higher than 2×10^{15} molecules cm^{-2} were observed in the west part of the circle along the M2 motorway. An asphalt plant is also located adjacent to this section of the road. The high VCDs here can probably be attributed to the emissions from the asphalt plant and high traffic density along the M2 motorway. For the second circle (Figure 4.29, right), enhanced VCDs around 1-1.5$\times10^{15}$ molecules cm^{-2} can be seen in the north and northeast segments. These elevated values are most probably due to the iron industries in the north and agricultural fields in the east part of the circle.

On 3 June (Figure 4.30, top panel) measurements were also performed on the Ferozepur Road and the Canal Road. These roads almost bisect the circle, and the measurements can give an idea of the trace gas distribution in the busy parts of the city. For both the measurements performed on that day, glyoxal VCDs $\sim1\times10^{15}$ molecules cm^{-2} were observed in the north. Figure 4.30 also represents the measurements performed on 5 and 6 June 2017. On 5 June, measurements along two circles were performed and for 6 June, measurements were extended in the northwest along the Lahore-Sheikhupura Road. On these two days VCDs below 1×10^{15} molecules cm^{-2} were most prevalent.

On 4 June measurements were performed in three periods. Figure 4.31 depicts the measurements carried out on that day. These include measurements along one large and one small circle to encircle the densely populated part of the city. An additional loop along the main roads of the city like the Ferozepur Road, Canal Road and Raiwind Road was also executed. Overall low VCDs were observed on that day and the highest values observed were around 0.8×10^{15} molecules cm^{-2} along the eastern half of the small circle.

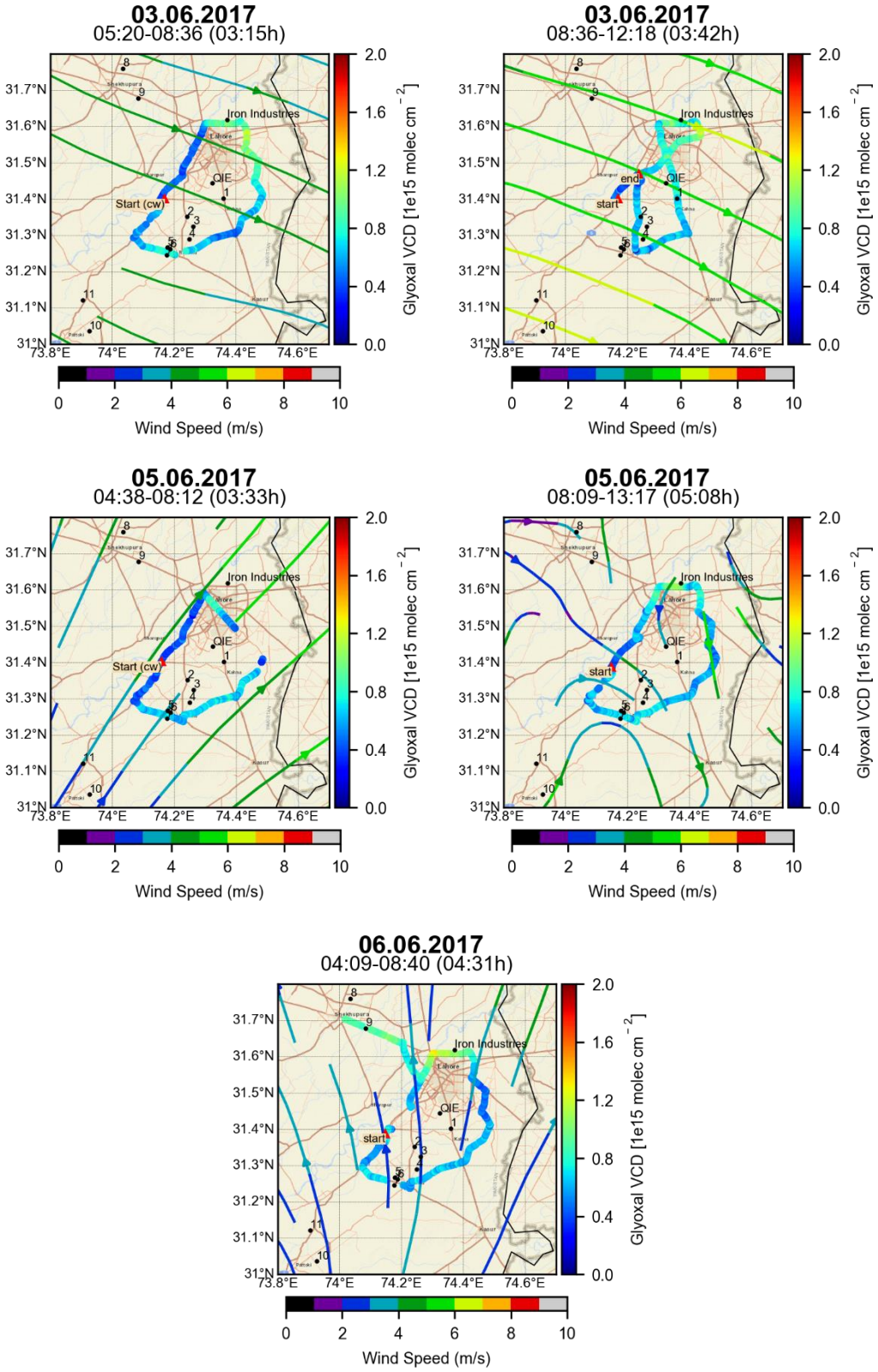

Figure 4.30: Glyoxal VCDs derived from the car MAX-DOAS measurements performed on 3, 5 and 6 June 2017. The streamlines represent the closest ECMWF wind outputs.

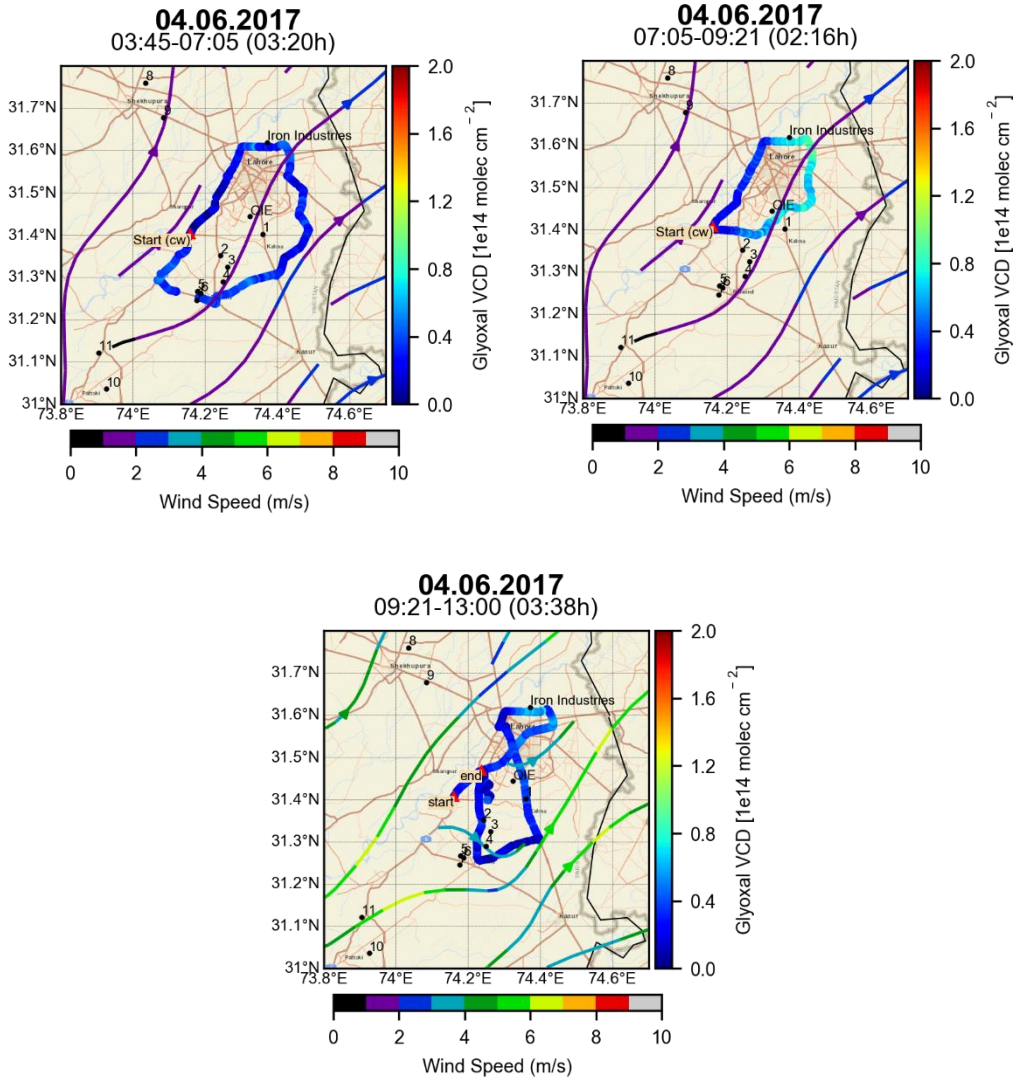

Figure 4.31: Glyoxal VCDs derived from the car MAX-DOAS measurements performed on 4 June 2017. The streamlines represent the closest ECMWF wind outputs.

4.4.1.2.Spatial Distributions of Glyoxal during Spring 2018

The measurements for the spring period were performed during the months of February and March 2018. During this period 35 circles (22 small and 13 large) were executed to study the spatial distribution of CHOCHO around Lahore. For the whole period glyoxal VCDs ranging between ~3×10^{12} and ~2×10^{15} molecules cm^{-2} were observed and enhancements above 1×10^{15} molecules cm^{-2} were found less prevalent as compared to the observations performed during the summer campaign.

On 13 and 23 February 2018 elevated VCDs around 2×10^{15} molecules cm^{-2} were found in the east to the southeast sides of the smaller circles. Figure 4.32 represents the measurements performed on these days. Along this part of the route, several industries e.g., textile, paper, and plastic industries are located. All these activities use organic compounds at different stages of the manufacturing processes and can be the potential emitters of glyoxal. A gas station is also present alongside of the road in the east. As fuel stations are strong sources of benzene, toluene, and p-xylene (BTX) in the ambient air (Kerchich & Kerbachi, 2012) the high glyoxal VCDs around the gas station might be explained by this source. The reaction between BTX and OH yields glyoxal as major primary product (Volkamer et al., 2001).

For 13 (6 large and 7 small) out of 35 circles, elevated VCDs were observed predominantly in the east sides. The large circles with the enhancements in the east are shown in Figure 4.33 while the smaller circles with the elevated VCDs in the same side are presented in Figures 4.34 and 4.35. Various industries and gas station are located in the east, along the smaller circles as already discussed for the enhancements of 23 February. Moreover, the wind directions during these measurements were going towards the east and that also augmented the buildup of the trace gas concentrations in the eastern parts of the circles.

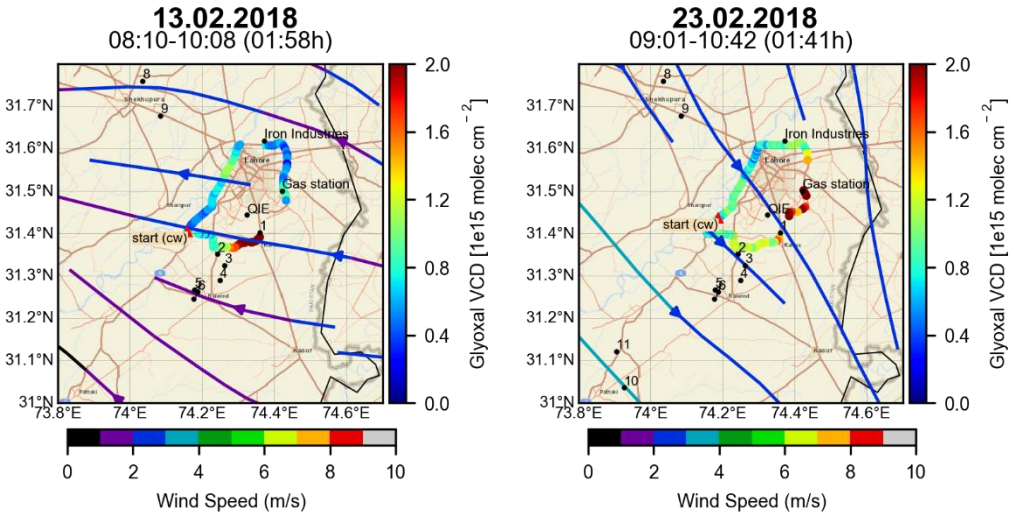

Figure 4.32: Measurements performed on 13 and 23 Feb 2018 along the smaller circles around Lahore. Elevated Glyoxal VCDs can be seen from east to the southern segment of the circles.

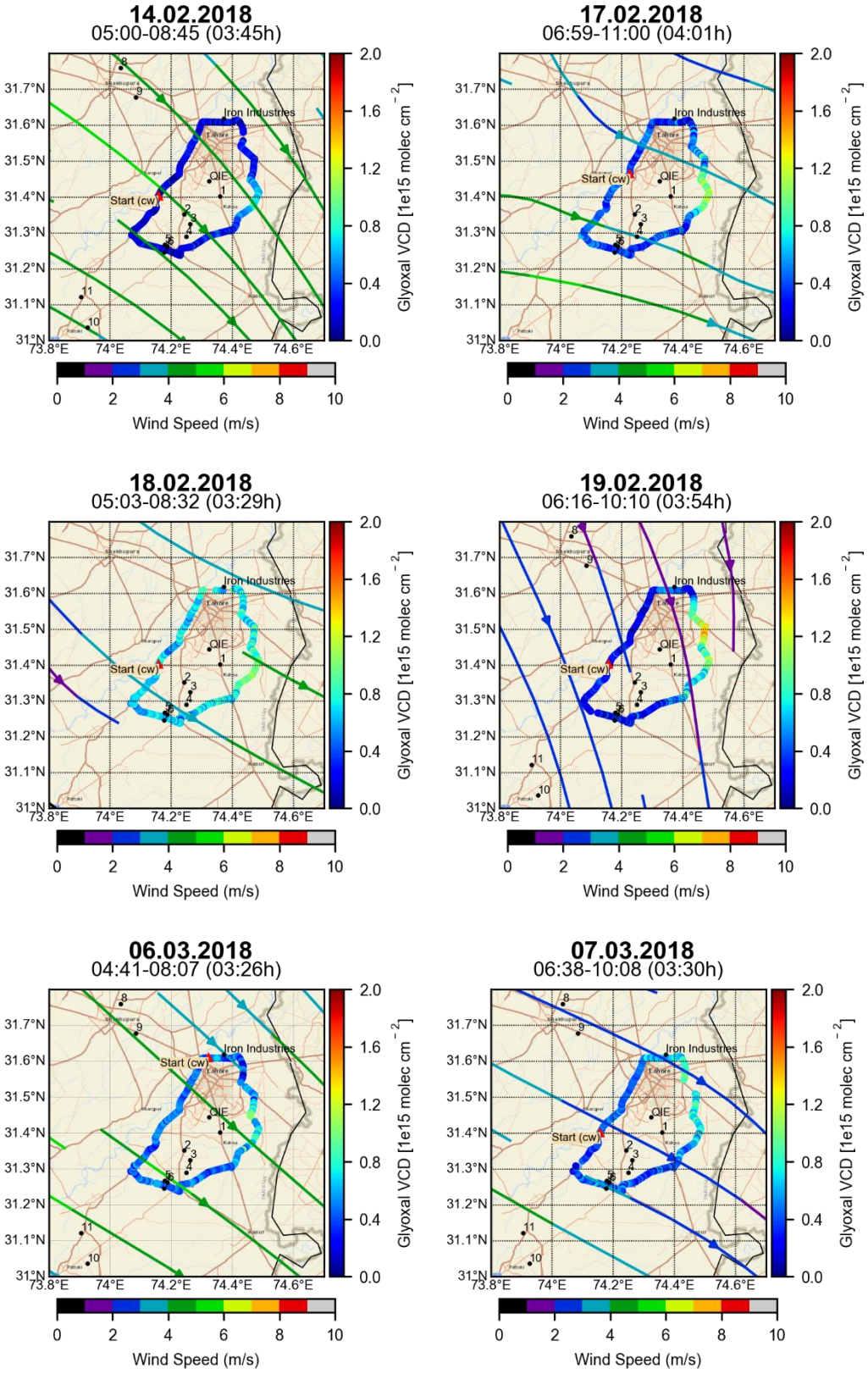

Figure 4.33: Glyoxal VCDs derived on selected days during the 2018 campaign with enhanced VCDs observed on the eastern side of the circles. The streamlines represent the ECMWF wind outputs at 6 UTC.

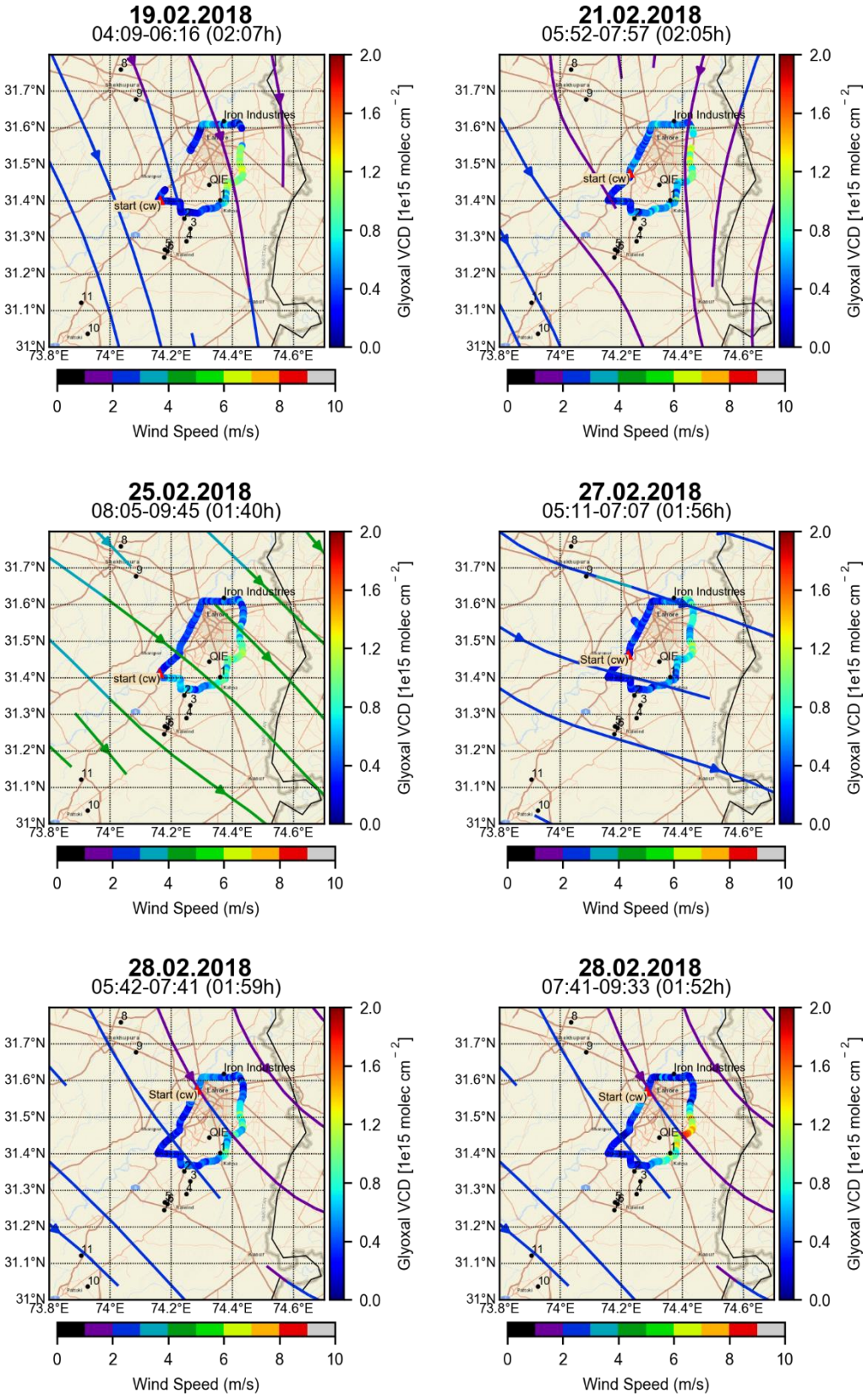

Figure 4.34: Glyoxal VCDs derived on the selected days during the 2018 campaign along the smaller route around Lahore showing enhanced VCDs on the eastern side of the circles. The streamlines represent the ECMWF wind outputs at 6 UTC.

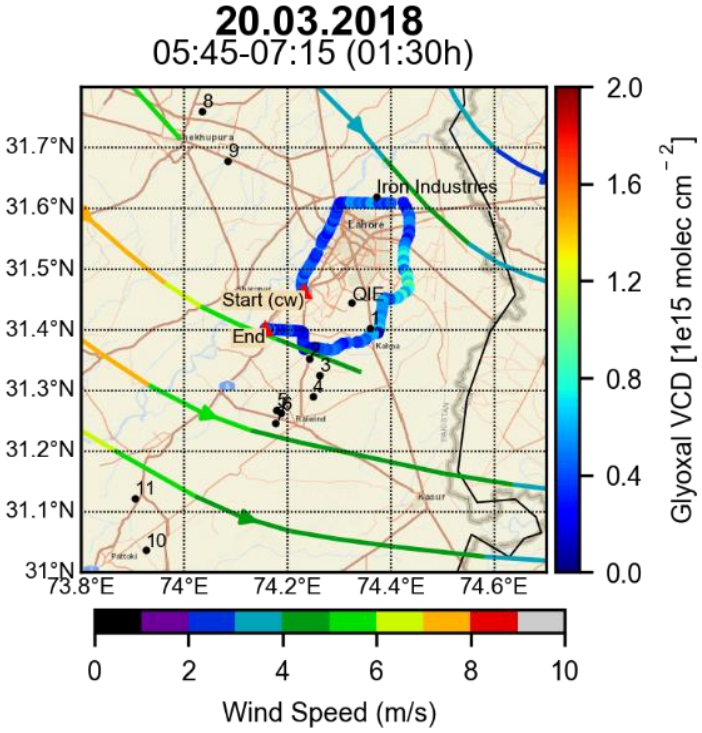

Figure 4.35: Glyoxal VCDs derived on 20 March 2018 along the smaller route around Lahore showing slight enhancements on the eastern side of the circle. The streamlines represent the ECMWF wind output at 6 UTC.

For the rest of the 19 circles (12 small and 7 large), presented in Figures 4.36 - 4.39 weak enhancements with no regular patterns were observed. The lowest VCDs ($\sim \leq 0.5\times10^{15}$ molecules cm^{-2}) were observed on 15.02 along the smaller circle.

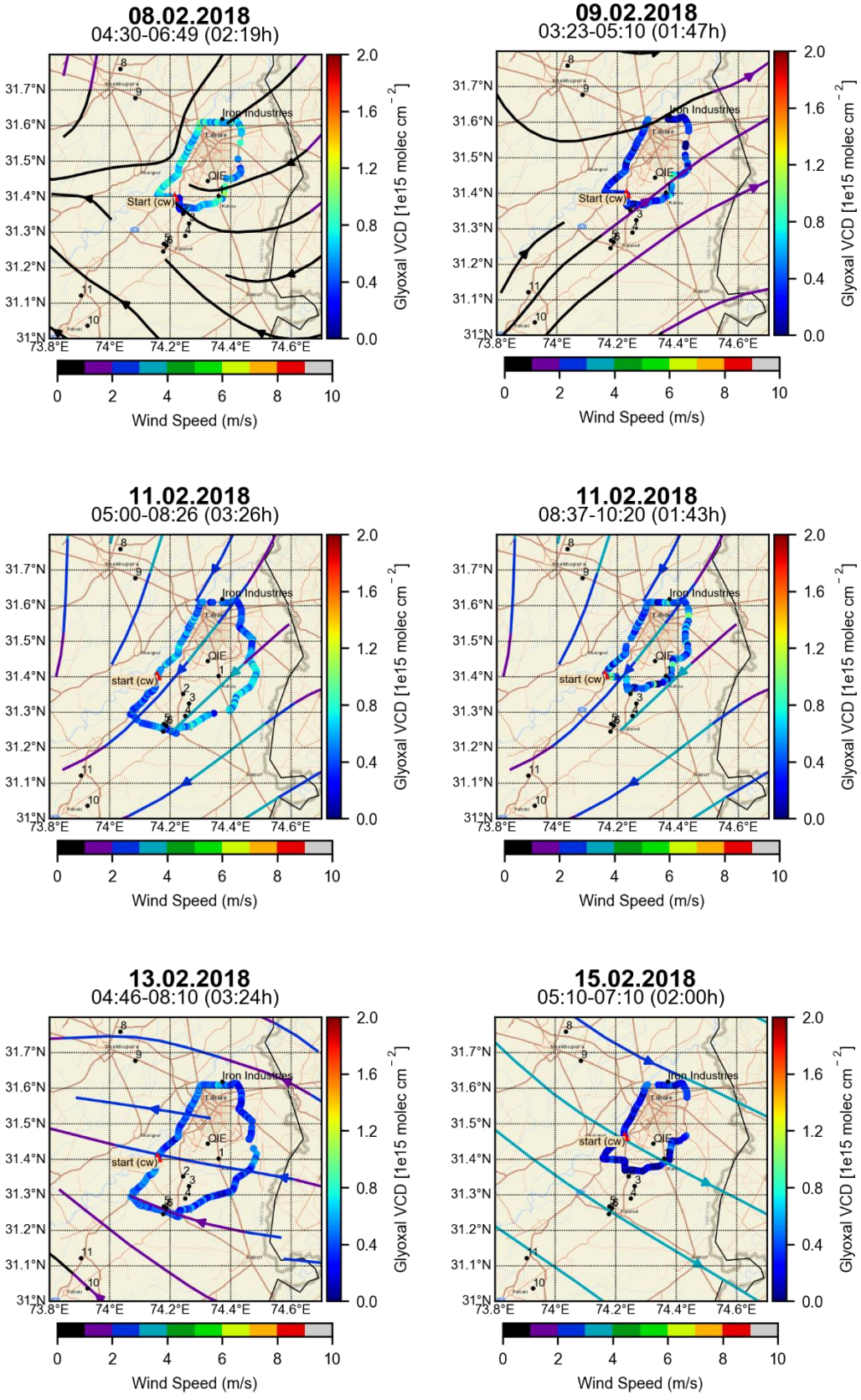

Figure 4.36: Glyoxal VCDs derived on selected days during the 2018 campaign around Lahore during the spring campaign, 2018. The streamlines represent the ECMWF wind outputs at 6 UTC.

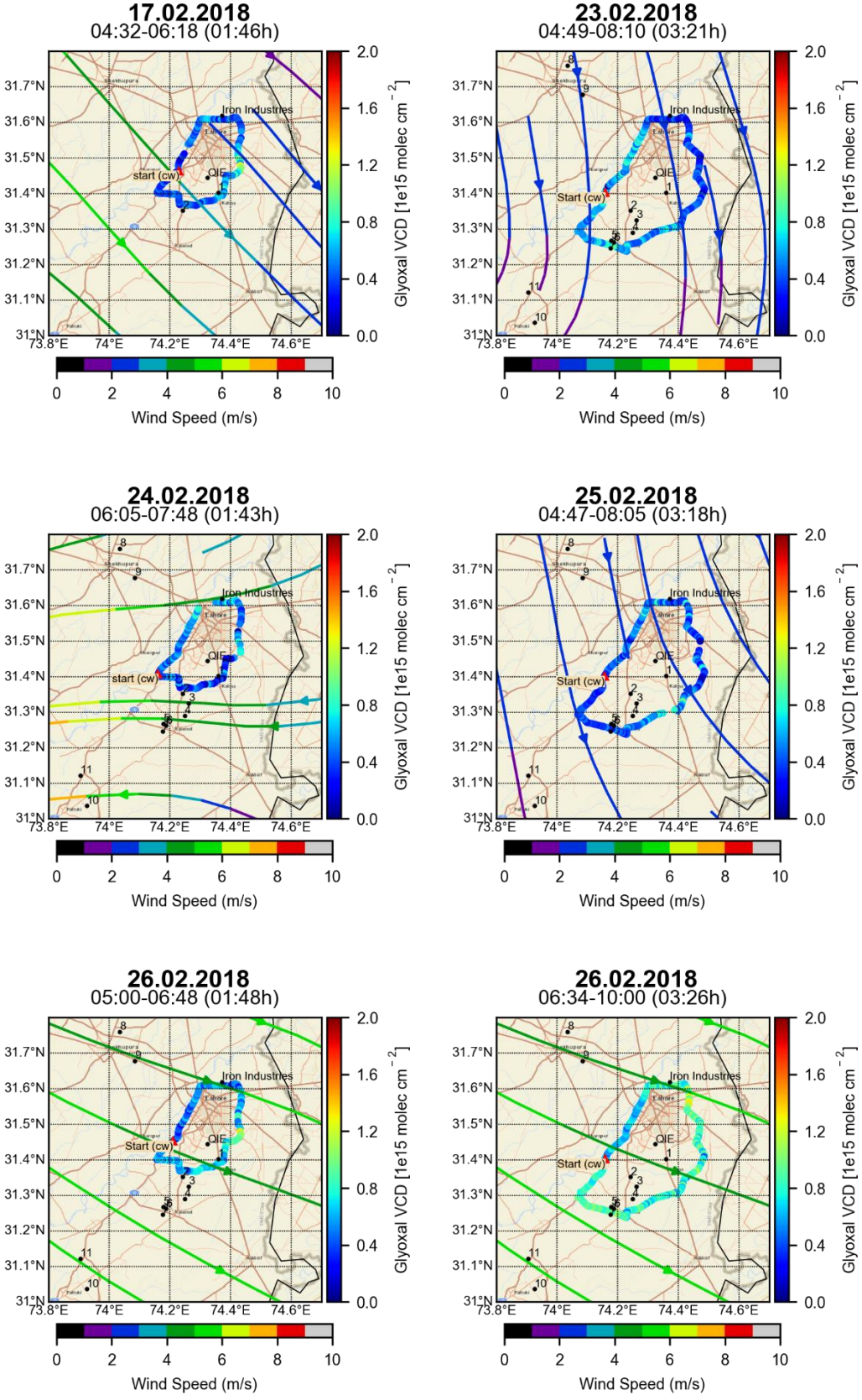

Figure 4.37: Glyoxal VCDs derived on selected days during the 2018 campaign around Lahore showing slight enhancements at different sides of the circles. The streamlines represent the ECMWF wind outputs at 6 UTC.

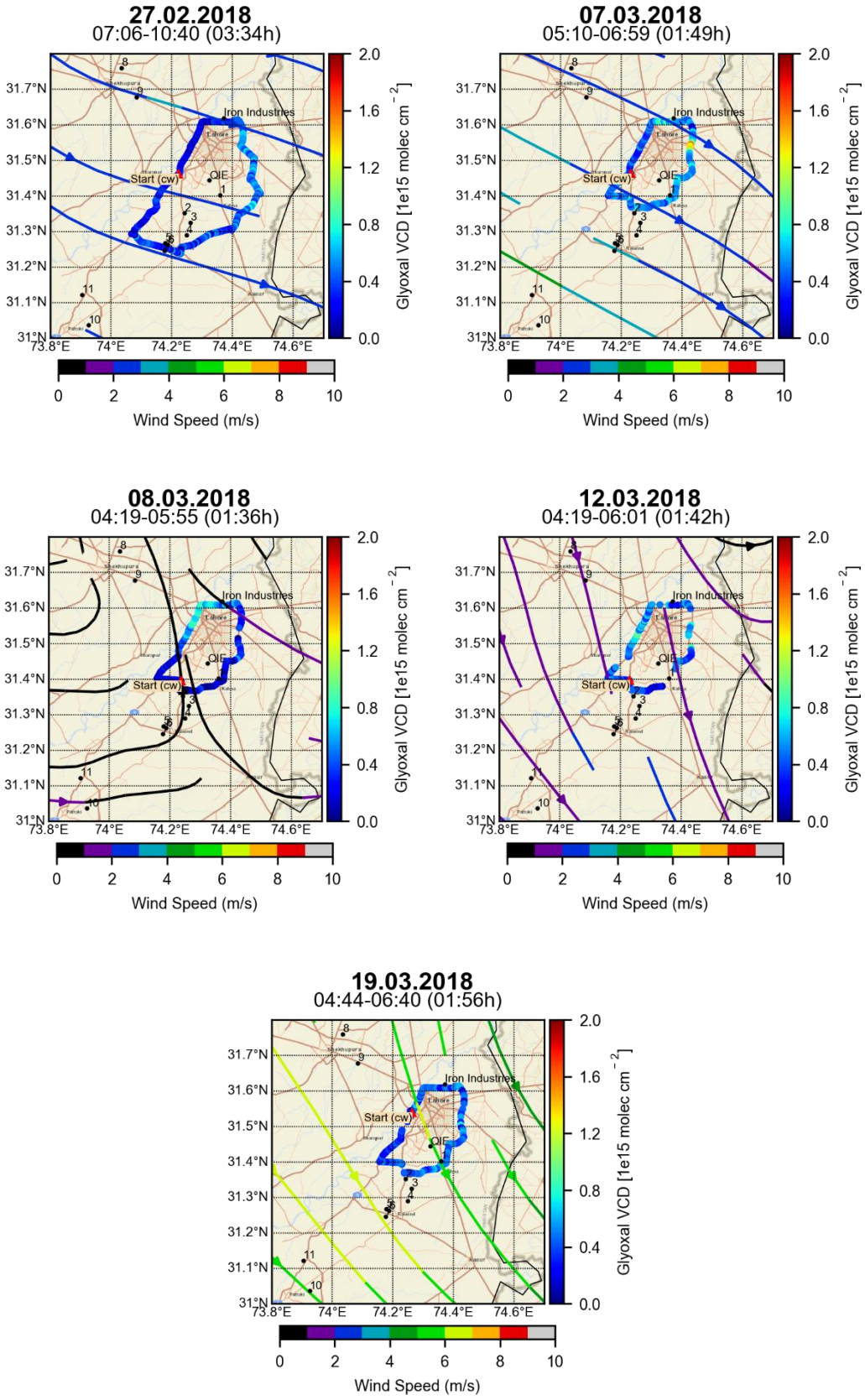

Figure 4.38: Glyoxal VCDs derived on selected days during the 2018 campaign around Lahore showing slight enhancements at different side of the circles. The streamlines represent the ECMWF wind outputs at 6 UTC.

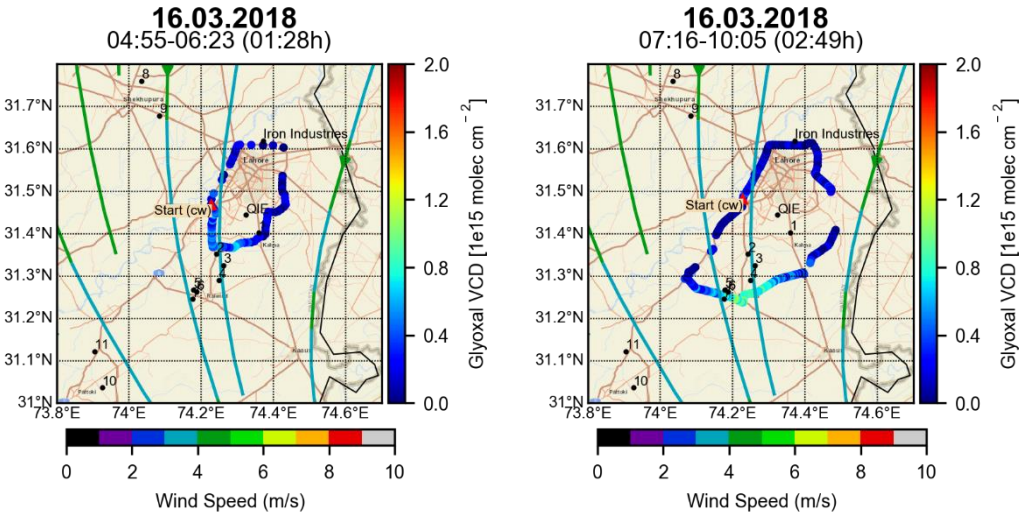

Figure 4.39: Glyoxal VCDs derived on 16 March around Lahore showing slight enhancements at the south and south east sides of the circles. The streamlines represent the ECMWF wind outputs at 6 UTC.

4.5. CORRELATION ANALYSIS

In order to assess the relationship between the observed trace gases, correlation analyses were performed. The simultaneous study of various trace gases over the same area allows to compare and correlate these gases and this kind of analysis can be used to identify the sources of these trace gases more accurately. Trace gas relationships have also been studied previously e.g. by Donner. (2016); Marbach et al. (2007) and Zeb et al., 2019. Marbach et al. (2007) used satellite observations and compared HCHO with NO_2 and CO to identify the tropospheric sources (anthropogenic and biogenic) of these trace gases and also proposed to study the comparison between formaldehyde and glyoxal.

In the current study, the Pearson correlation (Pearson, 1895) was estimated between the six trace gas pairs. The correlation analyses were performed for the 2017, 2018-I and 2018-II campaigns. For the two 2015 campaigns, no correlation analysis was possible as only NO_2 was observed during these periods. In this section, correlation analysis results for the summer 2017 and spring 2018 campaigns executed around Lahore are presented. The correlation results for the 2018-II campaign (performed around the power plants in the area) are presented in chapter 5. The correlation coefficient (R) values were used to assess the direction and strength of the relationship between the two variables. In Table 4.17, the R values for each trace gas pair is given for the measurements performed in the two seasons separately. The scatterplots for each trace gas pair for summer and spring are presented in Figures 4.40 and 4.41, respectively, and the scatterplots for the individual days can be found in appendix C.

Table 4.19: Correlation coefficients (R) for the trace gases pairs.

Season	NO_2 - SO_2	HCHO - CHOCHO	NO_2 - HCHO	NO_2 - CHOCHO	SO_2 - HCHO	SO_2 - CHOCHO
Summer (2017)	0.62	0.85	0.35	0.27	0.29	0.23
Spring (2018-I)	0.74	0.58	0.49	0.36	0.30	0.19

A strong correlation was found between NO_2 and SO_2 in spring and summer with R values of 0.74 and 0.62, respectively. In a previous study, Haider et al. (2017) reported a similar R value of 0.57 for the NO_2-SO_2, measured from two fixed ambient air quality monitoring stations in Lahore for the period of around five years (2007-11 and 2014-15). From these results, it can be assumed that NO_2 and SO_2 have similar sources along the driving route.

An even stronger correlation between HCHO and CHOCHO was found in summer with R = 0.85 and a slightly weaker correlation (R=0.58) was found in spring. From these figures, it can be concluded that also formaldehyde and glyoxal have common sources especially during the summer period. As a result of biomass burning in summer, formaldehyde and glyoxal are emitted and/or formed in considerable amounts (Marbach et al., 2008). In the periphery of Lahore, crop residues are burnt during summer, and according to Miller et al. (2016) and references therein, open fires also emit glyoxal and HCHO and/or their precursors. These burnings (and possibly also other sources of VOCs) may be the reason for a strong correlation between these two trace gases for the summer measurements.

Additionally, the ratio between glyoxal and formaldehyde (R_{GF}), [CHOCHO]/[HCHO] has been determined. R_{GF} values of 0.04 to 0.06 are typical for biogenic sources like isoprene whereas, R_{Gf} values below 0.04 refer to anthropogenic sources and are also linked to high NO_2 levels (Vrekoussis et al., 2010). In the current study, an R_{GF} value of 0.04 (± 0.013) was found for the measurements performed in the summer, whereas R_{GF} = 0.03 (±0.026) was found for the spring measurements. From the derived ratios between glyoxal and formaldehyde and the R values, it can be assumed that in summer biogenic sources might dominate, while in spring, anthropogenic sources are more prominent. For the NO_2-HCHO and NO_2-CHOCHO pairs, weaker correlations were found in both seasons with R values ranging between 0.27 and 0.49. The correlation coefficients are still much larger than zero probably indicating that part of emission sources of HCHO, CHOCHO and NO_2 (most probably vehicular emissions) are the same.

Also for the SO_2-HCHO and SO_2-CHOCHO pairs, weaker correlations were observed indicating that SO_2 and these VOCs have mostly different emission sources. The R values for the SO_2-HCHO for summer and spring were 0.29 and 0.30, respectively. For SO_2 and CHOCHO, these values were even lower i.e. 0.23 and 0.19 for summer and spring, respectively. Like for the correlation with NO2 the correlation coefficients are still much

larger than zero probably indicating that part of emission sources of HCHO, CHOCHO and SO2 (most probably vehicular emissions) are the same.

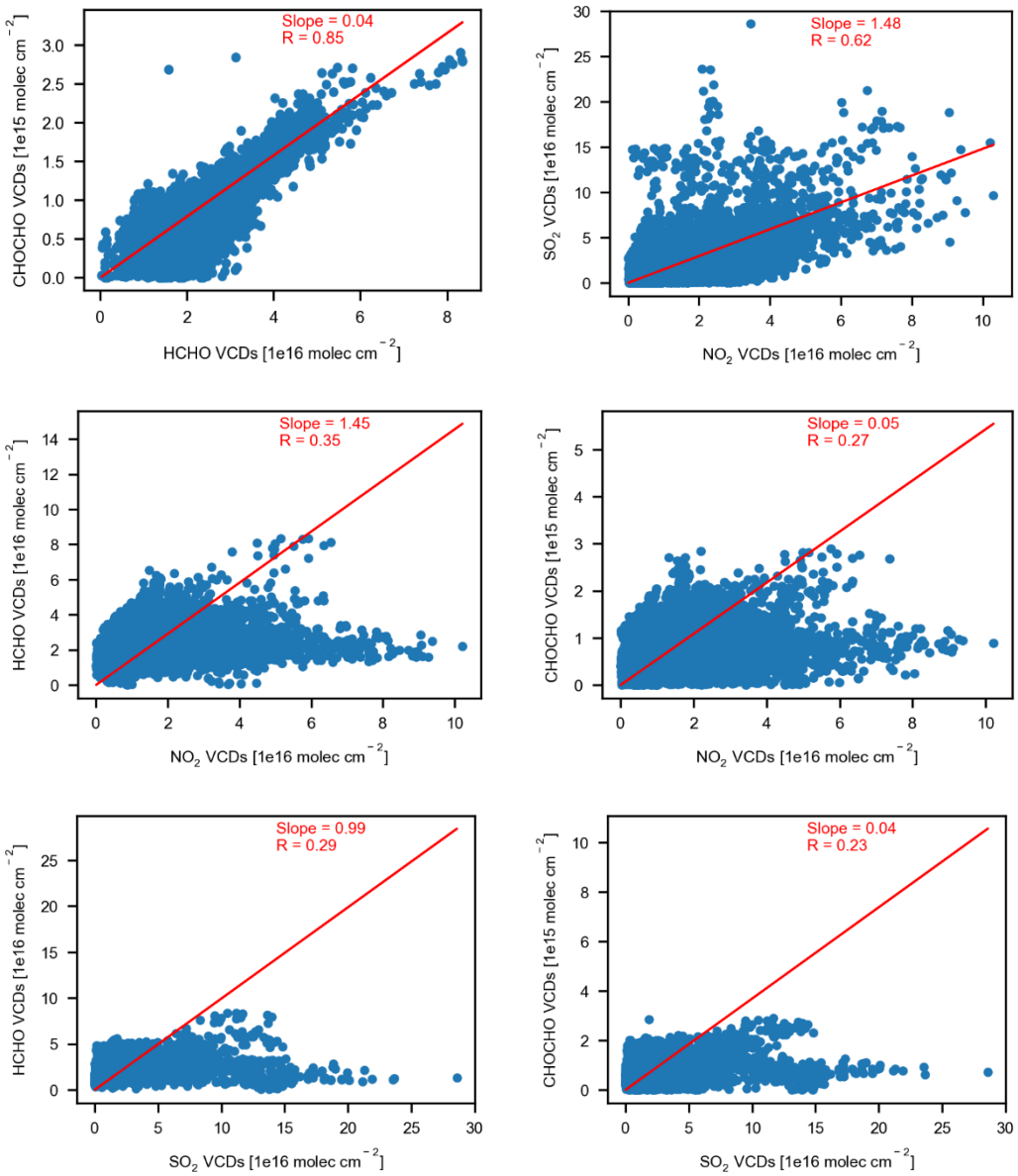

Figure 4.40: Scatter plots showing the correlations between six pairs of the trace gases observed during the summer 2017 campaign around Lahore.

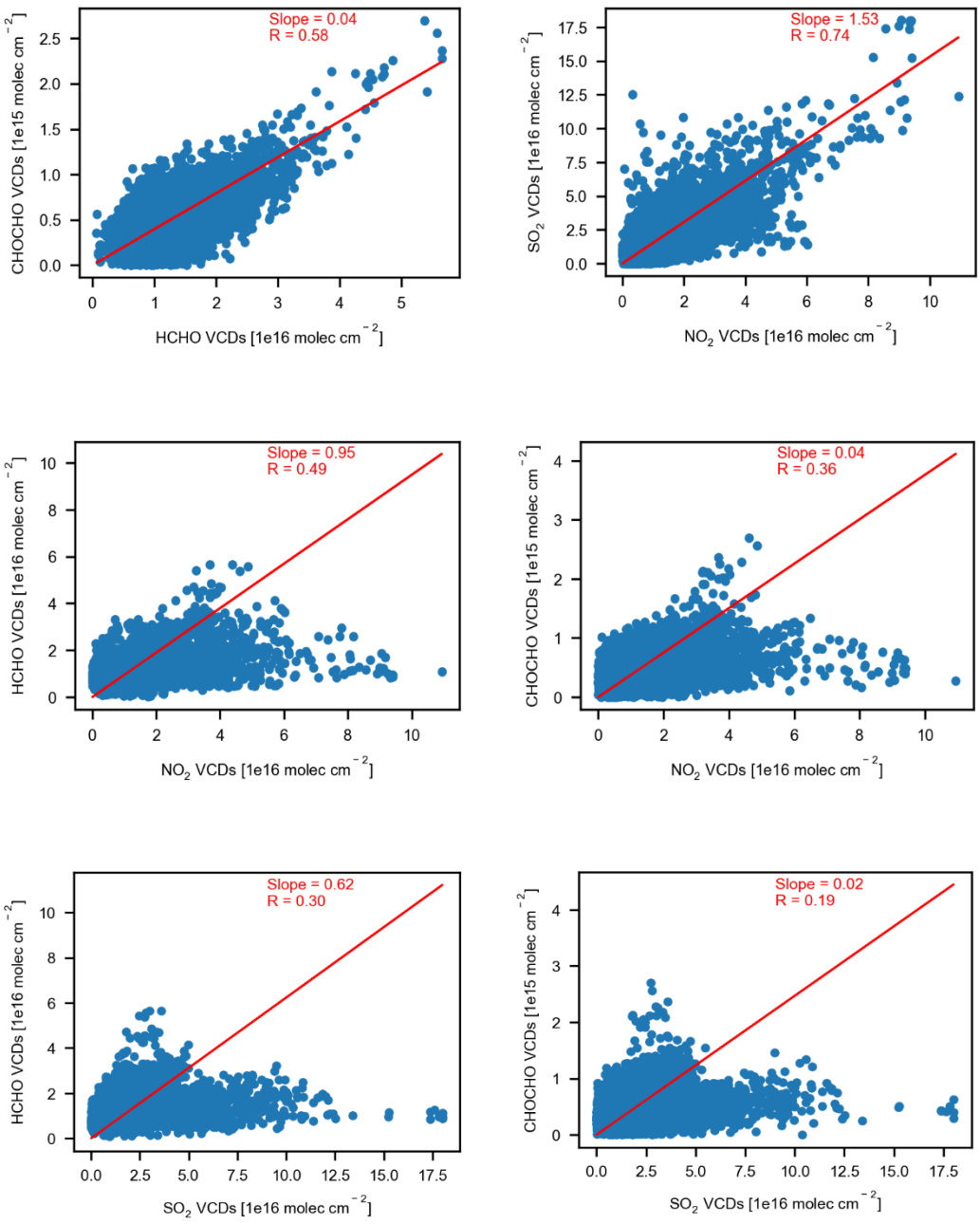

Figure 4.41: Scatter plots showing the correlations between the six pairs of the trace gases observed during the spring 2018 campaign performed around Lahore.

4.6. SUMMARY

This chapter presented the results for the four trace gases (nitrogen dioxide, sulfur dioxide, formaldehyde and glyoxal) analyzed from the spectra measured around and in the city of Lahore during the winter 2015, summer 2017 and spring 2018 campaigns.

For the winter 2015 campaign, NO_2 was analyzed alone, so for this period, only NO_x emissions and NO_2 distributions are presented. For the 2017 and 2018 campaigns, results for the other three trace gases were also presented. On most of the measurement days, accurate flux estimations were not possible due to unsuitable wind conditions like low wind speeds and/or highly variable directions.

NO_x emissions from the city, were estimated for 17 out of 50 circles performed during the three campaigns. The mean NO_x emissions for the one small circle performed in winter, six large circles in summer and five large and five small circles in spring were found quite similar ($\sim 1.40\times10^{25}$ molecules s^{-1}) indicating that the major NO_x sources in the city are transport and industrial emissions which remain rather constant throughout the year. Interestingly the area emissions for the large and the small circles were found to be systematically different i.e., around 1.60×10^{16} molecules s^{-1} m^{-2} for large circles performed in summer and spring and 3.27×10^{16} molecules s^{-1} m^{-2} for the small circles. In addition to the NO_x emission estimates, the spatial distributions of NO_2 measured along the driving routes performed during the three measurement periods (2015-II, 2017 and 2018-I) were presented. For the smaller circles, the predominant sources were the vehicular emissions and emissions from the iron industries in the north while along the larger circles, in addition to these two sources, also power plants and industries in the south were identified as the NO_x emitters.

In the second section of the chapter, SO_2 emission estimates for 15 circles performed during the summer and spring seasons around Lahore were presented. The mean emissions estimated for the large circles ($\sim 1.5\times10^{16}$ molecules s^{-1} m^{-2}) performed in spring 2018 were found almost two times higher than the averaged SO_2 emissions estimated for the 6 large circles ($\sim 7.2\times10^{15}$ molecules s^{-1} m^{-2}) performed in summer. It was speculated that the change of fuel type in the industrial sector during the colder months is probably responsible for the higher SO_2 emissions in spring. From the spatial distribution it was concluded that iron industries in the north, power plants and industries in the south and heavy-duty diesel vehicles on the N5 highway and M2 motorway are the prominent SO_2 sources in Lahore.

The third section encompassed the results for formaldehyde. Unlike NO_x and SO_2, formaldehyde fluxes were derived instead of the emissions. Emission estimates were not derived as HCHO undergoes rather complicated chemistry e.g., predominant secondary formation in contrast to only primary emission as for NO_x and SO_2. Also the short HCHO lifetime complicates the interpretation of the HCHO fluxes. and short lifetime. Formaldehyde fluxes were derived for 15 circles performed during the two campaigns. The flux values for the large circles performed in summer (6.72×10^{24} molecules s^{-1}) and spring (6.82×10^{24} molecules s^{-1}) were found quite similar. From this it can be concluded that anthropogenic sources like industrial emissions and fossil fuel combustion from vehicles

are the predominant formaldehyde sources in Lahore as emissions from these sources remain similar throughout the year. From the spatial distribution different stationary (e.g., a waste dumping site in the north, crop residue burning activities in the east and industries like paper mills, paint industries etc.) and mobile (traffic) emission sources of formaldehyde or its precursors are identified.

The fourth section of the chapter presented the spatial distribution results of glyoxal observed along the driving routes around and in Lahore, performed during the summer and spring campaigns. From these results it is concluded that enhanced glyoxal VCDs were found most prevalent in the summer as compared to the spring season. The prominent identified sources of glyoxal or its precursors in the study area were steel industries, gas stations and vehicular emissions.

For all the four trace gases, a general dependence on the wind was observed. On the days with stable and strong winds, the trace gas plumes were predominantly found at the downwind sides of the circles. In contrast, the days with calm wind conditions showed localized enhancements along the driving routes. On the days with high wind speeds (≥ 4 m s^{-1}) low VCD values were observed.

In the last section, correlation analyses between the analyzed trace gases were shown. These results revealed strong linear relationships between NO_2 and SO_2 as well as HCHO and CHOCHO indicating that these gas pairs might have similar sources in the study area. In contrast, for rest of the four pairs; NO_2-HCHO, NO_2-CHOCHO, SO_2-HCHO and SO_2-CHOCHO, weaker correlations were found in both seasons. But also these correlations were found to be significantly above zero indicating that part of emission sources of all trace gases (most probably vehicular emissions) are the same.

5. ADDITIONAL MOBILE MAX-DOAS MEASUREMENTS

This chapter presents the results from the measurements performed along the routes other than around Lahore. The first and last campaigns, 2015-I and 2018-II, were exclusively performed along the N-5 National Highway and the power plants in the area, respectively. There were also a few days in other campaigns where measurements were executed to investigate the trace gas distributions and/or emissions from other potential hotspots in the region. In the subsequent sections, the corresponding campaign-wise results are discussed.

5.1. MOBILE MAX-DOAS OBSERVATIONS DURING 2015-I

This campaign was performed along the main highways of Punjab for six days in February 2015 to investigate the spatial distribution of NO_2 along the driving routes. The instrument and analyses detail along with the measurement conditions are presented in chapters 3 and 4.

On 17 February 2015, the route started from the capital of Pakistan, Islamabad, and ended at Gujranwala city. The route was executed along the N5 highway, and the total distance covered was around 350 km. Figure 5.1 illustrates the NO_2 spatial distribution along the driving route. The enhancements ($\sim 2 \times 10^{16}$ molecules cm^{-2}) at the start of the route illustrate the pollution from the twin cities of Islamabad and Rawalpindi.

A similar study by Shabbir et al, (2016) during two days in November 2012 also reported comparable NO_2 levels near the Rawalpindi-Islamabad area ($\sim 2.5 \times 10^{16}$ molecules cm^{-2}) and the rest of the route along the N5 highway ($0.5\text{-}1.5 \times 10^{16}$ molecules cm^{-2}).

On 18 February 2015, measurements were performed from Lahore to Faisalabad city. In between this main route, additional measurements were performed in the northwest of Lahore to investigate the NO_2 pollution levels from this side as well. There are small clusters of different industries, including metal works or iron industries mentioned in chapter 4. These industries are a strong NO_2 source in the area, and elevated NO_2 VCDs $\geq 3 \times 10^{16}$ molecules cm^{-2} can be seen along this segment (north of Lahore) of the route. Figure 5.2 (top) shows the spatial distribution patterns of NO_2 observed on that day. Enhanced VCDs were also observed between Sheikhupura and Faisalabad. Emissions from the power plant and several industries along the road are responsible for the elevated levels. High NO_2 levels can also be seen in Faisalabad.

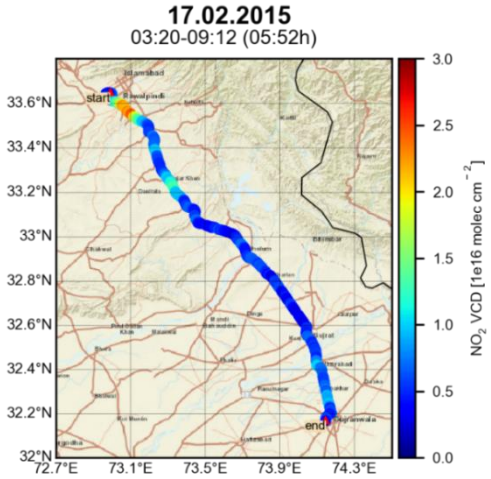

Figure 5.1: NO_2 VCDs derived from the car MAX-DOAS observations performed on 17.02.2015, along the N5 highway from Islamabad to Gujranwala.

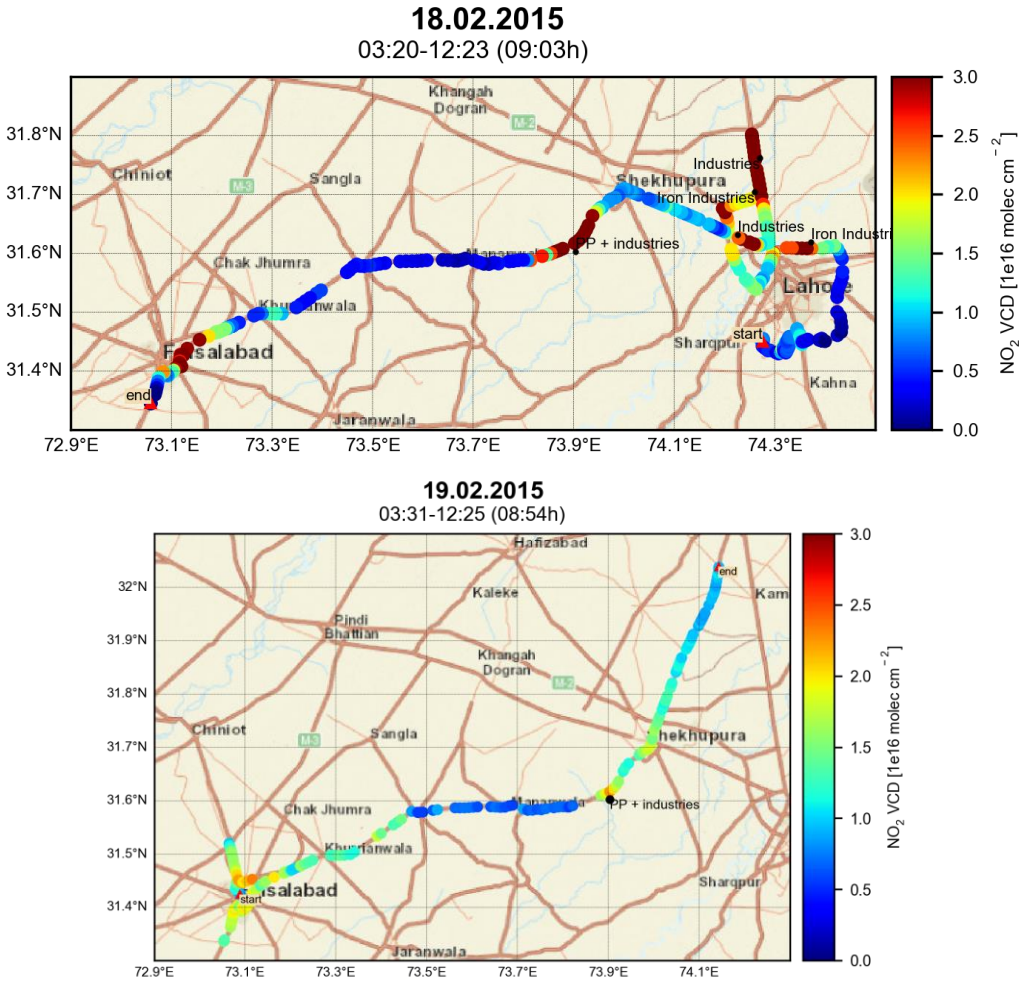

Figure 5.2:Tropospheric NO_2 VCDs measured on 18.02 (top) and 19.02 (bottom) by car MAX-DOAS between Lahore and Faisalabad.

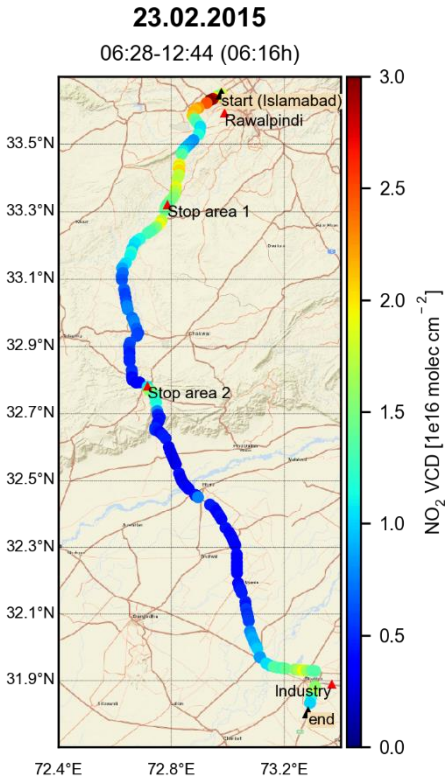

Figure 5.3: NO_2 VCDs derived from car MAX-DOAS observations from Islamabad to Pindi Bhattian along the M-2 Motorway on 23.02.2015.

On the third day of the campaign, i.e., 19.02.2015, measurements started from Faisalabad at 3:31 UTC and ended around 12:30 UTC, 10 km southwest of Gujranwala city. Enhanced VCDs ranging between $\sim 1.5\times10^{16}$ molecules cm^{-2} and $\sim 2.5\times10^{16}$ molecules cm^{-2} can be seen around Faisalabad in Figure 5.2 (bottom). On 18 February (Fig 5.2), NO_2 VCDs were $\sim \geq 3\times10^{16}$ molecules cm^{-2} in the power plant area, whereas on the next day (19.02), lower values around 2×10^{16} molecules cm^{-2} were observed at the same location.

On 23 February 2015, measurements were performed along the 270 km long route on the M2 motorway. The car MAX DOAS observations were started at Islamabad around noontime at 11:28 local time or 06:28 UTC and ended along the M4 Motorway near a small town named Pindi Bhattian after about 6 hours. Enhanced NO_2 VCDs near the starting point can be attributed to the emissions from the cities of Rawalpindi and Islamabad (Figure 5.3). Succeeding enhancements can be seen at the rest or stop areas along the motorway. Close to the end of the route, a large textile industry along the road and the vehicular NO_2 emissions from Pindi Bhattian are probable reasons for these enhancements.

On 26 February 2015, mobile measurements started from the city of Dera Ghazi Khan and ended near a sugar mill near the small town of Sanawan (Figure 5.4). Elevated NO_2 levels were observed in the vicinity of the power plant near Kot Addu.

On 27 February 2015, the measurements were performed 400 km south of Lahore to investigate the NO_2 spatial distribution in that region. The route adopted that day covered around 250 km along the N55, N70 and N5 highways. The measurements started around

10 am local time (4:59 UTC). Enhanced NO_2 VCDs observed in the first half of the route (Figure 5.5) can be attributed to three power plants, an oil refinery and other industries along the N55 road.

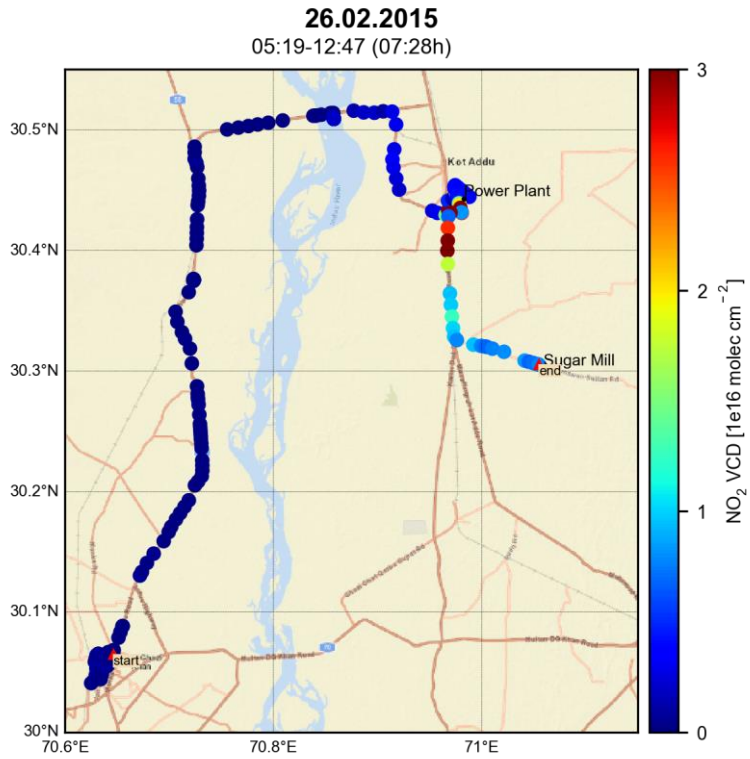

Figure 5.4: NO_2 VCDs observed from the car MAX-DOAS measurements on 26 February 2015 in southern Punjab.

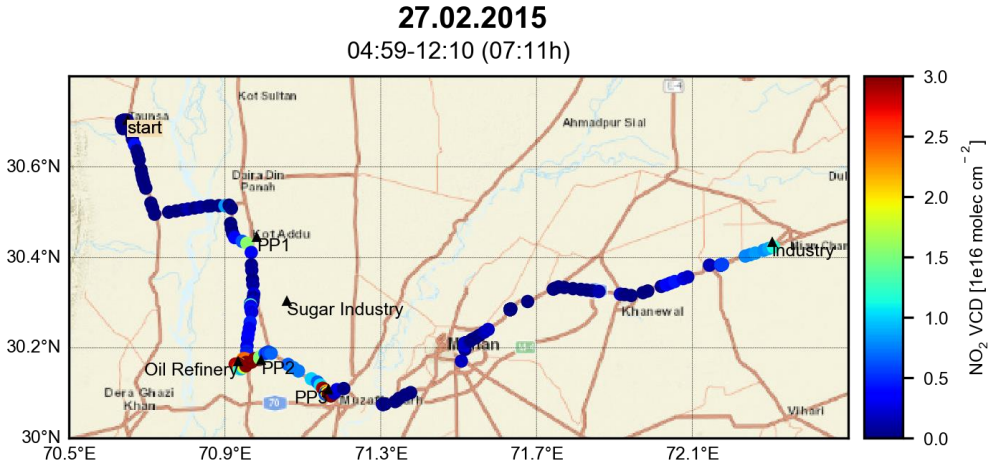

Figure 5.5: NO_2 VCDs derived from the car MAX-DOAS observations on 27 February 2015 along the N5 highway. The potential NO_2 sources like power plants and industries are also indicated.

5.2. MOBILE MAX-DOAS OBSERVATIONS DURING 2018-I

On three days during the 2018-I campaign, measurements were performed in addition to encircling Lahore. The spatial distributions of the four trace gases for these days are presented in this section.

5.2.1. Measurements around the Sahiwal Coal Power Plant

On 5 March 2018, measurements were performed to investigate the emissions from the Sahiwal coal power plant. The power plant is located around 150 km southwest of Lahore and has an installed capacity of 1320 megawatt (MW) (Government of Pakistan, 2020). Four circles were executed around the plant and each circle took approximately half an hour. Another power plant (Saif Power plant) with a capacity of 225 MW is also located on the opposite side of the road (Saif Group, 2020.). The spatial distributions of all the four trace gases observed during circle number four are shown in Figure 5.6. Enhancements for NO_2 and SO_2 can be seen at the downwind side (southeast). The other three circles also showed similar enhancement patterns, i.e., elevated values at the highway and the downwind part of the route. Figures for these circles can be found in appendix D.1.

Measurements were also performed along the way from Lahore to the power plant via the N5 highway. Figure 5.7 presents measurement results for the four trace gases along this part. Elevated NO_2 and SO_2 VCDs can be seen near the Nishat power plant. The plant is located approximately one km away from the road. For HCHO and CHOCHO, no clear enhancements with values around 1.2×10^{16} molecules cm^{-2} and below 1×10^{15} molecules cm^{-2} were observed.

5.2.2. Measurements around Faisalabad

Observations were performed on 9 March 2018 to investigate the spatial distributions of the trace gases around Faisalabad city. In Figure 5.8 NO_2, SO_2, HCHO and CHOCHO distributions are exhibited. The powerplants and industrial regions along the driving route are also indicated in the figure. The measurements started from Sheikhupura at 6:44 UTC and the circle started at 8:14 UTC and was completed in around 3 hours. At the south side of the circle, enhanced levels of all four species were observed. These elevated levels can be attributed to vehicular emissions. High NO_2 and SO_2 VCDs can also be seen on the eastern side of the circle. These enhancements are probably due to the emissions from various industries located along this part of the route. Along the highway, elevated SO_2 VCDs were observed in the vicinity of the powerplant 2 (Figure 5.8 b).

5.2.3. Measurements at Islamabad/Rawalpindi

Car MAX-DOAS measurements were performed to explore the trace gases abundance along the N5 highway from Lahore to Islamabad on 15 March 2018. The mobile measurements were also performed around Gujranwala. Gujranwala is an industrial city with approximately 2 million inhabitants and located 60 km north of Lahore. Measurements were started from Lahore at 3:26 UTC along the N5 highway and Gujranwala was encircled

from 4:35 to 5:23 UTC. Enhanced VCDs were not observed for any trace gas around the city of Gujranwala. The figures can be found in appendix D.2. The measurements continued across the Islamabad Expressway and Srinagar Highway, the two major roads of Islamabad. High levels of NO_2 and SO_2 were observed along these roads. Near the end of the measurements, enhanced VCDs for all trace gases were observed. Very high SO_2 VCDs ($\geq 4\times10^{16}$ molecules cm^{-2}) can be seen in Figure 5.9. These enhancements may be attributed to the emissions from cement industries in that area. The fuel and raw materials used for cement production are responsible for the emissions of oxides of sulfur (SO_2) and nitrogen (NO and NO_2). Sulfur containing fuels in the cement kiln combust at high temperatures and are oxidized into SO_2. Fuel combustion also produces NO_x and non-methane volatile organic compounds (Berdowski et al., 2016). The sulfur content present in the organic raw material used for cement production is also a source of SO_2 (Horkoss, 2008; Ibrahim et al., 2012).

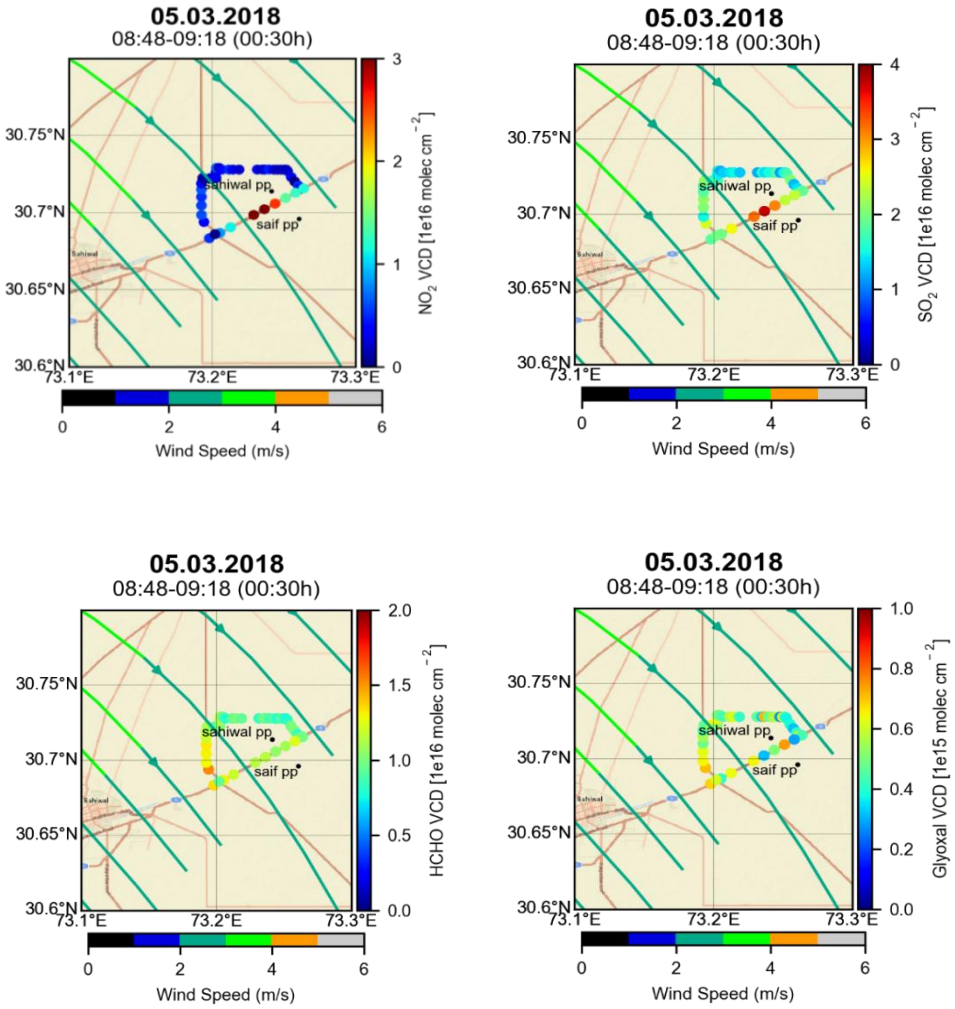

Figure 5.6: Spatial distribution of the four trace gases observed by the car MAX-DOAS measurements around the Sahiwal coal power plant. The wind streamlines shown represent the averaged ECMWF winds for the lower 500 m at 12 UTC.

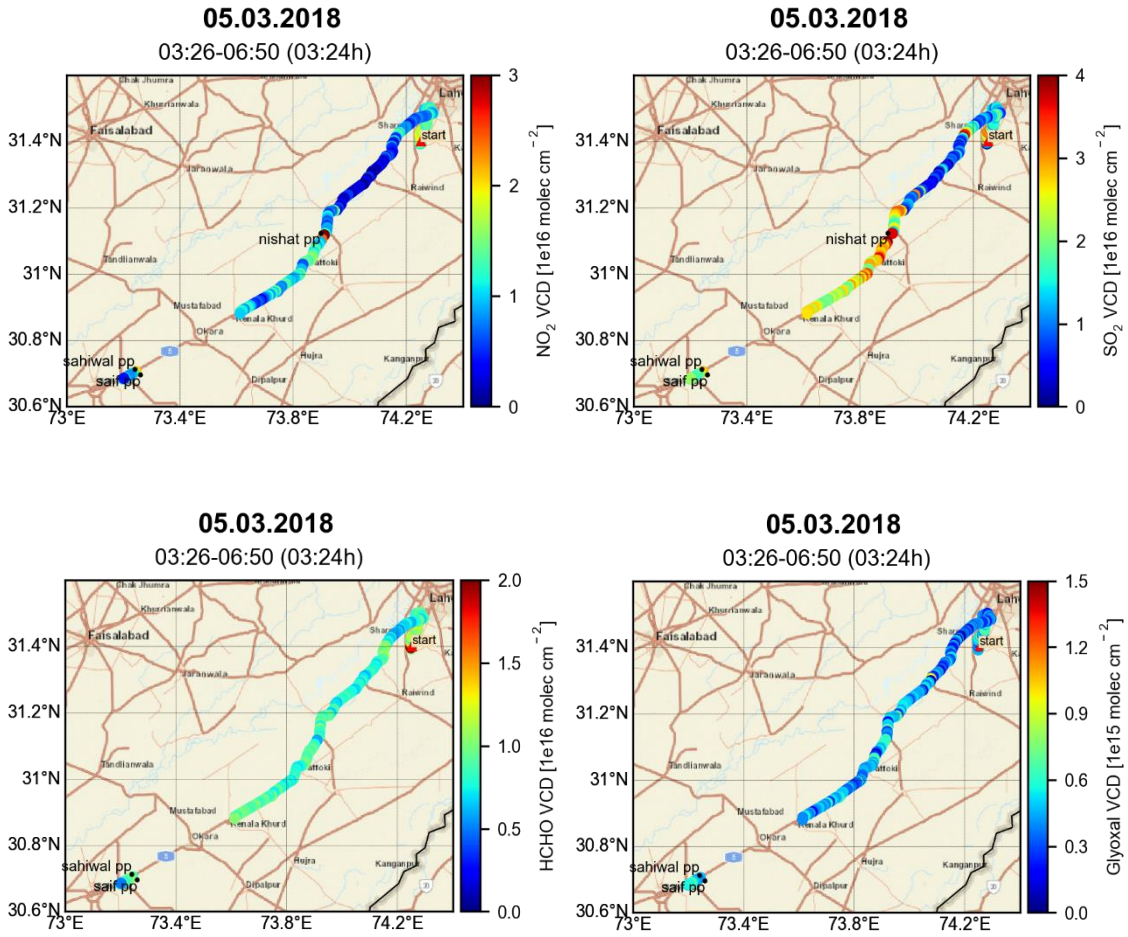

Figure 5.7: Tropospheric vertical column densities of all four trace gases derived from the car MAX-DOAS observations along the N5 highway on 5.3.2018 on the way to the power plant.

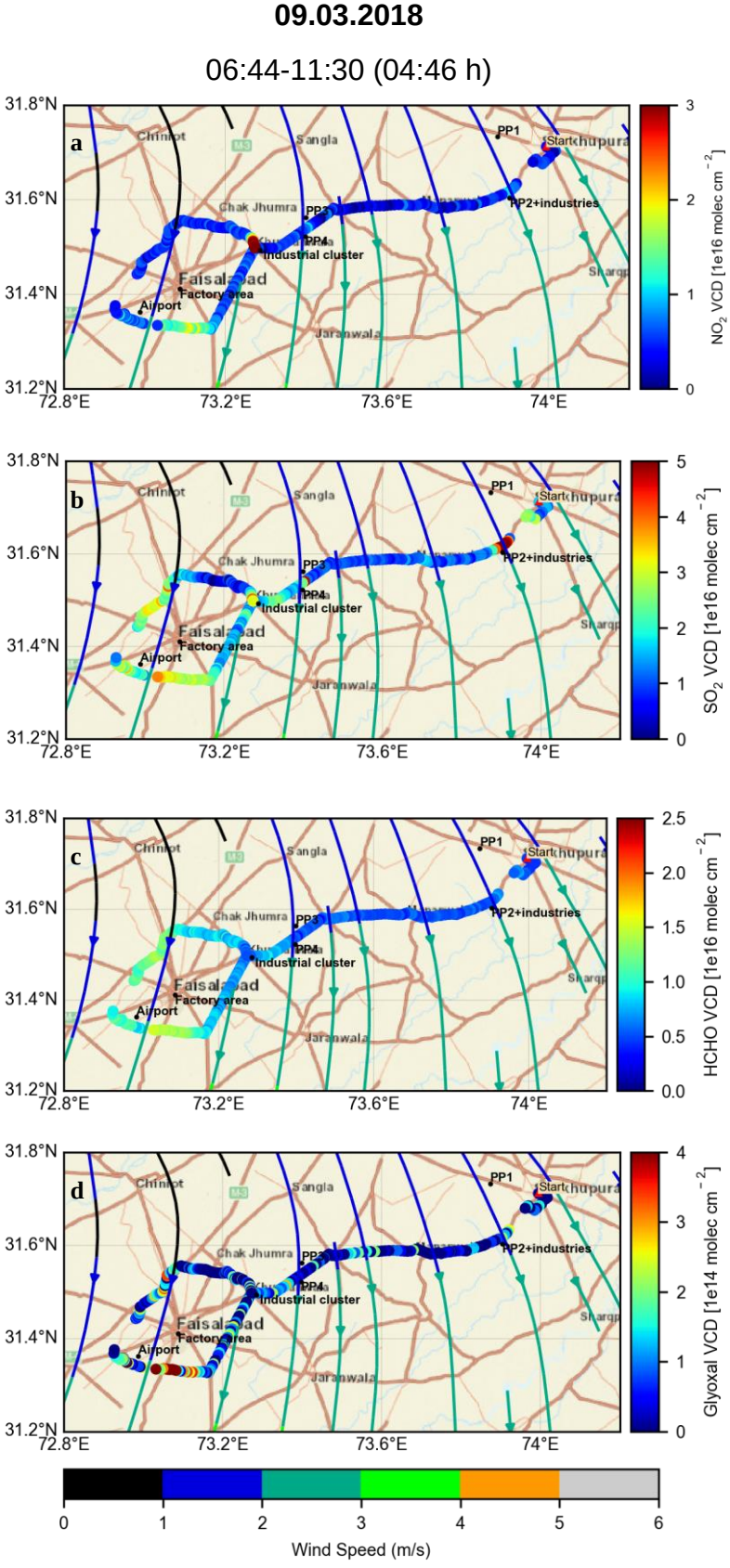

Figure 5.8: Tropospheric vertical column densities (VCDs) of NO_2(a), SO_2(b), CHOCHO(c) and HCHO(d) measured on 9 March 2018 from Sheikhupura to and around Faisalabad.

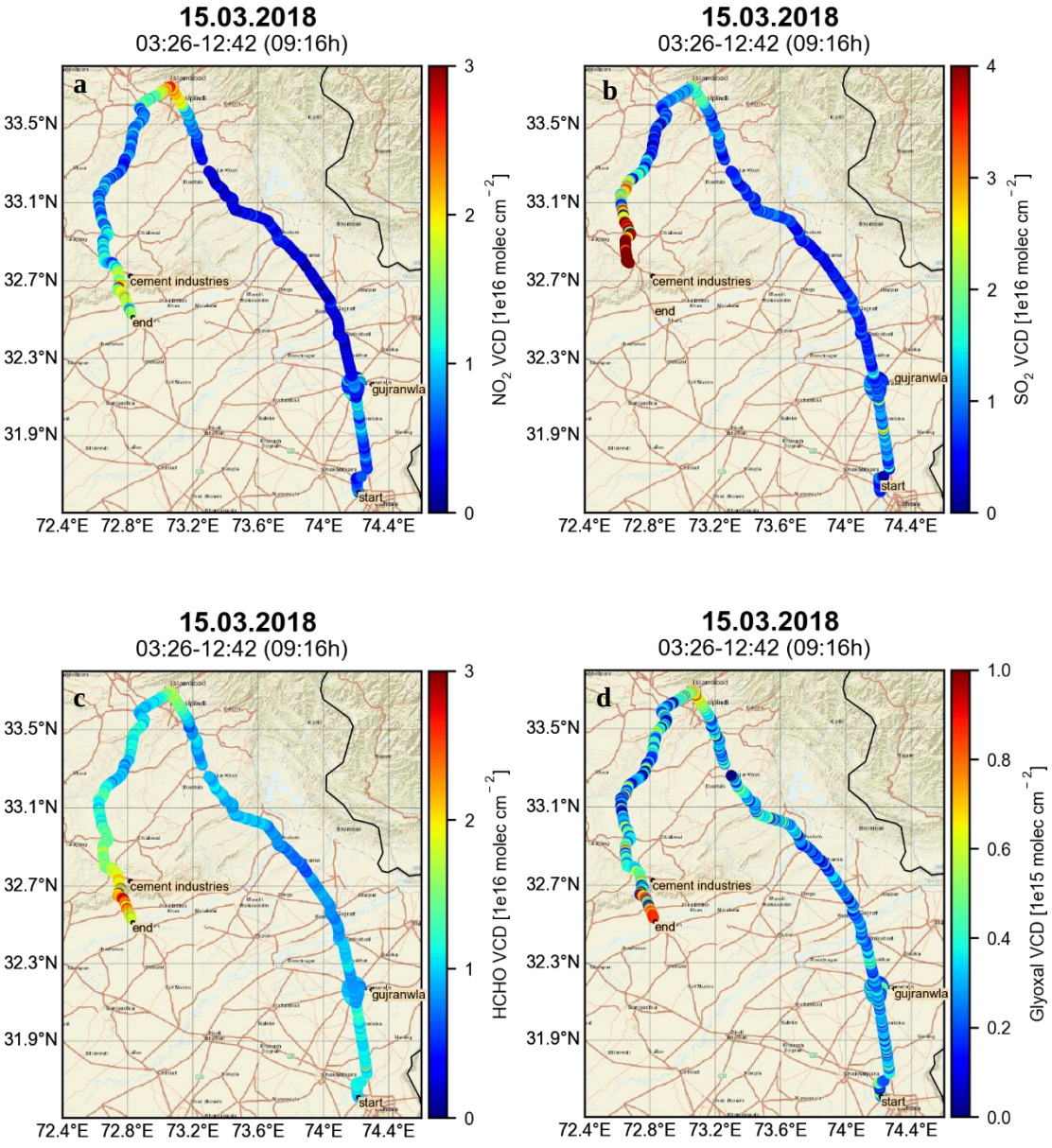

Figure 5.9: NO_2(a), SO_2(b), HCHO(c) and CHOCHO(d) VCDs for 15.03.2018, between Lahore and Islamabad along the N5 highway and the M2 Motorway derived from car MAX-DOAS.

5.3. POWER PLANT MEASUREMENTS (2018-II)

Measurements were performed for 13 days in June and July 2018 to estimate the trace gas emissions from the power plants in the region. Details of the study area, measurement conditions and analyses have already been discussed in chapters 2 and 3. Car MAX-DOAS measurements along the large circles around 17 power plants were made on three days, while on the rest of the ten days, smaller circles were performed to estimate the emissions from two or more power plants. According to the suitability criteria for the flux calculations described in section 2.3.2.1, only two smaller circles performed on 28.6.2018 got qualified for the emission estimation. For these and all other measurements performed during this campaign, the spatial distributions of the four trace gases are presented.

5.3.1. Emission Estimates

The power plants in the region were grouped under three zones as described in section 3.2.5, and Figures 3.8 and 3.9. On 28 June 2018, two circles around zone B and C powerplants were performed to estimate the NO_x and SO_2 emissions from the nine power plants. For this day, flux results of HCHO were not considered due to very high total errors and negative flux values. As mentioned in the previous chapter (section 4.3.1) the HCHO flux cannot be quantified straightforwardly due to the short lifetime and secondary formation of the trace gas. Moreover, power plants are not significant HCHO sources, which may be the reason for the total negative flux values.

The first circle was performed around the three zone-C power plants (Figure 5.10). The duration of the measurements was 2 hours and 21 minutes. The averaged wind speeds were > 4 ms^{-1} in the measurement area. The estimated NO_x emissions were $7.8 \times 10^{24} \pm 2.8 \times 10^{24}$ molecules s^{-1} and SO_2 emissions for the same circle were estimated as $1.3 \times 10^{25} \pm 0.4 \times 10^{24}$ molecules s^{-1}. The enhanced VCDs at the north and northwest side of the route indicate that the Orient and Nishat power plants were operational on that day while the Balloki power plant seems not functional.

The second circle was performed around the zone-B power plants between 9:11 and 11:07 UTC (Figure 5.11). The NO_x emissions estimated from the six zone-B power plants were $3.6 \times 10^{24} \pm 1.8 \times 10^{24}$ molecules s^{-1} whereas, the estimated SO_2 emissions were $4.7 \times 10^{24} \pm 1.9 \times 10^{24}$. Enhanced VCDs for both trace gases can be seen at the downwind side of the circle. Total estimated errors for emissions from both circles are presented in Table 5.1. For details of the error analysis, refer to section 4.1.1.3.

Table 5.1: Relative errors (%) of the NO_x and SO_2 emissions for 28.06.2018

Error of	Uncertainty sources		NO_x		SO_2	
			Zone C	**Zone B**	**Zone C**	**Zone B**
SCDs	Spectral retrieval		15.0	15.0	15.0	15.0
VCDs	Geometric approximation		20.0	20.0	20.0	20.0
Flux	Wind	45° shift	13.0	37.8	8.1	26.7
		Temporal interpolation	0.01	0.00	0.04	0.00
Flux	Gaps		11.0	11.4	13.7	17.4
NO_x emissions	Partitioning factor		15.0	15.0	---	---
NO_x emissions	Lifetime Factor		10.0	10.0	---	---
Total Error (±%)			**35.2**	**50.1**	**29.6**	**40.5**

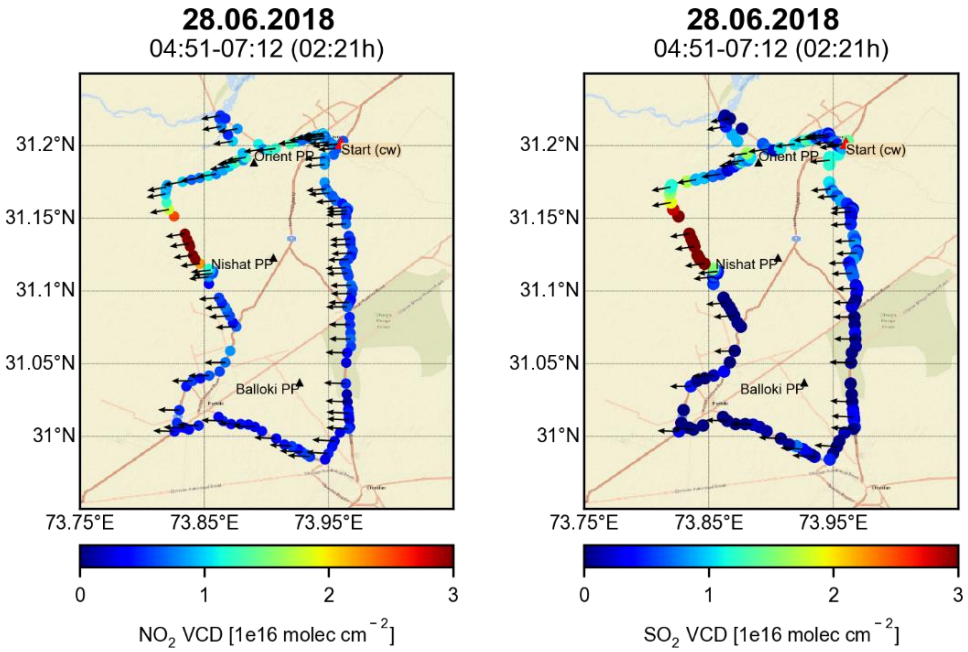

Figure 5.10: Tropospheric NO_2 (left) and SO_2 (right) VCDs measured on 28.06.2018 to estimate the NO_x and SO_2 emissions respectively, from the zone C power plants. The black arrows represent the corresponding wind vectors and the black triangles indicate the encircled power plants.

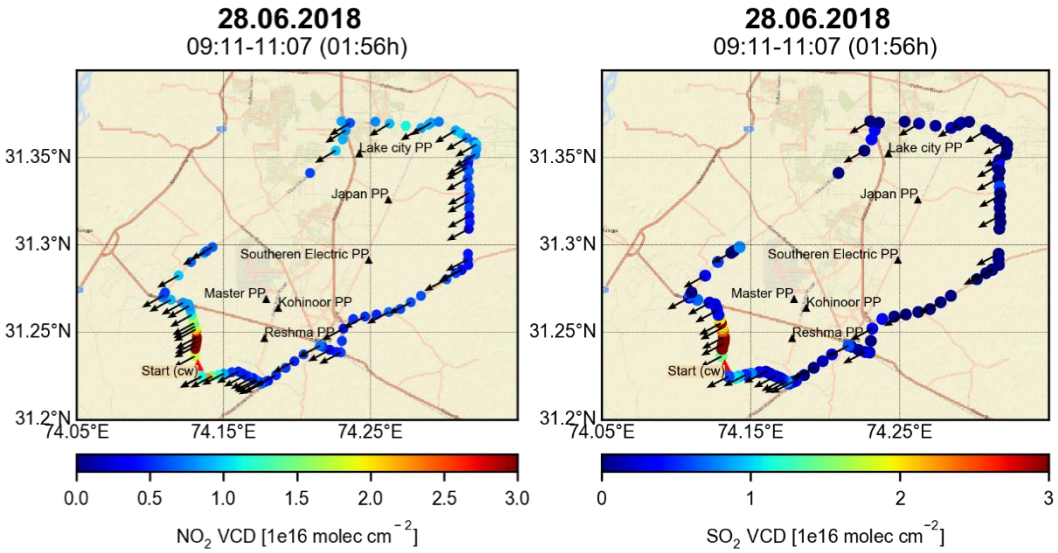

Figure 5.11: Tropospheric NO_2 (left) and SO_2 (right) VCDs measured on 28.06.2018 to estimate the trace gases emissions from the zone B power plants. The black arrows represent the corresponding wind vectors and the black triangles indicate the encircled power plants.

5.3.2. Spatial Distributions

The spatial distributions of the four trace gases (NO_2, SO_2, HCHO and CHOCHO) around the power plants measured for 12 days are discussed in this section. On three days (18 and 25 June and 5 July 2018), large circles were executed to encircle all 17 power plants in the area. In Figure 5.12, measurements performed on 25 June 2018 are shown, whereas measurement results for 18 June and 5 July can be found in appendix D.3. On 25 June, enhanced VCDs of all four trace gases are visible at the eastern sides of the circles. These enhancements for NO_2 and SO_2 are mainly from the steel industries in the north of Lahore and the industrial zone (QIE), whereas for formaldehyde and glyoxal, these elevated values can be attributed to the paper industry and crop residue burnings.

In Figure 5.13 measurements performed on 20 June are shown. On this day, measurements were performed to investigate the spatial distributions of the trace gases around the zone-A and zone-C power plants. The zone-A circle measurements were performed between 4:47 and 7:10 UTC, and the zone-B measurements were executed between 9:22 and 11:22 UTC. The measurements were also performed on the way between the two circles along the N60 and N5 highways. The part of the route adopted in the north of the zone-A circle showed enhanced SO_2 VCDs whereas, for NO_2, no enhancements were observed. The SO_2 enhancements can be attributed to the cluster of the brick kilns located along this segment of the road. The brick kilns in Pakistan use low-quality coal with high sulfur content and are especially a potential source of SO_2 (Khan et al., 2019; Mirza et al., 2013). For the zone-C circle, enhanced SO_2 and NO_2 VCDs were observed in the west, which can be attributed to the emissions from the power plant no. 8. For the other two trace gases, no enhancements were observed around the power plants. Enhanced HCHO and CHOCHO VCDs were

observed along the road connecting the two circles. These elevated values can be attributed to the industries present in the vicinity.

On 21 June 2018, measurements along the three power plant zones were performed, as shown in Figure 5.14. The first circle (3:56-6:00 UTC) was performed to investigate the trace gas distributions around the zone-C power plants. Elevated NO_2 and SO_2 VCDs ($>5\times10^{16}$ molecules cm^{-2}) were observed in the west to north sides of the circles (figure 5.15, top panel). These high levels are caused by the emissions from the power plants 9 and 10.

Enhanced levels of NO_2 and SO_2 were also observed in the northwest of the zone-B circles. The measurements along this circle were performed between 6:28 and 8:08 UTC.

The observations around the zone-A circle were executed from 10:35 to 13:37 UTC. No NO_2 and SO_2 enhancements were observed along this circle and it can be assumed that except for the power plant no. 16 and 17 no power plants in this zone were operational during the driving period as elevated NO_2 and SO_2 VCDs larger than 5×10^{16} molecules cm^{-2} were observed in their vicinity. HCHO VCDs around 2×10^{16} molecules cm^{-2} were observed along the southwestern segment of the zone-A circle.

25.06.2018

2:45-12:36 (9:50 h)

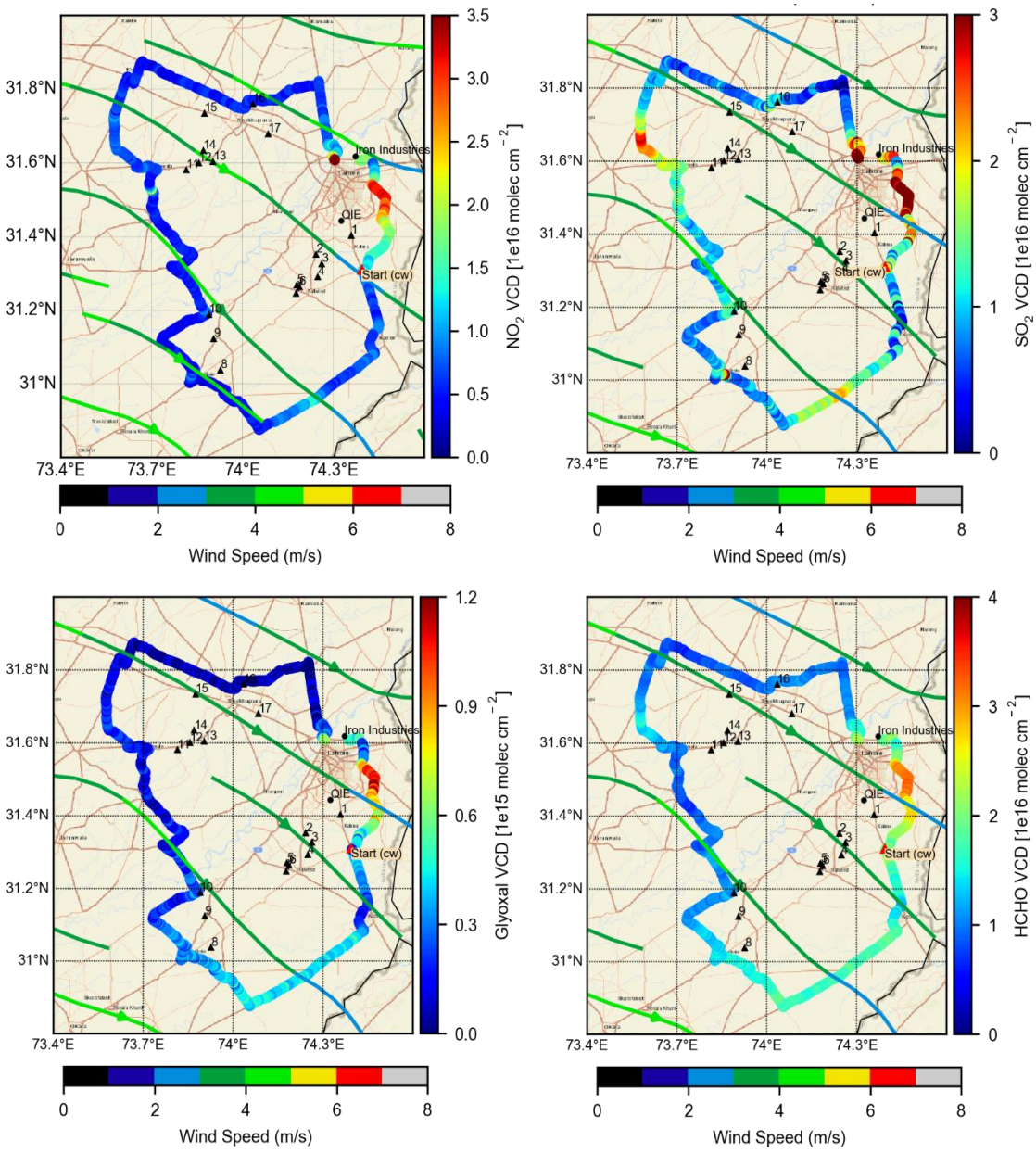

Figure 5.12: Trace gas VCDs observed by car MAX-DOAS on 25.06.2018, performed along the larger route around the 17 power plants in the region. The full circle was completed in around 10 hours. The wind stream lines represent the ECMWF averaged wind at 12 UTC.

20.06.2018

4:47-11:22 (6:35 h)

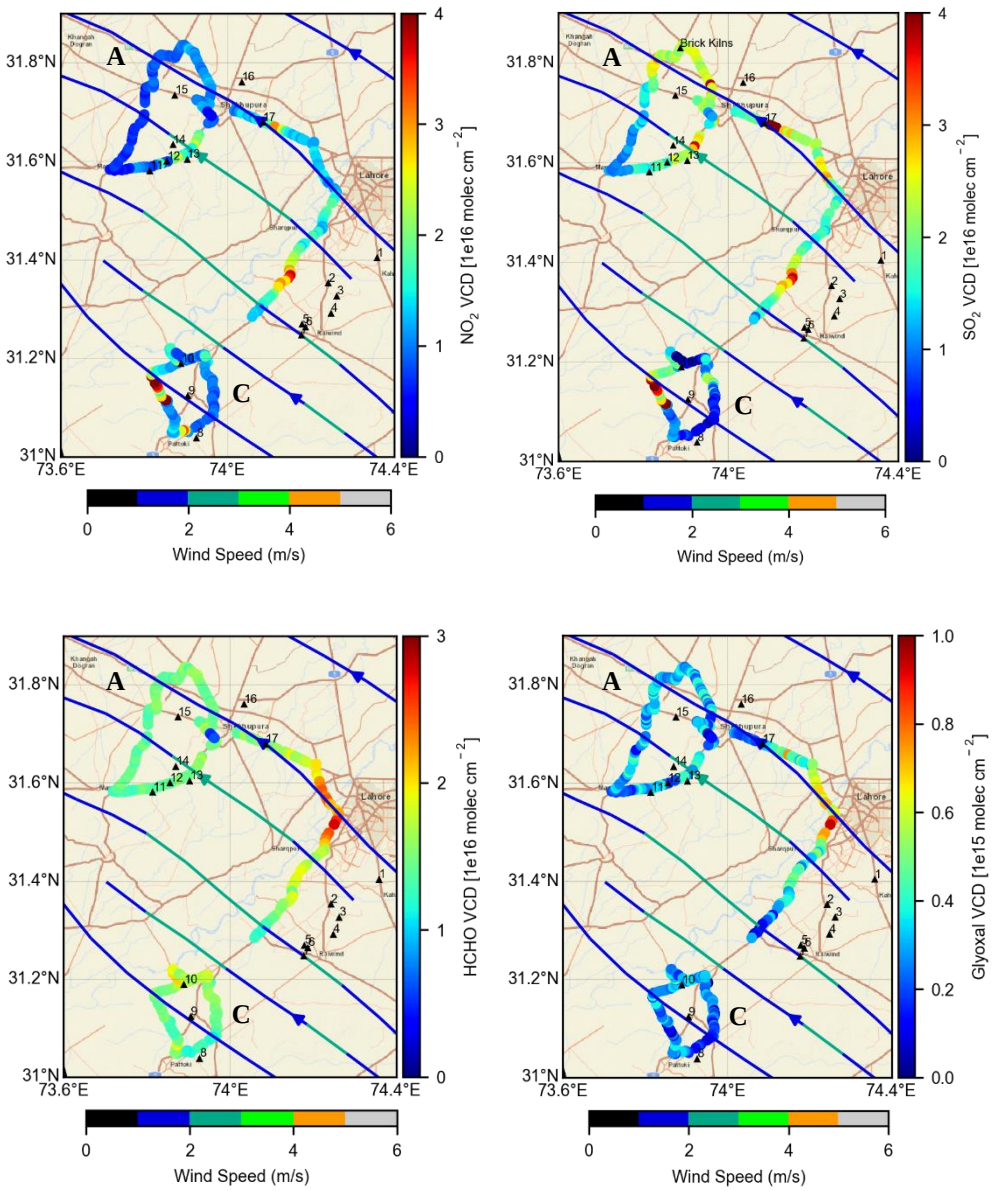

Figure 5.13: Tropospheric trace gas VCDs, observed by car MAX-DOAS measurements performed on 20.06.2018 to investigate the trace gas spatial distributions around the zone A and C power plants. The stream lines represent the 06 UTC averaged wind output.

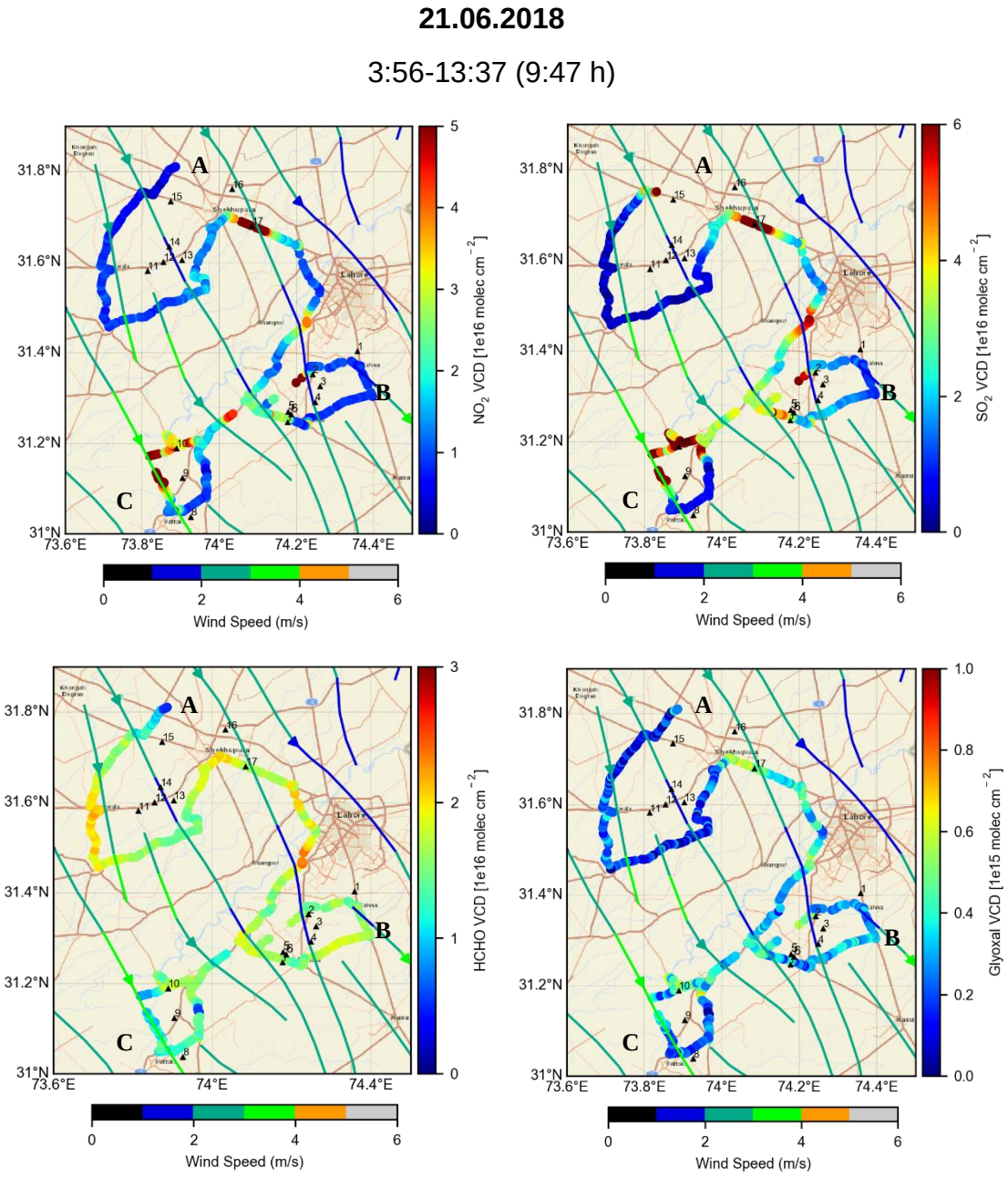

Figure 5.14: Tropospheric VCDs observed by the car MAX-DOAS measuremens on 21.06.2018 to investigate the spatial distributions around the 3 power plant zones. The streamlines represent the 12 UTC averaged wind output.

22.06.2018

A 3:50-6:50 (3:00 h)

B 10:12-12:17 (2:05 h)

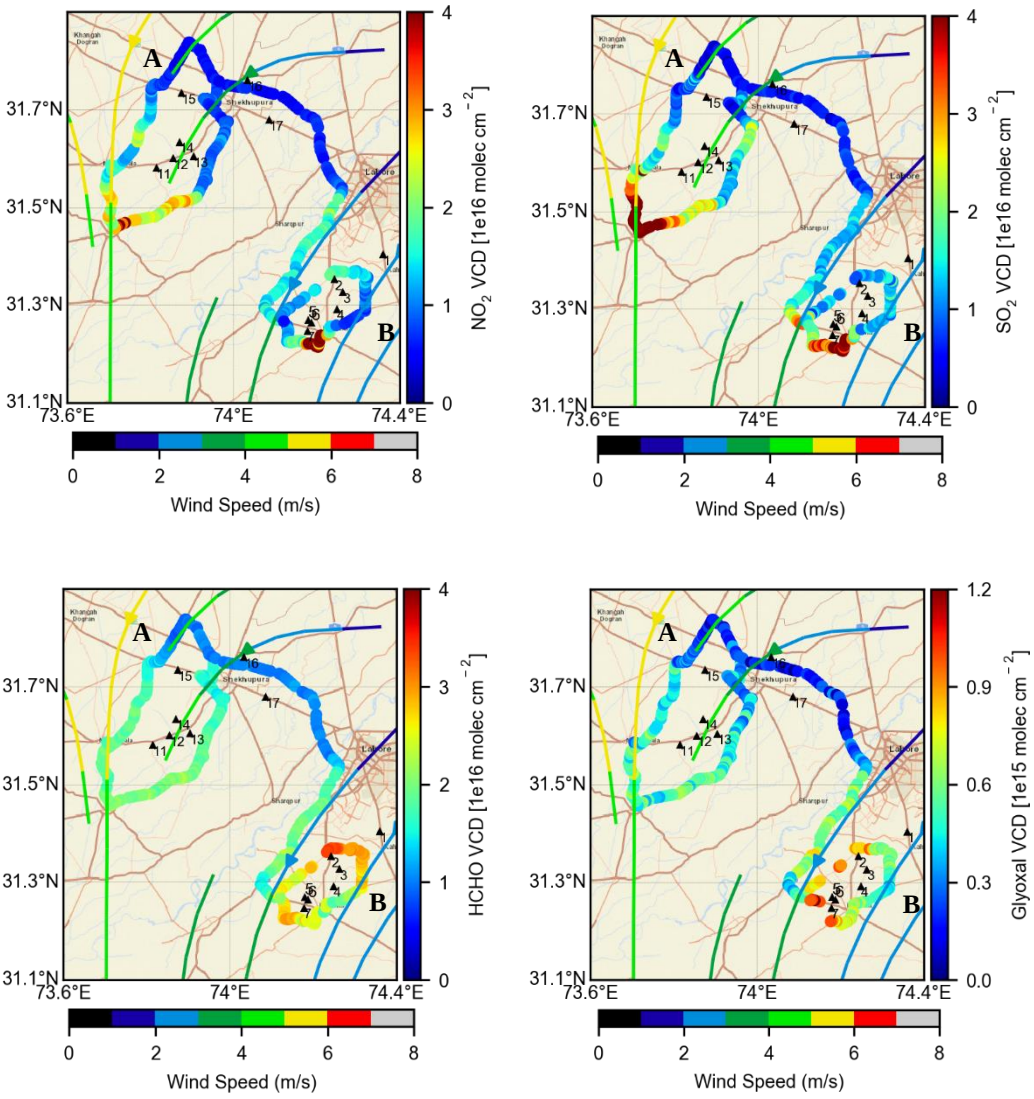

Figure 5.15: Tropospheric VCDs of NO_2, SO_2, HCHO and CHOCHO, observed by the car MAX-DOAS measurements on 22.06.2018 to investigate the spatial distributions around the zone A and B power plants. The streamlines represent the 6 UTC averaged wind output.

On 22 June 2018, measurements along the zones A and B power plants were performed, as shown in Figure 5.16. The first measurements (3:50-6:50 UTC) were performed along the zone-A circle. Elevated NO_2 and SO_2 VCDs around 4×10^{16} molecules cm^{-2} were observed at the downwind sides (south and west). These high values indicate that at least some of the encircled power plants were functional at the measurement time. For HCHO and CHOCHO, no obvious enhancements were found. The four trace gas distributions on the way from zone A to zone-B are also shown in Figure 5.16 Slightly enhanced levels of these trace gases were observed along the N5 highway part of the route and these elevated values can be most probably attributed to vehicular emissions. For the zone-B power plants, two circles were performed. In Figure 5.16 the results from the second circle (10:12-12:17 UTC) are presented. High NO_2 and SO_2 values were observed on the downwind sides of the circle. Also elevated VCDs of HCHO and glyoxal were observed, but with different spatial distributions compared to NO_2 and SO_2. These elevated glyoxal and formaldehyde VCDs can be attributed to the different industries in the vicinity. The trace gas distributions for the first circle performed around the zone-B power plants also showed a similar pattern, and the figure can be found in appendix D.3.

On the next day, i.e., 23 June 2018, again the zone A and B power plants were encircled (Figure 5.17). Observations around the zone-A circle were performed from 05:10 to 8:23 UTC. Elevated NO_2 and SO_2 VCDs around 6×10^{16} molecules cm^{-2} were observed in the vicinity of power plants 16 and 17. The low values along the rest of the circle indicate that the power plants 11-15 were not operational during the measurements. The observations around the zone B circle were performed from 09:45 to 11:50 UTC. For the zone-B circle, enhanced VCDs of NO_2 and SO_2 were observed on the west side of the circle that is also the lee side, whereas slight enhancements of HCHO and CHOCHO can also be seen along the same section. On the way between both circles, enhancements around 4×10^{16} molecules cm^{-2} and 1×10^{15} molecules cm^{-2} or above were observed for HCHO and CHOCHO, respectively. These elevated values can be attributed to industries along this section of the route.

The figures of the measurement results for the remaining days can be found in appendix D.3.

5.3.3. Correlation Analysis

To assess the relationship between the trace gases derived from the observations performed during the power plant campaign (2018-II), correlation analyses were performed between the six trace gas pairs. In this section, the results for these analyses are discussed. The correlation coefficients (R) were used to assess the direction and strength of the relationship between the two variables. In table 5.2, the R value for each trace gas pair is given for the measurements performed during this period. The scatterplots for each trace gas pair are presented in Figure 5.16, respectively.

Like the correlation analyses for the Lahore campaigns, similar results were also observed for this campaign. The NO_2-SO_2 and HCHO-CHOCHO pairs showed strong linear relationship with R values of 0.71 and 0.69, respectively, whereas for rest of the four pairs (NO_2-HCHO, NO_2-CHOCHO, SO_2-HCHO and SO_2-CHOCHO) weaker correlations were found. From these values one can conclude that NO_2-SO_2 and HCHO-CHOCHO probably have similar sources along the driving routes.

Table 5.2: Correlation coefficient (R) values for the trace gas pairs observed during the 2018-II campaign

NO_2-SO_2	**HCHO - CHOCHO**	**NO_2 - HCHO**	**NO_2 - CHOCHO**	**SO_2 - HCHO**	**SO_2 - CHOCHO**
0.71	0.69	0.29	0.46	0.28	0.34

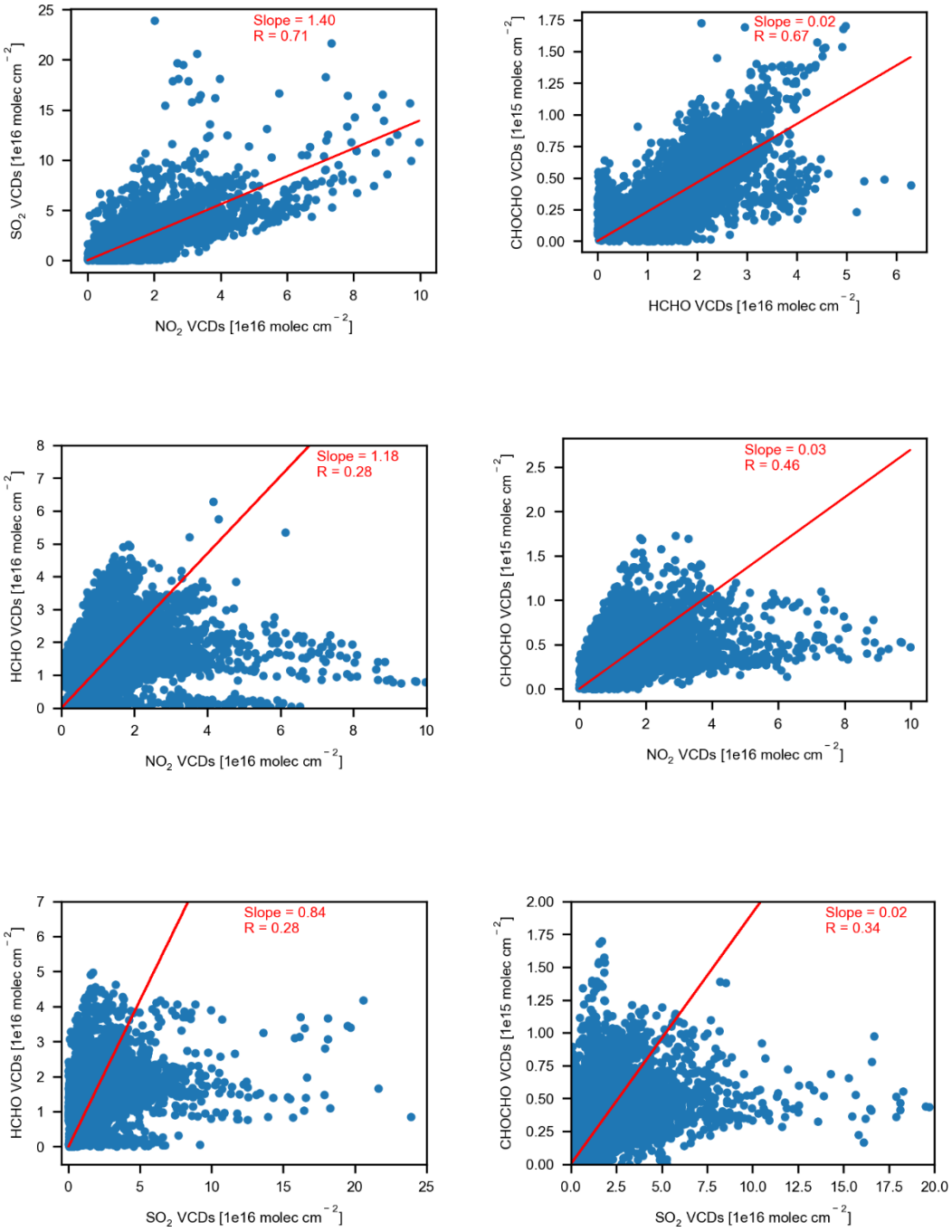

Figure 5.16: Scatter plots showing the correlations between the six pairs of trace gases observed during the 2018 II campaign around the power plants.

5.4. SUMMARY

In this chapter, results from the observations, which were not performed on the circles around Lahore, were presented.

For the 2015-I campaign, various potential sources of NO_2 were identified along the driving routes. Large cities like Rawalpindi, Islamabad and Faisalabad exhibited high NO_2 levels ($\sim 2.5 \times 10^{16}$ molecules cm^{-2}). Various power plants and industries were also spotted as potential emitters of nitrogen oxides. Compared to these regions, the parts of southern Punjab not in the vicinity of power plants and industries showed substantially lower levels of NO_2 ($\leq 1 \times 10^{15}$ molecules cm^{-2}).

For the 2018-I campaign, measurements at the Sahiwal coal power plant and at the cities of Faisalabad, Rawalpindi and Islamabad showed similarly elevated levels of the observed trace gases. The NO_2 levels for Rawalpindi and Islamabad remained quite consistent ($\sim 2.5 \times 10^{16}$ molecules cm^{-2}) over the period of three years.

The 2018-II campaign was initially planned to estimate the NO_x and SO_2 emissions from the power plants in the area. But due to the unsuitable wind conditions, NO_x and SO_2 emissions for only one day could be estimated for the two power plant clusters. The estimated NO_x emissions for these two conglomerates were estimated as 7.8×10^{24} and 3.6×10^{24} molecules s^{-1} and for SO_2, the emissions were estimated as 1.3×10^{25} and 4.7×10^{24} molecules s^{-1}. For the rest of the days, elevated levels of NO_2 ($\geq 4 \times 10^{16}$ molecules cm^{-2}) and SO_2 ($\geq 5 \times 10^{16}$ molecules cm^{-2}) were observed along the three power plant zones on different days.

From the correlation analyses, it was observed that SO_2 and NO_2 mostly showed similar emission patterns (R=0.71), which indicates that these two trace gases have common emission sources in this region, mainly the power plants. Also HCHO and CHOCHO showed enhanced correlations (R=0.69), indicating similar emission or formation processes, but different from those of NO_x and SO_2. These results were found consistent with the correlation analyses performed for the measurements executed around Lahore.

6. COMPARISON TO OTHER DATA SETS

In this chapter, the results of the MAX-DOAS observations are compared with other datasets. Comparison studies have been performed for two quantities, i.e., the derived trace gas emissions and the trace gas vertical column densities (VCDs). The emissions derived from MAX-DOAS measurements are compared to emission estimates from the TROPOspheric Monitoring Instrument (TROPOMI) and the Emission Database for Global Atmospheric Research (EDGAR) emission inventory. In addition, VCDs derived from mobile MAX- DOAS measurements are compared with TROPOMI satellite data. The comparisons were performed to evaluate the consistency of the MAX-DOAS data with other datasets. Table 6.1 presents an outline of the comparison scheme and the details of these datasets can be found in section 2.7.

Table 6.1: An overview of the comparison scheme performed between the different data sets.

Comparison Type	MAX-DOAS	TROPOMI	EDGAR
VCDs (molecules cm^{-2})	x	x	---
Emissions (molecules s^{-1})	x	x	x

6.1. VCD COMPARISONS

Vertical column densities (VCDs) retrieved from the car MAX-DOAS observations are compared to TROPOMI satellite data. In this thesis, a daily comparison is performed for co-located results of NO_2, while for SO_2 and HCHO, comparisons for monthly averages have been performed for the two measurement campaigns of 2018. In the following sub-sections, the details of these comparisons are presented.

6.1.1. Comparison with TROPOMI Satellite Data

6.1.1.1. Nitrogen Dioxide Comparison with TROPOMI Satellite Observations

Tropospheric NO_2 vertical column densities were taken from TROPOMI/S-5P, Level 2 data[5] (van Geffen et al., 2019). Measurements with cloud fraction (CF) $\leq$ 0.3 and quality

[5] Tropospheric NO_2 VCDs from TROPOMI were derived and provided by Christian Borger from the Satellite Remote Sensing Group, MPIC, Mainz.

assurance (QA) value ≥ 0.75 were selected. The satellite overpass time is around 13:30 local time (LT) or 8:30 UTC. For comparison, the MAX-DOAS observations performed ±15 minutes around the TROPOMI overpass time were considered. MAX-DOAS observations co-located within individual TROPOMI pixels were averaged and used for the comparison.

For the 2018-I campaign performed around Lahore (during Feb-Mar), the comparison was performed for 14 days; for the 2018-II measurements, the comparison was performed for 6 days. The coefficients of determination, R^2 for the two measurements, were found to be 0.56 and 0.58, respectively (Figure 6.1). All the compared days were clear with cloud fractions < 5%. To investigate the reason for the large variability in correlation strengths between the ground-based and satellite observations, aerosol optical depth (AOD) data (version 3, level 1.5) from AERONet (Holben et al., 2001) was considered for individual days. Daily averaged AOD at 440 nm was found to range from 0.28 to 0.90. The rather large AOD values during both campaigns indicate a strong effect of aerosols on the comparison result. Various previous studies, e.g. Boersma et al. (2004), Hong et al. (2017) and Leitão et al. (2010) also reported uncertainties in the satellite NO_2 retrieval due to aerosols.

The satellite data underestimated the ground-based measurements by around 40 to 50 % as the slope values for 2018-I and II were estimated around 0.51 and 0.61, respectively. The underestimation of the ground based measurements by TROPOMI data in the current study is compareable to previous studies. E.g., Dimitropoulou et al., 2020 also reported approximately 40-50 % underestimation of TROPOMI data by MAX-DOAS observation. Underestimation of satellite observations for tropospheric NO2, specifically over large urban areas, was also reported by various previous studies, e.g., Celarier et al. (2008); Irie et al. (2012); Kramer et al. (2008) and Pinardi et al. (2020). According to these studies, many factors can contribute to the underestimations e.g., different pixel sizes (instrumental characteristic), different retrieval methods, systematic uncertainties in the retrieval of column densities and uncertainties in the tropospheric air mass factor (AMF). For the present study, the main reason for the underestimations might be the satellite AMF, as for such high tropospheric NO_2 VCDs the other error sources probably have a minor influence.

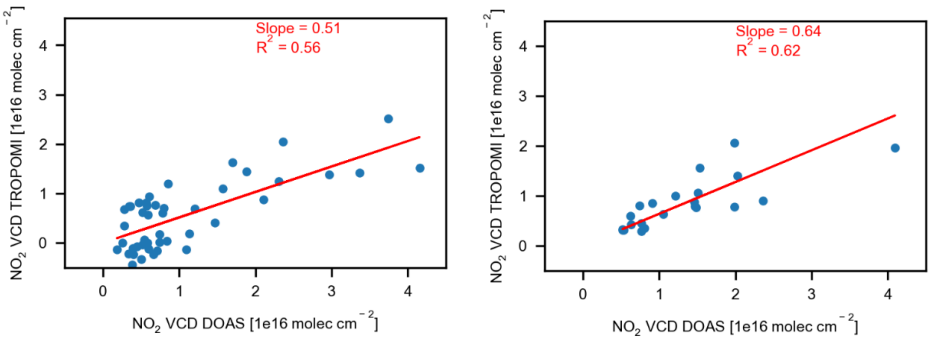

Figure 6.1: Correlation plots for NO_2 VCDs from MAX-DOAS and TROPOMI satellite observations for the two campaigns performed in 2018. The red lines show the regression lines, which were forced through zero.

6.1.1.2. Sulfur Dioxide Comparison with TROPOMI Satellite Observations

The TROPOMI data for the sulfur dioxide (SO_2) tropospheric vertical columns (TVCDs) was provided by Nicolas Theys[6] and retrieved according to the algorithm described in Theys et al. (2017). The SO_2 data for the months of February, March, June and July 2018 may contain large uncertainties as the processor was at a very early stage, and so the SO_2 profiles/averaging kernels may be subject to change. Similar to the NO_2 data set, measurements with cloud fractions $\leq$ 30% were selected. The preliminary SO_2 TROPOMI tropospheric vertical column densities are rather noisy, and thus a daily comparison is not reasonable. Instead, monthly averages (considering only the MAX-DOAS measurement days of the respective months) were calculated and compared with the MAX-DOAS monthly means. The TROPOMI SO_2 data for all available days were averaged for the above-mentioned four months in 2018. All MAX-DOAS observations performed during each month with $\pm$ half hour the overpass time of TROPOMI were averaged for 0.018× 0.018 degree grids. For February, MAX-DOAS measurements around Lahore were performed for 16 days; for March, measurements were performed for 10 days, whereas for June and July 2018 MAX-DOAS measurements were performed for 10 and 3 days, respectively. Figure 6.2 and Figure 6.3 show monthly averaged TROPOMI and MAX-DOAS SO_2 TVCDs for the Lahore region and, Table 6.2 presents the range of mean monthly SO_2 TVCDs from TROPOMI and MAX-DOAS over the MAX-DOAS measurement route for the months of February, March, June and July 2018, respectively.

The SO_2 TVCDs from TROPOMI ranged mainly between -4.5 and 4.9 $\times 10^{16}$ molecules cm^{-2}, over Lahore and the mean MAX-DOAS VCDs values were found be between 1.8 $\times 10^{15}$ and 5.6×10^{16} molecules cm^{-2}. For the power plants measurements, the maximum value for TROPOMI was 2.9 $\times 10^{16}$ molecules cm^{-2} whereas, for MAX-DOAS the maximum value in the power plants area was found to be 1.4 $\times 10^{17}$ molecules cm^{-2}. From these results, it can be assumed that the TVCDs from both the data sets to some extent showed a similar qualitative behaviour as the TVCDs from both data sets showed comparable ranges. However, the interpretation of this kind of comparison can not be straightforward, as the rather high standard deviations for the ground based measurements reveal a high variability of the MAX-DOAS VCDs along the driving routes. Also the satellite data are close or below their detection limit.

Here it should be noted that the spatial and temporal variability in the averaged SO_2 TROPOMI maps is rather high for the first three months (of the order of $\pm 4 \times 10^{16}$ molecules cm^{-2}). Moreover, no systematic spatial pattern can be identified in these maps. Probably the TROPOMI data quality during these first months is not good enough to allow a meaningful comparison to the MAX-DOAS measurements.

[6] Through personal communication.

Table 6.2: Tropospheric vertical column densities (TVCDs) for SO_2, obtained from ground based and satellite measurements for the 2018-I and 2018-II campaigns.

Month	TROPOMI TVCDs (molec cm^{-2})	MAX-DOAS TVCDs (molec cm^{-2})	MAX-DOAS TVCDs Standard Deviation (molec cm^{-2})
February	$-2.8 – 3.8 \times 10^{16}$	$2.8 \times 10^{15} – 4.5 \times 10^{16}$	$\pm 8.3 \times 10^{14} – \pm 4.2 \times 10^{16}$
March	$-4.5 – 4.9 \times 10^{16}$	$1.8 \times 10^{15} – 5.6 \times 10^{16}$	$\pm 1.3 \times 10^{14} – \pm 3.8 \times 10^{16}$
June	$-1.3 – 2.9 \times 10^{16}$	$1.1 \times 10^{15} – 1.4 \times 10^{17}$	$\pm 8.4 \times 10^{13} – \pm 7.8 \times 10^{16}$
July	$-1.6 – 2.0 \times 10^{16}$	$1.6 \times 10^{15} – 8.0 \times 10^{16}$	$\pm 5.6 \times 10^{11} – \pm 9.7 \times 10^{16}$

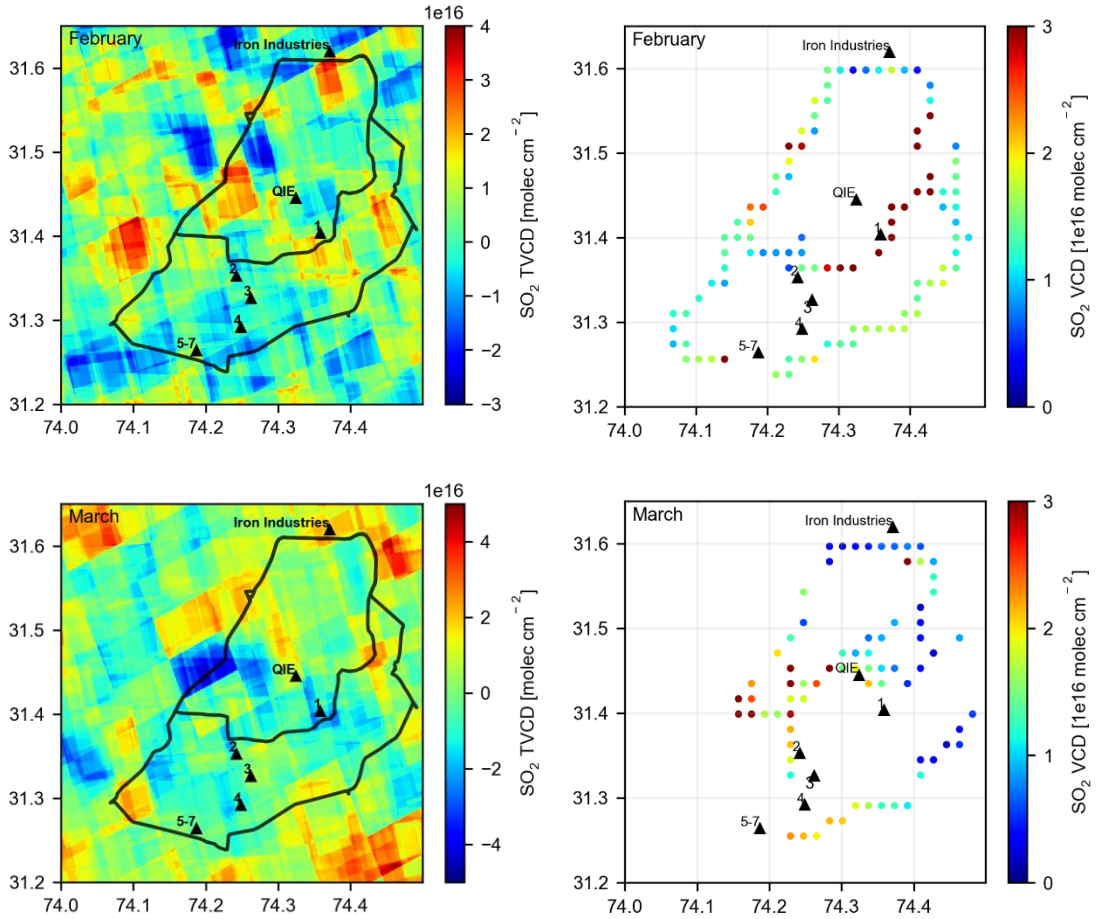

Figure 6.2: Mean SO_2 TVCDs retrieved from TROPOMI (left) and car MAX-DOAS (right) observations for February and March, 2018. The driving routes adopted during these periods are indicated as black lines in the left images, whereas, power plants and industries are indicated as black triangles.

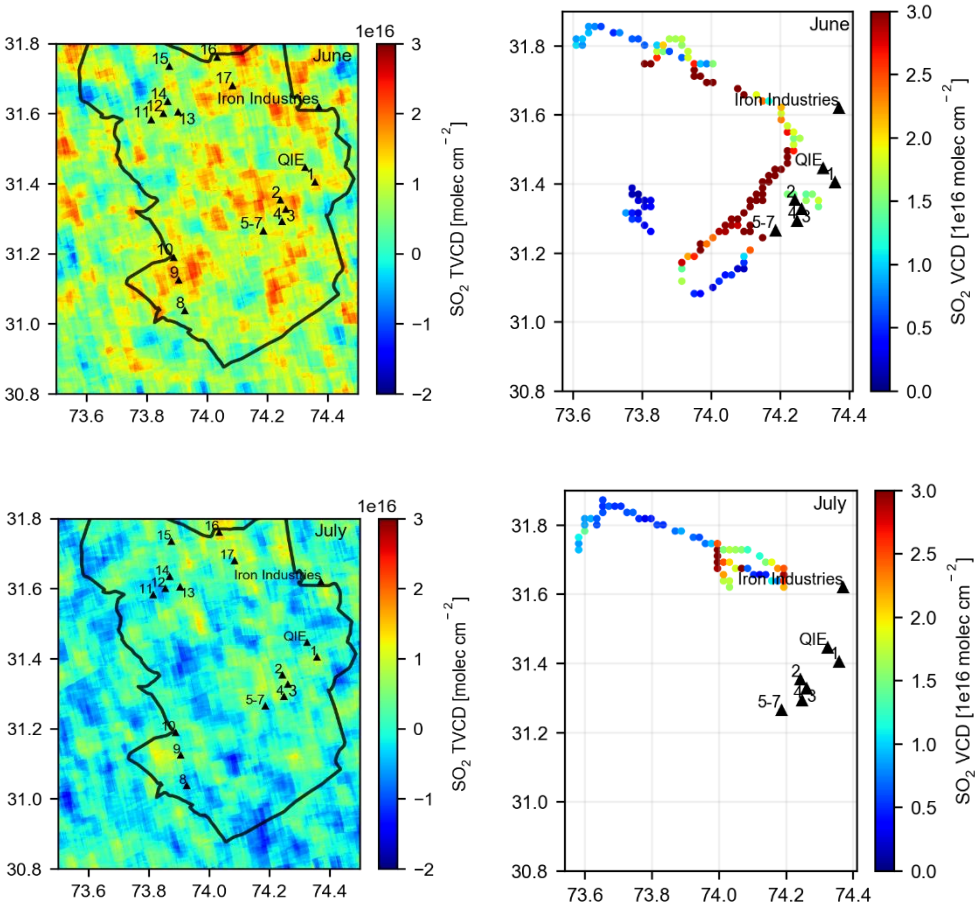

Figure 6.3: Mean SO_2 TVCDs retrieved from TROPOMI (left) and car MAX-DOAS (right) observations for June and July, 2018. The approximate boundary of the study area during these periods is indicated as black lines in the left images, whereas, power plants and industries are indicated as black triangles.

6.1.1.3. Formaldehyde Comparison with TROPOMI Satellite Observations

In this study, the offline TROPOMI formaldehyde tropospheric VCDs, provided by Isabelle De Smedt[7] from the Belgian Institute for Space Aeronomy, were used. For details of the TROPOMI formaldehyde retrieval algorithm, refer to De Smedt et al. (2018). MAX-DOAS formaldehyde VCDs measured during the months of February, March, June and July 2018 were averaged to be compared to the monthly averaged TROPOMI results. Like for SO_2, also the formaldehyde TVCDs from TROPOMI were rather noisy, as the instrument was at an initial stage during the aforementioned period. Therefore, also for HCHO monthly means were considered for the comparison. The calculated MAX-DOAS mean VCD values were obtained by averaging the whole data measured during each month. The MAX-DOAS observations, performed ± half hour of the TROPOMI overpass time (13:30 LT) were considered and the averaging was done for each 0.018 × 0.018 degrees grid.

[7] Through personal communication.

Figure 6.4 and Figure 6.5 show the TROPOMI monthly averaged HCHO TVCDs for the study area and Table 6.3 presents the range of mean monthly averaged HCHO TVCDs from TROPOMI over the MAX-DOAS measurement route and averaged MAX-DOAS VCDs with their corresponding standard deviations for the months of February, March, June and July 2018. The mean MAX-DOAS formaldehyde VCDs for February and March 2018 ranged between 5.5 $\times 10^{15}$ and 3.3×10^{16} molecules cm^{-2}. Figure 6.4 illustrates the monthly averaged spatial distribution of HCHO over Lahore for these months. During this period, enhanced TROPOMI values can be seen at the east and the center of Lahore for both datasets. TROPOMI TVCDs ranged from 3.3×10^{15} to 2.4 $\times 10^{16}$ molecules cm^{-2}. For the Lahore area, most of the TROPOMI values are around 1.25×10^{16}, comparable to the majority of MAX-DOAS monthly mean VCDs ranging between 1 and 1.5 $\times 10^{16}$ molecules cm^{-2}. For June and July 2018 (Figure 6.5), the averaged MAX-DOAS TVCDs were also found comparable to the TROPOMI VCDs over the study area. For all four months, the agreement between both data sets was much better than for SO_2. De Smedt et al. (2021) also reported monthly mean HCHO TVCDs over Lahore for 32 months (April 2018-December 2020). They used a modified version of the TROPOMI level 2 HCHO operational product and reported monthly mean HCHO TVCDs of 1.6×10^{16} molec cm^{-2} for the 20 km^2 area for Lahore. This value was comparable to the monthly mean VCDs (ranging between 5.5×10^{15} and 3.3×10^{16} molecules cm^{-2}) derived from the MAX-DOAS measurements in the current study. Chan et al. (2020) validated HCHO VCDs derived from TROPOMI observations using VCDs derived from MAX-DOAS measurements performed in Munich. They reported a quite good correlation for monthly averages with TROPOMI data underestimating the MAX-DOAS VCDs by around 30%.

Like for SO_2, also for the TROPOMI maps of HCHO, a rather large spatial and temporal variation is found. However, for HCHO, more systematic spatial structures are seen, which also have some similarities with the spatial structures measured by the car MAX-DOAS.

Table 6.3: Tropospheric vertical column densities for HCHO, obtained from ground based and satellite measurements for the 2018-I and 2018-II campaigns.

Month	TROPOMI TVCDs (molec cm^{-2})	Mean MAX-DOAS TVCDs (molec cm^{-2})	MAX-DOAS TVCD Standard Deviation (molec cm^{-2})
February	$3.3 \times 10^{15} – 2.2 \times 10^{16}$	$6.7 \times 10^{15} – 3.3 \times 10^{16}$	$\pm 2.5 \times 10^{13} – \pm 8.3 \times 10^{15}$
March	$4.2 \times 10^{15} – 1.8 \times 10^{16}$	$5.5 \times 10^{15} – 2.7 \times 10^{16}$	$\pm 2.0 \times 10^{13} – \pm 1.0 \times 10^{16}$
June	$1.2 \times 10^{16} – 2.2 \times 10^{16}$	$6.9 \times 10^{14} – 2.5 \times 10^{16}$	$\pm 2.5 \times 10^{12} – \pm 8.8 \times 10^{15}$
July	$8.0 \times 10^{15} – 1.8 \times 10^{16}$	$6.2 \times 10^{15} – 2.8 \times 10^{16}$	$\pm 7.8 \times 10^{12} – \pm 1.2 \times 10^{16}$

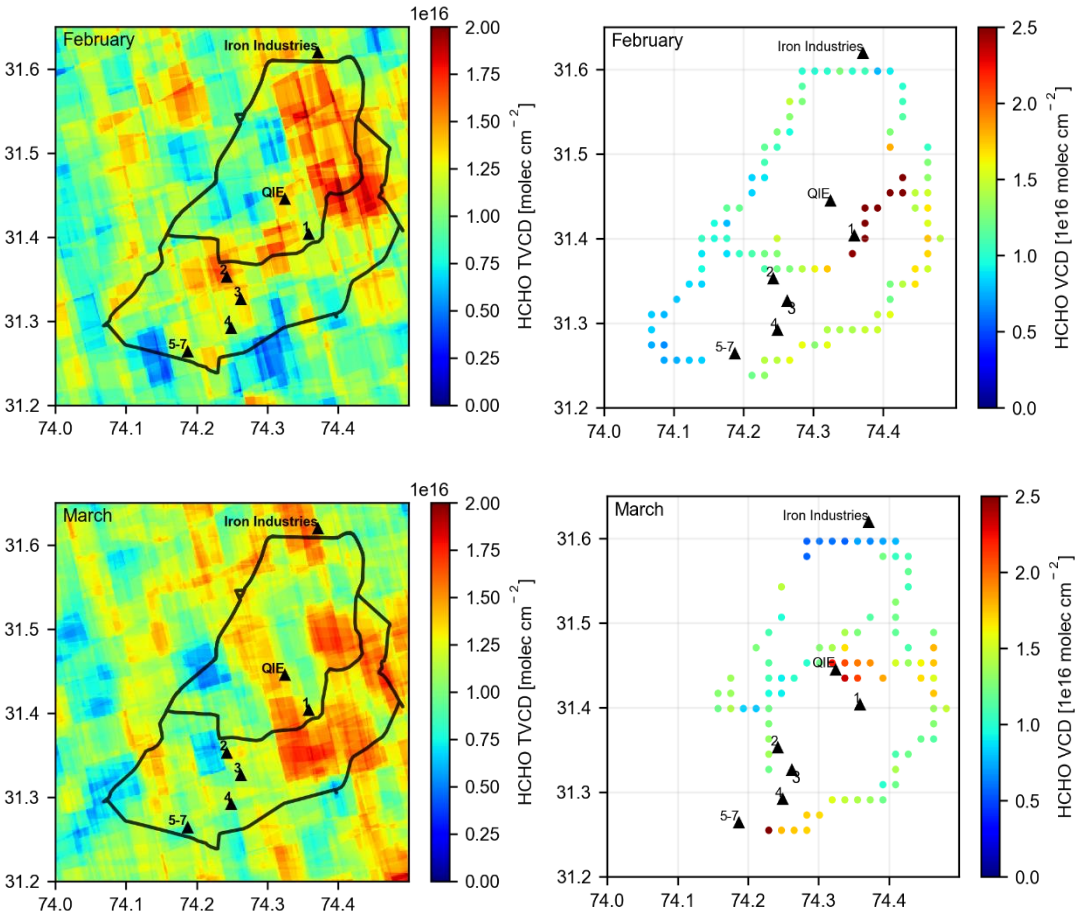

Figure 6.4: Mean HCHO TVCDs retrieved from TROPOMI (left) and car MAX-DOAS (right) observations for February and March 2018. The driving routes adopted during these periods are indicated as black lines in the left images, whereas, power plants and industries are indicated as black triangles.

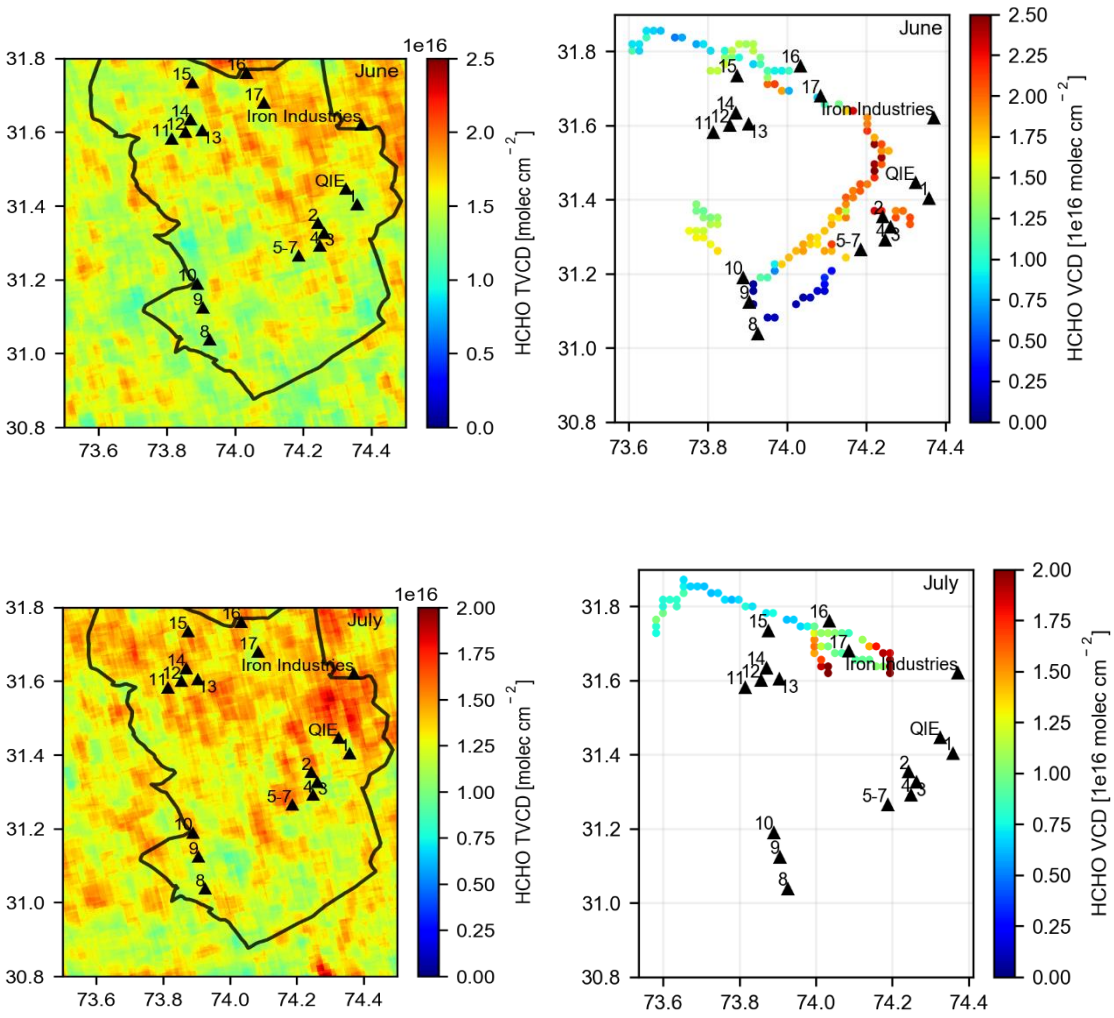

Figure 6.5: Mean HCHO TVCDs retrieved from TROPOMI (left) and car MAX-DOAS (right) observations for June and July, 2018. The approximate boundary of the study area during these periods is indicated as black lines in the left images, whereas, power plants and industries are indicated as black triangles.

6.1.2. Comparison with Regional Model Simulations

An attempt to compare the MAX-DOAS VCDs with a regional model, MECO(n), data was also made. However, it was found that the model failed to show any agreement with the obseravations. After searching for possible reasons for these discrepancies it was found that the model showed already large discrepencies in the meteorological input. Regional model simulations could in principle be improved by nudging the simulated meterology (temperature, specific humidity and u and v components of wind) towards the reanalysis dataset (e.g., ERA5). Unfortunately, it was not possible within the duration to overcome these fundamental defficiencies of the model set up. Thus the model comparison is not included in the main part of this thesis. The details and results obtained from the model simulations can be found in appendix E.

6.2. EMISSION ESTIMATE COMPARISON

In addition to the VCDs, also the estimated emissions for NO_2 and SO_2 were compared to other data sets. In this section, the comparison results of the emission estimates using the car MAX-DOAS measurements from two circles around Lahore are discussed. The NO_x and SO_2 emissions estimated from car MAX DOAS observations, were compared with the EDGAR (Emission Database for Global Atmospheric Research) emission inventory data and TROPOMI satellite data.

NO_x emissions were calculated and compared for the city of Lahore using the satellite data and the emissions from the EDGAR database. Emissions have also been estimated in earlier studies by using satellite observations, e.g., Leue et al. (2001), Beirle et. al. (2011), Shaiganfar (2012), Liu et al. (2016) and Beirle et al. (2019). With the knowledge of the NO_x lifetime (and possibly also wind information), emission estimates for a specific area are possible using satellite data. In the present work, TROPOMI satellite data[8] was spatially integrated to derive the NO_x emissions for Lahore, according to Beirle et al. (2019). The NO_x lifetime was assumed as 4 hours (Beirle et al., 2011) whereas a NO_x partitioning factor of 1.32 (Seinfeld & Pandis, 2006) was used to derive the NO_x emissions. The derived TROPOMI emissions were averaged for the period from December 2017 to October 2018. In Figure 6.6 (left), the NO_x emissions calculated from the three datasets are shown. It can be seen that the emissions from TROPOMI underestimate the emission estimates from MAX DOAS by around 29-65%. This underestimation is consistent with the underestimation of the true NO_2 VCDs by TROPOMI as shown above, and also mentioned in several studies, e.g. in (Beirle et al., 2019). Various other studies e.g., Griffin et al. (2019), Eskes et al. (2019), Lorente et al. (2019) and (Zhao et al., 2020), also reported that TROPOMI tropospheric columns might be low biased, up to 50%, which is most probably related to the errors in the air mass factor and the a-priori profiles. Thus, the

[8] NO_x emissions around Lahore, based on the NO_2 flux, derived from TROPOMI columns and ECMWF winds were provided by Steffen Beirle from the Satellite Remote Sensing Group, MPIC, Mainz.

underestimation of the NO_x emissions by TROPOMI can be explained by the underestimation of the NO_2 VCDs.

For the EDGAR emission estimates, the values were found to be in relatively good agreement with the MAX-DOAS results. For the large circles in summer and small circles in spring the MAX-DOAS emissions were higher by 5 and 16%, respectively, whereas for the large circles performed in spring, the MAX-DOAS emissions were lower than the EDGAR emissions by 13%. The reason for the different behaviors for the two sized circles in spring is not fully understood, but the differences are rather small. It should also be noted that TROPOMI emissions were estimated for an extended time period of ten months, while the EDGAR emissions are available as monthly means whereas, MAX DOAS emissions were calculated for a few days.

For SO_2 the MAX-DOAS emissions were compared only with EDGAR emissions. Due to high uncertainty and noise of the TROPOMI data, as mentioned in section 6.1.1.2, TROPOMI emission estimates were not possible for SO_2. In Figure 6.6 (right), the emissions from both datasets are shown. It can be seen that for the large circles in summer and the small circles in spring, the MAX-DOAS emissions are lower than the EDGAR emissions by 36% and 47%, respectively. The MAX-DOAS emissions for the large circles in spring are higher than the EDGAR emissions by around 12%. One probable reason for the lower EDGAR emissions for the large circles in spring is that the power plants in the south are not included in the EDGAR database (Figure 6.7). The higher EDGAR emissions of the small circles in spring, might be related to a drastic decline in diesel-driven vehicles in Lahore after 2010 as the government introduced policies to phase out diesel vehicles e.g., by converting them to CNG (compressed natural gas) (Government of Pakistan, 2012). All diesel-driven public transport was banned and replaced mainly by compressed natural gas-fueled vehicles (Wikipedia, (Transport in Lahore, 2020)). Moreover, MAX-DOAS measurements were performed during the daytime when all heavy-duty vehicles, including diesel trucks, are not allowed in the city (The News, 2009). This might also partly explain the low MAX-DOAS emissions for the large circles in summer.

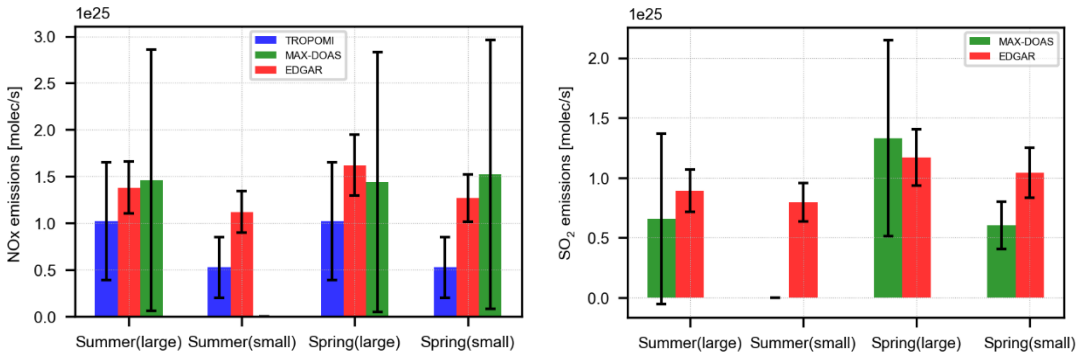

Figure 6.6: NO_x emissions (left) and SO_2 emissions (right) estimated from TROPOMI, MAX-DOAS and the EDGAR emission inventory. The black error bars represent the total uncertainties.

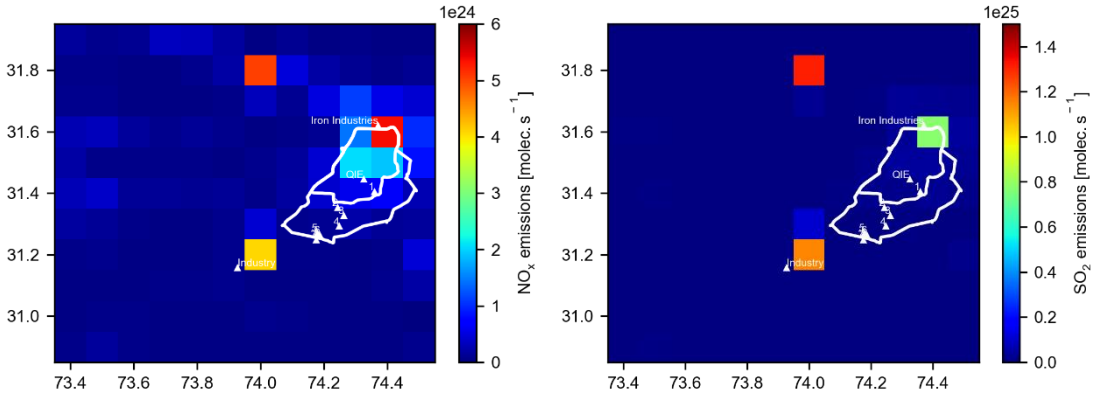

Figure 6.7: Annual average NO_x (left) and SO_2 (right) emissions from EDGAR v4.3.2,(2010). The power plants and other potential emission sources are indicated as white triangles. The white lines represent the routes of the large and small circles around Lahore. Very low emissions, from the cells in the south indicate that the emissions from the power plants are not included in the EDGAR database.

6.3. SUMMARY

This chapter presented a comparison of the MAX-DOAS results performed in 2017 and 2018 to other data sets. Two datasets were used to compare the emissions and trace gas VCDs derived from the MAX-DOAS measurements.

Tropospheric vertical column densities (TVCDs) derived from MAX-DOAS observations were compared with TROPOMI observations. For NO_2 quite good qualitative agreement was found on a satellite pixel basis. The R^2 values for the correlation between the MAX-DOAS and TROPOMI NO_2 VCDs showed values of 0.56 and 0.62 for the 2018-I and 2018-II campaigns, respectively. However, TROPOMI underestimated the ground-based observations by around 40 to 50%, which was found comparable with previous studies. The most probable reason for the underestimation of the TROPOMI data are deviations of the assumed a priori profiles and the true NO_2 profiles in Lahore.

The comparison for the SO_2 and HCHO VCDs could not be performed on a satellite pixel basis because both satellite data sets have large uncertainties and high noise levels (compared to the absolute trace gas VCDs over Lahore). Thus, comparisons for SO_2 and HCHO were performed for monthly means. Probably the TROPOMI data quality for both products were still rather poor at the initial stages of TROPOMI observations. For SO_2 no meaningful spatial patterns could be observed in the monthly means, but still the overall variability of the TROPOMI and MAX-DOAS SO_2 VCDs cover the same magnitude range. As compared to SO_2, the TROPOMI HCHO data showed a better agreement, and some systematic spatial patterns could be observed in the satellite data, which also showed similarities with the MAX-DOAS HCHO data. Especially the HCHO hotspot areas were found quite similar for HCHO above Lahore.

NO_x and SO_2 emissions from the city of Lahore were estimated from the MAX-DOAS observations and compared with the EDGAR emission inventory and emissions derived from the TROPOMI data. The NO_x emissions estimated from TROPOMI were found around 29-65% lower as compared to the emissions estimated from the MAX-DOAS observations. These differences are in good agreement with the comparison results for the NO_2 VCDs indicating that (besides the effect of the wrong satellite NO_2 VCDs) the derived emissions are very consistent. Also, the EDGAR emission estimates for NO_x showed a rather good agreement with the MAX-DOAS emission estimates. For SO_2 the comparison was only performed with the emissions estimated from the EDGAR database. The difference between both the datasets ranged between 12 and 47 %. The main reason assumed for large differences was a shift of the fuel for vehicles in the city from diesel to CNG and the prohibition of large trucks to enter the city during daytime.

7. CONCLUSIONS AND OUTLOOK

This thesis presents measurements of tropospheric column densities of NO_2, SO_2, HCHO and CHOCHO and corresponding emission estimates in and around Lahore, Pakistan by exploiting the ground based remote sensing technique of car MAX-DOAS observations. Simultaneous measurements of the above-mentioned trace gases with extended spatial coverage for the city of Lahore have been performed and analyzed in this thesis for the first time. The glyoxal VCDs measured in this study are the first ever reported results obtained from the car MAX-DOAS observations.

Trace gas emissions and fluxes[9] from the city were obtained by encircling it using the closed integral method (CIM) (Shaiganfar, 2012; Shaiganfar et al., 2017). The difference between the influx and outflux of the gases was calculated by taking into account the wind information.

In this study, a modified approach was introduced to calculate the VCDs derived from the spectra obtained during periods of technical failure of the instrument motor. The VCD retrieval for these periods required a special treatment due to the unavailability of the sequential 90° DSCDs. The modified method was tested for measurements where the motor worked well and the results of the modified method were compared to those of the standard method. Slightly higher uncertainties but overall good consistency with the standard method was found. Thus, also the results of the measurements during periods with motor problems could be used for the further analysis like the measurements without motor problems. The newly developed modified method will also be beneficial for future measurements with limited motor functionalities.

In addition to the motor problems, other technical problems of the instrument like low light intensity and the failure of the temperature stabilization occurred. For these measurements, larger errors in the spectral analysis were found in terms of high RMS (root mean square) values. Fortunately, a special treatment of the spectra during the additional analyses showed that they could still be used after further processing. However, unlike for various previous studies, a straightforward single RMS (root mean square) cut-off value to discard the low-quality data, obtained during these periods was not possible. To tackle this issue, a

[9]for all species the same technique is used, but for HCHO the determined fluxes from the city are not referred to as emissions, because HCHO is to a large part not directly emitted but produced by secondary formation from precursor species.

temporally varying threshold polynomial of fourth-order as a function of SZA was introduced to keep the good quality data at high SZA even with higher RMS values. The threshold polynomial was scaled after visual inspection of the NO_2 RMS values of the individual days. The RMS of the different trace gas analyses was found to be highly correlated, so the same NO_2 polynomial could also be applied to the differential slant column densities (DSCDs) of the other three trace gases (SO_2, HCHO and CHOCHO). The method might also become important for future measurements with similar problems.

At high SZA, a strong interference of O_3 with SO_2 was observed in the 2018-II measurements. This interference resulted in enhanced SO_2 DSCDs at high SZA. Similar problems have been found in earlier studies, and it was not possible to solve this problem by improving the spectral analysis. To deal with the issue, a post-processing method was developed: SO_2 VCDs were calculated using a time dependent $DSCD_{offset}$ which was determined by a polynomial fit to measurements with no SO_2 present. Subtracting this offset from the SO_2 DSCDs obtained from the spectral fit yielded the true atmospheric SO_2 signal. Also, this correction method will be beneficial for future studies.

Another challenge was also addressed in this thesis. Usually, wind data from the operational analysis from the European center for Medium-Range Weather Forecast (ECMWF) are used to determine trace gas fluxes/emissions from the MAX-DOAS measurements. However, for Lahore it turned out that there was a large discrepancy between the model wind data (especially the wind direction) and wind data measured from the aircrafts. Fortunately, the bias in the wind direction was found to be systematic and rather constant, with an average value of around 45°. This bias was addressed by taking the mean of several flux calculations performed by varying the wind direction in steps of 0.1° between the original and modified[10] ECMWF wind data. With this newly developed method, also the uncertainty of the flux calculations caused by uncertainties of the wind fields could be quantified.

With these improvements, it was possible to derive trace gas DSCDs and the corresponding fluxes/emissions for the first time for the city of Lahore. Measurements were conducted in different years and seasons and were analysed in a consistent way. A brief summary of the most important results is presented in the following sections.

7.1. NITROGEN OXIDES (NO_x)

NO_x emissions from Lahore for 17 circles were estimated during winter, spring and summer. The derived average emissions for all circles were found to be around 1.68×10^{25} molecules s^{-1}. The mean area emission fluxes for the populous part of the city were found 3.27×10^{16} molecules s^{-1} m^{-2} whereas the mean emissions for the circles including the peripheral area were found to be $\sim 1.60\times10^{16}$ molecules s^{-1} m^{-2}. These values also indicate that the NO_x sources are more concentrated in the densely populated part of the city.

[10] The modified ECMWF wind data was formulated by adding 45 degrees to the averaged original ECMWF data.

The derived emissions were found comparable with the NO_x emissions from other cities e.g., Houston, USA (~ 3.47 $\times 10^{16}$ molecules s^{-1} m^{-2}) and Shanghai, China (3.05×10^{16} molecules s^{-1} m^{-2}), but found to be quite low when compared to other large cities such as New York, Wuhan and Paris with emissions values of 2.38×10^{17}, 7.28×10^{16} and 2.37-5.69 molecules s^{-1} m^{-2}, respectively (Liu et al., 2016; Shaiganfar, 2012). NO_x emissions from Delhi ($\sim1.07\times10^{16}$ molecules s^{-1} m^{-2}) (Shaiganfar, 2012) were found close to the emissions from Lahore for the large circles.

The highest NO_2 VCDs in all Lahore campaigns were found to be around 9.0×10^{16} molecules cm^{-2}. NO_2 VCDs observed in other cities e.g. Beijing, China showed mean values around 4.6×10^{16} molecules cm^{-2} (Kang et al., 2021), and in Nanjing, China mean VCDs ranging between ~1 and 3.2×10^{16} molecules cm^{-2} (Chan et al., 2019). MAX-DOAS observations performed by Shaiganfar, (2012) around Delhi, India showed NO_2 VCDs $\sim \geq$ 5.0×10^{16} molecules cm^{-2}.

In addition to the measurements performed around Lahore, the 2018-II campaign was executed to estimate the NO_x and SO_2 emissions from the power plants in the region. The estimated NO_x emissions from two conglomerates of power plants were 3.63×10^{24} and 7.88×10^{24} molecules s^{-1}, respectively. These values are to the NO_x emissions from various power plants (in USA and China) ranging between 4.21×10^{24} and 3.82 $\times10^{25}$ molec s^{-1} (Liu et al., 2016).

There was no prominent seasonal variability found for the NO_x emissions from Lahore indicating that major NO_x sources in the city are transport and industrial emissions, which remain rather constant throughout the year. Interestingly, the impact of increased electricity consumption in the summer months has no substantial impact on the NO_x emissions as, during summer, the share of electricity generated from hydropower is also increased.

Another important result showing the advantages of mobile measurements was the determination of the spatial distribution of NO_x DSCDs, which helped to point out the major NO_2 sources along the driving routes. Spatial information was not only obtained in and around the city of Lahore, but also for other cities and the corresponding connecting roads. The most important results are:

- Major NO_x sources in Lahore are transport and industries located in the urban center. The per unit area emissions for spring for the urban center were calculated as 3.52 $\times10^{16}$ molecules s^{-1} m^{-2}, whereas far lower value (1.70 $\times10^{15}$ molecules s^{-1} m^{-2}) was found for the peripheral area.
- Along the peripheral part of the city in the south, power plants and industries were identified as the predominant NO_x emitters.
- The less industrialized and less populated southern part of the Punjab province showed substantially lower levels of NO_2.

NO_2 VCDs and NO_x emissions derived from the car MAX-DOAS observations during the 2018-I and 2018-II campaigns were also compared with TROPOMI observations and the

EDGAR emission inventory. The most important findings from these comparisons are given below.

Reasonably good agreement was observed for the tropospheric vertical densities (TVCDs) observed from ground-based and TROPOMI satellite observations on satellite pixel basis. The coefficients of determination (R^2) for the two datasets were found as 0.56 and 0.62 for the 2018-I and 2018-II campaigns, respectively, indicating an underestimation of ~ 40 to 50% of the TROPOMI TVCDs. This systematic difference is consistent with other studies and is most probably caused by imperfect a priori profile assumptions in the satellite retrieval.

Also the NO_x emissions from the city of Lahore estimated from the MAX-DOAS observations were compared with the EDGAR emission inventory and the emissions derived from the TROPOMI data.

Like for the NO_2 VCDs, also the NO_x emissions from TROPOMI were found lower than the emissions estimated from the MAX-DOAS observations by about 30-65% lower. These strong discrepancies indicate the limitations of the current TROPOMI satellite data for the determination of trace gas emissions.

The comparison between the NO_x emissions derived from MAX-DOAS observations and EDGAR data showed a very good agreement. For the large circles in summer and the small circles in spring, the MAX-DOAS emissions were found to be slightly higher by 5 to 16%, respectively, whereas for the large circles performed in spring, the MAX-DOAS emissions were slightly lower than the EDGAR emissions by 13%. This good agreement confirms both the EDGAR emission inventory for Lahore and the MAX-DOAS observations and analysis.

7.2. SULFUR DIOXIDE (SO_2)

The SO_2 emissions from Lahore for 15 circles performed during summer 2017 and spring 2018 were calculated; they ranged between 2.9 $\times 10^{24}$ and 3.0 $\times 10^{25}$ molecules s^{-1} for the small and large circles.

The highest SO_2 VCDs found around Lahore were ~ 2 $\times 10^{17}$ molecules cm^{-2}. In other large cities e.g. Hefei, Nanjing and Shanghai (China), the daily mean SO_2 VCDs ranged between ~ 2 and 3 $\times 10^{16}$ molecules cm^{-2} (Tian et al., 2018) and the monthly mean SO_2 VCDs in Xianghe, China, were found between 2 and 8 $\times 10^{16}$ molecules cm^{-2}. The average per unit area SO_2 emissions for large circles performed in summer and spring were found as 7.21 $\times 10^{15}$ and 1.48 $\times 10^{16}$ molecules s^{-1} m^{-2}, respectively, whereas for the small circles performed in spring, the averaged emissions were estimated as 1.40 $\times 10^{16}$ molec s^{-1} m^{-2}.

Like for NO_x, the SO_2 emissions from the power plants in the region were also estimated for one day. The estimated SO_2 emissions from two conglomerates of power plants were 1.82×10^{24} and 1.27×10^{25} molecules s^{-1}, respectively.

The emissions in summer were found approximately half of the emissions in spring. The change of fuel from natural gas to coal and residual fuel oil in summer and spring was identified as the most probable reason for higher emissions in the colder months.

The spatial distribution results helped to identify the major SO_2 sources along the driving routes. Iron industries in the north, power plants and industries in the south and diesel generators for backup energy sources in the southwest are the prominent stationary sources of SO_2 in the study area. Furthermore, heavy-duty diesel vehicles on the N5 highway and the M2 motorway are the prominent mobile SO_2 sources in Lahore. A clear seasonal variability was observed for SO_2 as mean emission values for spring were found around two times greater as compared to the emissions in summer. The reason behind the higher values in the colder months are probably related to the use of coal, diesel and residual fuel oil for standby power generation in industries and commercial hubs.

Also, the SO_2 VCDs and emissions were compared with TROPOMI satellite data and the EDGAR emission inventory. The satellite comparison for SO_2 was not performed on an individual satellite pixel basis because the satellite results are close to or below the detection limit. Therefore, averages of several days were compared. However, in spite of the comparison of averaged values, no similar spatial patterns could be identified in both data sets, probably because of the rather low signal to noise ratio for the satellite data. Nevertheless, similar magnitude ranges were observed for the VCDs from both data sets over Lahore.

The SO_2 emissions derived from the car MAX-DOAS observation were found to be lower than those of the EDGAR data base by 36% and 47% for the large circles in summer and the small circles in spring, respectively. The MAX-DOAS emissions for the large circles in spring were found around 12% higher as compared to the EDGAR emissions. Here it should be noted that the EDGAR database used for the comparison was for year 2010. One probable reason for the lower EDGAR emissions for the large circles in spring is that the power plants in the south are not included in the EDGAR database. The higher EDGAR emissions of the small circles in spring, might be linked to a ban of the entry of large trucks in the city at night and the shift of fuel for vehicles in the city from diesel to CNG (compressed natural gas) after 2010.

7.3. FORMALDEHYDE (HCHO)

For formaldehyde fluxes for 15 circles were derived from the car MAX-DOAS measurements. The fluxes were not referred to as emissions (like for NO_x and SO_2), because a major part of HCHO is formed as a secondary product by the oxidation of its precursors and not emitted directly.

The maximum HCHO VCDs measured around Lahore were ~ 8.35×10^{16} molecules cm^{-2}, in a similar range as HCHO values observed in other polluted regions, like e.g. the averaged HCHO in the Yangtze River Delta, China, (YRD) with average values around 4.0×10^{16} molecules cm^{-2} (Tian et al., 2018). The mean HCHO fluxes for the large circles in summer

and spring were found to be $6.72\times10^{24} \pm 2.97\times10^{24}$ and $6.82\times10^{24} \pm 2.76\times10^{24}$ molec s^{-1}, respectively. For the small circles performed in spring, the mean fluxes were calculated as $5.23\times10^{24} \pm 1.13\times10^{24}$ molecules s^{-1}.

The above-mentioned figures indicate that HCHO lacks any seasonality in the study area. Therefore, anthropogenic sources like vehicular and industrial emissions were assumed as the major sources of HCHO in the city, as they stay quite consistent throughout the year.

The mean flux per unit area calculated for the smaller circles (1.21×10^{16} molec s^{-1} m^{-2}) performed in spring were found to be higher than the per unit area flux for the large circles (7.56×10^{15} molecules s^{-1} m^{-2}). The per unit area flux of the additional area from the larger circle was found to be 3.38×10^{15} molecules s^{-1} m^{-2}. From these figures, it can be concluded that the populous part of the city dominates the total emissions of the HCHO precursor species.

Moreover, the spatial distribution results helped in identifying different stationary sources of formaldehyde or its precursor species along the driving routes. The major sources included a waste dumping site and metal industries in the north and crop residue burning activities in the east. High HCHO concentrations were also observed in the vicinity of industries like paper mills and paint industries. Also the range of the HCHO VCDs of both data sets was found to be similar.

No prominent HCHO enhancements were observed for the measurements performed around the power plant areas.

Like SO_2, the daily comparison on a satellite pixel basis was not possible for HCHO because the satellite HCHO VCDs are close to or below the detection limit. Thus, the averaged MAX-DOAS and TROPOMI VCD values were compared and showed partly similar spatial patterns (especially the locations of the highest values were similar) over the study area.

7.4. GLYOXAL (CHOCHO)

In the current study, the first ever car MAX-DOAS observations of glyoxal column densities were performed. The spatial distribution patterns of the trace gas were observed during the 2017 and 2018 campaigns. As compared to NO_2, glyoxal is a weak absorber and thus for the other campaigns performed in 2015 with the mini MAX-DOAS instruments, retrieval of CHOCHO VCDs was not possible due to the worse signal to noise ratio of the min MAX-DOAS instrument. Moreover, also no flux estimation for the glyoxal was possible, as in addition to the rather large uncertainties of the retrieved VCDs CHOCHO has also a rather short lifetime it is not predominantly emitted directly.

In the current study, the highest glyoxal VCDs ($\sim2.85\times10^{15}$ molecules cm^{-2}) around Lahore were found during the summer campaign. Spatial distribution results revealed that in general glyoxal VCDs higher than 1.0×10^{15} molecules cm^{-2} were mainly found during the summer measurement period. Overall the glyoxal VCDs around Lahore were found to be similar to glyoxal VCDs at other polluted regions like e.g. Beijing, China, with averaged maximum VCDs of 2.18×10^{15} molecules cm^{-2} (Javed et al., 2019).

Vehicular emissions, gas stations and steel industries were identified as the major sources of glyoxal or its precursors in the study area.

Like HCHO, low CHOCHO VCDs were also observed for the observations performed around the power plants during the 2018-II campaign.

7.5. CORRELATION BETWEEN THE TRACE GASES

From the car MAX-DOAS measurements the spatio-temporal patterns of the different trace gases were obtained during several campaigns. From the comparison of the observed patterns for the different trace gases, information about the responsible emission sources and/or atmospheric reactions can be obtained.

To study the interrelationship between all observed trace species, correlation analyses were performed for all possible trace gas pairs. These analyses indicated strong linear relationships between NO_2 and SO_2 (mostly during spring) as well as between HCHO and CHOCHO (mostly during summer) with correlation of coefficients (R) of 0.74 and 0.85, respectively. Much weaker correlations with R values less than 0.5 were observed for all other trace gas pairs. From these values it can be inferred that NO_x and SO_2 as well as HCHO and CHOCHO have similar emission sources in the study area. For NO_2 and SO_2, the similar sources are most probably fossil fuel combustion in industries, power plants and vehicles.

7.6. STRENGTHS

This study demonstrated the importance of ground-based monitoring. The most important advantages of the car MAX-DOAS method are:

- Ground-based monitoring has more liberty in terms of temporal resolution, as satellite observations are restricted usually to one (or less) per day. Moreover, for tropospheric studies, clouds are not as crucial for ground-based measurements as they are for satellite observations.
- The spatial resolution of car MAX-DOAS observations is much better than that of the satellite observations.
- The uncertainties of the emission estimates from car MAX-DOAS observations are smaller than for other measurement techniques (e.g., satellite observations). Thus, car MAX-DOAS measurements are an ideal tool to improve existing bottom-up inventories like EDGAR. This is especially important for developing countries as emission sources and abatement technologies are not always well documented.
- Car MAX-DOAS measurements are an ideal tool for the validation of satellite observations and model simulations because they cover the spatial and temporal dimension.
- This detailed study helped to understand the air quality of a megacity of a developing country in general and Lahore’s air quality in specific.

- The study may also provide policymakers with insights into the city's pollution sources and assist them to devise better air pollution reduction policies.
- This study provided detailed information about the status of the pollution control measures and energy infrastructure for the city of Lahore.

7.7. LIMITATIONS AND RECOMMENDATIONS

This study encountered a few limitations, some of which could be successfully addressed during the thesis. However, other limitations were more fundamental and corresponding improvements should be addressed in future studies. A brief discussion of the most important aspects which served as constraints to this study and suggestions for future improvements are given.

- The closed integral method technique for the determination of emissions used in this thesis is largely dependent upon stable wind conditions. During conditions of calm wind speeds and variable wind directions, it is not possible to estimate the trace gas emissions. In this study, around 2/3 of the observations got rejected for emission estimations due to the unsuitable wind conditions during the measurement period. For future studies it is recommended to take detailed weather forecasts into account for the planning of the car MAX-DOAS measurements. Measurements should only be performed for suitable wind conditions. Moreover, wind observations from weather stations should also be considered. If possible, the deployment of low cost weather sensors in the study area can also be done to get more reliable and readily accessible wind information.
- Simultaneous car MAX-DOAS measurements with two or more instruments may be performed in future studies to better cover the temporal variability and to better understand the trace gas emissions and their sources for large cities like Lahore.
- It is also recommended to perform simultaneous stationary measurements in addition to the mobile MAX-DOAS measurements. This would aid in understanding the dynamics of the tropospheric chemistry of the study area in more detail by providing the information of the vertical distribution of the trace species.

7.8. OUTLOOK

The current study successfully presented detailed information about the ambient air quality status of Lahore, Pakistan and adjoining areas. As a result of the limited temporal coverage and other constraints it was not possible to investigate several aspects in detail. Therefore, to further strengthen and elaborate the current knowledge, the following studies should be planned in the future.

- Satellite comparisons with other satellite sensors in addition to TROPOMI should be performed.
- A detailed comparison with the WRF-Chem regional model (Weather Research and Forecasting (WRF) model coupled with Chemistry) should be performed.

- Long term stationary measurements in Lahore should be performed to retrieve consistent time series of profiles of trace gases and aerosols.
- Results from the stationary measurements may also be compared with in-situ instruments. Further, car MAX-DOAS observations in all seasons may be performed in the future to study the seasonal variability in more detail. These measurements will help to better understand the seasonal trends of the trace gases.

APPENDIX

APPENDIX A

Fluxes calculated for different assumed wind directions for NO_2, SO_2 and HCHO are presented here.

A.1 NO_2 Fluxes

Fluxes calculated for different assumed wind directions for NO_2. The dashed vertical black lines indicate the averaged original ECMWF and shifted ECMWF wind directions, respectively.

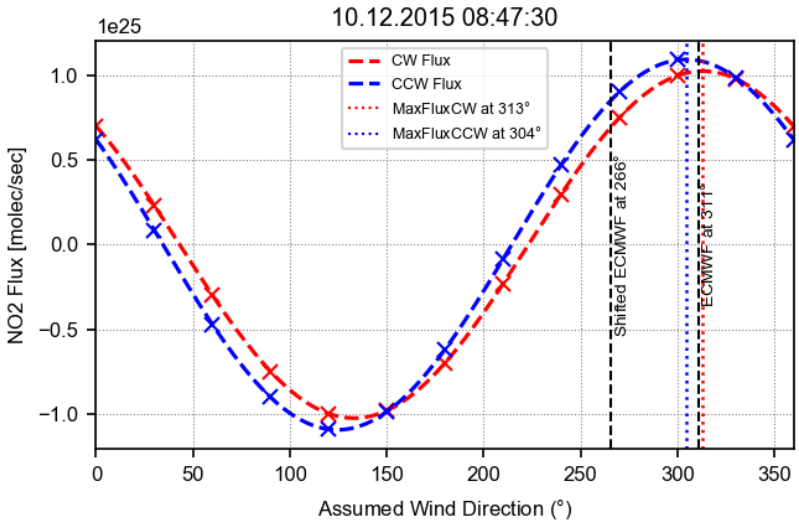

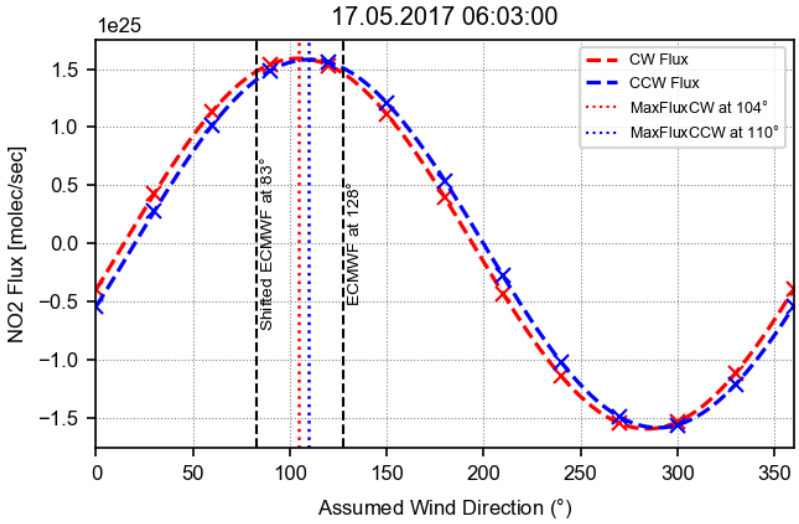

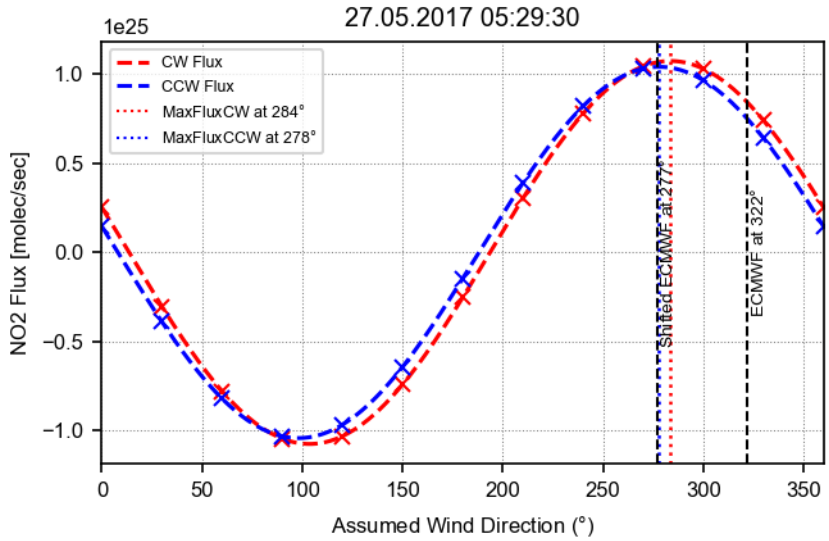
27.05.2017 05:29:30
1e25
CW Flux
CCW Flux
MaxFluxCW at 284°
MaxFluxCCW at 278°
Shifted ECMWF at 277°
ECMWF at 322°
NO2 Flux [molec/sec]
Assumed Wind Direction (°)

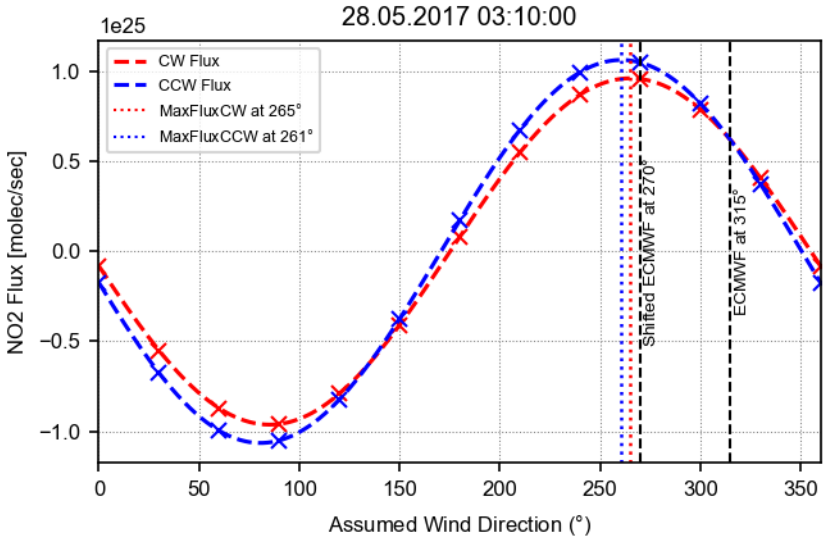
28.05.2017 03:10:00
1e25
CW Flux
CCW Flux
MaxFluxCW at 265°
MaxFluxCCW at 261°
Shifted ECMWF at 270°
ECMWF at 315°
NO2 Flux [molec/sec]
Assumed Wind Direction (°)

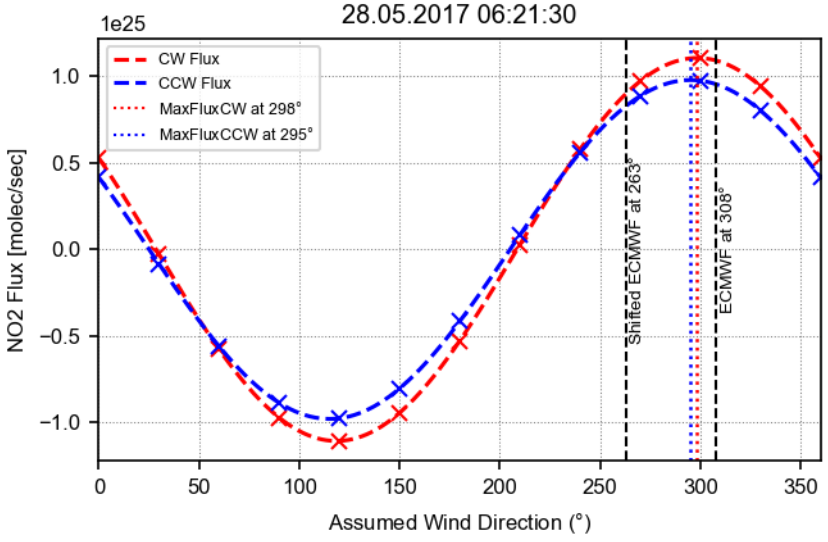
28.05.2017 06:21:30
1e25
CW Flux
CCW Flux
MaxFluxCW at 298°
MaxFluxCCW at 295°
Shifted ECMWF at 263°
ECMWF at 308°
NO2 Flux [molec/sec]
Assumed Wind Direction (°)

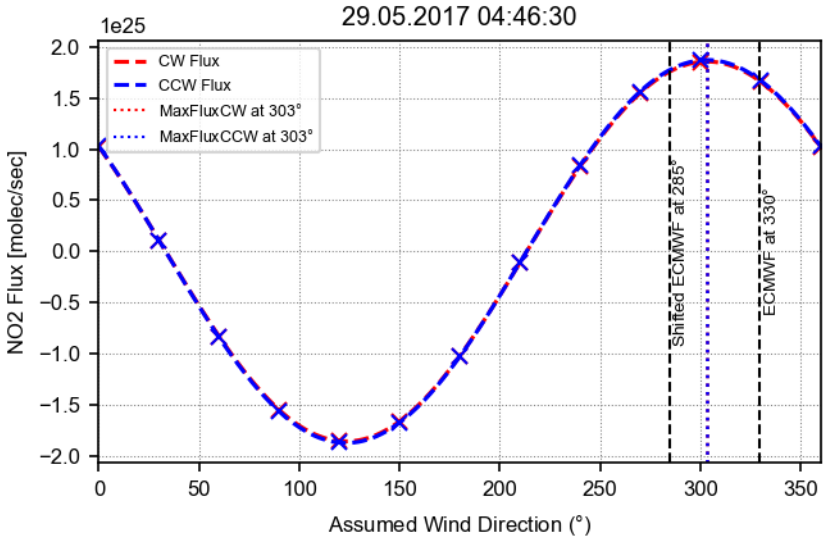
29.05.2017 04:46:30
1e25
CW Flux
CCW Flux
MaxFluxCW at 303°
MaxFluxCCW at 303°
Shifted ECMWF at 285°
ECMWF at 330°
NO2 Flux [molec/sec]
Assumed Wind Direction (°)

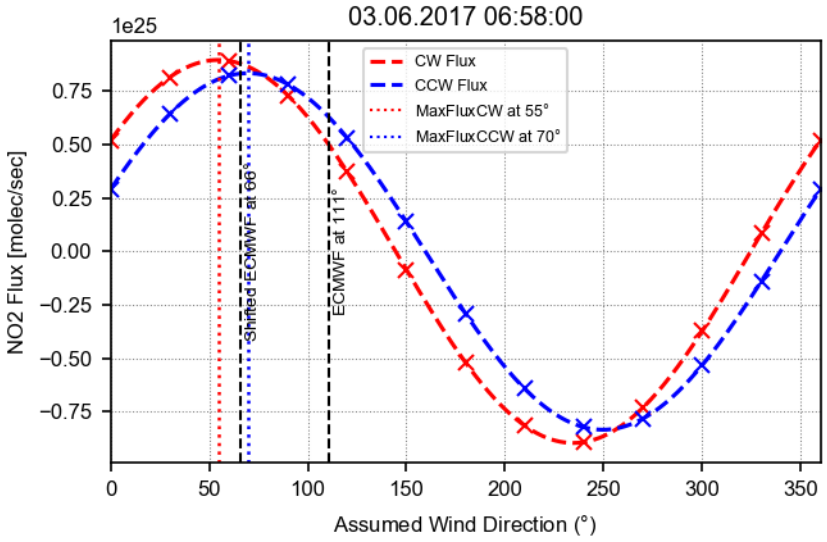
03.06.2017 06:58:00
1e25
CW Flux
CCW Flux
MaxFluxCW at 55°
MaxFluxCCW at 70°
Shifted ECMWF at 66°
ECMWF at 111°
NO2 Flux [molec/sec]
Assumed Wind Direction (°)

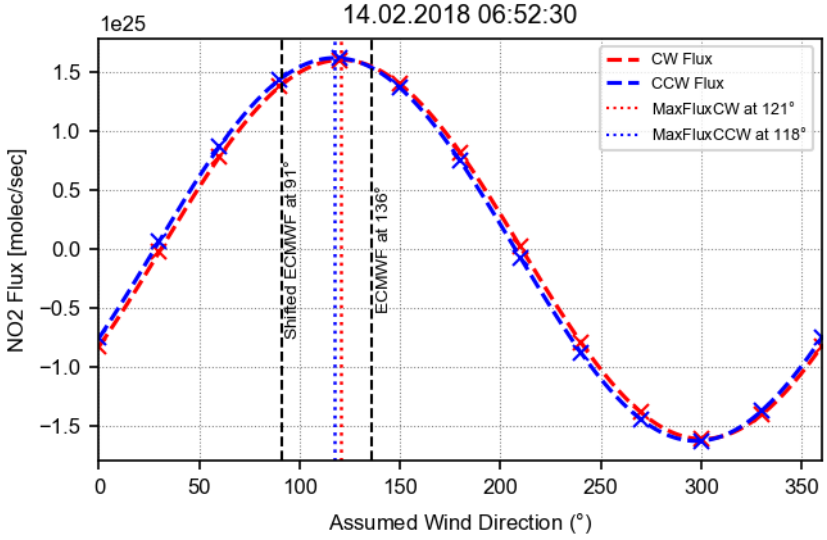
14.02.2018 06:52:30
1e25
CW Flux
CCW Flux
MaxFluxCW at 121°
MaxFluxCCW at 118°
Shifted ECMWF at 91°
ECMWF at 136°
NO2 Flux [molec/sec]
Assumed Wind Direction (°)

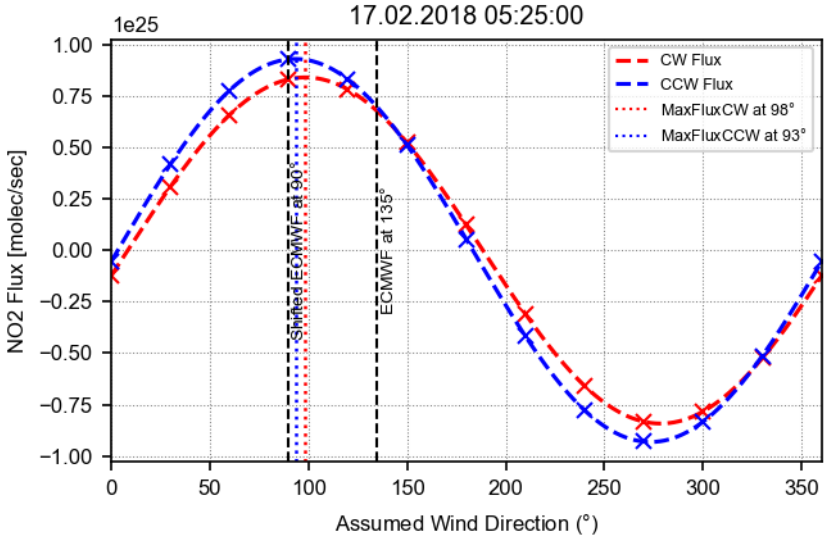
17.02.2018 05:25:00
1e25
NO2 Flux [molec/sec]
Assumed Wind Direction (°)
CW Flux
CCW Flux
MaxFluxCW at 98°
MaxFluxCCW at 93°
Shifted ECMWF at 90°
ECMWF at 135°

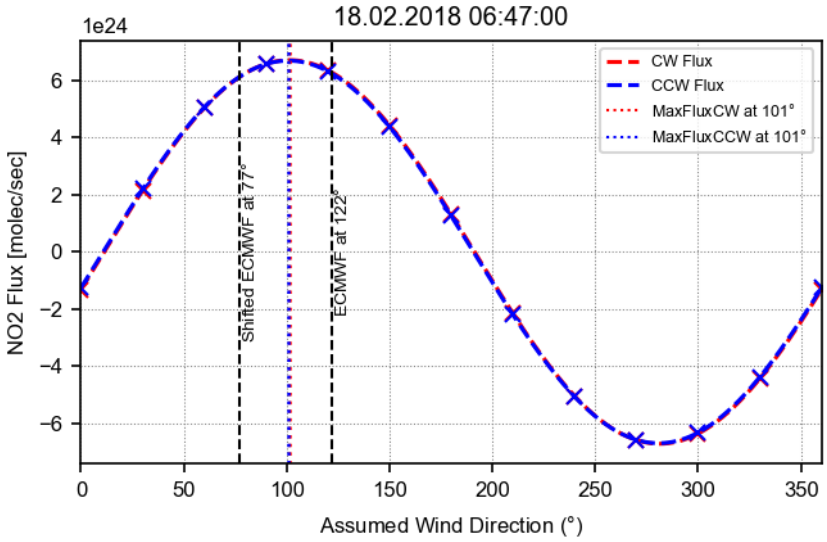
18.02.2018 06:47:00
1e24
NO2 Flux [molec/sec]
Assumed Wind Direction (°)
CW Flux
CCW Flux
MaxFluxCW at 101°
MaxFluxCCW at 101°
Shifted ECMWF at 77°
ECMWF at 122°

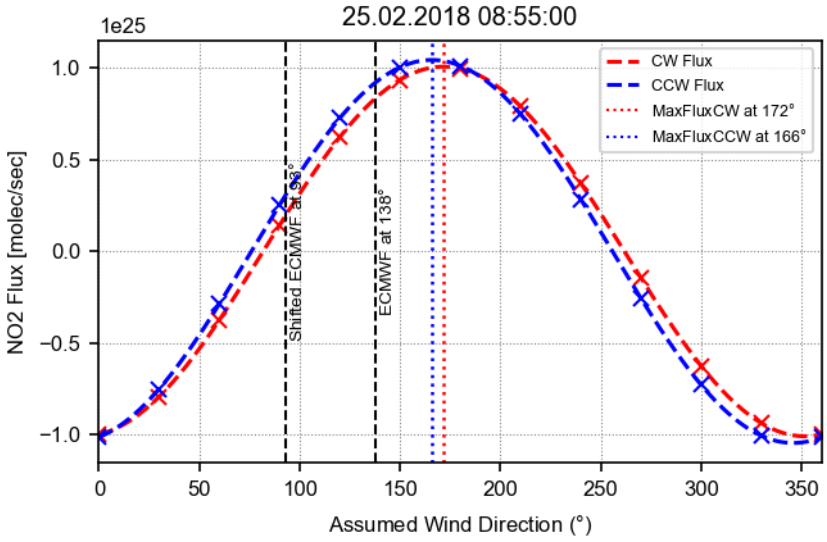
25.02.2018 08:55:00
1e25
NO2 Flux [molec/sec]
Assumed Wind Direction (°)
CW Flux
CCW Flux
MaxFluxCW at 172°
MaxFluxCCW at 166°
Shifted ECMWF at 93°
ECMWF at 138°

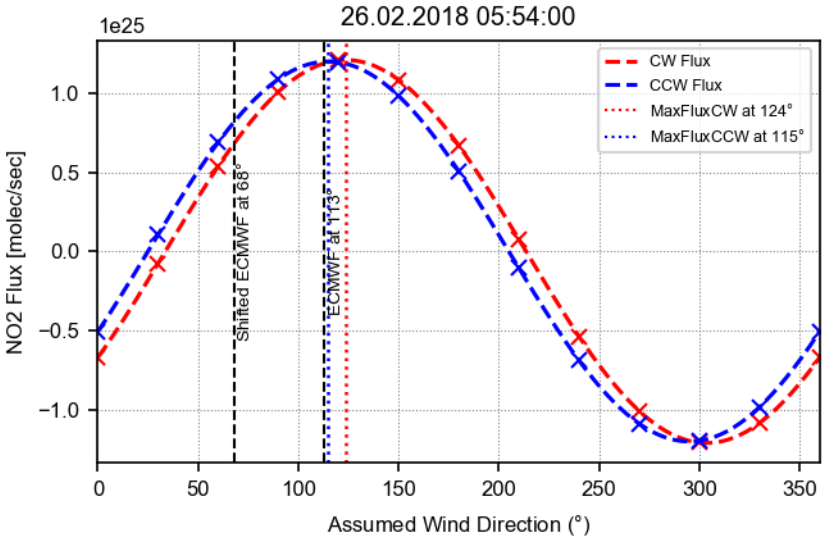
26.02.2018 05:54:00
1e25
CW Flux
CCW Flux
MaxFluxCW at 124°
MaxFluxCCW at 115°
Shifted ECMWF at 68°
ECMWF at 113°
NO2 Flux [molec/sec]
Assumed Wind Direction (°)

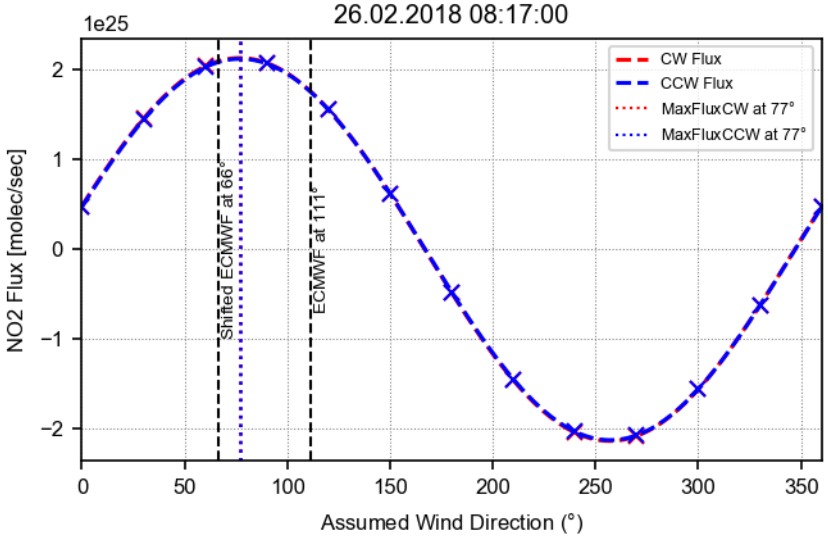
26.02.2018 08:17:00
1e25
CW Flux
CCW Flux
MaxFluxCW at 77°
MaxFluxCCW at 77°
Shifted ECMWF at 66°
ECMWF at 111°
NO2 Flux [molec/sec]
Assumed Wind Direction (°)

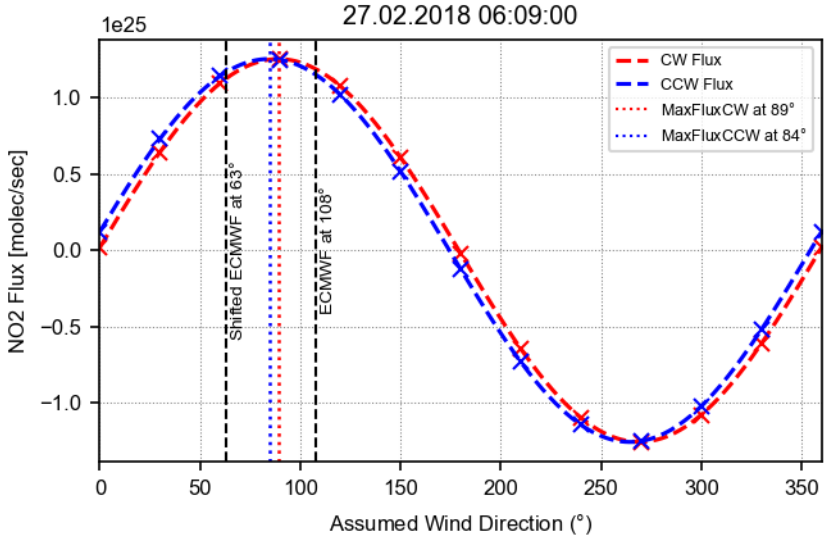
27.02.2018 06:09:00
1e25
CW Flux
CCW Flux
MaxFluxCW at 89°
MaxFluxCCW at 84°
Shifted ECMWF at 63°
ECMWF at 108°
NO2 Flux [molec/sec]
Assumed Wind Direction (°)

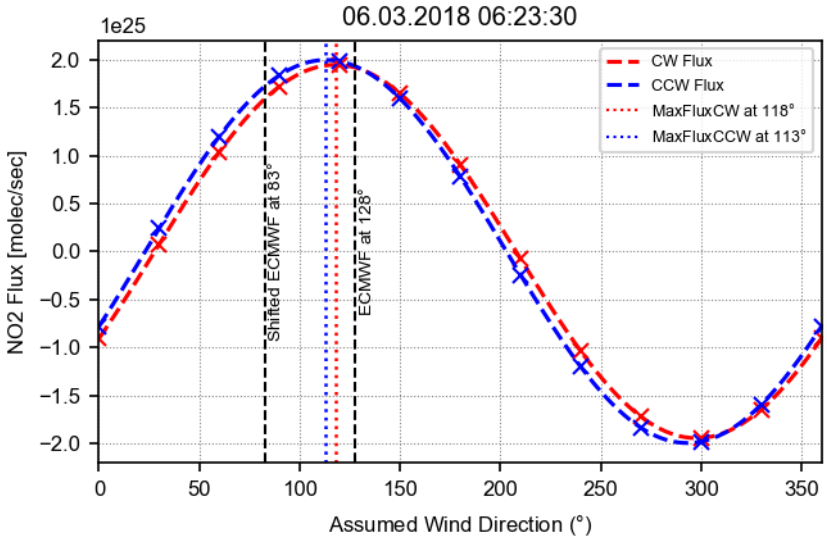
06.03.2018 06:23:30
1e25
NO2 Flux [molec/sec]
Assumed Wind Direction (°)
CW Flux
CCW Flux
MaxFluxCW at 118°
MaxFluxCCW at 113°
Shifted ECMWF at 83°
ECMWF at 128°

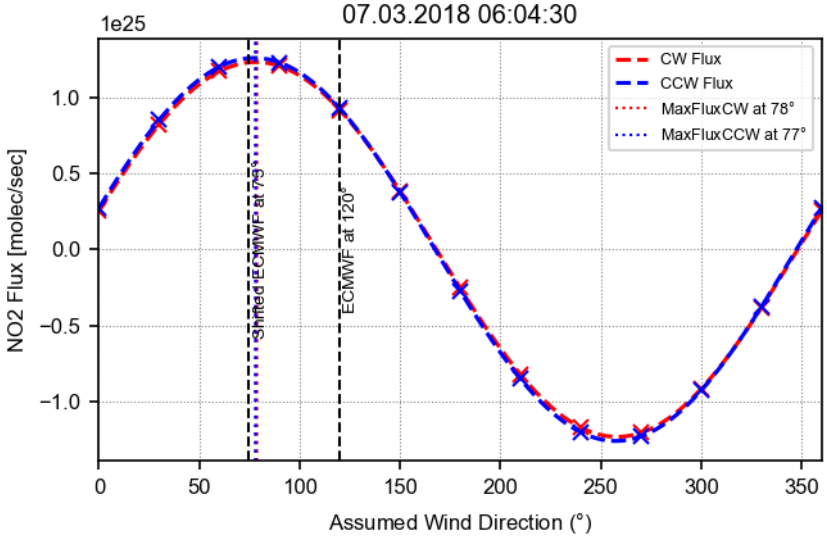
07.03.2018 06:04:30
1e25
NO2 Flux [molec/sec]
Assumed Wind Direction (°)
CW Flux
CCW Flux
MaxFluxCW at 78°
MaxFluxCCW at 77°
Shifted ECMWF at 75°
ECMWF at 120°

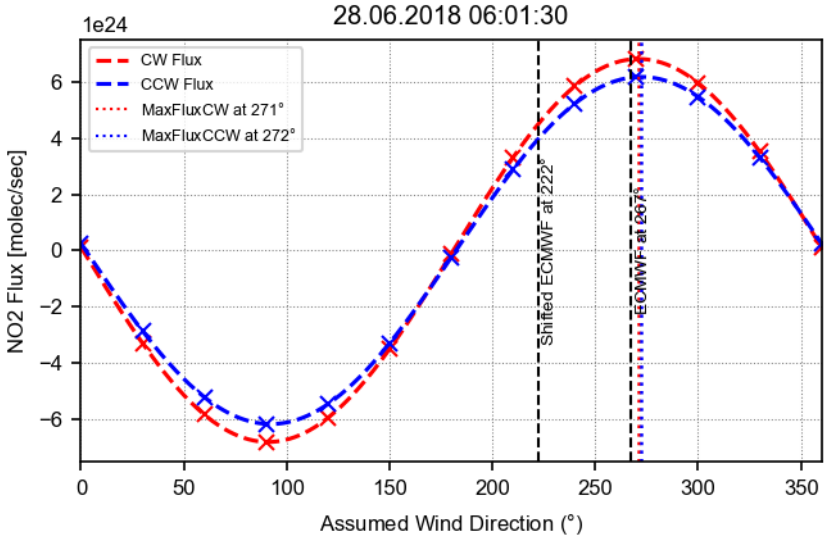
28.06.2018 06:01:30
1e24
NO2 Flux [molec/sec]
Assumed Wind Direction (°)
CW Flux
CCW Flux
MaxFluxCW at 271°
MaxFluxCCW at 272°
Shifted ECMWF at 222°
ECMWF at 267°

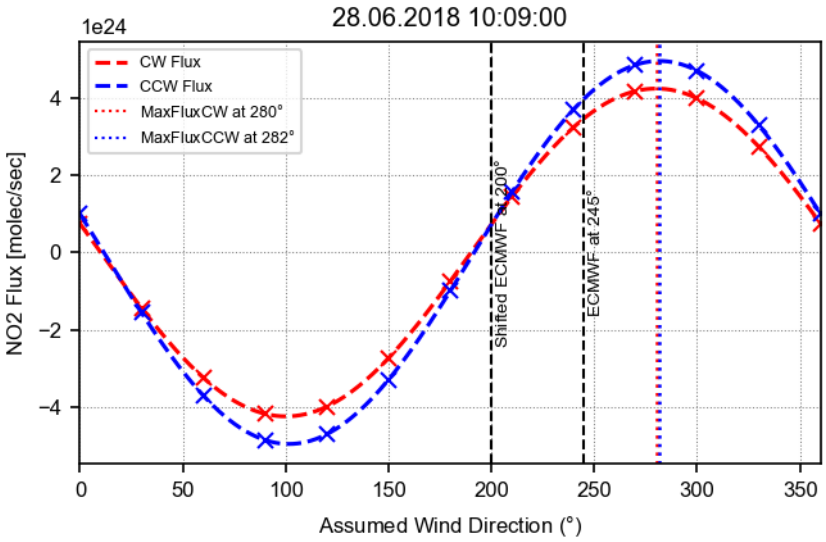
28.06.2018 10:09:00
1e24
CW Flux
CCW Flux
MaxFluxCW at 280°
MaxFluxCCW at 282°
NO2 Flux [molec/sec]
Assumed Wind Direction (°)
Shifted ECMWF at 200°
ECMWF at 245°
4
2
0
−2
−4
0
50
100
150
200
250
300
350

A.2 SO_2 Fluxes

Fluxes calculated for different assumed wind directions for SO_2. The dashed vertical black lines indicate the averaged original ECMWF and shifted ECMWF wind directions, respectively.

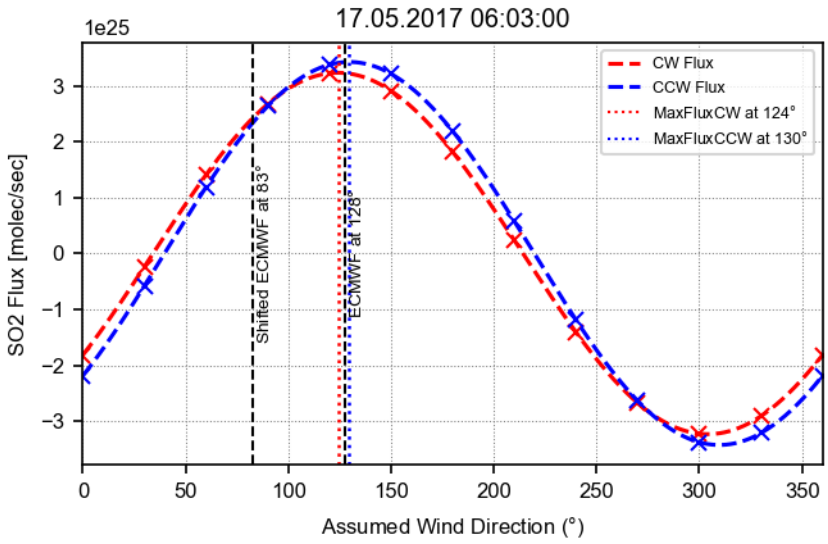

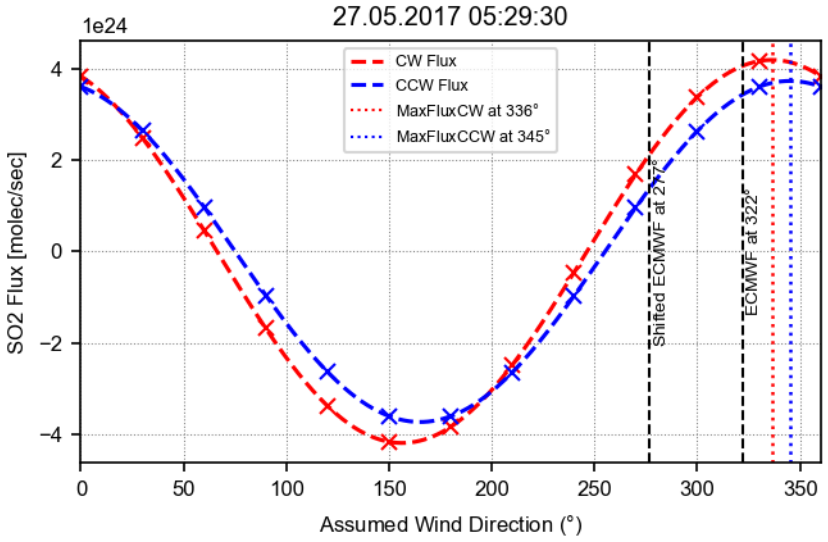

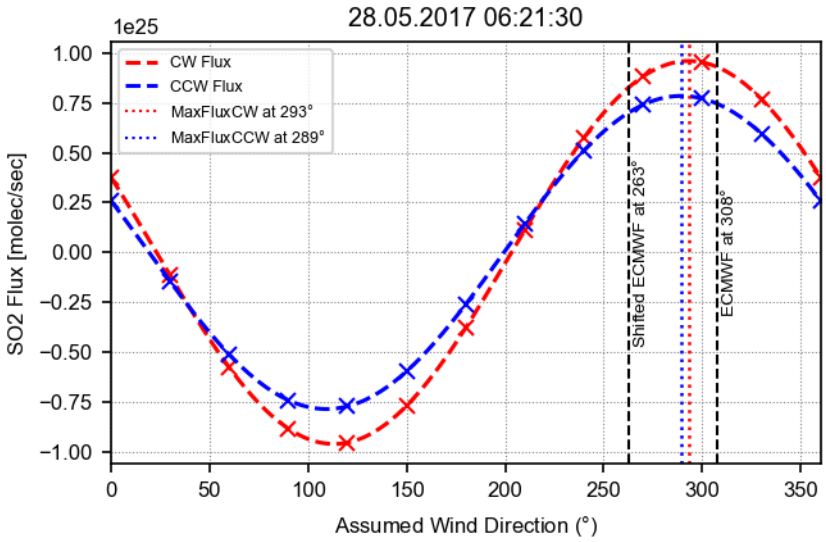
28.05.2017 06:21:30
1e25
CW Flux
CCW Flux
MaxFluxCW at 293°
MaxFluxCCW at 289°
Shifted ECMWF at 263°
ECMWF at 308°
SO2 Flux [molec/sec]
Assumed Wind Direction (°)

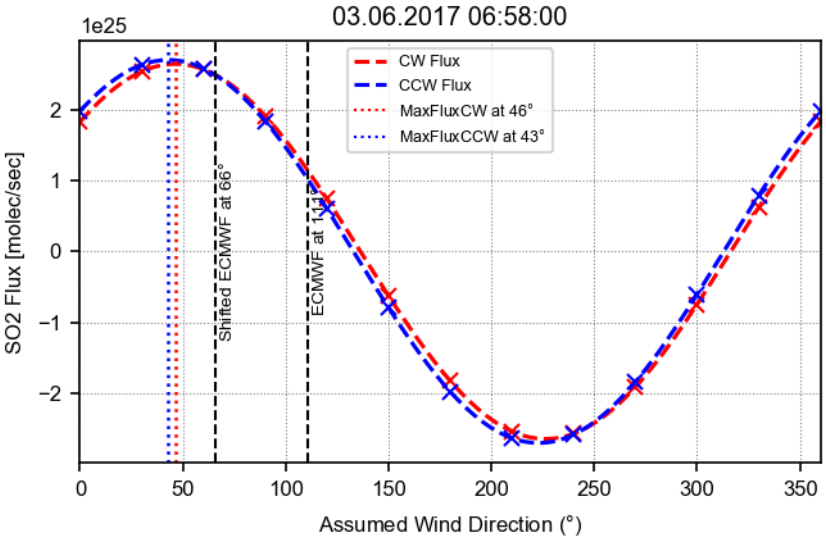
03.06.2017 06:58:00
1e25
CW Flux
CCW Flux
MaxFluxCW at 46°
MaxFluxCCW at 43°
Shifted ECMWF at 66°
ECMWF at 111°
SO2 Flux [molec/sec]
Assumed Wind Direction (°)

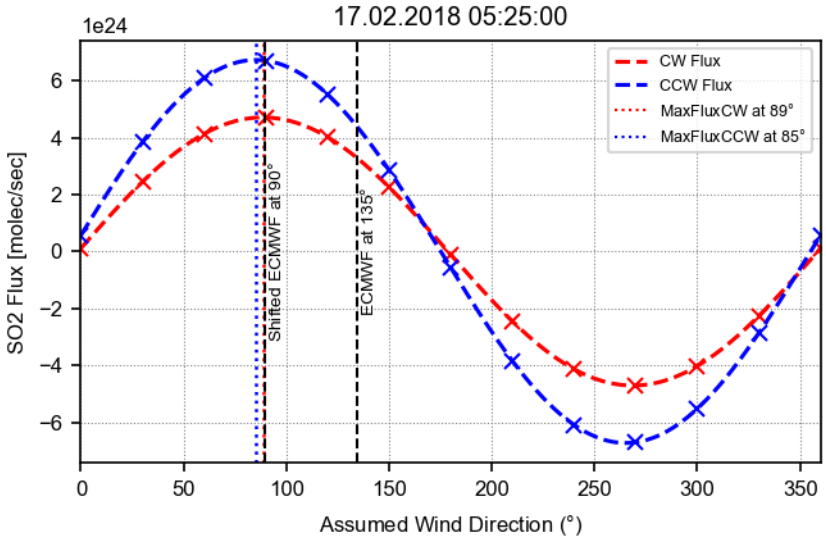
17.02.2018 05:25:00
1e24
CW Flux
CCW Flux
MaxFluxCW at 89°
MaxFluxCCW at 85°
Shifted ECMWF at 90°
ECMWF at 135°
SO2 Flux [molec/sec]
Assumed Wind Direction (°)

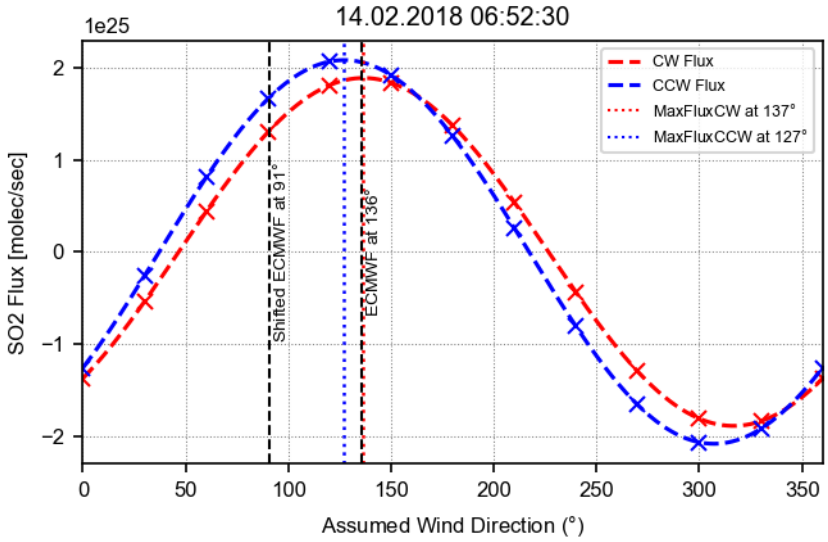
14.02.2018 06:52:30
1e25
CW Flux
CCW Flux
MaxFluxCW at 137°
MaxFluxCCW at 127°
Shifted ECMWF at 91°
ECMWF at 136°
SO2 Flux [molec/sec]
Assumed Wind Direction (°)

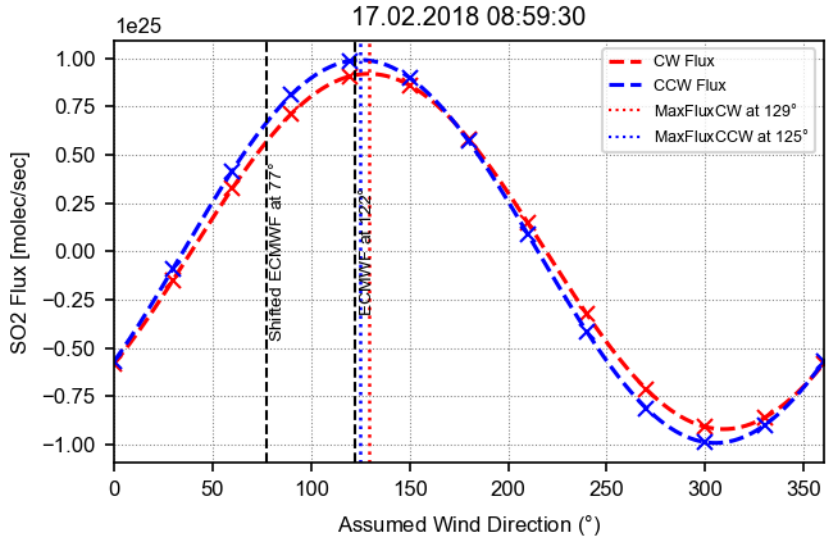
17.02.2018 08:59:30
1e25
CW Flux
CCW Flux
MaxFluxCW at 129°
MaxFluxCCW at 125°
Shifted ECMWF at 77°
ECMWF at 122°
SO2 Flux [molec/sec]
Assumed Wind Direction (°)

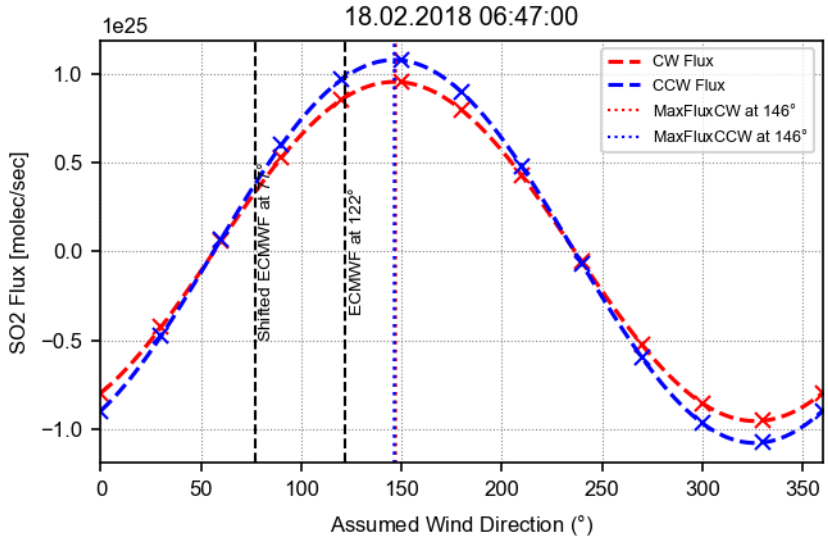
18.02.2018 06:47:00
1e25
CW Flux
CCW Flux
MaxFluxCW at 146°
MaxFluxCCW at 146°
Shifted ECMWF at 77°
ECMWF at 122°
SO2 Flux [molec/sec]
Assumed Wind Direction (°)

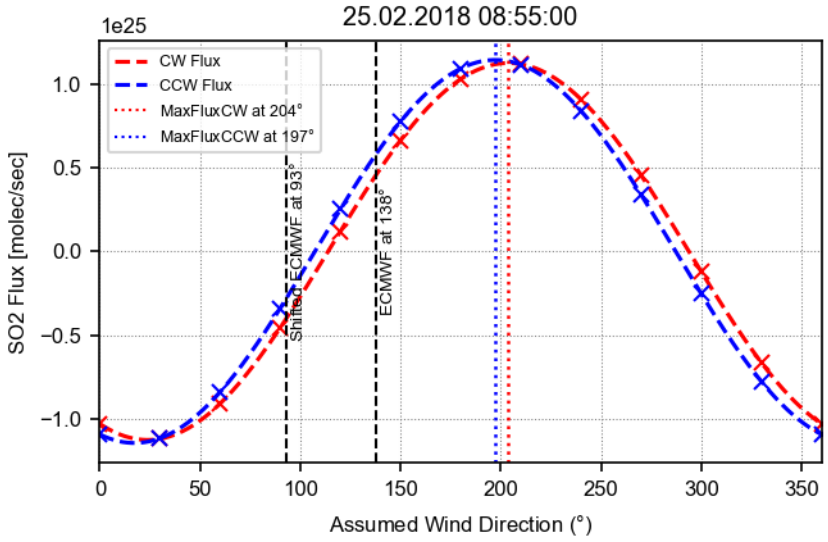
25.02.2018 08:55:00
1e25
CW Flux
CCW Flux
MaxFluxCW at 204°
MaxFluxCCW at 197°
Shifted ECMWF at 93°
ECMWF at 138°
SO2 Flux [molec/sec]
Assumed Wind Direction (°)

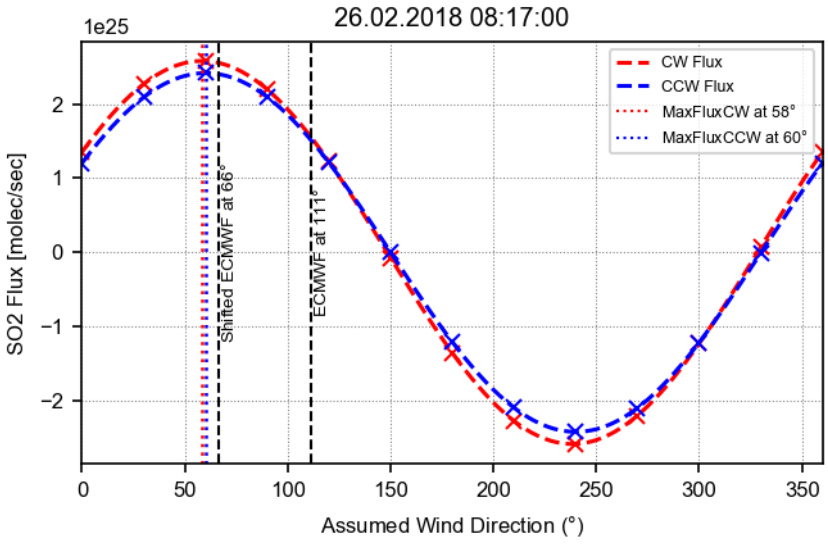
26.02.2018 08:17:00
1e25
CW Flux
CCW Flux
MaxFluxCW at 58°
MaxFluxCCW at 60°
Shifted ECMWF at 66°
ECMWF at 111°
SO2 Flux [molec/sec]
Assumed Wind Direction (°)

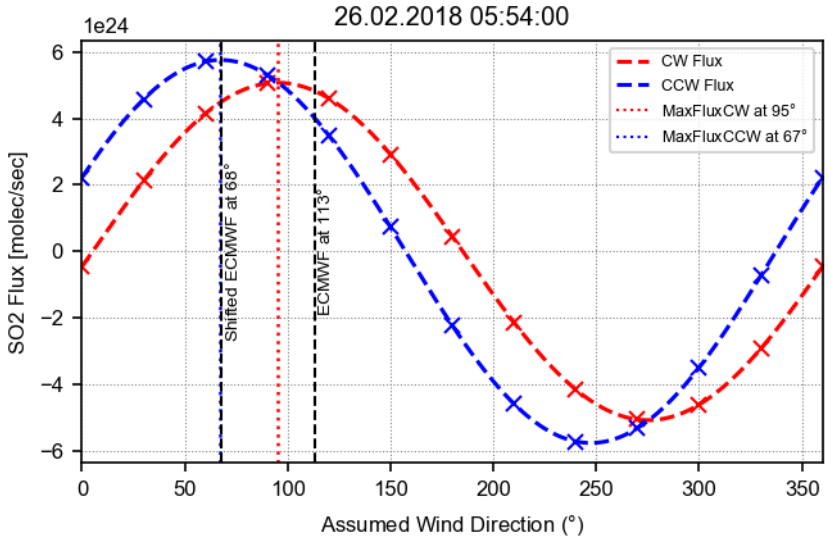
26.02.2018 05:54:00
1e24
CW Flux
CCW Flux
MaxFluxCW at 95°
MaxFluxCCW at 67°
Shifted ECMWF at 68°
ECMWF at 113°
SO2 Flux [molec/sec]
Assumed Wind Direction (°)

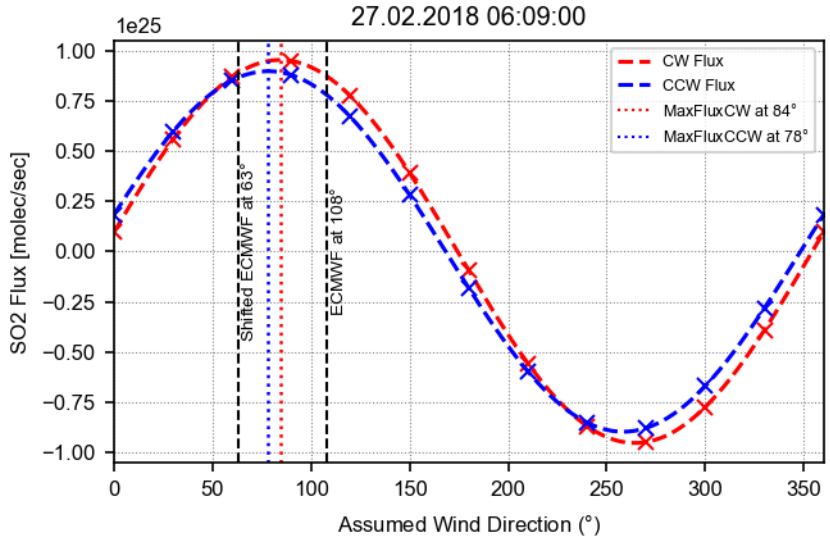
27.02.2018 06:09:00
1e25
SO2 Flux [molec/sec]
Assumed Wind Direction (°)
CW Flux
CCW Flux
MaxFluxCW at 84°
MaxFluxCCW at 78°
Shifted ECMWF at 63°
ECMWF at 108°

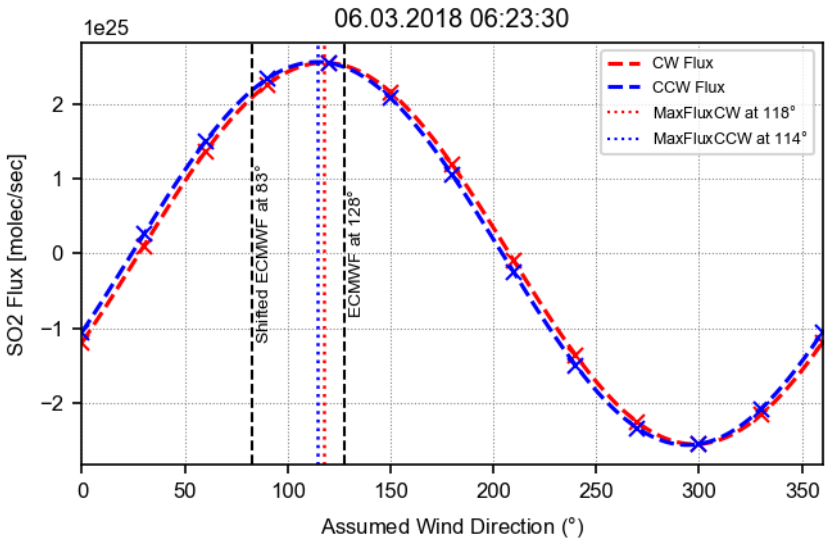
06.03.2018 06:23:30
1e25
SO2 Flux [molec/sec]
Assumed Wind Direction (°)
CW Flux
CCW Flux
MaxFluxCW at 118°
MaxFluxCCW at 114°
Shifted ECMWF at 83°
ECMWF at 128°

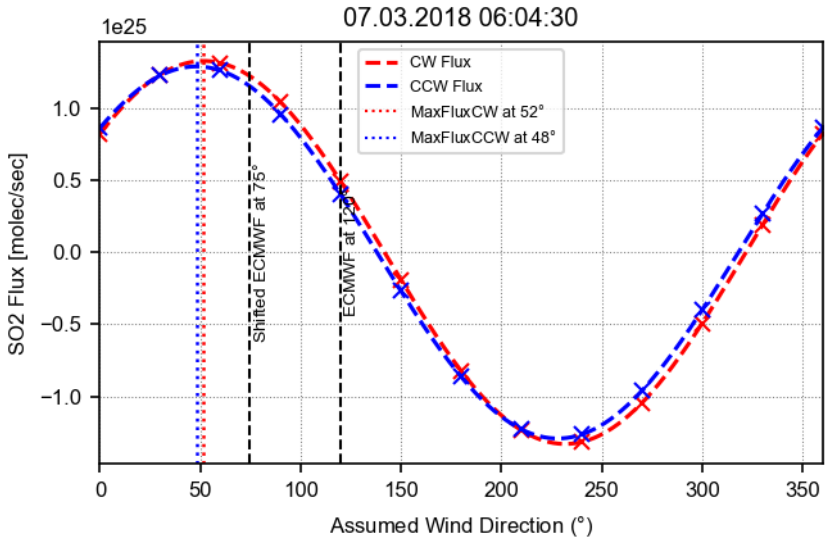
07.03.2018 06:04:30
1e25
SO2 Flux [molec/sec]
Assumed Wind Direction (°)
CW Flux
CCW Flux
MaxFluxCW at 52°
MaxFluxCCW at 48°
Shifted ECMWF at 75°

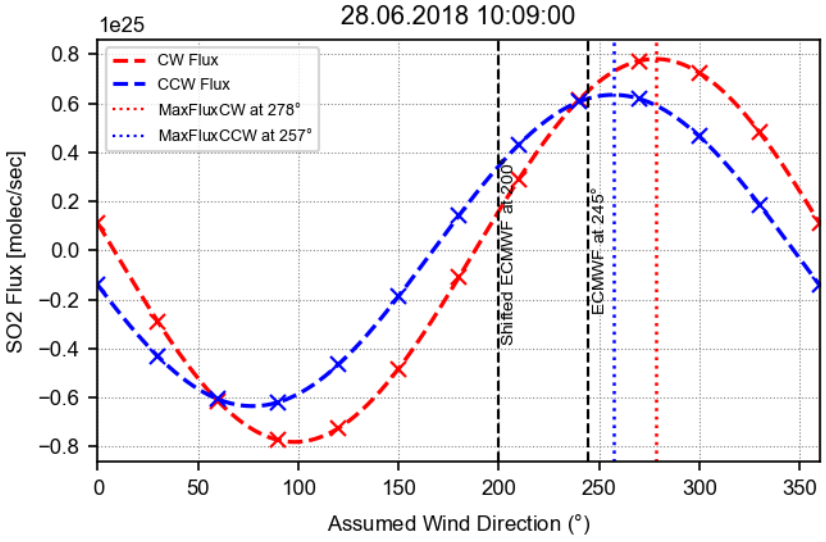
28.06.2018 10:09:00
1e25
CW Flux
CCW Flux
MaxFluxCW at 278°
MaxFluxCCW at 257°
Shifted ECMWF at 200°
ECMWF at 245°
SO2 Flux [molec/sec]
Assumed Wind Direction (°)
0.8
0.6
0.4
0.2
0.0
−0.2
−0.4
−0.6
−0.8
0
50
100
150
200
250
300
350

A.3 HCHO Fluxes

Fluxes calculated for different assumed wind directions for NO_2. The dashed vertical black lines indicate the averaged original ECMWF and shifted ECMWF wind directions, respectively.

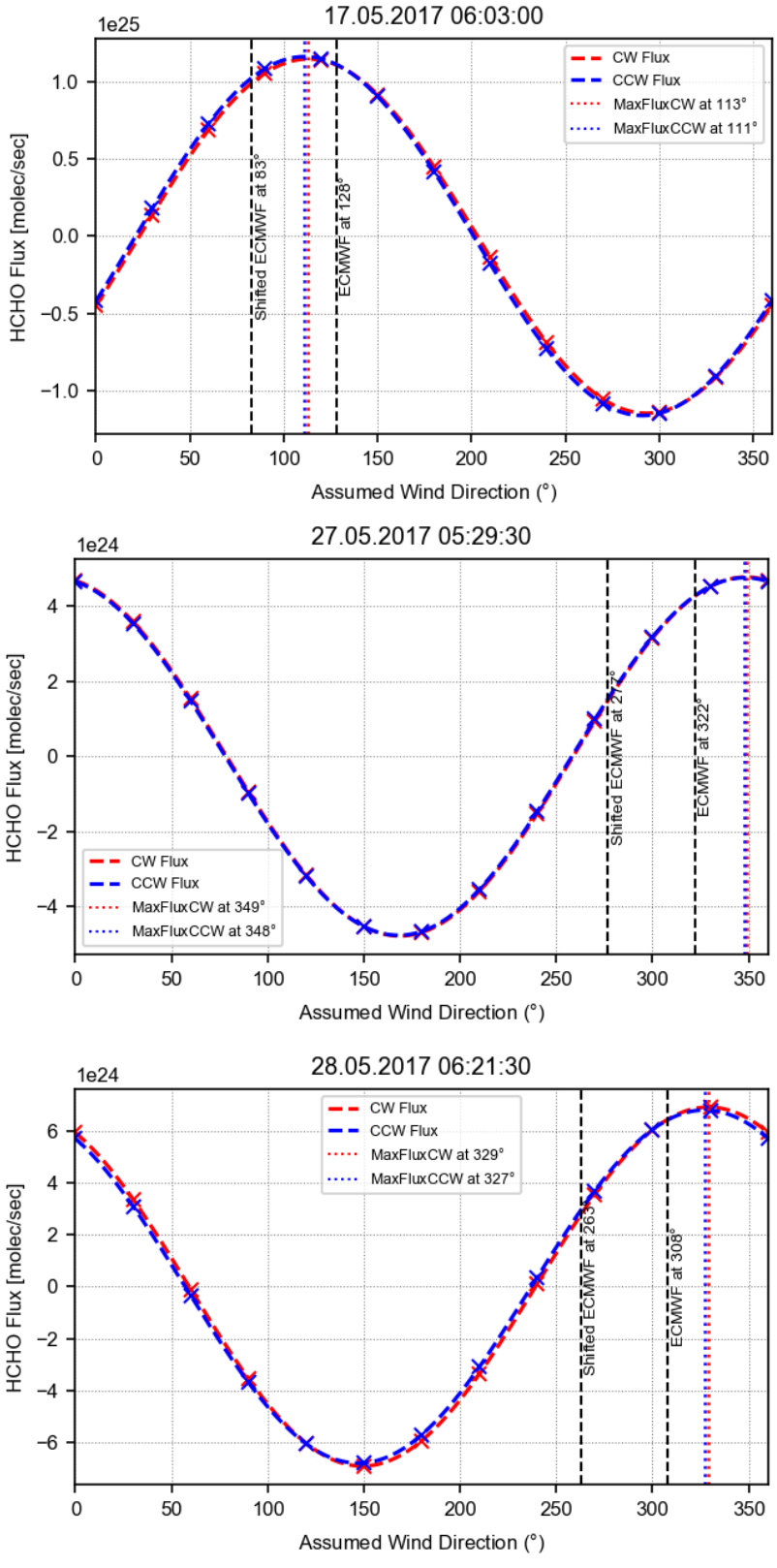

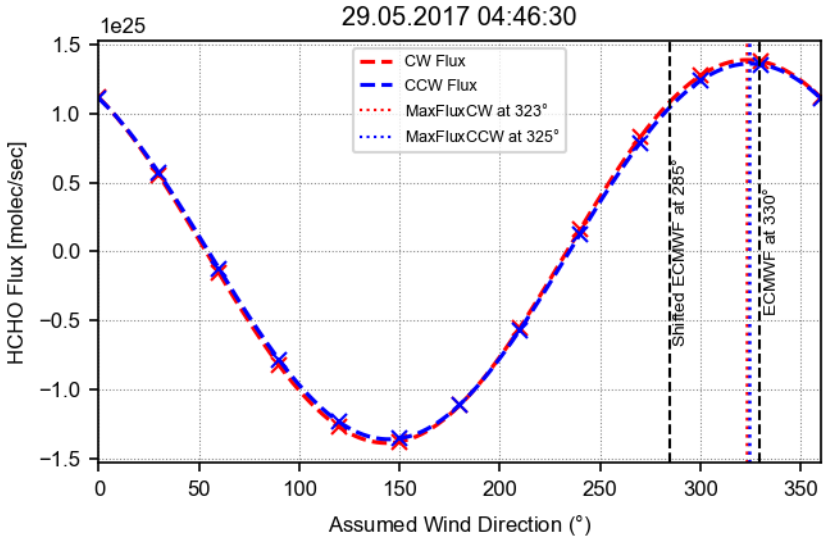
29.05.2017 04:46:30
1e25
CW Flux
CCW Flux
MaxFluxCW at 323°
MaxFluxCCW at 325°
Shifted ECMWF at 285°
ECMWF at 330°
HCHO Flux [molec/sec]
Assumed Wind Direction (°)

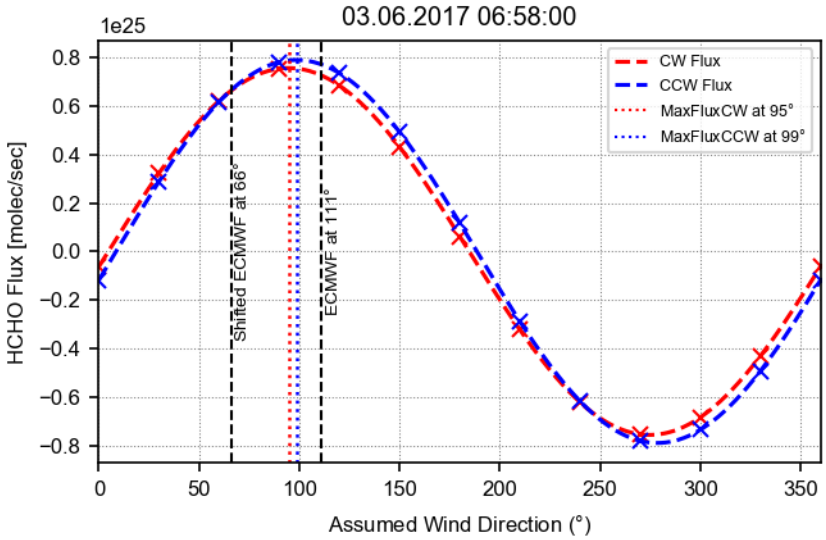
03.06.2017 06:58:00
1e25
CW Flux
CCW Flux
MaxFluxCW at 95°
MaxFluxCCW at 99°
Shifted ECMWF at 66°
ECMWF at 111°
HCHO Flux [molec/sec]
Assumed Wind Direction (°)

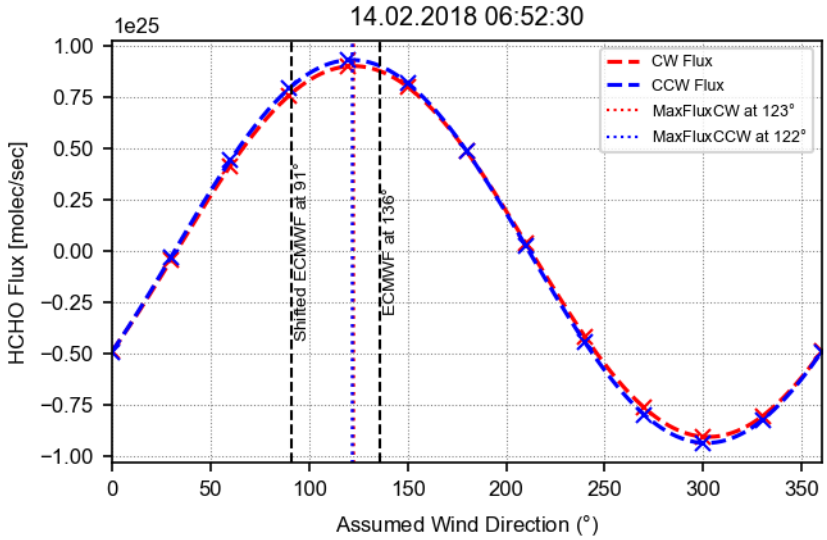
14.02.2018 06:52:30
1e25
CW Flux
CCW Flux
MaxFluxCW at 123°
MaxFluxCCW at 122°
Shifted ECMWF at 91°
ECMWF at 136°
HCHO Flux [molec/sec]
Assumed Wind Direction (°)

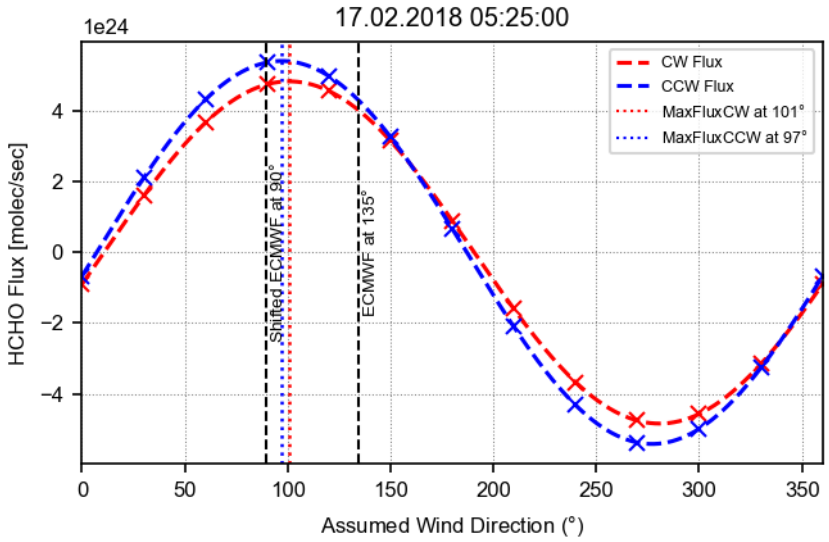
17.02.2018 05:25:00
1e24
CW Flux
CCW Flux
MaxFluxCW at 101°
MaxFluxCCW at 97°
Shifted ECMWF at 90°
ECMWF at 135°
HCHO Flux [molec/sec]
Assumed Wind Direction (°)

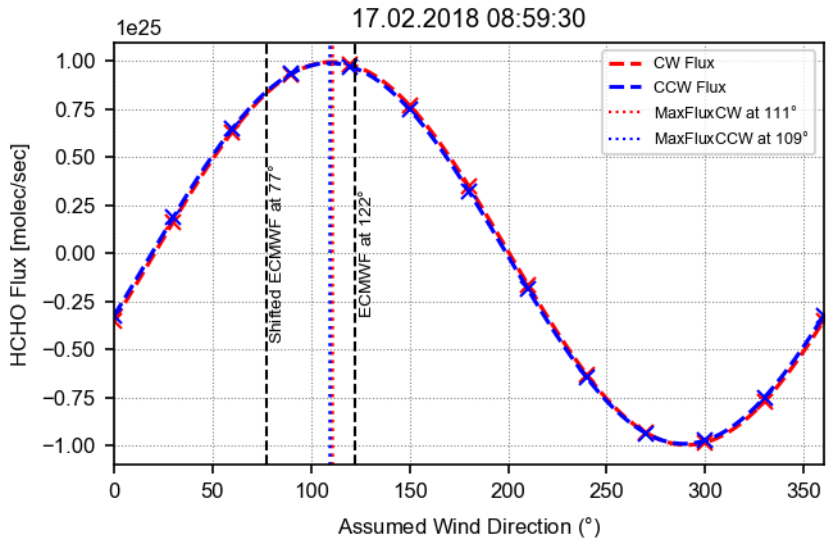
17.02.2018 08:59:30
1e25
CW Flux
CCW Flux
MaxFluxCW at 111°
MaxFluxCCW at 109°
Shifted ECMWF at 77°
ECMWF at 122°
HCHO Flux [molec/sec]
Assumed Wind Direction (°)

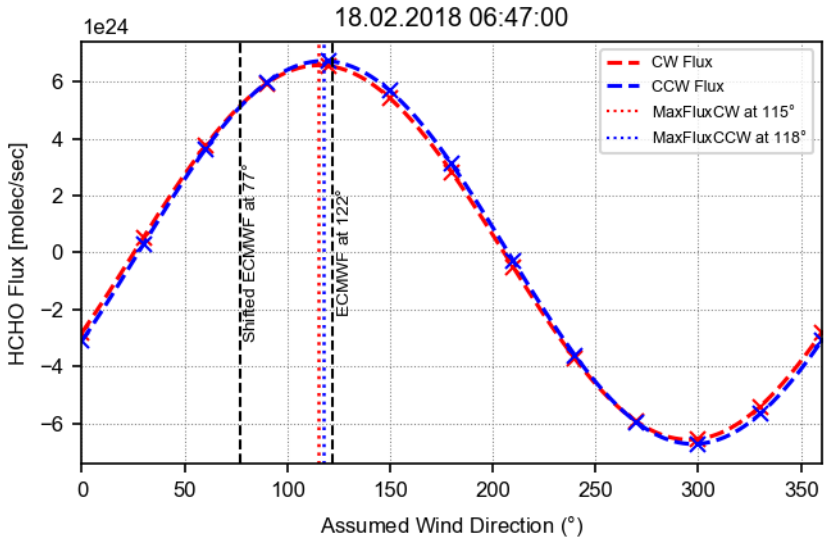
18.02.2018 06:47:00
1e24
CW Flux
CCW Flux
MaxFluxCW at 115°
MaxFluxCCW at 118°
Shifted ECMWF at 77°
ECMWF at 122°
HCHO Flux [molec/sec]
Assumed Wind Direction (°)

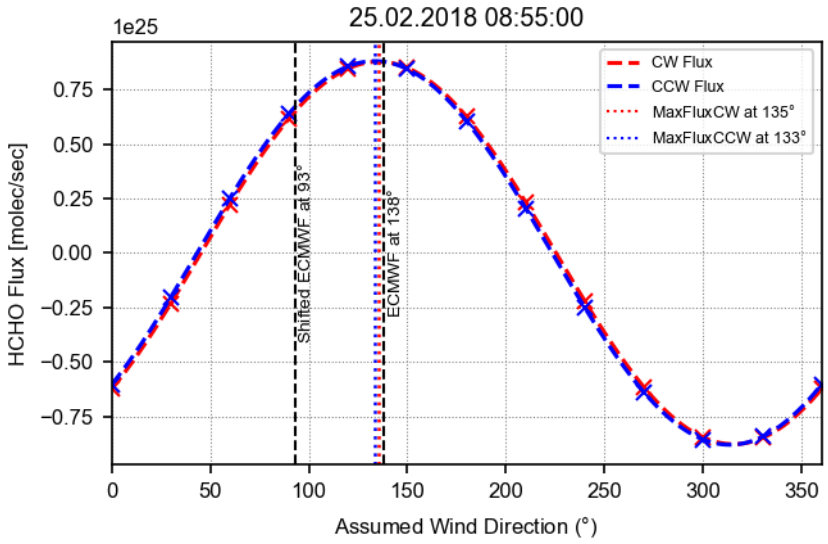
25.02.2018 08:55:00
1e25
HCHO Flux [molec/sec]
Assumed Wind Direction (°)
CW Flux
CCW Flux
MaxFluxCW at 135°
MaxFluxCCW at 133°
Shifted ECMWF at 93°
ECMWF at 138°

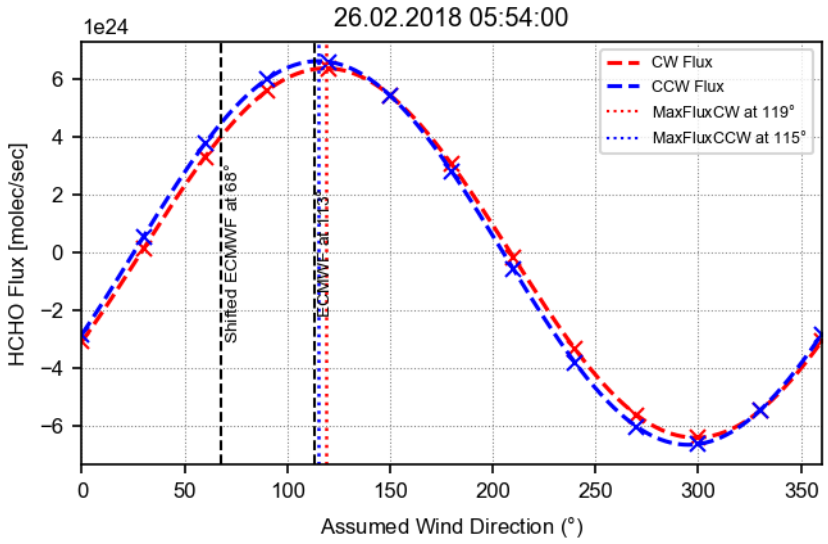
26.02.2018 05:54:00
1e24
HCHO Flux [molec/sec]
Assumed Wind Direction (°)
CW Flux
CCW Flux
MaxFluxCW at 119°
MaxFluxCCW at 115°
Shifted ECMWF at 68°
ECMWF at 113°

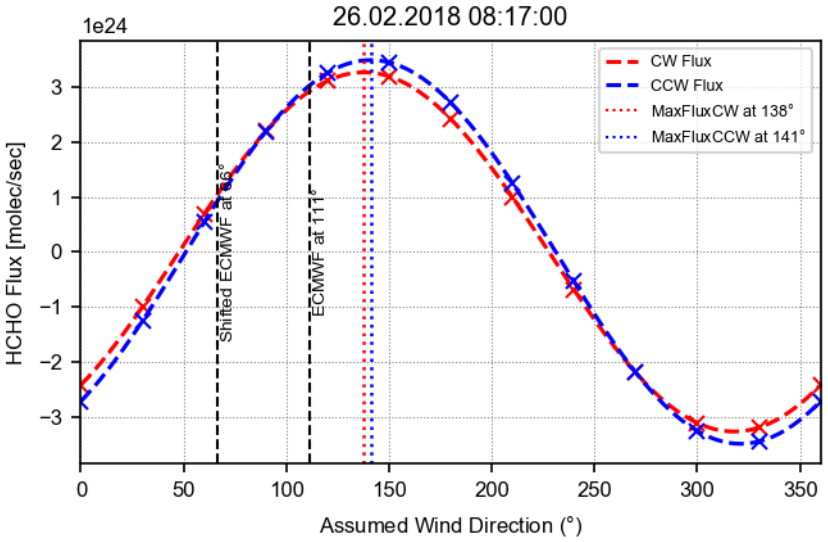
26.02.2018 08:17:00
1e24
HCHO Flux [molec/sec]
Assumed Wind Direction (°)
CW Flux
CCW Flux
MaxFluxCW at 138°
MaxFluxCCW at 141°
Shifted ECMWF at 66°
ECMWF at 111°

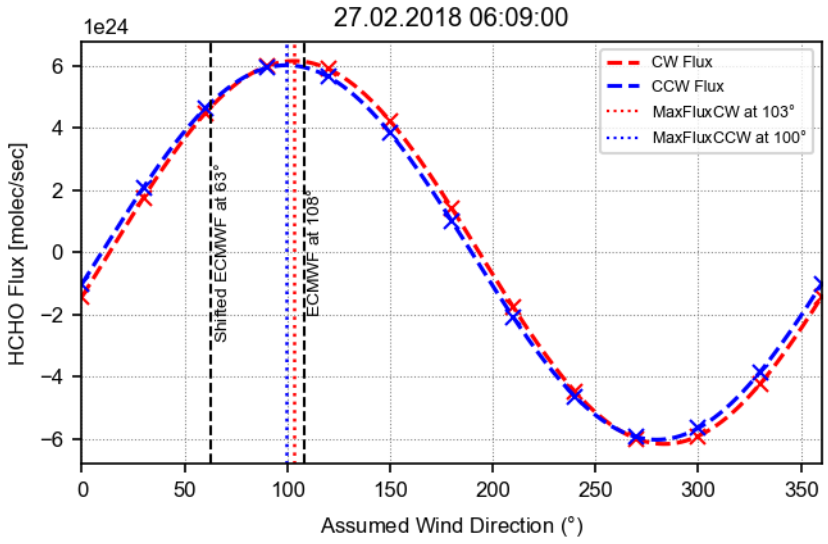
27.02.2018 06:09:00
1e24
HCHO Flux [molec/sec]
Assumed Wind Direction (°)
CW Flux
CCW Flux
MaxFluxCW at 103°
MaxFluxCCW at 100°
Shifted ECMWF at 63°
ECMWF at 108°

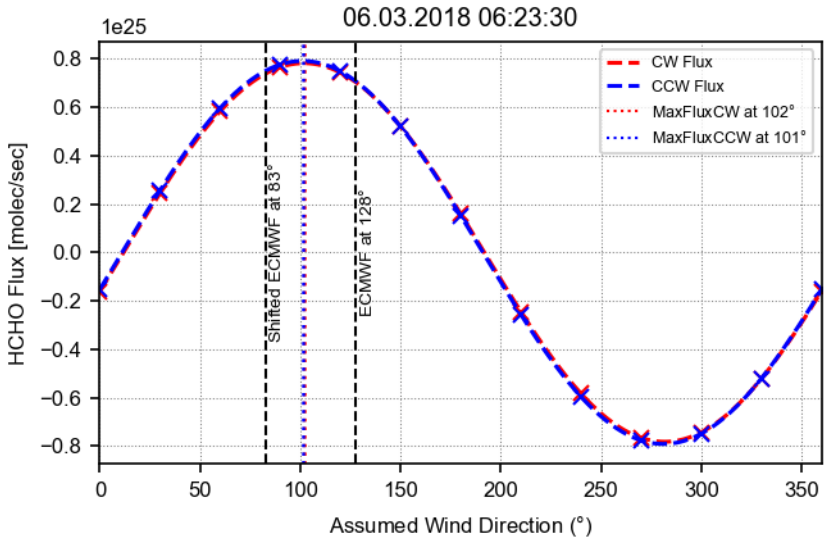
06.03.2018 06:23:30
1e25
HCHO Flux [molec/sec]
Assumed Wind Direction (°)
CW Flux
CCW Flux
MaxFluxCW at 102°
MaxFluxCCW at 101°
Shifted ECMWF at 83°
ECMWF at 128°

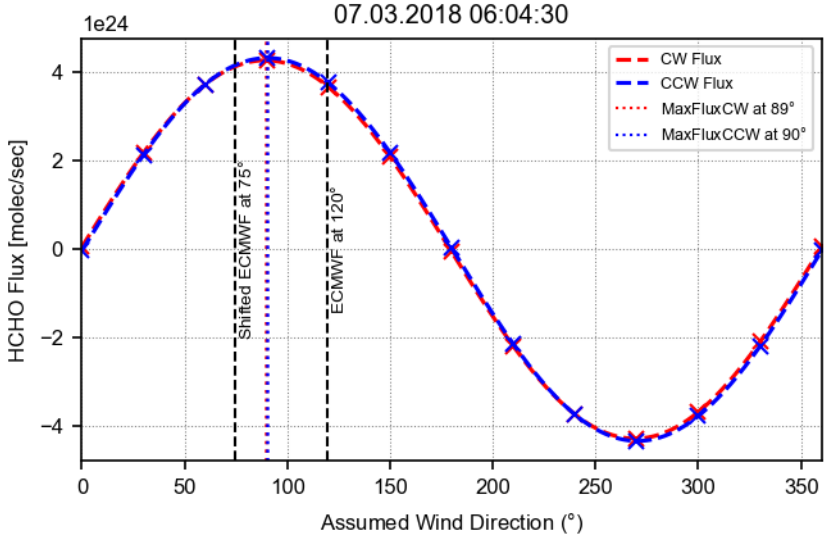
07.03.2018 06:04:30
1e24
HCHO Flux [molec/sec]
Assumed Wind Direction (°)
CW Flux
CCW Flux
MaxFluxCW at 89°
MaxFluxCCW at 90°
Shifted ECMWF at 75°
ECMWF at 120°

APPENDIX B

Spatial Distributions

B.1 NO_2 Spatial Distributions

NO_2 vertical column densities (VCDs) for the days grouped under category III, performed around Lahore during 2015-II, 2017 and 2018-I campaigns.

6.3.1.1.B.1.1. 2015 II

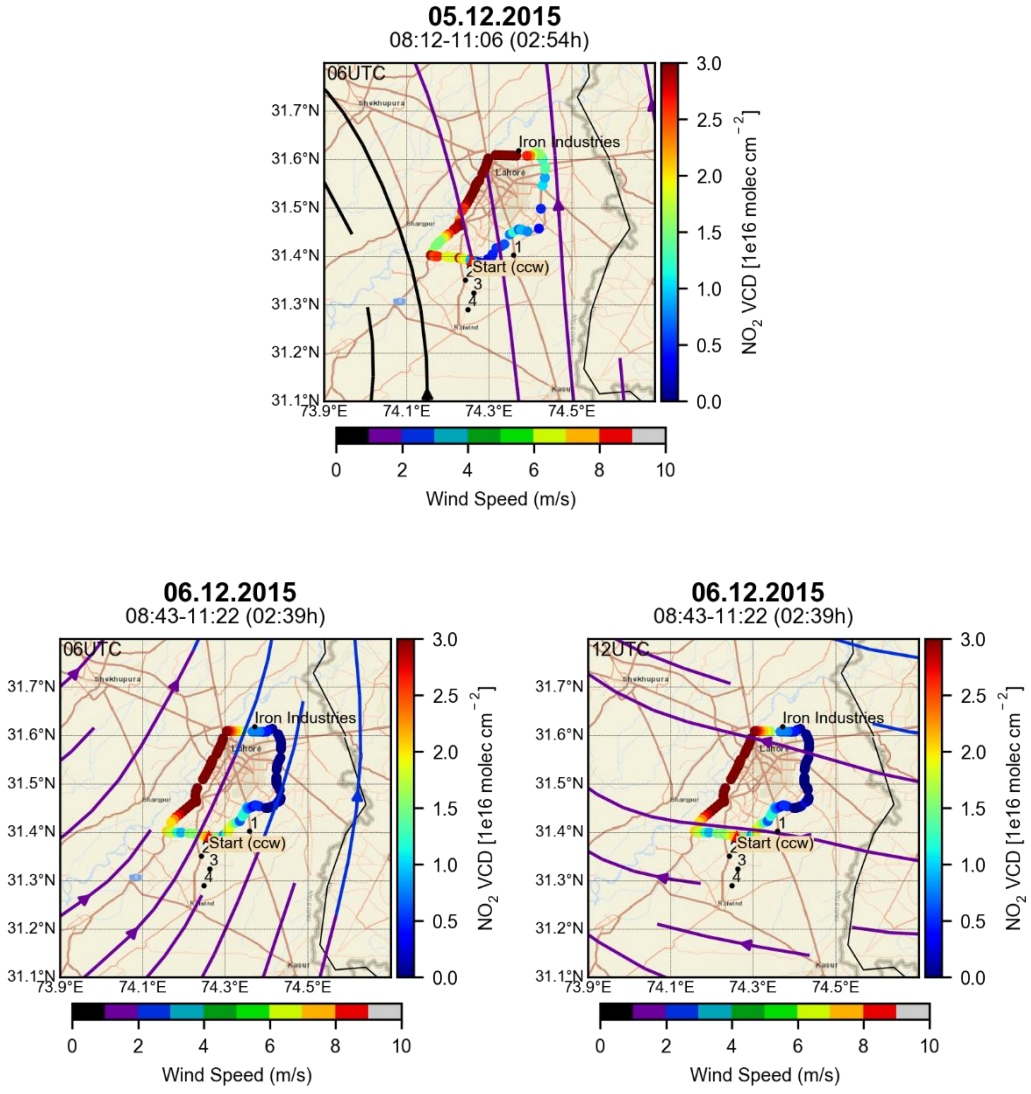

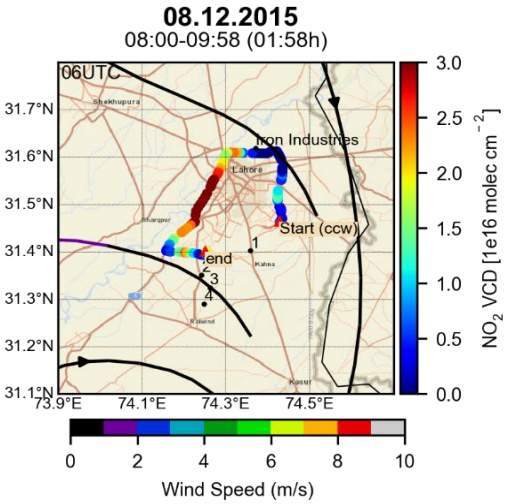
08.12.2015
08:00-09:58 (01:58h)
06UTC
Iron Industries
Start (ccw)
end
1
3
4
Lahore
Kasur
31.7°N
31.6°N
31.5°N
31.4°N
31.3°N
31.2°N
31.1°N
73.9°E
74.1°E
74.3°E
74.5°E
NO2 VCD [1e16 molec cm −2]
Wind Speed (m/s)

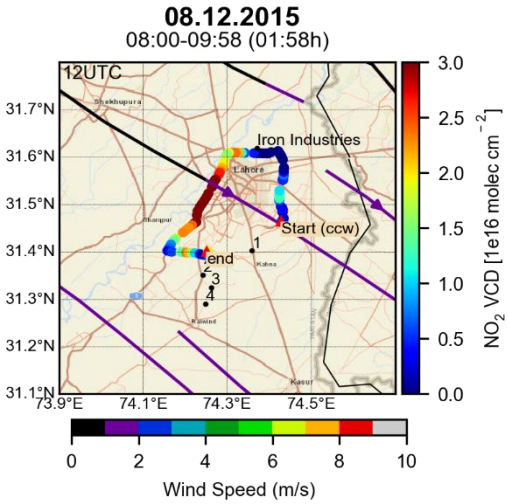
08.12.2015
08:00-09:58 (01:58h)
12UTC
Iron Industries
Start (ccw)
end
1
3
4
Lahore
Kasur
31.7°N
31.6°N
31.5°N
31.4°N
31.3°N
31.2°N
31.1°N
73.9°E
74.1°E
74.3°E
74.5°E
NO2 VCD [1e16 molec cm −2]
Wind Speed (m/s)

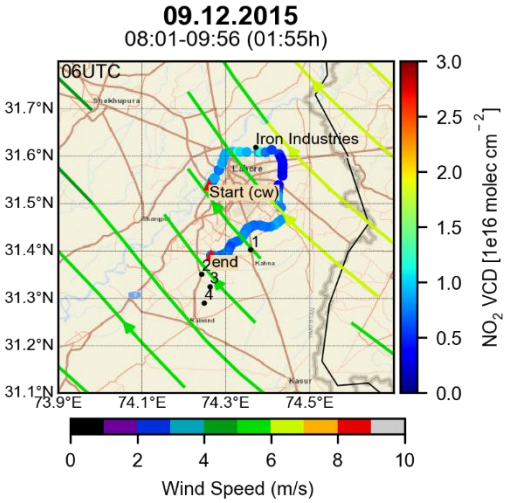
09.12.2015
08:01-09:56 (01:55h)
06UTC
Iron Industries
Start (cw)
end
1
3
4
Lahore
Kasur
31.7°N
31.6°N
31.5°N
31.4°N
31.3°N
31.2°N
31.1°N
73.9°E
74.1°E
74.3°E
74.5°E
NO2 VCD [1e16 molec cm −2]
Wind Speed (m/s)

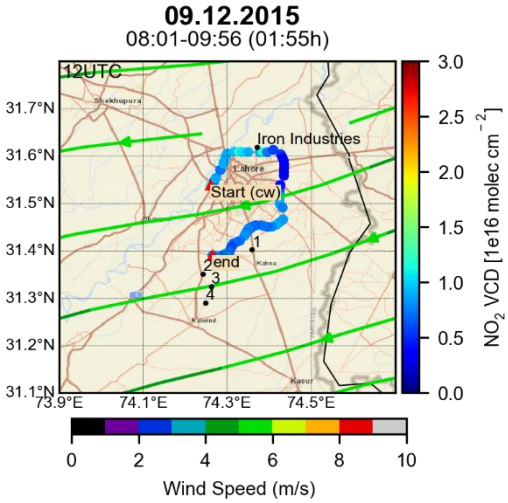
09.12.2015
08:01-09:56 (01:55h)
12UTC
Iron Industries
Start (cw)
end
1
3
4
Lahore
Kasur
31.7°N
31.6°N
31.5°N
31.4°N
31.3°N
31.2°N
31.1°N
73.9°E
74.1°E
74.3°E
74.5°E
NO2 VCD [1e16 molec cm −2]
Wind Speed (m/s)

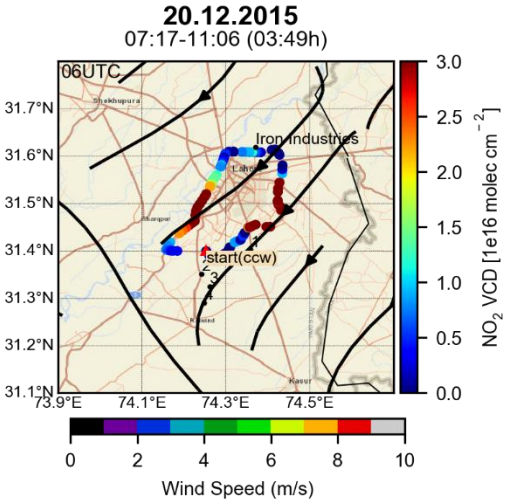
20.12.2015
07:17-11:06 (03:49h)
06UTC
Iron Industries
start(ccw)
1
3
Lahore
Kasur
31.7°N
31.6°N
31.5°N
31.4°N
31.3°N
31.2°N
31.1°N
73.9°E
74.1°E
74.3°E
74.5°E
NO2 VCD [1e16 molec cm −2]
Wind Speed (m/s)

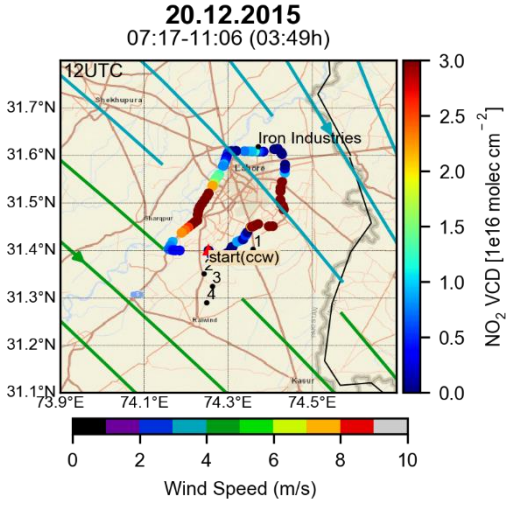
20.12.2015
07:17-11:06 (03:49h)
12UTC
Iron Industries
start(ccw)
1
3
Lahore
Kasur
31.7°N
31.6°N
31.5°N
31.4°N
31.3°N
31.2°N
31.1°N
73.9°E
74.1°E
74.3°E
74.5°E
NO2 VCD [1e16 molec cm −2]
Wind Speed (m/s)

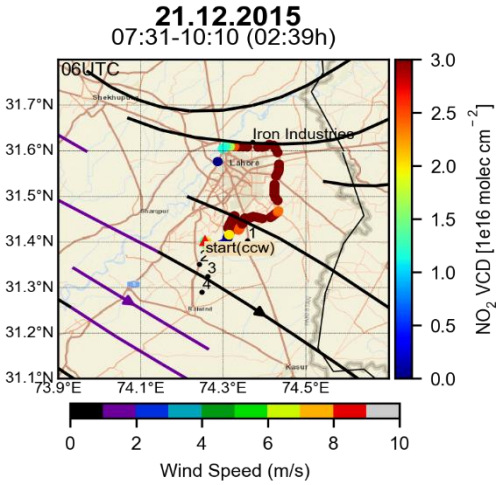

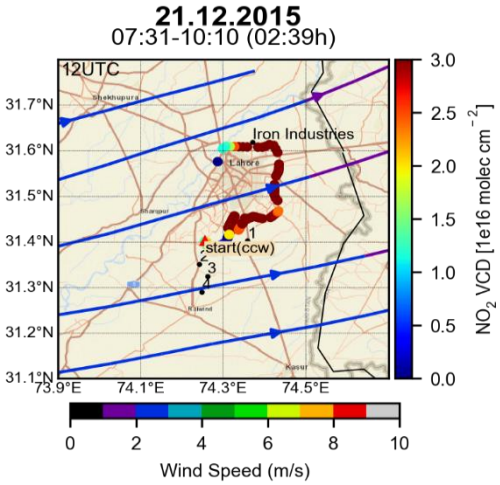

6.3.1.2.B.1.2. 2017

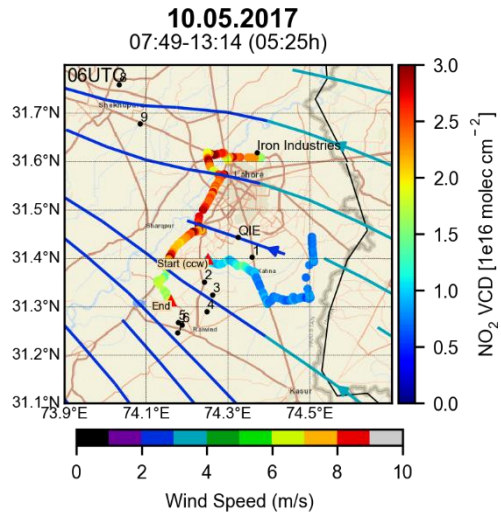

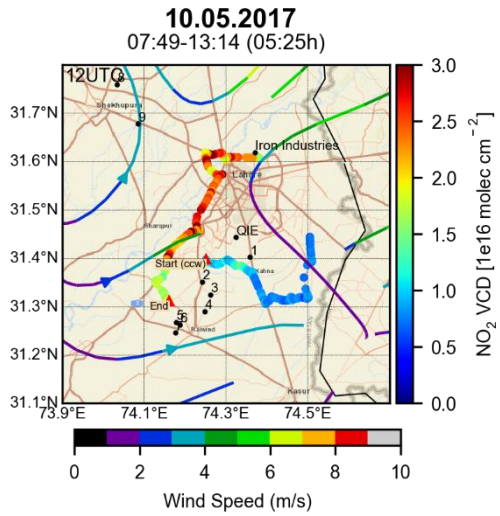

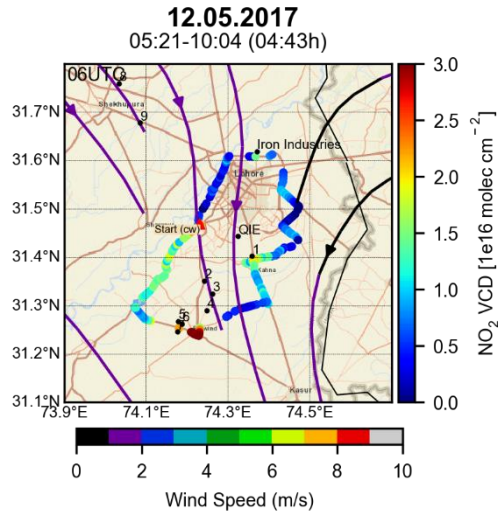

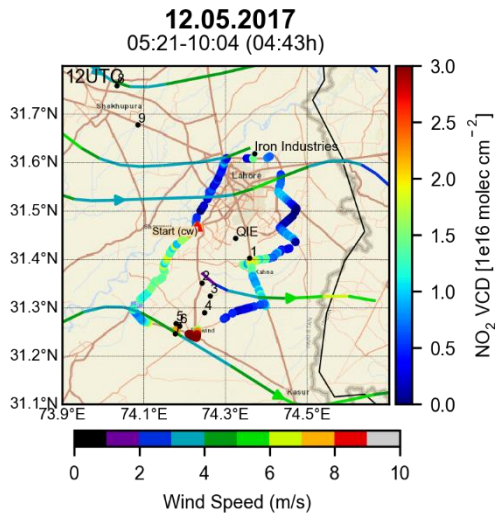

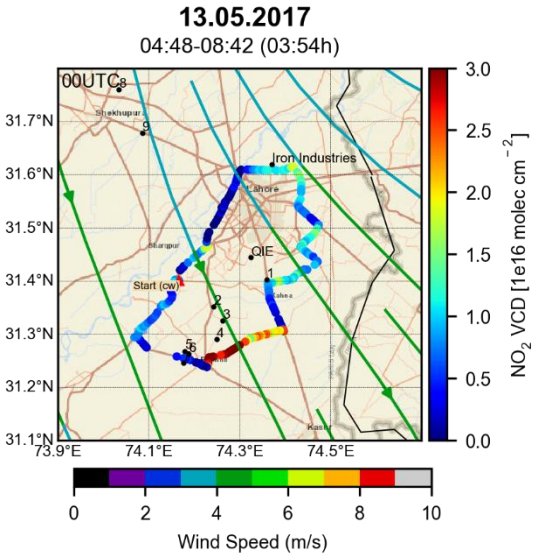
13.05.2017
04:48-08:42 (03:54h)
00UTC
Iron Industries
QIE
Start (cw)
Lahore
Kasur
31.7°N
31.6°N
31.5°N
31.4°N
31.3°N
31.2°N
31.1°N
73.9°E
74.1°E
74.3°E
74.5°E
NO2 VCD [1e16 molec cm−2]
Wind Speed (m/s)

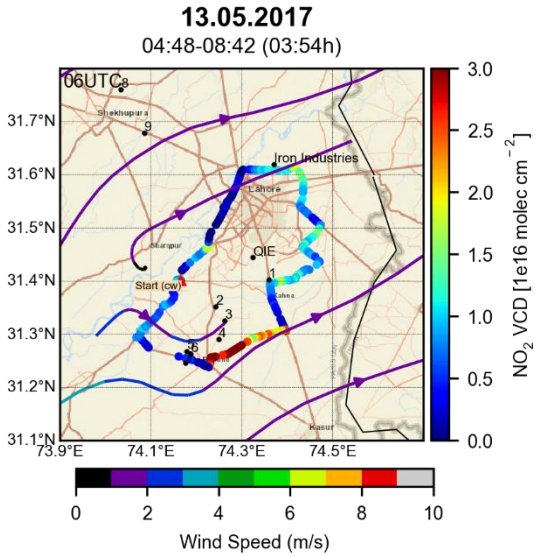
13.05.2017
04:48-08:42 (03:54h)
06UTC
Iron Industries
QIE
Start (cw)
Lahore
Kasur
31.7°N
31.6°N
31.5°N
31.4°N
31.3°N
31.2°N
31.1°N
73.9°E
74.1°E
74.3°E
74.5°E
NO2 VCD [1e16 molec cm−2]
Wind Speed (m/s)

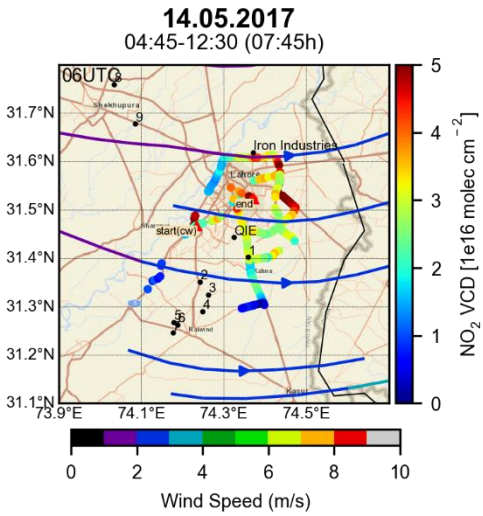
14.05.2017
04:45-12:30 (07:45h)
06UTC
Iron Industries
QIE
start(cw)
end
Lahore
Kasur
31.7°N
31.6°N
31.5°N
31.4°N
31.3°N
31.2°N
31.1°N
73.9°E
74.1°E
74.3°E
74.5°E
NO2 VCD [1e16 molec cm−2]
Wind Speed (m/s)

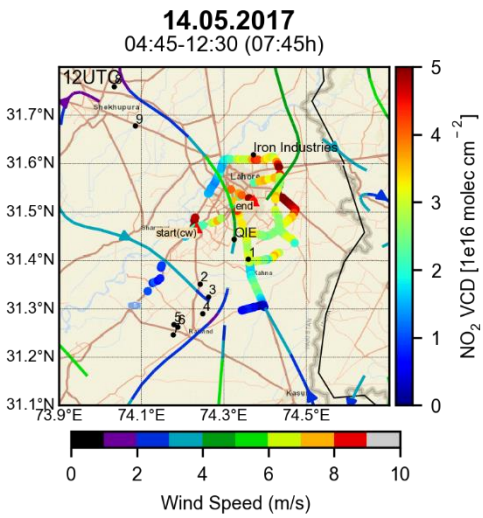
14.05.2017
04:45-12:30 (07:45h)
12UTC
Iron Industries
QIE
start(cw)
end
Lahore
Kasur
31.7°N
31.6°N
31.5°N
31.4°N
31.3°N
31.2°N
31.1°N
73.9°E
74.1°E
74.3°E
74.5°E
NO2 VCD [1e16 molec cm−2]
Wind Speed (m/s)

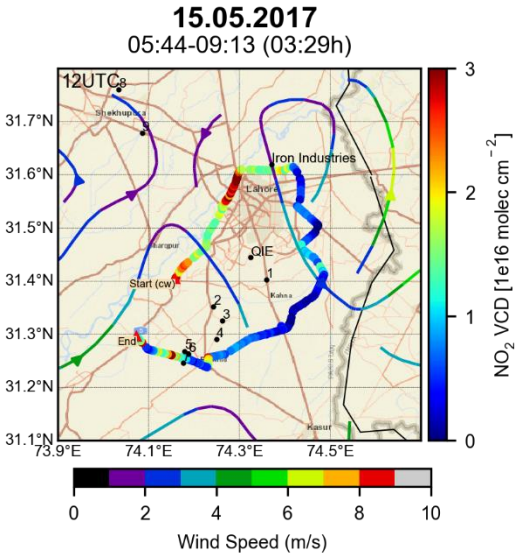
15.05.2017
05:44-09:13 (03:29h)
12UTC
Iron Industries
QIE
Start (cw)
End
Lahore
Kasur
31.7°N
31.6°N
31.5°N
31.4°N
31.3°N
31.2°N
31.1°N
73.9°E
74.1°E
74.3°E
74.5°E
NO2 VCD [1e16 molec cm−2]
Wind Speed (m/s)

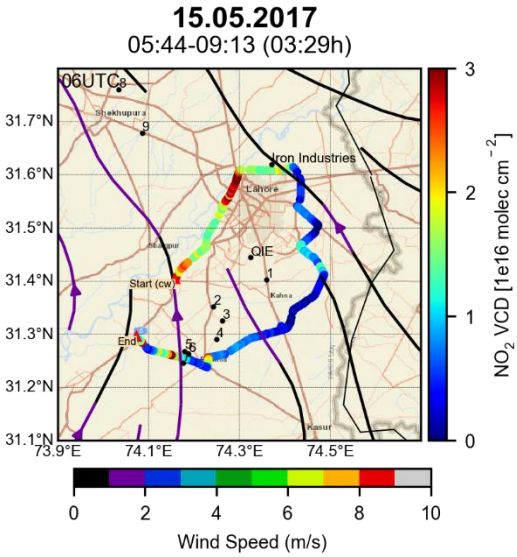
15.05.2017
05:44-09:13 (03:29h)
06UTC
Iron Industries
QIE
Start (cw)
End
Lahore
Kasur
31.7°N
31.6°N
31.5°N
31.4°N
31.3°N
31.2°N
31.1°N
73.9°E
74.1°E
74.3°E
74.5°E
NO2 VCD [1e16 molec cm−2]
Wind Speed (m/s)

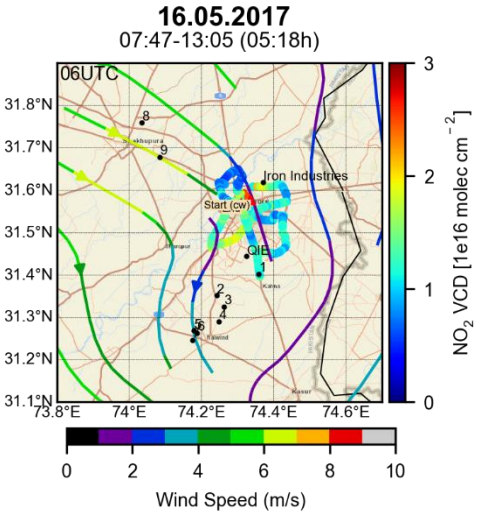
16.05.2017
07:47-13:05 (05:18h)
06UTC
Iron Industries
Start (cw)
QIE
NO2 VCD [1e16 molec cm-2]
Wind Speed (m/s)

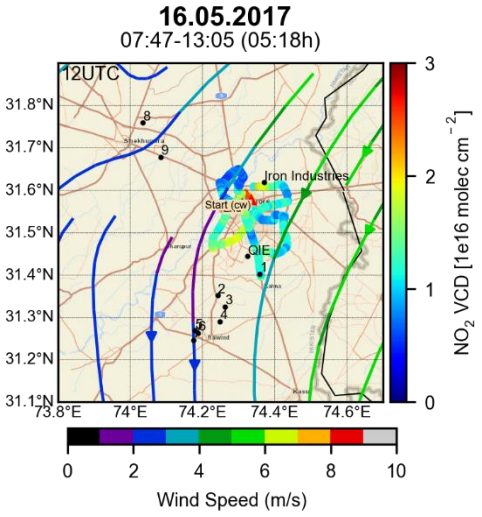
16.05.2017
07:47-13:05 (05:18h)
12UTC
Iron Industries
Start (cw)
QIE
NO2 VCD [1e16 molec cm-2]
Wind Speed (m/s)

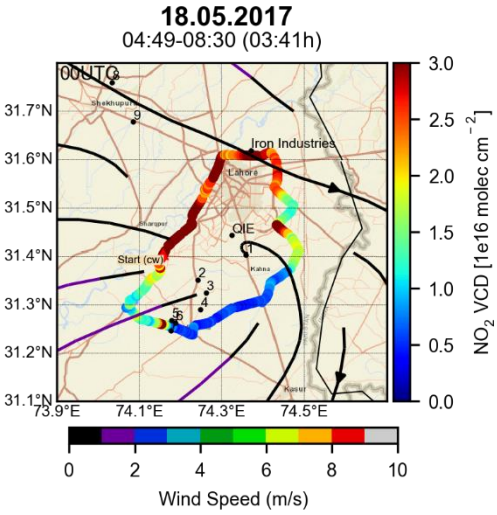
18.05.2017
04:49-08:30 (03:41h)
00UTC
Iron Industries
Lahore
Start (cw)
QIE
NO2 VCD [1e16 molec cm-2]
Wind Speed (m/s)

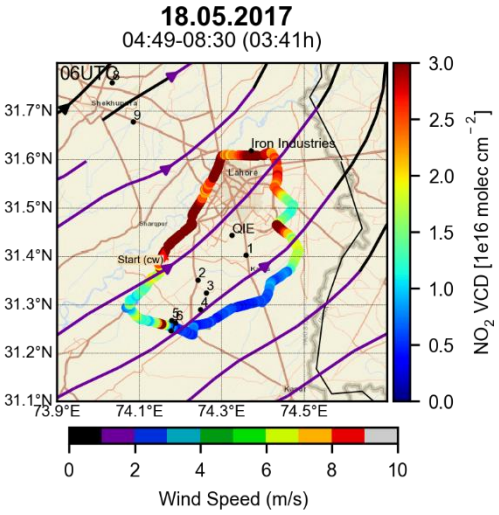
18.05.2017
04:49-08:30 (03:41h)
06UTC
Iron Industries
Lahore
Start (cw)
QIE
NO2 VCD [1e16 molec cm-2]
Wind Speed (m/s)

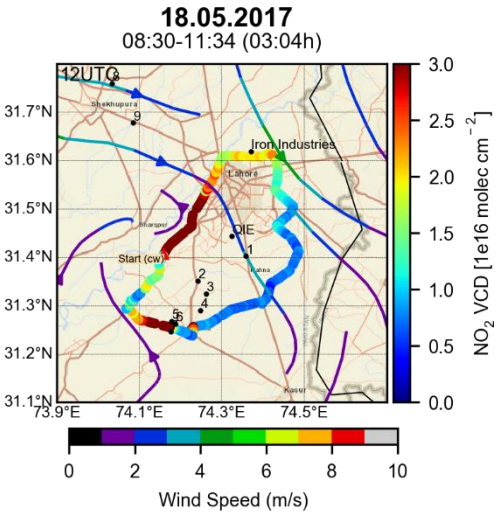
18.05.2017
08:30-11:34 (03:04h)
12UTC
Iron Industries
Lahore
Start (cw)
QIE
NO2 VCD [1e16 molec cm-2]
Wind Speed (m/s)

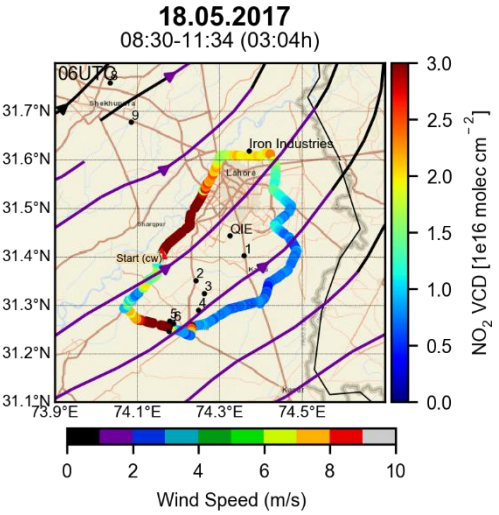
18.05.2017
08:30-11:34 (03:04h)
06UTC
Iron Industries
Lahore
Start (cw)
QIE
NO2 VCD [1e16 molec cm-2]
Wind Speed (m/s)

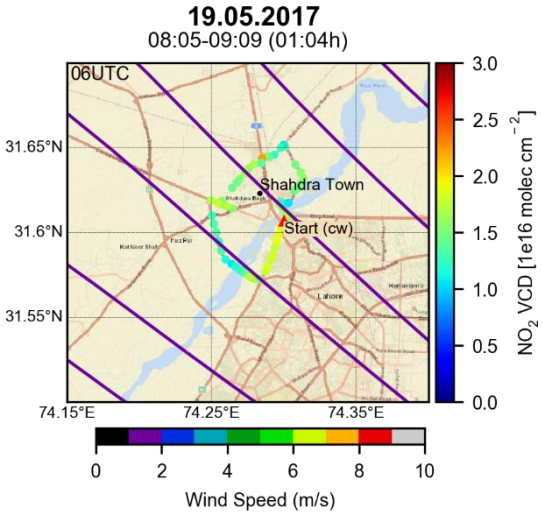
19.05.2017
08:05-09:09 (01:04h)
06UTC
Shahdra Town
Start (cw)
Lahore
31.65°N
31.6°N
31.55°N
74.15°E
74.25°E
74.35°E
NO2 VCD [1e16 molec cm−2]
Wind Speed (m/s)

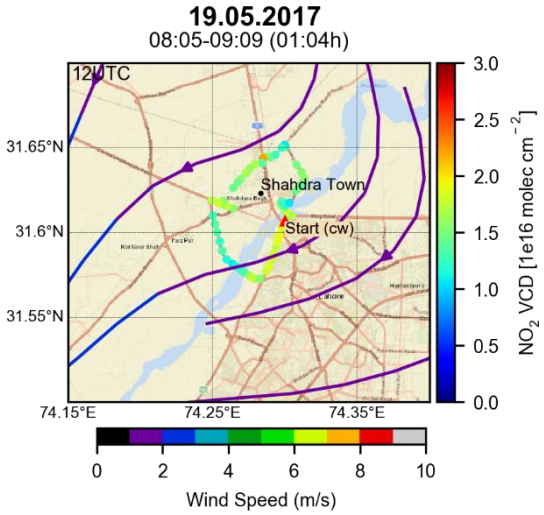
19.05.2017
08:05-09:09 (01:04h)
12UTC
Shahdra Town
Start (cw)
Lahore
31.65°N
31.6°N
31.55°N
74.15°E
74.25°E
74.35°E
NO2 VCD [1e16 molec cm−2]
Wind Speed (m/s)

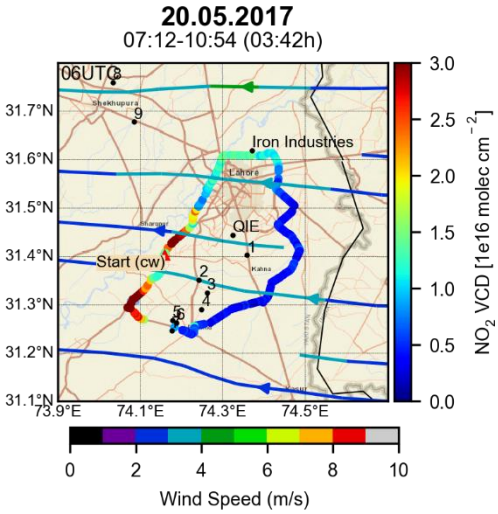
20.05.2017
07:12-10:54 (03:42h)
06UTC
Iron Industries
QIE
Start (cw)
Lahore
31.7°N
31.6°N
31.5°N
31.4°N
31.3°N
31.2°N
31.1°N
73.9°E
74.1°E
74.3°E
74.5°E
NO2 VCD [1e16 molec cm−2]
Wind Speed (m/s)

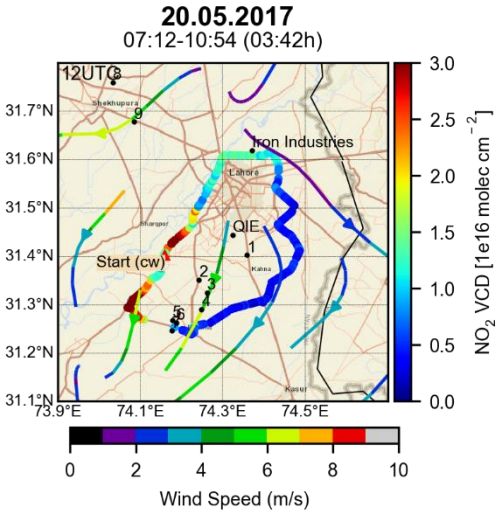
20.05.2017
07:12-10:54 (03:42h)
12UTC
Iron Industries
QIE
Start (cw)
Lahore
31.7°N
31.6°N
31.5°N
31.4°N
31.3°N
31.2°N
31.1°N
73.9°E
74.1°E
74.3°E
74.5°E
NO2 VCD [1e16 molec cm−2]
Wind Speed (m/s)

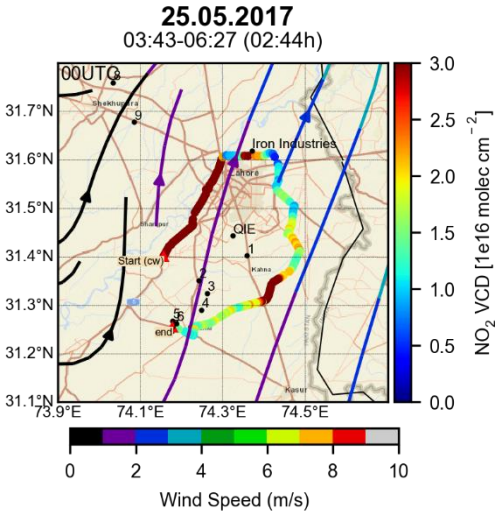
25.05.2017
03:43-06:27 (02:44h)
00UTC
Iron Industries
QIE
Start (cw)
Lahore
31.7°N
31.6°N
31.5°N
31.4°N
31.3°N
31.2°N
31.1°N
73.9°E
74.1°E
74.3°E
74.5°E
NO2 VCD [1e16 molec cm−2]
Wind Speed (m/s)

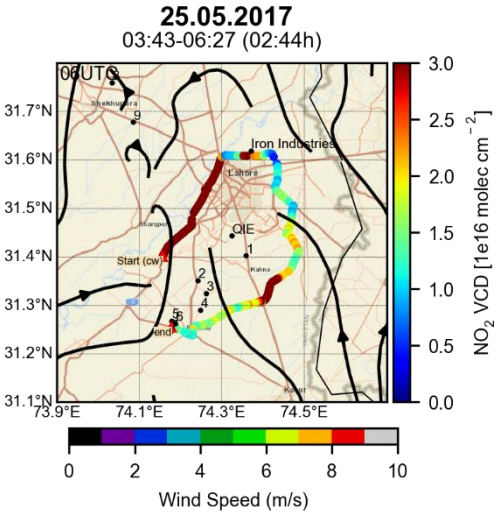
25.05.2017
03:43-06:27 (02:44h)
06UTC
Iron Industries
QIE
Start (cw)
Lahore
31.7°N
31.6°N
31.5°N
31.4°N
31.3°N
31.2°N
31.1°N
73.9°E
74.1°E
74.3°E
74.5°E
NO2 VCD [1e16 molec cm−2]
Wind Speed (m/s)

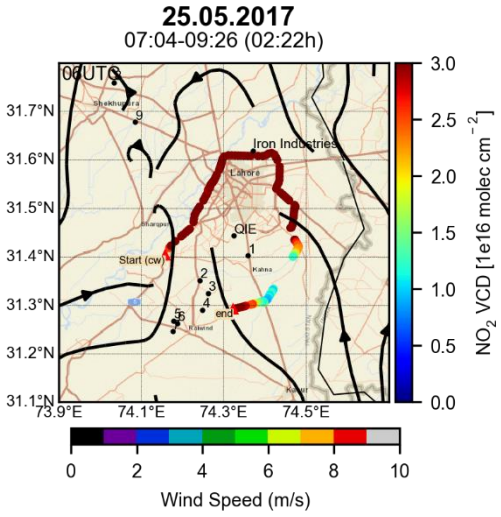
25.05.2017
07:04-09:26 (02:22h)
06UTC
Iron Industries
Lahore
OIE
Start (cw)
end
Kasur
31.7°N
31.6°N
31.5°N
31.4°N
31.3°N
31.2°N
31.1°N
73.9°E
74.1°E
74.3°E
74.5°E
NO2 VCD [1e16 molec cm−2]
Wind Speed (m/s)

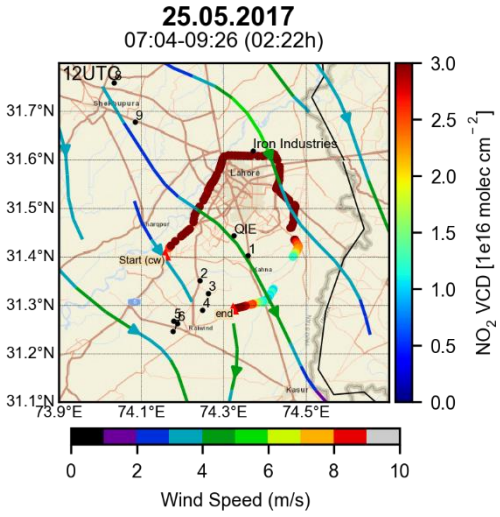
25.05.2017
07:04-09:26 (02:22h)
12UTC
Iron Industries
Lahore
OIE
Start (cw)
end
Kasur
31.7°N
31.6°N
31.5°N
31.4°N
31.3°N
31.2°N
31.1°N
73.9°E
74.1°E
74.3°E
74.5°E
NO2 VCD [1e16 molec cm−2]
Wind Speed (m/s)

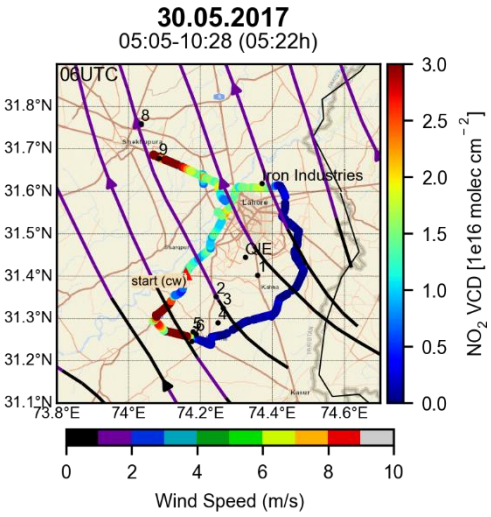
30.05.2017
05:05-10:28 (05:22h)
06UTC
Iron Industries
Lahore
OIE
start (cw)
Kasur
31.8°N
31.7°N
31.6°N
31.5°N
31.4°N
31.3°N
31.2°N
31.1°N
73.8°E
74°E
74.2°E
74.4°E
74.6°E
NO2 VCD [1e16 molec cm−2]
Wind Speed (m/s)

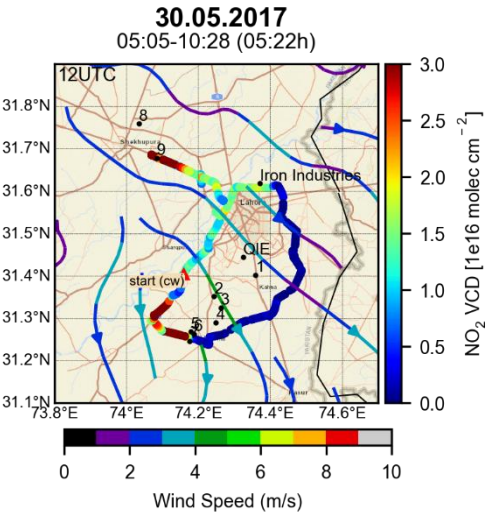
30.05.2017
05:05-10:28 (05:22h)
12UTC
Iron Industries
Lahore
OIE
start (cw)
Kasur
31.8°N
31.7°N
31.6°N
31.5°N
31.4°N
31.3°N
31.2°N
31.1°N
73.8°E
74°E
74.2°E
74.4°E
74.6°E
NO2 VCD [1e16 molec cm−2]
Wind Speed (m/s)

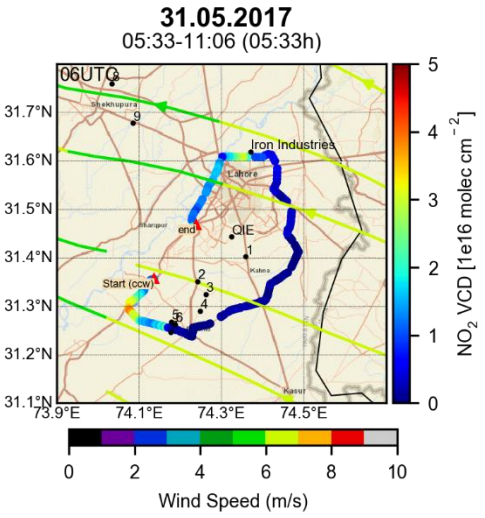
31.05.2017
05:33-11:06 (05:33h)
06UTC
Iron Industries
Lahore
OIE
end
Start (ccw)
Kasur
31.7°N
31.6°N
31.5°N
31.4°N
31.3°N
31.2°N
31.1°N
73.9°E
74.1°E
74.3°E
74.5°E
NO2 VCD [1e16 molec cm−2]
Wind Speed (m/s)

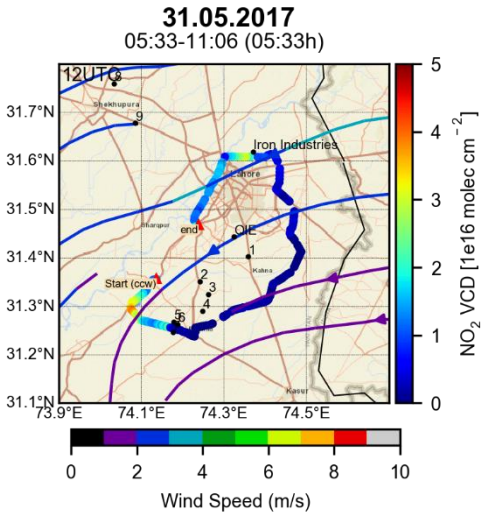
31.05.2017
05:33-11:06 (05:33h)
12UTC
Iron Industries
Lahore
OIE
end
Start (ccw)
Kasur
31.7°N
31.6°N
31.5°N
31.4°N
31.3°N
31.2°N
31.1°N
73.9°E
74.1°E
74.3°E
74.5°E
NO2 VCD [1e16 molec cm−2]
Wind Speed (m/s)

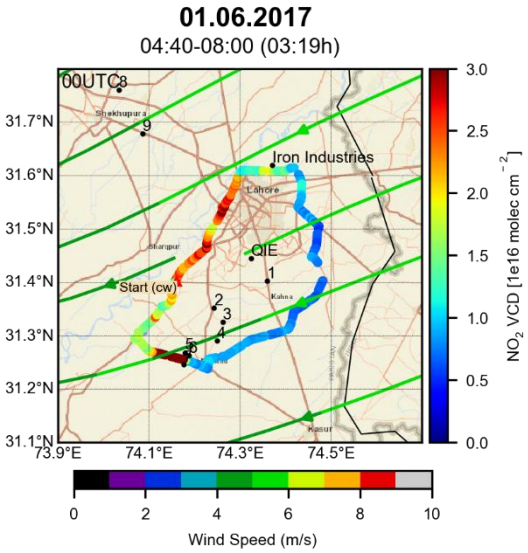
01.06.2017
04:40-08:00 (03:19h)
00UTC+8
Iron Industries
QIE
Start (cw)
1
2
3
4
5
6
9
Lahore
Kasur
31.7°N
31.6°N
31.5°N
31.4°N
31.3°N
31.2°N
31.1°N
73.9°E
74.1°E
74.3°E
74.5°E
NO2 VCD [1e16 molec cm-2]
0.0
0.5
1.0
1.5
2.0
2.5
3.0
Wind Speed (m/s)
0
2
4
6
8
10

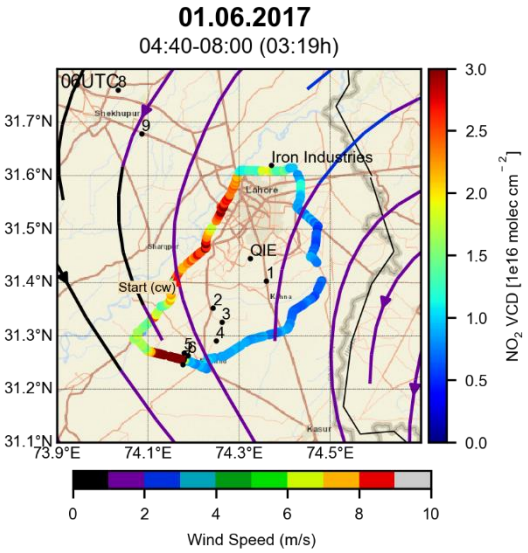
01.06.2017
04:40-08:00 (03:19h)
06UTC+8
Iron Industries
QIE
Start (cw)
1
2
3
4
5
6
9
Lahore
Kasur
31.7°N
31.6°N
31.5°N
31.4°N
31.3°N
31.2°N
31.1°N
73.9°E
74.1°E
74.3°E
74.5°E
NO2 VCD [1e16 molec cm-2]
0.0
0.5
1.0
1.5
2.0
2.5
3.0
Wind Speed (m/s)
0
2
4
6
8
10

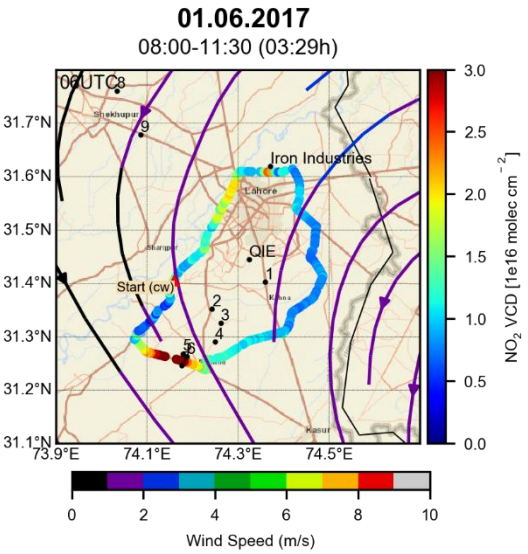
01.06.2017
08:00-11:30 (03:29h)
06UTC+8
Iron Industries
QIE
Start (cw)
1
2
3
4
5
6
9
Lahore
Kasur
31.7°N
31.6°N
31.5°N
31.4°N
31.3°N
31.2°N
31.1°N
73.9°E
74.1°E
74.3°E
74.5°E
NO2 VCD [1e16 molec cm-2]
0.0
0.5
1.0
1.5
2.0
2.5
3.0
Wind Speed (m/s)
0
2
4
6
8
10

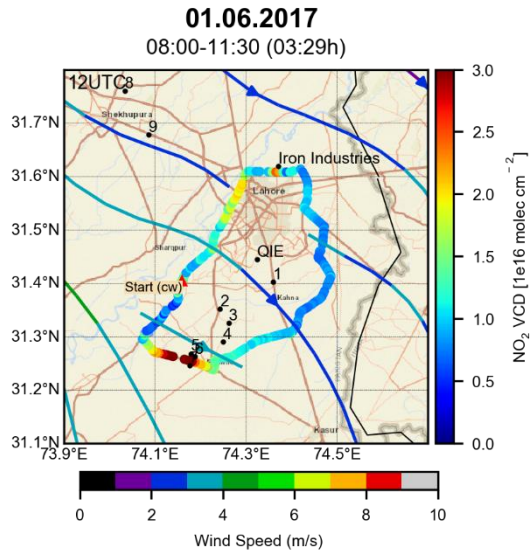
01.06.2017
08:00-11:30 (03:29h)
12UTC+8
Iron Industries
QIE
Start (cw)
1
2
3
4
5
6
9
Lahore
Kasur
31.7°N
31.6°N
31.5°N
31.4°N
31.3°N
31.2°N
31.1°N
73.9°E
74.1°E
74.3°E
74.5°E
NO2 VCD [1e16 molec cm-2]
0.0
0.5
1.0
1.5
2.0
2.5
3.0
Wind Speed (m/s)
0
2
4
6
8
10

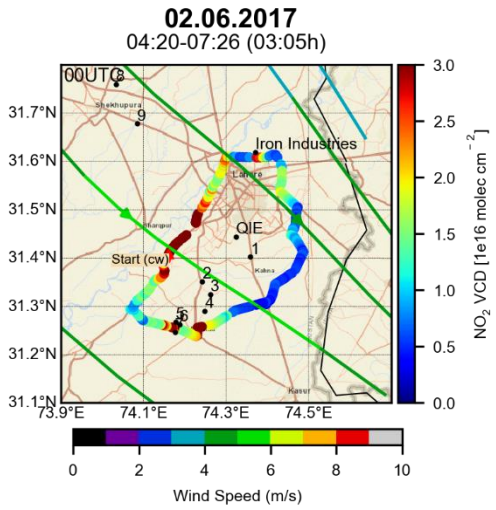
02.06.2017
04:20-07:26 (03:05h)
00UTC
Iron Industries
QIE
Start (cw)
31.7°N
31.6°N
31.5°N
31.4°N
31.3°N
31.2°N
31.1°N
73.9°E
74.1°E
74.3°E
74.5°E
3.0
2.5
2.0
1.5
1.0
0.5
0.0
NO2 VCD [1e16 molec cm−2]
0
2
4
6
8
10
Wind Speed (m/s)

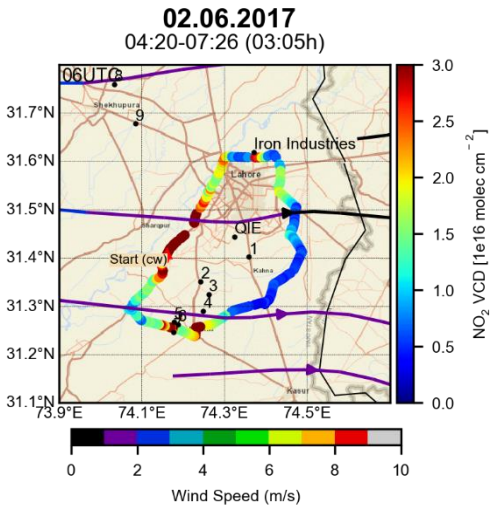
02.06.2017
04:20-07:26 (03:05h)
06UTC
Iron Industries
QIE
Start (cw)
31.7°N
31.6°N
31.5°N
31.4°N
31.3°N
31.2°N
31.1°N
73.9°E
74.1°E
74.3°E
74.5°E
3.0
2.5
2.0
1.5
1.0
0.5
0.0
NO2 VCD [1e16 molec cm−2]
0
2
4
6
8
10
Wind Speed (m/s)

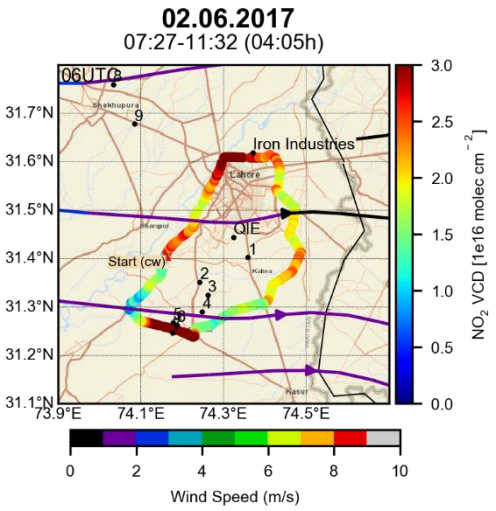
02.06.2017
07:27-11:32 (04:05h)
06UTC
Iron Industries
QIE
Start (cw)
31.7°N
31.6°N
31.5°N
31.4°N
31.3°N
31.2°N
31.1°N
73.9°E
74.1°E
74.3°E
74.5°E
3.0
2.5
2.0
1.5
1.0
0.5
0.0
NO2 VCD [1e16 molec cm−2]
0
2
4
6
8
10
Wind Speed (m/s)

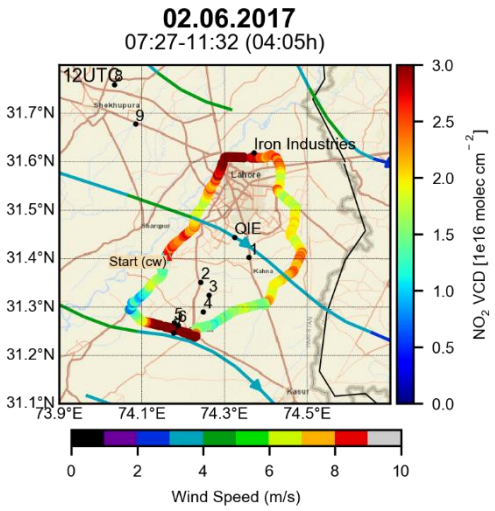
02.06.2017
07:27-11:32 (04:05h)
12UTC
Iron Industries
QIE
Start (cw)
31.7°N
31.6°N
31.5°N
31.4°N
31.3°N
31.2°N
31.1°N
73.9°E
74.1°E
74.3°E
74.5°E
3.0
2.5
2.0
1.5
1.0
0.5
0.0
NO2 VCD [1e16 molec cm−2]
0
2
4
6
8
10
Wind Speed (m/s)

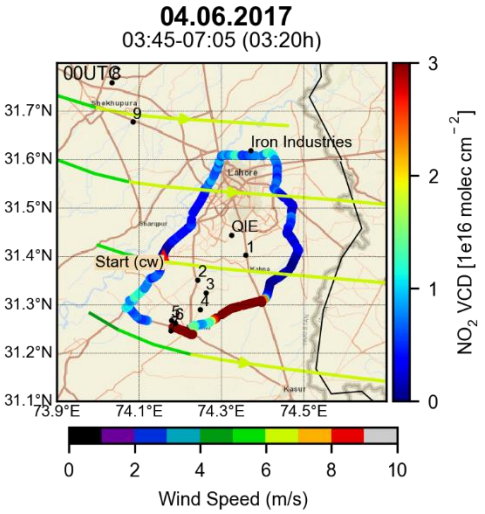
04.06.2017
03:45-07:05 (03:20h)
00UTC
Iron Industries
QIE
Start (cw)
Wind Speed (m/s)
NO2 VCD [1e16 molec cm-2]

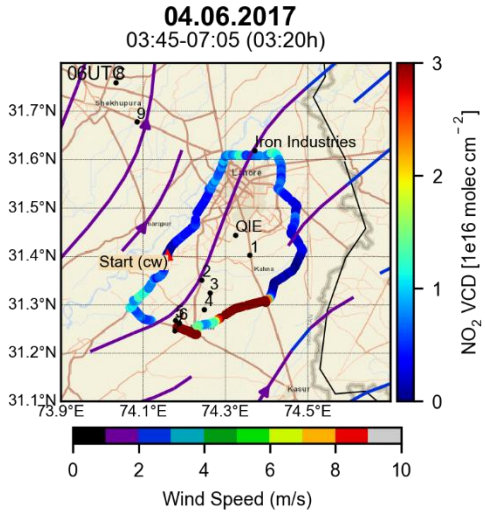
04.06.2017
03:45-07:05 (03:20h)
06UTC
Iron Industries
QIE
Start (cw)
Wind Speed (m/s)
NO2 VCD [1e16 molec cm-2]

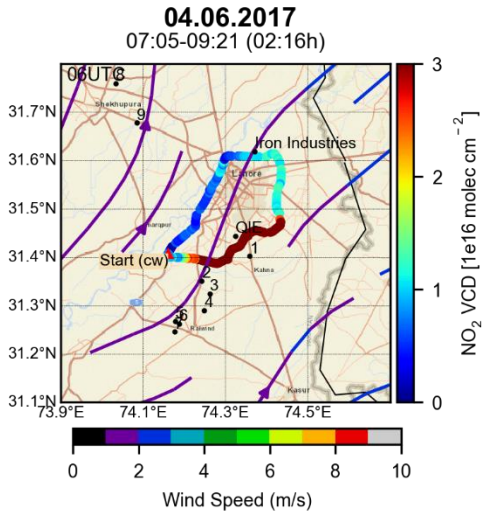
04.06.2017
07:05-09:21 (02:16h)
06UTC
Iron Industries
QIE
Start (cw)
Wind Speed (m/s)
NO2 VCD [1e16 molec cm-2]

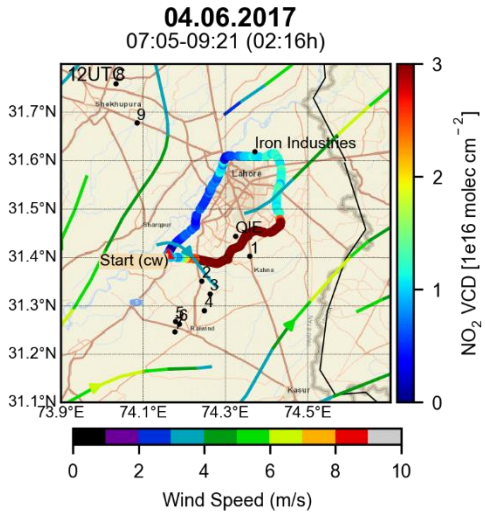
04.06.2017
07:05-09:21 (02:16h)
12UTC
Iron Industries
QIE
Start (cw)
Wind Speed (m/s)
NO2 VCD [1e16 molec cm-2]

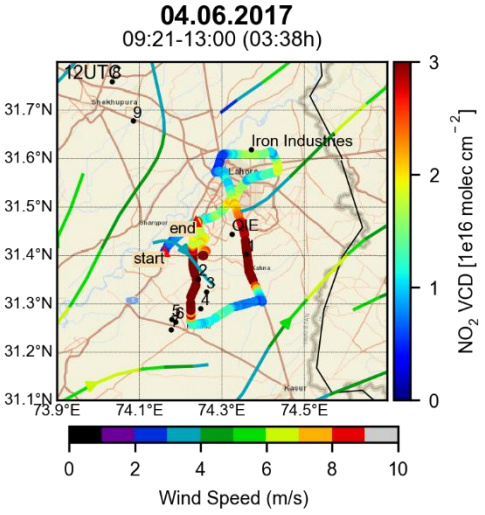
04.06.2017
09:21-13:00 (03:38h)
12UTC
Iron Industries
QIE
end
start
Wind Speed (m/s)
NO2 VCD [1e16 molec cm-2]

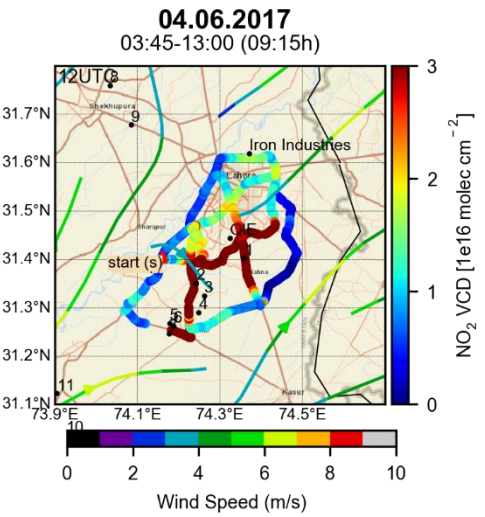
04.06.2017
03:45-13:00 (09:15h)
12UTC
Iron Industries
QIE
start (s)
Wind Speed (m/s)
NO2 VCD [1e16 molec cm-2]

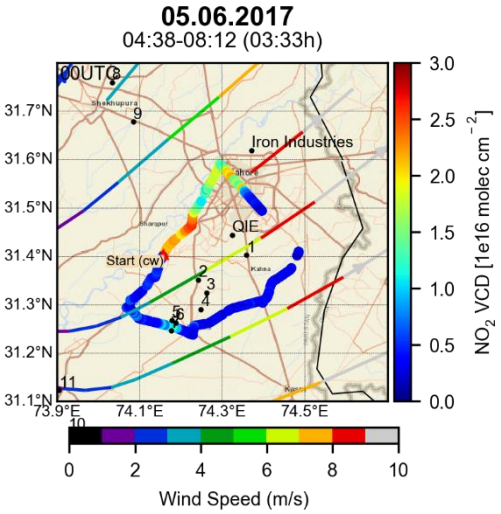
05.06.2017
04:38-08:12 (03:33h)
00UTC
Iron Industries
QIE
Start (cw)
31.7°N
31.6°N
31.5°N
31.4°N
31.3°N
31.2°N
31.1°N
73.9°E
74.1°E
74.3°E
74.5°E
NO2 VCD [1e16 molec cm -2]
Wind Speed (m/s)

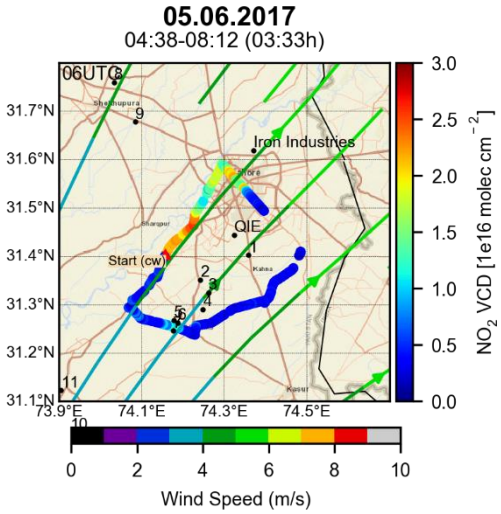
05.06.2017
04:38-08:12 (03:33h)
06UTC
Iron Industries
QIE
Start (cw)
31.7°N
31.6°N
31.5°N
31.4°N
31.3°N
31.2°N
31.1°N
73.9°E
74.1°E
74.3°E
74.5°E
NO2 VCD [1e16 molec cm -2]
Wind Speed (m/s)

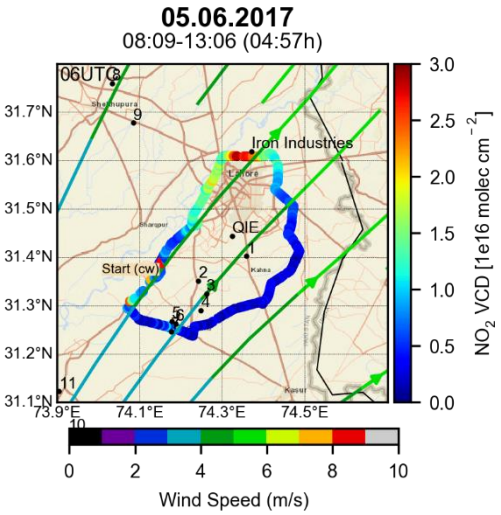
05.06.2017
08:09-13:06 (04:57h)
06UTC
Iron Industries
QIE
Start (cw)
31.7°N
31.6°N
31.5°N
31.4°N
31.3°N
31.2°N
31.1°N
73.9°E
74.1°E
74.3°E
74.5°E
NO2 VCD [1e16 molec cm -2]
Wind Speed (m/s)

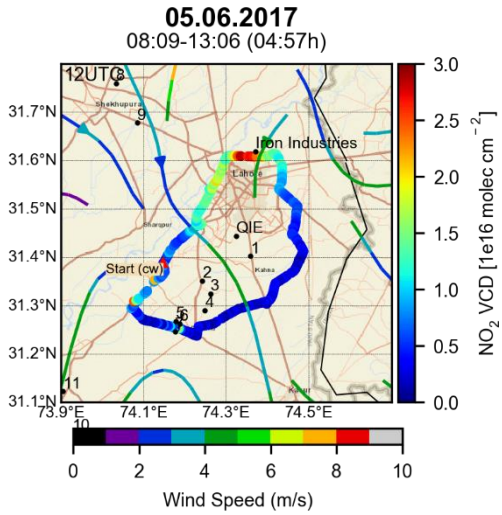
05.06.2017
08:09-13:06 (04:57h)
12UTC
Iron Industries
QIE
Start (cw)
31.7°N
31.6°N
31.5°N
31.4°N
31.3°N
31.2°N
31.1°N
73.9°E
74.1°E
74.3°E
74.5°E
NO2 VCD [1e16 molec cm -2]
Wind Speed (m/s)

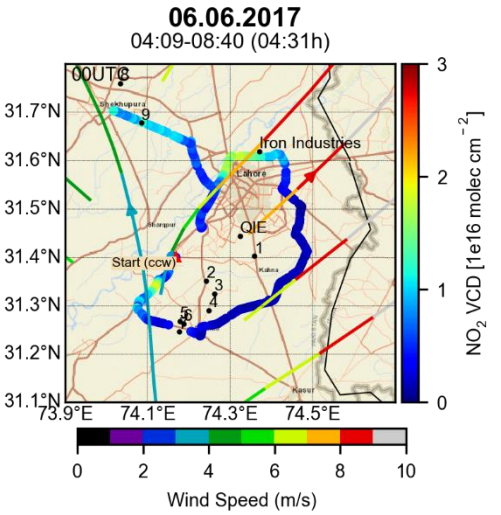
06.06.2017
04:09-08:40 (04:31h)
00UTC
Iron Industries
QIE
Start (ccw)
31.7°N
31.6°N
31.5°N
31.4°N
31.3°N
31.2°N
31.1°N
73.9°E
74.1°E
74.3°E
74.5°E
NO2 VCD [1e16 molec cm -2]
Wind Speed (m/s)

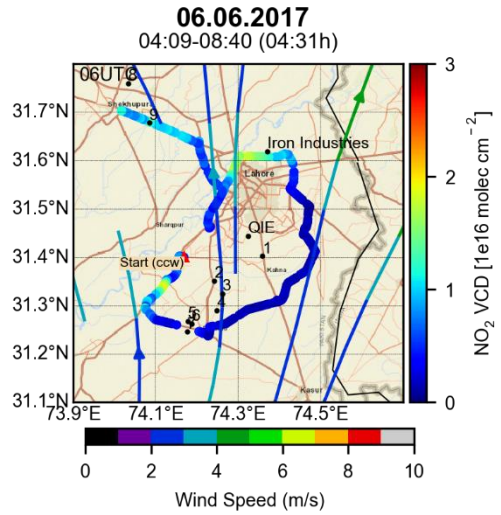
06.06.2017
04:09-08:40 (04:31h)
06UTC
Iron Industries
QIE
Start (ccw)
31.7°N
31.6°N
31.5°N
31.4°N
31.3°N
31.2°N
31.1°N
73.9°E
74.1°E
74.3°E
74.5°E
NO2 VCD [1e16 molec cm -2]
Wind Speed (m/s)

6.3.1.3.B.1.3. 2018 I

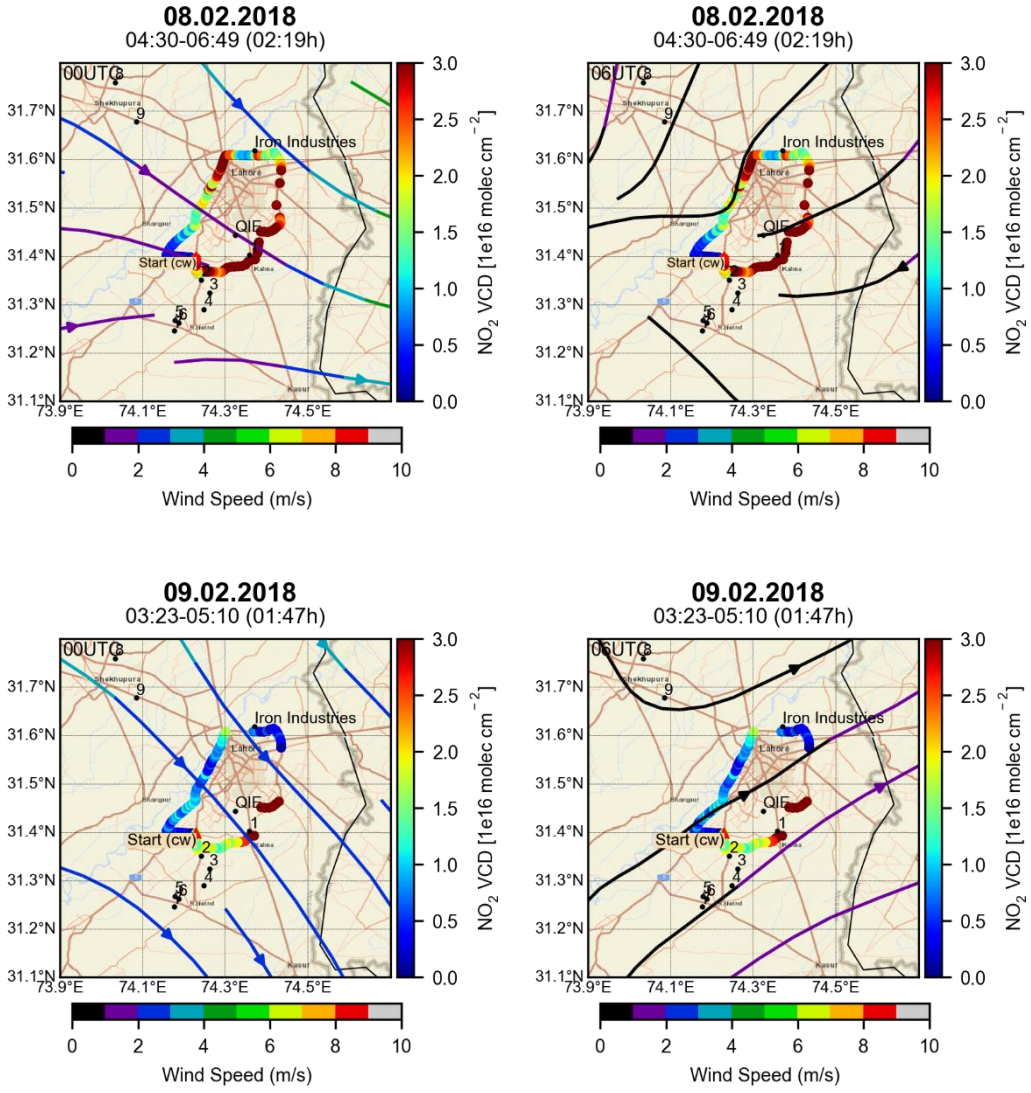

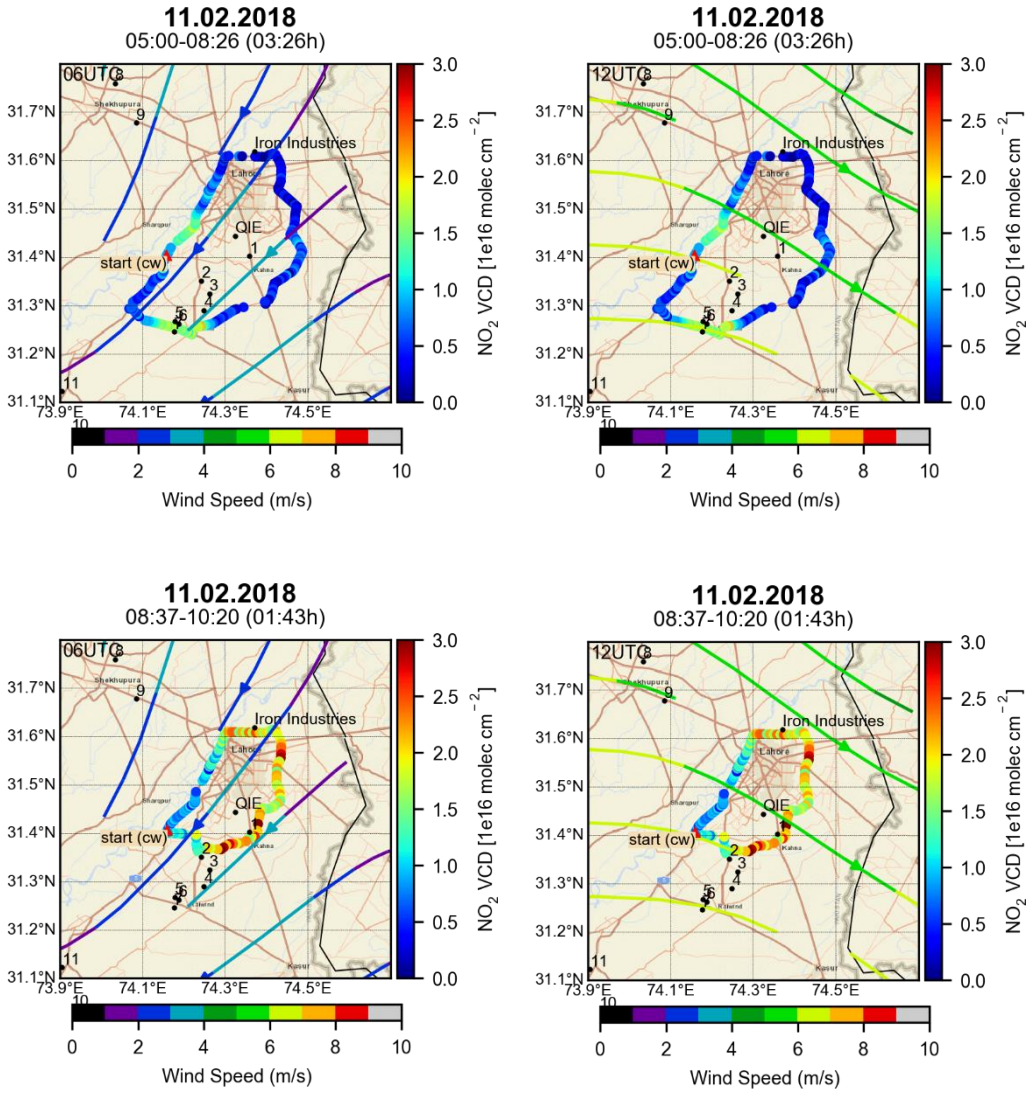
11.02.2018
05:00-08:26 (03:26h)
06UTC
12UTC
Iron Industries
QIE
start (cw)
Wind Speed (m/s)
NO2 VCD [1e16 molec cm-2]
11.02.2018
08:37-10:20 (01:43h)

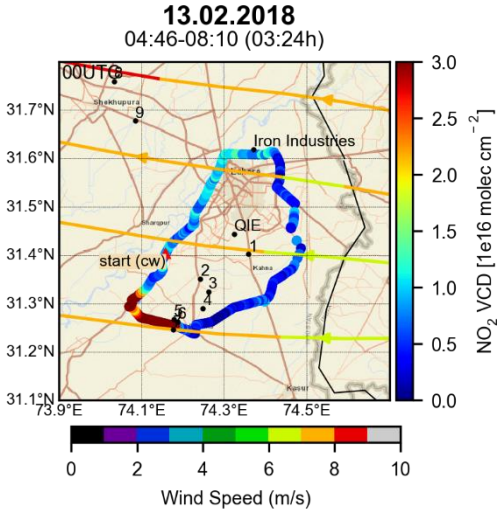
13.02.2018
04:46-08:10 (03:24h)
00UTC
Iron Industries
QIE
start (cw)
1
2
3
4
5
6
9
31.7°N
31.6°N
31.5°N
31.4°N
31.3°N
31.2°N
31.1°N
73.9°E
74.1°E
74.3°E
74.5°E
3.0
2.5
2.0
1.5
1.0
0.5
0.0
NO2 VCD [1e16 molec cm −2]
0
2
4
6
8
10
Wind Speed (m/s)

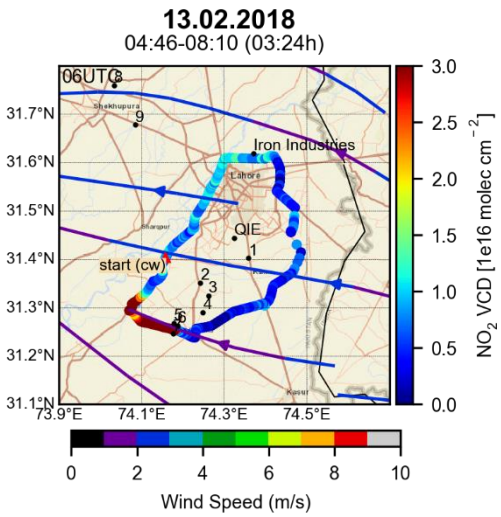
13.02.2018
04:46-08:10 (03:24h)
06UTC
Iron Industries
QIE
start (cw)
1
2
3
4
5
6
9
31.7°N
31.6°N
31.5°N
31.4°N
31.3°N
31.2°N
31.1°N
73.9°E
74.1°E
74.3°E
74.5°E
3.0
2.5
2.0
1.5
1.0
0.5
0.0
NO2 VCD [1e16 molec cm −2]
0
2
4
6
8
10
Wind Speed (m/s)

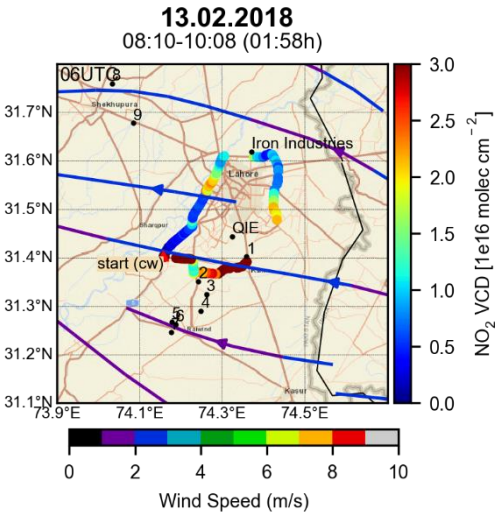
13.02.2018
08:10-10:08 (01:58h)
06UTC
Iron Industries
QIE
start (cw)
1
2
3
4
5
6
9
31.7°N
31.6°N
31.5°N
31.4°N
31.3°N
31.2°N
31.1°N
73.9°E
74.1°E
74.3°E
74.5°E
3.0
2.5
2.0
1.5
1.0
0.5
0.0
NO2 VCD [1e16 molec cm −2]
0
2
4
6
8
10
Wind Speed (m/s)

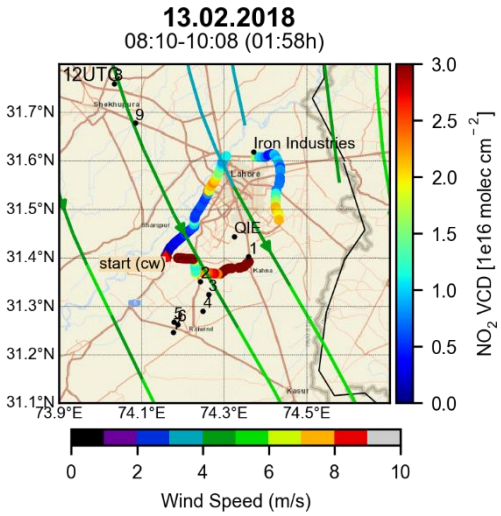
13.02.2018
08:10-10:08 (01:58h)
12UTC
Iron Industries
QIE
start (cw)
1
2
3
4
5
6
9
31.7°N
31.6°N
31.5°N
31.4°N
31.3°N
31.2°N
31.1°N
73.9°E
74.1°E
74.3°E
74.5°E
3.0
2.5
2.0
1.5
1.0
0.5
0.0
NO2 VCD [1e16 molec cm −2]
0
2
4
6
8
10
Wind Speed (m/s)

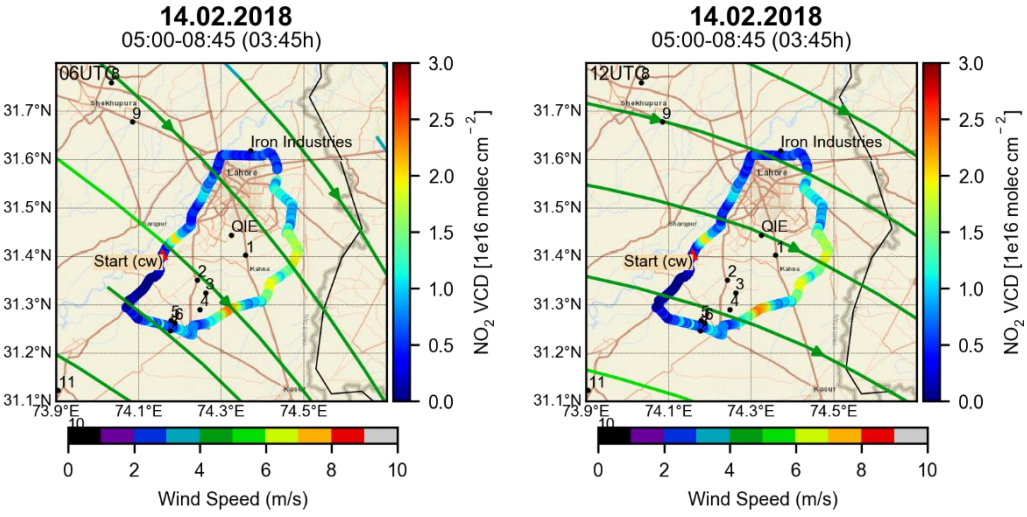
14.02.2018
05:00-08:45 (03:45h)
06UTC
Iron Industries
QIE
Start (cw)
Wind Speed (m/s)
NO2 VCD [1e16 molec cm -2]

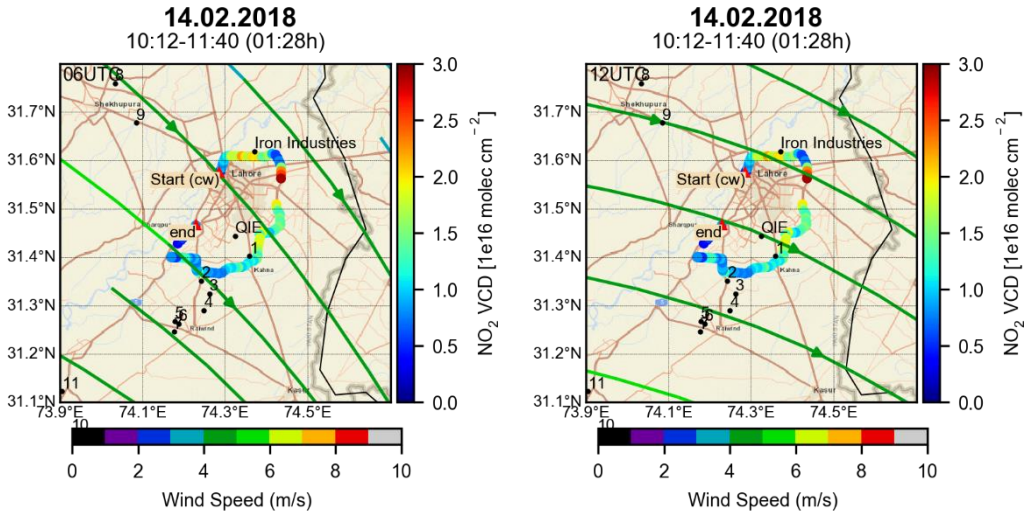
14.02.2018
10:12-11:40 (01:28h)
06UTC
Iron Industries
Start (cw)
end
QIE
Wind Speed (m/s)
NO2 VCD [1e16 molec cm -2]

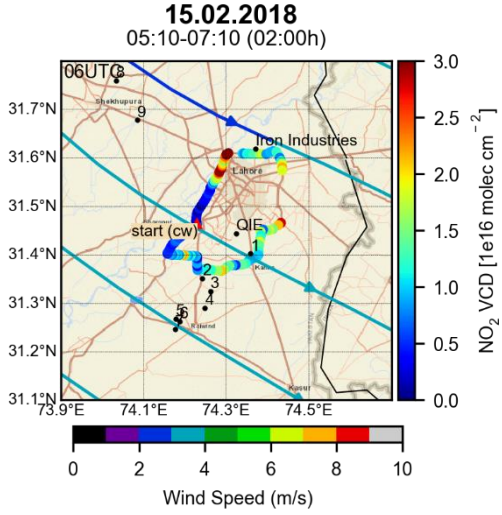
15.02.2018
05:10-07:10 (02:00h)
06UTC
Iron Industries
QIE
start (cw)
Wind Speed (m/s)
NO2 VCD [1e16 molec cm -2]

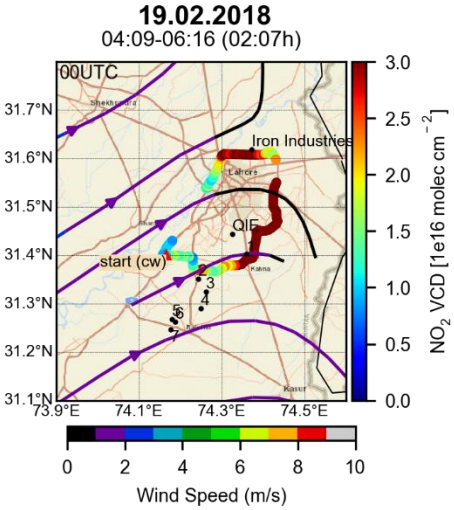
19.02.2018
04:09-06:16 (02:07h)
00UTC
Iron Industries
QIE
start (cw)
Lahore
Kasur
31.7°N
31.6°N
31.5°N
31.4°N
31.3°N
31.2°N
31.1°N
73.9°E
74.1°E
74.3°E
74.5°E
3.0
2.5
2.0
1.5
1.0
0.5
0.0
NO2 VCD [1e16 molec cm −2]
0
2
4
6
8
10
Wind Speed (m/s)

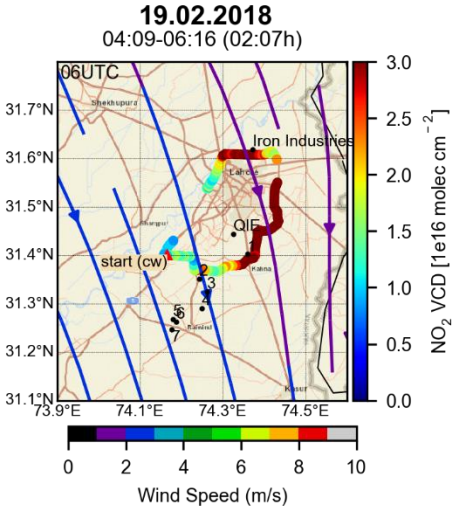
19.02.2018
04:09-06:16 (02:07h)
06UTC
Iron Industries
QIE
start (cw)
Lahore
Kasur
31.7°N
31.6°N
31.5°N
31.4°N
31.3°N
31.2°N
31.1°N
73.9°E
74.1°E
74.3°E
74.5°E
3.0
2.5
2.0
1.5
1.0
0.5
0.0
NO2 VCD [1e16 molec cm −2]
0
2
4
6
8
10
Wind Speed (m/s)

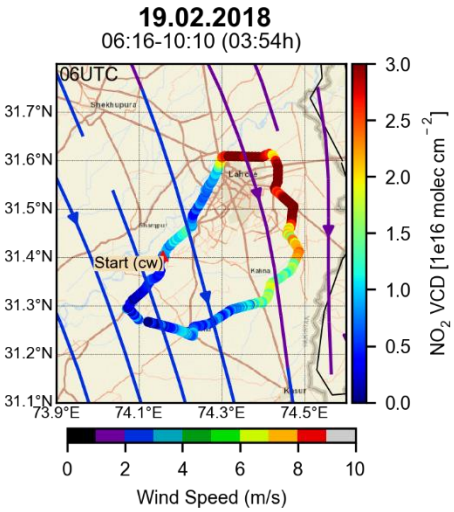
19.02.2018
06:16-10:10 (03:54h)
06UTC
Start (cw)
Lahore
Kasur
31.7°N
31.6°N
31.5°N
31.4°N
31.3°N
31.2°N
31.1°N
73.9°E
74.1°E
74.3°E
74.5°E
3.0
2.5
2.0
1.5
1.0
0.5
0.0
NO2 VCD [1e16 molec cm −2]
0
2
4
6
8
10
Wind Speed (m/s)

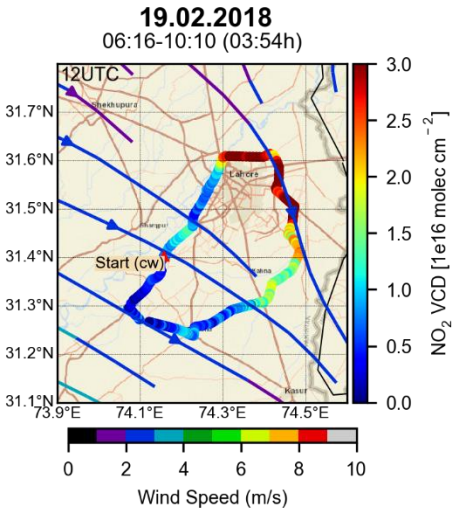
19.02.2018
06:16-10:10 (03:54h)
12UTC
Start (cw)
Lahore
Kasur
31.7°N
31.6°N
31.5°N
31.4°N
31.3°N
31.2°N
31.1°N
73.9°E
74.1°E
74.3°E
74.5°E
3.0
2.5
2.0
1.5
1.0
0.5
0.0
NO2 VCD [1e16 molec cm −2]
0
2
4
6
8
10
Wind Speed (m/s)

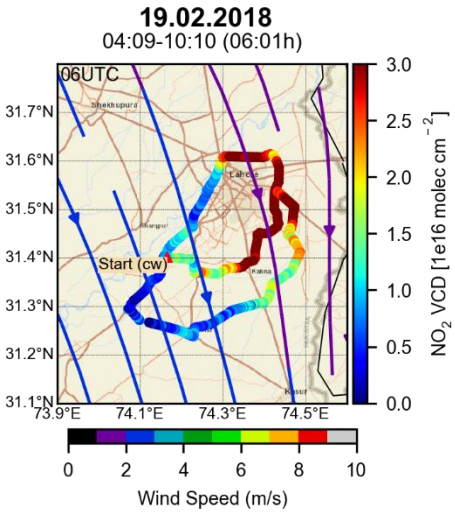
19.02.2018
04:09-10:10 (06:01h)
06UTC
Start (cw)
Lahore
Kasur
31.7°N
31.6°N
31.5°N
31.4°N
31.3°N
31.2°N
31.1°N
73.9°E
74.1°E
74.3°E
74.5°E
3.0
2.5
2.0
1.5
1.0
0.5
0.0
NO2 VCD [1e16 molec cm −2]
0
2
4
6
8
10
Wind Speed (m/s)

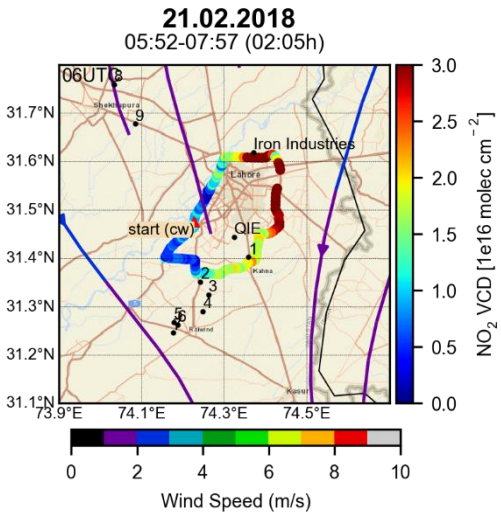
21.02.2018
05:52-07:57 (02:05h)
06UTC
Iron Industries
start (cw)
QIE
Lahore
Kasur
Kharian
Sheikhupura
31.7°N
31.6°N
31.5°N
31.4°N
31.3°N
31.2°N
31.1°N
73.9°E
74.1°E
74.3°E
74.5°E
NO2 VCD [1e16 molec cm−2]
0.0
0.5
1.0
1.5
2.0
2.5
3.0
Wind Speed (m/s)
0
2
4
6
8
10

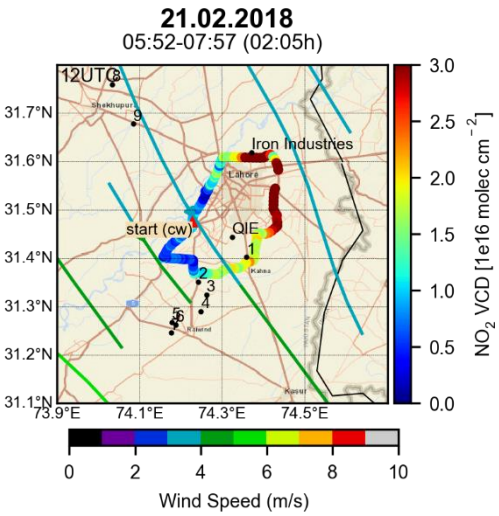
21.02.2018
05:52-07:57 (02:05h)
12UTC
Iron Industries
start (cw)
QIE
Lahore
Kasur
Kharian
Sheikhupura
31.7°N
31.6°N
31.5°N
31.4°N
31.3°N
31.2°N
31.1°N
73.9°E
74.1°E
74.3°E
74.5°E
NO2 VCD [1e16 molec cm−2]
0.0
0.5
1.0
1.5
2.0
2.5
3.0
Wind Speed (m/s)
0
2
4
6
8
10

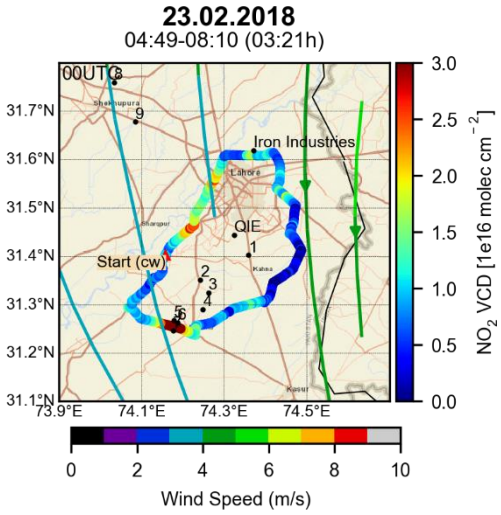
23.02.2018
04:49-08:10 (03:21h)
00UTC
Iron Industries
Start (cw)
QIE
Lahore
Kasur
Kharian
Sheikhupura
31.7°N
31.6°N
31.5°N
31.4°N
31.3°N
31.2°N
31.1°N
73.9°E
74.1°E
74.3°E
74.5°E
NO2 VCD [1e16 molec cm−2]
0.0
0.5
1.0
1.5
2.0
2.5
3.0
Wind Speed (m/s)
0
2
4
6
8
10

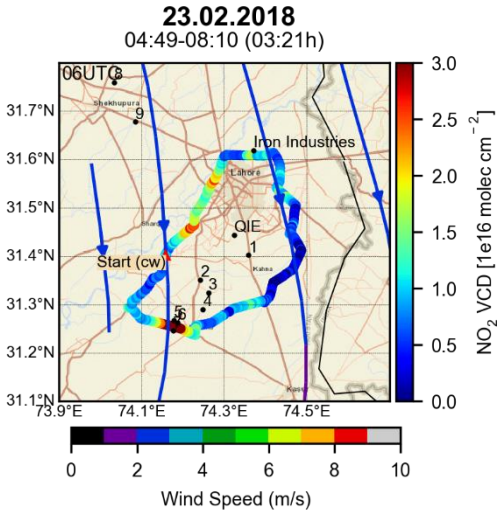
23.02.2018
04:49-08:10 (03:21h)
06UTC
Iron Industries
Start (cw)
QIE
Lahore
Kasur
Kharian
Sheikhupura
31.7°N
31.6°N
31.5°N
31.4°N
31.3°N
31.2°N
31.1°N
73.9°E
74.1°E
74.3°E
74.5°E
NO2 VCD [1e16 molec cm−2]
0.0
0.5
1.0
1.5
2.0
2.5
3.0
Wind Speed (m/s)
0
2
4
6
8
10

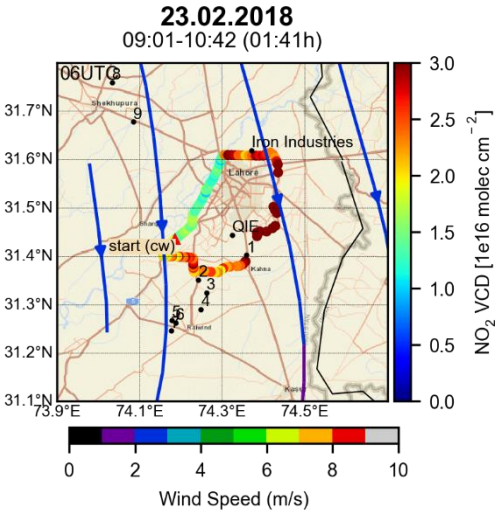
23.02.2018
09:01-10:42 (01:41h)
06UTC
Iron Industries
start (cw)
QIE
Lahore
Kasur
Kharian
Sheikhupura
31.7°N
31.6°N
31.5°N
31.4°N
31.3°N
31.2°N
31.1°N
73.9°E
74.1°E
74.3°E
74.5°E
NO2 VCD [1e16 molec cm−2]
0.0
0.5
1.0
1.5
2.0
2.5
3.0
Wind Speed (m/s)
0
2
4
6
8
10

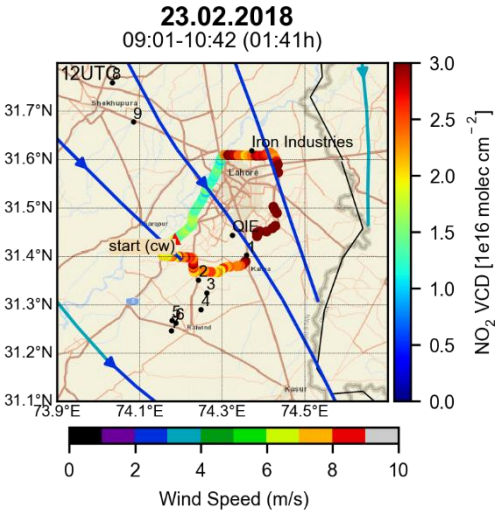
23.02.2018
09:01-10:42 (01:41h)
12UTC
Iron Industries
start (cw)
QIE
Lahore
Kasur
Kharian
Sheikhupura
31.7°N
31.6°N
31.5°N
31.4°N
31.3°N
31.2°N
31.1°N
73.9°E
74.1°E
74.3°E
74.5°E
NO2 VCD [1e16 molec cm−2]
0.0
0.5
1.0
1.5
2.0
2.5
3.0
Wind Speed (m/s)
0
2
4
6
8
10

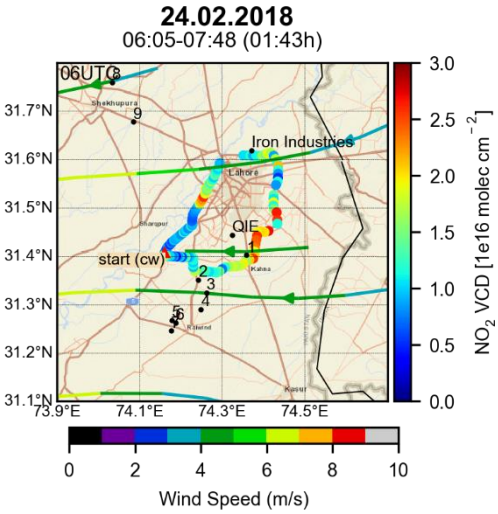
24.02.2018
06:05-07:48 (01:43h)
06UTC
Iron Industries
QIE
start (cw)
Lahore
Sheikhupura
Kasur
31.7°N
31.6°N
31.5°N
31.4°N
31.3°N
31.2°N
31.1°N
73.9°E
74.1°E
74.3°E
74.5°E
NO2 VCD [1e16 molec cm−2]
Wind Speed (m/s)

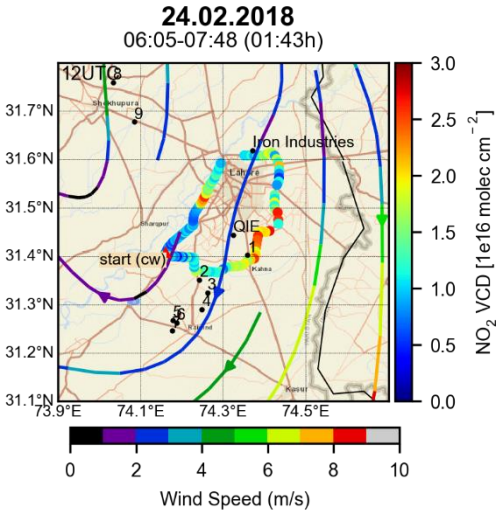
24.02.2018
06:05-07:48 (01:43h)
12UTC
Iron Industries
QIE
start (cw)
Lahore
Sheikhupura
Kasur
31.7°N
31.6°N
31.5°N
31.4°N
31.3°N
31.2°N
31.1°N
73.9°E
74.1°E
74.3°E
74.5°E
NO2 VCD [1e16 molec cm−2]
Wind Speed (m/s)

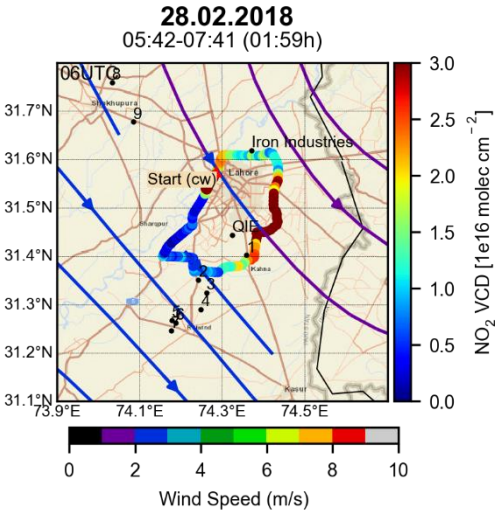
28.02.2018
05:42-07:41 (01:59h)
06UTC
Iron Industries
Start (cw)
QIE
Lahore
Sheikhupura
Kasur
31.7°N
31.6°N
31.5°N
31.4°N
31.3°N
31.2°N
31.1°N
73.9°E
74.1°E
74.3°E
74.5°E
NO2 VCD [1e16 molec cm−2]
Wind Speed (m/s)

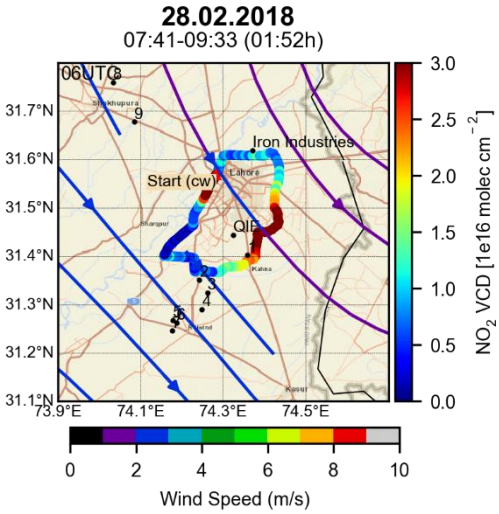
28.02.2018
07:41-09:33 (01:52h)
06UTC
Iron Industries
Start (cw)
QIE
Lahore
Sheikhupura
Kasur
31.7°N
31.6°N
31.5°N
31.4°N
31.3°N
31.2°N
31.1°N
73.9°E
74.1°E
74.3°E
74.5°E
NO2 VCD [1e16 molec cm−2]
Wind Speed (m/s)

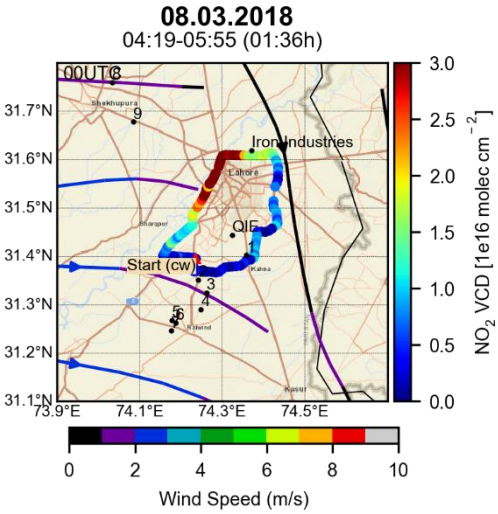
08.03.2018
04:19-05:55 (01:36h)
00UTC
Iron Industries
QIE
Start (cw)
Lahore
Sheikhupura
Kasur
31.7°N
31.6°N
31.5°N
31.4°N
31.3°N
31.2°N
31.1°N
73.9°E
74.1°E
74.3°E
74.5°E
NO2 VCD [1e16 molec cm−2]
Wind Speed (m/s)

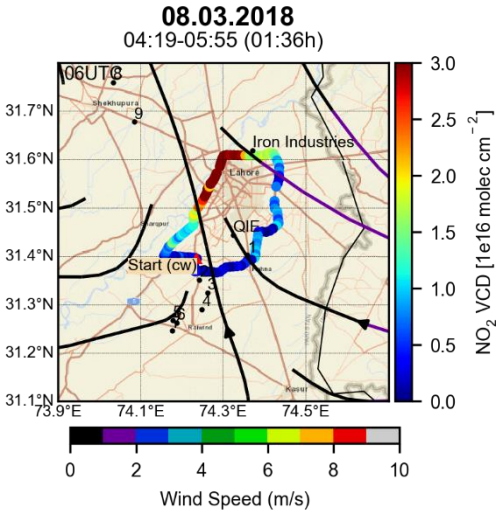
08.03.2018
04:19-05:55 (01:36h)
06UTC
Iron Industries
QIE
Start (cw)
Lahore
Sheikhupura
Kasur
31.7°N
31.6°N
31.5°N
31.4°N
31.3°N
31.2°N
31.1°N
73.9°E
74.1°E
74.3°E
74.5°E
NO2 VCD [1e16 molec cm−2]
Wind Speed (m/s)

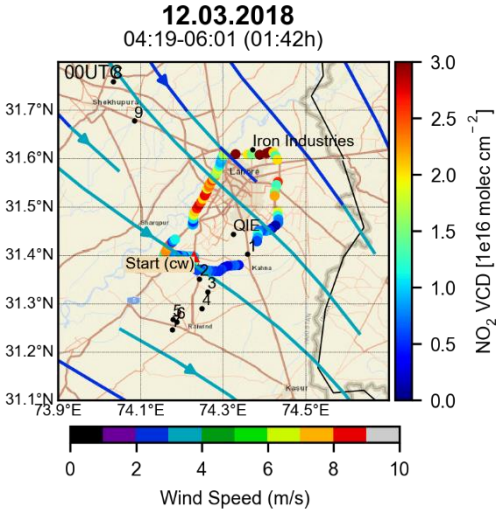
12.03.2018
04:19-06:01 (01:42h)
00UTC
Iron Industries
QIE
Start (cw)
Wind Speed (m/s)
NO2 VCD [1e16 molec cm -2]

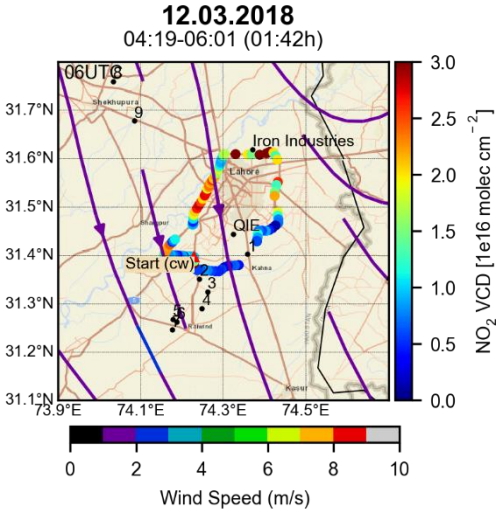
12.03.2018
04:19-06:01 (01:42h)
06UTC
Iron Industries
QIE
Start (cw)
Wind Speed (m/s)
NO2 VCD [1e16 molec cm -2]

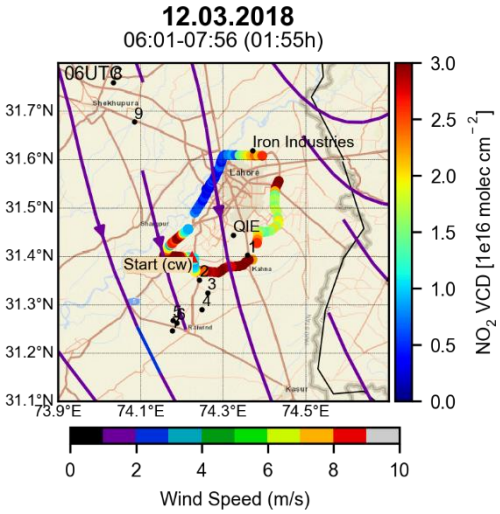
12.03.2018
06:01-07:56 (01:55h)
06UTC
Iron Industries
QIE
Start (cw)
Wind Speed (m/s)
NO2 VCD [1e16 molec cm -2]

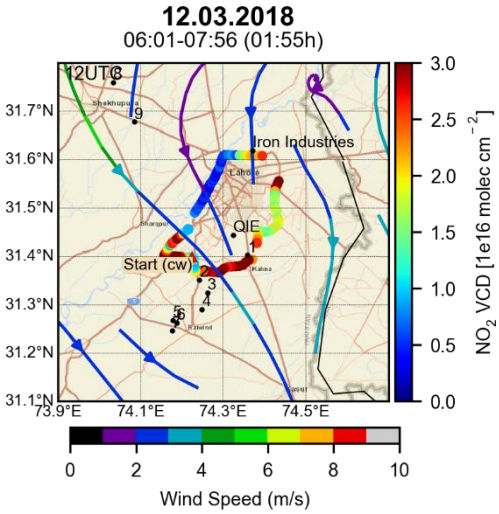
12.03.2018
06:01-07:56 (01:55h)
12UTC
Iron Industries
QIE
Start (cw)
Wind Speed (m/s)
NO2 VCD [1e16 molec cm -2]

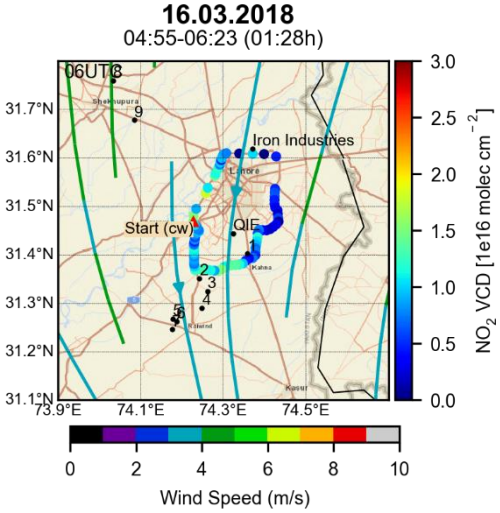
16.03.2018
04:55-06:23 (01:28h)
06UTC
Iron Industries
QIE
Start (cw)
Wind Speed (m/s)
NO2 VCD [1e16 molec cm -2]

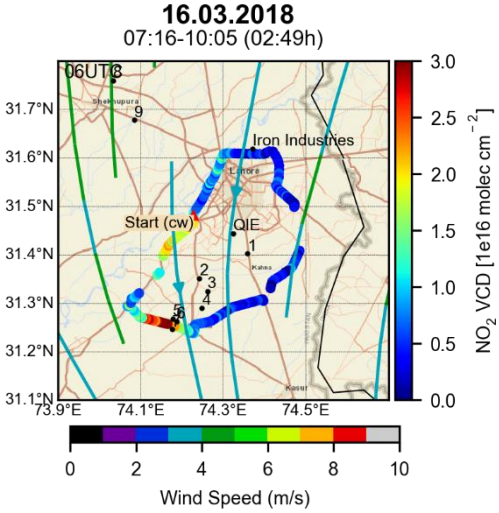
16.03.2018
07:16-10:05 (02:49h)
06UTC
Iron Industries
QIE
Start (cw)
Wind Speed (m/s)
NO2 VCD [1e16 molec cm -2]

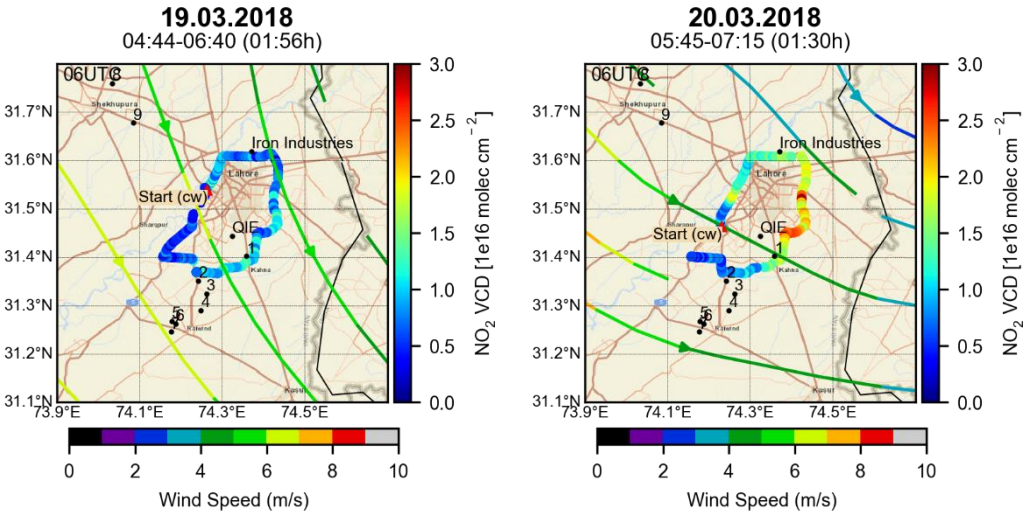
19.03.2018
04:44-06:40 (01:56h)
20.03.2018
05:45-07:15 (01:30h)
06UTC
Iron Industries
Start (cw)
QIE
Lahore
Sharqpur
Kasur
Kalasa
Khalid
Shekhupura
31.7°N
31.6°N
31.5°N
31.4°N
31.3°N
31.2°N
31.1°N
73.9°E
74.1°E
74.3°E
74.5°E
NO2 VCD [1e16 molec cm−2]
Wind Speed (m/s)

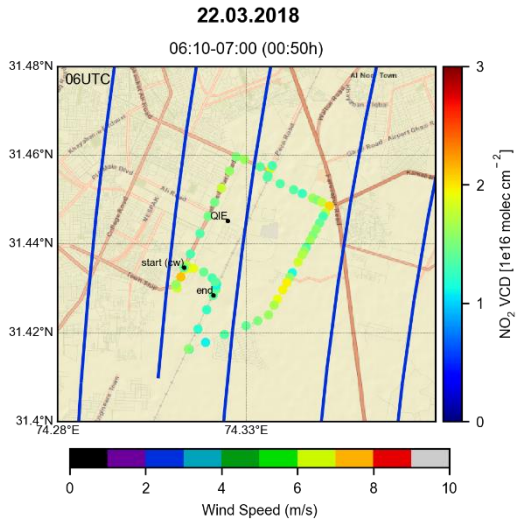
22.03.2018
06:10-07:00 (00:50h)
06UTC
QIE
start (cw)
end
31.48°N
31.46°N
31.44°N
31.42°N
31.4°N
74.28°E
74.33°E
NO2 VCD [1e16 molec cm−2]
Wind Speed (m/s)

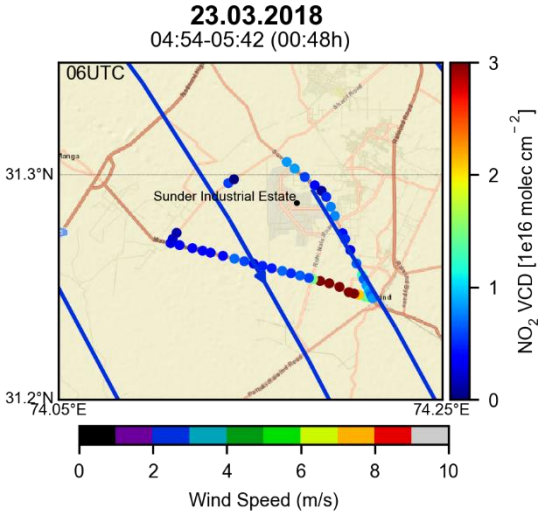
23.03.2018
04:54-05:42 (00:48h)
06UTC
Sunder Industrial Estate
31.3°N
31.2°N
74.05°E
74.25°E
NO2 VCD [1e16 molec cm−2]
Wind Speed (m/s)

B.2 SO_2 Spatial Distributions

SO_2 vertical column densities (VCDs) for the days grouped under category III, performed around Lahore during 2015-II, 2017 and 2018-I campaigns.

6.3.1.4.B.2.1. 2017

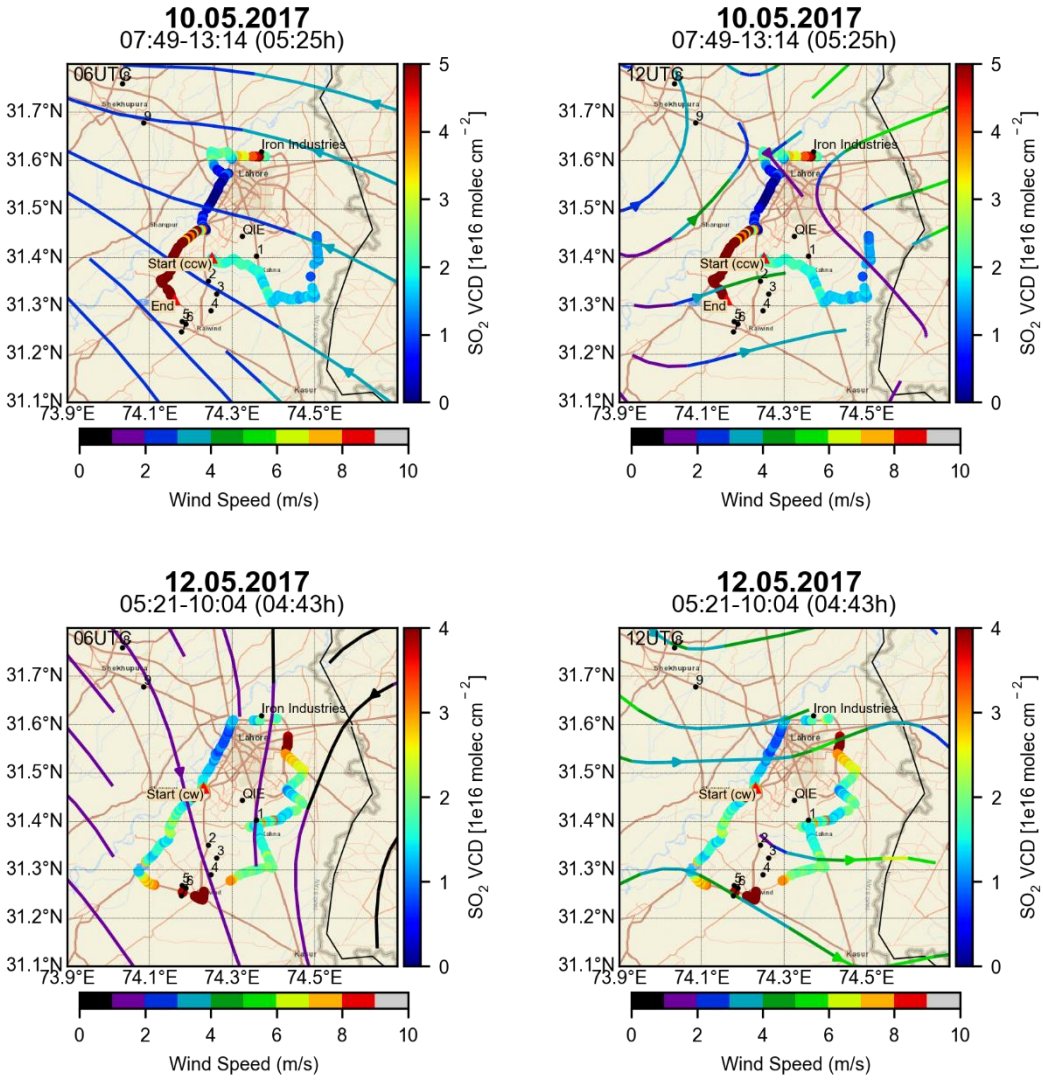

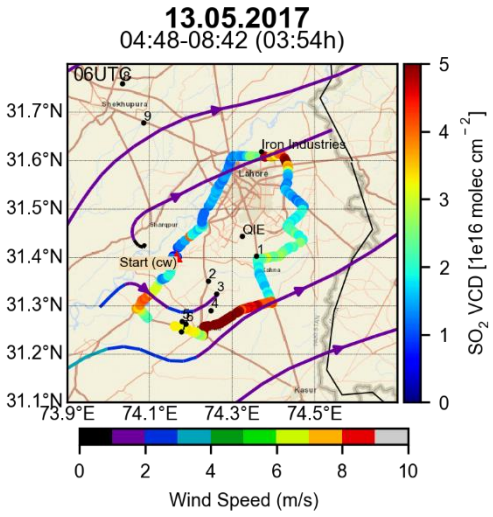
13.05.2017
04:48-08:42 (03:54h)
06UTC
Iron Industries
Lahore
OIE
Start (cw)
31.7°N
31.6°N
31.5°N
31.4°N
31.3°N
31.2°N
31.1°N
73.9°E
74.1°E
74.3°E
74.5°E
SO2 VCD [1e16 molec cm−2]
Wind Speed (m/s)

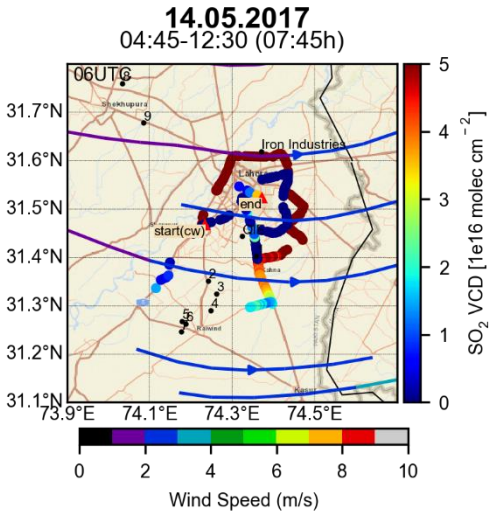
14.05.2017
04:45-12:30 (07:45h)
06UTC
Iron Industries
Lahore
end
start(cw)
31.7°N
31.6°N
31.5°N
31.4°N
31.3°N
31.2°N
31.1°N
73.9°E
74.1°E
74.3°E
74.5°E
SO2 VCD [1e16 molec cm−2]
Wind Speed (m/s)

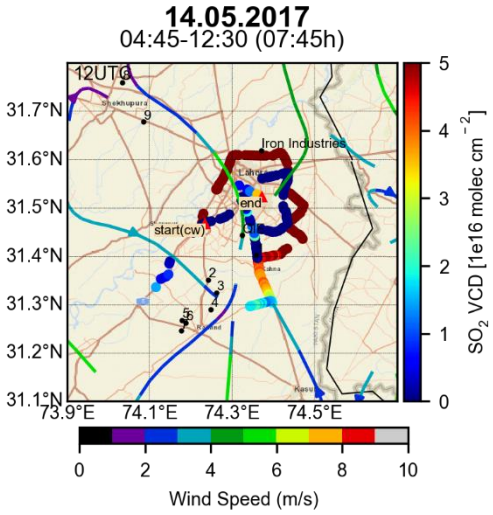
14.05.2017
04:45-12:30 (07:45h)
12UTC
Iron Industries
Lahore
end
start(cw)
31.7°N
31.6°N
31.5°N
31.4°N
31.3°N
31.2°N
31.1°N
73.9°E
74.1°E
74.3°E
74.5°E
SO2 VCD [1e16 molec cm−2]
Wind Speed (m/s)

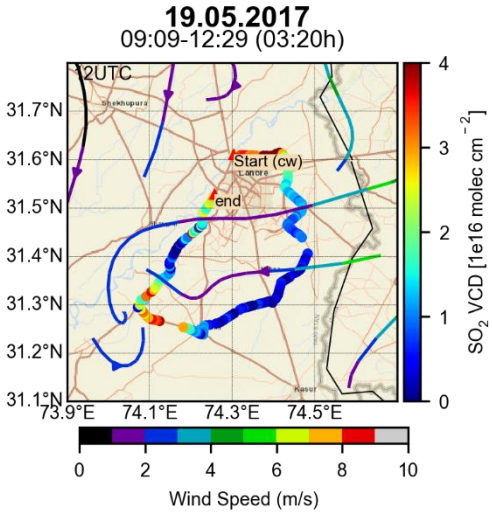
19.05.2017
09:09-12:29 (03:20h)
12UTC
Start (cw)
Lahore
end
31.7°N
31.6°N
31.5°N
31.4°N
31.3°N
31.2°N
31.1°N
73.9°E
74.1°E
74.3°E
74.5°E
SO2 VCD [1e16 molec cm−2]
Wind Speed (m/s)

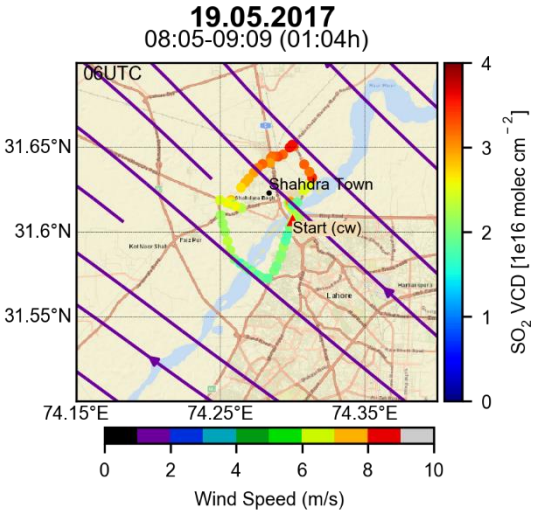
19.05.2017
08:05-09:09 (01:04h)
06UTC
Shahdra Town
Start (cw)
Lahore
31.65°N
31.6°N
31.55°N
74.15°E
74.25°E
74.35°E
SO2 VCD [1e16 molec cm−2]
Wind Speed (m/s)

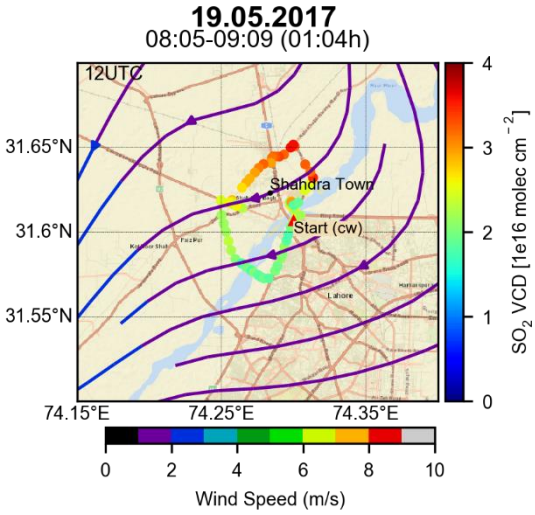
19.05.2017
08:05-09:09 (01:04h)
12UTC
Shahdra Town
Start (cw)
Lahore
31.65°N
31.6°N
31.55°N
74.15°E
74.25°E
74.35°E
SO2 VCD [1e16 molec cm−2]
Wind Speed (m/s)

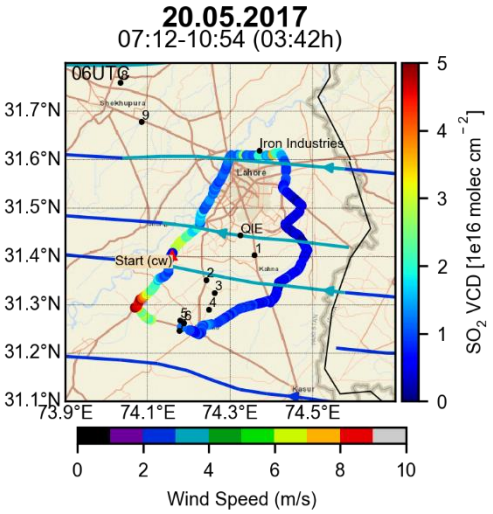
20.05.2017
07:12-10:54 (03:42h)
06UTC
Iron Industries
QIE
Start (cw)
Lahore
Kasur
31.7°N
31.6°N
31.5°N
31.4°N
31.3°N
31.2°N
31.1°N
73.9°E
74.1°E
74.3°E
74.5°E
SO2 VCD [1e16 molec cm-2]
Wind Speed (m/s)

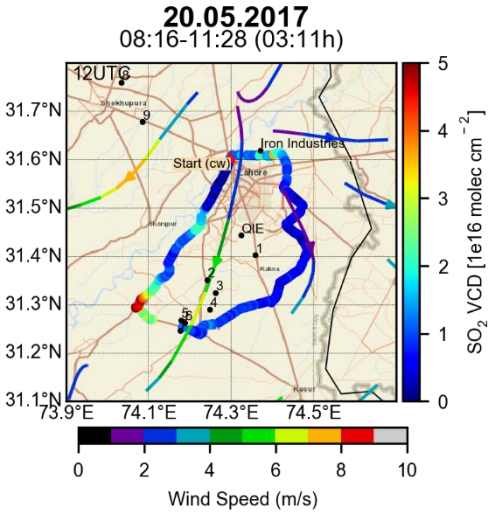
20.05.2017
08:16-11:28 (03:11h)
12UTC
Iron Industries
QIE
Start (cw)
Lahore
Kasur
31.7°N
31.6°N
31.5°N
31.4°N
31.3°N
31.2°N
31.1°N
73.9°E
74.1°E
74.3°E
74.5°E
SO2 VCD [1e16 molec cm-2]
Wind Speed (m/s)

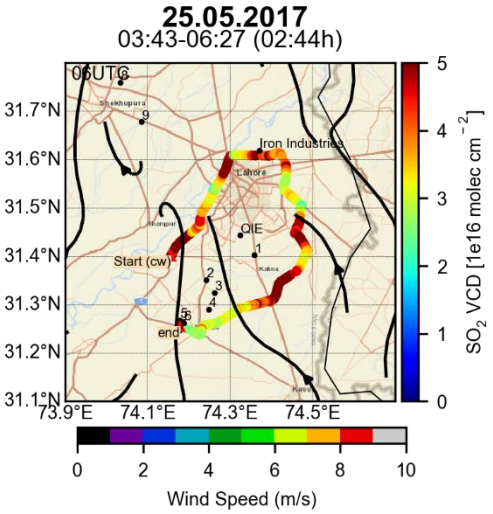
25.05.2017
03:43-06:27 (02:44h)
06UTC
Iron Industries
QIE
Start (cw)
end
Lahore
Kasur
31.7°N
31.6°N
31.5°N
31.4°N
31.3°N
31.2°N
31.1°N
73.9°E
74.1°E
74.3°E
74.5°E
SO2 VCD [1e16 molec cm-2]
Wind Speed (m/s)

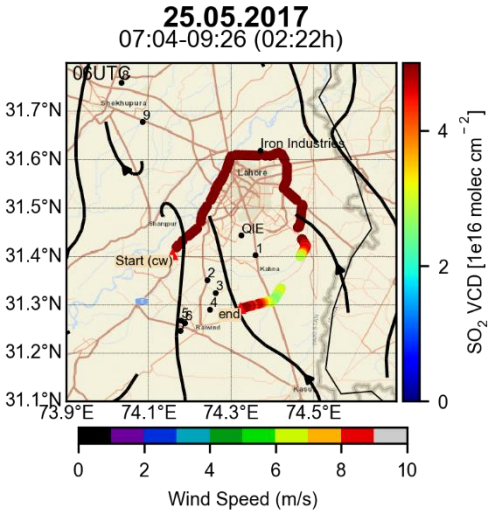
25.05.2017
07:04-09:26 (02:22h)
06UTC
Iron Industries
QIE
Start (cw)
end
Lahore
Kasur
31.7°N
31.6°N
31.5°N
31.4°N
31.3°N
31.2°N
31.1°N
73.9°E
74.1°E
74.3°E
74.5°E
SO2 VCD [1e16 molec cm-2]
Wind Speed (m/s)

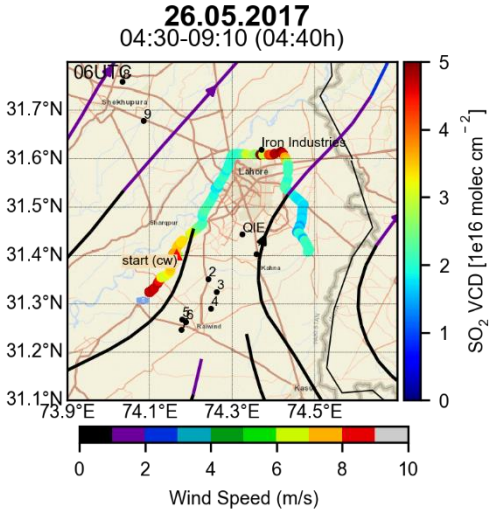
26.05.2017
04:30-09:10 (04:40h)
06UTC
Iron Industries
QIE
start (cw)
Lahore
Kasur
31.7°N
31.6°N
31.5°N
31.4°N
31.3°N
31.2°N
31.1°N
73.9°E
74.1°E
74.3°E
74.5°E
SO2 VCD [1e16 molec cm-2]
Wind Speed (m/s)

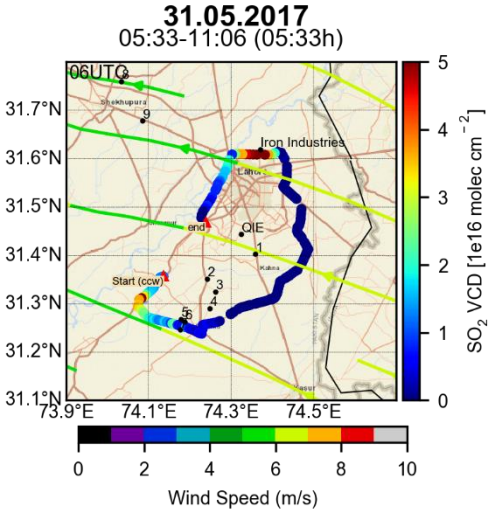
31.05.2017
05:33-11:06 (05:33h)
06UTC
Iron Industries
QIE
end
Start (ccw)
Lahore
Kasur
31.7°N
31.6°N
31.5°N
31.4°N
31.3°N
31.2°N
31.1°N
73.9°E
74.1°E
74.3°E
74.5°E
SO2 VCD [1e16 molec cm-2]
Wind Speed (m/s)

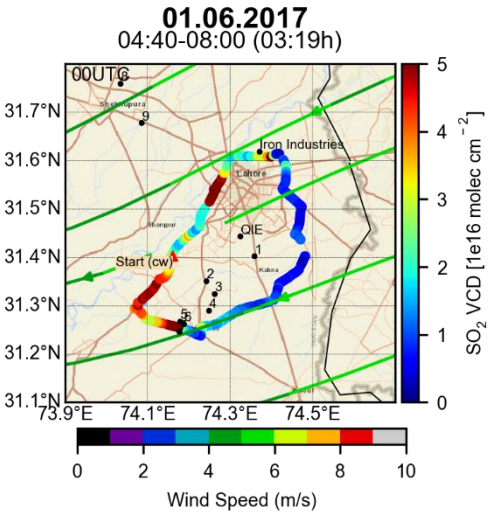
01.06.2017
04:40-08:00 (03:19h)
00UTC
Iron Industries
Lahore
OIE
Start (cw)
31.7°N
31.6°N
31.5°N
31.4°N
31.3°N
31.2°N
31.1°N
73.9°E
74.1°E
74.3°E
74.5°E
SO2 VCD [1e16 molec cm−2]
Wind Speed (m/s)

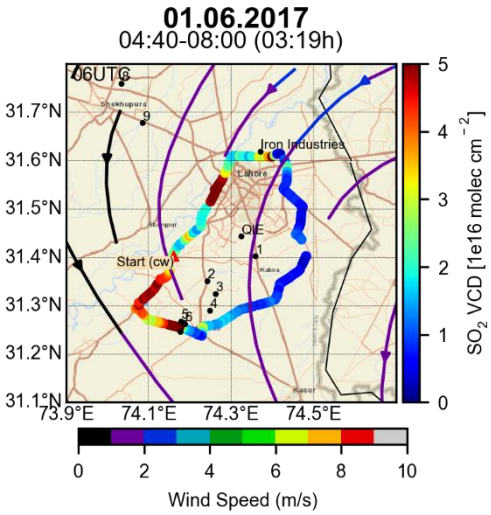
01.06.2017
04:40-08:00 (03:19h)
06UTC
Iron Industries
Lahore
OIE
Start (cw)
31.7°N
31.6°N
31.5°N
31.4°N
31.3°N
31.2°N
31.1°N
73.9°E
74.1°E
74.3°E
74.5°E
SO2 VCD [1e16 molec cm−2]
Wind Speed (m/s)

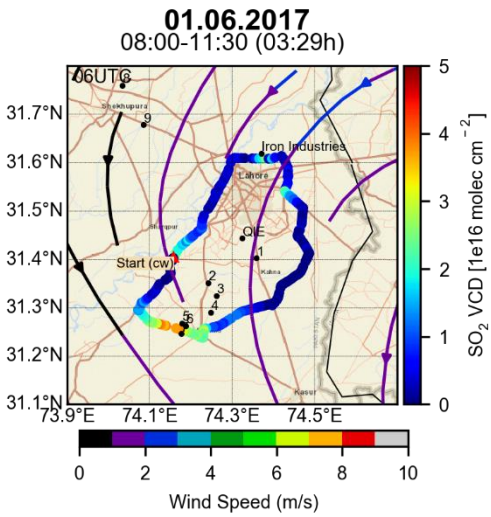
01.06.2017
08:00-11:30 (03:29h)
06UTC
Iron Industries
Lahore
OIE
Start (cw)
31.7°N
31.6°N
31.5°N
31.4°N
31.3°N
31.2°N
31.1°N
73.9°E
74.1°E
74.3°E
74.5°E
SO2 VCD [1e16 molec cm−2]
Wind Speed (m/s)

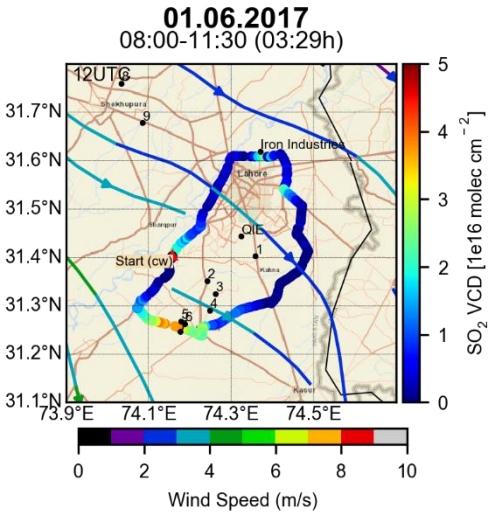
01.06.2017
08:00-11:30 (03:29h)
12UTC
Iron Industries
Lahore
OIE
Start (cw)
31.7°N
31.6°N
31.5°N
31.4°N
31.3°N
31.2°N
31.1°N
73.9°E
74.1°E
74.3°E
74.5°E
SO2 VCD [1e16 molec cm−2]
Wind Speed (m/s)

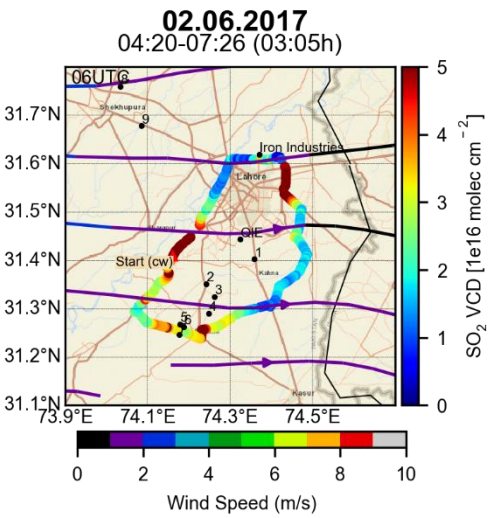
02.06.2017
04:20-07:26 (03:05h)
06UTC
Iron Industries
Lahore
OIE
Start (cw)
31.7°N
31.6°N
31.5°N
31.4°N
31.3°N
31.2°N
31.1°N
73.9°E
74.1°E
74.3°E
74.5°E
SO2 VCD [1e16 molec cm−2]
Wind Speed (m/s)

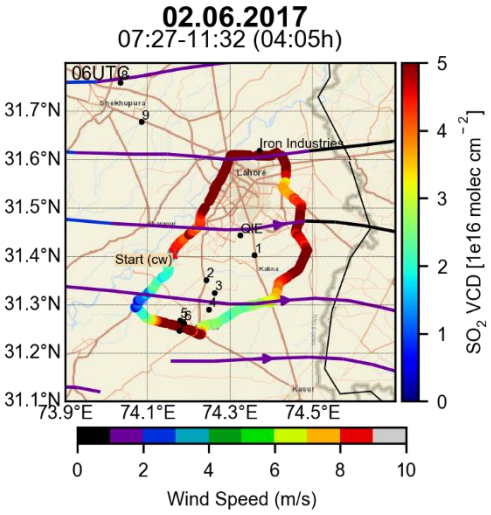
02.06.2017
07:27-11:32 (04:05h)
06UTC
Iron Industries
Lahore
OIE
Start (cw)
31.7°N
31.6°N
31.5°N
31.4°N
31.3°N
31.2°N
31.1°N
73.9°E
74.1°E
74.3°E
74.5°E
SO2 VCD [1e16 molec cm−2]
Wind Speed (m/s)

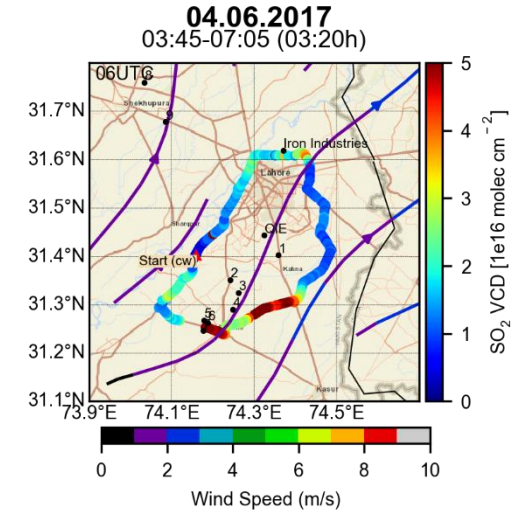
04.06.2017
03:45-07:05 (03:20h)
06UTC
Iron Industries
QIE
Start (cw)
31.7°N
31.6°N
31.5°N
31.4°N
31.3°N
31.2°N
31.1°N
73.9°E
74.1°E
74.3°E
74.5°E
SO2 VCD [1e16 molec cm-2]
Wind Speed (m/s)

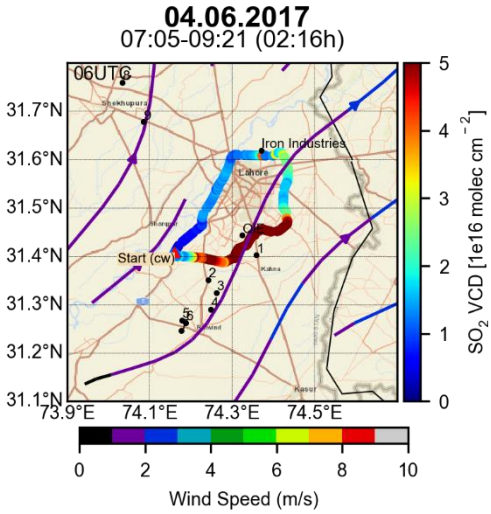
04.06.2017
07:05-09:21 (02:16h)
06UTC
Iron Industries
QIE
Start (cw)
31.7°N
31.6°N
31.5°N
31.4°N
31.3°N
31.2°N
31.1°N
73.9°E
74.1°E
74.3°E
74.5°E
SO2 VCD [1e16 molec cm-2]
Wind Speed (m/s)

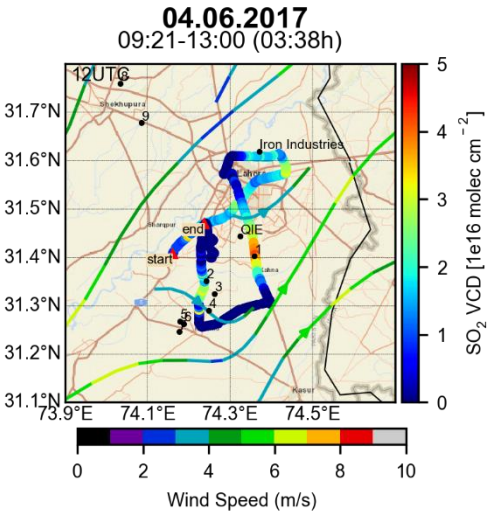
04.06.2017
09:21-13:00 (03:38h)
12UTC
Iron Industries
QIE
end
start
31.7°N
31.6°N
31.5°N
31.4°N
31.3°N
31.2°N
31.1°N
73.9°E
74.1°E
74.3°E
74.5°E
SO2 VCD [1e16 molec cm-2]
Wind Speed (m/s)

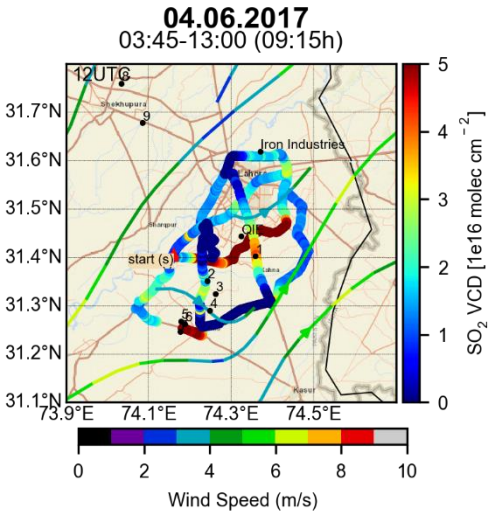
04.06.2017
03:45-13:00 (09:15h)
12UTC
Iron Industries
QIE
start (s)
31.7°N
31.6°N
31.5°N
31.4°N
31.3°N
31.2°N
31.1°N
73.9°E
74.1°E
74.3°E
74.5°E
SO2 VCD [1e16 molec cm-2]
Wind Speed (m/s)

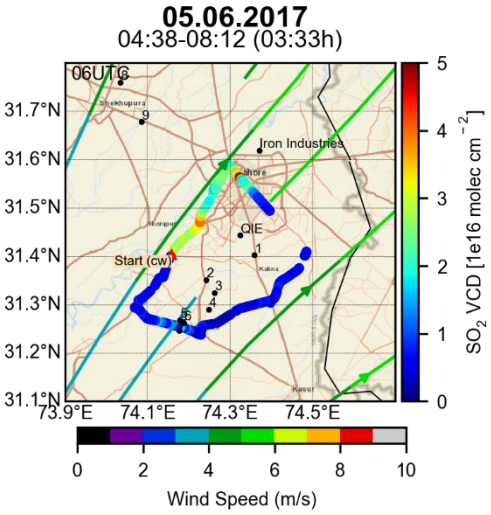
05.06.2017
04:38-08:12 (03:33h)
06UTC
Iron Industries
QIE
Start (cw)
31.7°N
31.6°N
31.5°N
31.4°N
31.3°N
31.2°N
31.1°N
73.9°E
74.1°E
74.3°E
74.5°E
SO2 VCD [1e16 molec cm-2]
Wind Speed (m/s)

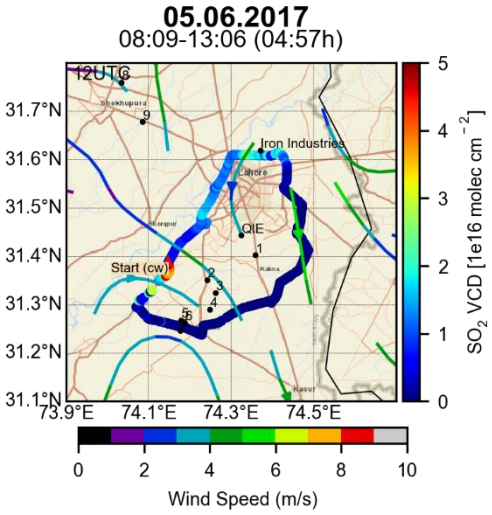
05.06.2017
08:09-13:06 (04:57h)
12UTC
Iron Industries
QIE
Start (cw)
31.7°N
31.6°N
31.5°N
31.4°N
31.3°N
31.2°N
31.1°N
73.9°E
74.1°E
74.3°E
74.5°E
SO2 VCD [1e16 molec cm-2]
Wind Speed (m/s)

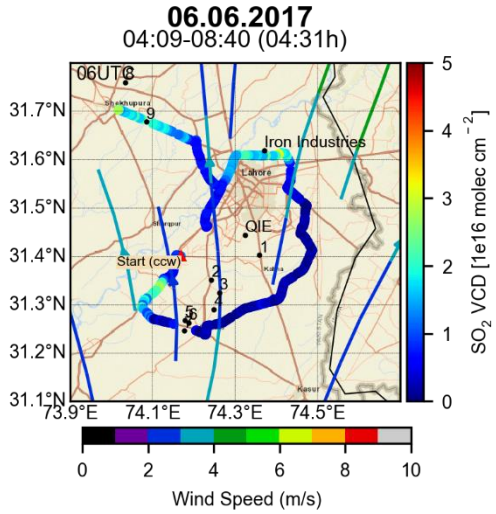

6.3.1.5.B.2.2. 2018 I

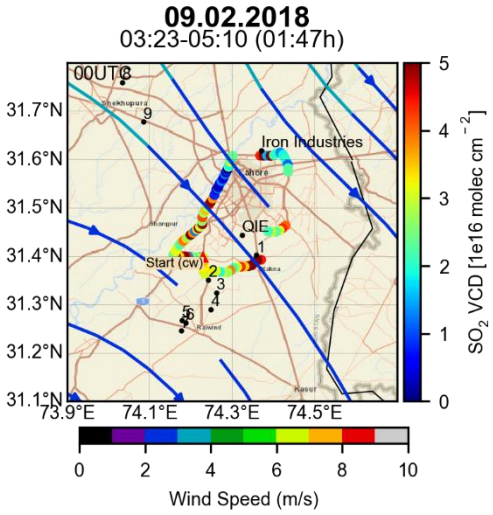

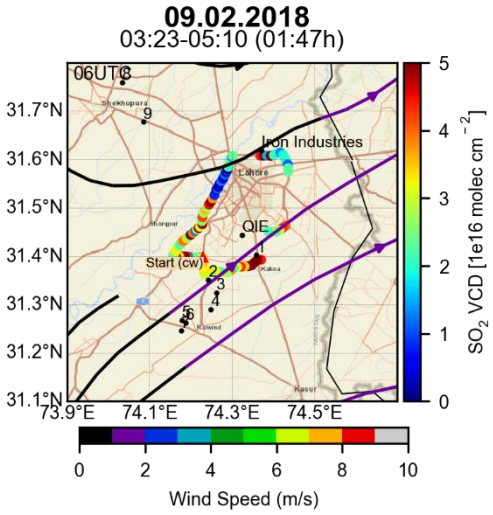

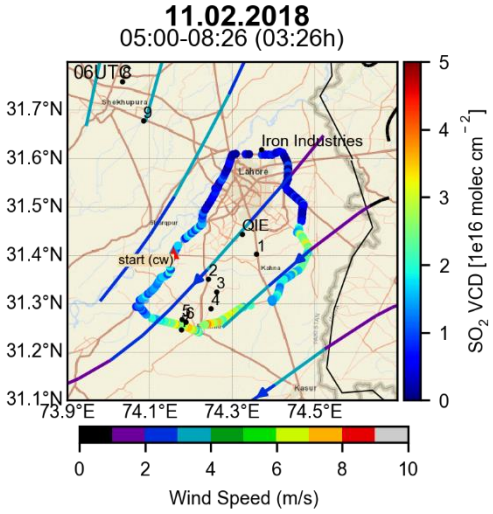

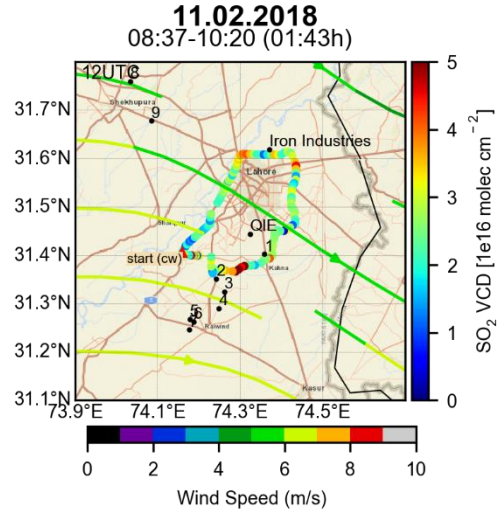

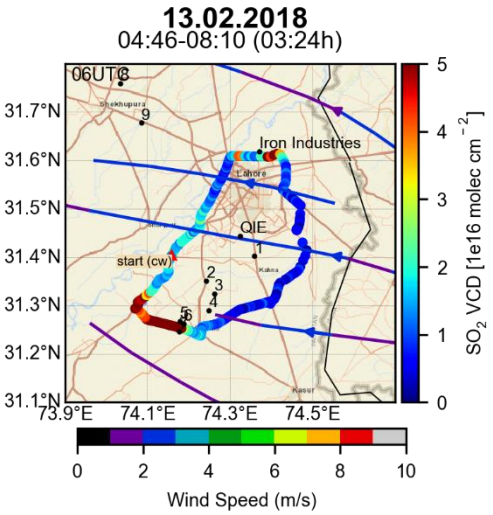
13.02.2018
04:46-08:10 (03:24h)
06UTC
Iron Industries
QIE
start (cw)
Lahore
Kasur
31.7°N
31.6°N
31.5°N
31.4°N
31.3°N
31.2°N
31.1°N
73.9°E
74.1°E
74.3°E
74.5°E
SO2 VCD [1e16 molec cm −2]
Wind Speed (m/s)

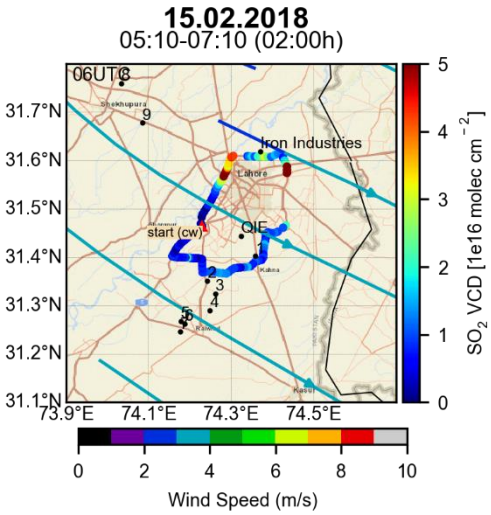
15.02.2018
05:10-07:10 (02:00h)
06UTC
Iron Industries
QIE
start (cw)
Lahore
Kasur
31.7°N
31.6°N
31.5°N
31.4°N
31.3°N
31.2°N
31.1°N
73.9°E
74.1°E
74.3°E
74.5°E
SO2 VCD [1e16 molec cm −2]
Wind Speed (m/s)

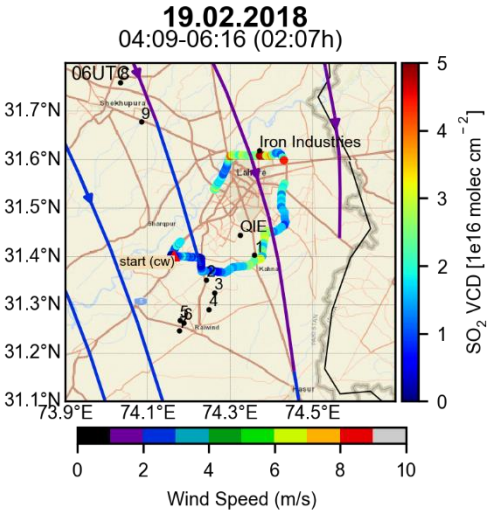
19.02.2018
04:09-06:16 (02:07h)
06UTC
Iron Industries
QIE
start (cw)
Lahore
Kasur
31.7°N
31.6°N
31.5°N
31.4°N
31.3°N
31.2°N
31.1°N
73.9°E
74.1°E
74.3°E
74.5°E
SO2 VCD [1e16 molec cm −2]
Wind Speed (m/s)

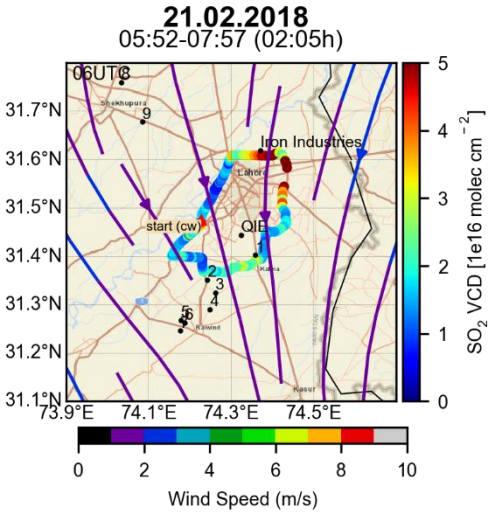
21.02.2018
05:52-07:57 (02:05h)
06UTC
Iron Industries
QIE
start (cw)
Lahore
Kasur
31.7°N
31.6°N
31.5°N
31.4°N
31.3°N
31.2°N
31.1°N
73.9°E
74.1°E
74.3°E
74.5°E
SO2 VCD [1e16 molec cm −2]
Wind Speed (m/s)

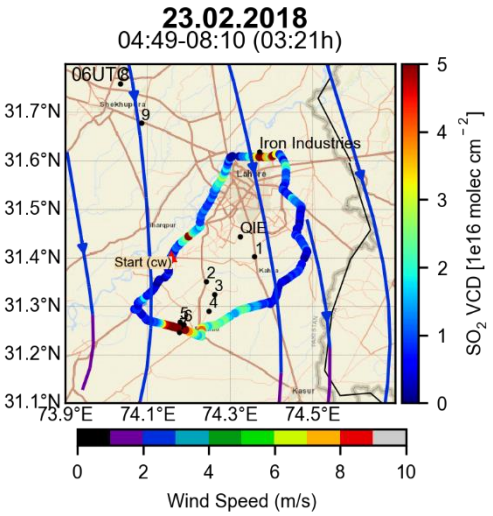
23.02.2018
04:49-08:10 (03:21h)
06UTC
Iron Industries
QIE
Start (cw)
Lahore
Kasur
31.7°N
31.6°N
31.5°N
31.4°N
31.3°N
31.2°N
31.1°N
73.9°E
74.1°E
74.3°E
74.5°E
SO2 VCD [1e16 molec cm −2]
Wind Speed (m/s)

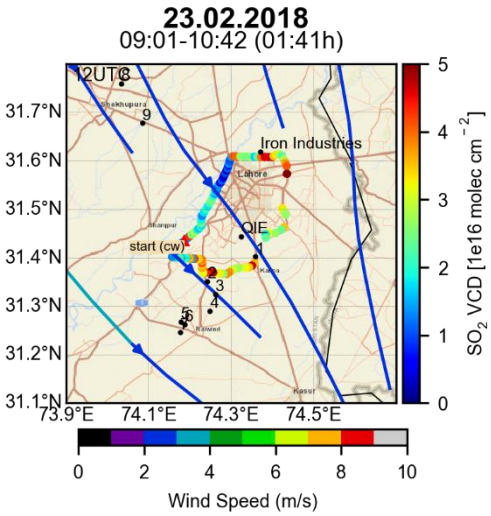
23.02.2018
09:01-10:42 (01:41h)
12UTC
Iron Industries
QIE
start (cw)
Lahore
Kasur
31.7°N
31.6°N
31.5°N
31.4°N
31.3°N
31.2°N
31.1°N
73.9°E
74.1°E
74.3°E
74.5°E
SO2 VCD [1e16 molec cm −2]
Wind Speed (m/s)

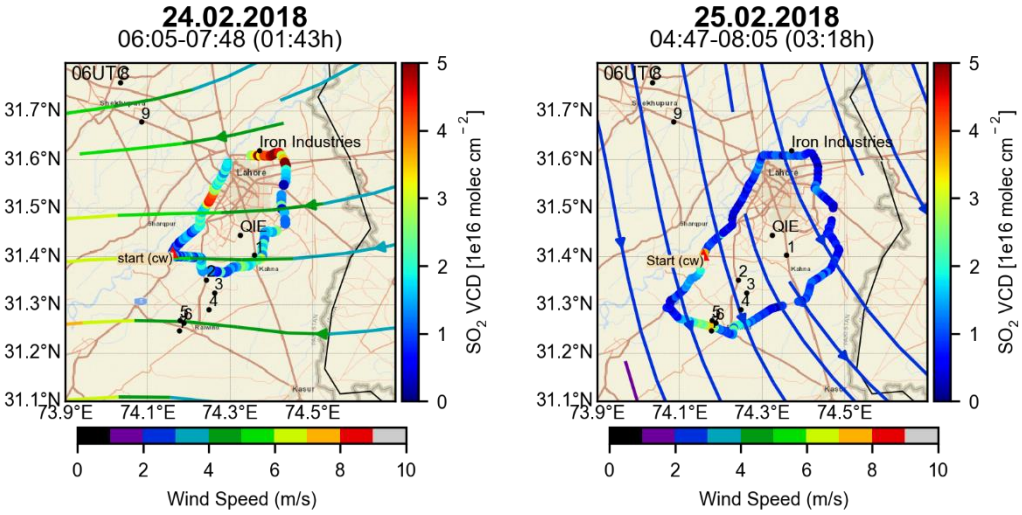
24.02.2018
06:05-07:48 (01:43h)
06UTC
Iron Industries
QIE
start (cw)
Lahore
Kasur
31.7°N
31.6°N
31.5°N
31.4°N
31.3°N
31.2°N
31.1°N
73.9°E
74.1°E
74.3°E
74.5°E
SO2 VCD [1e16 molec cm−2]
Wind Speed (m/s)

25.02.2018
04:47-08:05 (03:18h)
06UTC
Iron Industries
QIE
Start (cw)
Lahore
Kasur
31.7°N
31.6°N
31.5°N
31.4°N
31.3°N
31.2°N
31.1°N
73.9°E
74.1°E
74.3°E
74.5°E
SO2 VCD [1e16 molec cm−2]
Wind Speed (m/s)

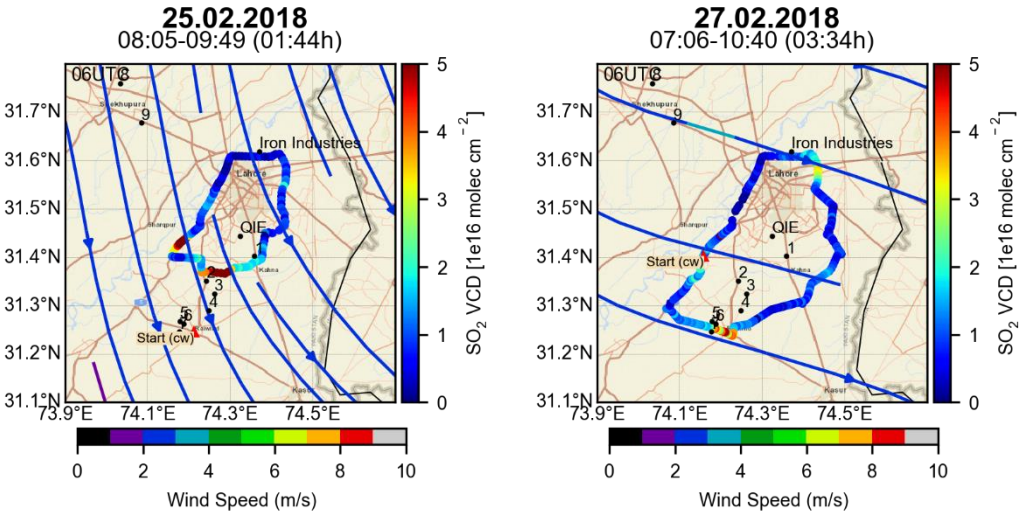
25.02.2018
08:05-09:49 (01:44h)
06UTC
Iron Industries
QIE
Start (cw)
Lahore
Kasur
31.7°N
31.6°N
31.5°N
31.4°N
31.3°N
31.2°N
31.1°N
73.9°E
74.1°E
74.3°E
74.5°E
SO2 VCD [1e16 molec cm−2]
Wind Speed (m/s)

27.02.2018
07:06-10:40 (03:34h)
06UTC
Iron Industries
QIE
Start (cw)
Lahore
Kasur
31.7°N
31.6°N
31.5°N
31.4°N
31.3°N
31.2°N
31.1°N
73.9°E
74.1°E
74.3°E
74.5°E
SO2 VCD [1e16 molec cm−2]
Wind Speed (m/s)

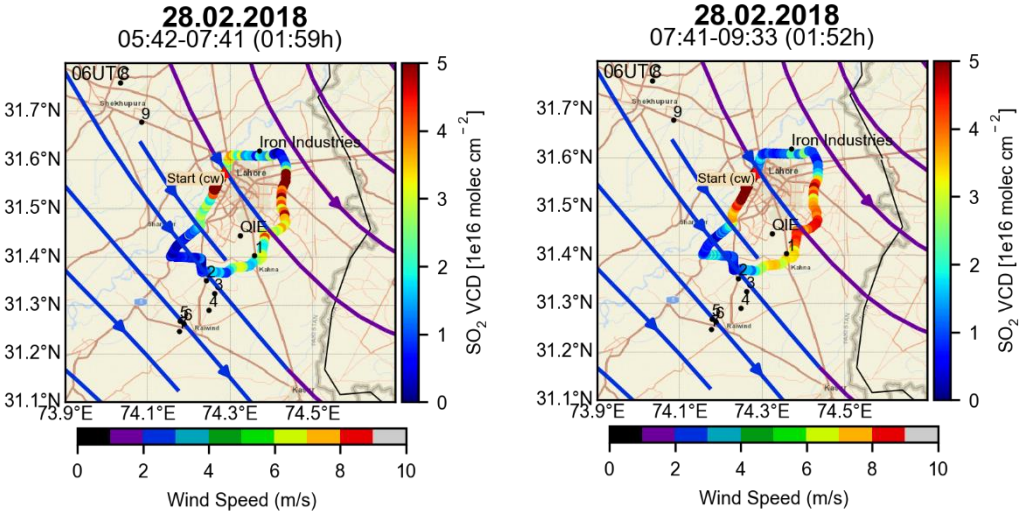
28.02.2018
05:42-07:41 (01:59h)
06UTC
Iron Industries
Start (cw)
QIE
Lahore
Kasur
31.7°N
31.6°N
31.5°N
31.4°N
31.3°N
31.2°N
31.1°N
73.9°E
74.1°E
74.3°E
74.5°E
SO2 VCD [1e16 molec cm−2]
Wind Speed (m/s)

28.02.2018
07:41-09:33 (01:52h)
06UTC
Iron Industries
Start (cw)
QIE
Lahore
Kasur
31.7°N
31.6°N
31.5°N
31.4°N
31.3°N
31.2°N
31.1°N
73.9°E
74.1°E
74.3°E
74.5°E
SO2 VCD [1e16 molec cm−2]
Wind Speed (m/s)

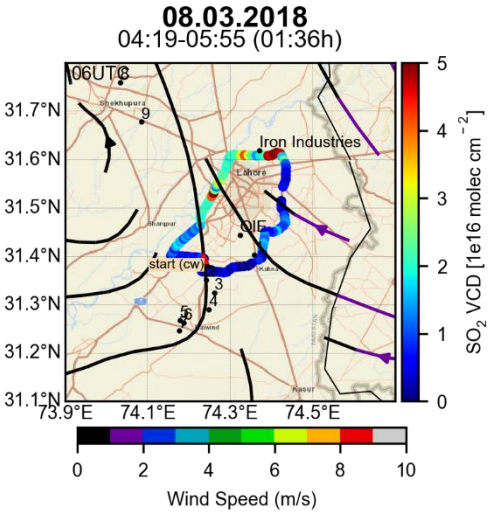
08.03.2018
04:19-05:55 (01:36h)
06UTC
Iron Industries
QIE
start (cw)
Lahore
Kasur
31.7°N
31.6°N
31.5°N
31.4°N
31.3°N
31.2°N
31.1°N
73.9°E
74.1°E
74.3°E
74.5°E
SO2 VCD [1e16 molec cm−2]
Wind Speed (m/s)

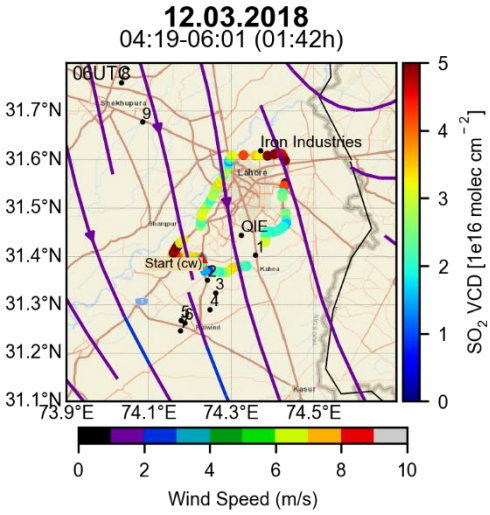
12.03.2018
04:19-06:01 (01:42h)
06UTC
Iron Industries
QIE
Start (cw)
Lahore
Kasur
31.7°N
31.6°N
31.5°N
31.4°N
31.3°N
31.2°N
31.1°N
73.9°E
74.1°E
74.3°E
74.5°E
SO2 VCD [1e16 molec cm−2]
Wind Speed (m/s)

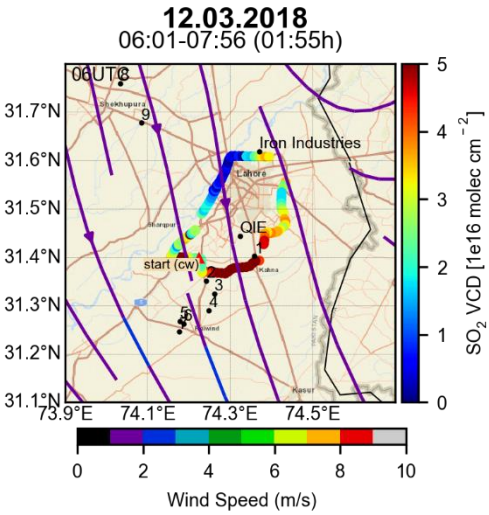
12.03.2018
06:01-07:56 (01:55h)
06UTC
Iron Industries
QIE
start (cw)
Lahore
Kasur
31.7°N
31.6°N
31.5°N
31.4°N
31.3°N
31.2°N
31.1°N
73.9°E
74.1°E
74.3°E
74.5°E
SO2 VCD [1e16 molec cm−2]
Wind Speed (m/s)

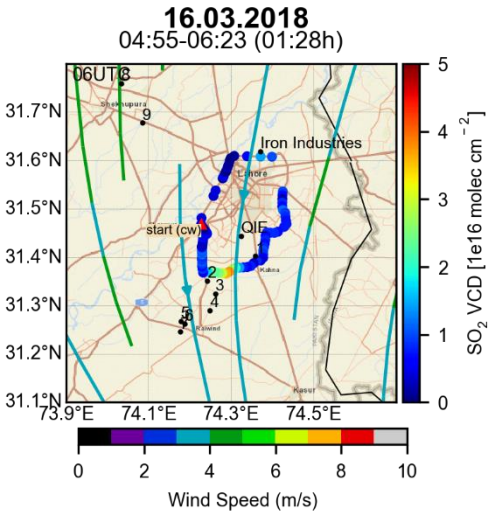
16.03.2018
04:55-06:23 (01:28h)
06UTC
Iron Industries
QIE
start (cw)
Lahore
Kasur
31.7°N
31.6°N
31.5°N
31.4°N
31.3°N
31.2°N
31.1°N
73.9°E
74.1°E
74.3°E
74.5°E
SO2 VCD [1e16 molec cm−2]
Wind Speed (m/s)

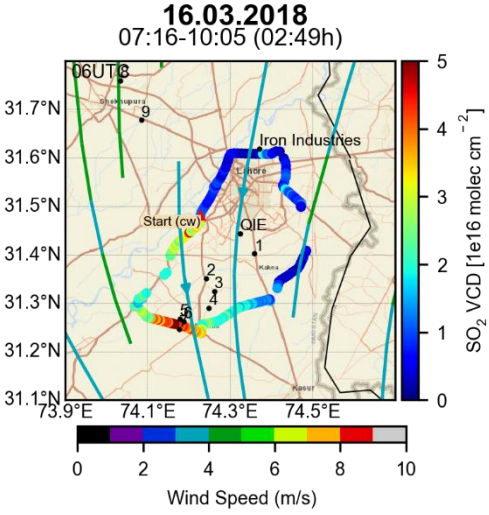
16.03.2018
07:16-10:05 (02:49h)
06UTC
Iron Industries
QIE
Start (cw)
Lahore
Kasur
31.7°N
31.6°N
31.5°N
31.4°N
31.3°N
31.2°N
31.1°N
73.9°E
74.1°E
74.3°E
74.5°E
SO2 VCD [1e16 molec cm−2]
Wind Speed (m/s)

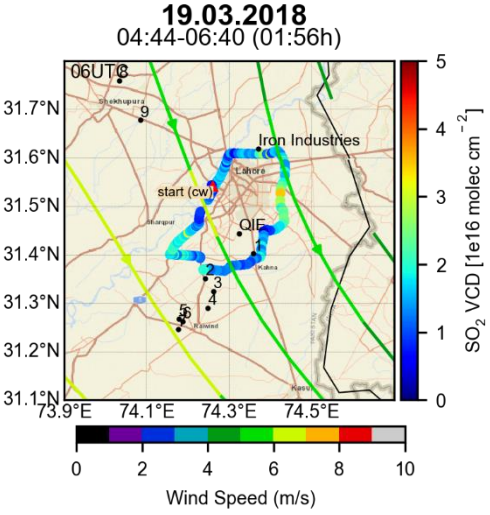
19.03.2018
04:44-06:40 (01:56h)
06UTC
Iron Industries
QIE
start (cw)
Lahore
Kasur
31.7°N
31.6°N
31.5°N
31.4°N
31.3°N
31.2°N
31.1°N
73.9°E
74.1°E
74.3°E
74.5°E
SO2 VCD [1e16 molec cm−2]
Wind Speed (m/s)

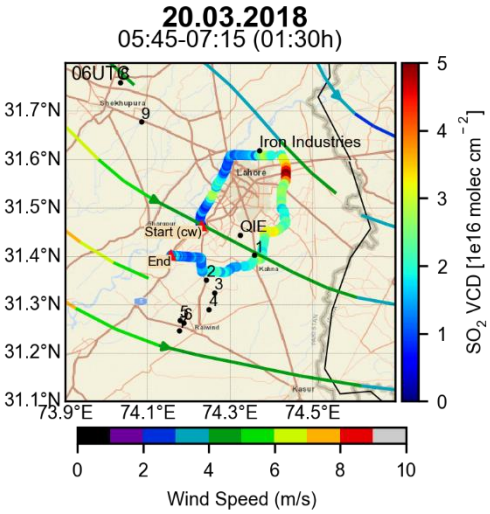
20.03.2018
05:45-07:15 (01:30h)
06UTC
Iron Industries
QIE
Start (cw)
End
Lahore
Kasur
31.7°N
31.6°N
31.5°N
31.4°N
31.3°N
31.2°N
31.1°N
73.9°E
74.1°E
74.3°E
74.5°E
SO2 VCD [1e16 molec cm−2]
Wind Speed (m/s)

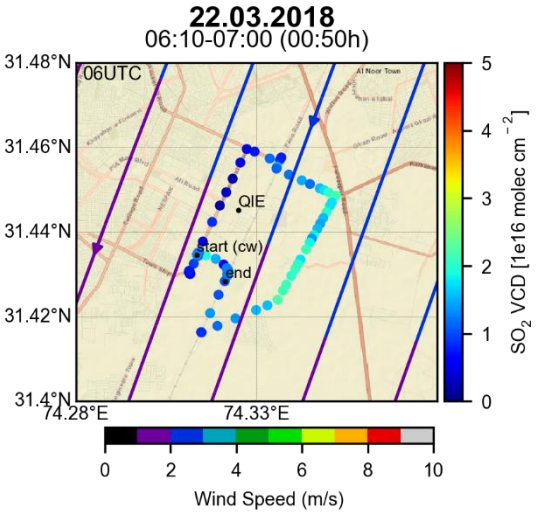
22.03.2018
06:10-07:00 (00:50h)
06UTC
QIE
Start (cw)
End
31.48°N
31.46°N
31.44°N
31.42°N
31.4°N
74.28°E
74.33°E
SO2 VCD [1e16 molec cm−2]
Wind Speed (m/s)

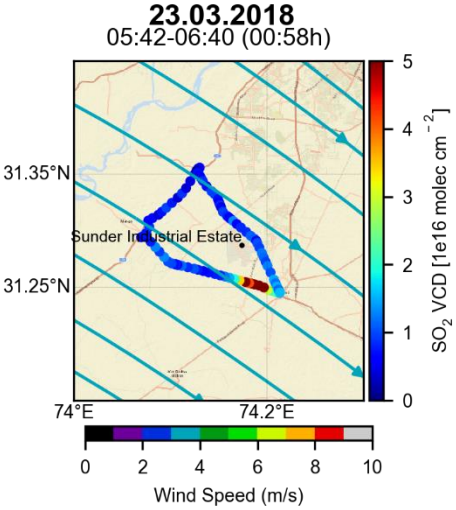
23.03.2018
05:42-06:40 (00:58h)
Sunder Industrial Estate
31.35°N
31.25°N
74°E
74.2°E
SO2 VCD [1e16 molec cm−2]
Wind Speed (m/s)

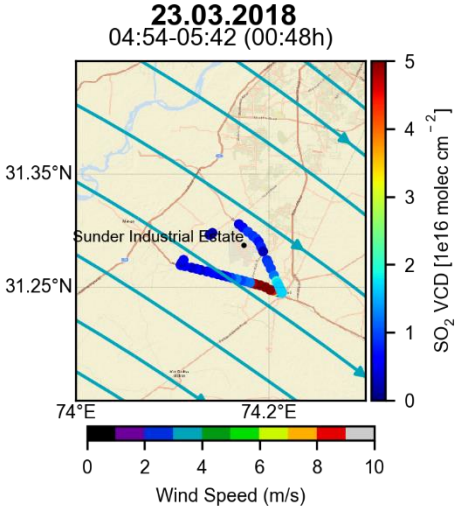
23.03.2018
04:54-05:42 (00:48h)
Sunder Industrial Estate
31.35°N
31.25°N
74°E
74.2°E
SO2 VCD [1e16 molec cm−2]
Wind Speed (m/s)

B.3 Formaldehyde Spatial Distributions

HCHO vertical column densities (VCDs) for the days grouped under category III, performed around Lahore during 2015-II, 2017 and 2018-I campaigns are presented here.

6.3.1.6.B.3.1. 2017

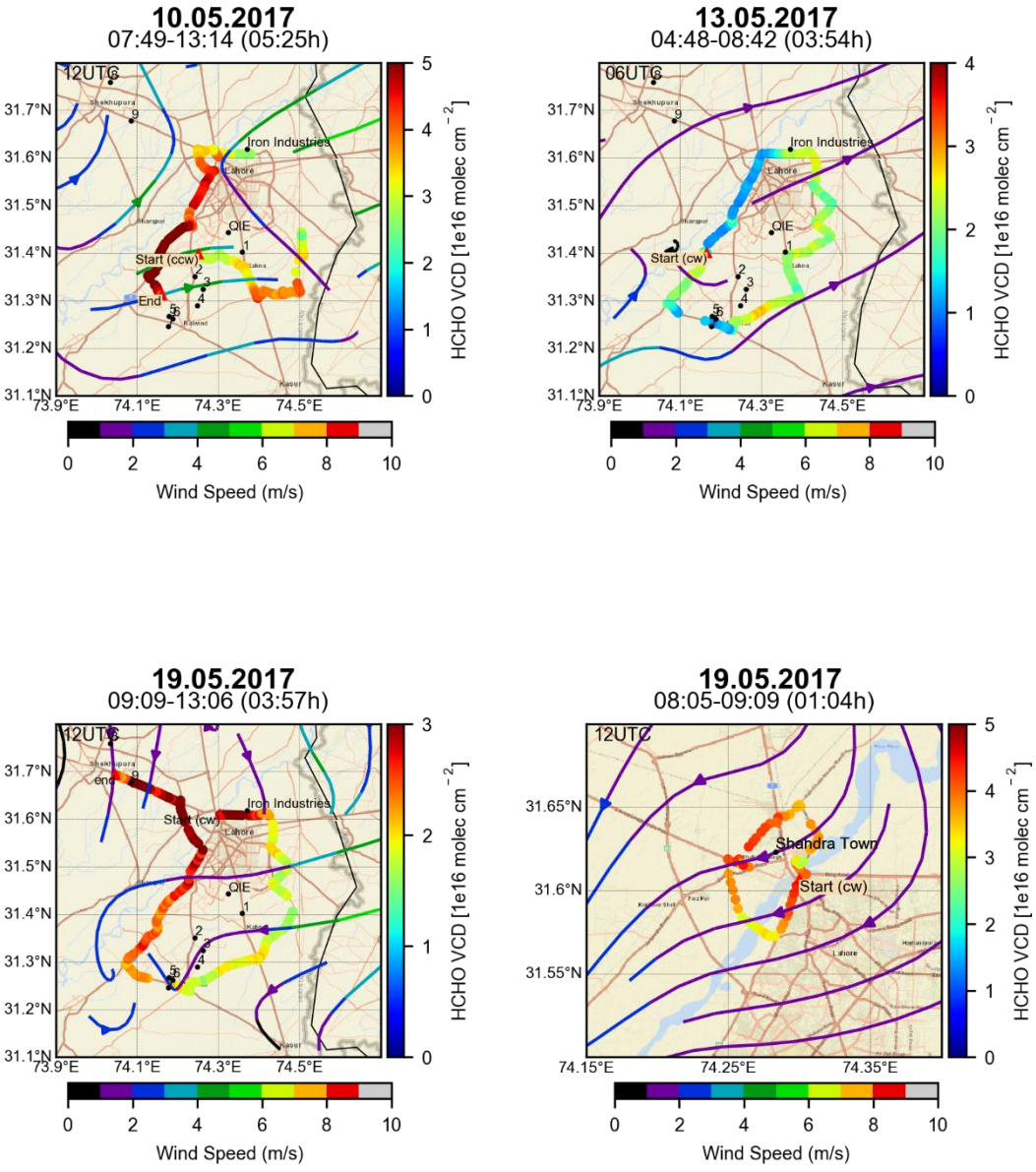

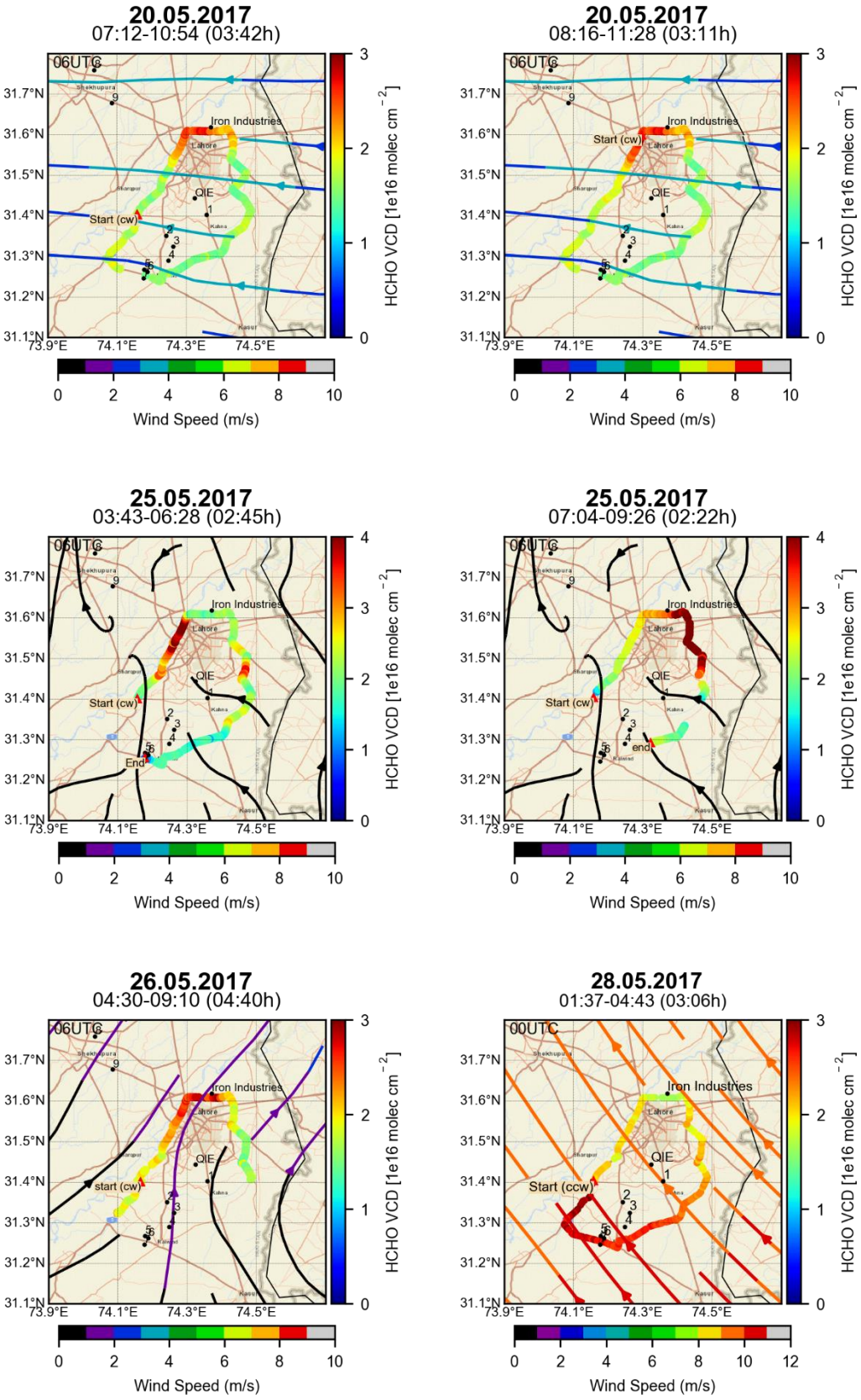
20.05.2017
07:12-10:54 (03:42h)
06UTC
Iron Industries
Lahore
QIE
Start (cw)
End
HCHO VCD [1e16 molec cm $^{-2}$]
Wind Speed (m/s)
20.05.2017
08:16-11:28 (03:11h)
06UTC
Iron Industries
Start (cw)
QIE
HCHO VCD [1e16 molec cm $^{-2}$]
Wind Speed (m/s)
25.05.2017
03:43-06:28 (02:45h)
06UTC
Iron Industries
QIE
Start (cw)
End
HCHO VCD [1e16 molec cm $^{-2}$]
Wind Speed (m/s)
25.05.2017
07:04-09:26 (02:22h)
06UTC
Iron Industries
QIE
Start (cw)
end
HCHO VCD [1e16 molec cm $^{-2}$]
Wind Speed (m/s)
26.05.2017
04:30-09:10 (04:40h)
06UTC
Iron Industries
QIE
start (cw)
HCHO VCD [1e16 molec cm $^{-2}$]
Wind Speed (m/s)
28.05.2017
01:37-04:43 (03:06h)
00UTC
Iron Industries
QIE
Start (ccw)
HCHO VCD [1e16 molec cm $^{-2}$]
Wind Speed (m/s)

29.05.2017
06:26-09:53 (03:27h)

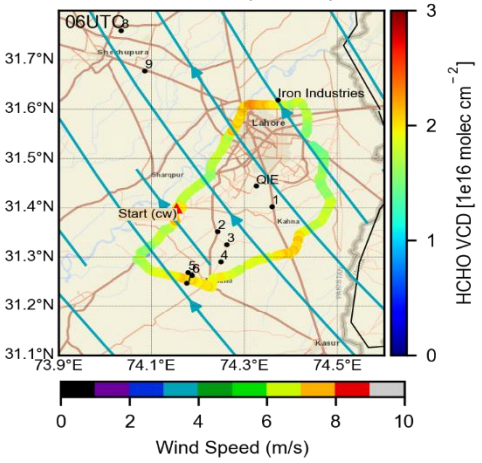

31.05.2017
05:33-11:06 (05:33h)

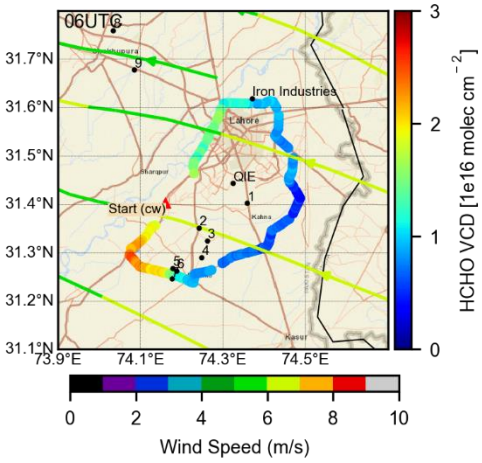

01.06.2017
04:40-08:00 (03:19h)

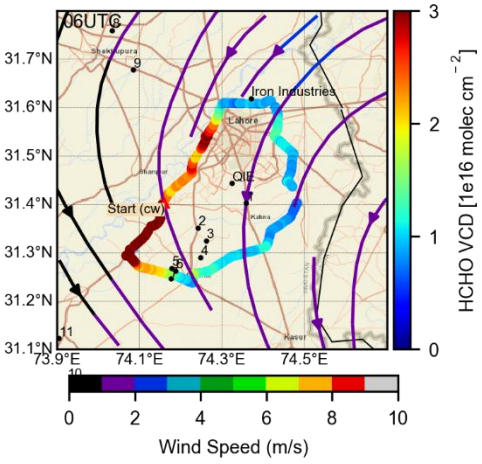

01.06.2017
08:00-11:30 (03:29h)

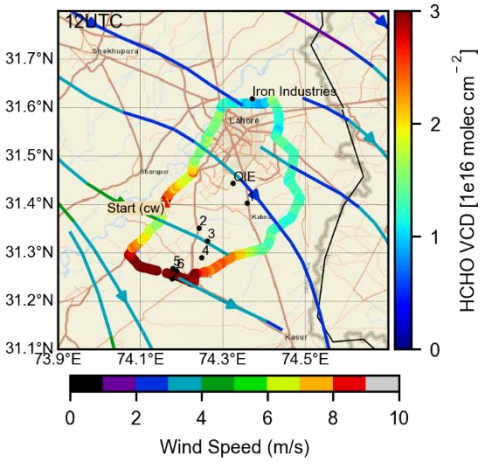

03.06.2017
08:36-12:18 (03:42h)

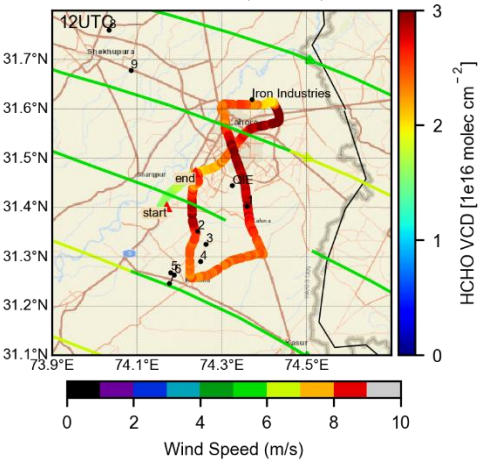

05.06.2017
04:38-08:12 (03:33h)

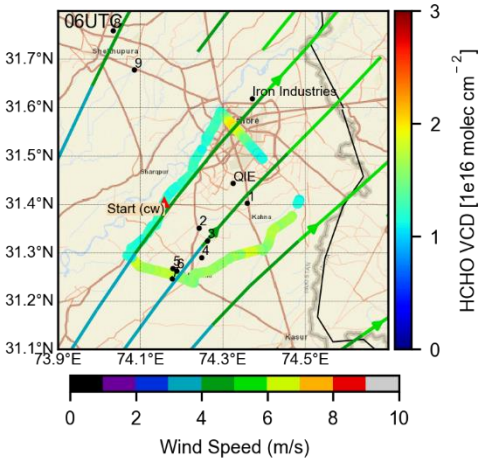

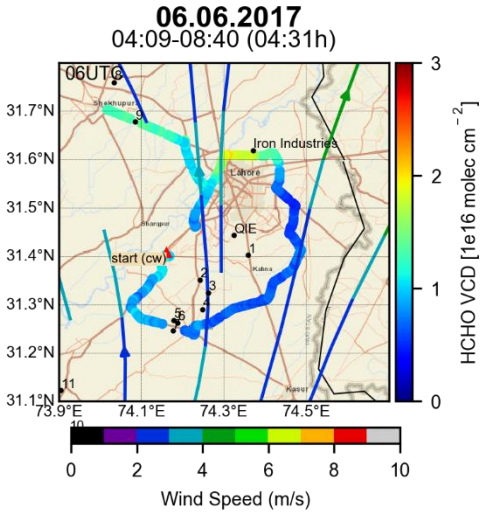
06.06.2017
04:09-08:40 (04:31h)
06UTC
Iron Industries
Lahore
QIE
start (cw)
31.7°N
31.6°N
31.5°N
31.4°N
31.3°N
31.2°N
31.1°N
73.9°E
74.1°E
74.3°E
74.5°E
HCHO VCD [1e16 molec cm^{-2}]
0
1
2
3
Wind Speed (m/s)
0
2
4
6
8
10

6.3.1.7.B.3.2. 2018 I

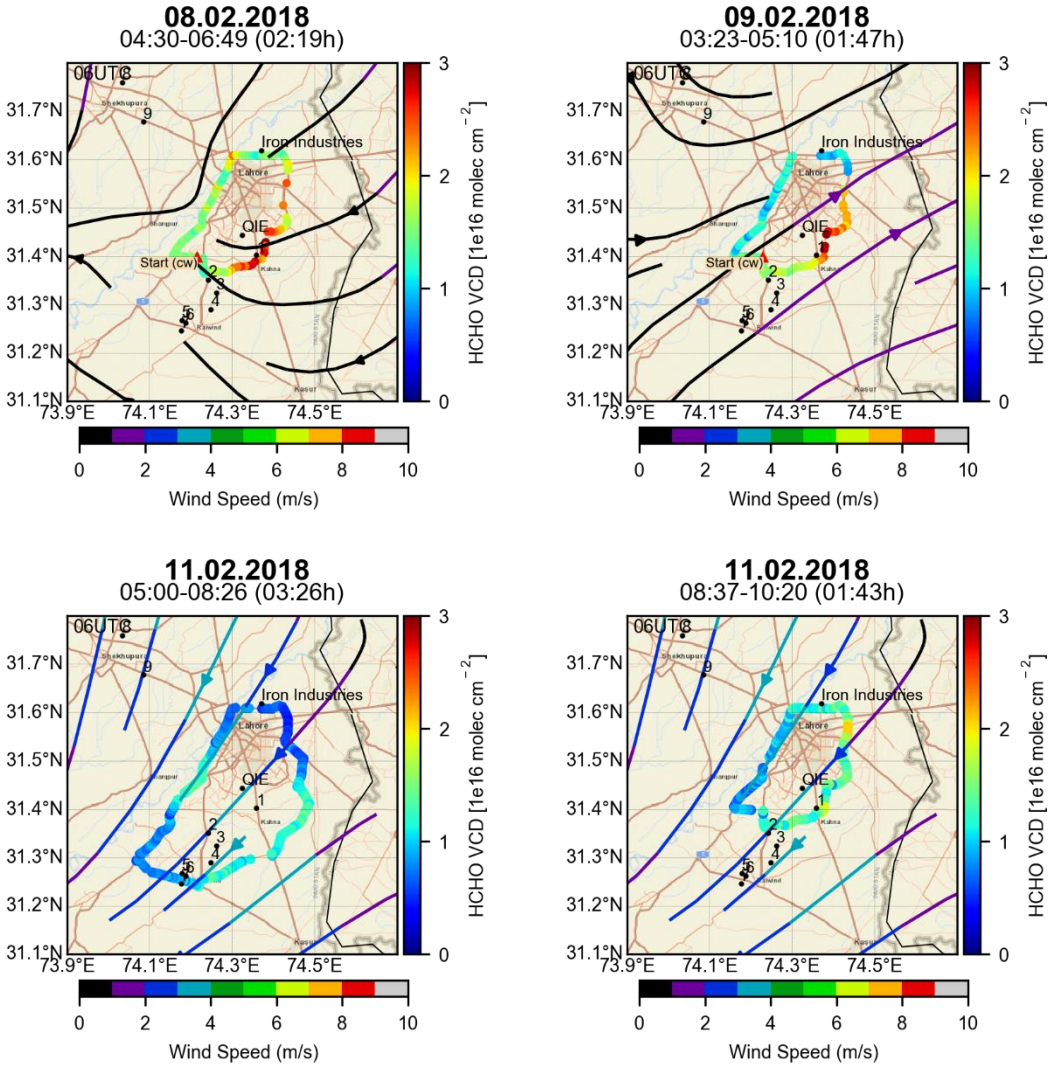

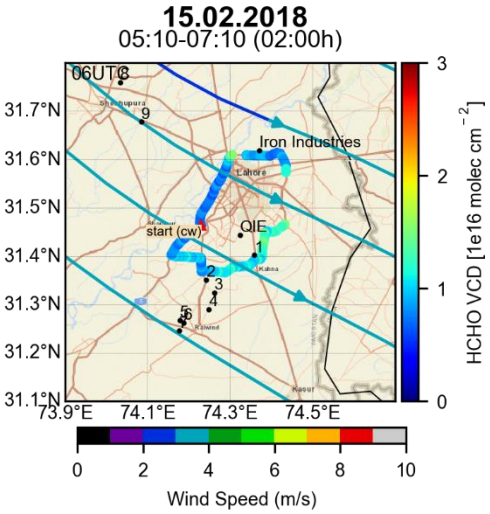
15.02.2018
05:10-07:10 (02:00h)
06UTC
Iron Industries
QIE
start (cw)
HCHO VCD [1e16 molec cm^{-2}]
Wind Speed (m/s)

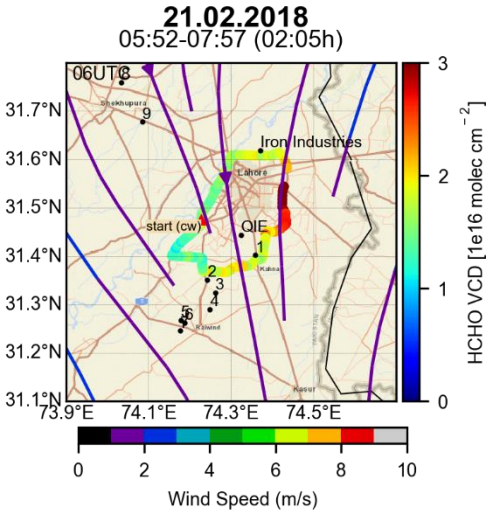
21.02.2018
05:52-07:57 (02:05h)
06UTC
Iron Industries
QIE
start (cw)
HCHO VCD [1e16 molec cm^{-2}]
Wind Speed (m/s)

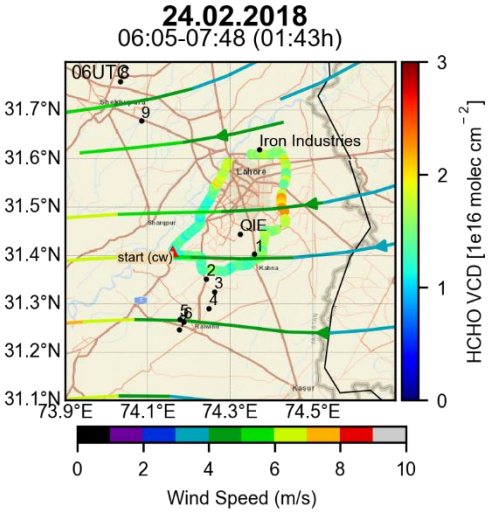
24.02.2018
06:05-07:48 (01:43h)
06UTC
Iron Industries
QIE
start (cw)
HCHO VCD [1e16 molec cm^{-2}]
Wind Speed (m/s)

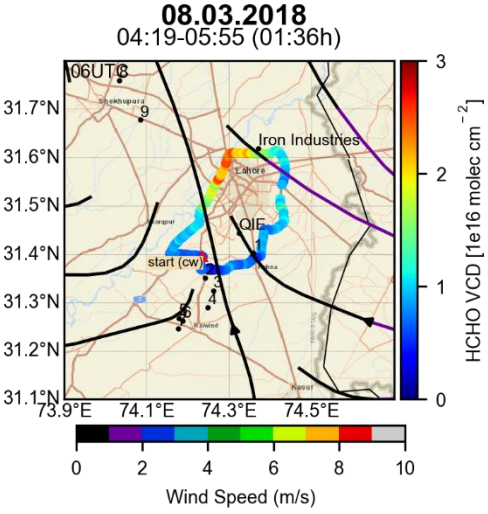
08.03.2018
04:19-05:55 (01:36h)
06UTC
Iron Industries
QIE
start (cw)
HCHO VCD [1e16 molec cm^{-2}]
Wind Speed (m/s)

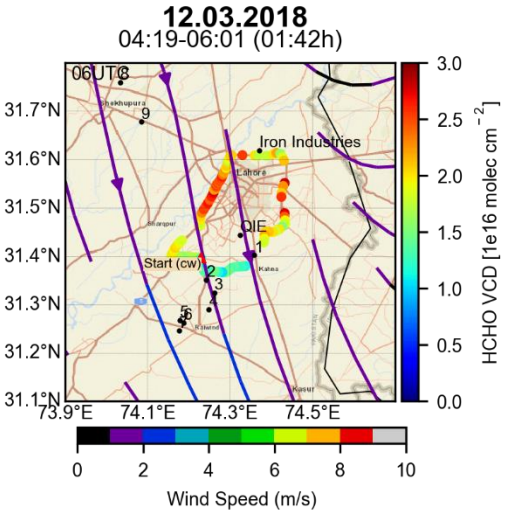
12.03.2018
04:19-06:01 (01:42h)
06UTC
Iron Industries
QIE
Start (cw)
HCHO VCD [1e16 molec cm^{-2}]
Wind Speed (m/s)

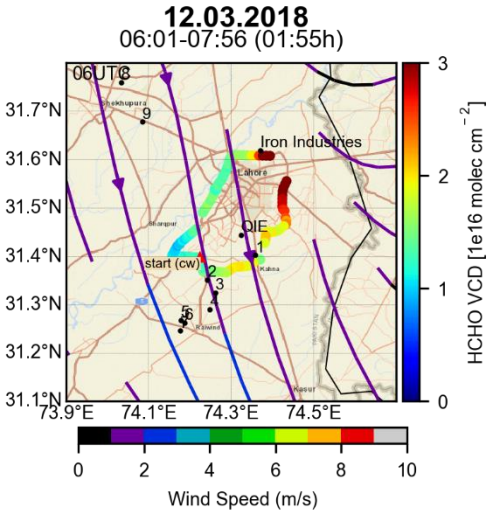
12.03.2018
06:01-07:56 (01:55h)
06UTC
Iron Industries
QIE
start (cw)
HCHO VCD [1e16 molec cm^{-2}]
Wind Speed (m/s)

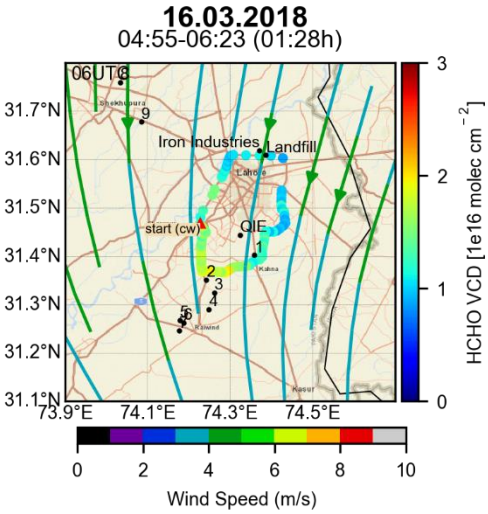
16.03.2018
04:55-06:23 (01:28h)
06UTC
Iron Industries
Landfill
start (cw)
QIE
Lahore
Kasur
31.7°N
31.6°N
31.5°N
31.4°N
31.3°N
31.2°N
31.1°N
73.9°E
74.1°E
74.3°E
74.5°E
HCHO VCD [1e16 molec cm $^{-2}$]
Wind Speed (m/s)

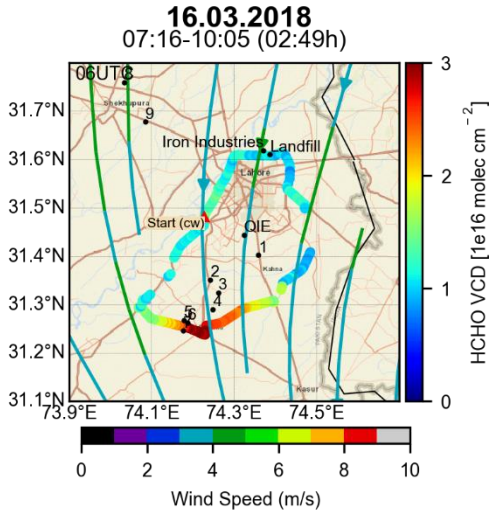
16.03.2018
07:16-10:05 (02:49h)
06UTC
Iron Industries
Landfill
Start (cw)
QIE
Lahore
Kasur
31.7°N
31.6°N
31.5°N
31.4°N
31.3°N
31.2°N
31.1°N
73.9°E
74.1°E
74.3°E
74.5°E
HCHO VCD [1e16 molec cm $^{-2}$]
Wind Speed (m/s)

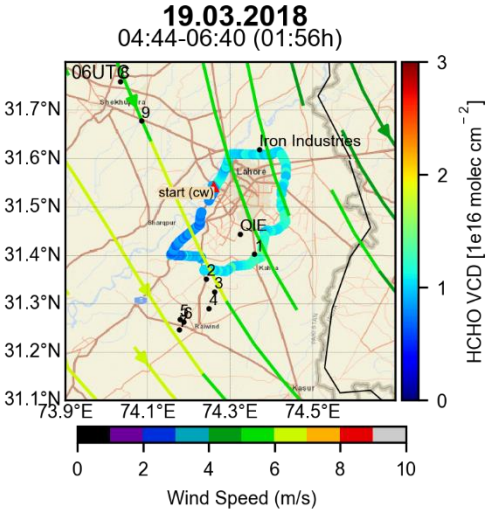
19.03.2018
04:44-06:40 (01:56h)
06UTC
Iron Industries
start (cw)
QIE
Lahore
Kasur
31.7°N
31.6°N
31.5°N
31.4°N
31.3°N
31.2°N
31.1°N
73.9°E
74.1°E
74.3°E
74.5°E
HCHO VCD [1e16 molec cm $^{-2}$]
Wind Speed (m/s)

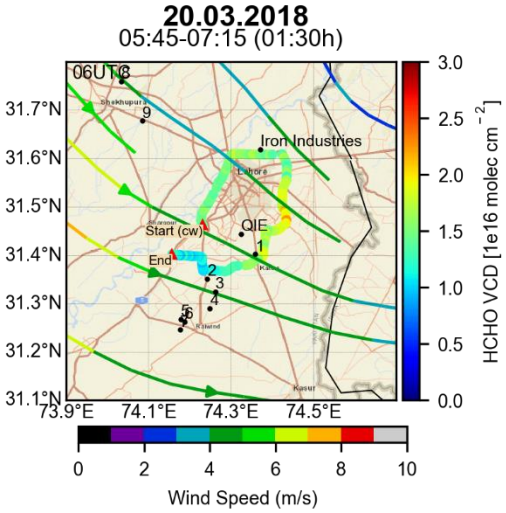
20.03.2018
05:45-07:15 (01:30h)
06UTC
Iron Industries
Start (cw)
End
QIE
Lahore
Kasur
31.7°N
31.6°N
31.5°N
31.4°N
31.3°N
31.2°N
31.1°N
73.9°E
74.1°E
74.3°E
74.5°E
HCHO VCD [1e16 molec cm $^{-2}$]
Wind Speed (m/s)

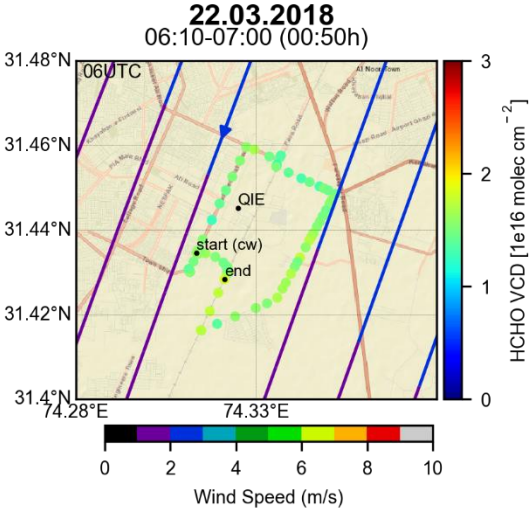
22.03.2018
06:10-07:00 (00:50h)
06UTC
QIE
start (cw)
end
31.48°N
31.46°N
31.44°N
31.42°N
31.4°N
74.28°E
74.33°E
HCHO VCD [1e16 molec cm $^{-2}$]
Wind Speed (m/s)

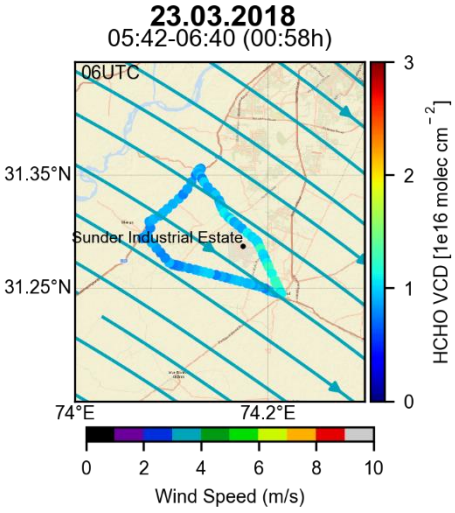
23.03.2018
05:42-06:40 (00:58h)
06UTC
Sunder Industrial Estate
31.35°N
31.25°N
74°E
74.2°E
HCHO VCD [1e16 molec cm $^{-2}$]
Wind Speed (m/s)

APPENDIX C

In this section correlation plots for the six trace gas pairs, observed in 2017 and 2018-II campaigns are presented.

C.1 2017

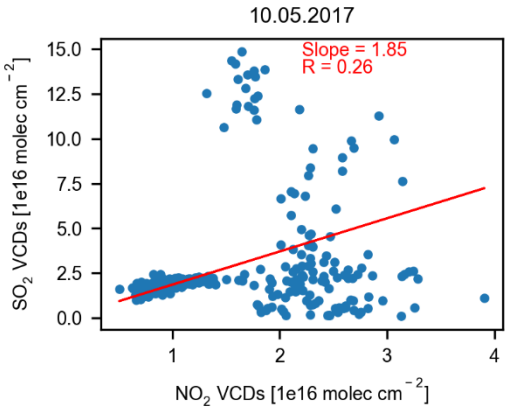

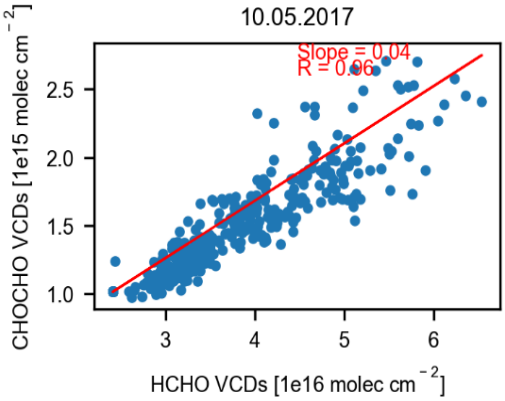

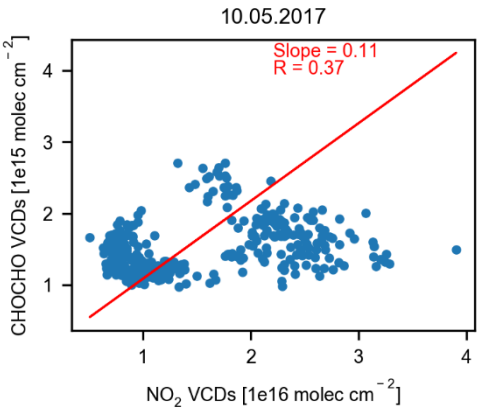

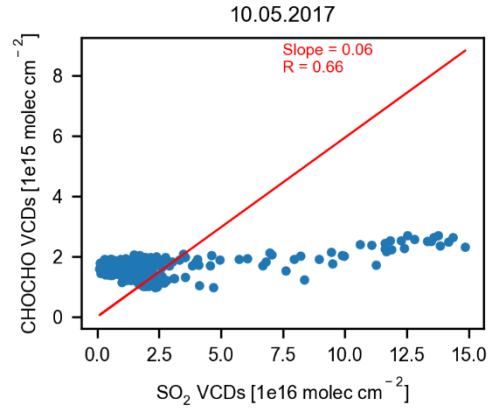

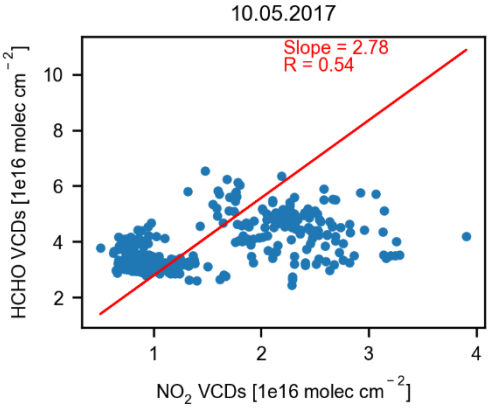

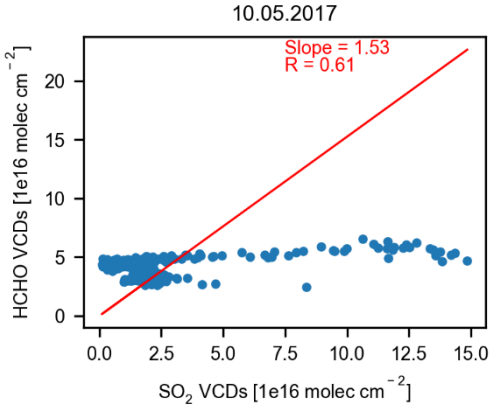

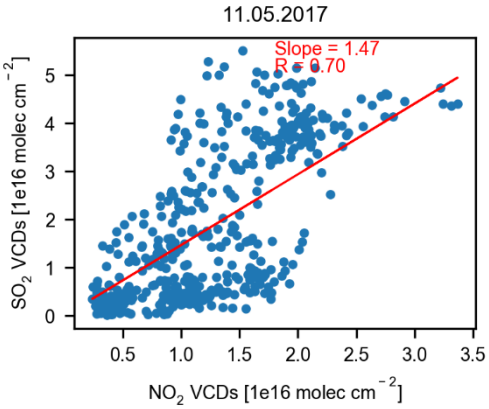
11.05.2017
Slope = 1.47
R = 0.70
SO2 VCDs [1e16 molec cm-2]
NO2 VCDs [1e16 molec cm-2]

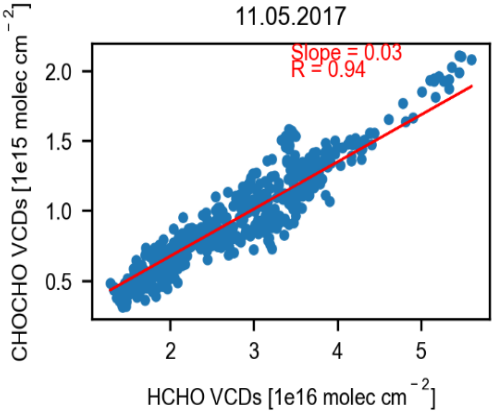
11.05.2017
Slope = 0.03
R = 0.94
CHOCHO VCDs [1e15 molec cm-2]
HCHO VCDs [1e16 molec cm-2]

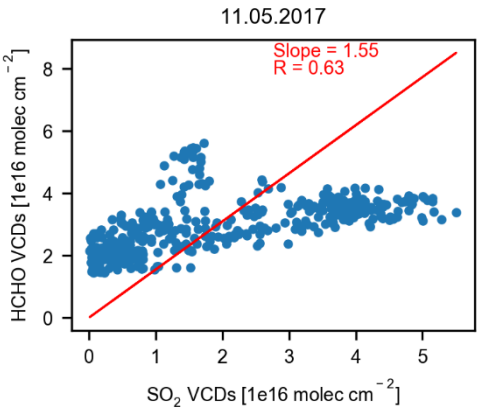
11.05.2017
Slope = 1.55
R = 0.63
HCHO VCDs [1e16 molec cm-2]
SO2 VCDs [1e16 molec cm-2]

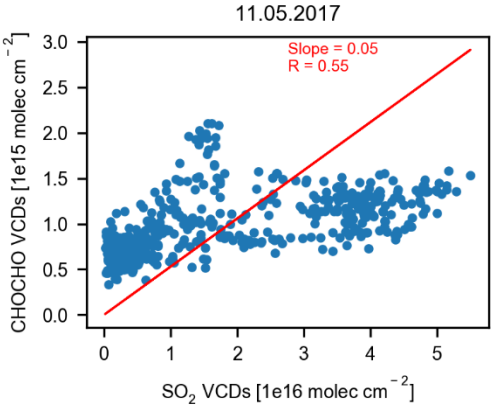
11.05.2017
Slope = 0.05
R = 0.55
CHOCHO VCDs [1e15 molec cm-2]
SO2 VCDs [1e16 molec cm-2]

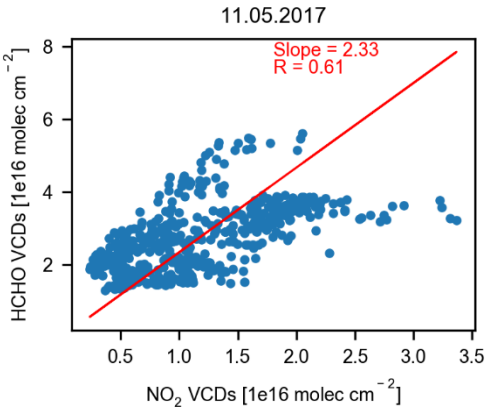
11.05.2017
Slope = 2.33
R = 0.61
HCHO VCDs [1e16 molec cm-2]
NO2 VCDs [1e16 molec cm-2]

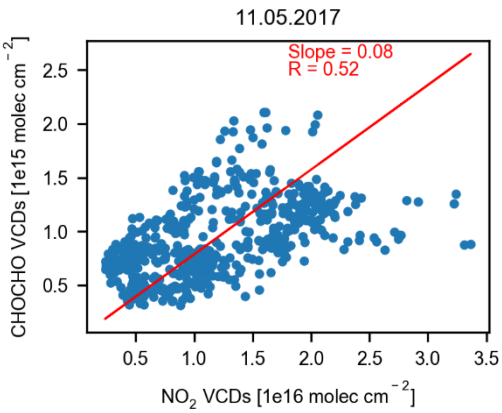
11.05.2017
Slope = 0.08
R = 0.52
CHOCHO VCDs [1e15 molec cm-2]
NO2 VCDs [1e16 molec cm-2]

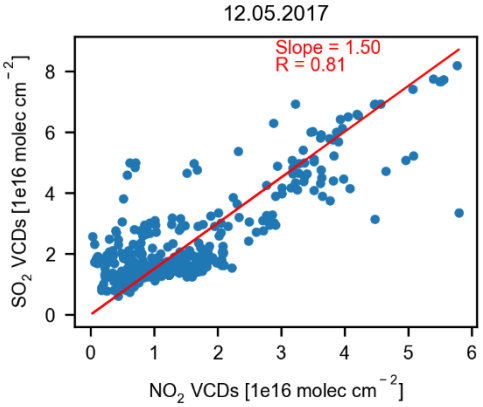
12.05.2017
Slope = 1.50
R = 0.81
SO2 VCDs [1e16 molec cm-2]
NO2 VCDs [1e16 molec cm-2]

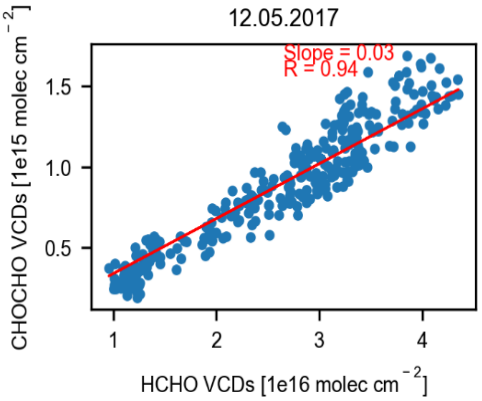
12.05.2017
Slope = 0.03
R = 0.94
CHOCHO VCDs [1e15 molec cm-2]
HCHO VCDs [1e16 molec cm-2]

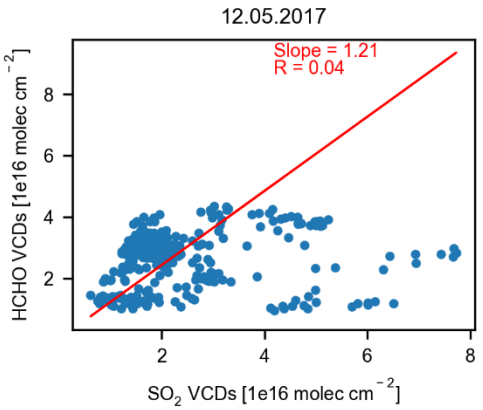
12.05.2017
Slope = 1.21
R = 0.04
HCHO VCDs [1e16 molec cm-2]
SO2 VCDs [1e16 molec cm-2]

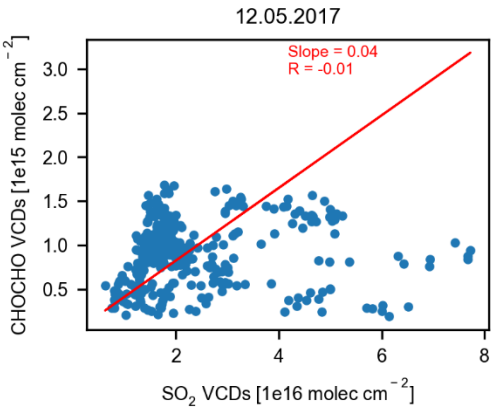
12.05.2017
Slope = 0.04
R = -0.01
CHOCHO VCDs [1e15 molec cm-2]
SO2 VCDs [1e16 molec cm-2]

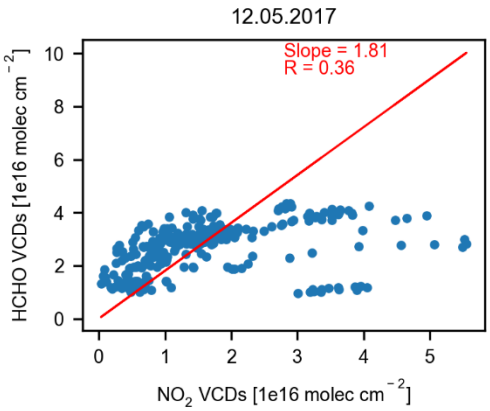
12.05.2017
Slope = 1.81
R = 0.36
HCHO VCDs [1e16 molec cm-2]
NO2 VCDs [1e16 molec cm-2]

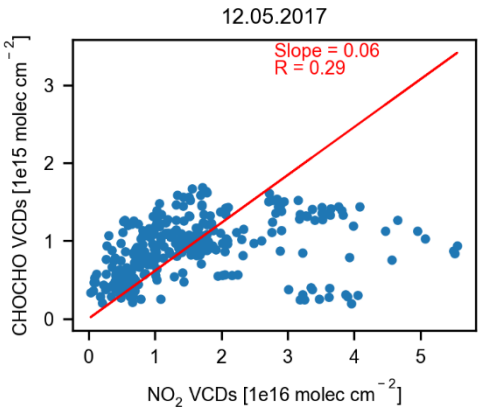
12.05.2017
Slope = 0.06
R = 0.29
CHOCHO VCDs [1e15 molec cm-2]
NO2 VCDs [1e16 molec cm-2]

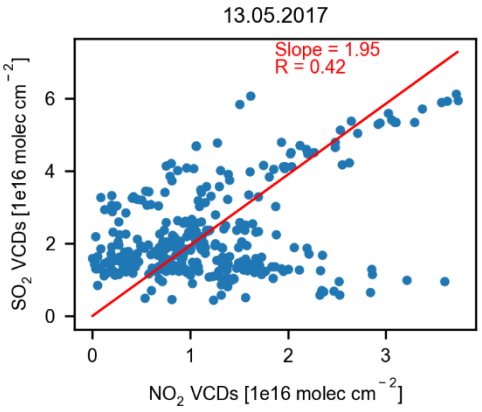
13.05.2017
Slope = 1.95
R = 0.42
SO2 VCDs [1e16 molec cm-2]
NO2 VCDs [1e16 molec cm-2]

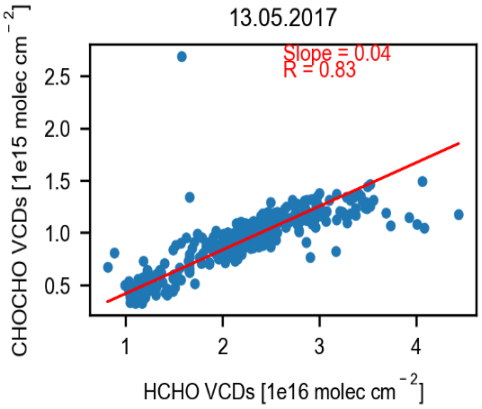
13.05.2017
Slope = 0.04
R = 0.83
CHOCHO VCDs [1e15 molec cm-2]
HCHO VCDs [1e16 molec cm-2]

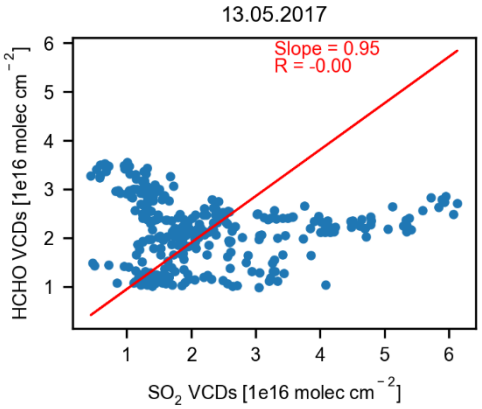
13.05.2017
Slope = 0.95
R = -0.00
HCHO VCDs [1e16 molec cm-2]
SO2 VCDs [1e16 molec cm-2]

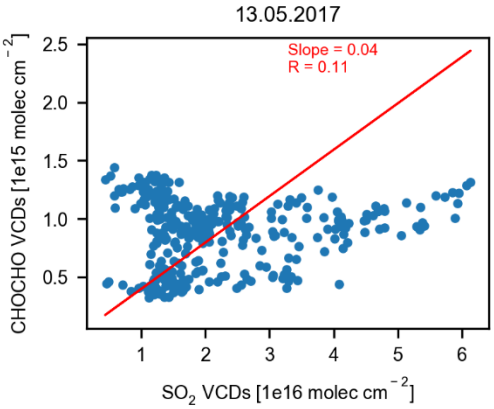
13.05.2017
Slope = 0.04
R = 0.11
CHOCHO VCDs [1e15 molec cm-2]
SO2 VCDs [1e16 molec cm-2]

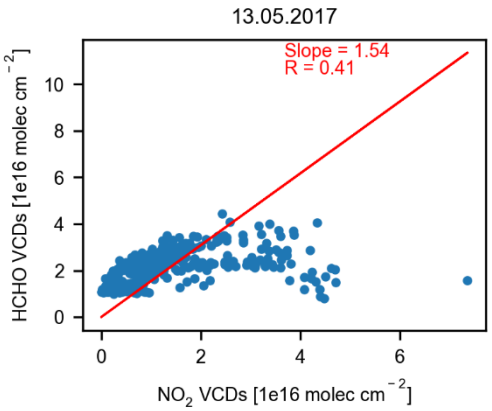
13.05.2017
Slope = 1.54
R = 0.41
HCHO VCDs [1e16 molec cm-2]
NO2 VCDs [1e16 molec cm-2]

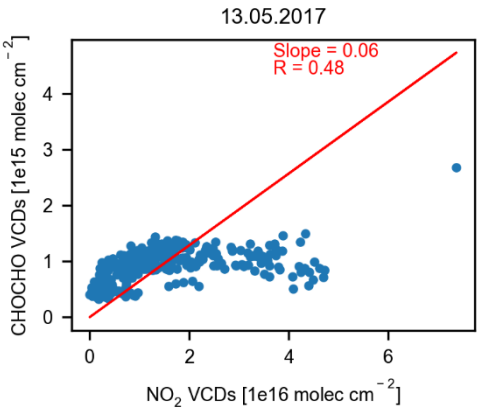
13.05.2017
Slope = 0.06
R = 0.48
CHOCHO VCDs [1e15 molec cm-2]
NO2 VCDs [1e16 molec cm-2]

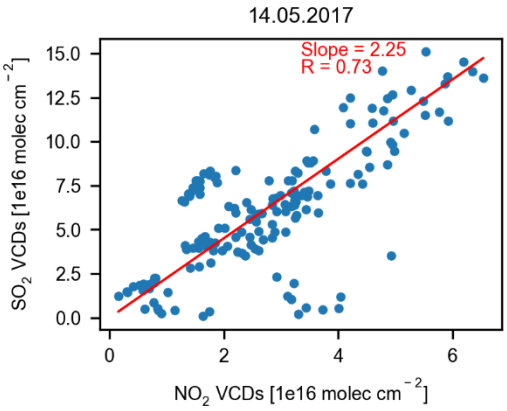
14.05.2017
Slope = 2.25
R = 0.73
SO2 VCDs [1e16 molec cm-2]
NO2 VCDs [1e16 molec cm-2]

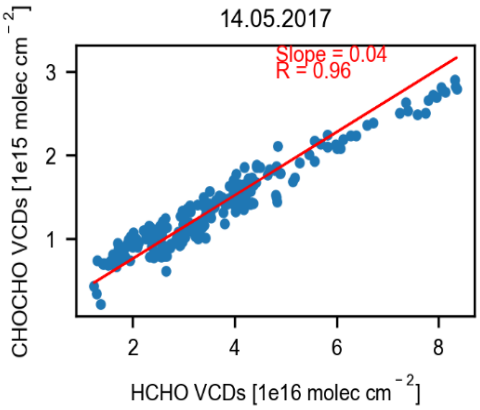
14.05.2017
Slope = 0.04
R = 0.96
CHOCHO VCDs [1e15 molec cm-2]
HCHO VCDs [1e16 molec cm-2]

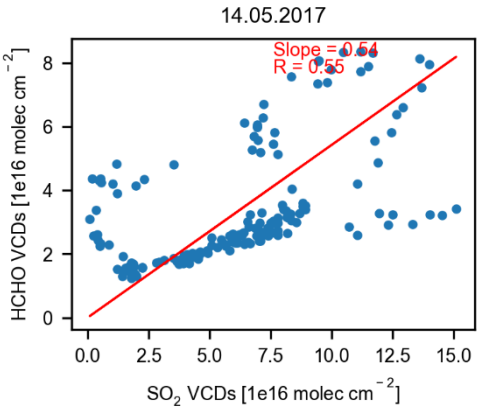
14.05.2017
Slope = 0.54
R = 0.55
HCHO VCDs [1e16 molec cm-2]
SO2 VCDs [1e16 molec cm-2]

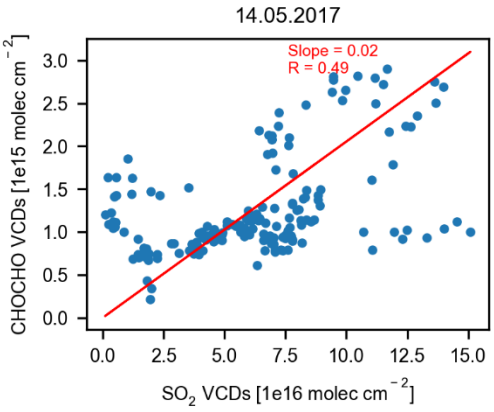
14.05.2017
Slope = 0.02
R = 0.49
CHOCHO VCDs [1e15 molec cm-2]
SO2 VCDs [1e16 molec cm-2]

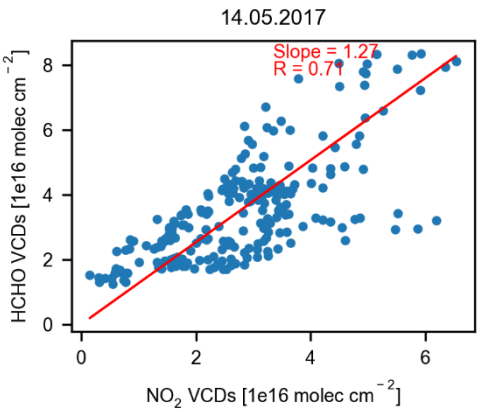
14.05.2017
Slope = 1.27
R = 0.71
HCHO VCDs [1e16 molec cm-2]
NO2 VCDs [1e16 molec cm-2]

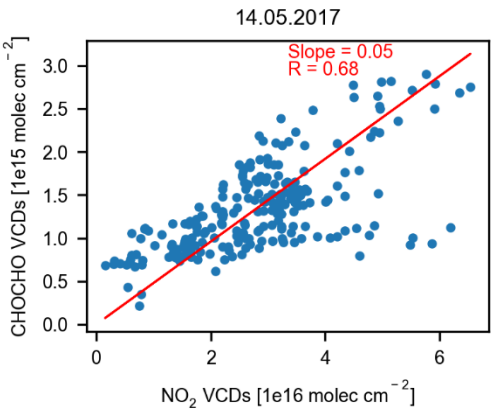
14.05.2017
Slope = 0.05
R = 0.68
CHOCHO VCDs [1e15 molec cm-2]
NO2 VCDs [1e16 molec cm-2]

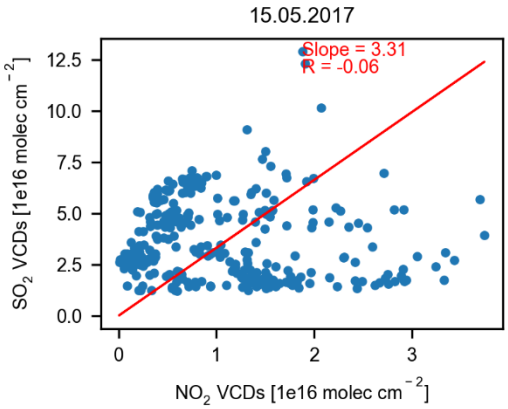
15.05.2017
Slope = 3.31
R = -0.06
SO2 VCDs [1e16 molec cm-2]
NO2 VCDs [1e16 molec cm-2]

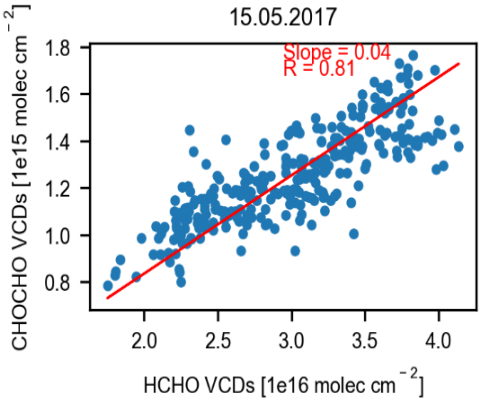
15.05.2017
Slope = 0.04
R = 0.81
CHOCHO VCDs [1e15 molec cm-2]
HCHO VCDs [1e16 molec cm-2]

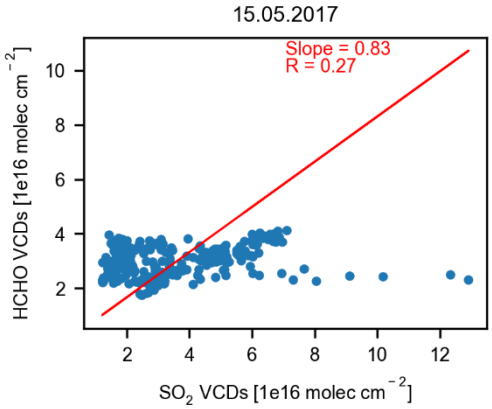
15.05.2017
Slope = 0.83
R = 0.27
HCHO VCDs [1e16 molec cm-2]
SO2 VCDs [1e16 molec cm-2]

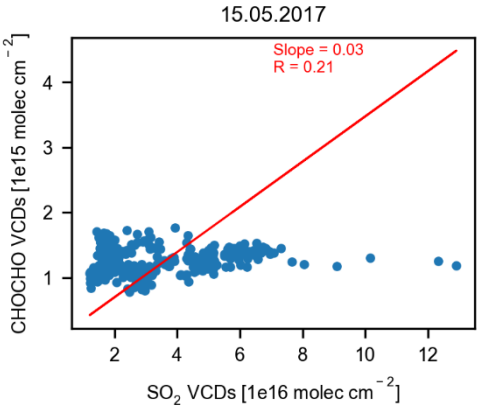
15.05.2017
Slope = 0.03
R = 0.21
CHOCHO VCDs [1e15 molec cm-2]
SO2 VCDs [1e16 molec cm-2]

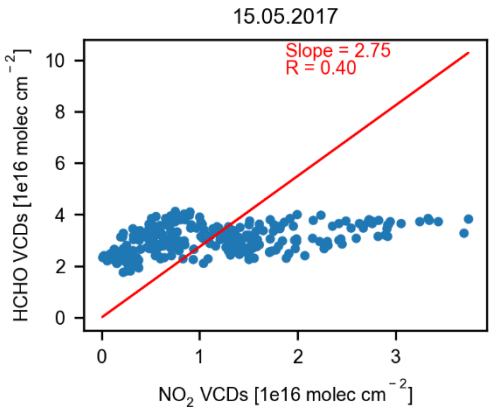
15.05.2017
Slope = 2.75
R = 0.40
HCHO VCDs [1e16 molec cm-2]
NO2 VCDs [1e16 molec cm-2]

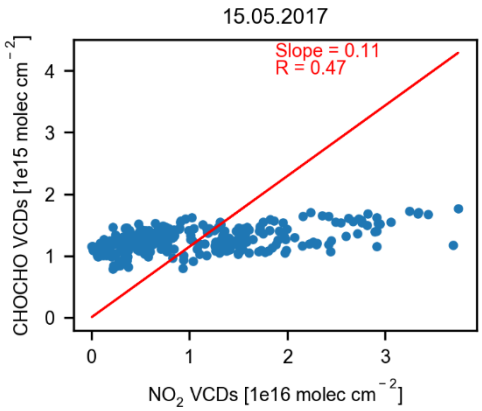
15.05.2017
Slope = 0.11
R = 0.47
CHOCHO VCDs [1e15 molec cm-2]
NO2 VCDs [1e16 molec cm-2]

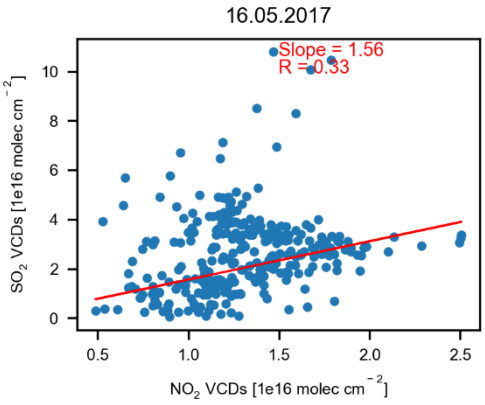
16.05.2017
Slope = 1.56
R = 0.33
SO2 VCDs [1e16 molec cm−2]
NO2 VCDs [1e16 molec cm−2]

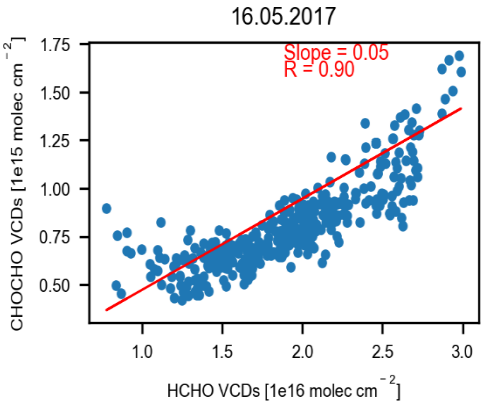
16.05.2017
Slope = 0.05
R = 0.90
CHOCHO VCDs [1e15 molec cm−2]
HCHO VCDs [1e16 molec cm−2]

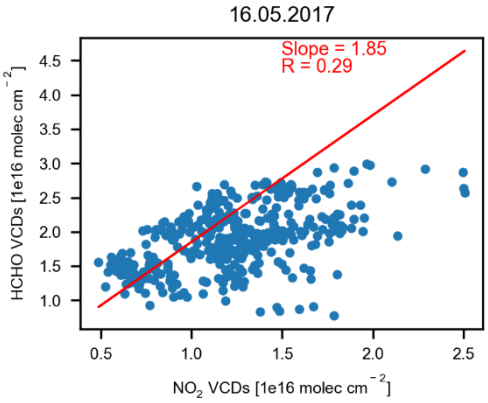
16.05.2017
Slope = 1.85
R = 0.29
HCHO VCDs [1e16 molec cm−2]
NO2 VCDs [1e16 molec cm−2]

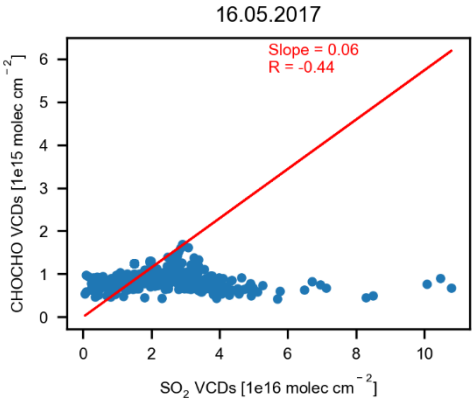
16.05.2017
Slope = 0.06
R = -0.44
CHOCHO VCDs [1e15 molec cm−2]
SO2 VCDs [1e16 molec cm−2]

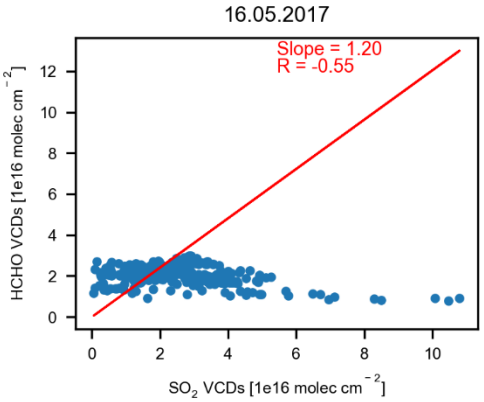
16.05.2017
Slope = 1.20
R = -0.55
HCHO VCDs [1e16 molec cm−2]
SO2 VCDs [1e16 molec cm−2]

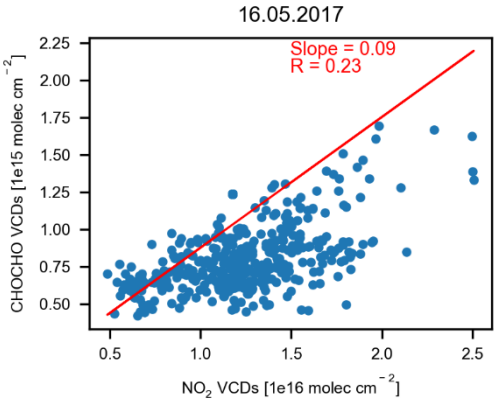
16.05.2017
Slope = 0.09
R = 0.23
CHOCHO VCDs [1e15 molec cm−2]
NO2 VCDs [1e16 molec cm−2]

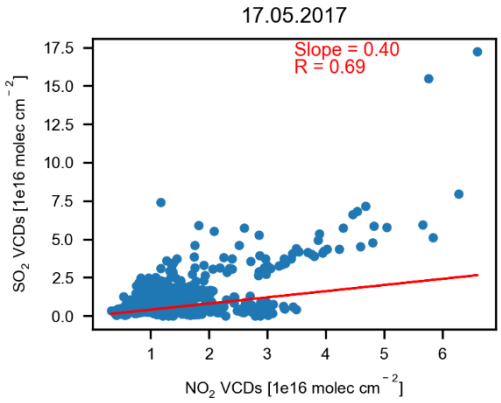
17.05.2017
Slope = 0.40
R = 0.69
SO2 VCDs [1e16 molec cm-2]
NO2 VCDs [1e16 molec cm-2]

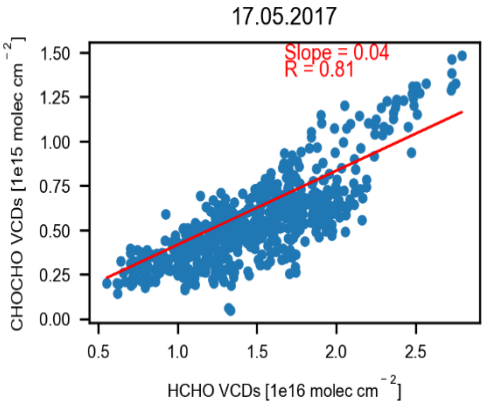
17.05.2017
Slope = 0.04
R = 0.81
CHOCHO VCDs [1e15 molec cm-2]
HCHO VCDs [1e16 molec cm-2]

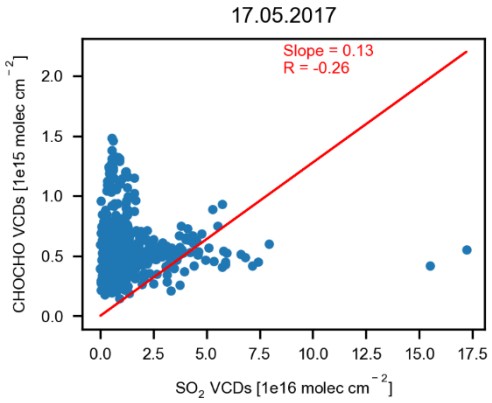
17.05.2017
Slope = 0.13
R = -0.26
CHOCHO VCDs [1e15 molec cm-2]
SO2 VCDs [1e16 molec cm-2]

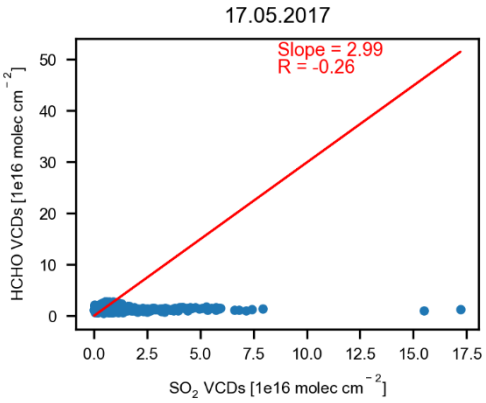
17.05.2017
Slope = 2.99
R = -0.26
HCHO VCDs [1e16 molec cm-2]
SO2 VCDs [1e16 molec cm-2]

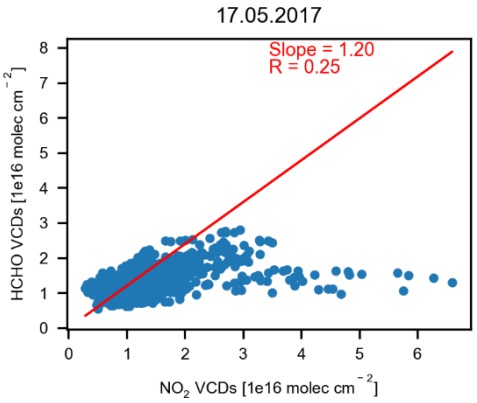
17.05.2017
Slope = 1.20
R = 0.25
HCHO VCDs [1e16 molec cm-2]
NO2 VCDs [1e16 molec cm-2]

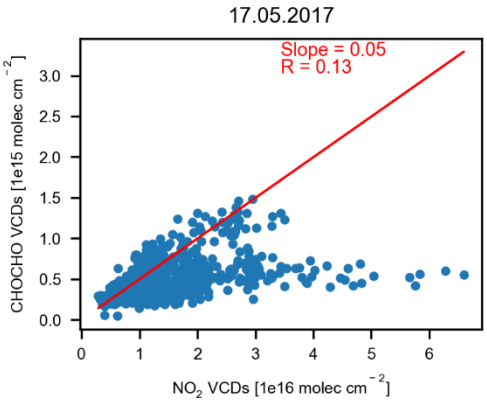
17.05.2017
Slope = 0.05
R = 0.13
CHOCHO VCDs [1e15 molec cm-2]
NO2 VCDs [1e16 molec cm-2]

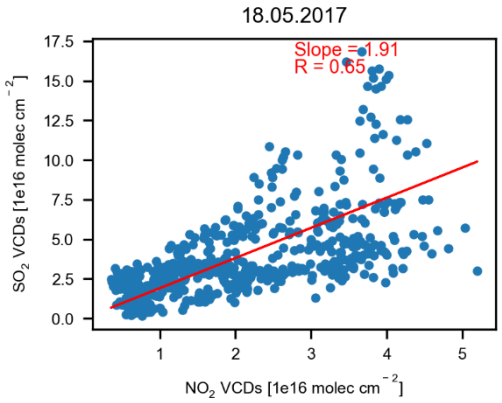
18.05.2017
Slope = 1.91
R = 0.65
SO2 VCDs [1e16 molec cm-2]
NO2 VCDs [1e16 molec cm-2]

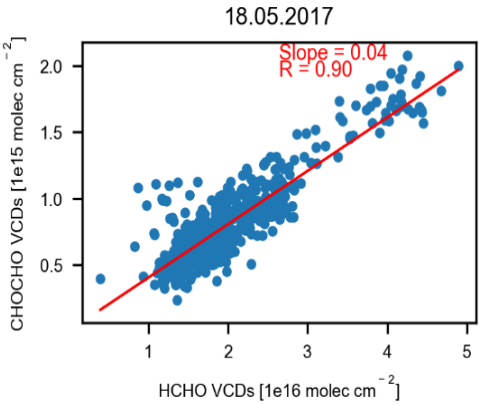
18.05.2017
Slope = 0.04
R = 0.90
CHOCHO VCDs [1e15 molec cm-2]
HCHO VCDs [1e16 molec cm-2]

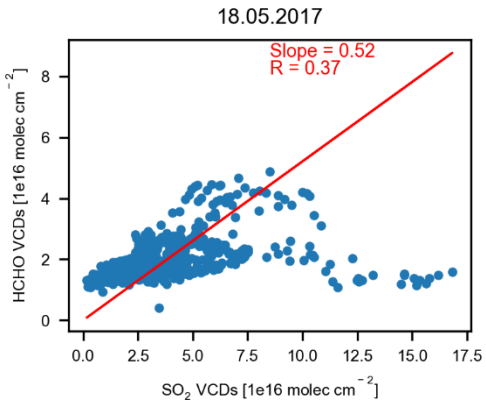
18.05.2017
Slope = 0.52
R = 0.37
HCHO VCDs [1e16 molec cm-2]
SO2 VCDs [1e16 molec cm-2]

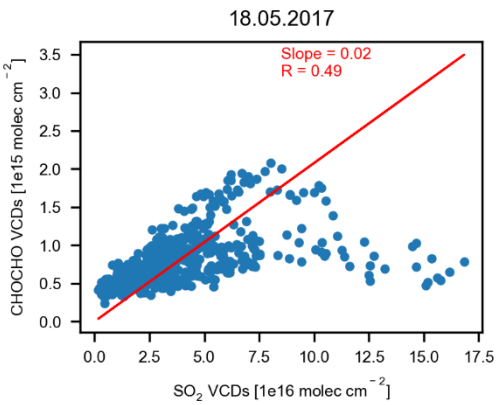
18.05.2017
Slope = 0.02
R = 0.49
CHOCHO VCDs [1e15 molec cm-2]
SO2 VCDs [1e16 molec cm-2]

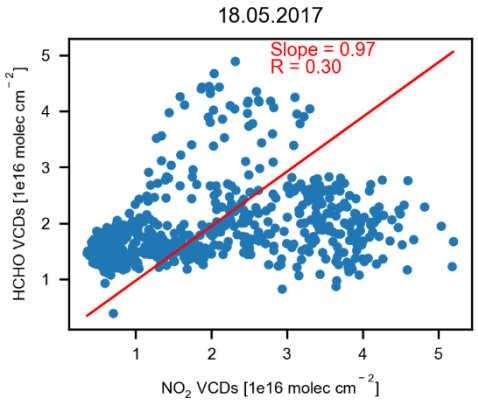
18.05.2017
Slope = 0.97
R = 0.30
HCHO VCDs [1e16 molec cm-2]
NO2 VCDs [1e16 molec cm-2]

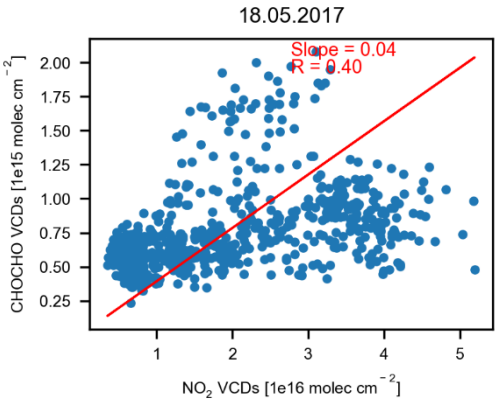
18.05.2017
Slope = 0.04
R = 0.40
CHOCHO VCDs [1e15 molec cm-2]
NO2 VCDs [1e16 molec cm-2]

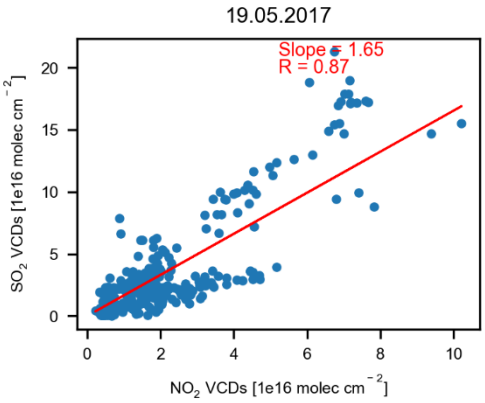
19.05.2017
Slope = 1.65
R = 0.87
SO2 VCDs [1e16 molec cm−2]
NO2 VCDs [1e16 molec cm−2]

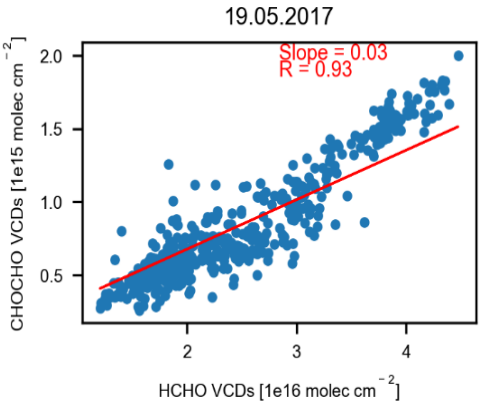
19.05.2017
Slope = 0.03
R = 0.93
CHOCHO VCDs [1e15 molec cm−2]
HCHO VCDs [1e16 molec cm−2]

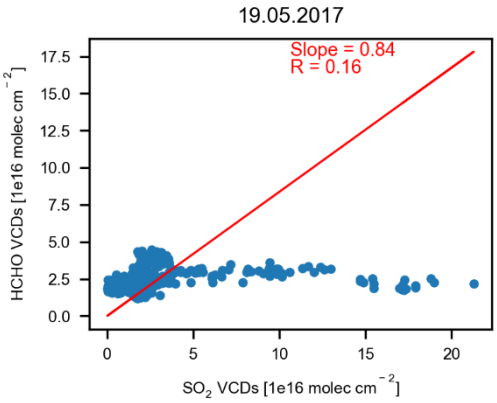
19.05.2017
Slope = 0.84
R = 0.16
HCHO VCDs [1e16 molec cm−2]
SO2 VCDs [1e16 molec cm−2]

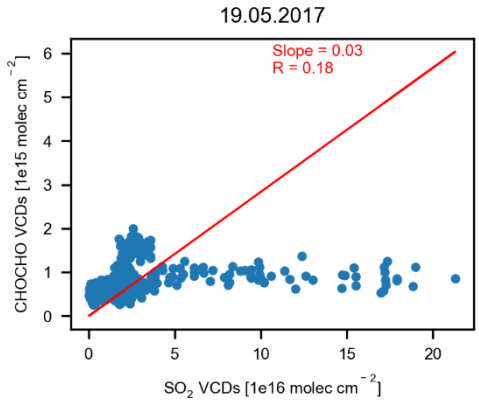
19.05.2017
Slope = 0.03
R = 0.18
CHOCHO VCDs [1e15 molec cm−2]
SO2 VCDs [1e16 molec cm−2]

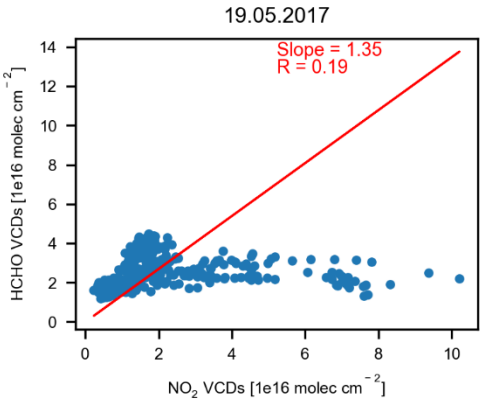
19.05.2017
Slope = 1.35
R = 0.19
HCHO VCDs [1e16 molec cm−2]
NO2 VCDs [1e16 molec cm−2]

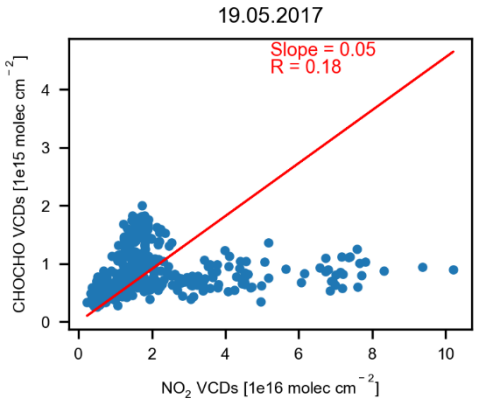
19.05.2017
Slope = 0.05
R = 0.18
CHOCHO VCDs [1e15 molec cm−2]
NO2 VCDs [1e16 molec cm−2]

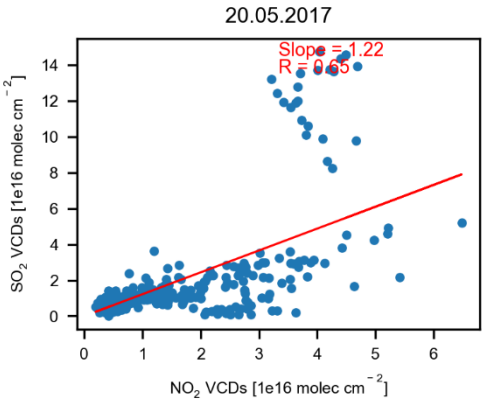
20.05.2017
Slope = 1.22
R = 0.65
SO2 VCDs [1e16 molec cm−2]
NO2 VCDs [1e16 molec cm−2]

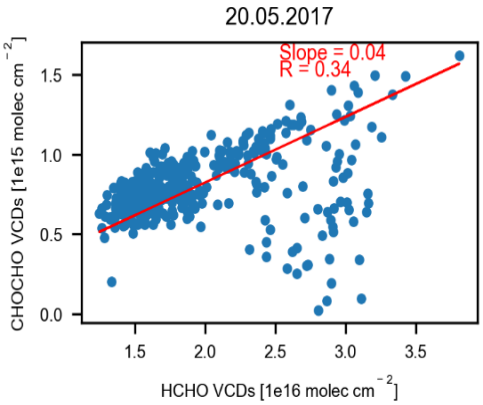
20.05.2017
Slope = 0.04
R = 0.34
CHOCHO VCDs [1e15 molec cm−2]
HCHO VCDs [1e16 molec cm−2]

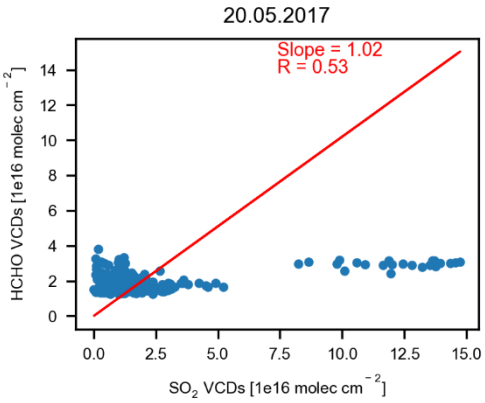
20.05.2017
Slope = 1.02
R = 0.53
HCHO VCDs [1e16 molec cm−2]
SO2 VCDs [1e16 molec cm−2]

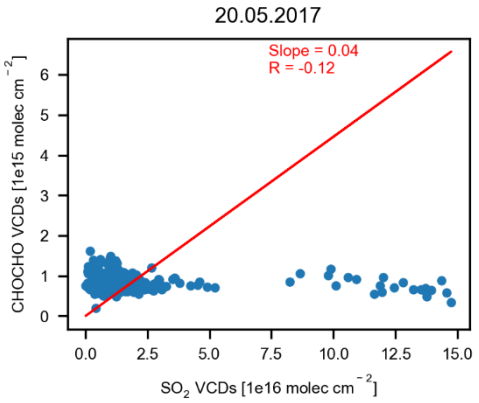
20.05.2017
Slope = 0.04
R = -0.12
CHOCHO VCDs [1e15 molec cm−2]
SO2 VCDs [1e16 molec cm−2]

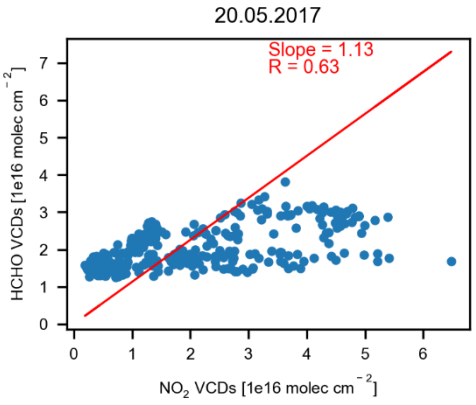
20.05.2017
Slope = 1.13
R = 0.63
HCHO VCDs [1e16 molec cm−2]
NO2 VCDs [1e16 molec cm−2]

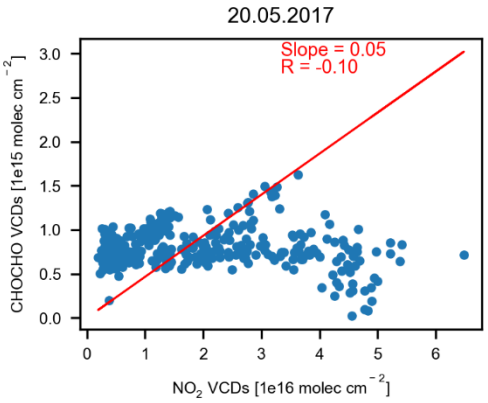
20.05.2017
Slope = 0.05
R = -0.10
CHOCHO VCDs [1e15 molec cm−2]
NO2 VCDs [1e16 molec cm−2]

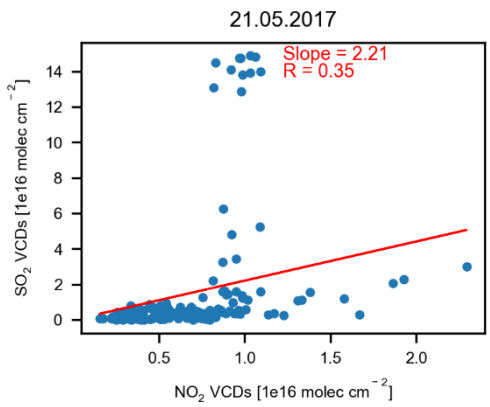
21.05.2017
Slope = 2.21
R = 0.35
SO2 VCDs [1e16 molec cm-2]
NO2 VCDs [1e16 molec cm-2]

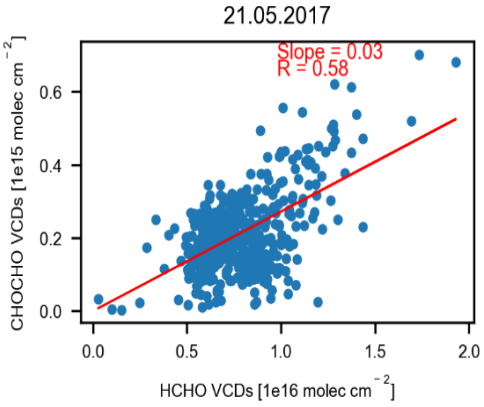
21.05.2017
Slope = 0.03
R = 0.58
CHOCHO VCDs [1e15 molec cm-2]
HCHO VCDs [1e16 molec cm-2]

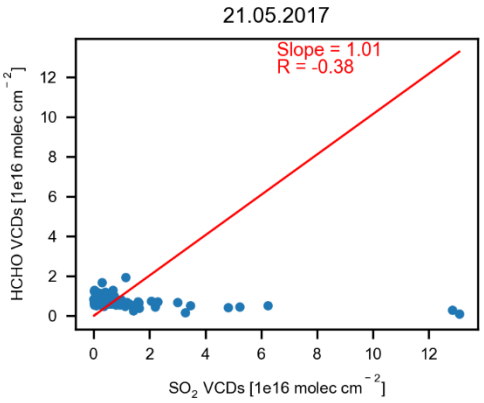
21.05.2017
Slope = 1.01
R = -0.38
HCHO VCDs [1e16 molec cm-2]
SO2 VCDs [1e16 molec cm-2]

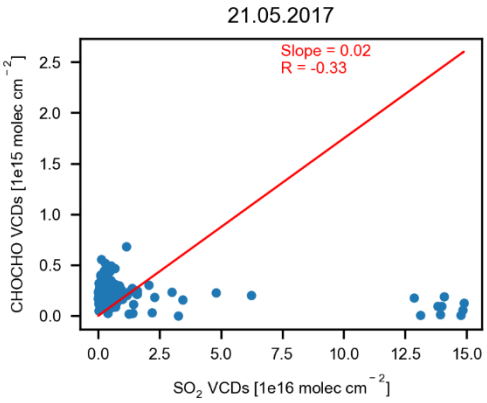
21.05.2017
Slope = 0.02
R = -0.33
CHOCHO VCDs [1e15 molec cm-2]
SO2 VCDs [1e16 molec cm-2]

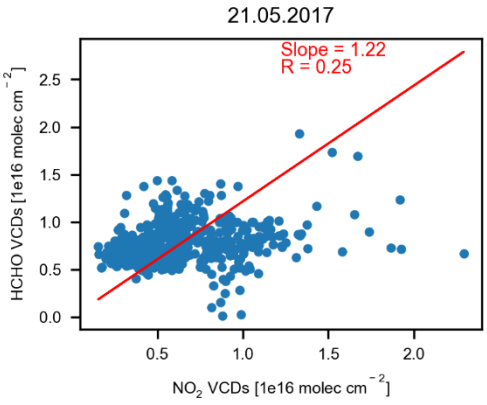
21.05.2017
Slope = 1.22
R = 0.25
HCHO VCDs [1e16 molec cm-2]
NO2 VCDs [1e16 molec cm-2]

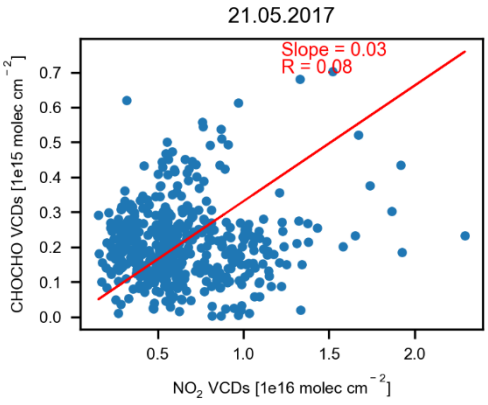
21.05.2017
Slope = 0.03
R = 0.08
CHOCHO VCDs [1e15 molec cm-2]
NO2 VCDs [1e16 molec cm-2]

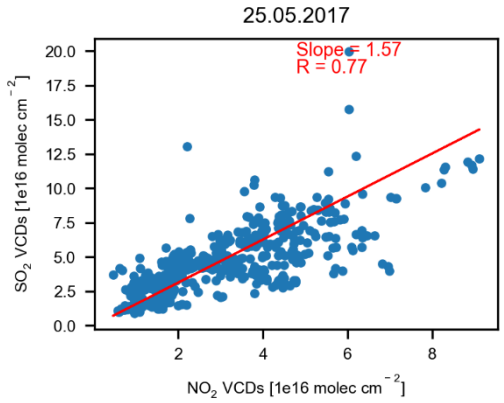
25.05.2017
Slope = 1.57
R = 0.77
SO2 VCDs [1e16 molec cm-2]
NO2 VCDs [1e16 molec cm-2]

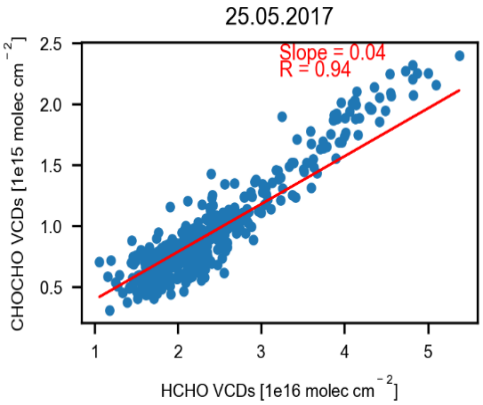
25.05.2017
Slope = 0.04
R = 0.94
CHOCHO VCDs [1e15 molec cm-2]
HCHO VCDs [1e16 molec cm-2]

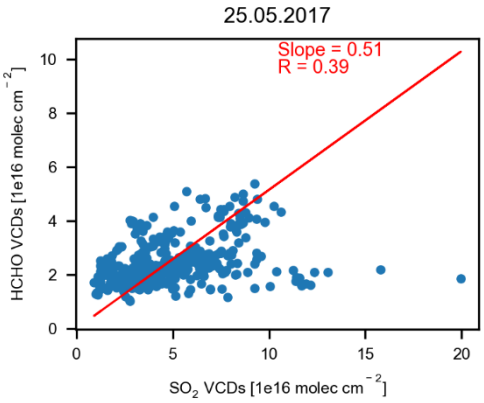
25.05.2017
Slope = 0.51
R = 0.39
HCHO VCDs [1e16 molec cm-2]
SO2 VCDs [1e16 molec cm-2]

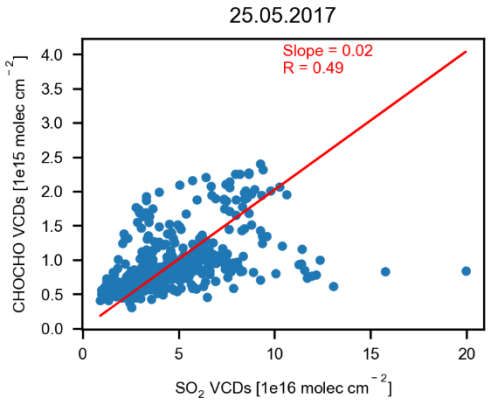
25.05.2017
Slope = 0.02
R = 0.49
CHOCHO VCDs [1e15 molec cm-2]
SO2 VCDs [1e16 molec cm-2]

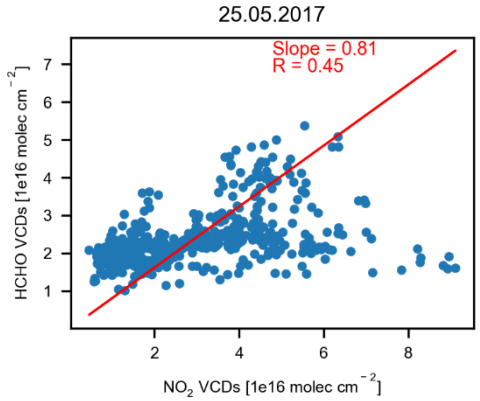
25.05.2017
Slope = 0.81
R = 0.45
HCHO VCDs [1e16 molec cm-2]
NO2 VCDs [1e16 molec cm-2]

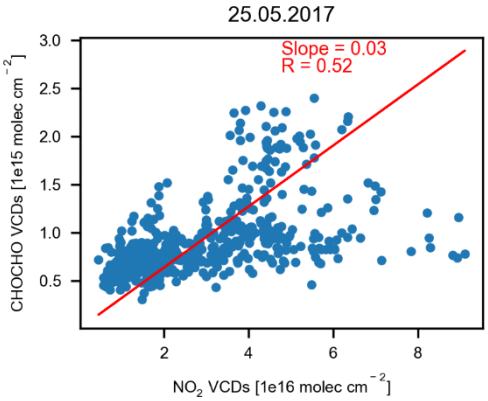
25.05.2017
Slope = 0.03
R = 0.52
CHOCHO VCDs [1e15 molec cm-2]
NO2 VCDs [1e16 molec cm-2]

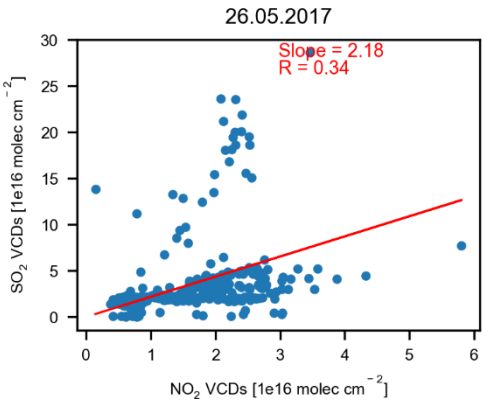
26.05.2017
Slope = 2.18
R = 0.34
SO2 VCDs [1e16 molec cm−2]
NO2 VCDs [1e16 molec cm−2]

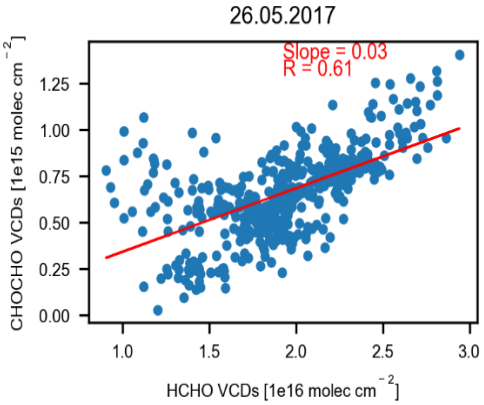
26.05.2017
Slope = 0.03
R = 0.61
CHOCHO VCDs [1e15 molec cm−2]
HCHO VCDs [1e16 molec cm−2]

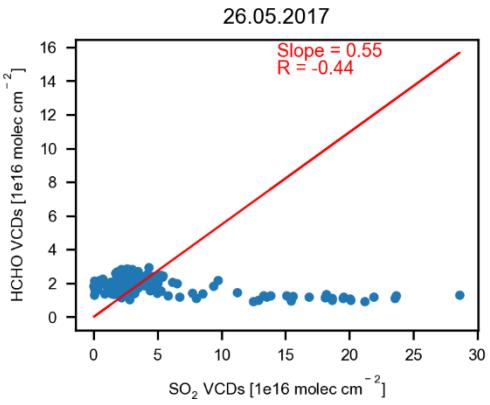
26.05.2017
Slope = 0.55
R = -0.44
HCHO VCDs [1e16 molec cm−2]
SO2 VCDs [1e16 molec cm−2]

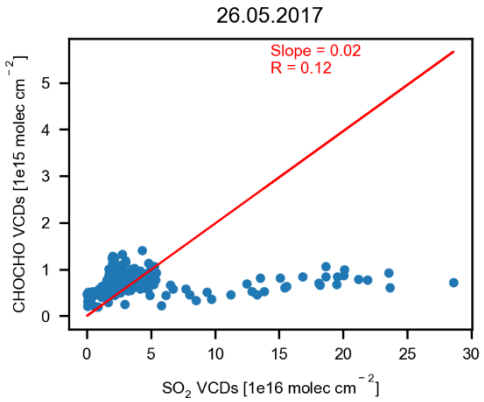
26.05.2017
Slope = 0.02
R = 0.12
CHOCHO VCDs [1e15 molec cm−2]
SO2 VCDs [1e16 molec cm−2]

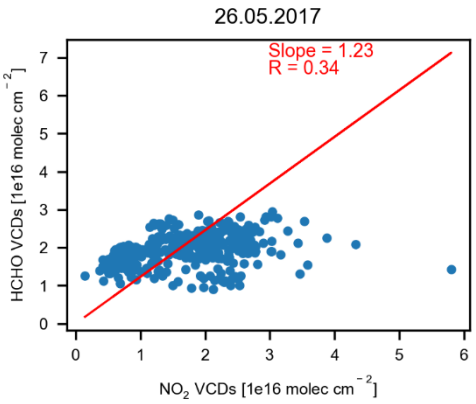
26.05.2017
Slope = 1.23
R = 0.34
HCHO VCDs [1e16 molec cm−2]
NO2 VCDs [1e16 molec cm−2]

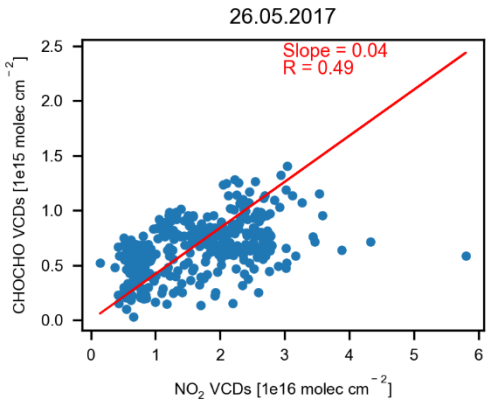
26.05.2017
Slope = 0.04
R = 0.49
CHOCHO VCDs [1e15 molec cm−2]
NO2 VCDs [1e16 molec cm−2]

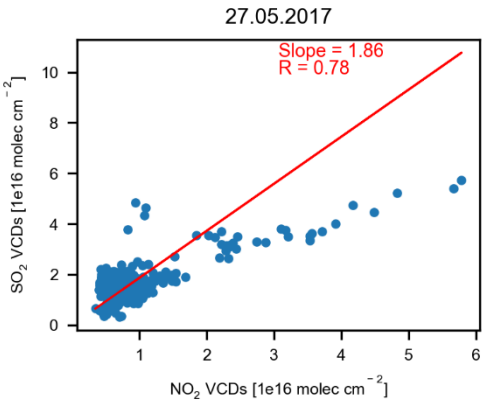
27.05.2017
Slope = 1.86
R = 0.78
SO2 VCDs [1e16 molec cm-2]
NO2 VCDs [1e16 molec cm-2]

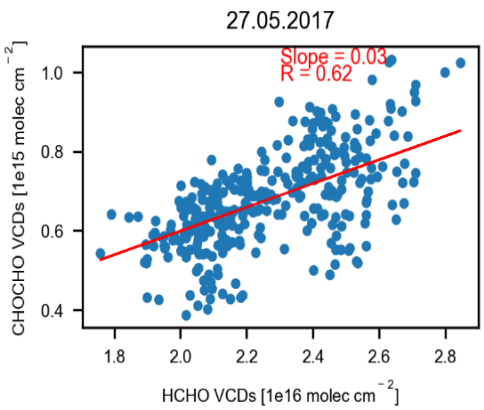
27.05.2017
Slope = 0.03
R = 0.62
CHOCHO VCDs [1e15 molec cm-2]
HCHO VCDs [1e16 molec cm-2]

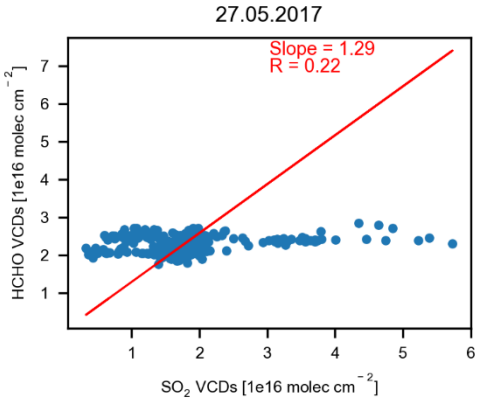
27.05.2017
Slope = 1.29
R = 0.22
HCHO VCDs [1e16 molec cm-2]
SO2 VCDs [1e16 molec cm-2]

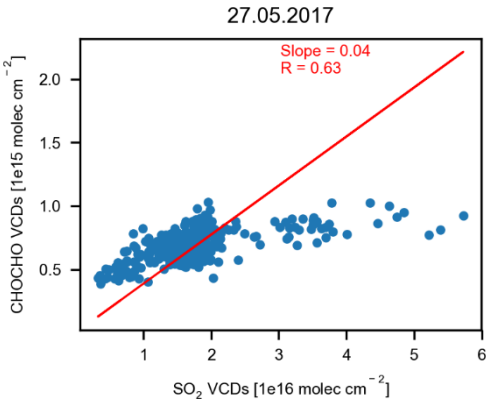
27.05.2017
Slope = 0.04
R = 0.63
CHOCHO VCDs [1e15 molec cm-2]
SO2 VCDs [1e16 molec cm-2]

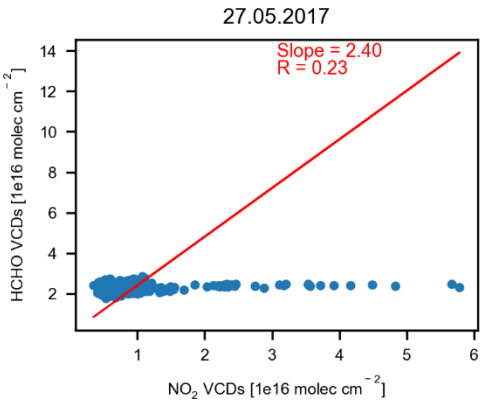
27.05.2017
Slope = 2.40
R = 0.23
HCHO VCDs [1e16 molec cm-2]
NO2 VCDs [1e16 molec cm-2]

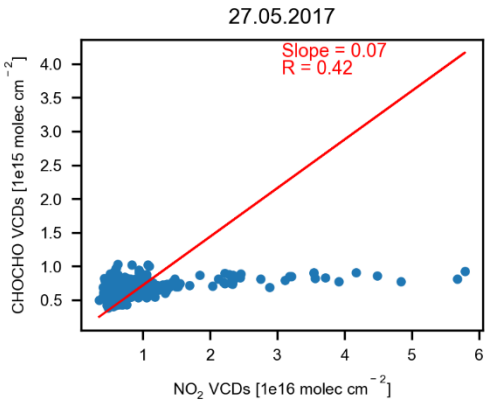
27.05.2017
Slope = 0.07
R = 0.42
CHOCHO VCDs [1e15 molec cm-2]
NO2 VCDs [1e16 molec cm-2]

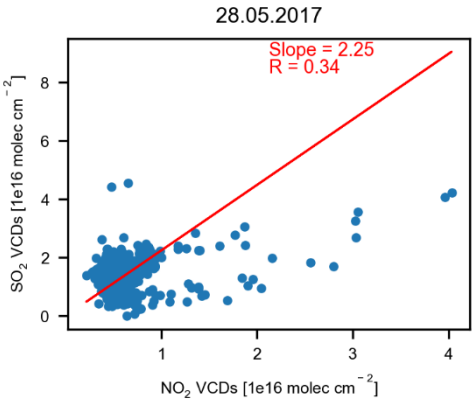
28.05.2017
Slope = 2.25
R = 0.34
SO2 VCDs [1e16 molec cm-2]
NO2 VCDs [1e16 molec cm-2]

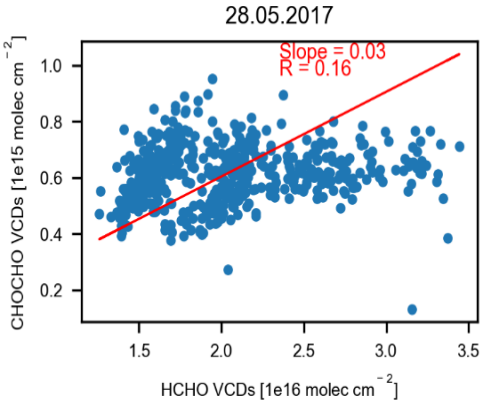
28.05.2017
Slope = 0.03
R = 0.16
CHOCHO VCDs [1e15 molec cm-2]
HCHO VCDs [1e16 molec cm-2]

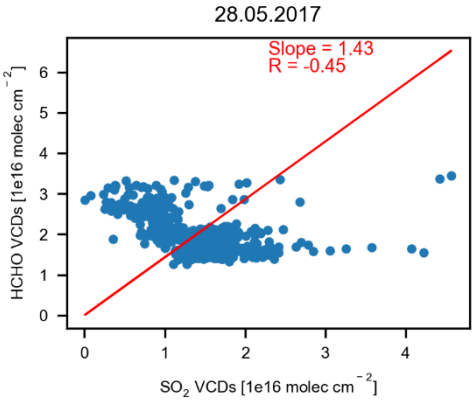
28.05.2017
Slope = 1.43
R = -0.45
HCHO VCDs [1e16 molec cm-2]
SO2 VCDs [1e16 molec cm-2]

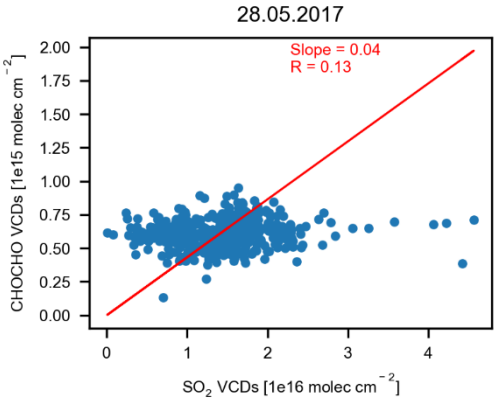
28.05.2017
Slope = 0.04
R = 0.13
CHOCHO VCDs [1e15 molec cm-2]
SO2 VCDs [1e16 molec cm-2]

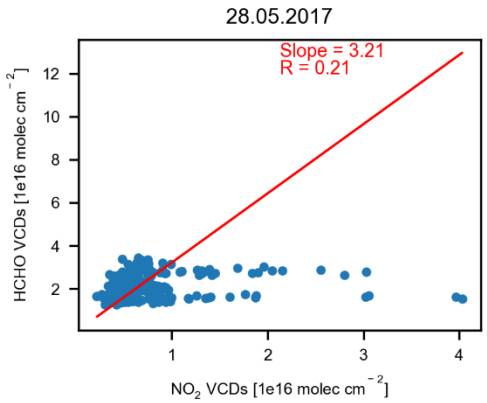
28.05.2017
Slope = 3.21
R = 0.21
HCHO VCDs [1e16 molec cm-2]
NO2 VCDs [1e16 molec cm-2]

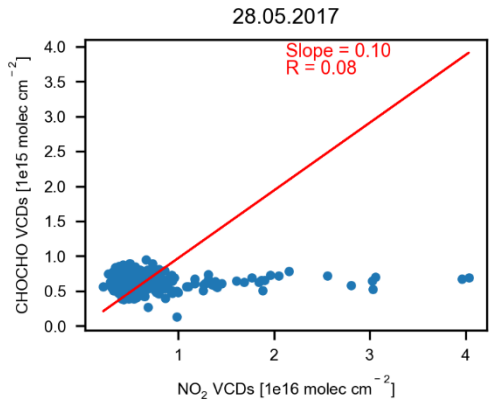
28.05.2017
Slope = 0.10
R = 0.08
CHOCHO VCDs [1e15 molec cm-2]
NO2 VCDs [1e16 molec cm-2]

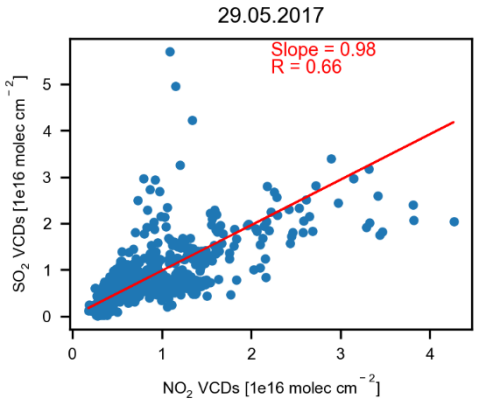
29.05.2017
Slope = 0.98
R = 0.66
SO2 VCDs [1e16 molec cm-2]
NO2 VCDs [1e16 molec cm-2]

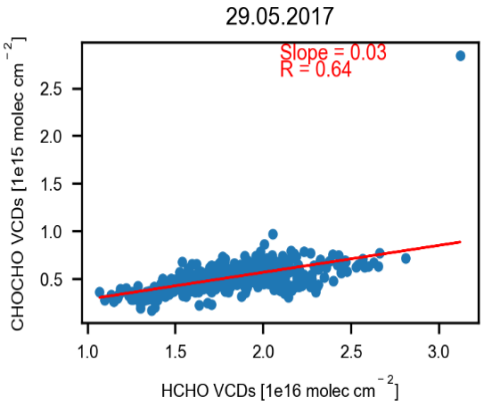
29.05.2017
Slope = 0.03
R = 0.64
CHOCHO VCDs [1e15 molec cm-2]
HCHO VCDs [1e16 molec cm-2]

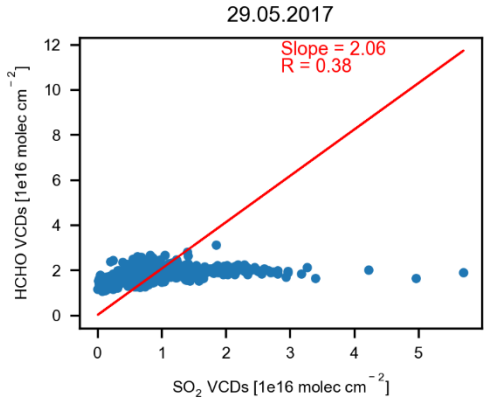
29.05.2017
Slope = 2.06
R = 0.38
HCHO VCDs [1e16 molec cm-2]
SO2 VCDs [1e16 molec cm-2]

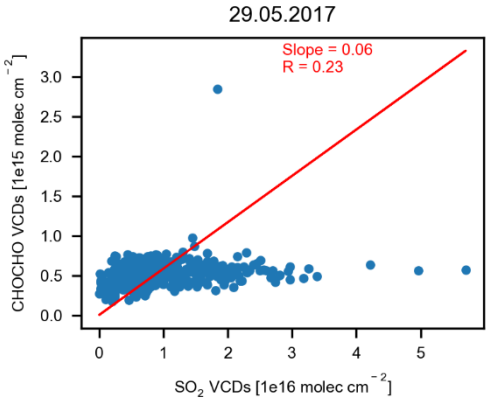
29.05.2017
Slope = 0.06
R = 0.23
CHOCHO VCDs [1e15 molec cm-2]
SO2 VCDs [1e16 molec cm-2]

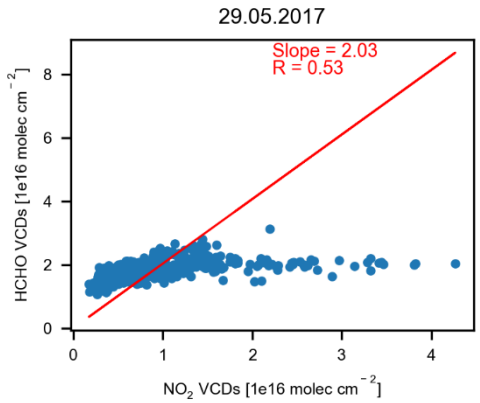
29.05.2017
Slope = 2.03
R = 0.53
HCHO VCDs [1e16 molec cm-2]
NO2 VCDs [1e16 molec cm-2]

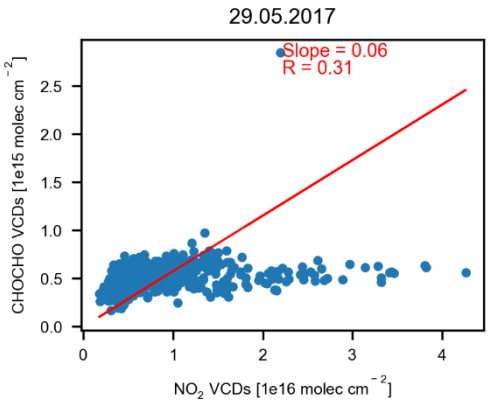
29.05.2017
Slope = 0.06
R = 0.31
CHOCHO VCDs [1e15 molec cm-2]
NO2 VCDs [1e16 molec cm-2]

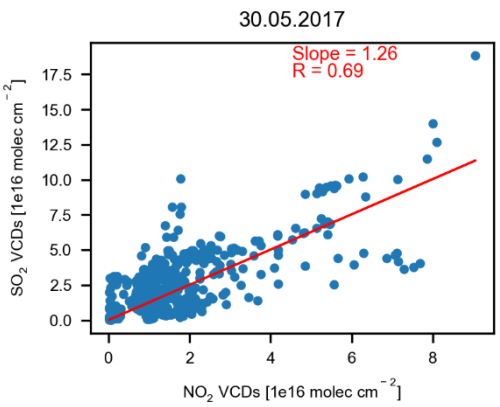
30.05.2017
Slope = 1.26
R = 0.69
SO2 VCDs [1e16 molec cm-2]
NO2 VCDs [1e16 molec cm-2]

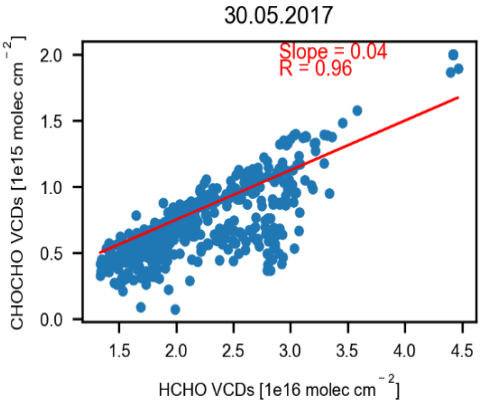
30.05.2017
Slope = 0.04
R = 0.96
CHOCHO VCDs [1e15 molec cm-2]
HCHO VCDs [1e16 molec cm-2]

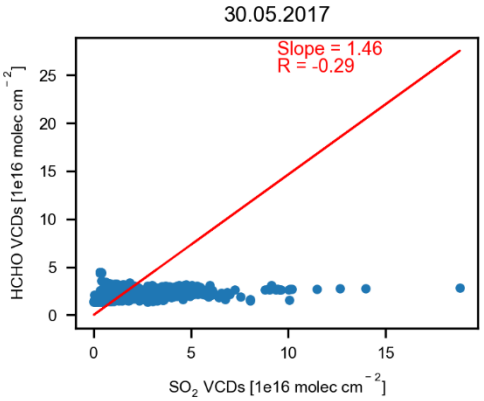
30.05.2017
Slope = 1.46
R = -0.29
HCHO VCDs [1e16 molec cm-2]
SO2 VCDs [1e16 molec cm-2]

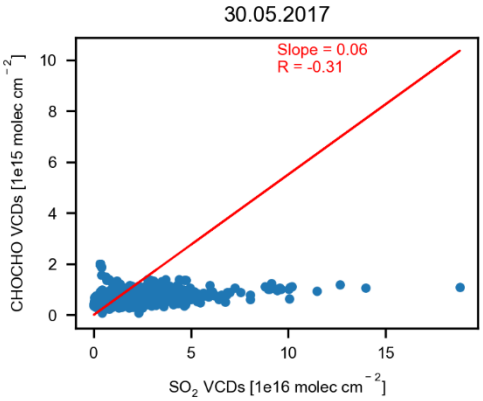
30.05.2017
Slope = 0.06
R = -0.31
CHOCHO VCDs [1e15 molec cm-2]
SO2 VCDs [1e16 molec cm-2]

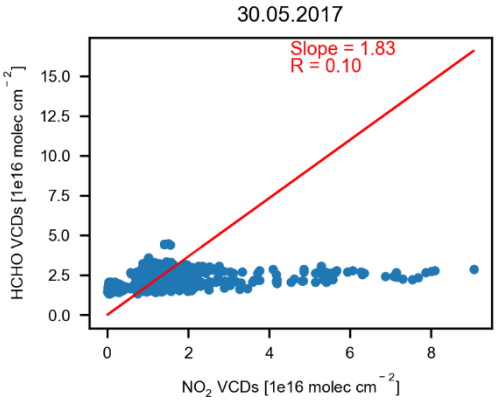
30.05.2017
Slope = 1.83
R = 0.10
HCHO VCDs [1e16 molec cm-2]
NO2 VCDs [1e16 molec cm-2]

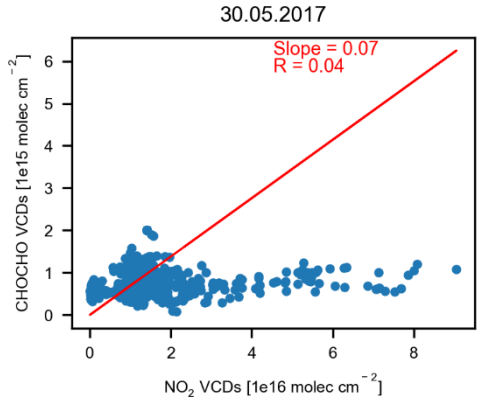
30.05.2017
Slope = 0.07
R = 0.04
CHOCHO VCDs [1e15 molec cm-2]
NO2 VCDs [1e16 molec cm-2]

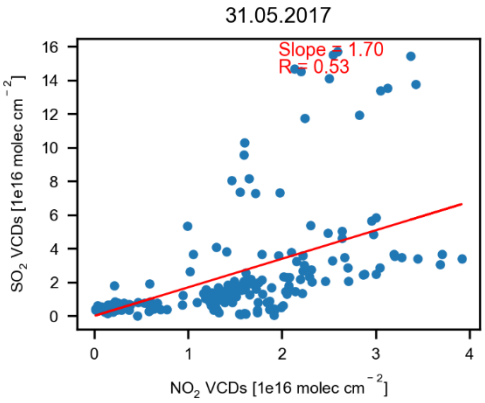
31.05.2017
Slope = 1.70
R = 0.53
SO2 VCDs [1e16 molec cm-2]
NO2 VCDs [1e16 molec cm-2]

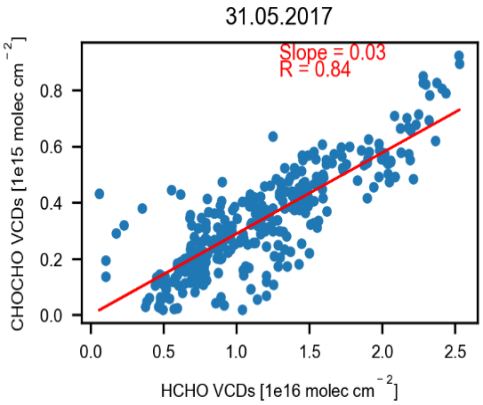
31.05.2017
Slope = 0.03
R = 0.84
CHOCHO VCDs [1e15 molec cm-2]
HCHO VCDs [1e16 molec cm-2]

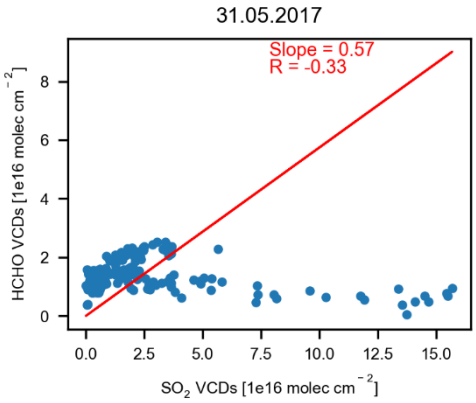
31.05.2017
Slope = 0.57
R = -0.33
HCHO VCDs [1e16 molec cm-2]
SO2 VCDs [1e16 molec cm-2]

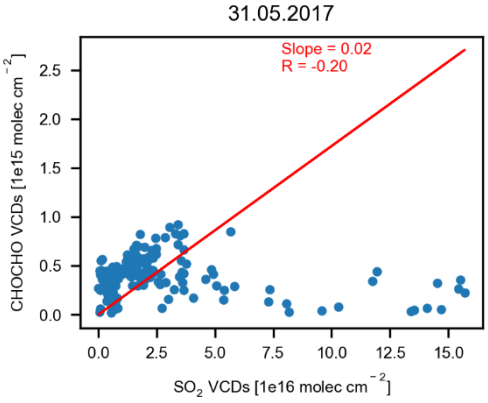
31.05.2017
Slope = 0.02
R = -0.20
CHOCHO VCDs [1e15 molec cm-2]
SO2 VCDs [1e16 molec cm-2]

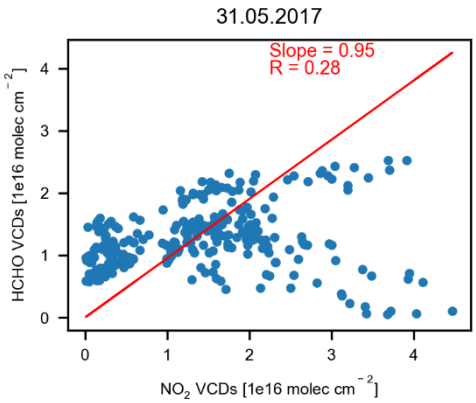
31.05.2017
Slope = 0.95
R = 0.28
HCHO VCDs [1e16 molec cm-2]
NO2 VCDs [1e16 molec cm-2]

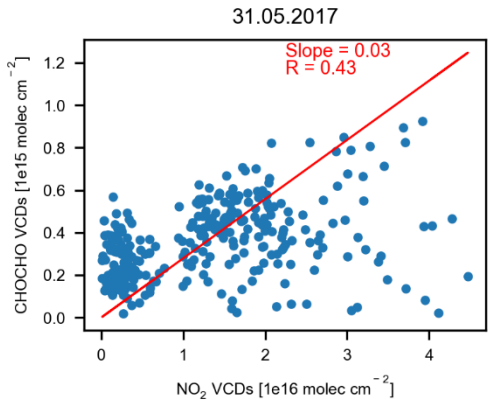
31.05.2017
Slope = 0.03
R = 0.43
CHOCHO VCDs [1e15 molec cm-2]
NO2 VCDs [1e16 molec cm-2]

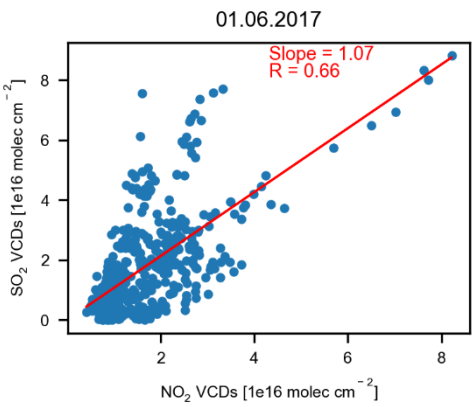
01.06.2017
Slope = 1.07
R = 0.66
SO2 VCDs [1e16 molec cm-2]
NO2 VCDs [1e16 molec cm-2]

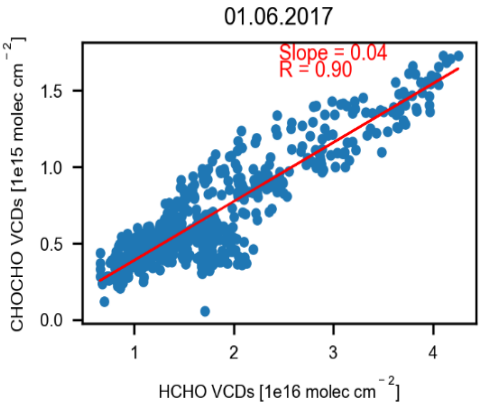
01.06.2017
Slope = 0.04
R = 0.90
CHOCHO VCDs [1e15 molec cm-2]
HCHO VCDs [1e16 molec cm-2]

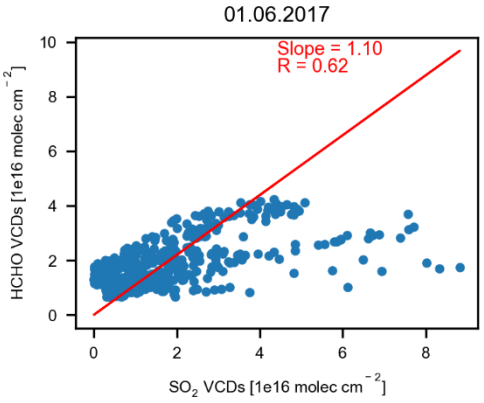
01.06.2017
Slope = 1.10
R = 0.62
HCHO VCDs [1e16 molec cm-2]
SO2 VCDs [1e16 molec cm-2]

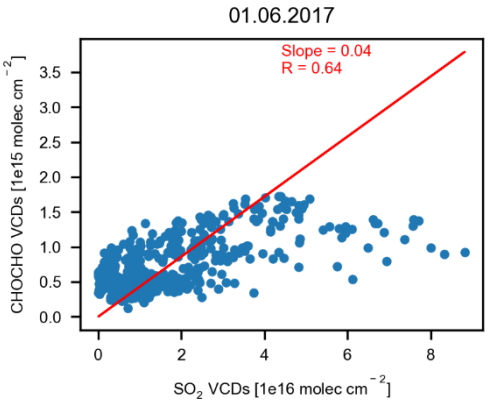
01.06.2017
Slope = 0.04
R = 0.64
CHOCHO VCDs [1e15 molec cm-2]
SO2 VCDs [1e16 molec cm-2]

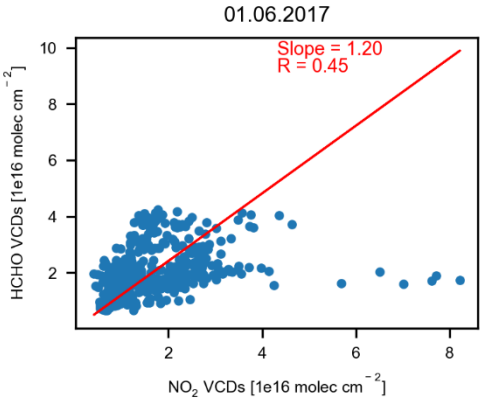
01.06.2017
Slope = 1.20
R = 0.45
HCHO VCDs [1e16 molec cm-2]
NO2 VCDs [1e16 molec cm-2]

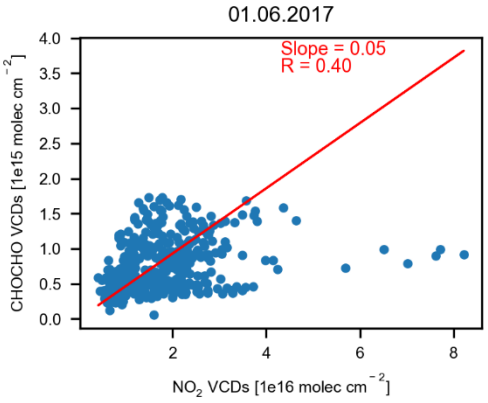
01.06.2017
Slope = 0.05
R = 0.40
CHOCHO VCDs [1e15 molec cm-2]
NO2 VCDs [1e16 molec cm-2]

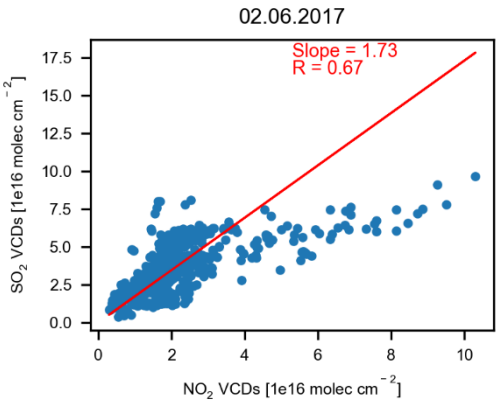
02.06.2017
Slope = 1.73
R = 0.67
SO2 VCDs [1e16 molec cm-2]
NO2 VCDs [1e16 molec cm-2]

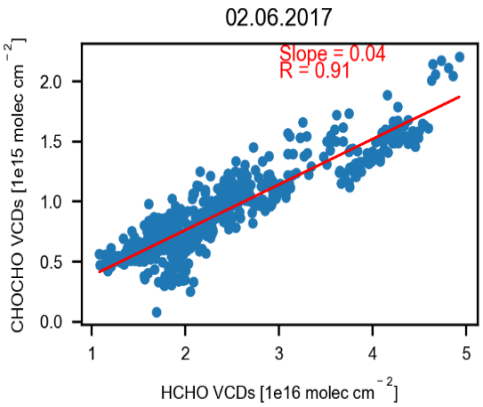
02.06.2017
Slope = 0.04
R = 0.91
CHOCHO VCDs [1e15 molec cm-2]
HCHO VCDs [1e16 molec cm-2]

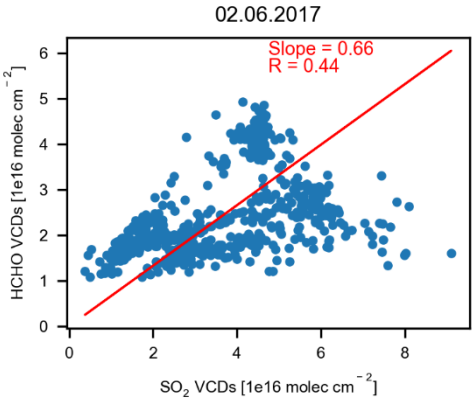
02.06.2017
Slope = 0.66
R = 0.44
HCHO VCDs [1e16 molec cm-2]
SO2 VCDs [1e16 molec cm-2]

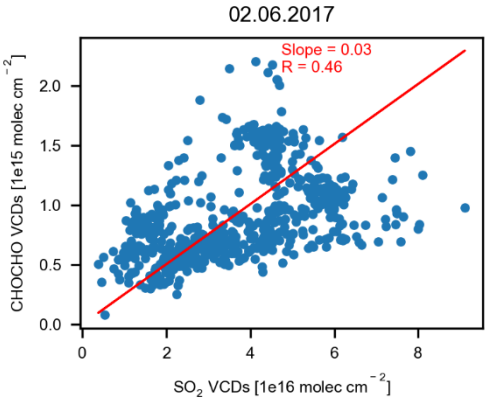
02.06.2017
Slope = 0.03
R = 0.46
CHOCHO VCDs [1e15 molec cm-2]
SO2 VCDs [1e16 molec cm-2]

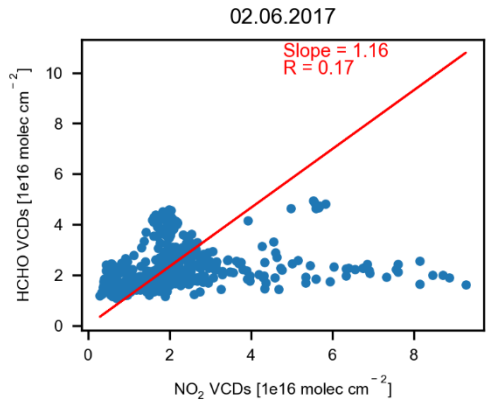
02.06.2017
Slope = 1.16
R = 0.17
HCHO VCDs [1e16 molec cm-2]
NO2 VCDs [1e16 molec cm-2]

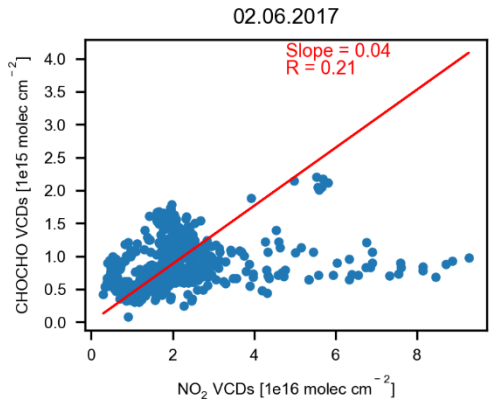
02.06.2017
Slope = 0.04
R = 0.21
CHOCHO VCDs [1e15 molec cm-2]
NO2 VCDs [1e16 molec cm-2]

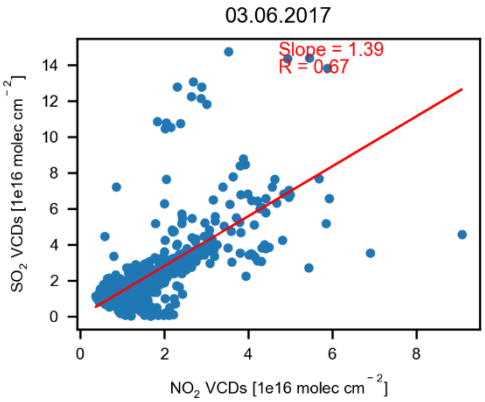
03.06.2017
Slope = 1.39
R = 0.67
SO2 VCDs [1e16 molec cm-2]
NO2 VCDs [1e16 molec cm-2]

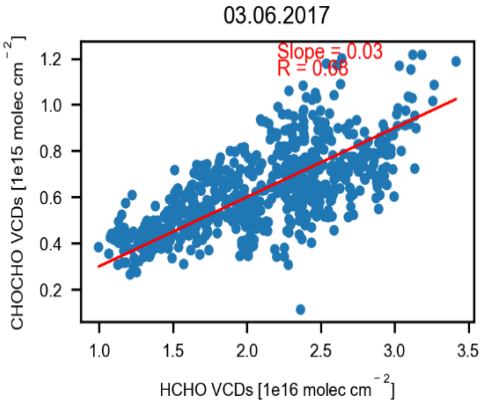
03.06.2017
Slope = 0.03
R = 0.68
CHOCHO VCDs [1e15 molec cm-2]
HCHO VCDs [1e16 molec cm-2]

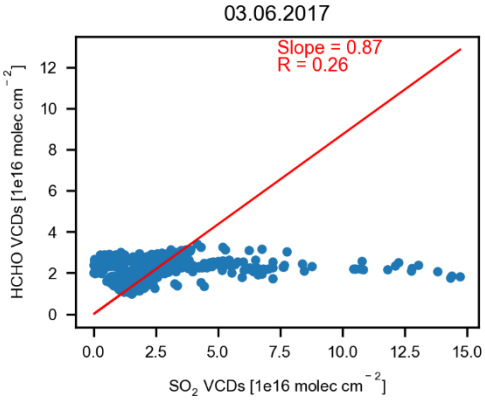
03.06.2017
Slope = 0.87
R = 0.26
HCHO VCDs [1e16 molec cm-2]
SO2 VCDs [1e16 molec cm-2]

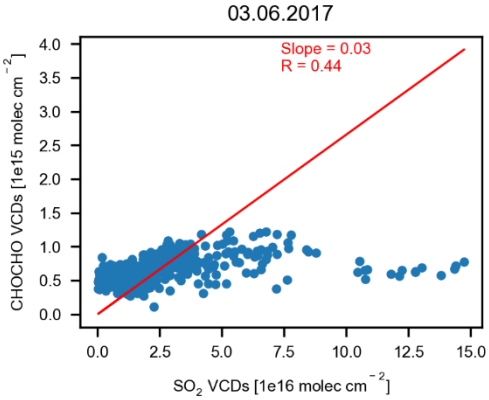
03.06.2017
Slope = 0.03
R = 0.44
CHOCHO VCDs [1e15 molec cm-2]
SO2 VCDs [1e16 molec cm-2]

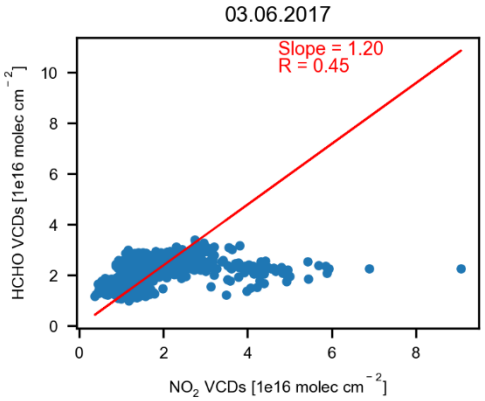
03.06.2017
Slope = 1.20
R = 0.45
HCHO VCDs [1e16 molec cm-2]
NO2 VCDs [1e16 molec cm-2]

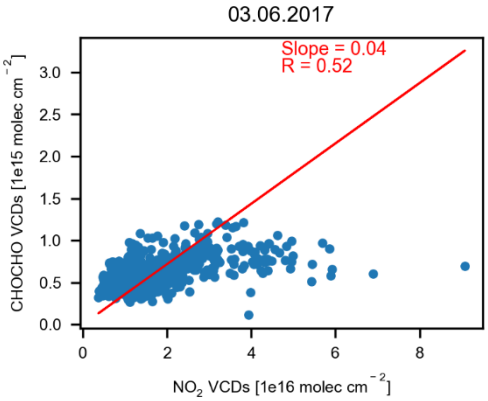
03.06.2017
Slope = 0.04
R = 0.52
CHOCHO VCDs [1e15 molec cm-2]
NO2 VCDs [1e16 molec cm-2]

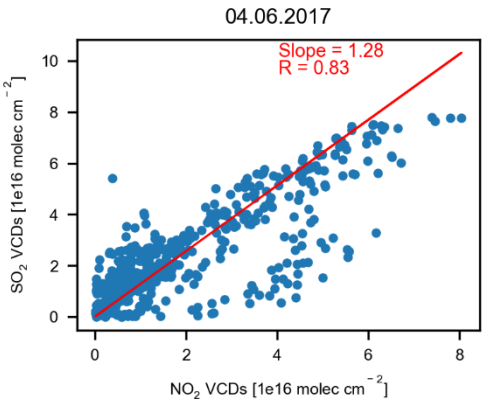
04.06.2017
Slope = 1.28
R = 0.83
SO2 VCDs [1e16 molec cm-2]
NO2 VCDs [1e16 molec cm-2]

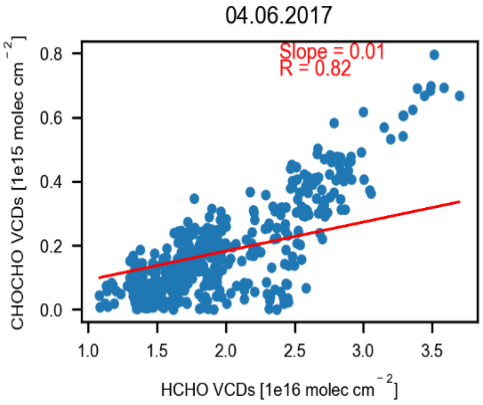
04.06.2017
Slope = 0.01
R = 0.82
CHOCHO VCDs [1e15 molec cm-2]
HCHO VCDs [1e16 molec cm-2]

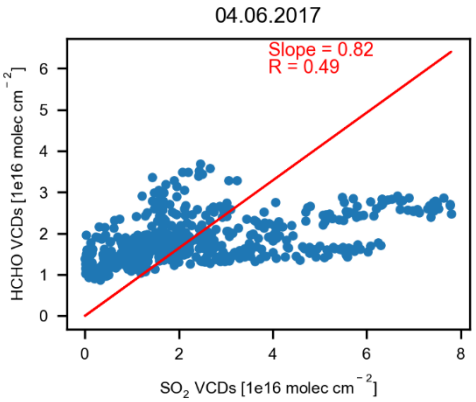
04.06.2017
Slope = 0.82
R = 0.49
HCHO VCDs [1e16 molec cm-2]
SO2 VCDs [1e16 molec cm-2]

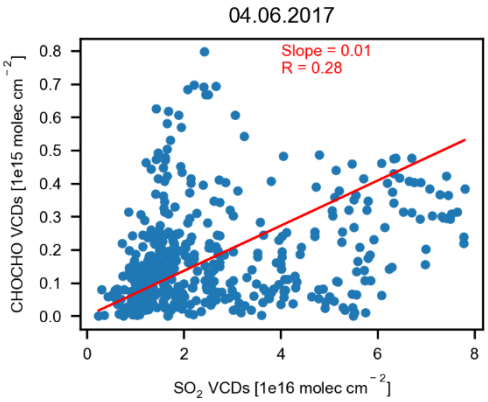
04.06.2017
Slope = 0.01
R = 0.28
CHOCHO VCDs [1e15 molec cm-2]
SO2 VCDs [1e16 molec cm-2]

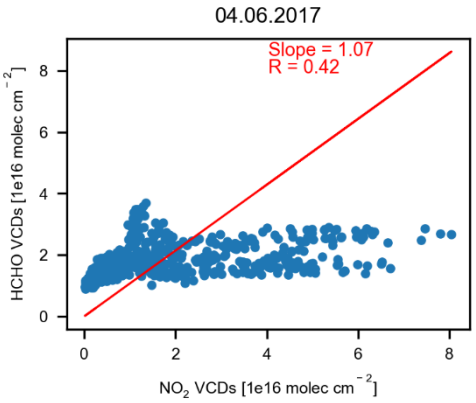
04.06.2017
Slope = 1.07
R = 0.42
HCHO VCDs [1e16 molec cm-2]
NO2 VCDs [1e16 molec cm-2]

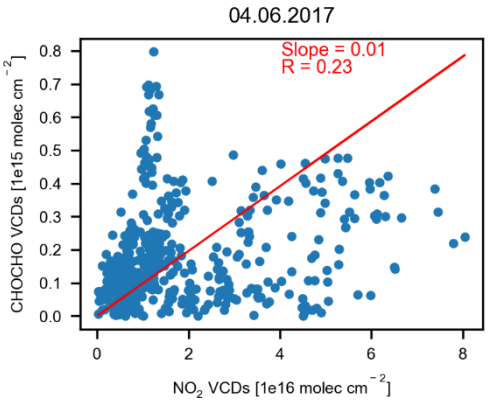
04.06.2017
Slope = 0.01
R = 0.23
CHOCHO VCDs [1e15 molec cm-2]
NO2 VCDs [1e16 molec cm-2]

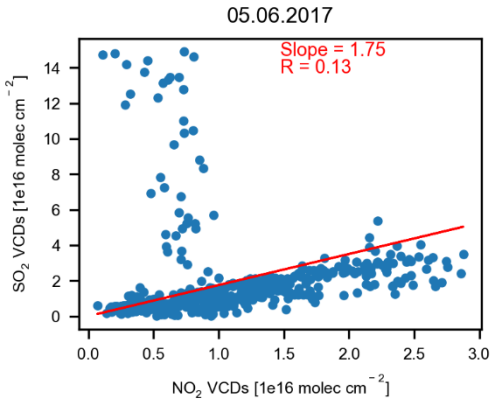
05.06.2017
Slope = 1.75
R = 0.13
SO2 VCDs [1e16 molec cm-2]
NO2 VCDs [1e16 molec cm-2]

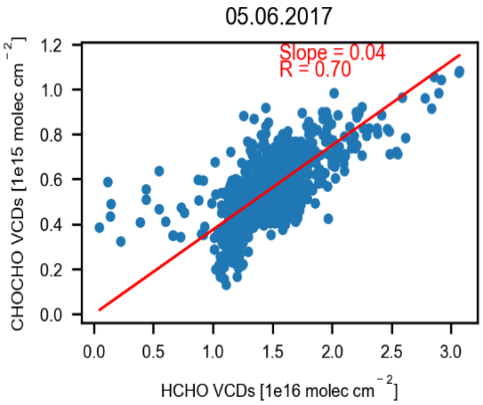
05.06.2017
Slope = 0.04
R = 0.70
CHOCHO VCDs [1e15 molec cm-2]
HCHO VCDs [1e16 molec cm-2]

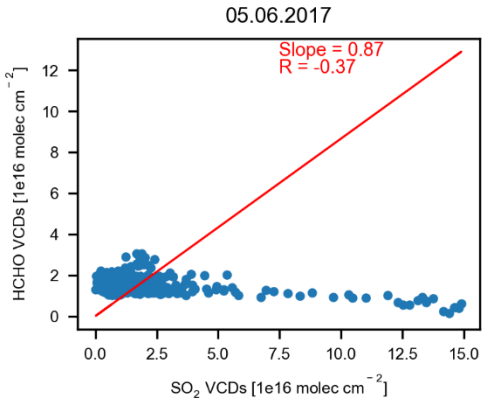
05.06.2017
Slope = 0.87
R = -0.37
HCHO VCDs [1e16 molec cm-2]
SO2 VCDs [1e16 molec cm-2]

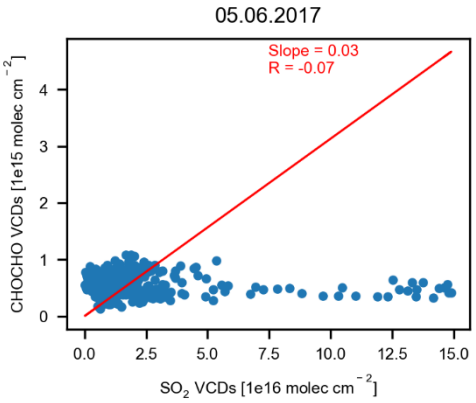
05.06.2017
Slope = 0.03
R = -0.07
CHOCHO VCDs [1e15 molec cm-2]
SO2 VCDs [1e16 molec cm-2]

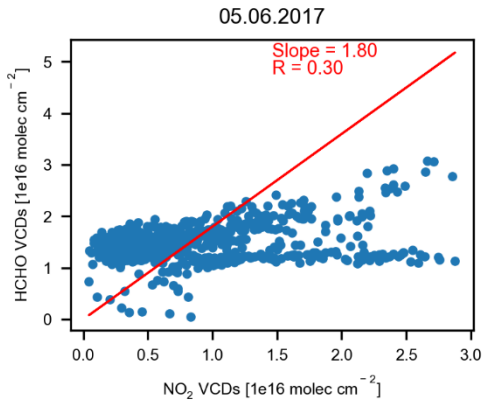
05.06.2017
Slope = 1.80
R = 0.30
HCHO VCDs [1e16 molec cm-2]
NO2 VCDs [1e16 molec cm-2]

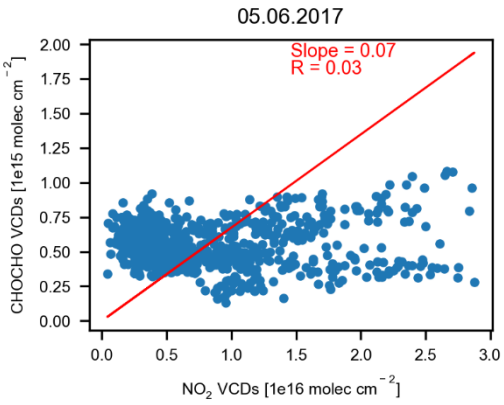
05.06.2017
Slope = 0.07
R = 0.03
CHOCHO VCDs [1e15 molec cm-2]
NO2 VCDs [1e16 molec cm-2]

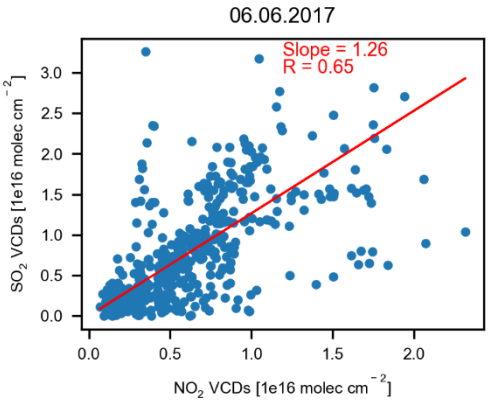
06.06.2017
Slope = 1.26
R = 0.65
SO2 VCDs [1e16 molec cm-2]
NO2 VCDs [1e16 molec cm-2]

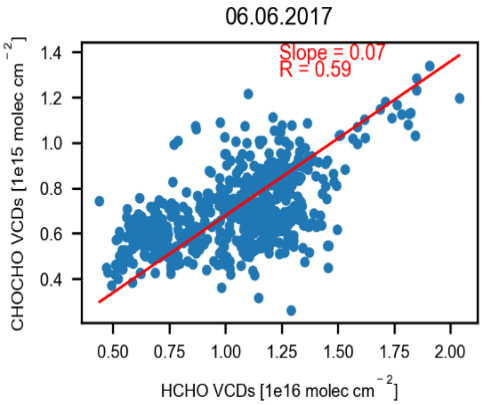
06.06.2017
Slope = 0.07
R = 0.59
CHOCHO VCDs [1e15 molec cm-2]
HCHO VCDs [1e16 molec cm-2]

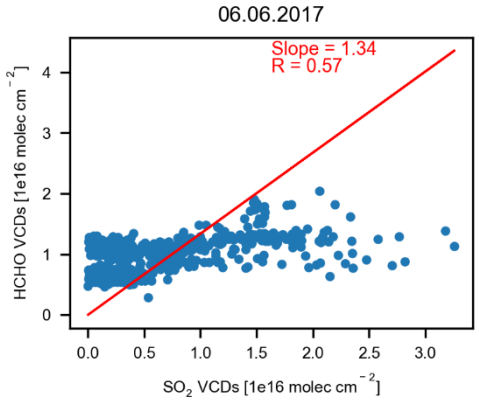
06.06.2017
Slope = 1.34
R = 0.57
HCHO VCDs [1e16 molec cm-2]
SO2 VCDs [1e16 molec cm-2]

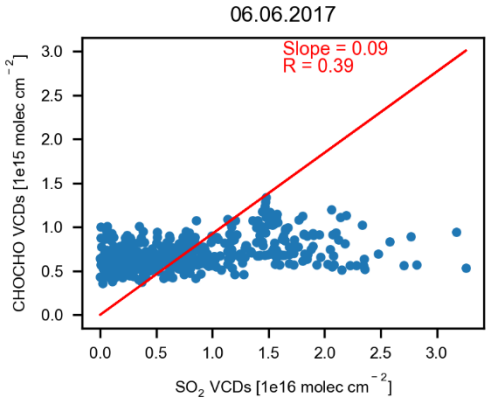
06.06.2017
Slope = 0.09
R = 0.39
CHOCHO VCDs [1e15 molec cm-2]
SO2 VCDs [1e16 molec cm-2]

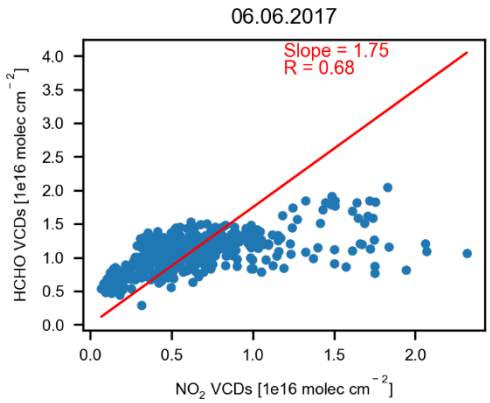
06.06.2017
Slope = 1.75
R = 0.68
HCHO VCDs [1e16 molec cm-2]
NO2 VCDs [1e16 molec cm-2]

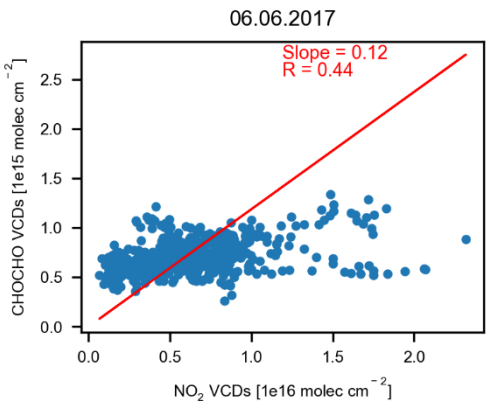
06.06.2017
Slope = 0.12
R = 0.44
CHOCHO VCDs [1e15 molec cm-2]
NO2 VCDs [1e16 molec cm-2]

C.2 2018-I

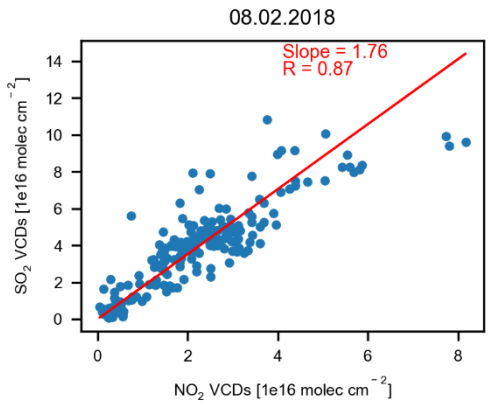
08.02.2018
Slope = 1.76
R = 0.87
SO2 VCDs [1e16 molec cm−2]
NO2 VCDs [1e16 molec cm−2]

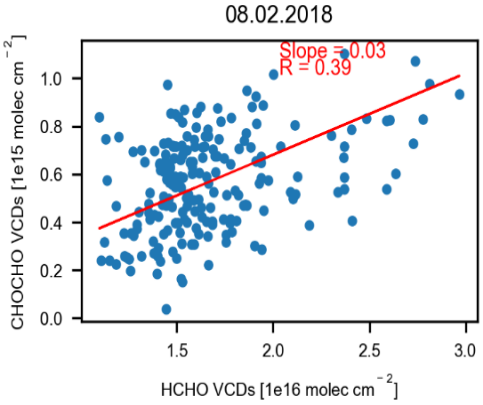
08.02.2018
Slope = 0.03
R = 0.39
CHOCHO VCDs [1e15 molec cm−2]
HCHO VCDs [1e16 molec cm−2]

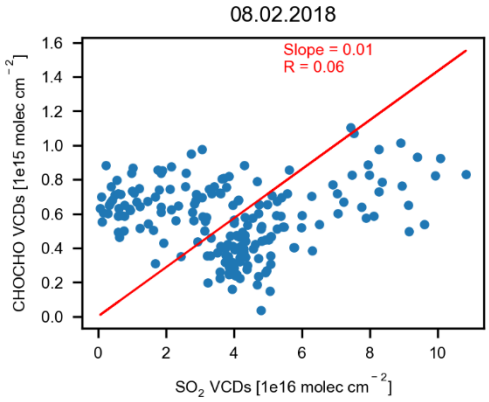
08.02.2018
Slope = 0.01
R = 0.06
CHOCHO VCDs [1e15 molec cm−2]
SO2 VCDs [1e16 molec cm−2]

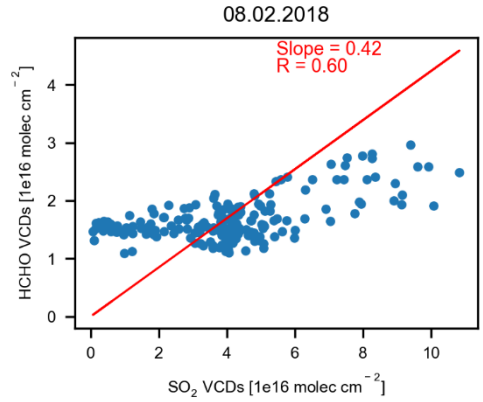
08.02.2018
Slope = 0.42
R = 0.60
HCHO VCDs [1e16 molec cm−2]
SO2 VCDs [1e16 molec cm−2]

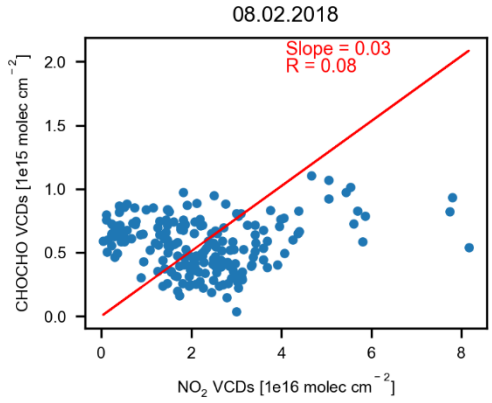
08.02.2018
Slope = 0.03
R = 0.08
CHOCHO VCDs [1e15 molec cm−2]
NO2 VCDs [1e16 molec cm−2]

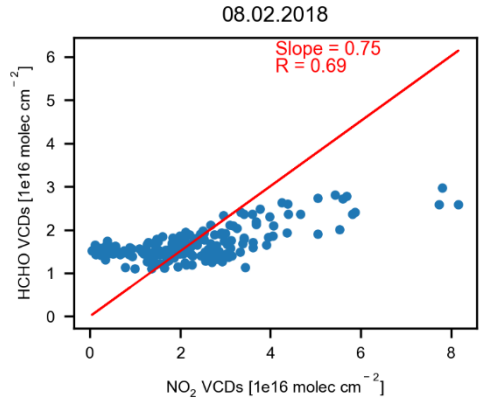
08.02.2018
Slope = 0.75
R = 0.69
HCHO VCDs [1e16 molec cm−2]
NO2 VCDs [1e16 molec cm−2]

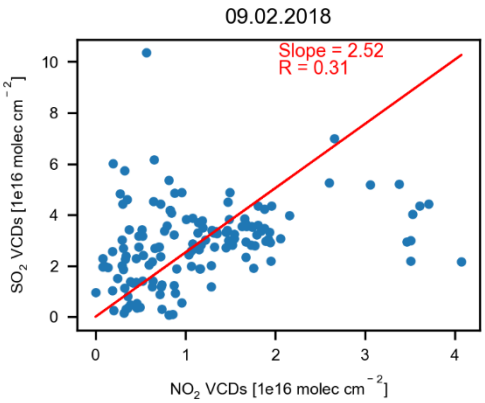
09.02.2018
Slope = 2.52
R = 0.31
SO2 VCDs [1e16 molec cm-2]
NO2 VCDs [1e16 molec cm-2]

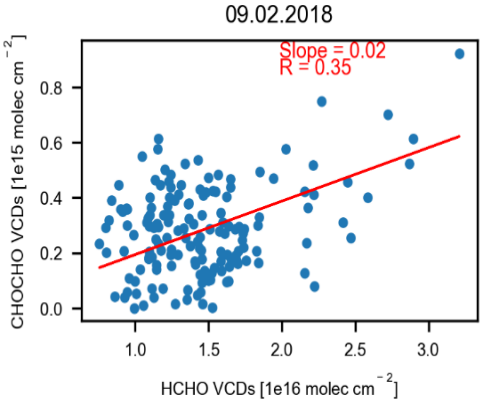
09.02.2018
Slope = 0.02
R = 0.35
CHOCHO VCDs [1e15 molec cm-2]
HCHO VCDs [1e16 molec cm-2]

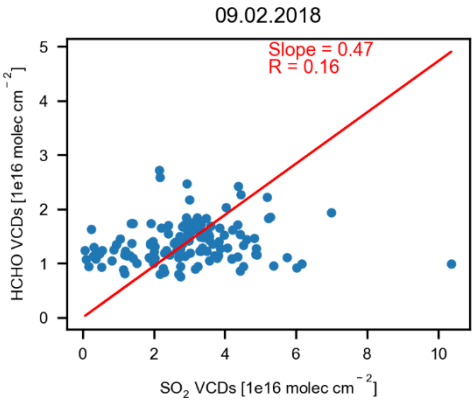
09.02.2018
Slope = 0.47
R = 0.16
HCHO VCDs [1e16 molec cm-2]
SO2 VCDs [1e16 molec cm-2]

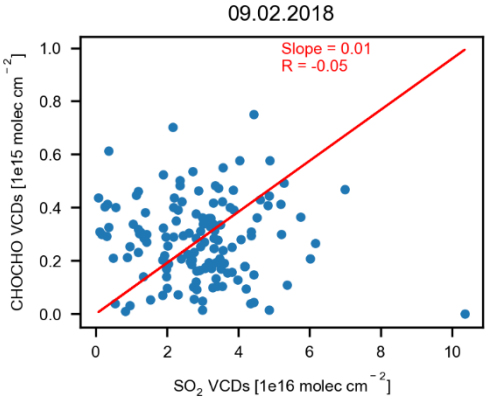
09.02.2018
Slope = 0.01
R = -0.05
CHOCHO VCDs [1e15 molec cm-2]
SO2 VCDs [1e16 molec cm-2]

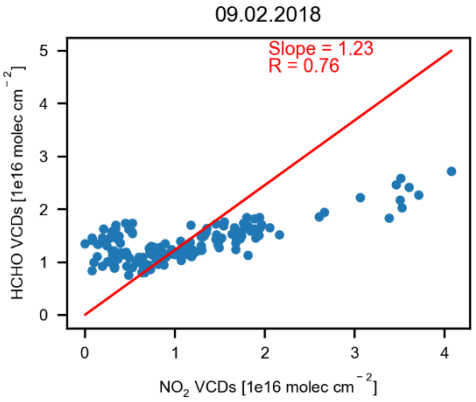
09.02.2018
Slope = 1.23
R = 0.76
HCHO VCDs [1e16 molec cm-2]
NO2 VCDs [1e16 molec cm-2]

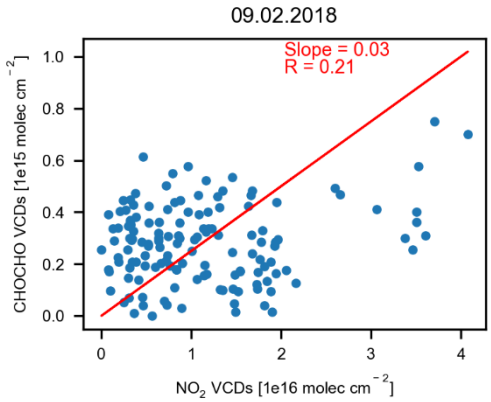
09.02.2018
Slope = 0.03
R = 0.21
CHOCHO VCDs [1e15 molec cm-2]
NO2 VCDs [1e16 molec cm-2]

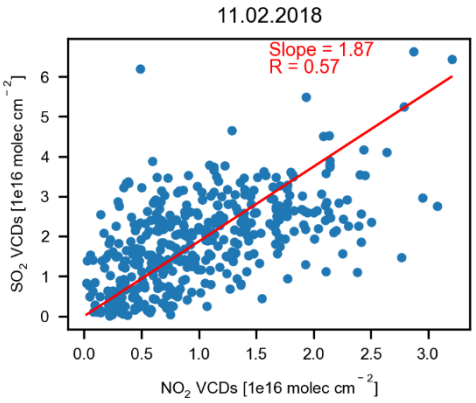
11.02.2018
Slope = 1.87
R = 0.57
SO2 VCDs [1e16 molec cm-2]
NO2 VCDs [1e16 molec cm-2]

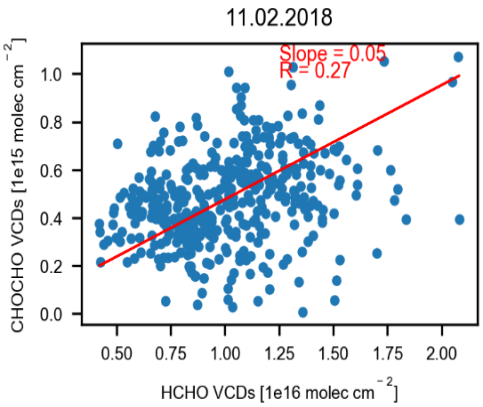
11.02.2018
Slope = 0.05
R = 0.27
CHOCHO VCDs [1e15 molec cm-2]
HCHO VCDs [1e16 molec cm-2]

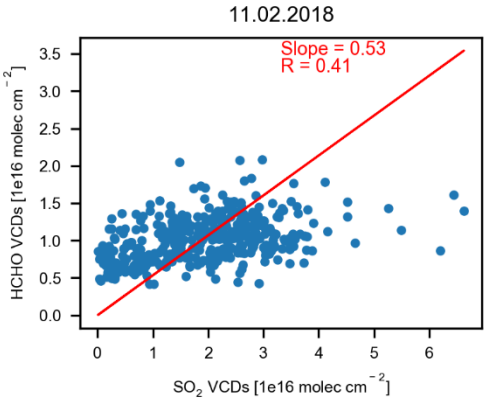
11.02.2018
Slope = 0.53
R = 0.41
HCHO VCDs [1e16 molec cm-2]
SO2 VCDs [1e16 molec cm-2]

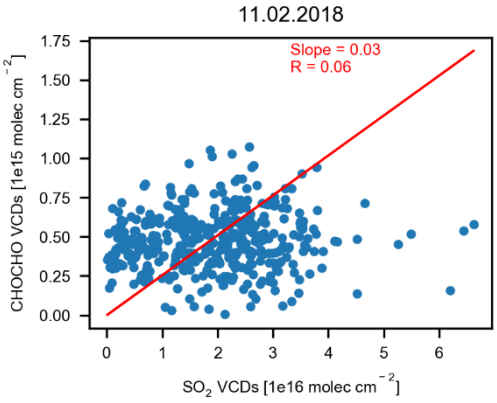
11.02.2018
Slope = 0.03
R = 0.06
CHOCHO VCDs [1e15 molec cm-2]
SO2 VCDs [1e16 molec cm-2]

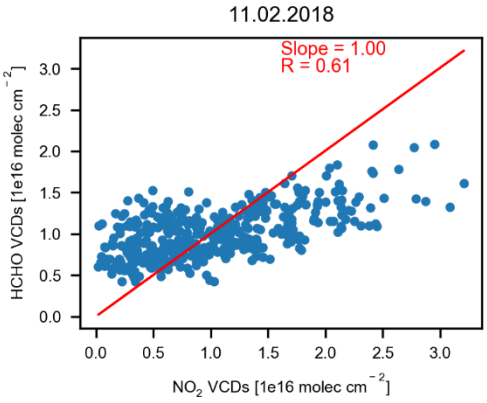
11.02.2018
Slope = 1.00
R = 0.61
HCHO VCDs [1e16 molec cm-2]
NO2 VCDs [1e16 molec cm-2]

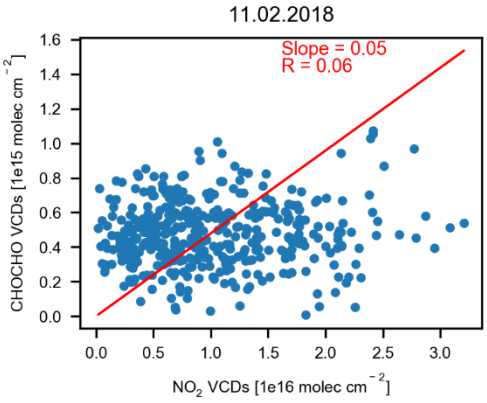
11.02.2018
Slope = 0.05
R = 0.06
CHOCHO VCDs [1e15 molec cm-2]
NO2 VCDs [1e16 molec cm-2]

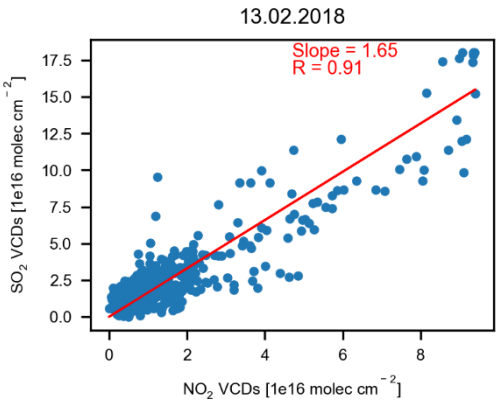
13.02.2018
Slope = 1.65
R = 0.91
SO2 VCDs [1e16 molec cm-2]
NO2 VCDs [1e16 molec cm-2]

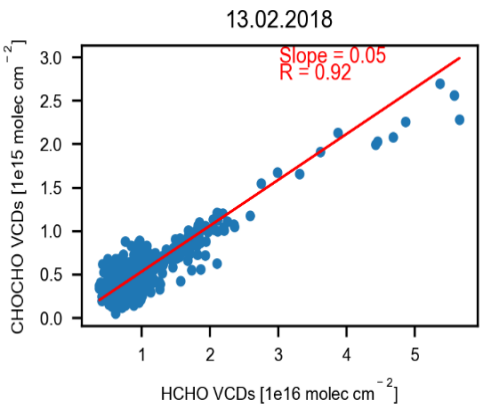
13.02.2018
Slope = 0.05
R = 0.92
CHOCHO VCDs [1e15 molec cm-2]
HCHO VCDs [1e16 molec cm-2]

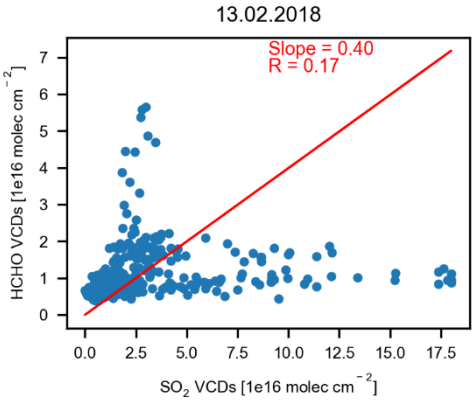
13.02.2018
Slope = 0.40
R = 0.17
HCHO VCDs [1e16 molec cm-2]
SO2 VCDs [1e16 molec cm-2]

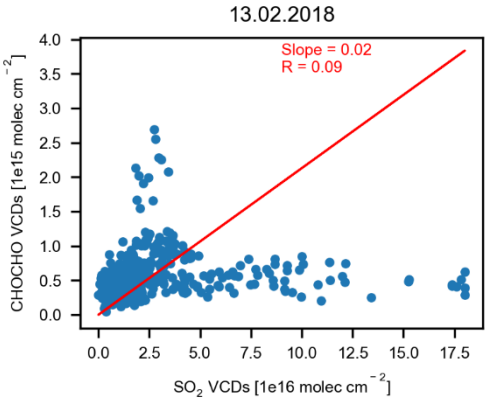
13.02.2018
Slope = 0.02
R = 0.09
CHOCHO VCDs [1e15 molec cm-2]
SO2 VCDs [1e16 molec cm-2]

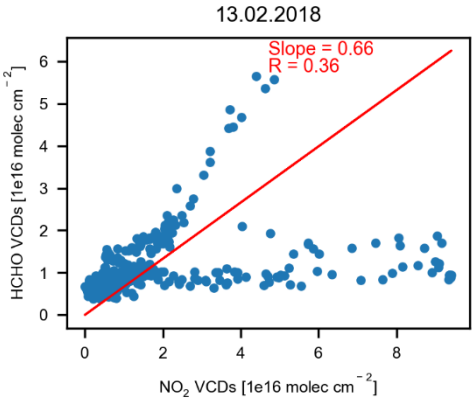
13.02.2018
Slope = 0.66
R = 0.36
HCHO VCDs [1e16 molec cm-2]
NO2 VCDs [1e16 molec cm-2]

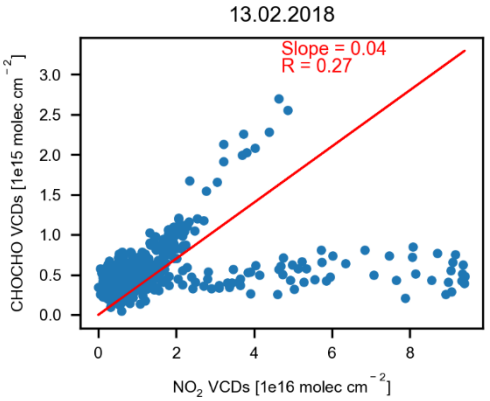
13.02.2018
Slope = 0.04
R = 0.27
CHOCHO VCDs [1e15 molec cm-2]
NO2 VCDs [1e16 molec cm-2]

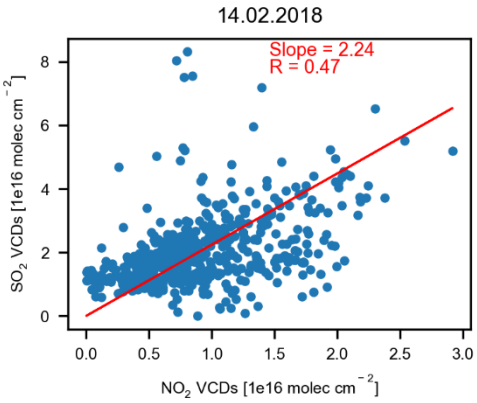
14.02.2018
Slope = 2.24
R = 0.47
SO2 VCDs [1e16 molec cm-2]
NO2 VCDs [1e16 molec cm-2]

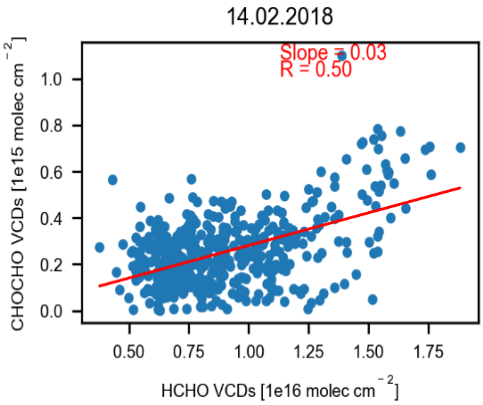
14.02.2018
Slope = 0.03
R = 0.50
CHOCHO VCDs [1e15 molec cm-2]
HCHO VCDs [1e16 molec cm-2]

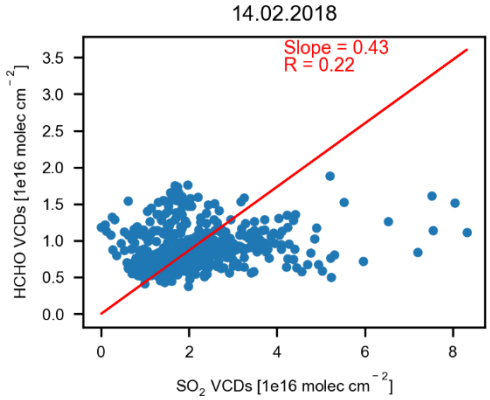
14.02.2018
Slope = 0.43
R = 0.22
HCHO VCDs [1e16 molec cm-2]
SO2 VCDs [1e16 molec cm-2]

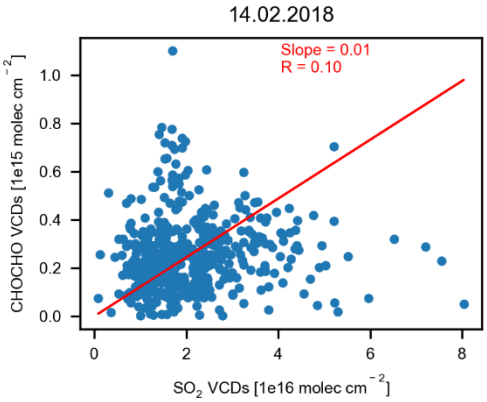
14.02.2018
Slope = 0.01
R = 0.10
CHOCHO VCDs [1e15 molec cm-2]
SO2 VCDs [1e16 molec cm-2]

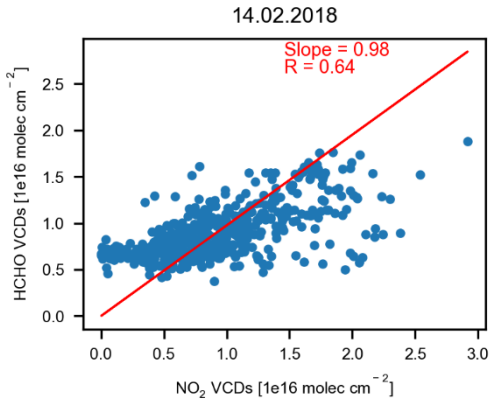
14.02.2018
Slope = 0.98
R = 0.64
HCHO VCDs [1e16 molec cm-2]
NO2 VCDs [1e16 molec cm-2]

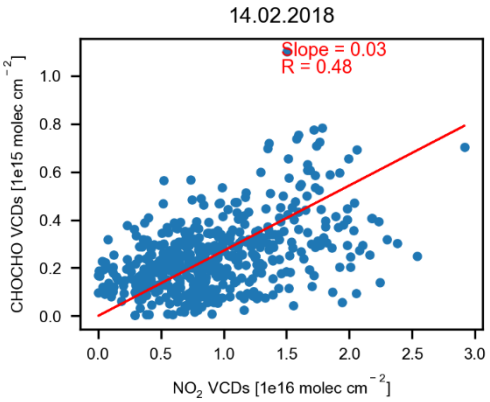
14.02.2018
Slope = 0.03
R = 0.48
CHOCHO VCDs [1e15 molec cm-2]
NO2 VCDs [1e16 molec cm-2]

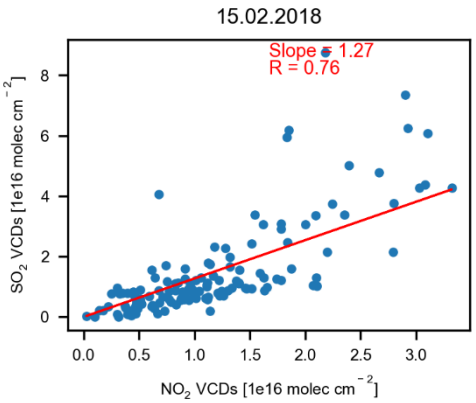
15.02.2018
Slope = 1.27
R = 0.76
SO2 VCDs [1e16 molec cm-2]
NO2 VCDs [1e16 molec cm-2]

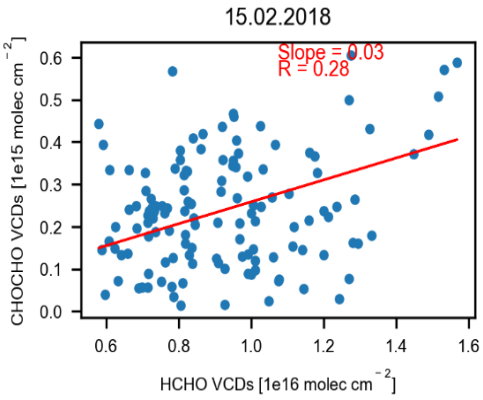
15.02.2018
Slope = 0.03
R = 0.28
CHOCHO VCDs [1e15 molec cm-2]
HCHO VCDs [1e16 molec cm-2]

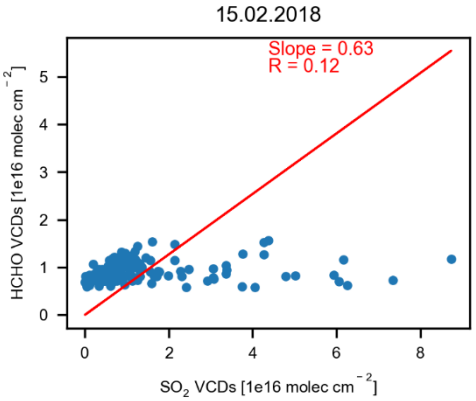
15.02.2018
Slope = 0.63
R = 0.12
HCHO VCDs [1e16 molec cm-2]
SO2 VCDs [1e16 molec cm-2]

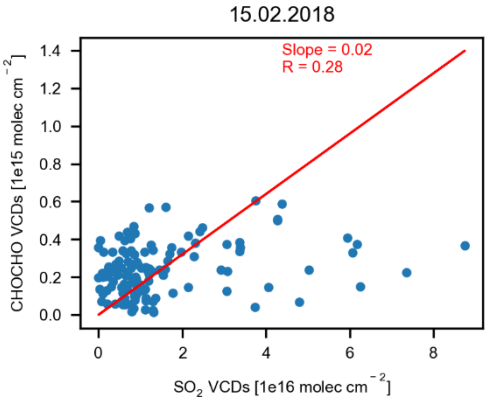
15.02.2018
Slope = 0.02
R = 0.28
CHOCHO VCDs [1e15 molec cm-2]
SO2 VCDs [1e16 molec cm-2]

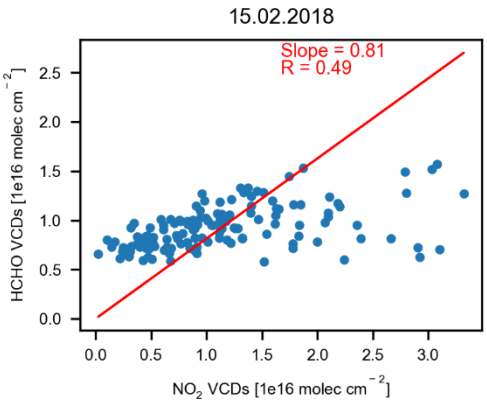
15.02.2018
Slope = 0.81
R = 0.49
HCHO VCDs [1e16 molec cm-2]
NO2 VCDs [1e16 molec cm-2]

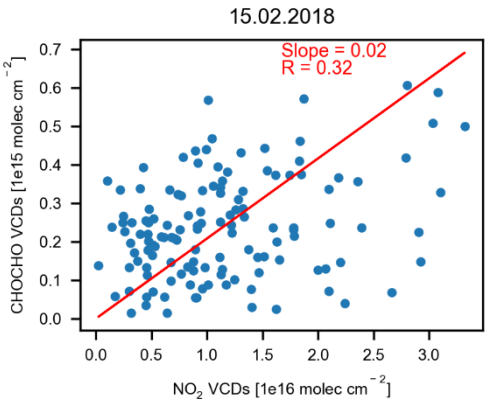
15.02.2018
Slope = 0.02
R = 0.32
CHOCHO VCDs [1e15 molec cm-2]
NO2 VCDs [1e16 molec cm-2]

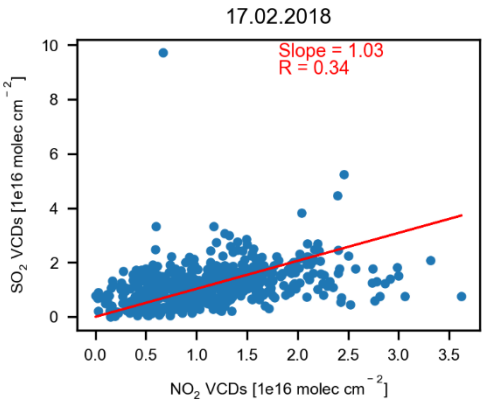
17.02.2018
Slope = 1.03
R = 0.34
SO2 VCDs [1e16 molec cm-2]
NO2 VCDs [1e16 molec cm-2]

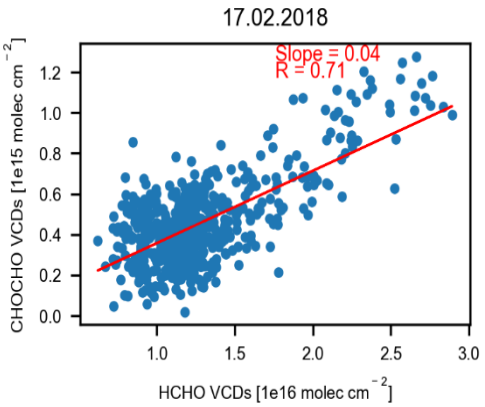
17.02.2018
Slope = 0.04
R = 0.71
CHOCHO VCDs [1e15 molec cm-2]
HCHO VCDs [1e16 molec cm-2]

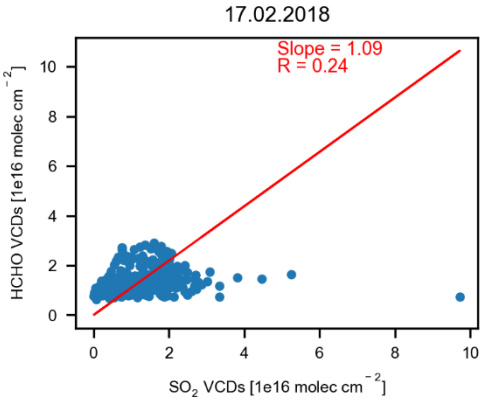
17.02.2018
Slope = 1.09
R = 0.24
HCHO VCDs [1e16 molec cm-2]
SO2 VCDs [1e16 molec cm-2]

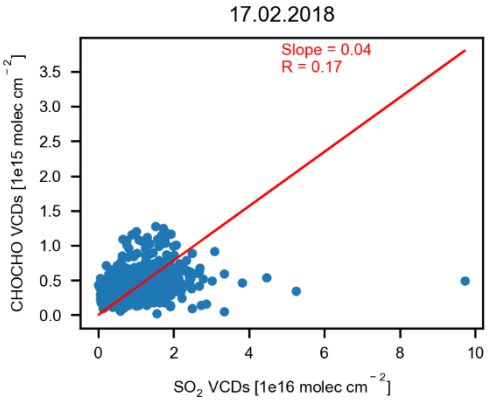
17.02.2018
Slope = 0.04
R = 0.17
CHOCHO VCDs [1e15 molec cm-2]
SO2 VCDs [1e16 molec cm-2]

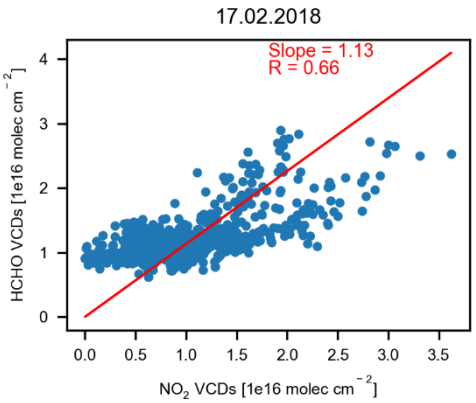
17.02.2018
Slope = 1.13
R = 0.66
HCHO VCDs [1e16 molec cm-2]
NO2 VCDs [1e16 molec cm-2]

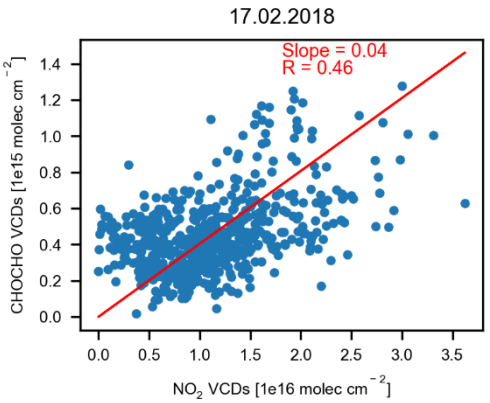
17.02.2018
Slope = 0.04
R = 0.46
CHOCHO VCDs [1e15 molec cm-2]
NO2 VCDs [1e16 molec cm-2]

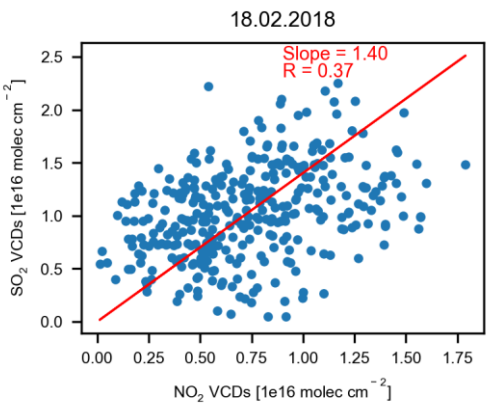
18.02.2018
Slope = 1.40
R = 0.37
SO2 VCDs [1e16 molec cm-2]
NO2 VCDs [1e16 molec cm-2]

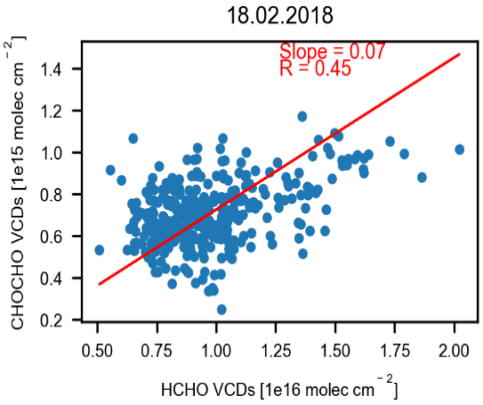
18.02.2018
Slope = 0.07
R = 0.45
CHOCHO VCDs [1e15 molec cm-2]
HCHO VCDs [1e16 molec cm-2]

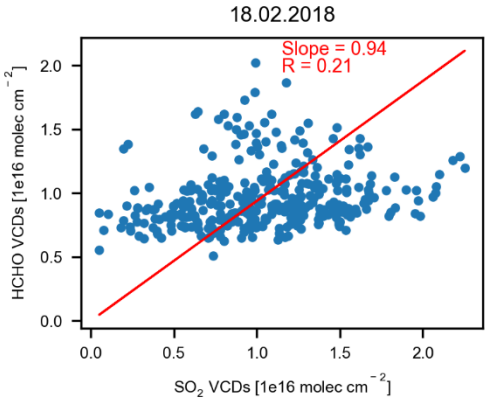
18.02.2018
Slope = 0.94
R = 0.21
HCHO VCDs [1e16 molec cm-2]
SO2 VCDs [1e16 molec cm-2]

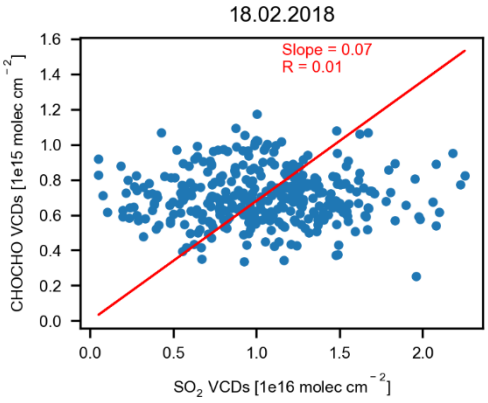
18.02.2018
Slope = 0.07
R = 0.01
CHOCHO VCDs [1e15 molec cm-2]
SO2 VCDs [1e16 molec cm-2]

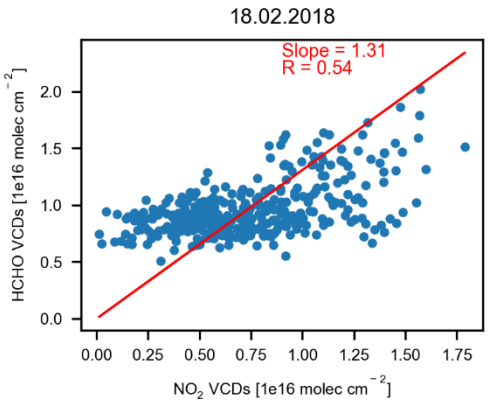
18.02.2018
Slope = 1.31
R = 0.54
HCHO VCDs [1e16 molec cm-2]
NO2 VCDs [1e16 molec cm-2]

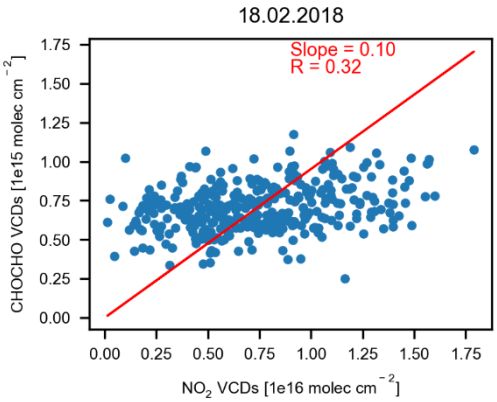
18.02.2018
Slope = 0.10
R = 0.32
CHOCHO VCDs [1e15 molec cm-2]
NO2 VCDs [1e16 molec cm-2]

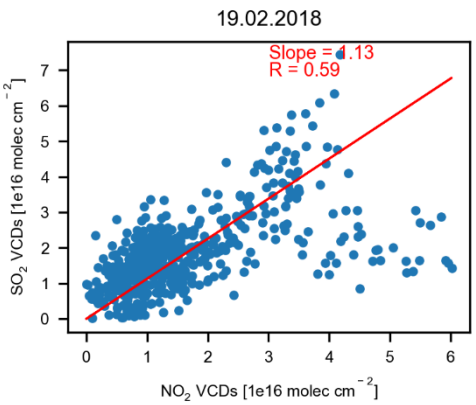
19.02.2018
Slope = 1.13
R = 0.59
SO2 VCDs [1e16 molec cm-2]
NO2 VCDs [1e16 molec cm-2]

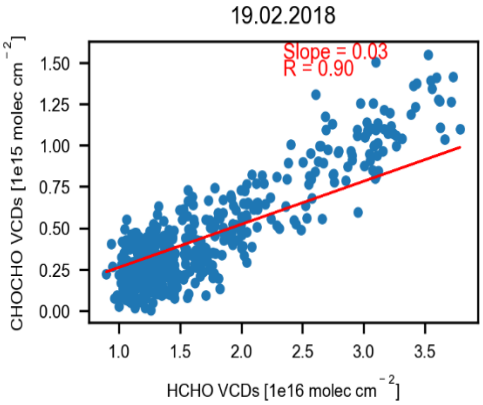
19.02.2018
Slope = 0.03
R = 0.90
CHOCHO VCDs [1e15 molec cm-2]
HCHO VCDs [1e16 molec cm-2]

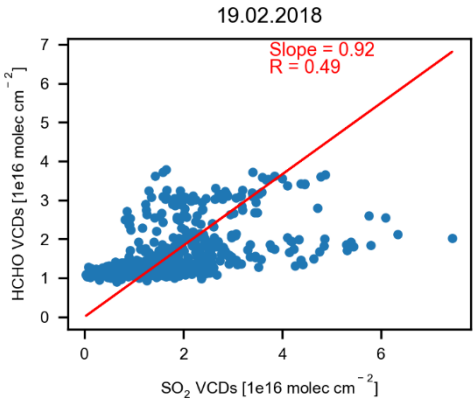
19.02.2018
Slope = 0.92
R = 0.49
HCHO VCDs [1e16 molec cm-2]
SO2 VCDs [1e16 molec cm-2]

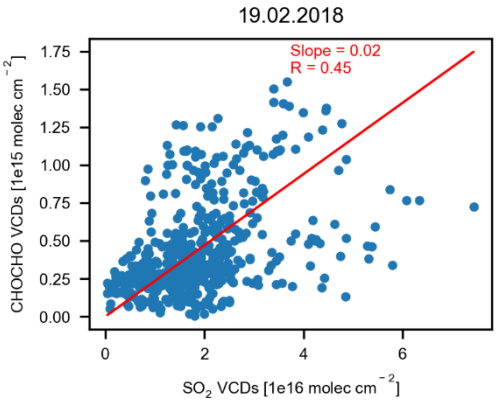
19.02.2018
Slope = 0.02
R = 0.45
CHOCHO VCDs [1e15 molec cm-2]
SO2 VCDs [1e16 molec cm-2]

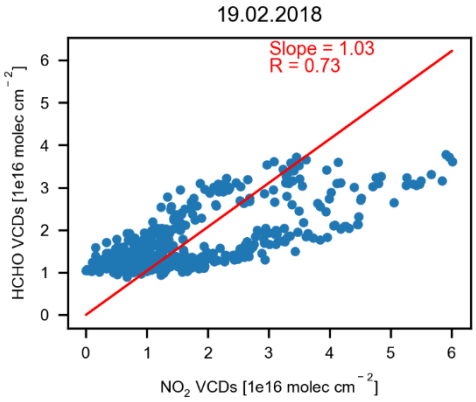
19.02.2018
Slope = 1.03
R = 0.73
HCHO VCDs [1e16 molec cm-2]
NO2 VCDs [1e16 molec cm-2]

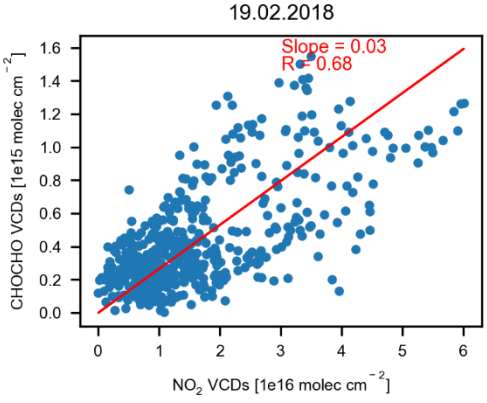
19.02.2018
Slope = 0.03
R = 0.68
CHOCHO VCDs [1e15 molec cm-2]
NO2 VCDs [1e16 molec cm-2]

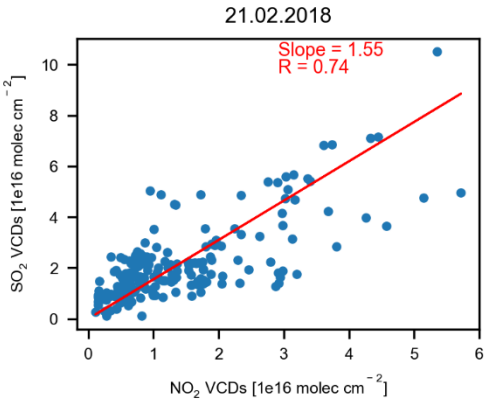
21.02.2018
Slope = 1.55
R = 0.74
SO2 VCDs [1e16 molec cm−2]
NO2 VCDs [1e16 molec cm−2]

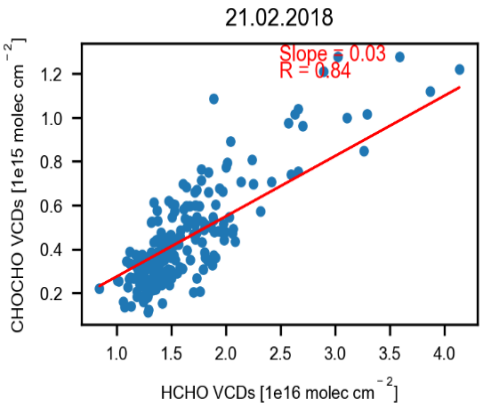
21.02.2018
Slope = 0.03
R = 0.84
CHOCHO VCDs [1e15 molec cm−2]
HCHO VCDs [1e16 molec cm−2]

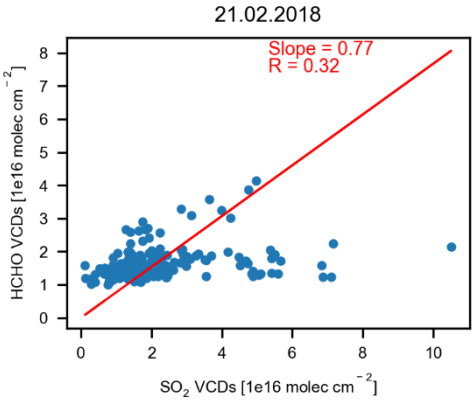
21.02.2018
Slope = 0.77
R = 0.32
HCHO VCDs [1e16 molec cm−2]
SO2 VCDs [1e16 molec cm−2]

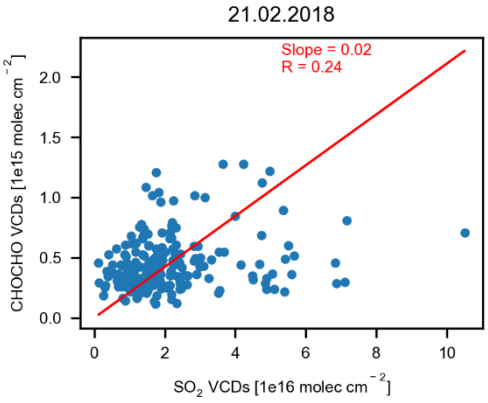
21.02.2018
Slope = 0.02
R = 0.24
CHOCHO VCDs [1e15 molec cm−2]
SO2 VCDs [1e16 molec cm−2]

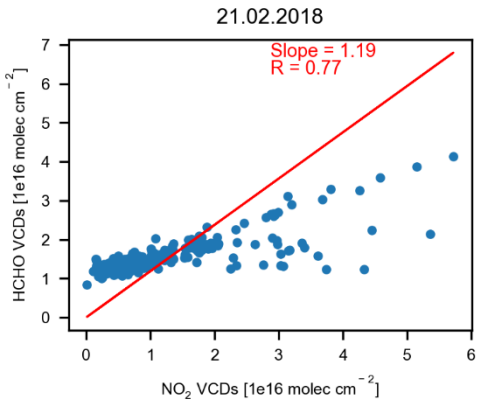
21.02.2018
Slope = 1.19
R = 0.77
HCHO VCDs [1e16 molec cm−2]
NO2 VCDs [1e16 molec cm−2]

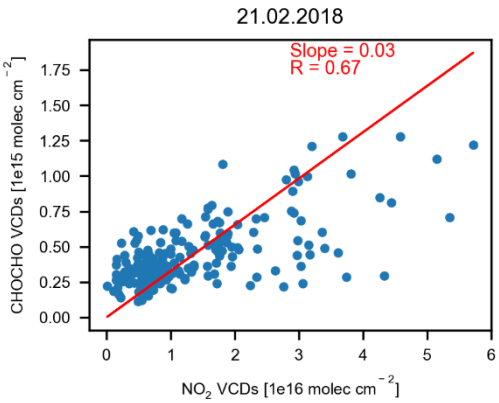
21.02.2018
Slope = 0.03
R = 0.67
CHOCHO VCDs [1e15 molec cm−2]
NO2 VCDs [1e16 molec cm−2]

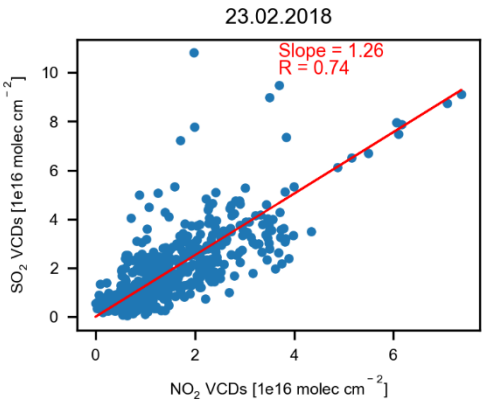
23.02.2018
Slope = 1.26
R = 0.74
SO2 VCDs [1e16 molec cm-2]
NO2 VCDs [1e16 molec cm-2]

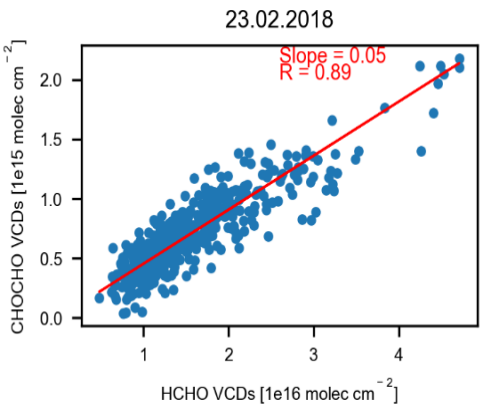
23.02.2018
Slope = 0.05
R = 0.89
CHOCHO VCDs [1e15 molec cm-2]
HCHO VCDs [1e16 molec cm-2]

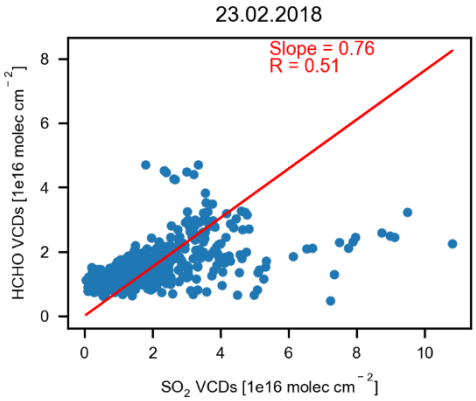
23.02.2018
Slope = 0.76
R = 0.51
HCHO VCDs [1e16 molec cm-2]
SO2 VCDs [1e16 molec cm-2]

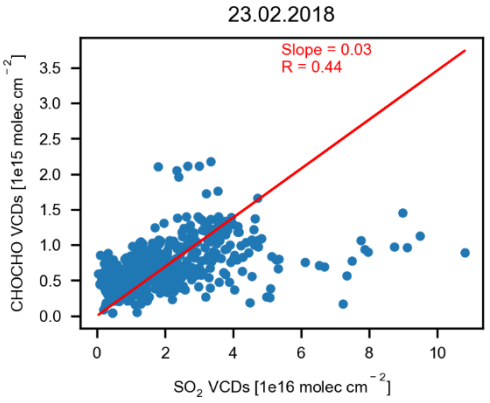
23.02.2018
Slope = 0.03
R = 0.44
CHOCHO VCDs [1e15 molec cm-2]
SO2 VCDs [1e16 molec cm-2]

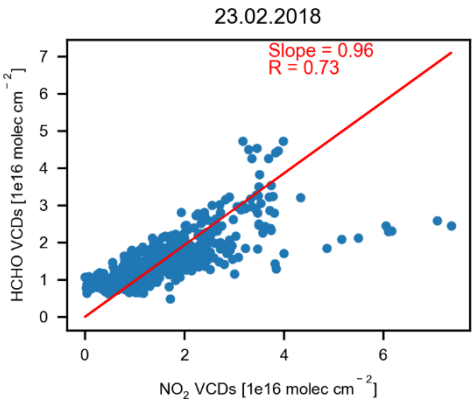
23.02.2018
Slope = 0.96
R = 0.73
HCHO VCDs [1e16 molec cm-2]
NO2 VCDs [1e16 molec cm-2]

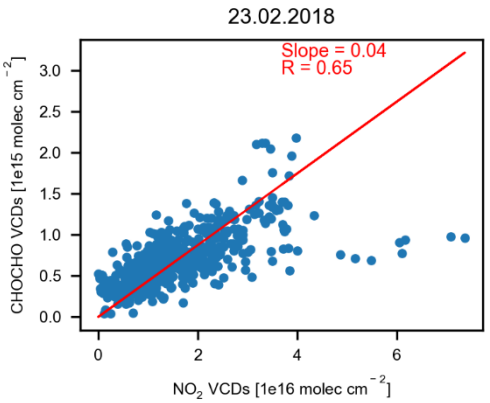
23.02.2018
Slope = 0.04
R = 0.65
CHOCHO VCDs [1e15 molec cm-2]
NO2 VCDs [1e16 molec cm-2]

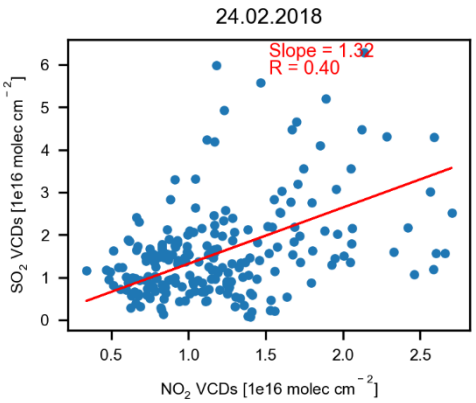
24.02.2018
Slope = 1.32
R = 0.40
SO2 VCDs [1e16 molec cm-2]
NO2 VCDs [1e16 molec cm-2]

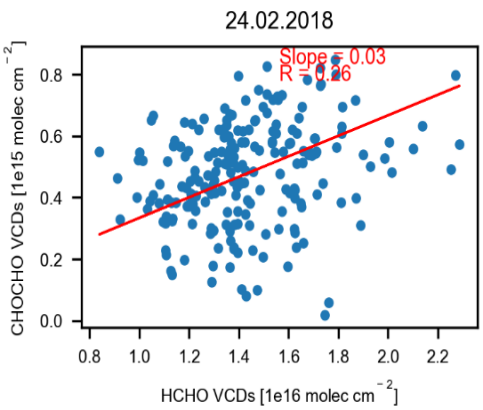
24.02.2018
Slope = 0.03
R = 0.26
CHOCHO VCDs [1e15 molec cm-2]
HCHO VCDs [1e16 molec cm-2]

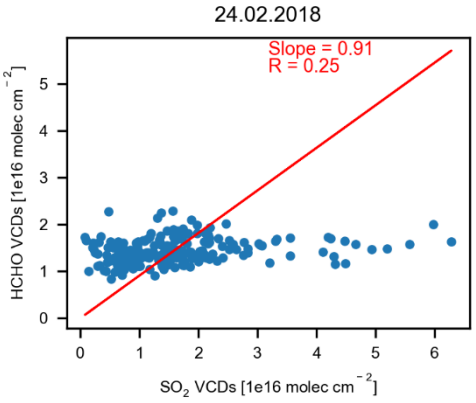
24.02.2018
Slope = 0.91
R = 0.25
HCHO VCDs [1e16 molec cm-2]
SO2 VCDs [1e16 molec cm-2]

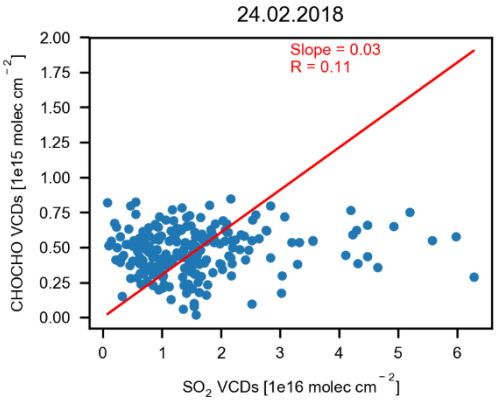
24.02.2018
Slope = 0.03
R = 0.11
CHOCHO VCDs [1e15 molec cm-2]
SO2 VCDs [1e16 molec cm-2]

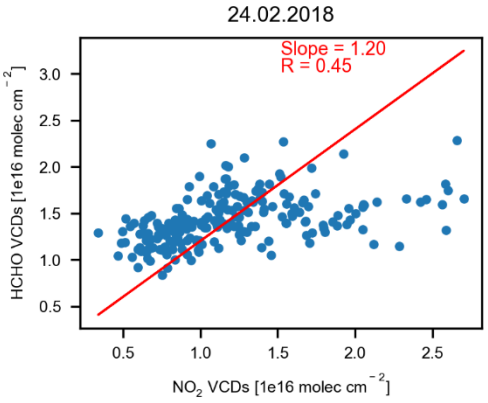
24.02.2018
Slope = 1.20
R = 0.45
HCHO VCDs [1e16 molec cm-2]
NO2 VCDs [1e16 molec cm-2]

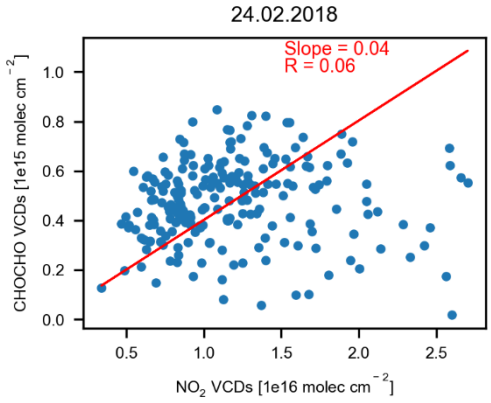
24.02.2018
Slope = 0.04
R = 0.06
CHOCHO VCDs [1e15 molec cm-2]
NO2 VCDs [1e16 molec cm-2]

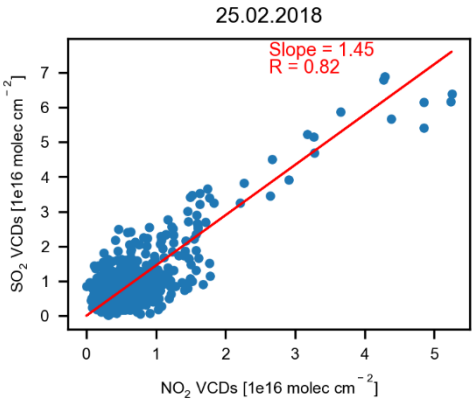
25.02.2018
Slope = 1.45
R = 0.82
SO2 VCDs [1e16 molec cm-2]
NO2 VCDs [1e16 molec cm-2]

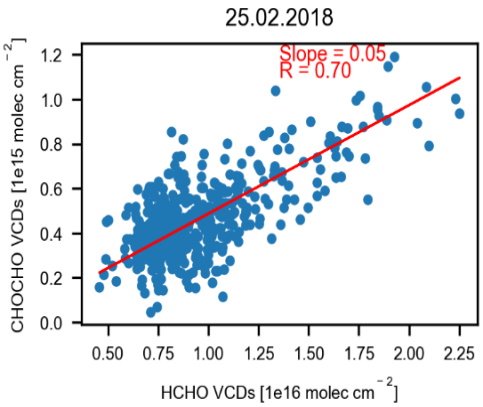
25.02.2018
Slope = 0.05
R = 0.70
CHOCHO VCDs [1e15 molec cm-2]
HCHO VCDs [1e16 molec cm-2]

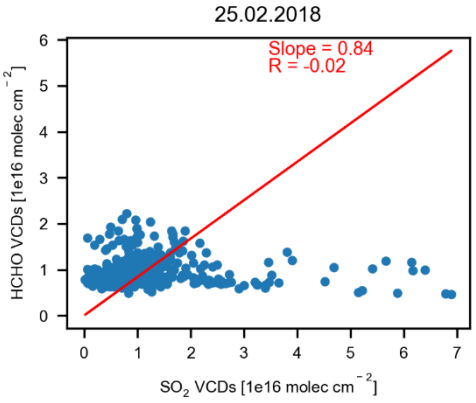
25.02.2018
Slope = 0.84
R = -0.02
HCHO VCDs [1e16 molec cm-2]
SO2 VCDs [1e16 molec cm-2]

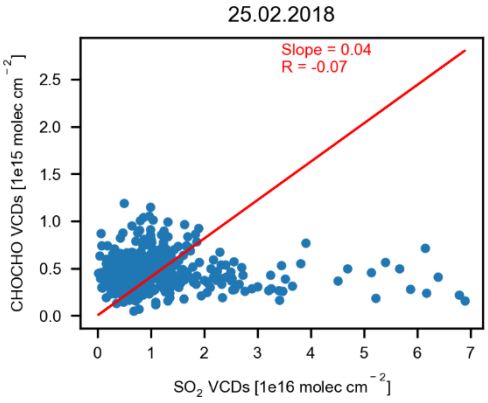
25.02.2018
Slope = 0.04
R = -0.07
CHOCHO VCDs [1e15 molec cm-2]
SO2 VCDs [1e16 molec cm-2]

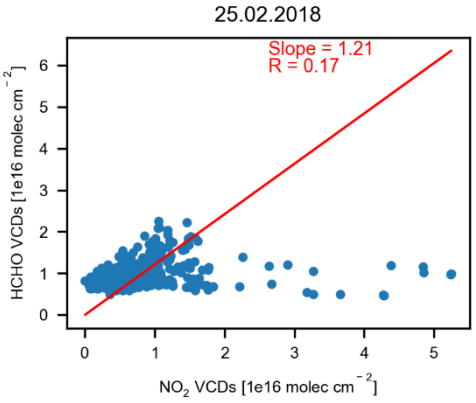
25.02.2018
Slope = 1.21
R = 0.17
HCHO VCDs [1e16 molec cm-2]
NO2 VCDs [1e16 molec cm-2]

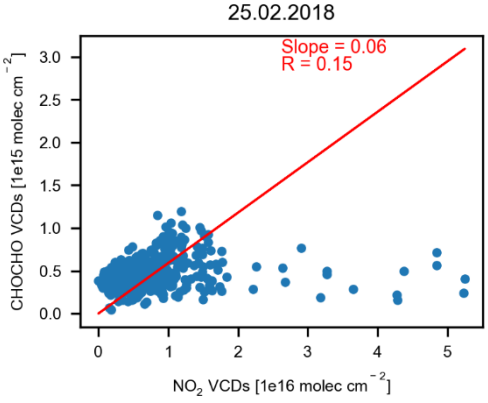
25.02.2018
Slope = 0.06
R = 0.15
CHOCHO VCDs [1e15 molec cm-2]
NO2 VCDs [1e16 molec cm-2]

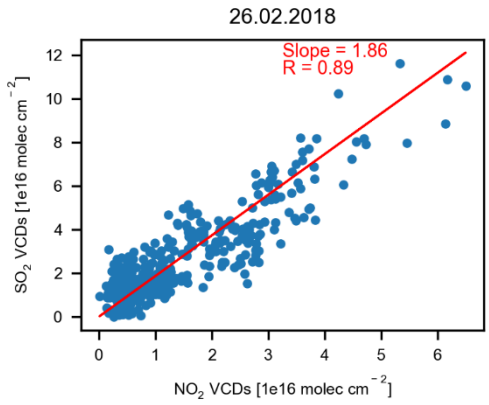
26.02.2018
Slope = 1.86
R = 0.89
SO2 VCDs [1e16 molec cm−2]
NO2 VCDs [1e16 molec cm−2]

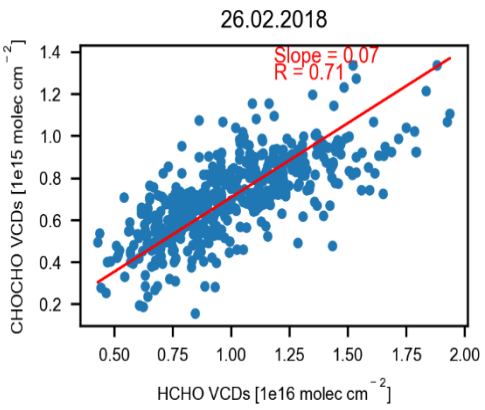
26.02.2018
Slope = 0.07
R = 0.71
CHOCHO VCDs [1e15 molec cm−2]
HCHO VCDs [1e16 molec cm−2]

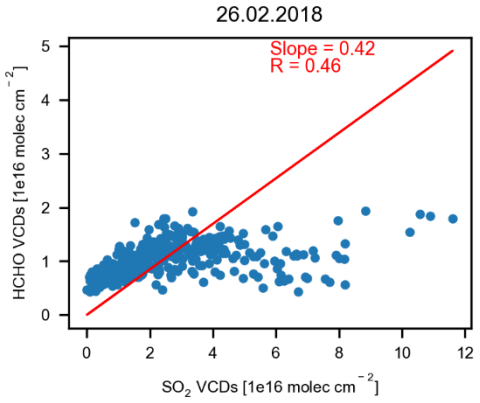
26.02.2018
Slope = 0.42
R = 0.46
HCHO VCDs [1e16 molec cm−2]
SO2 VCDs [1e16 molec cm−2]

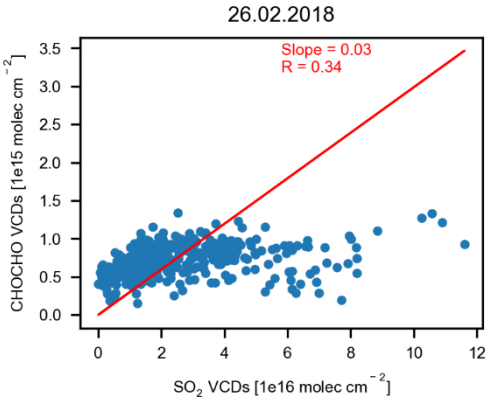
26.02.2018
Slope = 0.03
R = 0.34
CHOCHO VCDs [1e15 molec cm−2]
SO2 VCDs [1e16 molec cm−2]

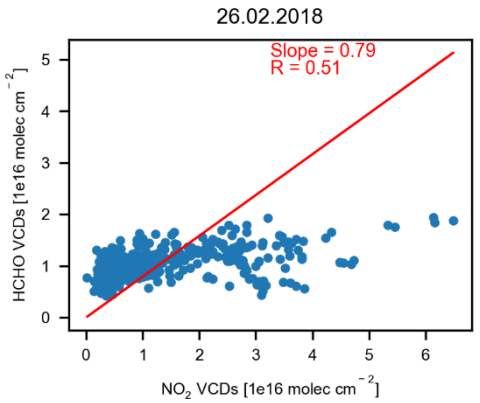
26.02.2018
Slope = 0.79
R = 0.51
HCHO VCDs [1e16 molec cm−2]
NO2 VCDs [1e16 molec cm−2]

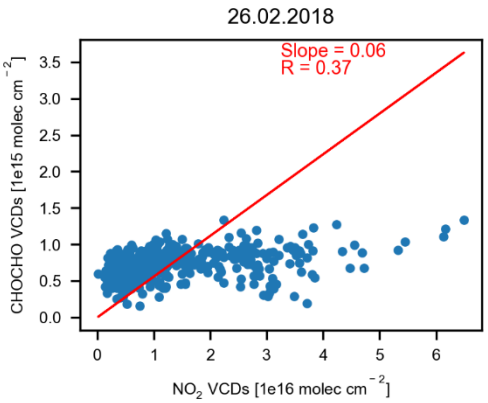
26.02.2018
Slope = 0.06
R = 0.37
CHOCHO VCDs [1e15 molec cm−2]
NO2 VCDs [1e16 molec cm−2]

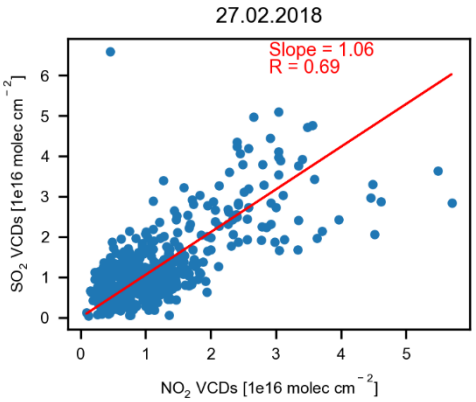
27.02.2018
Slope = 1.06
R = 0.69
SO2 VCDs [1e16 molec cm-2]
NO2 VCDs [1e16 molec cm-2]

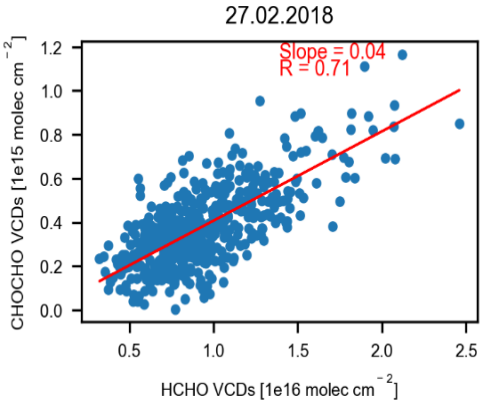
27.02.2018
Slope = 0.04
R = 0.71
CHOCHO VCDs [1e15 molec cm-2]
HCHO VCDs [1e16 molec cm-2]

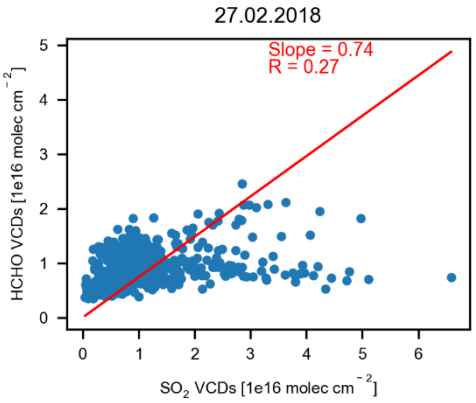
27.02.2018
Slope = 0.74
R = 0.27
HCHO VCDs [1e16 molec cm-2]
SO2 VCDs [1e16 molec cm-2]

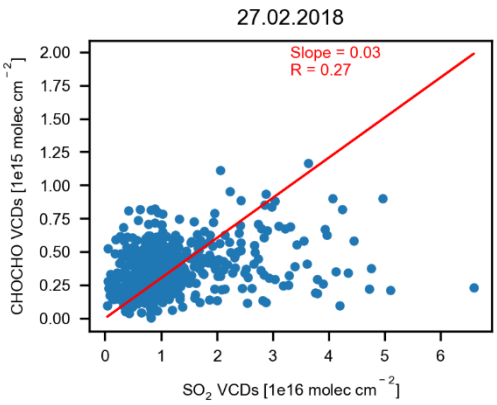
27.02.2018
Slope = 0.03
R = 0.27
CHOCHO VCDs [1e15 molec cm-2]
SO2 VCDs [1e16 molec cm-2]

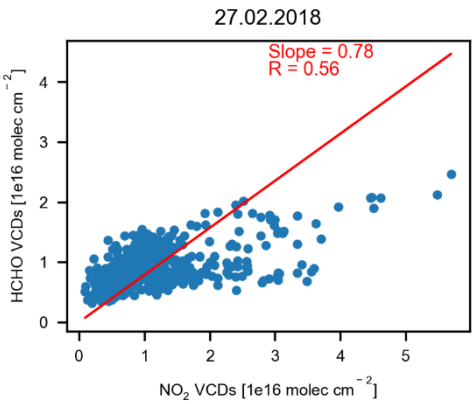
27.02.2018
Slope = 0.78
R = 0.56
HCHO VCDs [1e16 molec cm-2]
NO2 VCDs [1e16 molec cm-2]

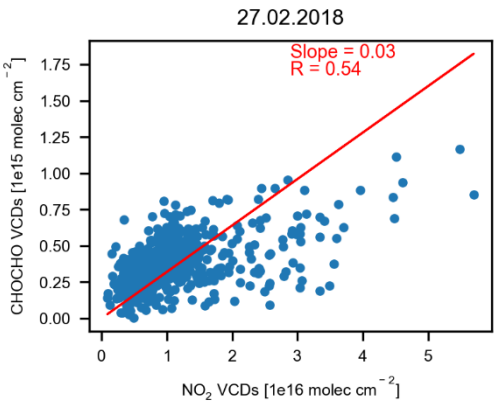
27.02.2018
Slope = 0.03
R = 0.54
CHOCHO VCDs [1e15 molec cm-2]
NO2 VCDs [1e16 molec cm-2]

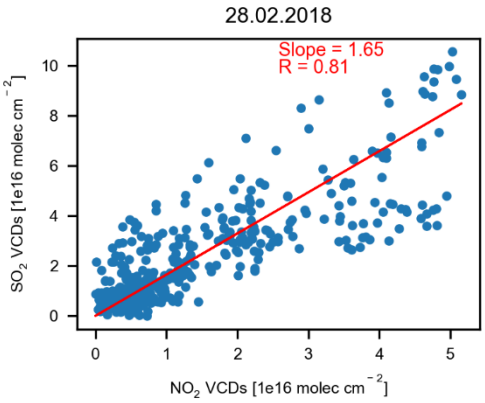
28.02.2018
Slope = 1.65
R = 0.81
SO2 VCDs [1e16 molec cm−2]
NO2 VCDs [1e16 molec cm−2]

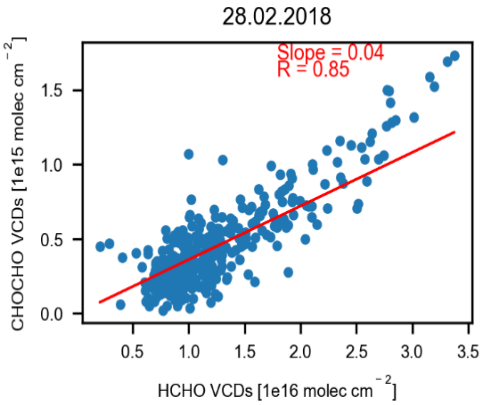
28.02.2018
Slope = 0.04
R = 0.85
CHOCHO VCDs [1e15 molec cm−2]
HCHO VCDs [1e16 molec cm−2]

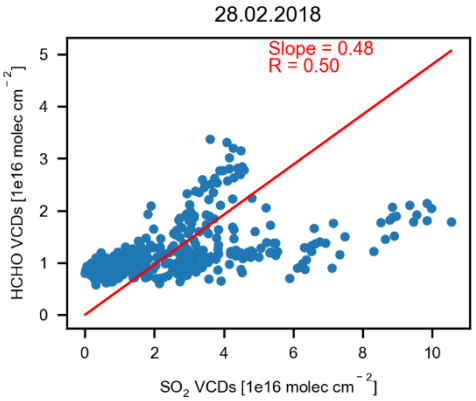
28.02.2018
Slope = 0.48
R = 0.50
HCHO VCDs [1e16 molec cm−2]
SO2 VCDs [1e16 molec cm−2]

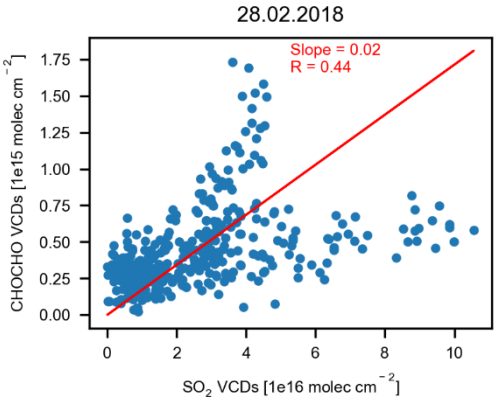
28.02.2018
Slope = 0.02
R = 0.44
CHOCHO VCDs [1e15 molec cm−2]
SO2 VCDs [1e16 molec cm−2]

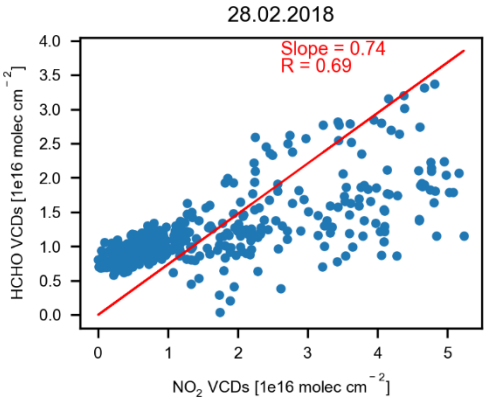
28.02.2018
Slope = 0.74
R = 0.69
HCHO VCDs [1e16 molec cm−2]
NO2 VCDs [1e16 molec cm−2]

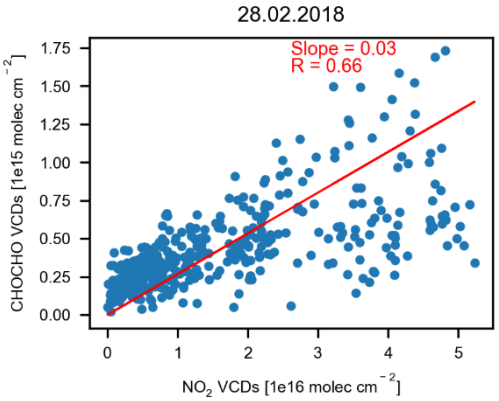
28.02.2018
Slope = 0.03
R = 0.66
CHOCHO VCDs [1e15 molec cm−2]
NO2 VCDs [1e16 molec cm−2]

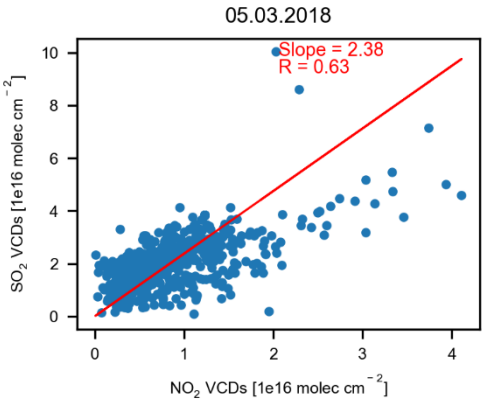
05.03.2018
Slope = 2.38
R = 0.63
SO2 VCDs [1e16 molec cm-2]
NO2 VCDs [1e16 molec cm-2]

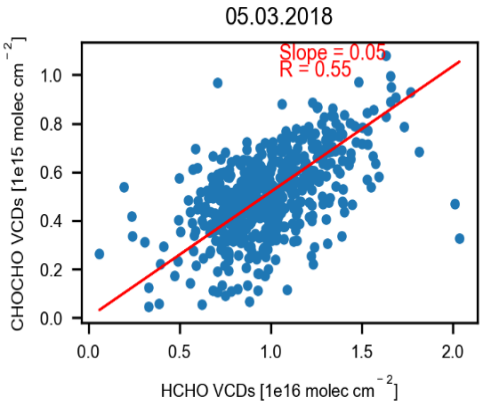
05.03.2018
Slope = 0.05
R = 0.55
CHOCHO VCDs [1e15 molec cm-2]
HCHO VCDs [1e16 molec cm-2]

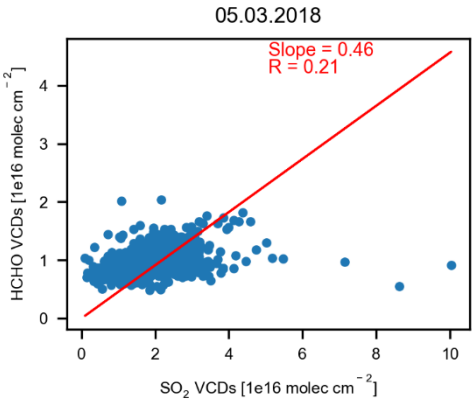
05.03.2018
Slope = 0.46
R = 0.21
HCHO VCDs [1e16 molec cm-2]
SO2 VCDs [1e16 molec cm-2]

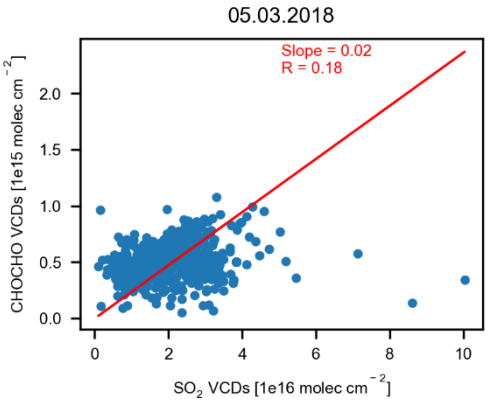
05.03.2018
Slope = 0.02
R = 0.18
CHOCHO VCDs [1e15 molec cm-2]
SO2 VCDs [1e16 molec cm-2]

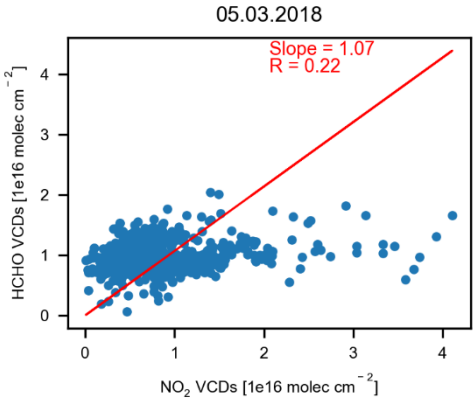
05.03.2018
Slope = 1.07
R = 0.22
HCHO VCDs [1e16 molec cm-2]
NO2 VCDs [1e16 molec cm-2]

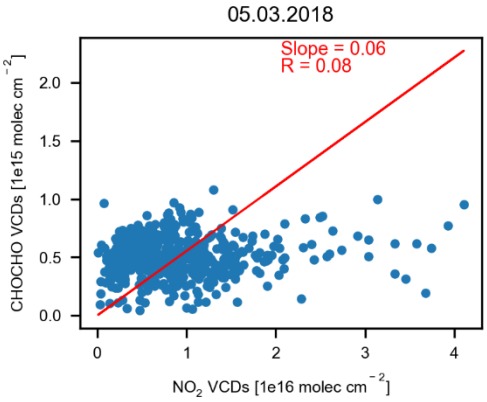
05.03.2018
Slope = 0.06
R = 0.08
CHOCHO VCDs [1e15 molec cm-2]
NO2 VCDs [1e16 molec cm-2]

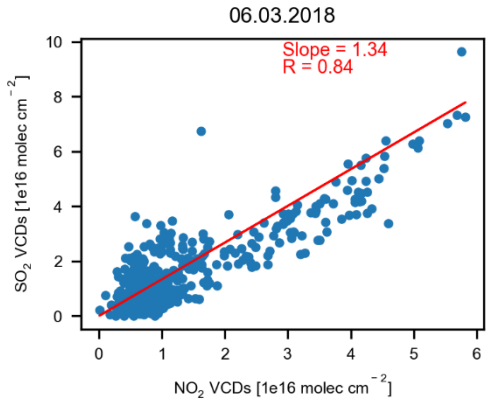
06.03.2018
Slope = 1.34
R = 0.84
SO2 VCDs [1e16 molec cm-2]
NO2 VCDs [1e16 molec cm-2]

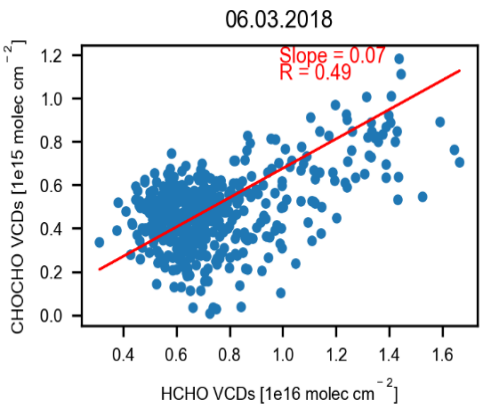
06.03.2018
Slope = 0.07
R = 0.49
CHOCHO VCDs [1e15 molec cm-2]
HCHO VCDs [1e16 molec cm-2]

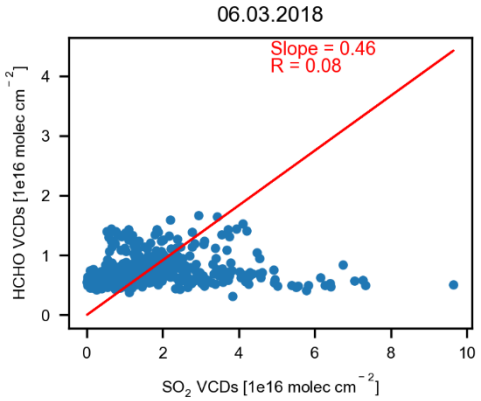
06.03.2018
Slope = 0.46
R = 0.08
HCHO VCDs [1e16 molec cm-2]
SO2 VCDs [1e16 molec cm-2]

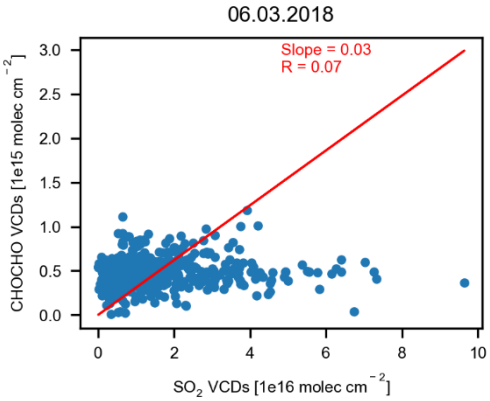
06.03.2018
Slope = 0.03
R = 0.07
CHOCHO VCDs [1e15 molec cm-2]
SO2 VCDs [1e16 molec cm-2]

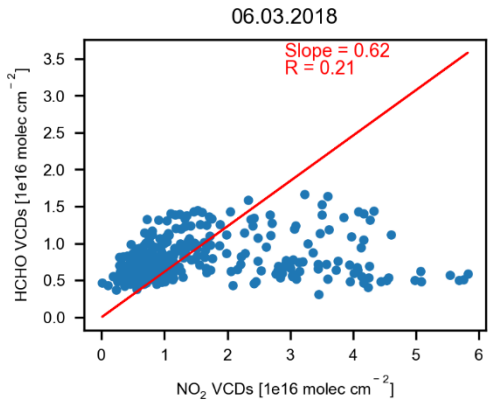
06.03.2018
Slope = 0.62
R = 0.21
HCHO VCDs [1e16 molec cm-2]
NO2 VCDs [1e16 molec cm-2]

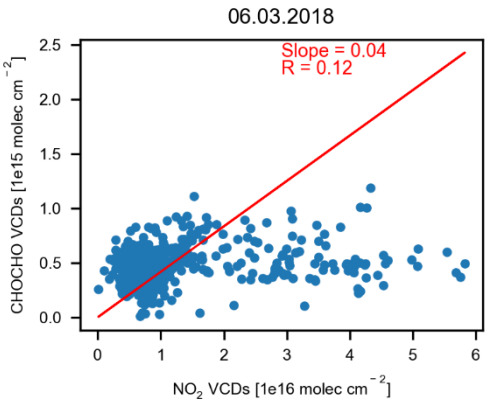
06.03.2018
Slope = 0.04
R = 0.12
CHOCHO VCDs [1e15 molec cm-2]
NO2 VCDs [1e16 molec cm-2]

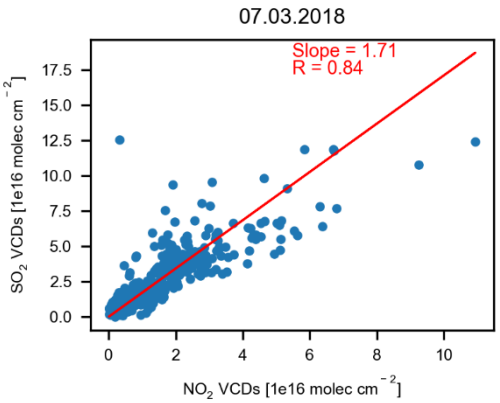
07.03.2018
Slope = 1.71
R = 0.84
SO2 VCDs [1e16 molec cm-2]
NO2 VCDs [1e16 molec cm-2]

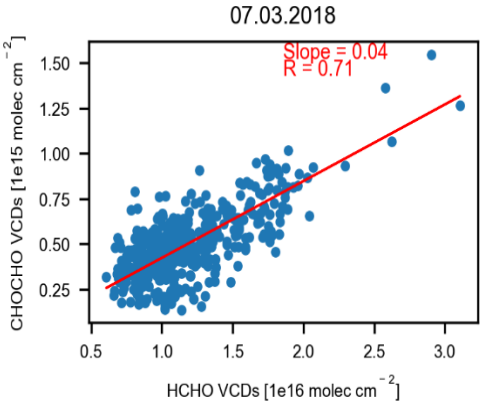
07.03.2018
Slope = 0.04
R = 0.71
CHOCHO VCDs [1e15 molec cm-2]
HCHO VCDs [1e16 molec cm-2]

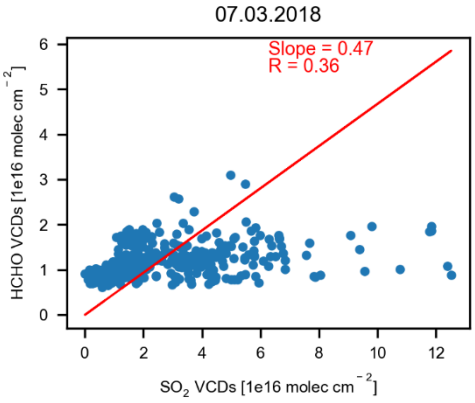
07.03.2018
Slope = 0.47
R = 0.36
HCHO VCDs [1e16 molec cm-2]
SO2 VCDs [1e16 molec cm-2]

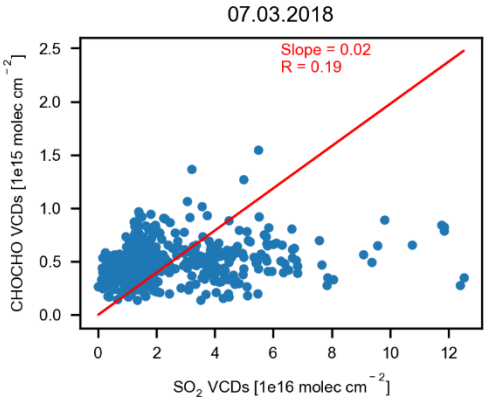
07.03.2018
Slope = 0.02
R = 0.19
CHOCHO VCDs [1e15 molec cm-2]
SO2 VCDs [1e16 molec cm-2]

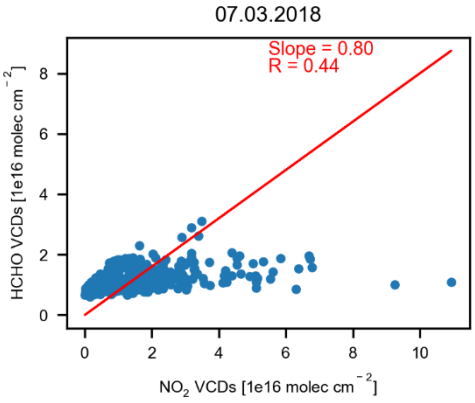
07.03.2018
Slope = 0.80
R = 0.44
HCHO VCDs [1e16 molec cm-2]
NO2 VCDs [1e16 molec cm-2]

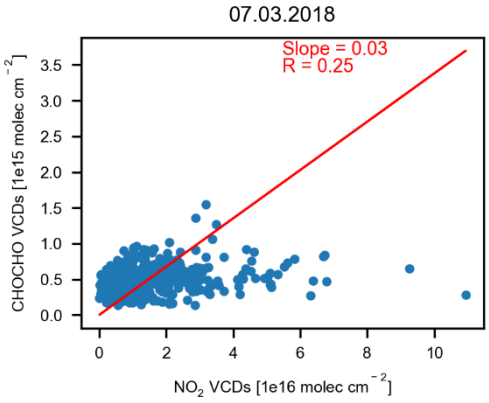
07.03.2018
Slope = 0.03
R = 0.25
CHOCHO VCDs [1e15 molec cm-2]
NO2 VCDs [1e16 molec cm-2]

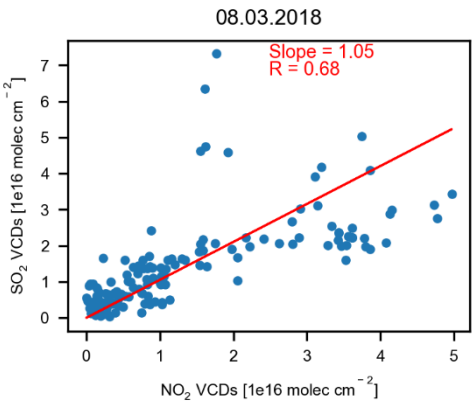
08.03.2018
Slope = 1.05
R = 0.68
SO2 VCDs [1e16 molec cm-2]
NO2 VCDs [1e16 molec cm-2]

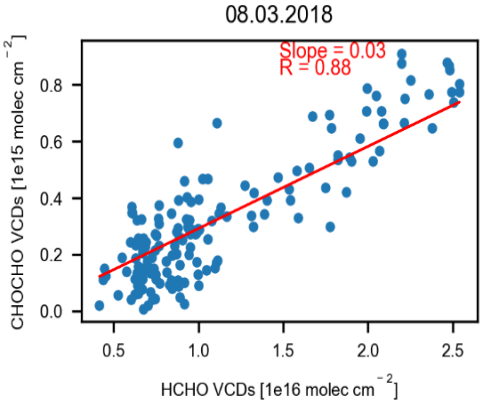
08.03.2018
Slope = 0.03
R = 0.88
CHOCHO VCDs [1e15 molec cm-2]
HCHO VCDs [1e16 molec cm-2]

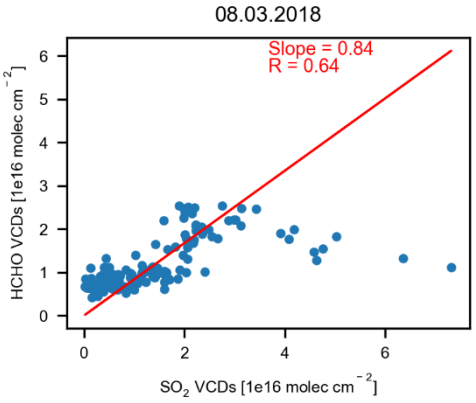
08.03.2018
Slope = 0.84
R = 0.64
HCHO VCDs [1e16 molec cm-2]
SO2 VCDs [1e16 molec cm-2]

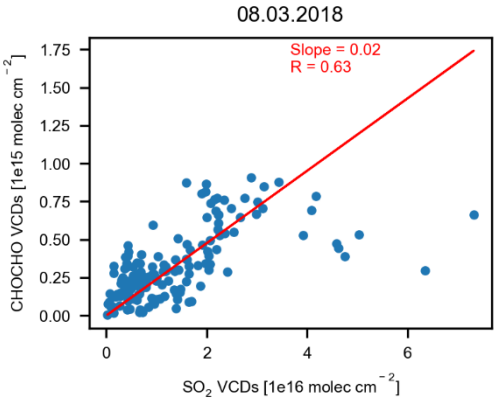
08.03.2018
Slope = 0.02
R = 0.63
CHOCHO VCDs [1e15 molec cm-2]
SO2 VCDs [1e16 molec cm-2]

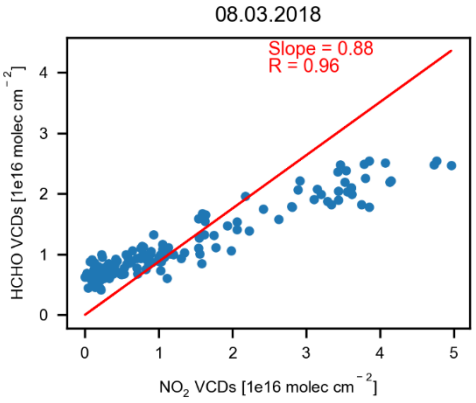
08.03.2018
Slope = 0.88
R = 0.96
HCHO VCDs [1e16 molec cm-2]
NO2 VCDs [1e16 molec cm-2]

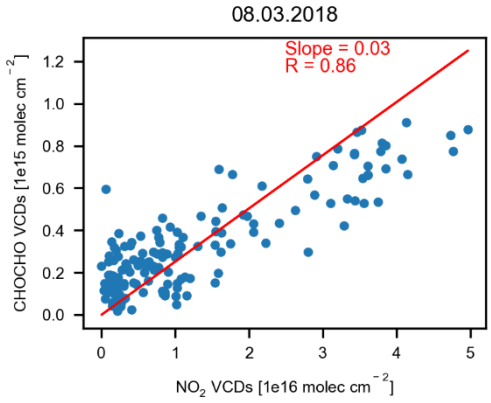
08.03.2018
Slope = 0.03
R = 0.86
CHOCHO VCDs [1e15 molec cm-2]
NO2 VCDs [1e16 molec cm-2]

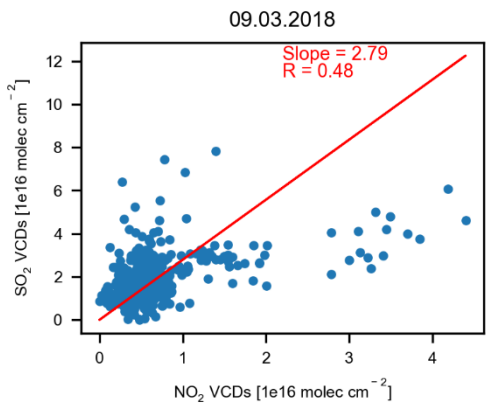
09.03.2018
Slope = 2.79
R = 0.48
SO2 VCDs [1e16 molec cm-2]
NO2 VCDs [1e16 molec cm-2]

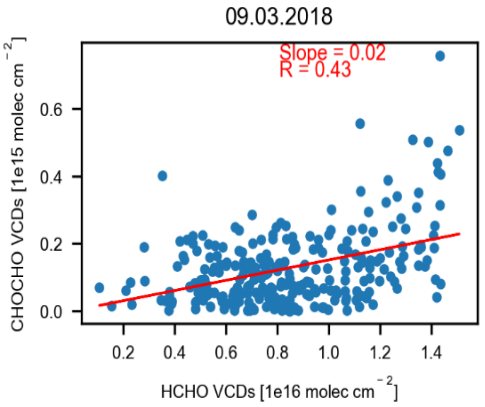
09.03.2018
Slope = 0.02
R = 0.43
CHOCHO VCDs [1e15 molec cm-2]
HCHO VCDs [1e16 molec cm-2]

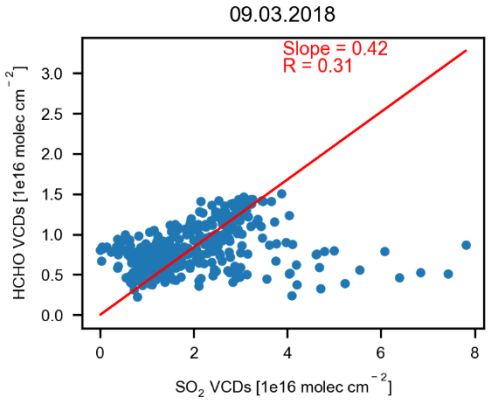
09.03.2018
Slope = 0.42
R = 0.31
HCHO VCDs [1e16 molec cm-2]
SO2 VCDs [1e16 molec cm-2]

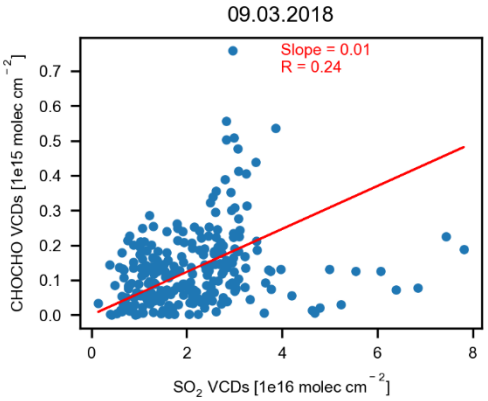
09.03.2018
Slope = 0.01
R = 0.24
CHOCHO VCDs [1e15 molec cm-2]
SO2 VCDs [1e16 molec cm-2]

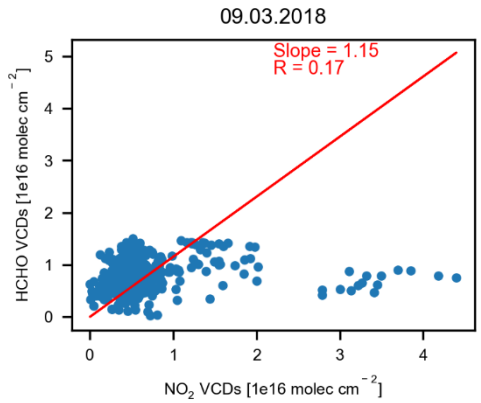
09.03.2018
Slope = 1.15
R = 0.17
HCHO VCDs [1e16 molec cm-2]
NO2 VCDs [1e16 molec cm-2]

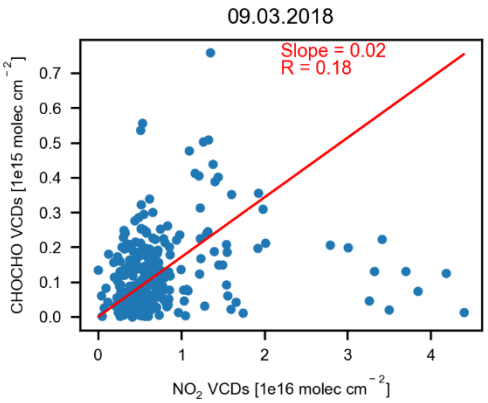
09.03.2018
Slope = 0.02
R = 0.18
CHOCHO VCDs [1e15 molec cm-2]
NO2 VCDs [1e16 molec cm-2]

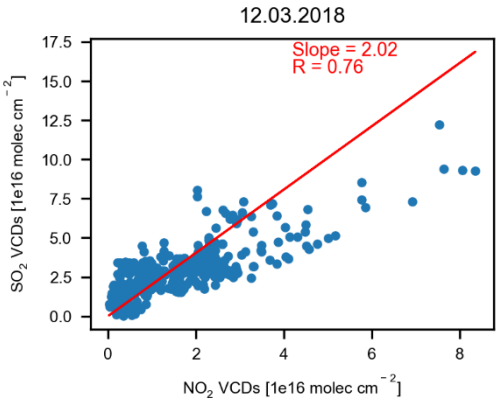
12.03.2018
Slope = 2.02
R = 0.76
SO2 VCDs [1e16 molec cm-2]
NO2 VCDs [1e16 molec cm-2]

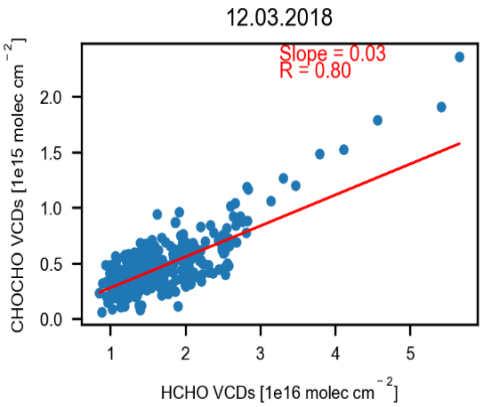
12.03.2018
Slope = 0.03
R = 0.80
CHOCHO VCDs [1e15 molec cm-2]
HCHO VCDs [1e16 molec cm-2]

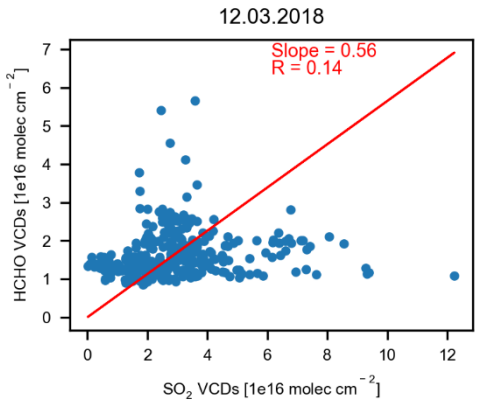
12.03.2018
Slope = 0.56
R = 0.14
HCHO VCDs [1e16 molec cm-2]
SO2 VCDs [1e16 molec cm-2]

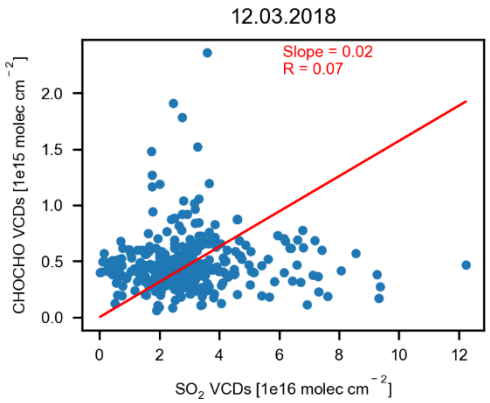
12.03.2018
Slope = 0.02
R = 0.07
CHOCHO VCDs [1e15 molec cm-2]
SO2 VCDs [1e16 molec cm-2]

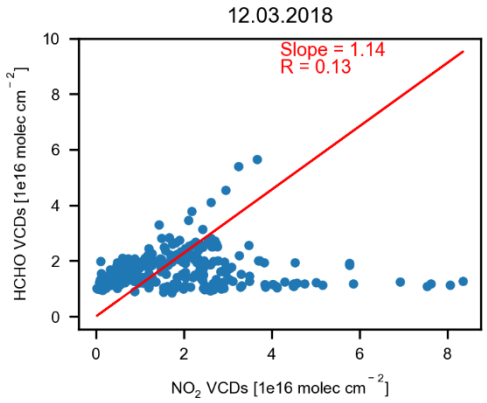
12.03.2018
Slope = 1.14
R = 0.13
HCHO VCDs [1e16 molec cm-2]
NO2 VCDs [1e16 molec cm-2]

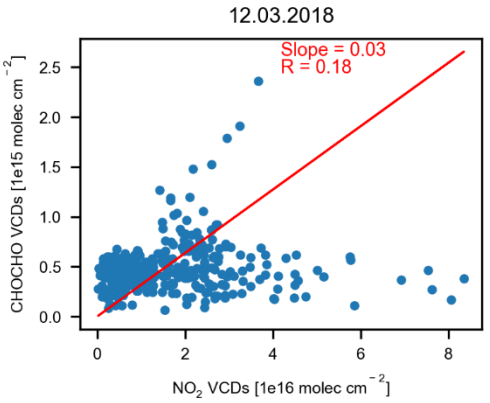
12.03.2018
Slope = 0.03
R = 0.18
CHOCHO VCDs [1e15 molec cm-2]
NO2 VCDs [1e16 molec cm-2]

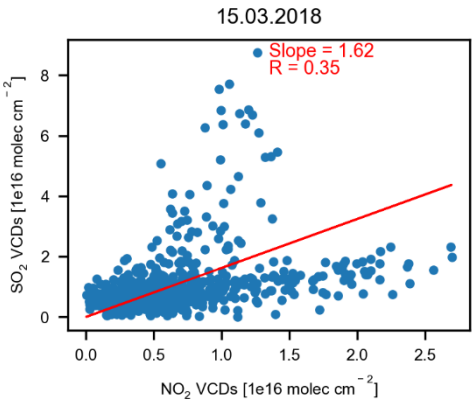
15.03.2018
Slope = 1.62
R = 0.35
SO2 VCDs [1e16 molec cm-2]
NO2 VCDs [1e16 molec cm-2]

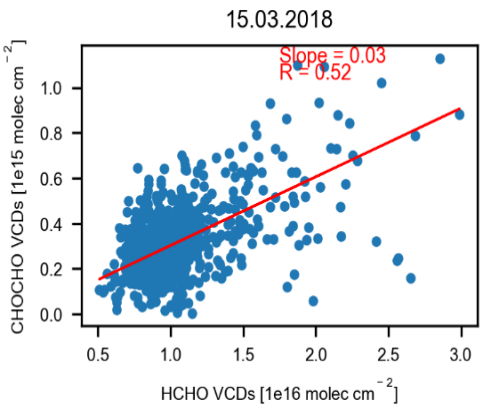
15.03.2018
Slope = 0.03
R = 0.52
CHOCHO VCDs [1e15 molec cm-2]
HCHO VCDs [1e16 molec cm-2]

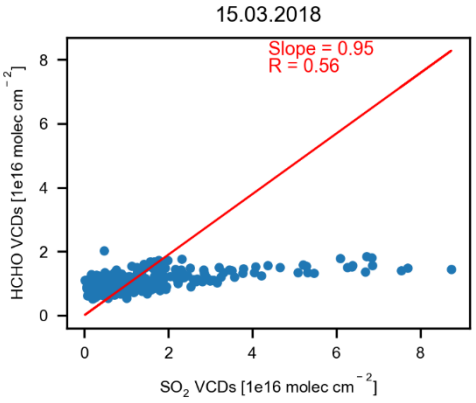
15.03.2018
Slope = 0.95
R = 0.56
HCHO VCDs [1e16 molec cm-2]
SO2 VCDs [1e16 molec cm-2]

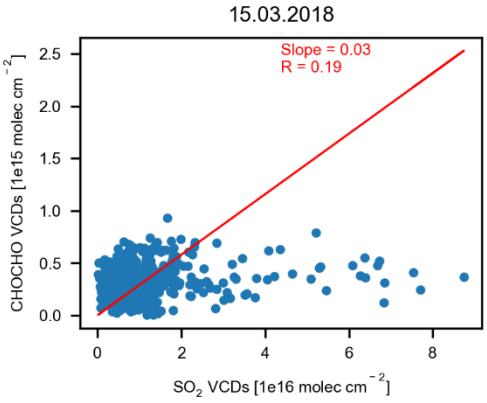
15.03.2018
Slope = 0.03
R = 0.19
CHOCHO VCDs [1e15 molec cm-2]
SO2 VCDs [1e16 molec cm-2]

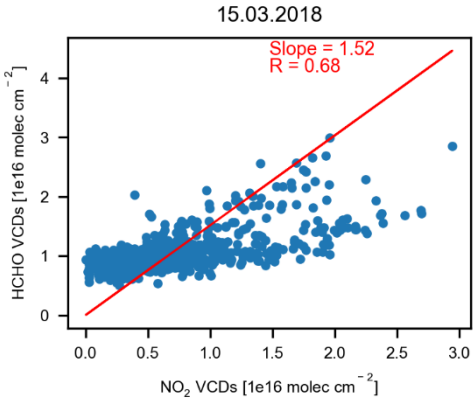
15.03.2018
Slope = 1.52
R = 0.68
HCHO VCDs [1e16 molec cm-2]
NO2 VCDs [1e16 molec cm-2]

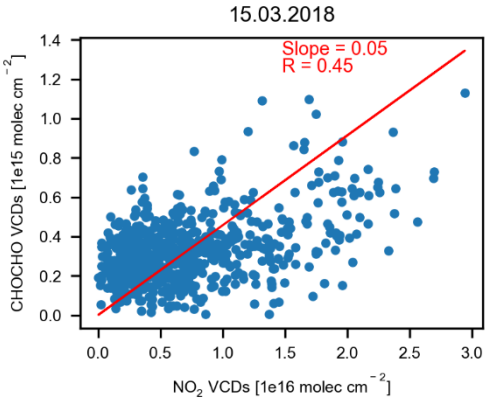
15.03.2018
Slope = 0.05
R = 0.45
CHOCHO VCDs [1e15 molec cm-2]
NO2 VCDs [1e16 molec cm-2]

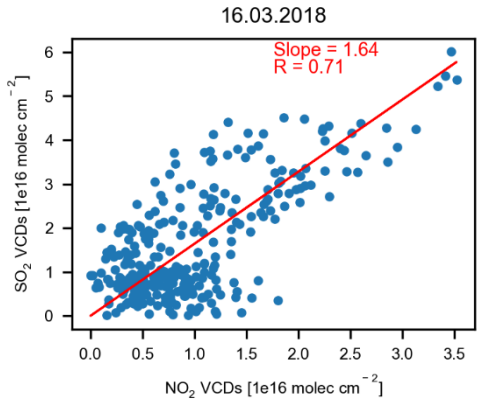
16.03.2018
Slope = 1.64
R = 0.71
SO2 VCDs [1e16 molec cm-2]
NO2 VCDs [1e16 molec cm-2]

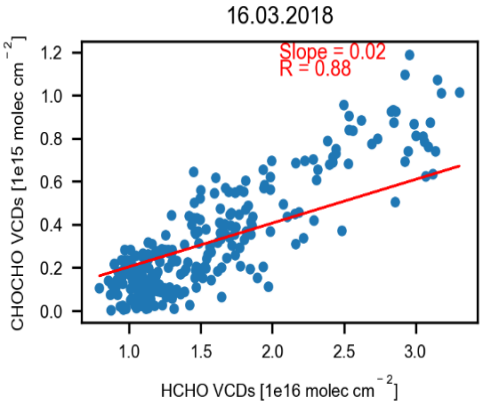
16.03.2018
Slope = 0.02
R = 0.88
CHOCHO VCDs [1e15 molec cm-2]
HCHO VCDs [1e16 molec cm-2]

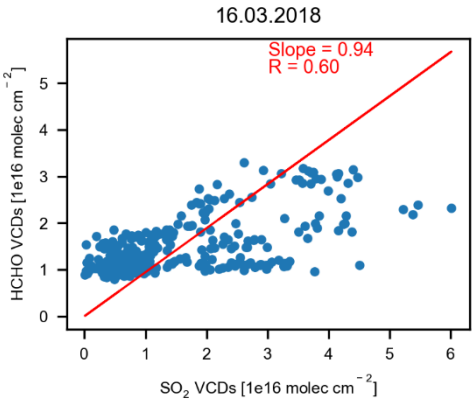
16.03.2018
Slope = 0.94
R = 0.60
HCHO VCDs [1e16 molec cm-2]
SO2 VCDs [1e16 molec cm-2]

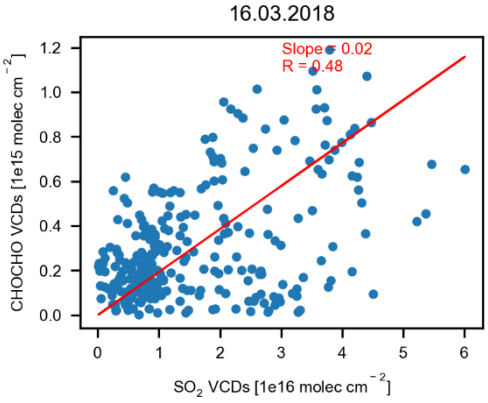
16.03.2018
Slope = 0.02
R = 0.48
CHOCHO VCDs [1e15 molec cm-2]
SO2 VCDs [1e16 molec cm-2]

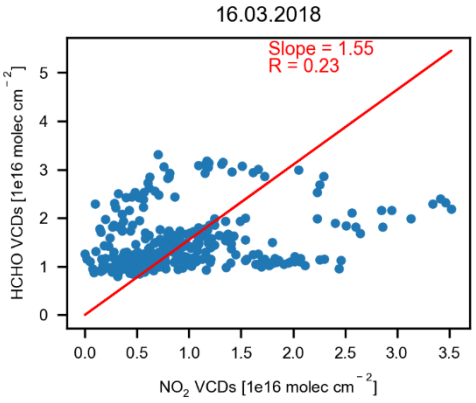
16.03.2018
Slope = 1.55
R = 0.23
HCHO VCDs [1e16 molec cm-2]
NO2 VCDs [1e16 molec cm-2]

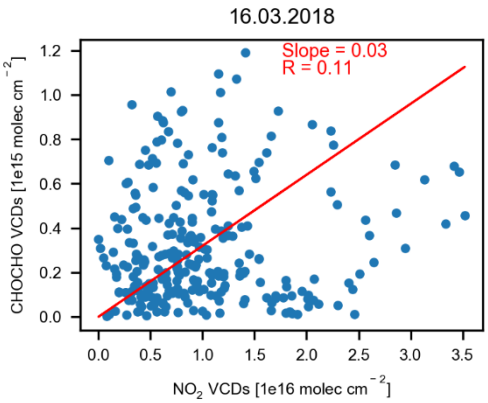
16.03.2018
Slope = 0.03
R = 0.11
CHOCHO VCDs [1e15 molec cm-2]
NO2 VCDs [1e16 molec cm-2]

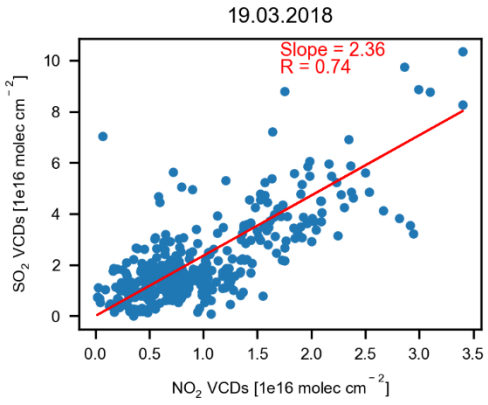
19.03.2018
Slope = 2.36
R = 0.74
SO2 VCDs [1e16 molec cm-2]
NO2 VCDs [1e16 molec cm-2]

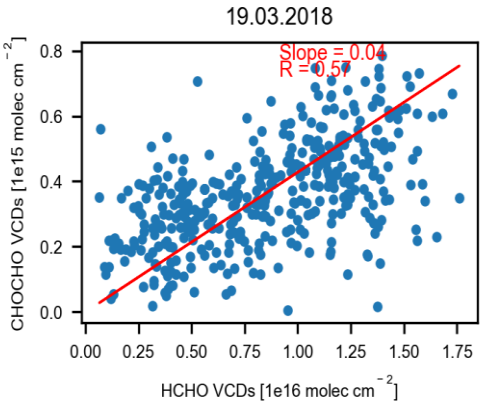
19.03.2018
Slope = 0.04
R = 0.57
CHOCHO VCDs [1e15 molec cm-2]
HCHO VCDs [1e16 molec cm-2]

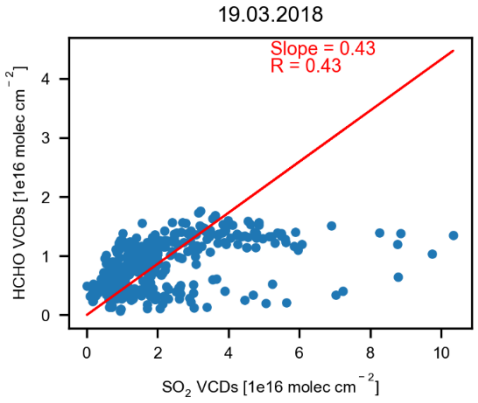
19.03.2018
Slope = 0.43
R = 0.43
HCHO VCDs [1e16 molec cm-2]
SO2 VCDs [1e16 molec cm-2]

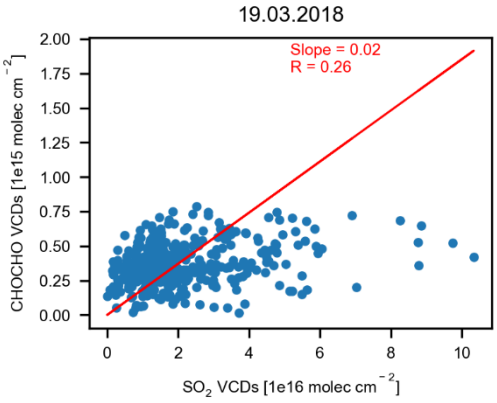
19.03.2018
Slope = 0.02
R = 0.26
CHOCHO VCDs [1e15 molec cm-2]
SO2 VCDs [1e16 molec cm-2]

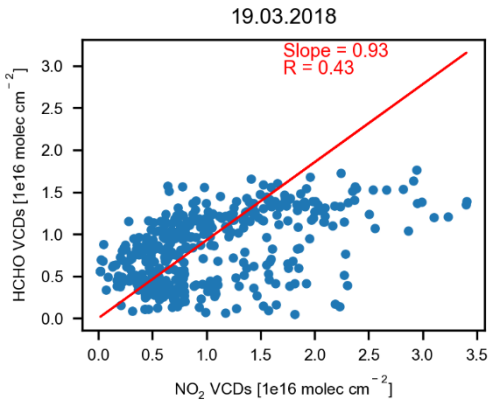
19.03.2018
Slope = 0.93
R = 0.43
HCHO VCDs [1e16 molec cm-2]
NO2 VCDs [1e16 molec cm-2]

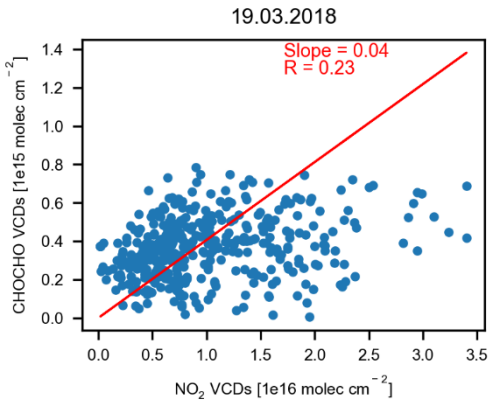
19.03.2018
Slope = 0.04
R = 0.23
CHOCHO VCDs [1e15 molec cm-2]
NO2 VCDs [1e16 molec cm-2]

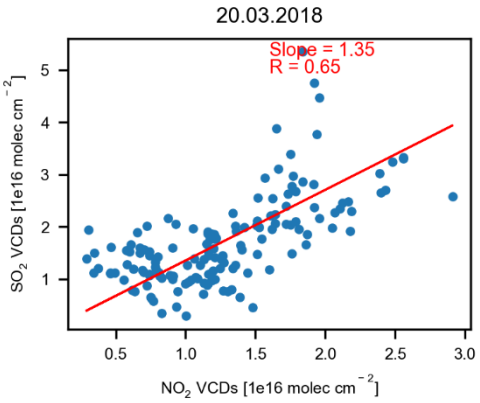
20.03.2018
Slope = 1.35
R = 0.65
SO2 VCDs [1e16 molec cm-2]
NO2 VCDs [1e16 molec cm-2]

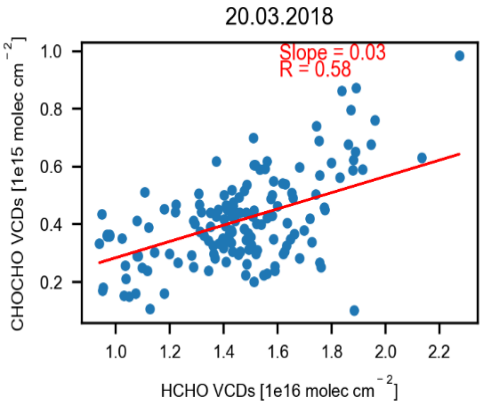
20.03.2018
Slope = 0.03
R = 0.58
CHOCHO VCDs [1e15 molec cm-2]
HCHO VCDs [1e16 molec cm-2]

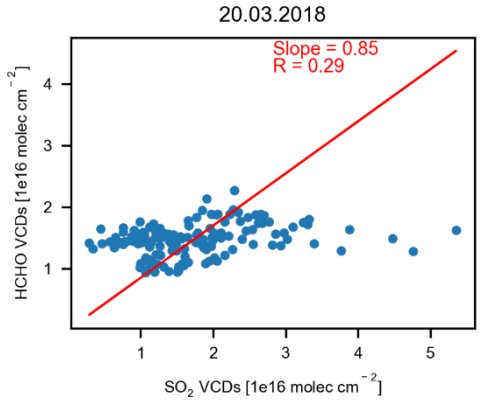
20.03.2018
Slope = 0.85
R = 0.29
HCHO VCDs [1e16 molec cm-2]
SO2 VCDs [1e16 molec cm-2]

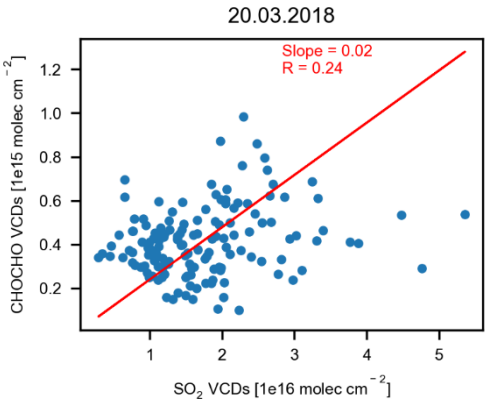
20.03.2018
Slope = 0.02
R = 0.24
CHOCHO VCDs [1e15 molec cm-2]
SO2 VCDs [1e16 molec cm-2]

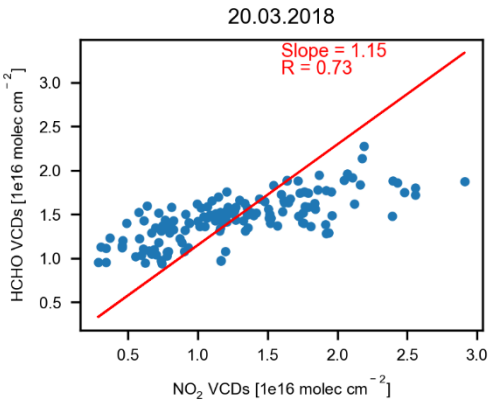
20.03.2018
Slope = 1.15
R = 0.73
HCHO VCDs [1e16 molec cm-2]
NO2 VCDs [1e16 molec cm-2]

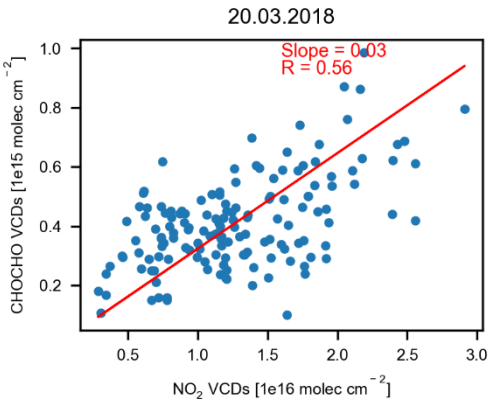
20.03.2018
Slope = 0.03
R = 0.56
CHOCHO VCDs [1e15 molec cm-2]
NO2 VCDs [1e16 molec cm-2]

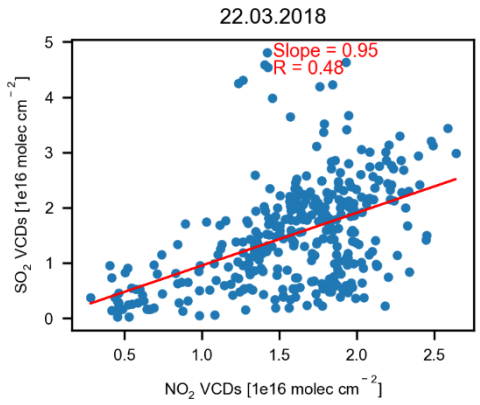
22.03.2018
Slope = 0.95
R = 0.48
SO2 VCDs [1e16 molec cm−2]
NO2 VCDs [1e16 molec cm−2]

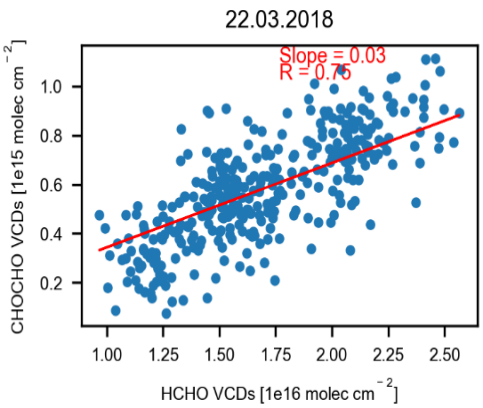
22.03.2018
Slope = 0.03
R = 0.75
CHOCHO VCDs [1e15 molec cm−2]
HCHO VCDs [1e16 molec cm−2]

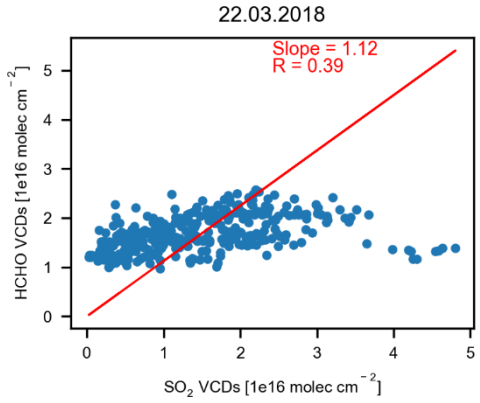
22.03.2018
Slope = 1.12
R = 0.39
HCHO VCDs [1e16 molec cm−2]
SO2 VCDs [1e16 molec cm−2]

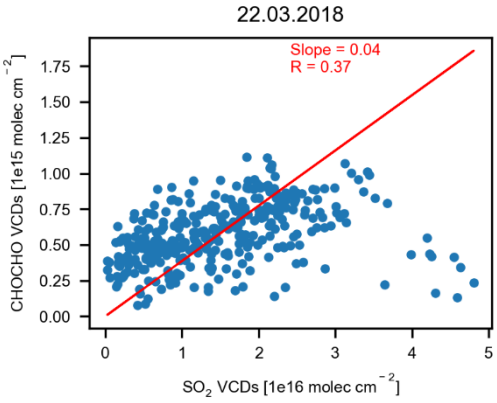
22.03.2018
Slope = 0.04
R = 0.37
CHOCHO VCDs [1e15 molec cm−2]
SO2 VCDs [1e16 molec cm−2]

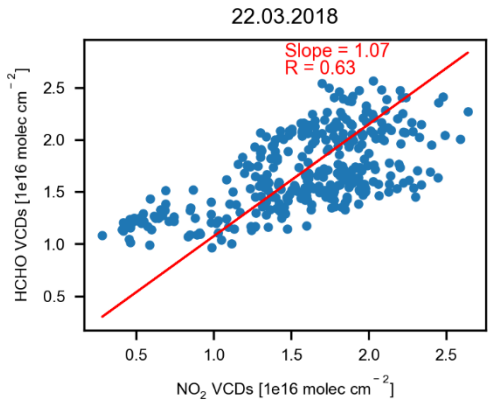
22.03.2018
Slope = 1.07
R = 0.63
HCHO VCDs [1e16 molec cm−2]
NO2 VCDs [1e16 molec cm−2]

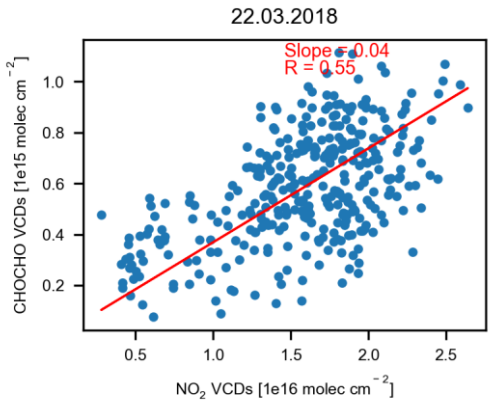
22.03.2018
Slope = 0.04
R = 0.55
CHOCHO VCDs [1e15 molec cm−2]
NO2 VCDs [1e16 molec cm−2]

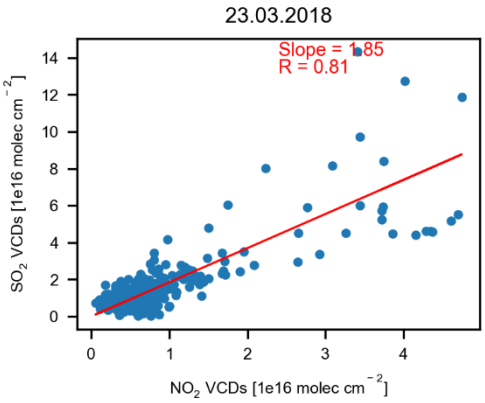
23.03.2018
Slope = 1.85
R = 0.81
SO2 VCDs [1e16 molec cm-2]
NO2 VCDs [1e16 molec cm-2]

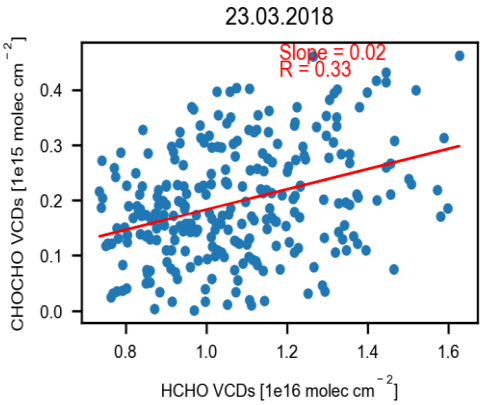
23.03.2018
Slope = 0.02
R = 0.33
CHOCHO VCDs [1e15 molec cm-2]
HCHO VCDs [1e16 molec cm-2]

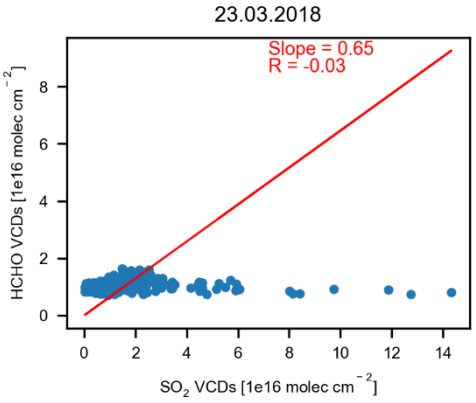
23.03.2018
Slope = 0.65
R = -0.03
HCHO VCDs [1e16 molec cm-2]
SO2 VCDs [1e16 molec cm-2]

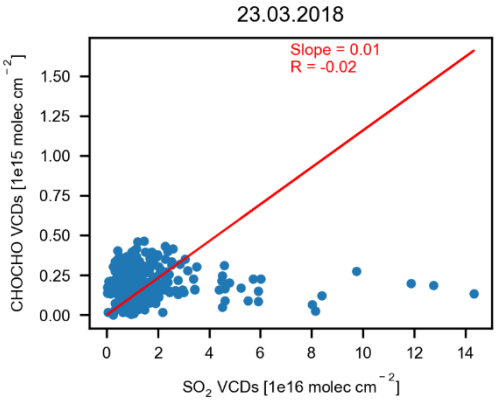
23.03.2018
Slope = 0.01
R = -0.02
CHOCHO VCDs [1e15 molec cm-2]
SO2 VCDs [1e16 molec cm-2]

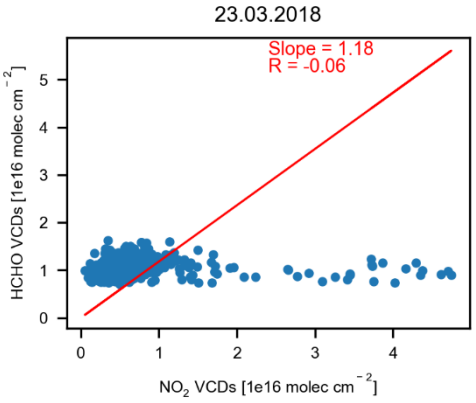
23.03.2018
Slope = 1.18
R = -0.06
HCHO VCDs [1e16 molec cm-2]
NO2 VCDs [1e16 molec cm-2]

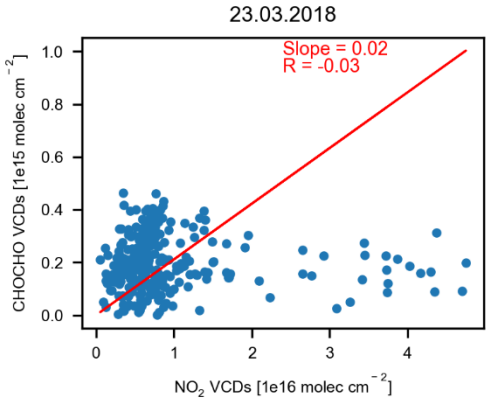
23.03.2018
Slope = 0.02
R = -0.03
CHOCHO VCDs [1e15 molec cm-2]
NO2 VCDs [1e16 molec cm-2]

APPENDIX D

The supplementary figures for chapter 5 are presented in this appendix.

D.1. Sahiwal Power Plant

In this section, vertical column densities (VCDs) of the four trace gases derived from the observations performed around the Sahiwal coal power plant on March 2018 are presented.

6.3.1.8.D.1.1. NO_2

NO_2 VCDs derived from the observations performed in three circles around the Sahiwal coal power plant are presented.

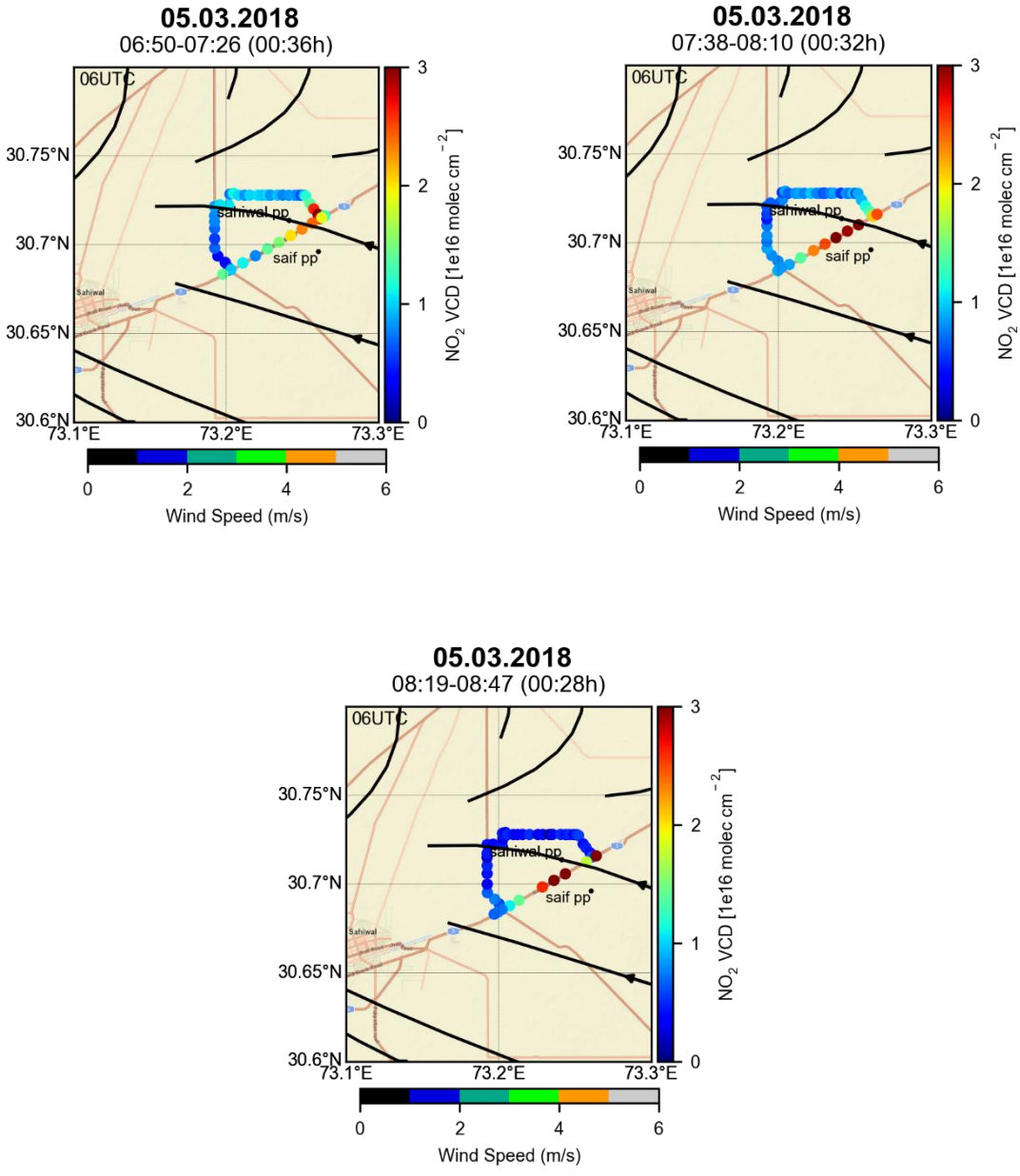

6.3.1.9.D.1.2. SO_2

SO_2 VCDs derived from the observations performed in three circles around the Sahiwal coal power plant are presented.

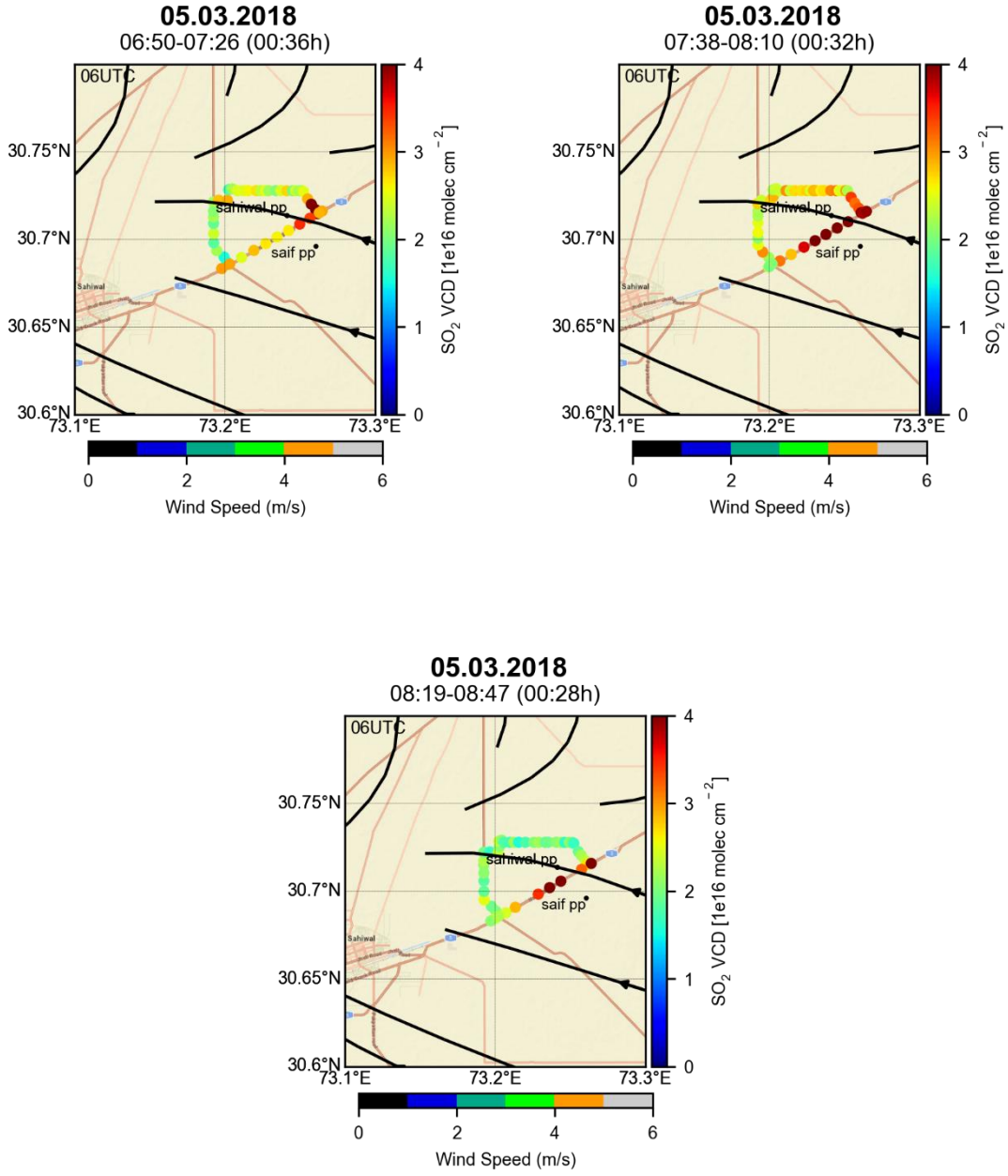

6.3.1.10. D.1.3. Formaldehyde

HCHO VCDs derived from the observations performed in three circles around the Sahiwal coal power plant are presented.

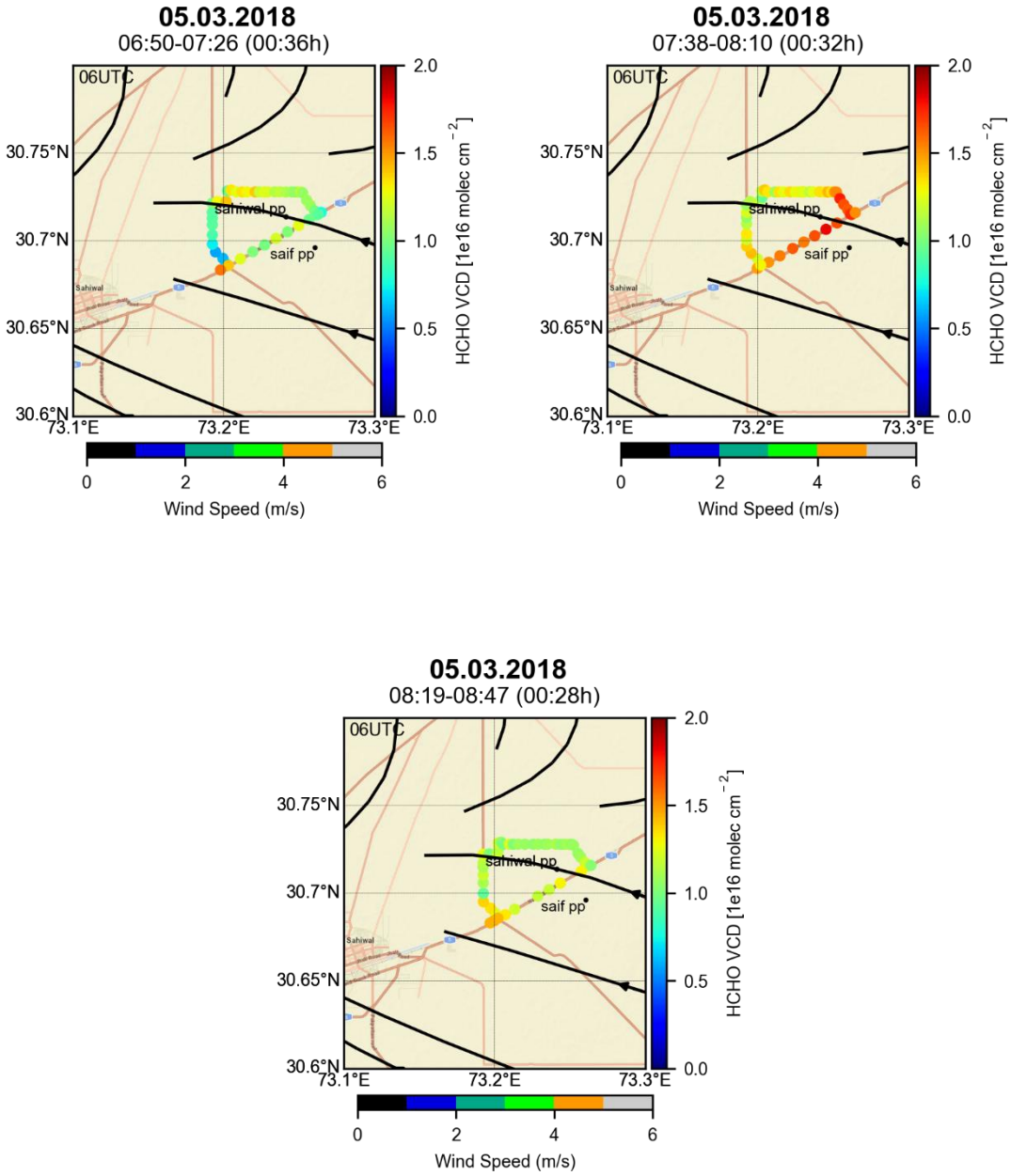

6.3.1.11. D.1.4. Glyoxal

Glyoxal VCDs derived from the observations performed in three circles around the Sahiwal coal power plant are presented.

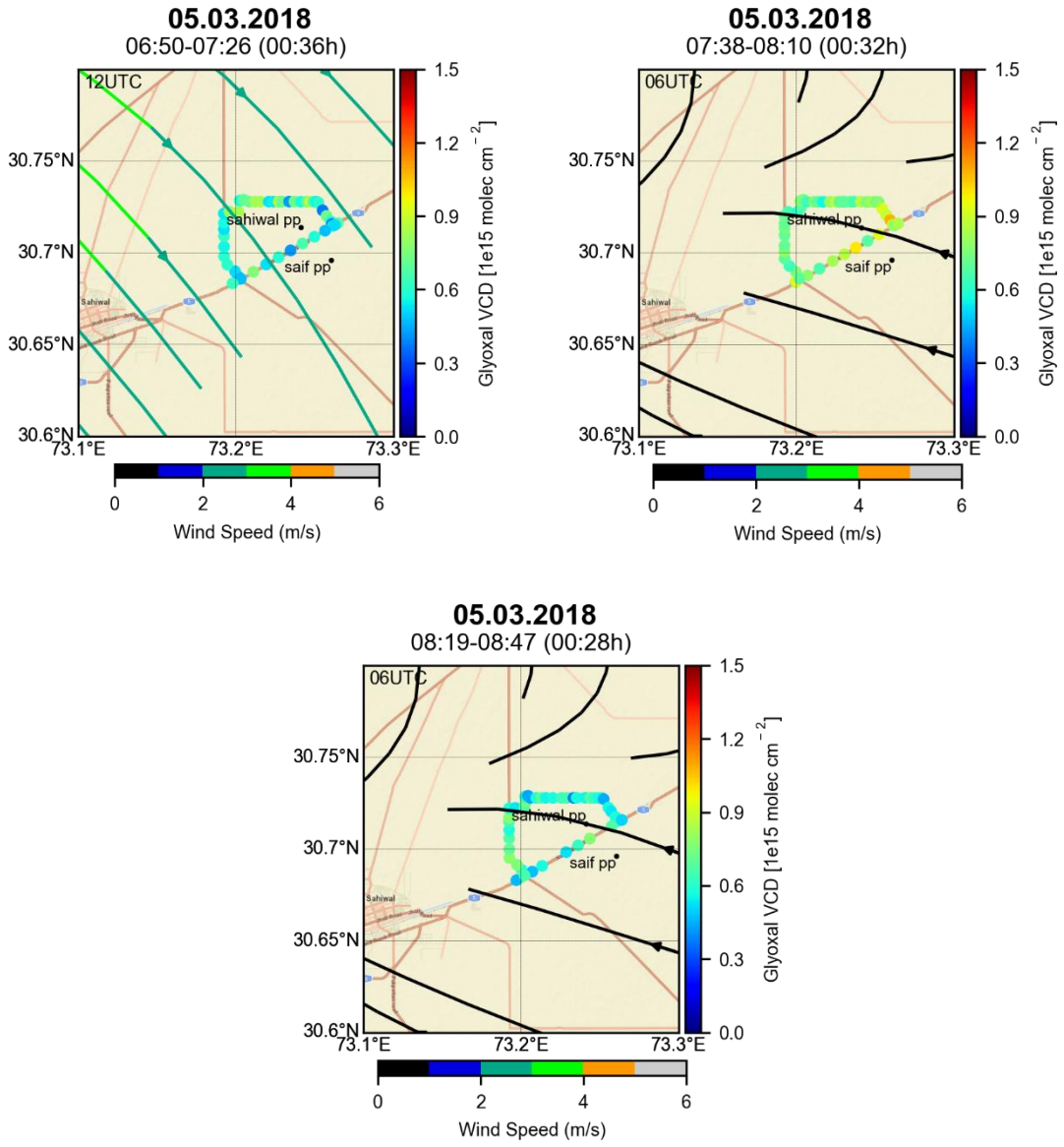

D.2. Spatial Distribution around Gujranwala

In this section trace gas VCDs derived from the observations performed around the city of Gujranwala on 15 March 2018 are presented. The streamlines indicate ECMWF winds at 6 UTC.

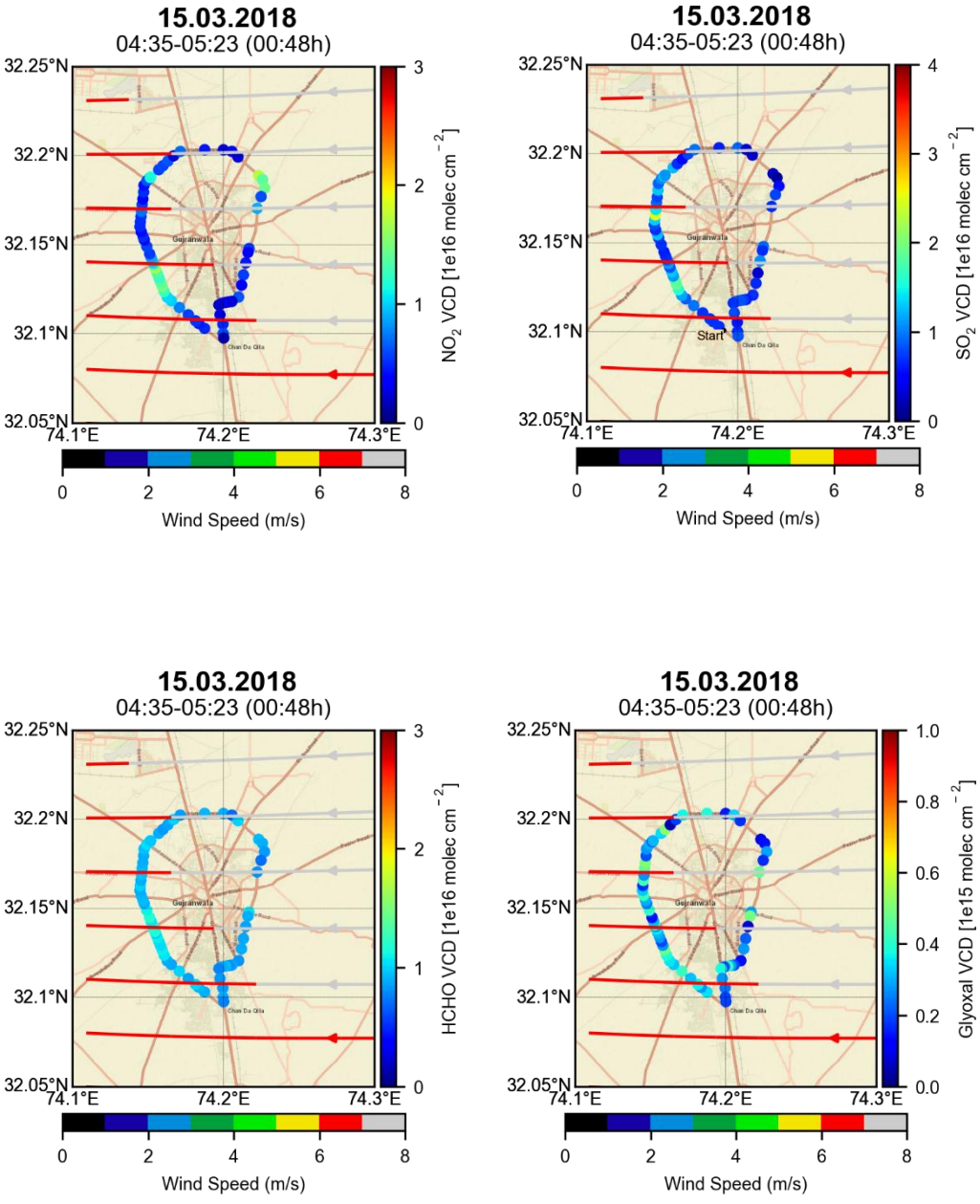

D.3. Trace gas spatial distributions around power plants

In this section NO_2, SO_2, HCHO and CHOCHO VCDs derived from the observations executed around the power plants on different days during the 2018-II campaign are presented date wise.

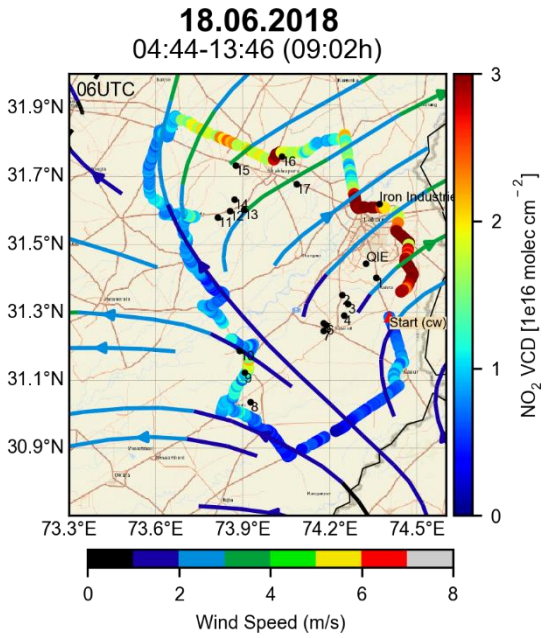

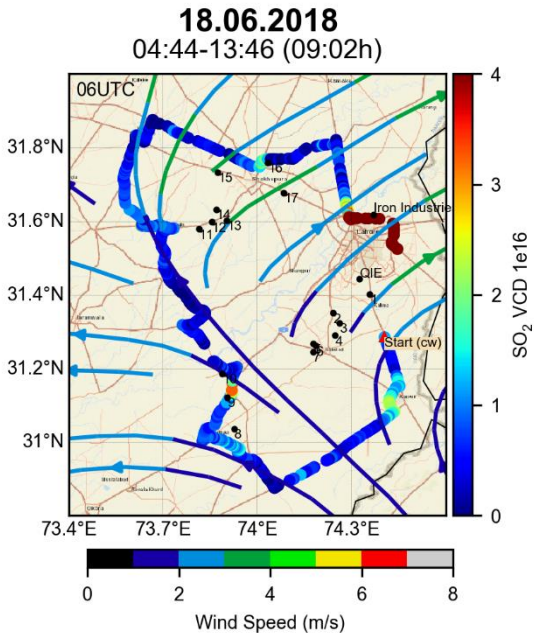

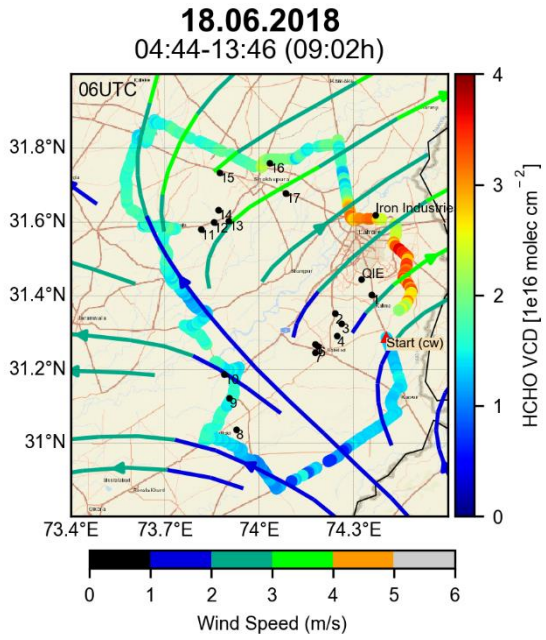

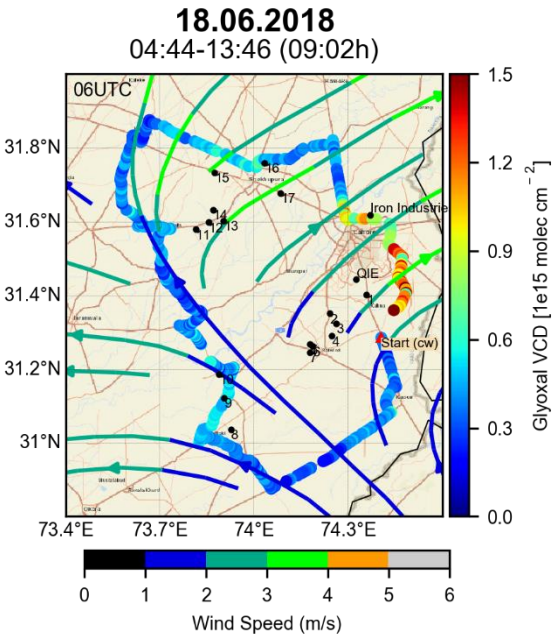

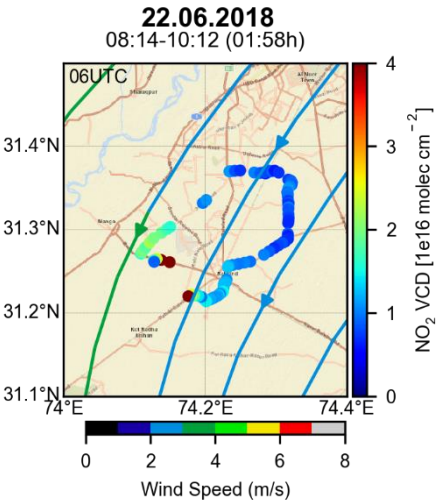
22.06.2018
08:14-10:12 (01:58h)
06UTC
31.4°N
31.3°N
31.2°N
31.1°N
74°E
74.2°E
74.4°E
NO2 VCD [1e16 molec cm−2]
Wind Speed (m/s)

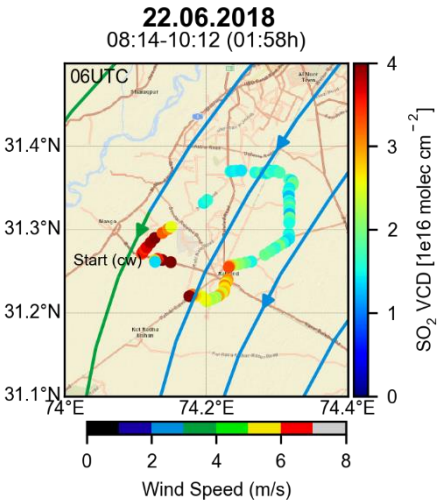
22.06.2018
08:14-10:12 (01:58h)
06UTC
Start (cw)
SO2 VCD [1e16 molec cm−2]
Wind Speed (m/s)

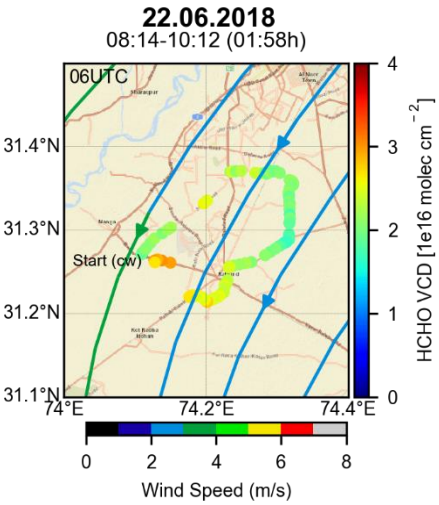
22.06.2018
08:14-10:12 (01:58h)
06UTC
Start (cw)
HCHO VCD [1e16 molec cm−2]
Wind Speed (m/s)

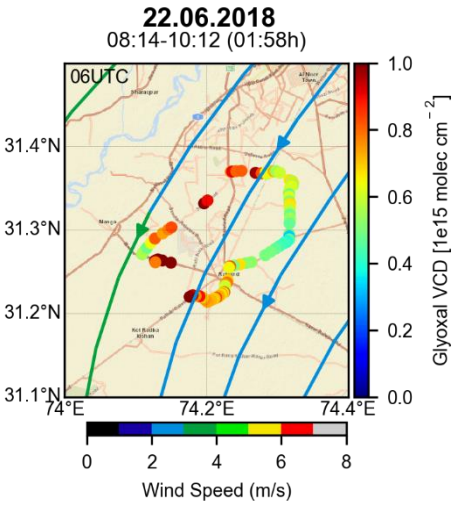
22.06.2018
08:14-10:12 (01:58h)
06UTC
Glyoxal VCD [1e15 molec cm−2]
Wind Speed (m/s)

26.06.2018

02:45-13:41 (10:56h)

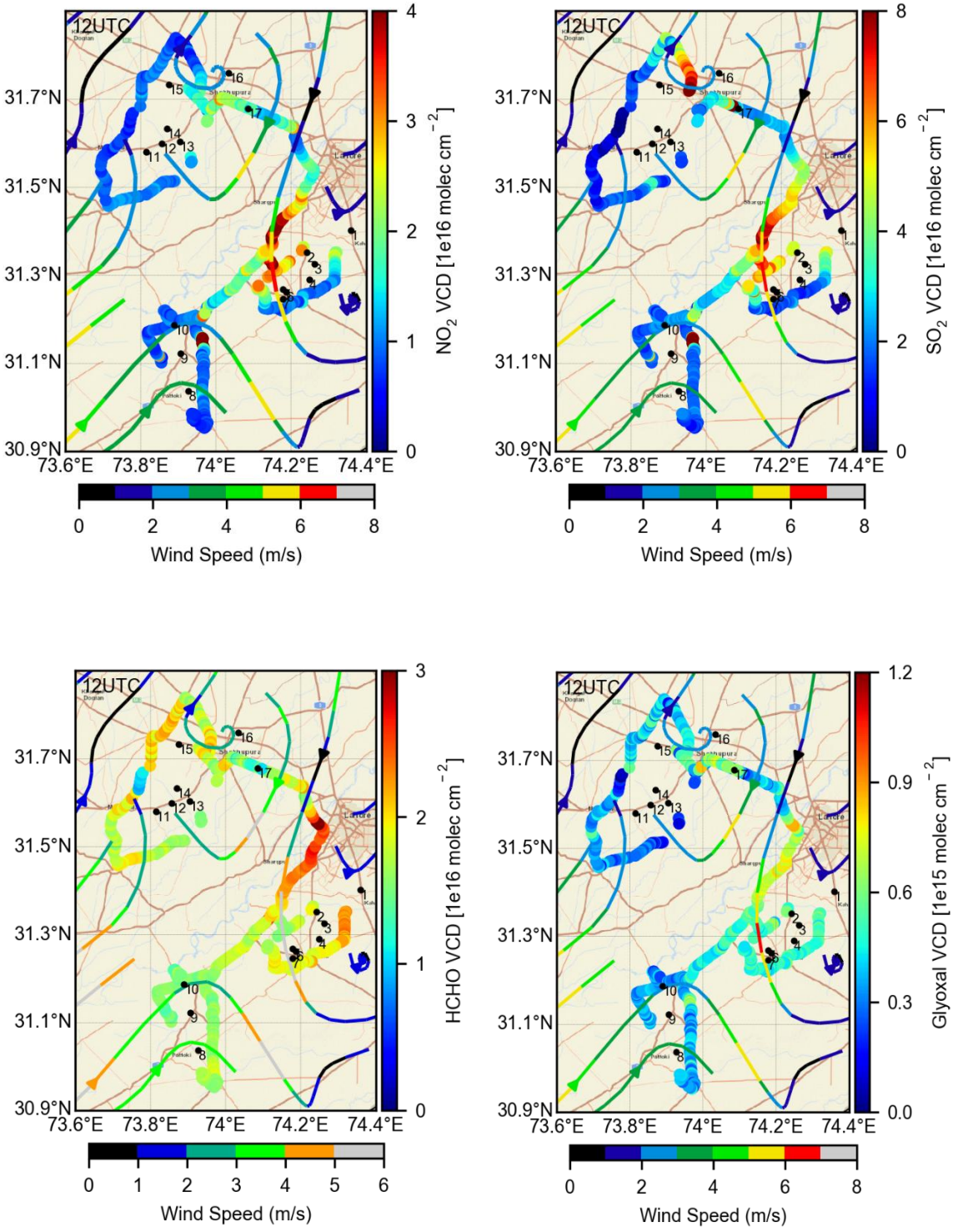

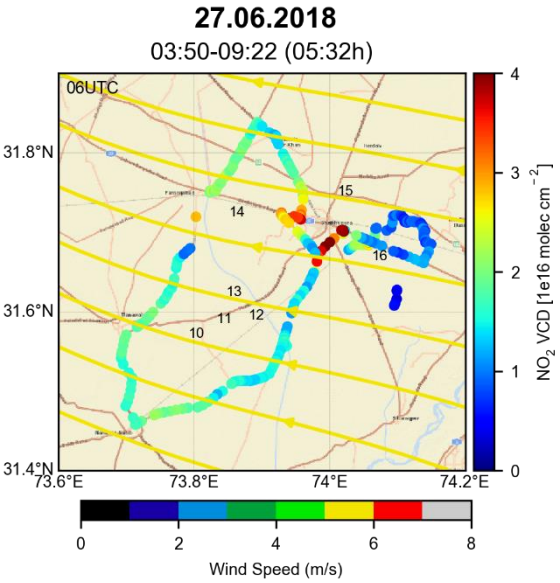
27.06.2018
03:50-09:22 (05:32h)
06UTC
31.8°N
31.6°N
31.4°N
73.6°E
73.8°E
74°E
74.2°E
10
11
12
13
14
15
16
0
1
2
3
4
NO2 VCD [1e16 molec cm−2]
0
2
4
6
8
Wind Speed (m/s)

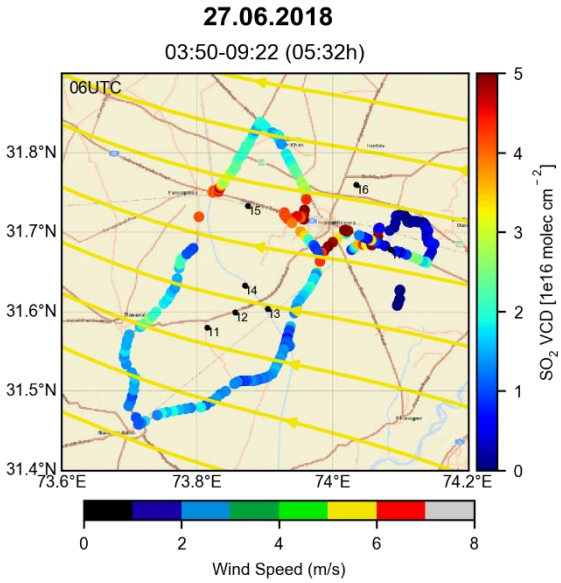
27.06.2018
03:50-09:22 (05:32h)
06UTC
31.8°N
31.7°N
31.6°N
31.5°N
31.4°N
73.6°E
73.8°E
74°E
74.2°E
11
12
13
14
15
16
0
1
2
3
4
5
SO2 VCD [1e16 molec cm−2]
0
2
4
6
8
Wind Speed (m/s)

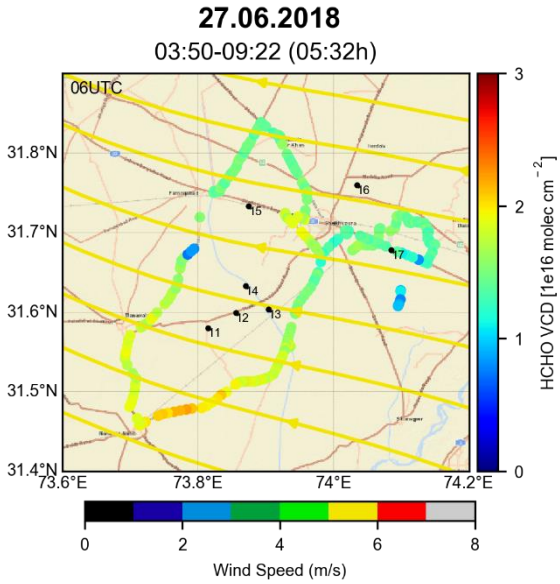
27.06.2018
03:50-09:22 (05:32h)
06UTC
31.8°N
31.7°N
31.6°N
31.5°N
31.4°N
73.6°E
73.8°E
74°E
74.2°E
11
12
13
14
15
16
17
0
1
2
3
HCHO VCD [1e16 molec cm−2]
0
2
4
6
8
Wind Speed (m/s)

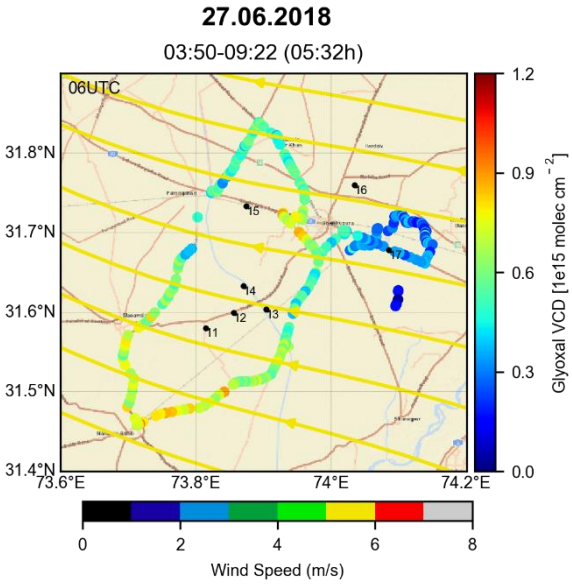
27.06.2018
03:50-09:22 (05:32h)
06UTC
31.8°N
31.7°N
31.6°N
31.5°N
31.4°N
73.6°E
73.8°E
74°E
74.2°E
11
12
13
14
15
16
17
0.0
0.3
0.6
0.9
1.2
Glyoxal VCD [1e15 molec cm−2]
0
2
4
6
8
Wind Speed (m/s)

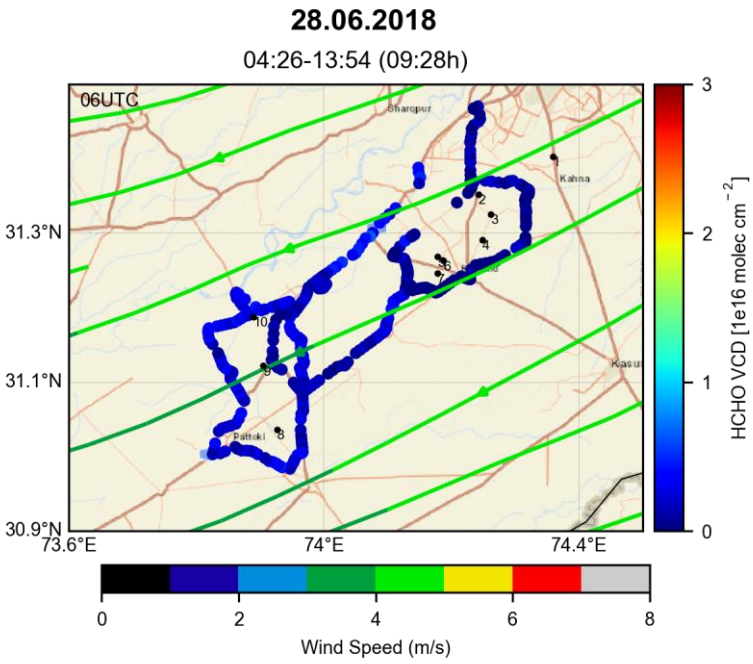
28.06.2018
04:26-13:54 (09:28h)
06UTC
Kahna
Kasur
Pattoki
31.3°N
31.1°N
30.9°N
73.6°E
74°E
74.4°E
HCHO VCD [1e16 molec cm $^{-2}$]
0
1
2
3
0
2
4
6
8
Wind Speed (m/s)

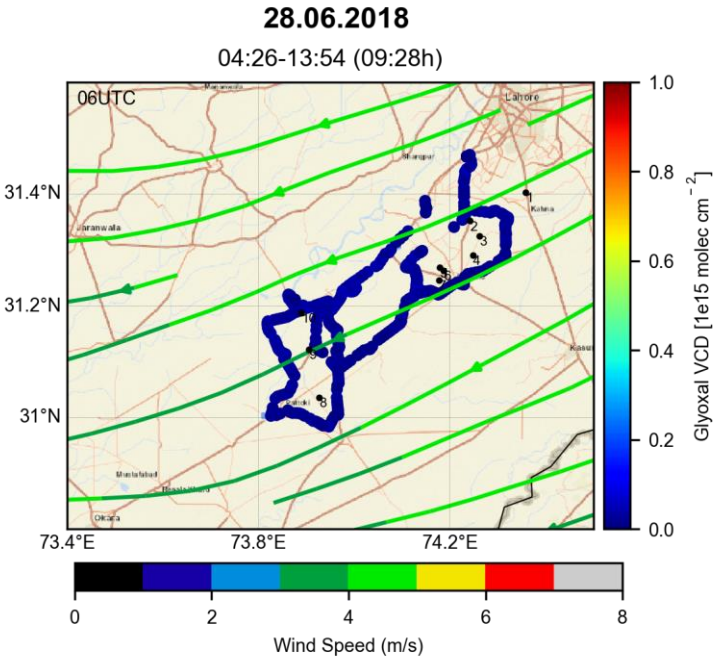
28.06.2018
04:26-13:54 (09:28h)
06UTC
Lahore
Kahna
Kasur
31.4°N
31.2°N
31°N
73.4°E
73.8°E
74.2°E
Glyoxal VCD [1e15 molec cm $^{-2}$]
0.0
0.2
0.4
0.6
0.8
1.0
0
2
4
6
8
Wind Speed (m/s)

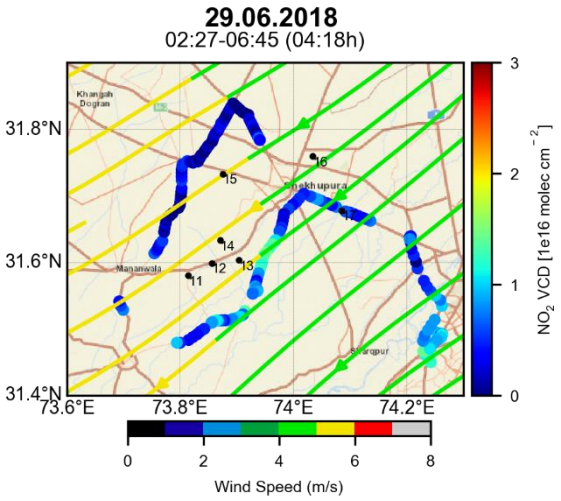
29.06.2018
02:27-06:45 (04:18h)
31.8°N
31.6°N
31.4°N
73.6°E
73.8°E
74°E
74.2°E
Khangah Dogran
Nankhupura
Mananwala
Sharqpur
11
12
13
14
15
16
0
2
4
6
8
Wind Speed (m/s)
0
1
2
3
NO2 VCD [1e16 molec cm −2]

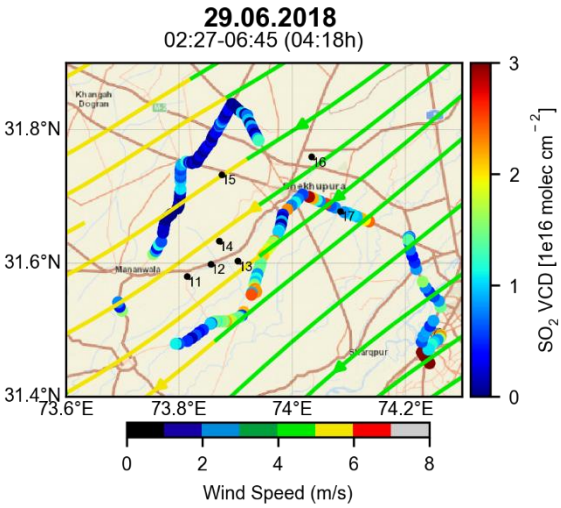
29.06.2018
02:27-06:45 (04:18h)
31.8°N
31.6°N
31.4°N
73.6°E
73.8°E
74°E
74.2°E
Khangah Dogran
Nankhupura
Mananwala
Sharqpur
11
12
13
14
15
16
17
0
2
4
6
8
Wind Speed (m/s)
0
1
2
3
SO2 VCD [1e16 molec cm −2]

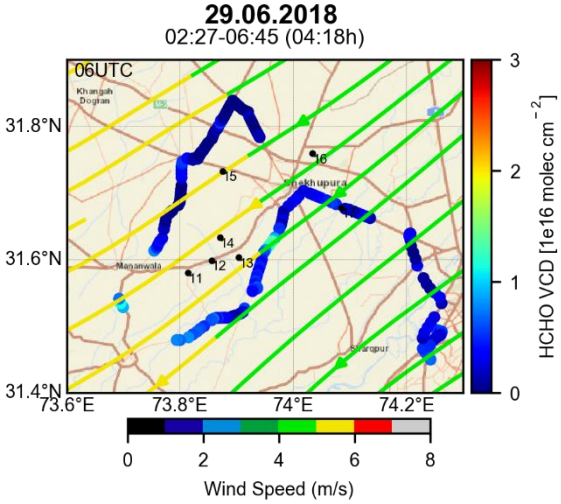
29.06.2018
02:27-06:45 (04:18h)
06UTC
31.8°N
31.6°N
31.4°N
73.6°E
73.8°E
74°E
74.2°E
Khangah Dogran
Nankhupura
Mananwala
Sharqpur
11
12
13
14
15
16
0
2
4
6
8
Wind Speed (m/s)
0
1
2
3
HCHO VCD [1e16 molec cm −2]

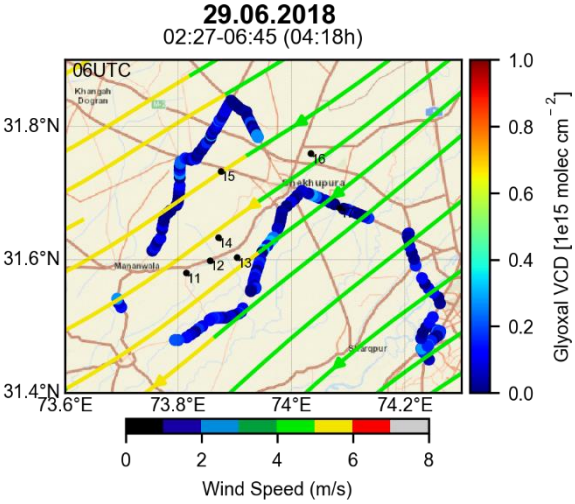
29.06.2018
02:27-06:45 (04:18h)
06UTC
31.8°N
31.6°N
31.4°N
73.6°E
73.8°E
74°E
74.2°E
Khangah Dogran
Nankhupura
Mananwala
Sharqpur
11
12
13
14
15
16
0
2
4
6
8
Wind Speed (m/s)
0.0
0.2
0.4
0.6
0.8
1.0
Glyoxal VCD [1e15 molec cm −2]

02.07.2018

03:15-13:41 (11:26 h)

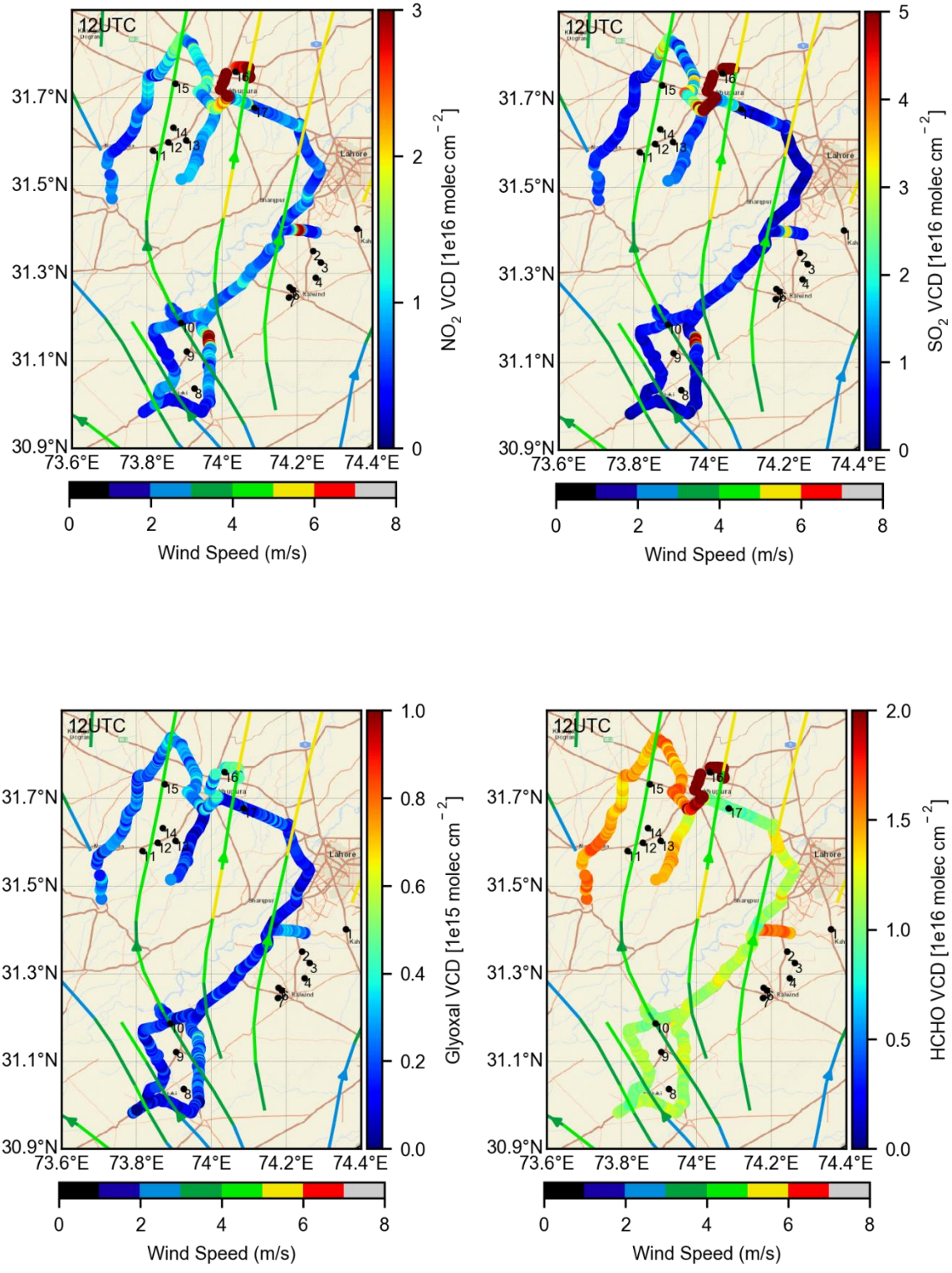

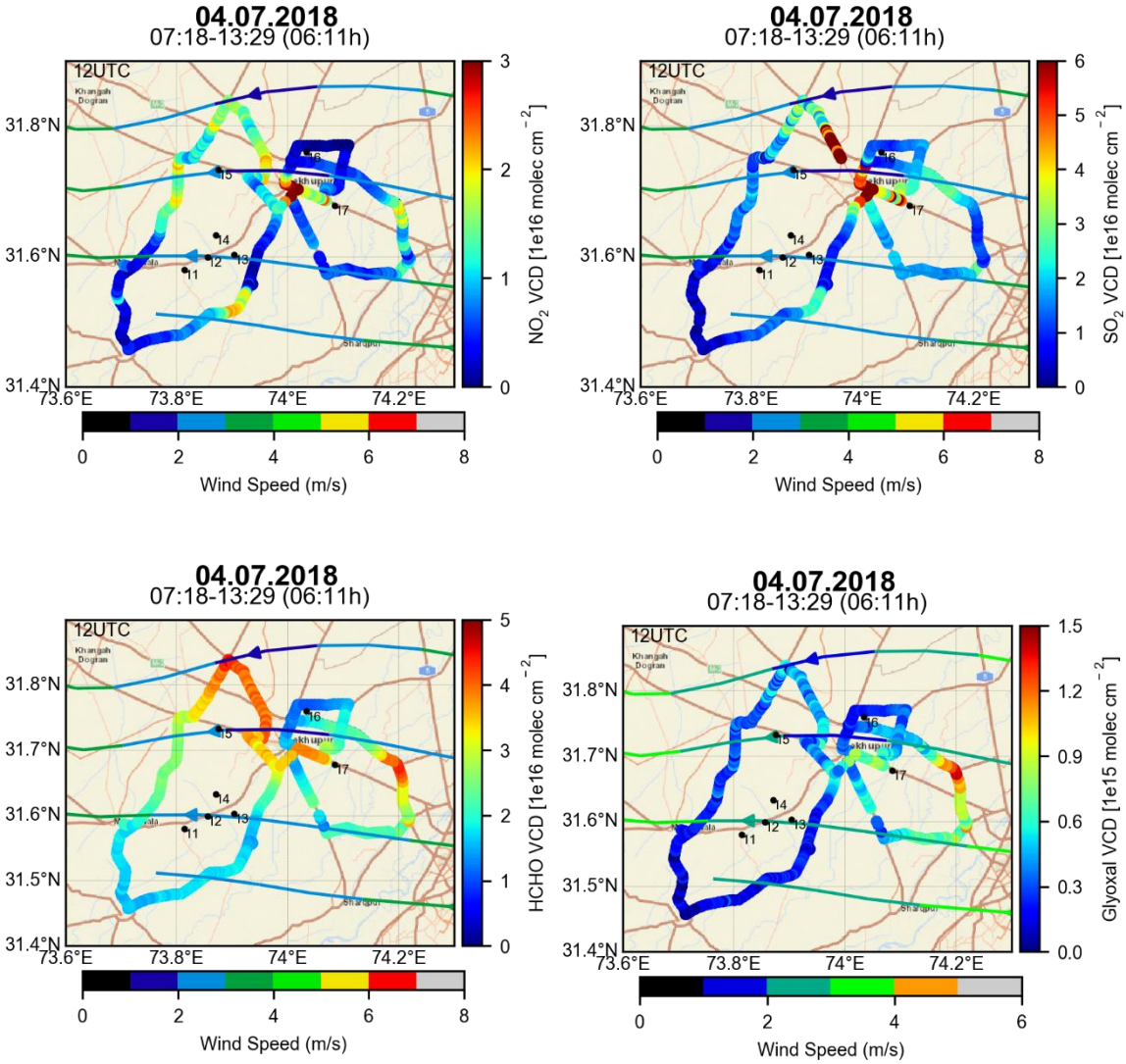
04.07.2018
07:18-13:29 (06:11h)
12UTC
31.8°N
31.6°N
31.4°N
73.6°E
73.8°E
74°E
74.2°E
NO2 VCD [1e16 molec cm −2]
SO2 VCD [1e16 molec cm −2]
HCHO VCD [1e16 molec cm −2]
Glyoxal VCD [1e15 molec cm −2]
Wind Speed (m/s)

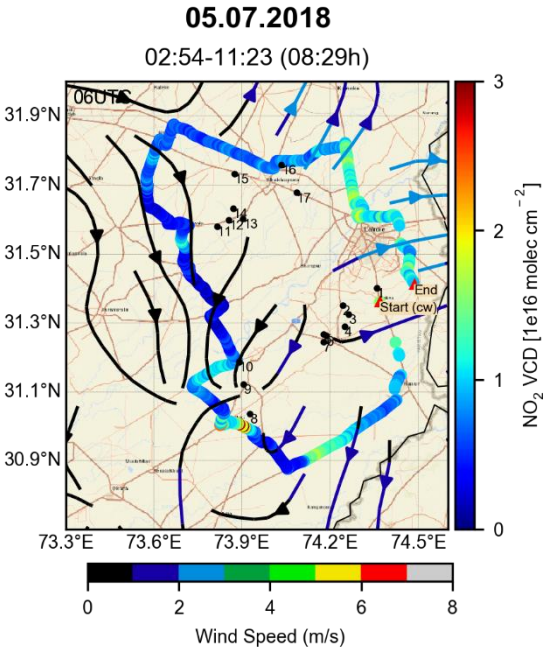
05.07.2018
02:54-11:23 (08:29h)
06UTC
31.9°N
31.7°N
31.5°N
31.3°N
31.1°N
30.9°N
73.3°E
73.6°E
73.9°E
74.2°E
74.5°E
Start (cw)
End
NO2 VCD [1e16 molec cm−2]
Wind Speed (m/s)

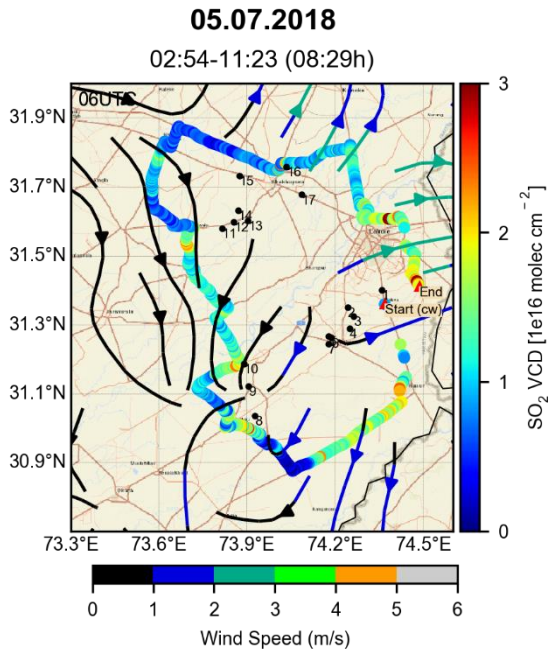
05.07.2018
02:54-11:23 (08:29h)
06UTC
31.9°N
31.7°N
31.5°N
31.3°N
31.1°N
30.9°N
73.3°E
73.6°E
73.9°E
74.2°E
74.5°E
Start (cw)
End
SO2 VCD [1e16 molec cm−2]
Wind Speed (m/s)

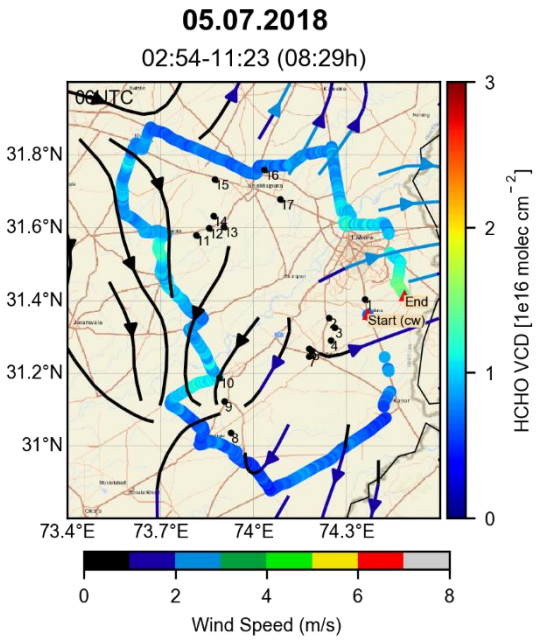
05.07.2018
02:54-11:23 (08:29h)
06UTC
31.8°N
31.6°N
31.4°N
31.2°N
31°N
73.4°E
73.7°E
74°E
74.3°E
Start (cw)
End
HCHO VCD [1e16 molec cm−2]
Wind Speed (m/s)

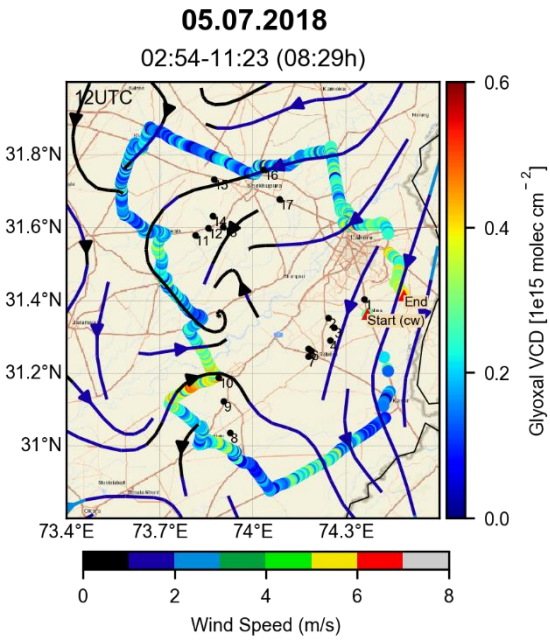
05.07.2018
02:54-11:23 (08:29h)
12UTC
31.8°N
31.6°N
31.4°N
31.2°N
31°N
73.4°E
73.7°E
74°E
74.3°E
Start (cw)
End
Glyoxal VCD [1e15 molec cm−2]
Wind Speed (m/s)

APPENDIX E

E.1. Regional Model (MECO(n))

In this appendix comparison between MAX-DOAS and MECO(n) VCDs is presented.

The simulation results were obtained from the on-line coupled atmospheric chemistry model system called "MECO(n)", i.e. MESSy-fied ECHAM and COSMO models nested n times (Hofmann et al., 2012; Kerkweg & Jöckel, 2012). In the current study, the COSMO/MESSY model is nested 2 times. The first instance has a spatial resolution of around 50×50 km^2 while the second instance has a spatial resolution of ~7×7 km^2 or 0.0625×0.0625 degrees. The model output was sampled online at the time and geolocation of the car MAX DOAS observations using the diagnostic submodel S4D. EDGAR 4.3.2 (Crippa et al., 2018) is used as the anthropogenic emission inventory input. The base year for the inventory is 2010. Further details of the model can be found in Kumar et al. (2021)

E.1.1. MAX-DOAS VCDs' comparison with simulated VCDs

TROPOMI satellite observations are available only once per day at noontime. As a result, the comparison between ground-based MAX-DOAS measurements and the satellite data set can only be performed for a short time slot of the day. Compared to satellite data, MECO(n) simulations have a higher temporal coverage and resolution and are therefore well suited for the comparison with ground-based observations. Thus, comparisons were also performed with the regional model MECO(n). MAX-DOAS observations have also been previously compared with regional air quality models, e.g. by Vlemmix et al. (2015), Shaiganfar et al. (2015), Blechschmidt et al. (2020) and Kumar et al. (2021). In the present study, three trace gas VCDs (NO_2, SO_2 and HCHO) from two measurement campiagns performed during summer 2017 and 2018 are compared with VCDs obtained from the regional model run.

Comparison between nitrogen dioxide vertical column densities obtained from the two datasets are performed for 20 days during the 2017 and for 10 days during the 2018-II campaigns. As already mentioned, the 2017 measurements were performed around Lahore city, whereas the 2018-II campaign was executed to measure the trace gas distributions around the region's power plants. Figure E.1 illustrates the scatter plots for the two datasets for both measurement periods. If all data are considered, no correlation was found, and the coefficients of determination (R^2) were found to be 0.07 and 0.00 for the 2017 and 2018-II measurements, respectively. However, a weak to moderate correlation was observed on individual days, e.g. on 18 June 2018. On this day, a moderate correlation ($R^2 = 0.54$) between the data sets was found. Comparison results for this day are shown in Figures E.2 and E.3. On this day, measurements were performed from 4:11 to 13:38 UTC along the large circle around the powerplants in the region. From the time series plot (Figure E.2, b) it can be observed that although the MECO(n) results are underestimated by more than a factor of 3, still a similar qualitative behavior was found.

The comparison results for the other two trace gases (SO_2 and HCHO) also showed differences in the spatial distributions between measurements and simulations.

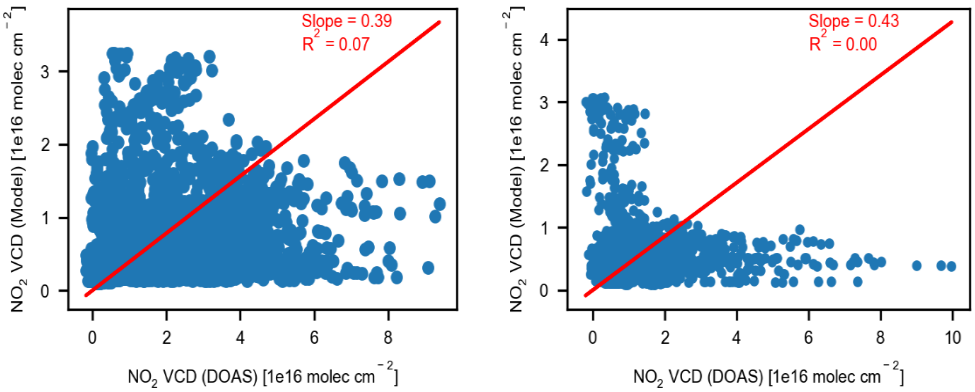

Figure E.1: Correlation plots for the NO_2 VCDs observed from car MAX-DOAS and simulated by the regional model for 2017 (left) and 2018-II (right) measurement periods.

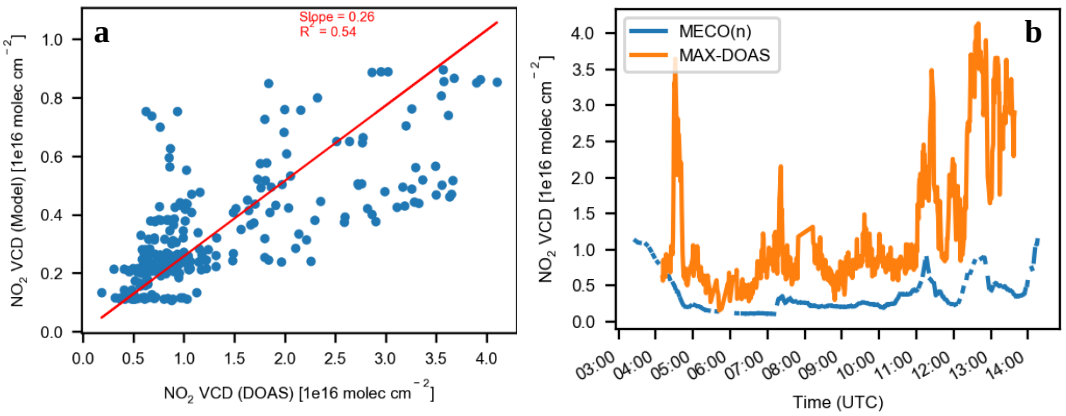

Figure E.2: Comparison plots for the observed and modelled NO_2 VCDs on 18.06.2018. The figure (a) exhibits the correlation analysis, while the figure (b) represents the timeseries of the NO_2 VCDs obtained from both datasets.

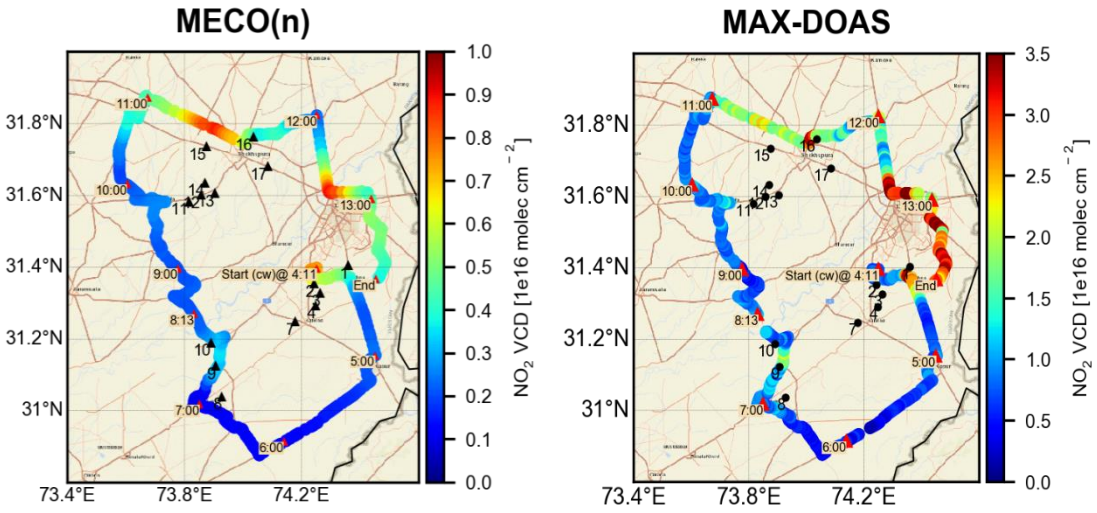

Figure E.3: Spatial distribution of NO_2 VCDs from model and MAX-DOAS on 18.06.2018 around the power plants in the region. The timestamps are also indicated along the whole route. The color bars for both the datasets are scaled differently.

The disagreement between the MAX-DOAS and MECO(n) may be partly due to the errors in the meteorological data used for the model simulations. To confirm this, the wind data used for the model was compared with the ERA 5 hourly wind data (Copernicus Climate Change Service (C3S), 2017) and with the measurements obtained from the aircraft observations. The details of the aircraft observations are discussed in section 2.6.1. Figure and Figure illustrate the results for the comparison of the wind speed and wind direction. The three data sets were compared with each other for a period of around two weeks in June and July 2018. All datasets were averaged over a horizontal grid of 0.27° ×0.49° for an altitude range of ~600-950 m above sea level. The coefficient of determination (R^2) for the correlation analyses between the wind speeds of the aircraft and ERA5 versus the MECO(n) winds were found to be 0.0 and 0.02, respectively. The R^2 value for the ERA 5 and aircraft observations was found to be 0.23 (R=0.48). These values indicate that the MECO winds show no agreement with the other two datasets, whereas the ERA 5 results and the aircraft observations showed a weak relationship. Figure 6.10 shows the wind roses for the three datasets. Therefore, it can be assumed that the discrepancies in the wind data might be the main reason for the erroneous simulated VCDs. This assumption can also be supported by the comparison for the wind data between MECO(n) and ERA 5 for 18.06.2018 (the day with $R^2 = 0.54$). In Figure E.2 (b), it can be observed, that for the last two hours (~11:00-13:00 UTC) the VCDs from both the datasets showed similar relative behaviour. Also wind data for the same time period showed quite similar values. Figure exhibits the timeseries plots for the wind speeds and wind directions during the measurement time on 18 June 2018.

Another reason for the disagreement of MAX-DOAS VCDs and the simulated VCDs can be found in the emission inventory's base year, i.e. 2010, since then the emission sources for the city have very probably changed significantly.

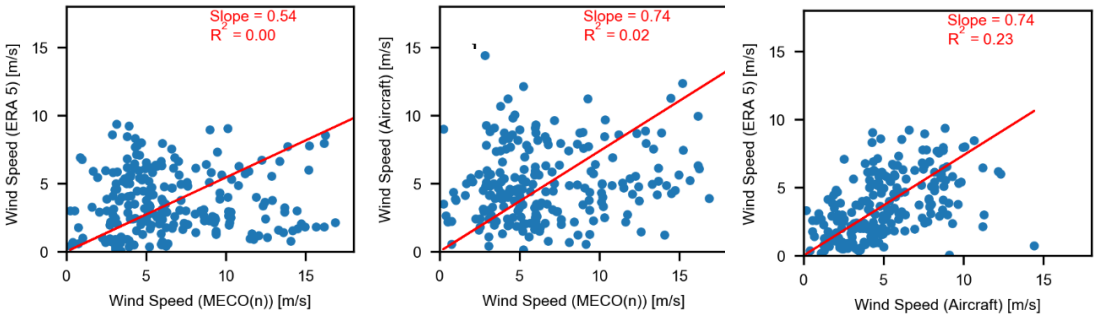

Figure E.4: Scatter plots for the wind speeds of the three datasets. Plots a and b represent the correlation between the wind speeds from MECO(n) and ERA 5 and the aircraft observations, respectively. The plot c illustrates the relationship between the wind speeds obtained from the aircraft and ERA 5 data.

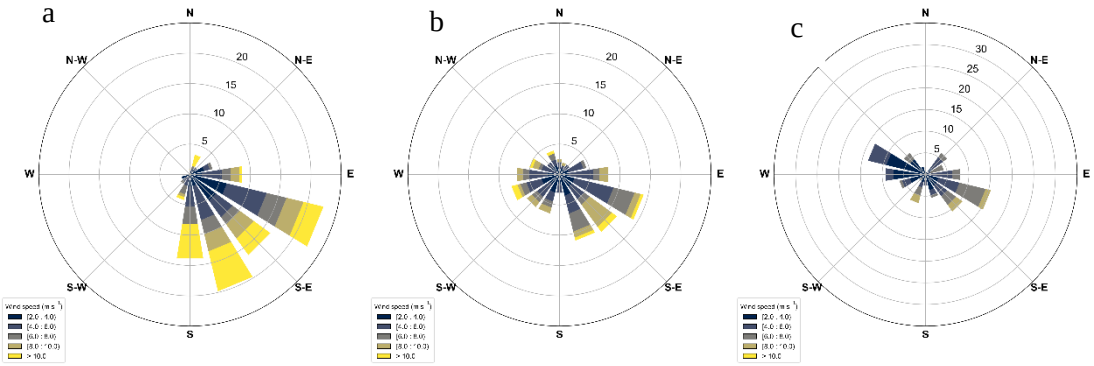

Figure E.5: Windrose plots of the wind conditions used in MECO(n) (a) and obtained from aircraft (b) and ERA 5 (c) data.

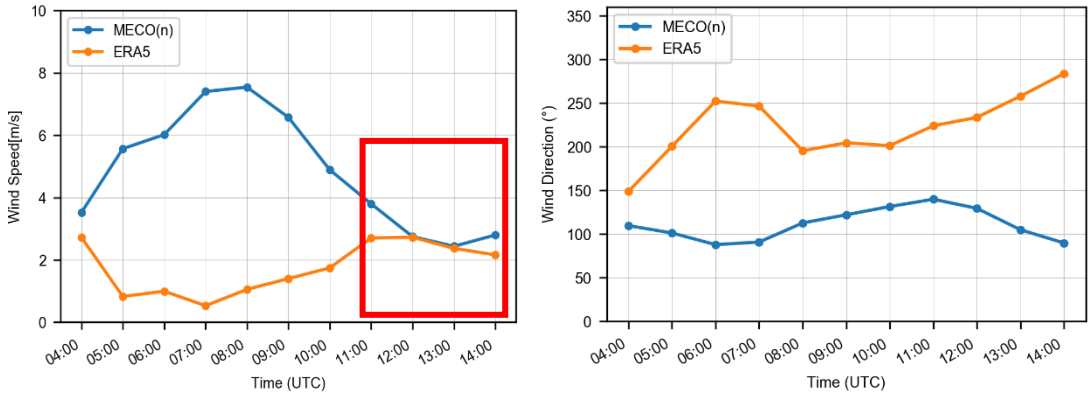

Figure E.6: Timeseries plots for wind speeds (left) and wind directions (right) from MECO(n) and ERA 5 on 18.06.2018. Comparable wind speeds can be observed between 11 and 14 UTC, highlighted by the red box.

BIBLIOGRAPHY

Abubakar Syed Muhammad. (2016). Lahore a city of gardens, now a city of concrete - Pakistan DAWN.COM. Retrieved November 22, 2020, from https://www.dawn.com/news/1238407

Ahmad, N., Hussain, K., Ahmad, N., Khaleeq-Ur-Rahman, M., & Hussnainn, A. (2014). A Study of Concentration of Lahore (Pakistan) Suspended Particulates and Their Trace Elemental Loadings. *World Applied Sciences Journal*, *32*(9), 1952–1961. https://doi.org/10.5829/idosi.wasj.2014.32.09.1128

Alam, A., Tabinda, A. B., Qadir, A., Butt, T. E., Siddique, S., & Mahmood, A. (2017). Ecological risk assessment of an open dumping site at Mehmood Booti Lahore, Pakistan. *Environmental Science and Pollution Research*, *24*(21), 17889–17899. https://doi.org/10.1007/s11356-017-9215-y

Ali, M., & Athar, M. (2010). Impact of transport and industrial emissions on the ambient air quality of Lahore City, Pakistan. *Environmental Monitoring and Assessment*, *171*(1–4), 353–363. https://doi.org/10.1007/s10661-009-1283-0

Ali, Z., Rauf, A., Sidra, S., Nasir, Z. A., & Colbeck, I. (2015). Air quality(particulate matter) at heavy traffic sites in Lahore, Pakistan. *Journal of Animal and Plant Sciences*, *25*(3), 644–648.

Aliwell, S. R., Van Roozendael, M., Johnston, P. V., Richter, A., Wagner, T., Arlander, D. W., … Pundt, I. (2002). Analysis for BrO in zenith-sky spectra: An intercomparison exercise for analysis improvement. *Journal of Geophysical Research Atmospheres*, *107*(14), 1–20.

Anderson, L. G., Lanning, J. A., Barrel, R., Miyagishima, J., Jones, R. H., & Wolfe, P. (1996). Sources and sinks of formaldehyde and acetaldehyde: An analysis of Denver's ambient concentration data. *Atmos. Environ.*, *30*(12), 2113–2123.

Anjum, M. S., Ali, S. M., Imad-ud-din, M., Subhani, M. A., Anwar, M. N., Nizami, A. S., … Khokhar, M. F. (2021). An Emerged Challenge of Air Pollution and Ever-Increasing Particulate Matter in Pakistan; A Critical Review. *Journal of Hazardous Materials*, *402*(August 2020), 123943. https://doi.org/10.1016/j.jhazmat.2020.123943

Arlander, D. W., Brüning, D., Schmidt, U., & Ehhalt, D. H. (1995). The tropospheric distribution of formaldehyde during TROPOZ II. *Journal of Atmospheric Chemistry*, *22*(3), 251–269. https://doi.org/10.1007/BF00696637

Ashraf, A., Butt, A., Khalid, I., Alam, R. U., & Ahmad, S. R. (2019). Smog analysis and its effect on reported ocular surface diseases: A case study of 2016 smog event of Lahore. *Atmospheric Environment*, *198*(September 2017), 257–264. https://doi.org/10.1016/j.atmosenv.2018.10.029

Ashraf, N., Mushtaq, M., Sultana, B., & Iqbal, M. (2013). Preliminary monitoring of

tropospheric air quality of Lahore City in Pakistan. *Sustainable Development*, *3*(2), 19–28.

Atkinson, R., Baulch, D. L., Cox, R. A., Crowley, J. N., Hampson, R. F., Hynes, R. G., … Wallington, T. J. (2008). Evaluated kinetic and photochemical data for atmospheric chemistry: Volume IV - Gas phase reactions of organic\newline halogen species. *Atmospheric Chemistry and Physics*, *8*(15), 4141–4496. https://doi.org/10.5194/acp-8-4141-2008

Atkinson, Roger. (2000). Atmospheric chemistry of VOCs and NO(x). *Atmospheric Environment*, *34*(12–14), 2063–2101. https://doi.org/10.1016/S1352-2310(99)00460-4

Bastien, L., Brown, N., & Harley, R. (2018). Contributions to local and regional-scale formaldehyde concentrations. *Atmospheric Chemistry and Physics Discussions*, 1–29. https://doi.org/10.5194/acp-2018-496

Beirle, S., Boersma, K. F., Platt, U., Lawrence, M. G., & Wagner, T. (2011). Megacity emissions and lifetimes of nitrogen oxides probed from space. *Science*, *333*(6050), 1737–1739. https://doi.org/10.1126/science.1207824

Beirle, S., Borger, C., Dörner, S., Li, A., Hu, Z., Liu, F., … Wagner, T. (2019a). Pinpointing nitrogen oxide emissions from space. *Science Advances*, *5*(11), 1–7. https://doi.org/10.1126/sciadv.aax9800

Beirle, S., Borger, C., Dörner, S., Li, A., Hu, Z., Liu, F., … Wagner, T. (2019b). Pinpointing nitrogen oxide emissions from space. *Science Advances*, *5*(11). https://doi.org/10.1126/sciadv.aax9800

Berdowski, J., Most, P. Van Der, Boer, R. W., Rentz, O., Oertel, D., Pacyna, J. M., … Appelman, W. (2016). *Cement Production*.

Bigi, A., & Harrison, R. M. (2010). Analysis of the air pollution climate at a central urban background site. *Atmospheric Environment*, *44*(16), 2004–2012. https://doi.org/10.1016/j.atmosenv.2010.02.028

Blechschmidt, A. M., Arteta, J., Coman, A., Curier, L., Eskes, H., Foret, G., … P. Burrows, J. (2020). Comparison of tropospheric NO2 columns from MAX-DOAS retrievals and regional air quality model simulations. *Atmospheric Chemistry and Physics*, *20*(5), 2795–2823. https://doi.org/10.5194/acp-20-2795-2020

Boersma, K. F., Eskes, H. J., & Brinksma, E. J. (2004). Error analysis for tropospheric NO2 retrieval from space. *Journal of Geophysical Research: Atmospheres*, *109*(4). https://doi.org/10.1029/2003jd003962

Brinksma, E. J., Pinardi, G., Volten, H., Braak, R., Richter, A., Schönhardt, A., … Levelt, P. F. (2008). The 2005 and 2006 DANDELIONS NO<inf>2</inf> and aerosol intercomparison campaigns. *Journal of Geophysical Research Atmospheres*, *113*(16), 1–18. https://doi.org/10.1029/2007JD008808

Calvert, J. G., Atkinson, R., Kerr, J. A., Madronich, S., Moortgat, G., Wallington, T. J., & Yarwood, G. (2000). *THE MECHANISMS OF ATMOSPHERIC OXIDATION OF THE ALKENES*. Retrieved from https://opensky.ucar.edu/islandora/object/books%3A153

Celarier, E. A., Brinksma, E. J., Gleason, J. F., Veerkind, J. P., Cede, A., Herman, J. R., … Levelt, P. F. (2008). Validation of ozone monitoring instrument nitrogen dioxide

columns. *Journal of Geophysical Research Atmospheres*, *113*(15), 1–23. https://doi.org/10.1029/2007JD008908

Chan, K. L., Wang, Z., Ding, A., Heue, K., Shen, Y., Wang, J., … Wenig, M. (2019). MAX-DOAS measurements of tropospheric NO 2 and HCHO in Nanjing and the comparison to OMI observations. *MAX-DOAS Measurements of Tropospheric NO₂ and HCHO in Nanjing and the Comparison to OMI Observations*, (2), 1–25. https://doi.org/10.5194/acp-2018-1266

Chan, K. L., Wiegner, M., Alberti, C., & Wenig, M. (2020). MAX-DOAS measurements of tropospheric NO2 and HCHO in Munich and the comparison to OMI and TROPOMI satellite observations. *Atmospheric Measurement Techniques Discussions*, (2), 1–31. https://doi.org/10.5194/amt-2020-35

Chance, K., & Kurucz, R. L. (2010). An improved high-resolution solar reference spectrum for earth's atmosphere measurements in the ultraviolet, visible, and near infrared. *Journal of Quantitative Spectroscopy and Radiative Transfer*, *111*(9), 1289–1295. https://doi.org/10.1016/j.jqsrt.2010.01.036

Chel Jung, M., Park, J., & Kim, S. (2019). *Spatial Relationships between Urban Structures and Air Pollution in Korea*. https://doi.org/10.3390/su11020476

Cheremisinoff, N. P., & Rosenfeld, P. E. (2010). Sources of air emissions from pulp and paper mills. *Handbook of Pollution Prevention and Cleaner Production*, *2*, 179–259. https://doi.org/10.1016/b978-0-08-096446-1.10006-1

Choi, Y., & Souri, A. H. (2015). Seasonal behavior and long-term trends of tropospheric ozone, its precursors and chemical conditions over Iran: A view from space. *Atmospheric Environment*, *106*, 232–240. https://doi.org/10.1016/j.atmosenv.2015.02.012

Colbeck, I., Sidra, S., Ali, Z., Ahmed, S., & Nasir, Z. A. (2019). Spatial and temporal variations in indoor air quality in Lahore, Pakistan. *International Journal of Environmental Science and Technology*, *16*(6), 2565–2572. https://doi.org/10.1007/s13762-018-1693-z

Colbeck, Ian, Nasir, Z. A., & Ali, Z. (2010). The state of indoor air quality in Pakistan-a review. *Environmental Science and Pollution Research*, *17*(6), 1187–1196. https://doi.org/10.1007/s11356-010-0293-3

Copernicus Climate Change Service (C3S). (2017). ERA5: Fifth generation of ECMWF atmospheric reanalyses of the global climate . Copernicus Climate Change Service Climate Data Store (CDS). Retrieved from https://cds.climate.copernicus.eu/cdsapp#!/home

Crippa, M., Oreggioni, G., Guizzardi, D., Muntean, M., Schaaf, E., Lo Vullo, E., … Vignati, E. (2019). *Fossil CO2 and GHG emissions of all world countries*. https://doi.org/10.2760/687800

Crippa, Monica, Guizzardi, D., Muntean, M., Schaaf, E., Dentener, F., Van Aardenne, J. A., … Janssens-Maenhout, G. (2018). Gridded emissions of air pollutants for the period 1970-2012 within EDGAR v4.3.2. *Earth System Science Data*, *10*(4), 1987–2013. https://doi.org/10.5194/essd-10-1987-2018

Danckaert, T., Fayt, C., & Van Roozendael, M. (2017). Qdoas 3.2. *Software User Manual*, (September). Retrieved from http://uv-vis.aeronomie.be/software/QDOAS/QDOAS_manual.pdf

De Smedt, I., Müller, J. F., Stavrakou, T., Van Der A, R., Eskes, H., & Van Roozendael, M. (2008). Twelve years of global observations of formaldehyde in the troposphere using GOME and SCIAMACHY sensors. *Atmospheric Chemistry and Physics*, *8*(16), 4947–4963. https://doi.org/10.5194/acp-8-4947-2008

De Smedt, Isabelle, Theys, N., Yu, H., Danckaert, T., Lerot, C., Compernolle, S., … Veefkind, P. (2018). Algorithm theoretical baseline for formaldehyde retrievals from S5P TROPOMI and from the QA4ECV project. *Atmospheric Measurement Techniques*, *11*(4), 2395–2426. https://doi.org/10.5194/amt-11-2395-2018

Dimitropoulou, E., Hendrick, F., Pinardi, G., Friedrich, M., Merlaud, A., Tack, F., … Roozendael, M. Van. (2020). Validation of TROPOMI tropospheric NO2 columns using dual-scan MAX-DOAS measurements in Uccle, Brussels. *Atmospheric Measurement Techniques Discussions*, *30*(2), 1–50. https://doi.org/10.5194/amt-2020-33

Dios, M., Souto, J. A., Casares, J. J., Gallego, N., Sáez, A., Macho, M. L., … Vellón, J. M. (2012). A mixed top-down and bottom-up methodology in spatial segregation of emissions based on GIS tools. *WIT Transactions on Ecology and the Environment*, *157*, 225–236. https://doi.org/10.2495/AIR120201

Donner, S. (2016a). *MOBILE MAX-DOAS MEASUREMENTS OF THE TROPOSPHERIC FORMALDEHYDE COLUMN IN THE RHEIN - MAIN REGION Master - Thesis*. (May).

Donner, S. (2016b). *MOBILE MAX-DOAS MEASUREMENTS OF THE TROPOSPHERIC FORMALDEHYDE COLUMN IN THE RHEIN - MAIN REGION Master - Thesis*.

Environmental Protection Agency (EPA). (1999). Nitrogen oxides (NOx), why and how they are controlled. In *Epa-456/F-99-006R*. Retrieved from http://www.epa.gov/ttncatc1/dir1/fnoxdoc.pdf

Eskes, R. H. J., Product, M. P. C., Mpc, L., Coordinator, V., Lead, M. P. C. E., Mpc, L., … Mission, E. S. A. (2019). *S5P Mission Performance Centre Henk Eskes Angelik a Dehn Claus*.

European Environment Agency. (2015). *SOER 2015 European briefings Air Pollution*. (Figure 1), 4. Retrieved from http://www.eea.europa.eu/soer-2015/europe/air

Express Tribune. (2017). *Natural gas supply*. Retrieved from https://tribune.com.pk/story/1482404/domestic-consumers-likely-receive-gas-winter

Fayt, C., Letocart, V., & van Roozendael, M. (2011). *QDOAS Software user manual*. (July). Retrieved from http://uv-vis.aeronomie.be/software/QDOAS/index.php

Finlayson-Pitts, B. J., & Pitts, J. N. (2000). Kinetics and Atmospheric Chemistry. *Chemistry of the Upper and Lower Atmosphere*, 130–178. https://doi.org/10.1016/b978-012257060-5/50007-1

Fioletov, V., McLinden, C., Krotkov, N., Li, C., Joiner, J., Theys, N., … Moran, M. (2016). A global catalogue of large SO 2 sources and emissions derived from the Ozone Monitoring Instrument. *Atmospheric Chemistry and Physics*, *16*(18), 11497–11519. https://doi.org/10.5194/acp-16-11497-2016-supplement

Fishman, J., & Crutzen, P. J. (1978). The origin of ozone in the troposphere. *Nature*, *274*(5674), 855–858. https://doi.org/10.1038/274855a0

Fleischmann, O. C., Hartmann, M., Burrows, J. P., & Orphal, J. (2004). New ultraviolet

absorption cross-sections of BrO at atmospheric temperatures measured by time-windowing Fourier transform spectroscopy. *Journal of Photochemistry and Photobiology A: Chemistry*, *168*(1–2), 117–132. https://doi.org/10.1016/j.jphotochem.2004.03.026

Frins, E., Shaiganfar, R., Platt, U., & Wagner, T. (2016). Determination of NO_x emissions from Frankfurt Airport by optical spectroscopy (DOAS) – A feasibility study. *Atmospheric Measurement Techniques Discussions*, (x), 1–18. https://doi.org/10.5194/amt-2016-255

Fu, T. M., Jacob, D. J., Wittrock, F., Burrows, J. P., Vrekoussis, M., & Henze, D. K. (2008). Global budgets of atmospheric glyoxal and methylglyoxal, and implications for formation of secondary organic aerosols. *Journal of Geophysical Research Atmospheres*, *113*(15). https://doi.org/10.1029/2007JD009505

Ghafoor, G. Z., Sharif, F., Khan, A. U., Hayyat, M. U., Farhan, M., & Shahzad, L. (2020). Energy consumption and carbon dioxide emissions of residential buildings in Lahore, Pakistan. *Polish Journal of Environmental Studies*, *29*(2), 1613–1623. https://doi.org/10.15244/pjoes/109305

Ghauri, B., Lodhi, A., & Mansha, M. (2007). Development of baseline (air quality) data in Pakistan. *Environmental Monitoring and Assessment*, *127*(1–3), 237–252. https://doi.org/10.1007/s10661-006-9276-8

Government of Pakistan. (n.d.). Sahiwal 2x660MW Coal-fired Power Plant, Punjab China Pakistan Economic Corridor (CPEC) Official Website. Retrieved October 21, 2020, from http://cpec.gov.pk/project-details/2

Greenstone, M., & (Claire) Fan, Q. (2019). *Pakistan's Air Pollution Challenge & Potential for Longer Lives*.

Griffin, D., Zhao, X., McLinden, C. A., Boersma, F., Bourassa, A., Dammers, E., … Wolde, M. (2019). High-Resolution Mapping of Nitrogen Dioxide With TROPOMI: First Results and Validation Over the Canadian Oil Sands. *Geophysical Research Letters*, *46*(2), 1049–1060. https://doi.org/10.1029/2018GL081095

Grosjean, D., Grosjean, E., & Gertler, A. W. (2001). On-road emissions of carbonyls from light-duty and heavy-duty vehicles. *Environmental Science and Technology*, *35*(1), 45–53. https://doi.org/10.1021/es001326a

Grosjean, D., Miguel, A. H., & Tavares, T. M. (1990). *and Other Carbonyls ~ Acetone*. (1), 101–106.

Gurjar, B. R., Jain, A., Sharma, A., Agarwal, A., Gupta, P., Nagpure, A. S., & Lelieveld, J. (2010). Human health risks in megacities due to air pollution. *Atmospheric Environment*, *44*(36), 4606–4613. https://doi.org/10.1016/j.atmosenv.2010.08.011

Haider, R., Yasar, A., & Tabinda, A. B. (2017). Urban emission patterns at a semi-arid site in lahore, pakistan. *Polish Journal of Environmental Studies*, *26*(1), 59–68. https://doi.org/10.15244/pjoes/64284

Hameed, S., Mirza, M. I., Ghauri, B. M., Siddiqui, Z. R., Javed, R., Khan, A. R., … Husain, L. (2000). On the widespread winter fog in Northeastern Pakistan and India. *Geophysical Research Letters*, *27*(13), 1891–1894. https://doi.org/10.1029/1999GL011020

Hamid, A., Akhtar, S., Atique, S. A., Huma, Z., Uddin, S. G. M., & Asghar, S. (2019).

Ambient air quality & noise level monitoring of different areas of lahore (Pakistan) and its health impacts. *Polish Journal of Environmental Studies*, *28*(2), 623–629. https://doi.org/10.15244/pjoes/81702

Haq, G. (2012). *Urban Air Pollution in Asian Cities: Status, Challenges and Management*. Retrieved from http://books.google.fr/books?id=0q0eBAAAQBAJ

Harrison, R. M. (2018). Urban atmospheric chemistry: a very special case for study. *Npj Climate and Atmospheric Science*, *1*(1), 1–5. https://doi.org/10.1038/s41612-017-0010-8

Haydar, S., Haider, H., Bari, A. J., & Faragh, A. (2012). Effect of Mehmood Booti Dumping Site in Lahore on Ground Water Quality. *Pakistan Journal of Engineering and Applied Sciences*, *10*(January 2012), 51–56.

Health Effects Institute. (2020). *Soga-2020-Report.Pdf*.

Ho, S. S. H., Ip, H. S. S., Ho, K. F., Ng, L. P. T., Chan, C. S., Dai, W. T., & Cao, J. J. (2013). Hazardous airborne carbonyls emissions in industrial workplaces in China. *Journal of the Air and Waste Management Association*, *63*(7), 864–877. https://doi.org/10.1080/10962247.2013.797519

Ho, S. S. H., & Yu, J. Z. (2002). Feasibility of collection and analysis of airborne carbonyls by on-sorbent derivatization and thermal desorption. *Analytical Chemistry*, *74*(6), 1232–1240. https://doi.org/10.1021/ac015708q

Hofmann, C., Kerkweg, A., Wernli, H., & Jöckel, P. (2012). The 1-way on-line coupled atmospheric chemistry model system MECO(n) – Part 3: Meteorological evaluation of the on-line coupled system. *Geoscientific Model Development*, *5*(1), 129–147. https://doi.org/10.5194/gmd-5-129-2012

Holben, B. N., Tanré, D., Smirnov, A., Eck, T. F., Slutsker, I., Abuhassan, N., … Zibordi, G. (2001). An emerging ground-based aerosol climatology: Aerosol optical depth from AERONET. *Journal of Geophysical Research Atmospheres*, *106*(D11), 12067–12097. https://doi.org/10.1029/2001JD900014

Hong, H., Kim, J., Jeong, U., Han, K., & Lee, H. (n.d.). *The Effects of Aerosol on the Retrieval Accuracy of NO 2 Slant Column Density*. (2). https://doi.org/10.3390/rs9080867

Hönninger, G., von Friedeburg, C., & Platt, U. (2003). Multi Axis Differential Optical Absorption Spectroscopy (MAX-DOAS). *Atmospheric Chemistry and Physics Discussions*, *3*(6), 5595–5658. https://doi.org/10.5194/acpd-3-5595-2003

Hönninger, Gerd, & Platt, U. (2002). Observations of BrO and its vertical distribution during surface ozone depletion at Alert. *Atmospheric Environment*, *36*(15–16), 2481–2489. https://doi.org/10.1016/S1352-2310(02)00104-8

Horkoss, S. (2008). *Reducing the SO2 emission from a cement kiln*. (January 2008).

Ibrahim, H. G., Okasha, A. Y., Elatrash, M. S., & Al-Meshragi1, M. A. (2012). *Emissions of SO2, NOx and PMs from Cement Plant in Vicinity of Khoms City in Northwestern Libya*. 620–628.

Ibrahim, O., Shaiganfar, R., Sinreich, R., Stein, T., Platt, U., & Wagner, T. (2010). Car MAX-DOAS measurements around entire cities: Quantification of NOx emissions from the cities of Mannheim and Ludwigshafen (Germany). *Atmospheric Measurement Techniques*, *3*(3), 709–721. https://doi.org/10.5194/amt-3-709-2010

Ibrahim, Ossama. (2009). *Applications on Ground-based Tropospheric Measurements using Multi-Axis Differential Optical Absorption Spectroscopy*. 294. Retrieved from http://www.ub.uni-heidelberg.de/archiv/9455

Ilyas, S. Z. (2007). A Review of Transport and Urban Air Pollution in Pakistan. *Journal of Applied Sciences and Environmental Management*, *11*(2), 113–121. https://doi.org/10.4314/jasem.v11i2.55004

IQAir. (2019). 2019 World Air Quality Report Region & City PM2.5 Ranking. *Air Quality Report*, (August), 1–35. Retrieved from https://www.iqair.com/world-most-polluted-cities/world-air-quality-report-2019-en.pdf

IQAIR. (2018). *2018 World Air Quality Report PM2.5 Ranking*. 22.

Irie, H., Boersma, K. F., Kanaya, Y., Takashima, H., Pan, X., & Wang, Z. F. (2012). Quantitative bias estimates for tropospheric NO2 columns retrieved from SCIAMACHY, OMI, and GOME-2 using a common standard for East Asia. *Atmospheric Measurement Techniques*, *5*(10), 2403–2411. https://doi.org/10.5194/amt-5-2403-2012

Jacob, D. J. (1999a). 11. Oxidizing Power of the Troposphere. In *Introduction to Atmospheric Chemistry* (Vol. 3). https://doi.org/10.1515/9781400841547-012

Jacob, D. J. (1999b). 12. Ozone Air Pollution. In *Introduction to Atmospheric Chemistry*. https://doi.org/10.1515/9781400841547-013

Jacob, D. J. (1999c). *Introduction to Atmospheric Chemistry, by Daniel Jacob (Harvard University)*. Retrieved from http://acmg.seas.harvard.edu/people/faculty/djj/book/

Jafary, Z. A., & Faridi, I. A. (2006). Air Pollution By Roadside Dust and Automobile Exhaust At Busy Road-Crossings of Lahore. *Pak J Physiol*, *2*(2), 31–34.

Jalees, M. I., & Asim, Z. (2016). Statistical modeling of atmospheric trace metals in Lahore, Pakistan for correlation and source identification. *Environmental Earth Sciences*, *75*(9), 1–12. https://doi.org/10.1007/s12665-016-5604-7

Jamal, N. (2016). *A renewable electricity supply system in Pakistan by 2050 : assessment of generation capacity and transmission system requirements*. (December), 1–213.

Javed, Z., Liu, C., Khokhar, M. F., Tan, W., Liu, H., Xing, C., … Rehman, A. (2019). Ground-based MAX-DOAS observations of CHOCHO and HCHO in Beijing and Baoding, China. *Remote Sensing*, *11*(13). https://doi.org/10.3390/rs11131524

Johansson, M., Galle, B., Yu, T., Tang, L., Chen, D., Li, H., … Zhang, Y. (2008). Quantification of total emission of air pollutants from Beijing using mobile mini-DOAS. *Atmospheric Environment*, *42*(29), 6926–6933. https://doi.org/10.1016/j.atmosenv.2008.05.025

Kang, Y., Tang, G., Li, Q., Liu, B., Cao, J., Hu, Q., & Wang, Y. (2021). Evaluation and Evolution of MAX-DOAS-observed Vertical NO2 Profiles in Urban Beijing. *Advances in Atmospheric Sciences*, *38*(7), 1188–1196. https://doi.org/10.1007/s00376-021-0370-1

Kashif, S.-R., Ismail Shah, S., & Arooj, F. (2019). Outdoor Air Quality as Influenced by Vehicular Exhaust in Metropolitan City of Lahore, Pakistan. *Pakistan Journal of Scientific and Industrial Research Series A: Physical Sciences*, (x), 190–196. Retrieved from https://v3.pjsir.org/index.php/physical-sciences/article/view/336

Kerchich, Y., & Kerbachi, R. (2012). Measurement of BTEX (benzene, toluene,

ethybenzene, and xylene) levels at urban and semirural areas of Algiers City using passive air samplers. *Journal of the Air and Waste Management Association*, *62*(12), 1370–1379. https://doi.org/10.1080/10962247.2012.712606

Kerkweg, A., & Jöckel, P. (2012). The 1-way on-line coupled atmospheric chemistry model system MECO(n) – Part 1: Description of the limited-area atmospheric chemistry model COSMO/MESSy. *Geoscientific Model Development*, *5*(1), 87–110. https://doi.org/10.5194/gmd-5-87-2012

Kesselmeier, J. (2001). Exchange of short-chain oxygenated volatile organic compounds (VOCs) between plants and the atmosphere: A compilation of field and laboratory studies. *Journal of Atmospheric Chemistry*, *39*(3), 219–233. https://doi.org/10.1023/A:1010632302076

Khalil, H. B., & Zaidi, S. J. H. (2014). Energy crisis and potential of solar energy in Pakistan. *Renewable and Sustainable Energy Reviews*, *31*, 194–201. https://doi.org/10.1016/j.rser.2013.11.023

Khan, M. W., Ali, Y., De Felice, F., Salman, A., & Petrillo, A. (2019). Impact of brick kilns industry on environment and human health in Pakistan. *Science of the Total Environment*, *678*, 383–389. https://doi.org/10.1016/j.scitotenv.2019.04.369

Khoder, M. I. (2009). Diurnal, seasonal and weekdays-weekends variations of ground level ozone concentrations in an urban area in greater Cairo. *Environmental Monitoring and Assessment*, *149*(1–4), 349–362. https://doi.org/10.1007/s10661-008-0208-7

Khokhar, M. F., Khalid, T., Yasmin, N., & De Smedt, I. (2015). Spatio-temporal analyses of formaldehyde over Pakistan by using SCIAMACHY and GOME-2 observations. *Aerosol and Air Quality Research*, *15*(5), 1760–1773. https://doi.org/10.4209/aaqr.2014.12.0339

Khokhar, M. F., Naveed, S. I., Butt, J. K., & Abbas, Z. (2016). Comparative analysis of atmospheric glyoxal column densities retrieved from MAX-DOAS observations in Pakistan and during MAD-CAT field campaign in Mainz, Germany. *Atmosphere*, *7*(5). https://doi.org/10.3390/atmos7050068

Khokhar, M. F., Yasmin, N., Fatima, N., Beirle, S., & Wagner, T. (2015). Detection of trends and seasonal variation in tropospheric nitrogen dioxide over Pakistan. *Aerosol and Air Quality Research*, *15*(7), 2508–2524. https://doi.org/10.4209/aaqr.2015.03.0157

Koppmann, R. (2007). Volatile Organic Compounds in the Atmosphere. In *Volatile Organic Compounds in the Atmosphere*. https://doi.org/10.1002/9780470988657

Kramer, L. J., Leigh, R. J., Remedios, J. J., & Monks, P. S. (2008). Comparison of OMI and ground-based in situ and MAX-DOAS measurements of tropospheric nitrogen dioxide in an urban area. *Journal of Geophysical Research Atmospheres*, *113*(16), 1–12. https://doi.org/10.1029/2007JD009168

Kraus, S. G. (2006). *DOASIS --- A framework design for DOAS*. Retrieved from http://www.shaker.eu/catalogue/Details.asp?ISBN=3-8322-5452-8

Kumar, V., Remmers, J., Beirle, S., Fallmann, J., Kerkweg, A., Lelieveld, J., … Wagner, T. (2021). *Evaluation of the coupled high-resolution atmospheric chemistry model system MECO (n) using in situ and MAX-DOAS NO 2 measurements*. (2), 1–40.

Landrigan, P. J., Fuller, R., Acosta, N. J. R., Adeyi, O., Arnold, R., Basu, N. (Nil), …

Zhong, M. (2018). The Lancet Commission on pollution and health. *The Lancet*, *391*(10119), 462–512. https://doi.org/10.1016/S0140-6736(17)32345-0

Leitão, J., Richter, A., Vrekoussis, M., Kokhanovsky, A., Zhang, Q. J., Beekmann, M., & Burrows, J. P. (2010). On the improvement of NO2 satellite retrievals - Aerosol impact on the airmass factors. *Atmospheric Measurement Techniques*, *3*(2), 475–493. https://doi.org/10.5194/amt-3-475-2010

Lerot, C., Stavrakou, T., De Smedt, I., M̈uller, J. F., & Van Roozendael, M. (2010). Glyoxal vertical columns from GOME-2 backscattered light measurements and comparisons with a global model. *Atmospheric Chemistry and Physics*, *10*(24), 12059–12072. https://doi.org/10.5194/acp-10-12059-2010

LESCO. (2020). FESCO_Pattern. Retrieved November 10, 2020, from http://www.lesco.gov.pk/FESCO_Pattern

Leser, H., Hönninger, G., & Platt, U. (2003). MAX-DOAS measurements of BrO and NO2 in the marine boundary layer. *Geophysical Research Letters*, *30*(10), 3–6. https://doi.org/10.1029/2002gl015811

Leue, C., Wenig, M., Wagner, T., Klimm, O., Platt, U., & Jähne, B. (2001). *Quantitative analysis of NOx emissions from Global Ozone Monitoring Experiment satellite image sequences*. *106*, 5493–5505.

Levenberg, K. (1944). a Method for the Solution of Certain Non-Linear Problems in Least Squares. *Quarterly of Applied Mathematics*, *2*(2), 164–168. https://doi.org/10.1177/002205741408001401

Li, X., Wang, S., Zhou, R., & Zhou, B. (2014). Urban atmospheric formaldehyde concentrations measured by a differential optical absorption spectroscopy method. *Environmental Sciences: Processes and Impacts*, *16*(2), 291–297. https://doi.org/10.1039/c3em00545c

Liteplo, R. G., Beauchamp, R., Meek, M. E., & Chénier, R. (2002). Concise International Chemical Assessment Document 40: Formaldehyde. *IPCS Concise International Chemical Assessment Documents*, (40).

Liu, F., Beirle, S., Zhang, Q., Dörner, S., He, K., & Wagner, T. (2016). NOx lifetimes and emissions of cities and power plants in polluted background estimated by satellite observations. *Atmospheric Chemistry and Physics*, *16*(8), 5283–5298. https://doi.org/10.5194/acp-16-5283-2016

Liu, M., Lin, J., Kong, H., Boersma, K. F., Eskes, H., Kanaya, Y., … Wang, J. (2020). A new TROPOMI product for tropospheric NO₂ columns over East Asia with explicit aerosol corrections. *Atmospheric Measurement Techniques Discussions*, (2), 1–22. https://doi.org/10.5194/amt-2019-500

Lok Chan, K., Wiegner, M., Van Geffen, J., De Smedt, I., Alberti, C., Cheng, Z., … Wenig, M. (2020). MAX-DOAS measurements of tropospheric NO2and HCHO in Munich and the comparison to OMI and TROPOMI satellite observations. *Atmospheric Measurement Techniques*, *13*(8), 4499–4520. https://doi.org/10.5194/amt-13-4499-2020

Lorente, A., Boersma, K. F., Eskes, H. J., Veefkind, J. P., van Geffen, J. H. G. M., de Zeeuw, M. B., … Krol, M. C. (2019). Quantification of nitrogen oxides emissions from build-up of pollution over Paris with TROPOMI. *Scientific Reports*, *9*(1), 1–10. https://doi.org/10.1038/s41598-019-56428-5

Luecken, D. J., Hutzell, W. T., Strum, M. L., & Pouliot, G. A. (2012). Regional sources of atmospheric formaldehyde and acetaldehyde, and implications for atmospheric modeling. *Atmospheric Environment*, *47*(2), 477–490. https://doi.org/10.1016/j.atmosenv.2011.10.005

MacDonald, S. M., Oetjen, H., Mahajan, A. S., Whalley, L. K., Edwards, P. M., Heard, D. E., … Plane, J. M. C. (2012). DOAS measurements of formaldehyde and glyoxal above a south-east Asian tropical rainforest. *Atmospheric Chemistry and Physics*, *12*(13), 5949–5962. https://doi.org/10.5194/acp-12-5949-2012

Marbach, T. (2021). Satellite Group Mainz. Retrieved July 24, 2021, from http://joseba.mpch-mainz.mpg.de/hcho.htm

Marbach, T., Beirle, S., Frankenberg, C., Platt, U., & Wagner, T. (2007). Identification of tropospheric trace gas sources: Synergistic use of HCHO and other satellite observations. *European Space Agency, (Special Publication) ESA SP*, *2007*(SP-636). Retrieved from https://authors.library.caltech.edu/57414/1/461886ma.pdf

Marbach, T., Beirle, S., Liu, C., Platt, U., & Wagner, T. (2008). Biomass burning emissions from satellite observations: synergistic use of formaldehyde (HCHO), fire counts, and surface temperature. *Remote Sensing of Fire: Science and Application*, *7089*, 70890J. https://doi.org/10.1117/12.793654

Marlier, M. E., Jina, A. S., Kinney, P. L., & DeFries, R. S. (2016). Extreme Air Pollution in Global Megacities. *Current Climate Change Reports*, *2*(1), 15–27. https://doi.org/10.1007/s40641-016-0032-z

Marquez, L. O., & Smith, N. C. (1999). A framework for linking urban form and air quality. *Environmental Modelling and Software*, *14*(6), 541–548. https://doi.org/10.1016/S1364-8152(99)00018-3

Meller, R. (1992). *hcho_297K_Meller*. Retrieved from http://satellite.mpic.de/spectral_atlas/cross_sections/Organics (carbonyls)/Aldehydes(aliphatic)/CH2O_Meller(1992)_297K_224.55-376.01nm.txt

Mie, G. (1908). *Der physik. 1*.

Miller, C. C., Jacob, D. J., Marais, E. A., Yu, K., Travis, K. R., Kim, P. S., … Chance, K. (2016). Glyoxal yield from isoprene oxidation and relation to formaldehyde: chemical mechanism, constraints from SENEX aircraft observations, and interpretation of OMI satellite data. *Atmospheric Chemistry and Physics Discussions*, (x), 1–25. https://doi.org/10.5194/acp-2016-1042

Mirza, A. I., Kazmi, J. H., & Shirazi, S. A. (2013). Spatio-periodic monitoring and analysis of atmospheric sulphur dioxide (so2) in the metropolitan areas of lahore -pakistan. *Pakistan Journal of Science*, *65*(1), 83–90.

Moesl, K. G. (2012). *On the Formation of Nitrogen Oxides During the Combustion of Partially Pre-Vaporized Droplets*.

Munger, J. W., Jacob, D. J., Daube, B. C., & Horowitz, L. W. (1995). *C-4 carbonyls*. *100*, 9325–9333.

Myriokefalitakis, S., Vrekoussis, M., Tsigaridis, K., Wittrock, F., Richter, A., Brühl, C., … Kanakidou, M. (2008). The influence of natural and anthropogenic secondary sources on the glyoxal global distribution. *Atmospheric Chemistry and Physics*, *8*(16), 4965–4981. https://doi.org/10.5194/acp-8-4965-2008

National Cancer Institute. (2011). Formaldehyde and Cancer Risk - National Cancer Institute. Retrieved July 6, 2021, from https://www.cancer.gov/about-cancer/causes-prevention/risk/substances/formaldehyde/formaldehyde-fact-sheet

NEPRA. (2018). Power System Statistics 2017-18. In *State of Industry Report 2018*. Retrieved from https://nepra.org.pk/publications/State of Industry Reports/State of Industry Report 2018.pdf

Olatunji, S. O., Fakinle, B. S., Jimoda, L. A., Adeniran, J. A., & Adesanmi, A. J. (2015). Air emissions of sulphur dioxide from gasoline and diesel consumption in the southwestern states of nigeria. *Petroleum Science and Technology*, *33*(6), 678–685. https://doi.org/10.1080/10916466.2014.1002929

Pakistan Bureau of Statistics Government of. (2017). census 2017. Retrieved from http://www.pbs.gov.pk/content/block-wise-provisional-summary-results-6th-population-housing-census-2017-january-03-2018

Pakistan, P. B. of S. G. of. (2017). *District and Tehsil Level Population Summary With Region Breakup Region*. *52*(280), 815. Retrieved from http://www.pbs.gov.pk/sites/default/files/bwpsr/punjab/LAHORE_SUMMARY.pdf

Parrish, D. D., Ryerson, T. B., Mellqvist, J., Johansson, J., Fried, A., Richter, D., … Herndon, S. C. (2012). Primary and secondary sources of formaldehyde in urban atmospheres: Houston Texas region. *Atmospheric Chemistry and Physics*, *12*(7), 3273–3288. https://doi.org/10.5194/acp-12-3273-2012

Pearson, K. (1895). Note on regression and inheritance in the case of two parents. *Proceedings of the Royal Society of London 58*, 240–242. https://doi.org/https://doi.org/10.1098/rspl.1895.0041

Pinardi, G., Van Roozendael, M., Abuhassan, N., Adams, C., Cede, A., Clémer, K., … Yilmaz, S. (2013). MAX-DOAS formaldehyde slant column measurements during CINDI: intercomparison and analysis improvement. *Atmospheric Measurement Techniques*, *6*(1), 167–185. https://doi.org/10.5194/amt-6-167-2013

Pinardi, Gaia, Roozendael, M. Van, Hendrick, F., Theys, N., Abuhassan, N., Bais, A., … Wittrock, F. (2020). Validation of tropospheric NO2 column measurements of GOME-2A and OMI using MAX-DOAS and direct sun network observations. *Atmospheric Measurement Techniques Discussions*, (2), 1–55. https://doi.org/10.5194/amt-2020-76

Platt, U., & Stutz, J. (2008). *Differential Optical Absorption Spectroscopy*.

Platt, U, Stutz, J., Stutz, J., Optical, D., Spectroscopy, A., & Environments, S. (2008). Differential Optical Absorption Spectroscopy. *Differential Optical Absorption Spectroscopy*, *112*, 91–112. https://doi.org/10.1007/978-3-540-75776-4

Platt, Ulrich, & Stutz, J. (2008). *Differential Optical Absorption Spectroscopy Principles & Applications*.

Poot, B., Fabiani, F., Reuvers, L., Selvaggi, A., White, L., & Goodsell, P. J. (2002). Sulphur dioxide emissions from oil refineries and combustion of oil products in western Europe and Hungary (1998). *CONCAWE Reports*, (10).

Punjab Bureau of Statistics. (2015). *2015 Punjab Development Statistics BUREAU OF STATISTICS GOVERNMENT OF THE PUNJAB LAHORE*.

Punjab Bureau of Statistics. (2017). Punjab census. Retrieved November 22, 2020, from

https://web.archive.org/web/20170829162305/http://www.pbscensus.gov.pk/sites/default/files/population_of_major_cities_census_2017 _0.pdf

Raja, S., Biswas, K. F., Husain, L., & Hopke, P. K. (2010). Source apportionment of the atmospheric aerosol in Lahore, Pakistan. *Water, Air, and Soil Pollution*, *208*(1–4), 43–57. https://doi.org/10.1007/s11270-009-0148-z

Rasheed, A. (2014). *Dynamic Analysis of Ambient Air Pollution and Assessment of Effects of Climate Change on Air Dynamic Analysis of Ambient Air Pollution and Assessment of Effects of Climate Change on Air*.

Rayleigh, Lord. (1899). XXXIV. On the transmission of light through an atmosphere containing small particles in suspension, and on the origin of the blue of the sky . *The London, Edinburgh, and Dublin Philosophical Magazine and Journal of Science*, *47*(287), 375–384. https://doi.org/10.1080/14786449908621276

Riaz, R., & Hamid, K. (2018). Existing Smog in Lahore, Pakistan: An Alarming Public Health Concern. *Cureus*, *10*(1), 1–2. https://doi.org/10.7759/cureus.2111

Rivera, C., Sosa, G., Wöhrnschimmel, H., De Foy, B., Johansson, M., & Galle, B. (2009). Tula industrial complex (Mexico) emissions of so2 and NO 2 during the MCMA 2006 field campaign using a mobile mini-DOAS system. *Atmospheric Chemistry and Physics*, *9*(17), 6351–6361. https://doi.org/10.5194/acp-9-6351-2009

Rivera, Claudia, Mellqvist, J., Samuelsson, J., Lefer, B., Alvarez, S., & Patel, M. R. (2010). Quantification of NO2 and SO2 emissions from the houston ship channel and texas city industrial areas during the 2006 texas air quality study. *Journal of Geophysical Research Atmospheres*, *115*(8), 1–10. https://doi.org/10.1029/2009JD012675

Roberts-Semple, D., Song, F., & Gao, Y. (2012). Seasonal characteristics of ambient nitrogen oxides and ground-level ozone in metropolitan northeastern New Jersey. *Atmospheric Pollution Research*, *3*(2), 247–257. https://doi.org/10.5094/APR.2012.027

Roozendael, M. Van, Fayt, C., Post, P., Hermans, C., & Lambert, J. C. (2004). *UV-Visible Observations*.

Rothman, L. S., Gordon, I. E., Barber, R. J., Dothe, H., Gamache, R. R., Goldman, A., … Tennyson, J. (2010). HITEMP, the high-temperature molecular spectroscopic database. *Journal of Quantitative Spectroscopy and Radiative Transfer*, *111*(15), 2139–2150. https://doi.org/10.1016/j.jqsrt.2010.05.001

Saif Group. (n.d.). Saif Group - Power Generation. Retrieved October 21, 2020, from https://www.saifgroup.com/power.php

Seinfeld, J. H., & Pandis, S. N. (2006). Atmospheric Chemistry and Physics: From Air Pollution to Climate Change. In *Atmospheric Chemistry and Physics*. https://doi.org/10.1063/1.882420

Seinfeld, John H, & Pandis, S. N. (2006). *ATMOSPHERIC From Air Pollution to Climate Change SECOND EDITION*.

Serdyuchenko, A., Gorshelev, V., Weber, M., Chehade, W., & Burrows, J. P. (2014). High spectral resolution ozone absorption cross-sections – Part 2: Temperature dependence. *Atmospheric Measurement Techniques*, *7*(2), 625–636. https://doi.org/10.5194/amt-7-625-2014

Shaiganfar, R., Beirle, S., Petetin, H., Zhang, Q., Beekmann, M., & Wagner, T. (2015).

New concepts for the comparison of tropospheric NO2 column densities derived from car-MAX-DOAS observations, OMI satellite observations and the regional model CHIMERE during two MEGAPOLI campaigns in Paris 2009/10. *Atmospheric Measurement Techniques*, *8*(7), 2827–2852. https://doi.org/10.5194/amt-8-2827-2015

Shaiganfar, R., Beirle, S., Sharma, M., Chauhan, A., Singh, R. P., & Wagner, T. (2011). Estimation of NOx emissions from Delhi using Car MAX-DOAS observations and comparison with OMI satellite data. *Atmospheric Chemistry and Physics*, *11*(21), 10871–10887. https://doi.org/10.5194/acp-11-10871-2011

Shaiganfar, Reza. (2012). *Estimation of NOx Emissions from megacities using mobile MAX-DOAS and satellite observations*.

Shaiganfar, Reza, Beirle, S., Denier Van Der Gon, H., Jonkers, S., Kuenen, J., Petetin, H., … Wagner, T. (2017). Estimation of the Paris NOx emissions from mobile MAX-DOAS observations and CHIMERE model simulations during the MEGAPOLI campaign using the closed integral method. *Atmospheric Chemistry and Physics*, *17*(12), 7853–7890. https://doi.org/10.5194/acp-17-7853-2017

Sharma, S. K., Datta, A., Saud, T., Saxena, M., Mandal, T. K., Ahammed, Y. N., & Arya, B. C. (2010). Seasonal variability of ambient NH3, NO, NO2 and SO2 over Delhi. *Journal of Environmental Sciences*, *22*(7), 1023–1028. https://doi.org/10.1016/S1001-0742(09)60213-8

Sinreich, R, Volkamer, R., Filsinger, F., Frieß, U., Kern, C., Platt, U., … Sebasti, O. (2007). *MAX-DOAS detection of glyoxal during ICARTT 2004 To cite this version : HAL Id : hal-00296162 and Physics MAX-DOAS detection of glyoxal during ICARTT 2004*.

Sinreich, Roman. (2008). *Multi-Axis Differential Optical Absorption Spectroscopy Measurements in Polluted Environments*. 242. Retrieved from http://archiv.ub.uni-heidelberg.de/volltextserver/8069/1/Dissertation_Roman_Sinreich_final.pdf

Smedt, Isabelle De, Pinardi, G., Vigouroux, C., Compernolle, S., & Bais, A. (2021). *Comparative assessment of TROPOMI and OMI formaldehyde observations against MAX-DOAS network column measurements* . (May), 1–51.

Smith, S. J., Pitchera, H., & Wigley, T. M. L. (2001). Global and regional anthropogenic sulfur dioxide emissions. *Global and Planetary Change*. https://doi.org/10.1016/S0921-8181(00)00057-6

Solomon, S., & Sanders, R. W. (1987). *Su • • Zenith Point*. *92*, 8311–8319.

Stavrakou, T., Müller, J.-F., De Smedt, I., Van Roozendael, M., Kanakidou, M., Vrekoussis, M., … Burrows, J. P. (2009). The continental source of glyoxal estimated by the synergistic use of spaceborne measurements and inverse modelling. *Atmospheric Chemistry and Physics Discussions*, *9*(3), 13593–13628. https://doi.org/10.5194/acpd-9-13593-2009

Stavrakou, T., Müller, J. F., Bauwens, M., De Smedt, I., Lerot, C., Van Roozendael, M., … Song, Y. (2016). Substantial Underestimation of Post-Harvest Burning Emissions in the North China Plain Revealed by Multi-Species Space Observations. *Scientific Reports*, *6*(July), 1–11. https://doi.org/10.1038/srep32307

Stone, E., Schauer, J., Quraishi, T. A., & Mahmood, A. (2010). Chemical characterization and source apportionment of fine and coarse particulate matter in Lahore, Pakistan. *Atmospheric Environment*, *44*(8), 1062–1070. https://doi.org/10.1016/j.atmosenv.2009.12.015

Su, W., Liu, C., Hu, Q., Zhao, S., Sun, Y., Wang, W., … Kim, J. (2019). Primary and secondary sources of ambient formaldehyde in the Yangtze River Delta based on Ozone Mapping and Profiler Suite (OMPS) observations. *Atmospheric Chemistry and Physics*, *19*(10), 6717–6736. https://doi.org/10.5194/acp-19-6717-2019

Sun, J., Vu, H., Ellerbroek, J., & Hoekstra, J. M. (2019). PyModeS: Decoding Mode-S Surveillance Data for Open Air Transportation Research. *IEEE Transactions on Intelligent Transportation Systems*, *21*(7), 2777–2786. https://doi.org/10.1109/TITS.2019.2914770

Tabinda, A. B., Ali, H., Yasar, A., Rasheed, R., Mahmood, A., & Iqbal, A. (2020). Comparative Assessment of Ambient Air Quality of Major Cities of Pakistan. *Mapan - Journal of Metrology Society of India*, *35*(1), 25–32. https://doi.org/10.1007/s12647-019-00335-7

Taylor, E., & Ann, M. (2014). Visual air quality management. In *Air Quality Management: Canadian Perspectives on a Global Issue* (Vol. 9789400775). https://doi.org/10.1007/978-94-007-7557-2_8

Thalman, R., & Volkamer, R. (2013). Temperature dependent absorption cross-sections of O2-O 2 collision pairs between 340 and 630 nm and at atmospherically relevant pressure. *Physical Chemistry Chemical Physics*, *15*(37), 15371–15381. https://doi.org/10.1039/c3cp50968k

The News. (2009). Heavy vehicles allowed entry to city. Retrieved October 10, 2020, from https://www.thenews.com.pk/archive/print/159840-heavy-vehicles-allowed-entry-to-city)

Themelis, N. J., & Ulloa, P. A. (2007). Methane generation in landfills. *Renewable Energy*, *32*(7), 1243–1257. https://doi.org/10.1016/j.renene.2006.04.020

Theys, N., De Smedt, I., Yu, H., Danckaert, T., Van Gent, J., Hörmann, C., … Van Roozendael, M. (2017). Sulfur dioxide retrievals from TROPOMI onboard Sentinel-5 Precursor: Algorithm theoretical basis. *Atmospheric Measurement Techniques*, *10*(1), 119–153. https://doi.org/10.5194/amt-10-119-2017

Tian, X., Xie, P., Xu, J., Li, A., Wang, Y., Qin, M., & Hu, Z. (2018). Long-term observations of tropospheric NO2, SO2 and HCHO by MAX-DOAS in Yangtze River Delta area, China. *Journal of Environmental Sciences (China)*, *71*(2), 207–221. https://doi.org/10.1016/j.jes.2018.03.006

ul-Haq, Z., Tariq, S., Ali, M., Mahmood, K., Batool, S. A., & Rana, A. D. (2014). A study of tropospheric NO2 variability over Pakistan using OMI data. *Atmospheric Pollution Research*, *5*(4), 709–720. https://doi.org/10.5094/APR.2014.080

ul-Haq, Z., Tariq, S., Ali, M., Mahmood, K., & Rana, A. D. (2016). Sulphur dioxide loadings over megacity Lahore (Pakistan) and adjoining region of Indo-Gangetic Basin. *International Journal of Remote Sensing*, *37*(13), 3021–3041. https://doi.org/10.1080/01431161.2016.1192701

UNEP. (2019). Air pollution hurts the poorest most. Retrieved June 18, 2021, from https://www.unep.org/news-and-stories/story/air-pollution-hurts-poorest-most

United Nations. (2018). *World Urbanization Prospects The 2018 Revision*.

US EPA. (2000). Hot mix asphalt plants emission assessment report. In *North*.

US EPA. (2018). US epa criteria pollutants. Retrieved from https://www.epa.gov/criteria-

air-pollutants

US EPA. (2019). SO2 US epa. Retrieved from https://www.epa.gov/so2-pollution/sulfur-dioxide-basics#effects

US EPA. (2021a). Effects of Acid Rain. Retrieved August 31, 2021, from https://www.epa.gov/acidrain/effects-acid-rain

US EPA. (2021b, January 28). Sulfur Dioxide Basics. Retrieved August 31, 2021, from https://www.epa.gov/so2-pollution/sulfur-dioxide-basics

US EPA. (2021c, March 22). Criteria Air Pollutants | US EPA. Retrieved July 6, 2021, from https://www.epa.gov/criteria-air-pollutants#self

US EPA. (2021d, April 23). Ground-level Ozone Pollution | US EPA. Retrieved July 6, 2021, from https://www.epa.gov/ground-level-ozone-pollution

van Geffen, J. H. G. M., Eskes, H. J., Boersma, K. F., Maasakkers, J. D., & Veefkind, J. P. (2019). TROPOMI ATBD of the total and tropospheric NO2 data products. *S5p/TROPOMI*, (1.4.0), 1–76. Retrieved from https://sentinel.esa.int/documents/247904/2476257/Sentinel-5P-TROPOMI-ATBD-NO2-data-products

Vandaele, A. C., Hermans, C., & Fally, S. (2009). Fourier transform measurements of SO2 absorption cross sections: II. Temperature dependence in the 29 000-44 000 cm-1 (227-345 nm) region. *Journal of Quantitative Spectroscopy and Radiative Transfer*, *110*(18), 2115–2126. https://doi.org/10.1016/j.jqsrt.2009.05.006

Vandaele, A. C., Hermans, C., Simon, P. C., Carleer, M., Colin, R., Fally, S., … Coquart, B. (1998). Measurements of the NO2 absorption cross-section from 42 000 cm-1 to 10 000 cm-1 (238-1000 nm) at 220 K and 294 K. *Journal of Quantitative Spectroscopy and Radiative Transfer*, *59*(3–5), 171–184. https://doi.org/10.1016/S0022-4073(97)00168-4

Varshney, C. K., & Singh, A. P. (2003). Passive samplers for NOx monitoring: A critical review. *Environmentalist*, *23*(2), 127–136. https://doi.org/10.1023/A:1024883620408

Veefkind, J. P., Aben, I., McMullan, K., Förster, H., de Vries, J., Otter, G., … Levelt, P. F. (2012). TROPOMI on the ESA Sentinel-5 Precursor: A GMES mission for global observations of the atmospheric composition for climate, air quality and ozone layer applications. *Remote Sensing of Environment*, *120*(2012), 70–83. https://doi.org/10.1016/j.rse.2011.09.027

Vlemmix, T., Eskes, H. J., Piters, A. J. M., Schaap, M., Sauter, F. J., Kelder, H., & Levelt, P. F. (2015). MAX-DOAS tropospheric nitrogen dioxide column measurements compared with the Lotos-Euros air quality model. *Atmospheric Chemistry and Physics*, *15*(3), 1313–1330. https://doi.org/10.5194/acp-15-1313-2015

Volkamer, R., Platt, U., & Wirtz, K. (2001). Primary and secondary glyoxal formation from aromatics: Experimental evidence for the bicycloalkyl - radical pathway from benzene, toluene, and p-xylene. *Journal of Physical Chemistry A*, *105*(33), 7865–7874. https://doi.org/10.1021/jp010152w

Volkamer, Rainer, Molina, L. T., Molina, M. J., Shirley, T., & Brune, W. H. (2005). DOAS measurement of glyoxal as an indicator for fast VOC chemistry in urban air. *Geophysical Research Letters*, *32*(8), 1–4. https://doi.org/10.1029/2005GL022616

Volkamer, Rainer, Spietz, P., Burrows, J., & Platt, U. (2005). High-resolution absorption

cross-section of glyoxal in the UV-vis and IR spectral ranges. *Journal of Photochemistry and Photobiology A: Chemistry*, *172*(1), 35–46. https://doi.org/10.1016/j.jphotochem.2004.11.011

Vrekoussis, M., Wittrock, F., Richter, A., & Burrows, J. P. (2009). Temporal and spatial variability of glyoxal as observed from space. *Atmospheric Chemistry and Physics*, *9*(13), 4485–4504. https://doi.org/10.5194/acp-9-4485-2009

Vrekoussis, M., Wittrock, F., Richter, A., & Burrows, J. P. (2010). GOME-2 observations of oxygenated VOCs: What can we learn from the ratio glyoxal to formaldehyde on a global scale? *Atmospheric Chemistry and Physics*, *10*(21), 10145–10160. https://doi.org/10.5194/acp-10-10145-2010

Wagner, T., Beirle, S., & Deutschmann, T. (2009). Three-dimensional simulation of the Ring effect in observations of scattered sun light using Monte Carlo radiative transfer models. *Atmospheric Measurement Techniques*, *2*(1), 113–124. https://doi.org/10.5194/amt-2-113-2009

Wagner, Thomas, Dix, B., Friedeburg, C. V., Frieß, U., Sanghavi, S., Sinreich, R., & Platt, U. (2004). MAX-DOAS O4 measurements: A new technique to derive information on atmospheric aerosols - Principles and information content. *Journal of Geophysical Research D: Atmospheres*, *109*(22), 1–19. https://doi.org/10.1029/2004JD004904

Wagner, Thomas, Ibrahim, O., Shaiganfar, R., & Platt, U. (2010). Mobile MAX-DOAS observations of tropospheric trace gases. *Atmospheric Measurement Techniques*, *3*(1), 129–140. https://doi.org/10.5194/amt-3-129-2010

Wallace, J. M., & V. Hobbs, P. (2006). Atmospheric science : an introductory survey. In *Academic Press*.

Wenig, M., Kühl, S., Beirle, S., Bucsela, E., Jähne, B., Platt, U., … Wagner, T. (2004). Retrieval and analysis of stratospheric NO 2 from the Global Ozone Monitoring Experiment . *Journal of Geophysical Research: Atmospheres*, *109*(D4), n/a-n/a. https://doi.org/10.1029/2003jd003652

WHO. (2018). Air pollution.

Wikipedia. (n.d.). Transport in Lahore - Wikipedia. Retrieved September 11, 2020, from https://en.wikipedia.org/wiki/Transport_in_Lahore

Wikipedia. (2020). copd and air pollution. Retrieved from https://en.wikipedia.org/wiki/Chronic_obstructive_pulmonary_disease#:~:text=Chronic obstructive pulmonary disease (COPD,it typically worsens over time.

William, M., & Kenneth, D. (2000). Exacerbations of COPD. *CHEST*, *117*(5), 390S-397S. https://doi.org/10.1378/chest.117.5_suppl_2.390s

Wittrock, F., Richter, A., Oetjen, H., Burrows, J. P., Kanakidou, M., Myriokefalitakis, S., … Wagner, T. (2006). Simultaneous global observations of glyoxal and formaldehyde from space. *Geophysical Research Letters*, *33*(16), 1–5. https://doi.org/10.1029/2006GL026310

WMO. (2003). Aircraft Meteorological Data Relay (AMDAR) Reference Manual. *World Meteorological Organization Doc. WMO-958*, (958). Retrieved from https://library.wmo.int/opac/index.php?lvl=notice_display&id=7920#.WTqUhXrLJXU

Wolfe, G. M., Kaiser, J., Hanisco, T. F., Keutsch, F. N., De Gouw, J. A., Gilman, J. B., …

Warneke, C. (2016). Formaldehyde production from isoprene oxidation across NOx regimes. *Atmospheric Chemistry and Physics*, *16*(4), 2597–2610. https://doi.org/10.5194/acp-16-2597-2016

World Meteorological Organization. (2017). *Guide to Aircraft-based Observations*. Retrieved from https://library.wmo.int/doc_num.php?explnum_id=4120

Wu, F., Li, A., Xie, P., Chen, H., Hu, Z., Zhang, Q., … Liu, W. (2017). Emission flux measurement error with a mobile DOAS system and application to NOx flux observations. *Sensors (Switzerland)*, *17*(2), 1–14. https://doi.org/10.3390/s17020231

Yasar, A., Haider, R., Tabinda, A. B., Kausar, F., & Khan, M. (2013). Short communication a comparison of engine emissions from heavy, medium, and light vehicles for CNG, diesel, and gasoline fuels. *Polish Journal of Environmental Studies*, *22*(4), 1277–1281.

Yasin, G., Bhanger, M. I., Ansari, T. M., Muhammad, S., Naqvi, S. R., & Talpur, F. N. (2012). Quality of commercial high speed diesel and its environmental impact. *Journal of Petroleum Technology and Alternative Fuels*, *3*(March), 29–35. https://doi.org/10.5897/JPTAF11.031

Younes, I., Bukhari, O., Butt, I., & Shafiq, M. (2009). Air pollution patterns identification in Lahore city using GIS (1999-2007). *Pakistan Geographical Review*, *64*(1).

Zahid, A. (2020). Rise In Number Of Vehicles Creating Traffic Problems In Lahore - PakWheels Blog. Retrieved November 22, 2020, from https://www.pakwheels.com/blog/rise-in-number-of-vehicles-creating-traffic-problems-in-lahore/

Zarzana, K. J., Selimovic, V., Koss, A. R., Sekimoto, K., Coggon, M. M., Yuan, B., … Brown, S. S. (2018). Primary emissions of glyoxal and methylglyoxal from laboratory measurements of open biomass burning. *Atmospheric Chemistry and Physics*, *18*(20), 15451–15470. https://doi.org/10.5194/acp-18-15451-2018

Zeb, N., Khokhar, M. F., Pozzer, A., & Khan, S. A. (2019). Exploring the temporal trends and seasonal behaviour of tropospheric trace gases over Pakistan by exploiting satellite observations. *Atmospheric Environment*, *198*(October 2018), 279–290. https://doi.org/10.1016/j.atmosenv.2018.10.053

Zel'dovich, Y. B. (1946). The Oxidation of Nitrogen in Combustion and Explosions. *Acta Physicochimica U.R.S.S.*, (21), 577–628,.

Zhang, Q., Geng, G. N., Wang, S. W., Richter, A., & He, K. Bin. (2012). Satellite remote sensing of changes in NO x emissions over China during 1996-2010. *Chinese Science Bulletin*, *57*(22), 2857–2864. https://doi.org/10.1007/s11434-012-5015-4

Zhao, X., Griffin, D., Fioletov, V., McLinden, C., Cede, A., Tiefengraber, M., … Chi Lee, S. (2020). Assessment of the quality of tropomi high-spatial-resolution no2 data products in the greater toronto area. *Atmospheric Measurement Techniques*, *13*(4), 2131–2159. https://doi.org/10.5194/amt-13-2131-2020

Zhu, L., Jacob, D. J., Keutsch, F. N., Mickley, L. J., Scheffe, R., Strum, M., … Shah, V. (2017). Formaldehyde (HCHO) As a Hazardous Air Pollutant: Mapping Surface Air Concentrations from Satellite and Inferring Cancer Risks in the United States. *Environmental Science and Technology*, *51*(10), 5650–5657. https://doi.org/10.1021/acs.est.7b01356

ACKNOWLEDGEMENTS

ACKNOWLEDGEMENTS